SISSA
Scuola
Internazionale
Superiore di
Studi Avanzati

Physics Area - PhD course in
Statistical Physics

Circuit complexity and entanglement in many-body quantum systems

Candidate:
Giuseppe Di Giulio

Advisor:
Prof. Erik Tonni

Academic Year 2020-21

A Nonna Maria

Contents

Introduction

In the last two decades, it became clear that various concepts introduced and studied in quantum information theory are important also for many-body systems with ramifications to different lines of research, ranging from condensed matter theory to high energy physics and quantum gravity. One of these aspects is undoubtedly the entanglement, a characteristic trait of quantum mechanics since its early days [1, 2].

Given a spatial bipartition of a quantum system into A and B, the reduced density matrix of A is defined by tracing the density matrix of the system over the degrees of freedom of B. This is the starting point for determining the entanglement between A and its complement, whose most successful measures are the von Neumann and the Rényi entanglement entropies. The entanglement turns out to be particularly interesting in condensed matter theory and many-body physics [3–5]. It provides a powerful tool to distinguish whether the system is at criticality or in a gapped phase. Indeed, when a system described by a local and gapped Hamiltonian is in its ground state, the entanglement entropy of a subsystem A scales with the area of A: this fact is known as area law. On the other hand, at criticality, some violations of the area law are observed, as, for instance, in one-dimensional quantum systems [6, 7]. These universal properties have been studied also for systems with large correlation lengths that can be described by quantum field theories (QFTs), which flow to conformal field theories (CFTs) at criticality [6, 8–11]. Furthermore, the entanglement has found remarkable applications also in characterising systems with disorder [12, 13] and in detecting topological order [14, 15]. Entanglement has also attracted a lot of interest in high energy physicis as a fundamental tool for understanding the origin of the Bekenstein-Hawking entropy of black holes [16–22]. Besides the purely theoretical interest, in the last years, thanks to the advances that allow to prepare and manipulate systems made up of few atoms, experimental setups have been realised to detect the characteristic features of entanglement [23–25].

The von Neumann and the Rényi entanglement entropies quantify the amount of entanglement between a subsystem and its complement and depend only on the spectrum of the reduced density matrix (called entanglement spectrum [26]). Thus, a richer point of view can be achieved by studying the entire reduced density matrix, that provides the complete information about the entanglement of a given bipartition. Equivalently, one can consider the logarithm of the reduced density matrix, namely the entanglement Hamiltonian (introduced in the context of algebraic quantum field theory as modular Hamiltonian); since the reduced density matrix and the entanglement Hamiltonian are operators, they are in general highly non-trivial objects. A further useful entanglement quantifier is the contour for the entanglement entropies [27–29], which describes the contribution of the various points in A to the entanglement entropies.

Another quantity playing an important role in quantum information theory is the complexity of a quantum circuit. A quantum circuit constructs a target state by applying a specific sequence of elementary operations, called gates, to a reference state. The circuit complexity is given by the minimum number of allowed gates that is needed to construct the target state starting from the assigned reference state. This quantity depends on the target state, on the reference state, on the

set of allowed gates and, eventually, on the specified tolerance for the target state.

The circuit complexity is an insightful notion in quantum computer science because it provides the most efficient way to implement a certain operation on a given quantum state [30, 31]. Since an active study of this quantity in the context of many-body quantum systems just started a few years ago, its properties are much less understood than the ones of entanglement. A crucial step that has led to important progresses has been done by Nielsen and collaborators in [32–34]. They introduced a geometric approach that allows to compute the complexity by finding a geodesic in a suitable space of states. Adapting this method to various models, many results have been obtained in the case when the reference and the target states are pure states [35–46].

Remarkable insights in the framework of the AdS/CFT correspondence [47] can be obtained through various quantities borrowed from quantum information theory. In [48, 49] Ryu and Takayanagi conjectured a holographic prescription for computing the entanglement entropy which showed a deep relation between entanglement and quantum gravity, proposing the entropy as a useful way for probing the geometry of the spacetime. Since the Ryu-Takayanagi formula for the entanglement entropy does not capture the physics behind the horizon of black holes, Susskind and collaborators proposed that a good candidate for this purpose could be the holographic complexity [50, 51]. This sparked the interest in this quantity that has been investigated through various proposals in several geometries [52–59]. The existence of a holographic conjecture for the complexity of CFT states strongly motivated the development of approaches for studying this quantity in a field theoretical setup [60–76].

An important playground for evaluating the entanglement and the circuit complexity in many-body systems is provided by the Gaussian states. Thanks to the efforts of the quantum information theorists, these states have been framed in an elegant mathematical formalism and several results have been obtained in this context [77, 78]. The set of Gaussian states includes some cases of great physical relevance as the ground states and the thermal states of free theories. Determining the circuit complexity [35–44, 79] and the entanglement [4, 5, 10] for these particular states, despite their simplicity, is very important. Indeed, it is the first natural step towards the comprehension of these aspects in many-body quantum systems and it allows to obtained non-trivial explicit results that exhibit interesting physical features.

The out-of-equilibrium dynamics is another interesting arena for studying the universal properties of many-body systems. One of the most known protocols for driving a quantum system out of equilibrium is the quantum quench (see [80, 81] for reviews). Given a system prepared in a state $|\psi_0\rangle$, consider a sudden change at $t = 0$ that provides the time-evolved state $|\psi(t)\rangle = e^{-\mathrm{i}\widehat{H}t}|\psi_0\rangle$ for $t > 0$. Since typically $|\psi_0\rangle$ is not an eigenstate of the evolution Hamiltonian $\widehat{H}$, this time-evolved pure state is highly non trivial. The kind of sudden change leads to identify two main classes of quantum quenches. Global quenches are characterised by sudden changes that involve the entire system (e.g. a modification of a parameter in the Hamiltonian) [82–84]. Instead, in local quenches the sudden change occurs only at a point [85–88]. The quantum quenches also allow to understand the relaxation and thermalisation properties of quantum systems [89, 90] and it is therefore insightful to study the temporal evolutions of the complexity and of entanglement-related quantities induced by these protocols.

An intriguing problem concerns understanding possible relations between circuit complexity and entanglement. Many entanglement measures are defined once a particular spatial bipartition is considered. In order to have a notion of complexity associated to a given subsystem, it is necessary a method for computing the complexity of mixed states; indeed, the reduced density matrix of a subsystem, obtained by partial tracing a pure state density matrix, describes a mixed state. Thus, a proper comparison, for instance, with the von Neumann entanglement entropy, requires an approach for the complexity of mixed states. The Part I of this thesis is devoted to

this issue: by employing the Fisher information geometry for the covariance matrices [91–93], we determine the optimal circuit connecting two mixed bosonic Gaussian states in harmonic lattices as a geodesic in the manifold identified by these states. The length of this path is interpreted as the complexity to create a target state from a reference state through the optimal circuit. This allows to compute not only the complexity between reduced density matrices, but also the complexity between thermal states, which provide another important class of mixed states. Furthermore, in this setting, by exploiting the Williamson's theorem [94], we can consider circuits whose reference and target states have either the same spectrum or can be associated to the same basis. This allows to propose some ways to quantify the spectrum and the basis complexity for bosonic Gaussian states.

Studying the complexity as distance in the space of mixed states requires a deep knowledge of the structure of the density matrices that, for the case of reduced density matrices, is equivalently provided by the entanglement Hamiltonians. The Part II of this thesis is dedicated to the study of the entanglement Hamiltonians and the entanglement spectra in free systems. We consider critical and gapped lattice models in static and out of equilibrium configurations, addressing also the interesting question of how recovering the underlying QFT results from them.

Nowadays, guided by some recent theoretical [95–97] and experimental [25] results, entanglement is used also for studying systems endowed with a global symmetry. Indeed, an evergreen research topic is the characterisation of how the presence of symmetries, a pillar of modern physics, influences the properties of a given system. The Part III of this thesis is devoted to the question of how the entanglement splits into the different sectors of an internal symmetry: the answer is encoded in the so-called symmetry resolved entanglement entropies. These quantities turn out to be strictly related to the probability distribution of the conserved charges or, equivalently, to its generating function, called full counting statistics.

In this thesis, we mainly deal with free systems (with some exceptions), which provide the easiest setting for understanding the properties of complexity and entanglement in many-body quantum systems. The questions we address turn out to be far from being trivial even in these models, despite their simplicity.

In the remaining part of this introduction we briefly outline the organisation and the contents of the thesis.

Organisation of the thesis

This thesis collects most of the results obtained during the years of Ph.D. at SISSA. Chapter 1 contains the main concepts about circuit complexity and entanglement necessary to understand the subsequent chapters. The rest of the thesis is organised into three parts, as explained below.

Part I

In Part I we develop a formalism for computing the circuit complexity between mixed bosonic Gaussian states based on the Fisher information geometry. This allows, for instance, to compute the complexity between thermal states and the complexity between reduced density matrices, also called subsystem complexity.

- In Chapter 2 we set up the formalism and we employ it for computing the complexity between thermal states and the subsystem complexity in harmonic lattices in static configurations. Explicit proposals to quantify the spectrum complexity and the basis complexity and to determine the purification of the mixed states are also discussed.

- In Chapter 3 we study the temporal evolution of the circuit complexity in harmonic lattices after a global quantum quench of the mass parameter. Analytical results are obtained for the complexity of entire systems and a numerical analysis of the subsystem complexity of a block of consecutive sites in harmonic chains is reported.

- Chapter 4 contains a numerical analysis of the temporal evolution of the complexity of entire systems and of the subsystem complexity after a local quench where two harmonic chains are suddenly joined.

The results discussed in this part are contained in the following works:

[98] G. Di Giulio and E. Tonni, *Complexity of mixed Gaussian states from Fisher information geometry*, JHEP **2012**, 101 (2020).

[99] G. Di Giulio and E. Tonni, *Subsystem complexity after a global quantum quench*, JHEP **2105**, 022 (2021).

[100] G. Di Giulio and E. Tonni, *Subsystem complexity after a local quantum quench*, accepted by JHEP, arXiv:2106.08282.

Part II

Part II is devoted to the study of the entanglement Hamiltonians and the entanglement spectra in free lattice models. We consider both bosonic and fermionic models in static and out of equilibrium settings.

- In Chapter 5 we study the continuum limit of the entanglement Hamiltonians of a block of consecutive sites in massless harmonic chains and the corresponding entanglement spectra, recovering the results predicted by conformal field theory.

- In Chapter 6 we study the entanglement Hamiltonians for finite intervals in infinite non-critical quantum chains, considering coupled harmonic oscillators and fermionic hopping models with dimerization.

- Chapter 7 contains an analysis of the temporal evolution of the entanglement Hamiltonian of an interval after a global quantum quench in free lattice models of bosons and fermions in one spatial dimension. The temporal evolutions of the gaps in the entanglement spectrum and of the contour for the entanglement entropies are also discussed.

This part is mainly based on the following papers:

[101] G. Di Giulio and E. Tonni, *On entanglement hamiltonians of an interval in massless harmonic chains* , J. Stat. Mech. **2003**, 033102 (2020).

[102] V. Eisler, G. Di Giulio, E. Tonni and I. Peschel, *Entanglement Hamiltonians for non-critical quantum chains*, J. Stat. Mech. **2010**, 103102 (2020) .

[103] G. Di Giulio, R. Arias and E. Tonni, *Entanglement hamiltonians in 1D free lattice models after a global quantum quench*, J. Stat. Mech. **1912**, 123103 (2019).

Part III

Finally, in Part III we address the problem of determining the symmetry resolution of the entanglement entropies in models endowed with a $U(1)$ symmetry. We focus in particular on gapped systems, both on the lattice and in a field theoretical formulation.

- An analysis of the entanglement entropies related to different symmetry sectors of free quantum field theories with an internal U(1) symmetry is presented in Chapter 8. We provide explicit analytic computations for the symmetry resolved entropies of Dirac and complex scalar fields in two spacetime dimensions, both in the massive and massless cases.

- In Chapter 9 we study the symmetry resolved entanglement entropies in gapped integrable lattice models, finding exact results for a free bosonic system and the XXZ spin-chain (the latter is an interacting model). The connection between the symmetry resolved entanglement and the full counting statistics is also discussed.

The results reported in this part have been obtained in the following works:

[104] S. Murciano, G. Di Giulio and P. Calabrese, *Entanglement and symmetry resolution in two dimensional free quantum field theories*, JHEP **2008** , 073 (2020).

[105] S. Murciano, G. Di Giulio and P. Calabrese, *Symmetry resolved entanglement in gapped integrable systems: a corner transfer matrix approach*, SciPost **8** , 046 (2020) .

[106] P. Calabrese, M. Collura, G. Di Giulio and S. Murciano, *Full counting statistics in the gapped XXZ spin chain*, EPL **129** , 60007 (2020).

At the end of these three parts, in the Conclusions, we report some final remarks and interesting directions for future research. Finally, in Appendix B we report some additional results about the complexity in harmonic lattices, while the Appendices A and C are devoted to some technical details about the numerical computations whose results are discussed throughout the thesis.

Chapter 1

Aspects of circuit complexity and entanglement

1.1 Circuit Complexity

In this section we provide the definition of circuit complexity and we discuss some of its qualitative properties and their relation with black hole physics.

1.1.1 Complexity and quantum circuits

In physics (and not only), a fruitful approach to deal with a complicated task is carrying it out through a sequence of *simple operations*. This turns out to be very useful also in quantum information theory in order to construct a certain quantum state.

Consider a pure quantum state $|\psi_{\rm R}\rangle$, called *reference state*, and suppose we want to construct the *target state* $|\psi_{\rm T}\rangle$ acting on $|\psi_{\rm R}\rangle$ with a series of elementary operations. In quantum information theory, such elementary operations are called gates and, since the reference and the target states are assumed to be pure states, are realised by unitary operators. If we consider a reference state made up of K qubits (as we are going to do in the following), the gates that we apply to it are *elementary* in the sense that they involve only $k \ll K$ qubits, namely a *small* number of them. The sequence of gates we apply to $|\psi_{\rm R}\rangle$ to obtain $|\psi_{\rm T}\rangle$ is called *quantum circuit*. Clearly, once we have fixed the reference and the target states, the possible circuits we can realise depend on the properties of the allowed gates, as for instance on how many qubits they act. We call $\mathcal{G}$ the set of the allowed gates, which, by definition, contains unitary operators. A legitimate question that can be asked is whether a target state can be obtained up to a certain precision δ. Usually δ is called *tolerance* and it also influences the way in which the quantum circuit connecting $|\psi_{\rm R}\rangle$ to $|\psi_{\rm T}\rangle$ can be constructed.

We are interested in understanding which is the optimal way to construct, up to a certain tolerance, the target state applying the gates drawn from $\mathcal{G}$ to the reference state. The quantity providing the answer is the *quantum circuit complexity* defined as the minimum number of gates required for obtaining a target state $|\psi_{\rm T}\rangle$ from a reference state $|\psi_{\rm R}\rangle$ through the quantum circuit

$$g_1\, g_2 \dots g_n |\psi_{\rm R}\rangle \qquad\qquad g_1,\, g_2, \dots, g_n \in \mathcal{G} \tag{1.1.1}$$

up to a tolerance δ given in terms of a certain norm $||.||$ as

$$||g_1\, g_2 \dots g_n |\psi_{\rm R}\rangle - |\psi_{\rm T}\rangle|| \leq \delta\,. \tag{1.1.2}$$

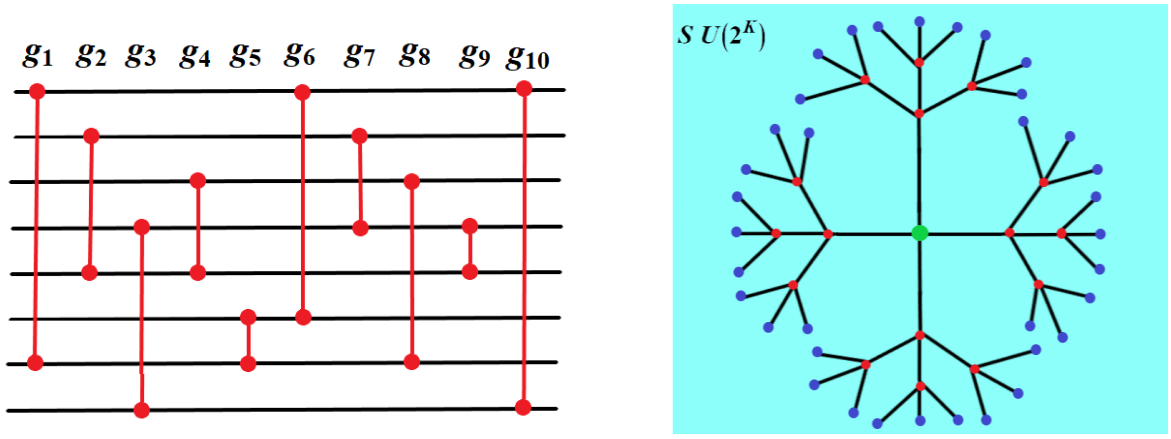

Figure 1.1: Left panel: graphical representation of a circuit with $K = 8$ qubits made by ten 2-local gates. Right panel: graph on the set of unitaries acting on the Hilbert space of K qubits. The coloured dots represent different unitaries and the blue ones provide the boundary of the graph. Each path starting from the initial point (green dot) and ending on one of the blue dots represent a possible quantum circuit with depth equal to three.

The quantum circuit associated to the minimum number of gates is called *optimal circuit*. Let us stress that, in general, the complexity depends not only on the chosen reference and target states, but also on the set $\mathcal{G}$ and on the tolerance δ that we allow.

The concept of quantum complexity is relevant in quantum information theory and quantum computer science [30, 31]. Indeed a central problem of quantum computation is to determine the most efficient way of implementing a given unitary operation. For this reason, the complexity turns out to be crucial in several applications ranging from *public-key quantum money* [107–109] to *copy-protected quantum software* [110, 111].

Recently, the quantum complexity has attracted also the attention of the community of high energy physics, given that, as we are going to discuss in Sec. 1.1.3, the features of this quantity present intriguing similarities with some properties of black holes [50–52, 54, 112, 113].

A toy model for the complexity

In order to discuss some of the properties of the circuit complexity, we consider a simple toy model where the states are made by K qubits, with $K \gg 1$ [50, 51]. The dimension of the associated Hilbert space is 2^K. The gates are chosen to be 2-*local*, namely each gate involves only $k = 2$ qubits of the state on which it acts (in this case, $2 \ll K$ and therefore these gates are elementary in the sense explained above). In the left panel of Fig. 1.1 we show a pictorial representation of a circuit with 2-local gates and $K = 8$. All the considerations that we make in the following can be generalised to the case where $k \neq 2$.

We start from a reference state and we construct a circuit as follows. Consider identical and consecutive time steps and, at each of them, let $K/2$ 2-local gates act. At each time step, we have to pair K qubits through $K/2$ gates and this provides the unitary transformation acting on the state. The number of possible resulting unitary transformations (or *unitaries*) at the first time step is simply obtained as

$$d \sim \frac{K!}{(K/2)!} \sim \left(\frac{2K}{e}\right)^{\frac{K}{2}} \tag{1.1.3}$$

where we have used the Stirling's approximation.

It turns out to be very useful providing a graphical representation for this circuit. Since each discrete step consists in applying one of the d possible unitaries, we can see the set of all the allowed circuits as a *graph* on the manifold $SU(2^K)$, as pictorially represented in the right panel of Fig. 1.1 [113–115]. Each vertex of such a graph represents a unitary operator that can implement a gate in the circuit that we are studying. Let us add another step to the graph. In doing this, we introduce a further technical restriction (not really relevant for large K), which simplifies the treatment. We assume that a pairing between qubits occurred at the first step, cannot be repeated in the second step. This means that the second layer of the graph has a number of branches equal to $d-1=\frac{K!}{(K/2)!}-1$ (which is very close to d in (1.1.3) as $K\gg 1$). We can then apply repeatedly this procedure obtaining a larger and larger graph.

Another important assumption is that, in the initial steps of this construction, no collisions occur in the graph, namely each unitary at the boundary of the graph is reached by only one branch [114]. After τ time steps (τ is also called *depth* of the circuit), the number of unitaries reached by the graph is given by

$$d^\tau \simeq \left(\frac{2K}{e}\right)^{\frac{\tau K}{2}} . \tag{1.1.4}$$

If we add to the *no-collision assumption* the fact that no vertices already visited can be reached again during the evolution of the graph (both these assumptions are reasonable during the first steps given that, for $K\gg 1$, the dimension of $SU(2^K)$ is extremely high), we straightforwardly have that each path starting from the initial point of the graph (green dot in the right panel of Fig. 1.1) and ending in one of the unitaries at the boundary of the graph (blue dots in the same panel) corresponds to an optimal circuit. The complexity is given by the number of steps τ multiplied by the number of gates in each step, namely [50, 51]

$$\mathcal{C}=\frac{\tau K}{2} . \tag{1.1.5}$$

This provides a very rough and intuitive argument for the initial linear growth of the circuit complexity. In the following we try to understand approximately until which time this linear growth occurs. Let us also remark that, using (1.1.4) and (1.1.5), we can say that the sub-volume of $SU(2^K)$ corresponding to unitaries of complexity $\mathcal{C}$ is exponential in $\mathcal{C}$ and it is given by $(2K/e)^{\mathcal{C}}$.

Before proceeding further in this discussion, let us mention some useful properties of $SU(2^K)$. In order to estimate the number of unitaries in $SU(2^K)$, we divide its volume by the volume of an ϵ-ball $\mathcal{B}_\epsilon$ (ball of radius ϵ) of the same dimensionality, namely 4^K-1. When $K\gg 1$, we have [116]

$$\mathrm{Vol}\big(SU(2^K)\big)\simeq\frac{2\pi^{\frac{(2^K+2)(2^K-1)}{2}}}{2!3!\dots(2^K-1)!}\qquad \mathrm{Vol}\big(\mathcal{B}_\epsilon\big)\simeq\frac{\pi^{\frac{4^K-1}{2}}}{\big(\frac{4^K-1}{2}\big)!} \tag{1.1.6}$$

whose ratio gives the number of unitaries in $SU(2^K)$ regulated by a cutoff ϵ, which reads (using the Stirling's approximation)

$$\frac{\mathrm{Vol}\big(SU(2^K)\big)}{\mathrm{Vol}\big(\mathcal{B}_\epsilon\big)}\simeq\left(\frac{2^K}{\epsilon^2}\right)^{4^K/2} . \tag{1.1.7}$$

The number of unitaries (1.1.7) is useful for giving an estimate of the maximal complexity that we can have in this model. Indeed, if we let the graph introduced before grow, at a certain point the number of unitaries reached by the graph becomes equal to (1.1.7), namely

$$\left(\frac{2K}{e}\right)^{\mathcal{C}_{\max}}=\left(\frac{2^K}{\epsilon^2}\right)^{4^K/2}\qquad\Rightarrow\qquad \mathcal{C}_{\max}=4^K\left[\frac{1}{2}+\frac{|\log\epsilon|}{\log K}\right] . \tag{1.1.8}$$

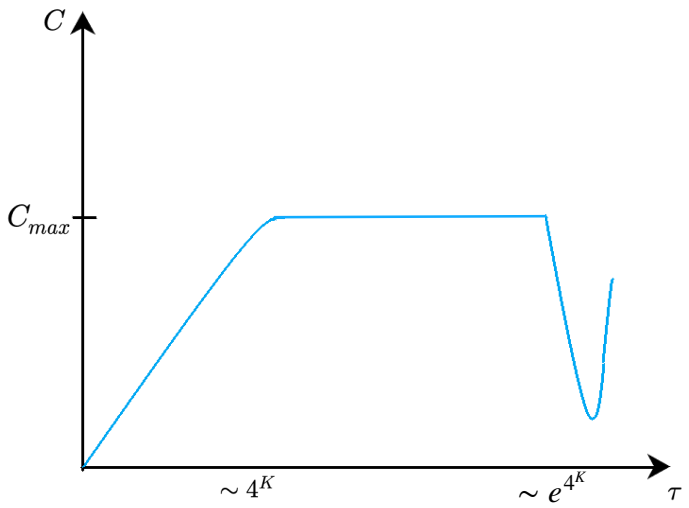

Figure 1.2: Sketch of the temporal evolution of the complexity in the toy model considered in this section. The initial growth is linear until $\tau_* \sim 4^K$ and then it becomes approximately constant with value $\mathcal{C}_{\max}$ given by (1.1.8). At $\tau_{\rm rec} \sim e^{4^K}$ the complexity returns close to its initial value because of quantum recurrences. Figure adapted from [117].

Let us stress that the maximum complexity in (1.1.8) has a strong (exponential) dependence on K and a weak (logarithmic) dependence on the cutoff ϵ.

In this picture, when the graph reaches the maximum complexity, it has no choice but visiting previously visited vertices, which, with very high probability, correspond to other (almost) maximally complex unitaries [113, 114]. Thus, we can conclude that complexity saturates (up to possible small oscillations) and this occurs at a value of time exponentially large in K, namely at $\tau_* \sim 4^K$ [50, 51]. This is consistent with the findings of [118], where it has been shown that almost all the unitary matrices require an exponential number of operations to be constructed by a circuit involving 2-local gates. In Fig. 1.2 we sketch the temporal evolution of the complexity described above (the possible oscillations in the constant regime have been neglected in this representation).

It is worth remarking that, after a doubly exponential time in K, because of quantum recurrences, the quantum circuit returns in the neighbourhood of the identity (which is the initial point) and therefore the complexity drops almost to zero and starts again its evolution [119]. The recurrence time is approximately given by $\tau_{\rm rec} \sim e^{4^K}$ and it grows with K in the same way as the number of states of a 2^K dimensional Hilbert space [117].

It is insightful to compare the complexity of this very simple model with another relevant quantity, namely the entropy. The maximum entropy of a system made by K qubits is simply given by $S_{\max} = K \log 2$ and therefore, for large K, $S_{\max} \ll \mathcal{C}_{\max}$. This suggests that the time scale of thermalisation for this model is much smaller than the time scale of saturation of the complexity. A further possible aspect to study is the effect of a perturbation on the complexity of a quantum circuit. This can be done by asking how much time the perturbation needs to spread throughout the whole circuit. For the toy model we are considering, this time scale, known as *scrambling time* and denoted by $\tau_{\rm s}$, has been estimated finding that [50, 52]

$$\tau_{\rm s} \sim \log K \,. \tag{1.1.9}$$

Clearly, for large K, $\tau_{\rm s} \ll \tau_*$. Thus, we can conclude that the saturation time of the complexity is definitely the largest time scale in our system and therefore in the toy model we have considered

something physically relevant happens long after the thermalisation and the scrambling and the complexity is the right quantity to detect it.

It is an interesting problem to understand whether these properties, that are easily understood for the simple model considered above, hold in many-body systems described either by lattice models or by continuum field theories. Many efforts have been done in this direction in the past years [35–46, 60–76, 79]. This very active line of research has been also motivated by recent progresses and insights coming from black hole physics and the AdS/CFT correspondence. We are going to briefly discuss some of them in Sec. 1.1.3.

1.1.2 A geometric approach to the complexity

Important concepts and tools, that have led to remarkable advances in understanding the circuit complexity in many-body quantum systems and quantum field theories, have been developed by Nielsen and his collaborators in [32–34]. This approach is based on the idea that it is easier to deal with smooth curves rather than with discrete circuits, as the ones described in Sec. 1.1.1. The set of all the states that can be possibly found along the circuits is thought as a smooth manifold and the circuits connecting a generic reference state to a generic target state as curves on this manifold. The Nielsen's approach introduces the notion of *local metric* as a way to parametrise the cost of each unitary transformation connecting two infinitesimally close quantum states, represented by close points in the manifold of all the states that can be connected through a quantum circuit. Given that the local metric encodes how we can move from a point to another one on the manifold, in this context, its choice contains information about the gates that are allowed in the quantum circuits. In other words, the metric can be thought as a *cost function* which assigns a weight to each of the possible gates in the circuit that we aim to construct. Furthermore, the metric provides a natural way to quantify the length of a curve, that we interpret as the depth of a quantum circuit, and allows to determine the geodesics, namely the curves with minimal length, between two points. From this perspective, given two points representing the reference and the target states, it is straightforward to interpret the geodesics connecting them as the optimal circuit and the length of this geodesics as the complexity. Thus, through the (properly adapted) methods of the Riemannian geometry, the geodesics analysis offers a powerful tool to the quantum computation.

The approach of Nielsen and collaborators has been developed specifically for quantum circuits that allow to construct a pure state from another pure state through a sequence of unitary gates. Nevertheless, one can try to generalise it to the case of quantum circuits involving mixed states [120], where the manifold of all the vectors describing a given physical system in a pure state has to be replaced by the set of density matrices associated to the mixed states in the same system. The latter space has in general a much more complicated structure (indeed it is made by operators rather than vectors) and therefore the underlying geometry is more difficult to study. Nonetheless, it is worth finding cases in which this analysis can be performed and the circuit complexity of mixed states can be investigated. The interest in studying the complexity of mixed states lies in several aspects. First of all, some of the quantum states that usually we have to deal with are mixed states. This is the case of thermal states and reduced density matrices of a given spatial subregion of a many-body system (see the definition in 1.2.1). Thus, in order to have a well defined notion of complexity for these classes of states, it is worth developing an approach for mixed states. Furthermore, while for pure states the gates are clearly given by unitary operators, it is interesting to investigate more on how to implement gates in circuits connecting mixed states using more general quantum operations [120].

Given the difficulty of the problem, it is natural to start by considering simple free lattice models, like the harmonic lattices with nearest neighbour spring-like interaction. The Hamiltonian

reads

$$\widehat{H} = \sum_{i=1}^{N} \left(\frac{1}{2m}\, \hat{p}_i^2 + \frac{m\omega^2}{2}\, \hat{q}_i^2 \right) + \sum_{\langle i,j \rangle} \frac{\kappa}{2} (\hat{q}_i - \hat{q}_j)^2 \tag{1.1.10}$$

where the second sum is performed over the nearest neighbour sites and the hermitian position and momentum operators satisfy the canonical commutation relations $[\hat{q}_i, \hat{q}_j] = [\hat{p}_i, \hat{p}_j] = 0$ and $[\hat{q}_i, \hat{p}_j] = \mathrm{i}\delta_{ij}$ (we set $\hbar = 1$ throughout this thesis). The states of the harmonic lattices can be equivalently represented either by density matrices or by Wigner functions, which are quasi-probability distribution functions (they are not positive definite) defined on a fictitious phase space (see also Sec. 2.2.1 for the definition). Thus, the geometry of these states can be seen as the one of the corresponding Wigner functions. An important class of states is the one of *Gaussian states*, which are characterised by Gaussian Wigner functions (hence, in this case, the Wigner functions are proper probability distribution functions). The space of this class of states is such that each point corresponds to a Gaussian probability distribution function (PDF) and therefore the manifold is parametrised in general by $(\boldsymbol{r}, \gamma)$, where $\boldsymbol{r}$ is the vector containing the first moments and γ is the *covariance matrix*, whose entries are given by two-point correlators of position and momentum operators. The *information geometry* is the branch of mathematics that studies the Riemannian geometry associated to spaces of PDFs [93,121,122] and, in this framework, various results for the geometry of Gaussian PDFs have been obtained [91–93, 121, 123].

In chapter 2 we exploit the geodesics in the manifold of Gaussian PDFs with vanishing first moments and the associated geodesic length, called Fisher-Rao distance [92, 124–128], to provide a possible circuit complexity for the mixed bosonic Gaussian states (see also [98]). If we denote by γ_{R} and γ_{T} the covariance matrices of the reference and the target mixed states respectively, the complexity of the circuit connecting them is given by

$$\mathcal{C} = \frac{1}{2\sqrt{2}} \sqrt{\mathrm{Tr}\big[\log(\gamma_{\mathrm{T}} \gamma_{\mathrm{R}}^{-1})\big]^2}\,. \tag{1.1.11}$$

When γ_{R} and γ_{T} are covariance matrices of pure states, (1.1.11) reduces to the results found in [35, 40].

More details are given in chapter 2, where properties and applications are reported and discussed. We find it worth mentioning here the possibility of defining through (1.1.11) the *subsystem complexity* as the complexity between two reduced density matrices associated to the same spatial subsystem (see Sec. 2.7.4). In chapters 3 and 4 we employ the proposal (1.1.11) for studying the temporal evolution of the complexity after some protocols driving the harmonic lattices out of equilibrium (see also [99, 100]).

Another approach to the complexity of mixed states, based on the purification of quantum states, has been introduced in [79] (further results can be found in [129,130]). The mixed reference and target states are first purified and then the complexity between the obtained pure states is computed. Given that there are many ways of purifying a state, the result is uniquely determined once the purifications corresponding to the minimal complexity have been selected. This approach is briefly reviewed in Sec. 2.6. Let us stress that the purifications realised in [79] for computing the complexity of mixed states requires the introduction of ancillary degrees of freedom, which is not necessary in the approach described in chapter 2.

A density matrix describing a quantum state is an operator and therefore is characterised by a spectrum and a basis. When a density matrix is associated to a pure state, its spectrum has a unique non vanishing element which is equal to one and, hence, the pure states are identified only by the basis of their density matrices. On the other hand, the density matrices describing mixed states are characterised both by their basis and their spectrum. We can therefore pictorially

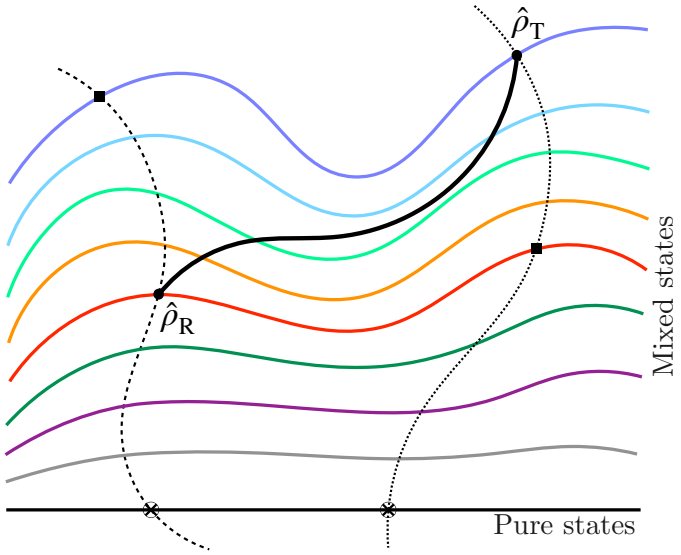

Figure 1.3: Pictorial representation of the space of mixed states. The coloured curves represent the sets of states having the same spectrum and, among these, the black straight line is the set of pure states. The dashed curves connect states with the same basis and different spectra, while the black thick curve represents the goedesic connecting two generic mixed states described by the density matrices $\hat{\rho}_{\mathrm{R}}$ and $\hat{\rho}_{\mathrm{T}}$. Figure adapted from [98].

represent the space of all the mixed states of a given system as in Fig. 1.3, where the coloured solid curves represent the sets of states having the same spectrum, with the black straight line which corresponds to the set of pure states. Within this space, one can move either along the slices at fixed spectrum or by fixing the basis and changing the spectrum only (as represented by the two dashed curves). These two possibilities lead to the notions of spectrum and basis complexity [46]. The former is the complexity restricted to a given slice, while the latter is the distance between states living in different slices and characterised by the same basis. Let us stress that, for two generic mixed states, it might be necessary to change both the basis and the spectrum for constructing the target state from the reference state in the most efficient way (as occurs, for instance, if the optimal circuit is the one represented by the black thick curve connecting $\hat{\rho}_{\mathrm{R}}$ and $\hat{\rho}_{\mathrm{T}}$ in Fig. 1.3). Nevertheless, it is insightful to find a precise prescription to compute the spectrum and the basis complexity and to understand in details their properties. In Sec. 2.3 we tackle this problem for bosonic Gaussian states using the proposal for the complexity based on the Fisher information geometry [98].

From the discussion above, it should be clear that the notion of complexity is intimately related to the geometry of quantum states [131] and to the way in which one measures the distance among them. The distance between two states can be evaluated also through the distance between the corresponding density matrices. Various expressions for distances have been constructed and it is natural to ask whether they have to satisfy some physical properties required for a measure of distance (and distinguishability) between states. The main of these features is known as contractivity [131–133] and it amounts to require that two generic quantum states are less distinguishable if we apply to both of them the same quantum operation. A quantum operation Θ is realised by a completely positive operator which acts on the density matrix $\hat{\rho}$, providing another quantum state $\Theta(\hat{\rho})$ [77, 131, 132] (see also Sec. 2.5). A distance d between two states characterised by their density matrices $\hat{\rho}_1$ and $\hat{\rho}_2$ is contractive when the action of a quantum operation Θ reduces the

distance between any two given states [132, 133], namely [1]

$$d(\hat{\rho}_1, \hat{\rho}_2) \geqslant d\big(\Theta(\hat{\rho}_1), \Theta(\hat{\rho}_2)\big)\,. \tag{1.1.12}$$

This is a crucial property imposed to a distance in quantum information theory. The main contractive distances are the Bures distance, defined in terms of the fidelity $\mathcal{F}$ as follows

$$d^2_{\rm B}(\hat{\rho}_1, \hat{\rho}_2) \equiv 2\,(1 - \mathcal{F}(\hat{\rho}_1, \hat{\rho}_2)) \qquad \mathcal{F}(\hat{\rho}_1, \hat{\rho}_2) \equiv \mathrm{Tr}\left(\sqrt{\sqrt{\hat{\rho}_1}\,\hat{\rho}_2\,\sqrt{\hat{\rho}_1}}\,\right) \tag{1.1.13}$$

the Hellinger distance

$$d^2_{\rm H}(\hat{\rho}_1, \hat{\rho}_2) \equiv 2\left[1 - \mathrm{Tr}\left(\sqrt{\hat{\rho}_1}\,\sqrt{\hat{\rho}_2}\right)\right] \tag{1.1.14}$$

and the trace distance

$$d_{L^1}(\hat{\rho}_1, \hat{\rho}_2) \equiv \mathrm{Tr}\big|\hat{\rho}_1 - \hat{\rho}_2\big|\,. \tag{1.1.15}$$

The trace distance is the L^p-distance with $p = 1$ and it is the only contractive distance among the L^p-distances. For $p = 2$ we have the Hilbert-Schmidt distance [131]

$$d_{\rm HS}(\hat{\rho}_1, \hat{\rho}_2) \equiv \sqrt{\mathrm{Tr}\big(\hat{\rho}_1 - \hat{\rho}_2\big)^2} \tag{1.1.16}$$

which is non contractive. The Bures distance and the Hellinger distance are Riemannian[2], being induced by a metric tensor, while the trace distance is not. Another difference occurs when we restrict to the subset of the pure states. It is well known that the only Riemannian distance between pure states is the Fubini-Study distance $d^2_{\rm FS} \equiv 2\,(1 - |\langle\psi_1|\psi_2\rangle|)$, where $\hat{\rho}_1 = |\psi_1\rangle\langle\psi_1|$ and $\hat{\rho}_2 = |\psi_2\rangle\langle\psi_2|$. Restricting to pure states, the Bures distance becomes exactly the Fubini-Study distance, while the Hellinger distance and trace distance become $d^2_{\rm H} = 2\left(1 - |\langle\psi_1|\psi_2\rangle|^2\right)$ and $d^2_{L^1} = 4\left(1 - |\langle\psi_1|\psi_2\rangle|^2\right)$ respectively, namely functions of the Fubini-Study distance [133].

It would be very interesting to employ some of the distances between density matrices reported in this subsection to define notions of optimal circuit and complexity for mixed states.

1.1.3 Complexity and black holes

The AdS/CFT correspondence is a conjectured duality between a quantum theory of gravity defined on a $d+1$-dimensional Anti-de Sitter (AdS_{d+1}) spacetime (which is a particular space with constant negative curvature) and a conformal field theory (CFT) with gauge fields defined on a d-dimensional spacetime without gravity [47, 135, 136] (see also the review [137]). This duality realises the *holographic principle* which states that all the information content of a quantum gravity theory in $d+1$ dimensions can be encoded in an effective theory in d dimensions. In this case, the CFT is defined on the boundary of the AdS spacetime. The AdS/CFT correspondence is a strong-weak coupling duality, namely, when the conformal field theory is strongly coupled, the dual gravity theory is classical. The first example of this duality was found by Maldacena in [47] between the type IIB superstring theory on $\mathrm{AdS}_5 \times S^5$ and the 4-dimensional $\mathcal{N} = 4$ superconformal Yang-Mills field theory with gauge group $SU(N)$. We find it worth mentioning that, for a two-dimensional CFT with central charge c, the regime described by a classical gravitational model in asymptotically AdS_3 is given by $c \to \infty$.

Within this duality, every state of the CFT corresponds to a specific geometry of the AdS bulk. For instance, the ground state of the CFT is dual to the empty AdS, while the CFT in a thermal

[1] Sometimes, as for instance in [131], this property is called monotonicity.

[2] In [134] Petz has classified all the contractive Riemannian metrics, finding a general formula that provides (1.1.13) and (1.1.14) as particular cases.

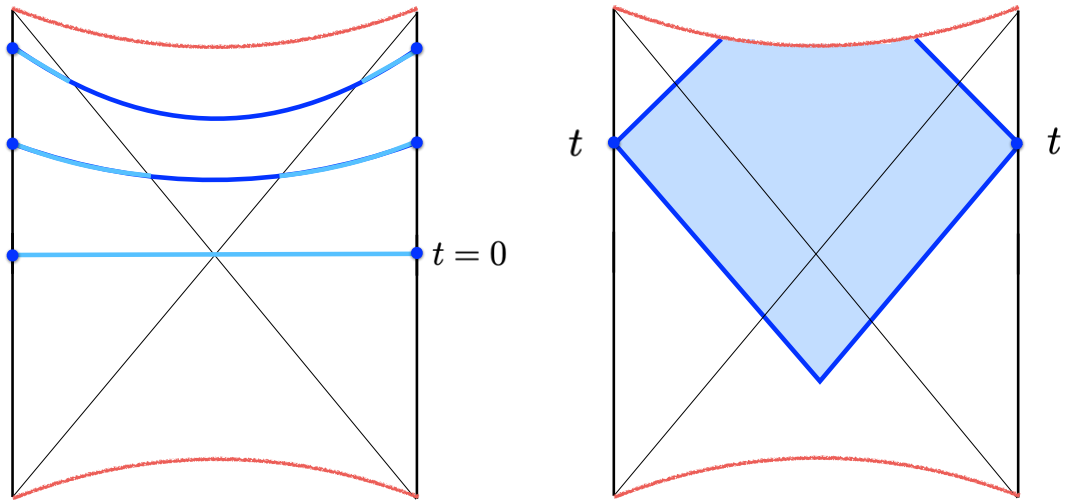

Figure 1.4: Two Penrose diagrams of the eternal black hole spacetime. In each diagram the diagonals represent the horizons of the two black holes and divide the spacetime into four parts: the left and the right ones are the exterior regions, while the top is the interior of the black holes. The red curves at the top and at the bottom of the diagrams represent the singularities and the black straight vertical lines are the boundaries of the spacetime where the entangled CFTs live. In the left panel we also sketch three space-like hypersurfaces anchored to the boundaries (blue curves), while in the right panel the blue region represents the Wheeler-DeWitt patch. Figure adapted from [51, 113].

state at a given temperature corresponds to have an asymptotically AdS black hole in the bulk. Furthermore, whenever we have a quantity defined on one side of the correspondence, there should be an holographic dual on the other side: this provides the so-called holographic dictionary. In the last twenty-five years the AdS/CFT correspondence has found several applications ranging from the elementary particle physics to condensed matter and quantum information theory. Recently, the quantum circuit complexity has become an attracting quantity in this context, in particular for its relation with black holes [50–52, 54, 112, 113].

In order to support the fact that the complexity is an insightful quantity in the study of black holes, let us consider the following fact: the spatial volume behind the horizon of a black hole grows in time and its growth continues long after the black hole has reached the thermal equilibrium. This means that the entropy of the black hole cannot encode this phenomenon since it stops to increase after the thermalisation. Thus, another quantity is expected to describe the growth of the black hole interior and, as we are going to briefly discuss, this quantity turns out to be the complexity.

To grab some intuitions about this connection, we exploit a pattern of similarities that has been developed in [138] between black holes and quantum circuits. Within this correspondence, a black hole with a given entropy S is described by a quantum circuit with K qubits, such that $K \sim S$. Indeed, as explained before, the maximum entropy of a system with K qubits is proportional to K and therefore a circuit describing a black hole with entropy S must have at least S qubits. We assume that this minimal setup is enough for our purposes. The correspondences between these two systems include also the identification between the time of the circuit and the Rindler time in the black hole geometry.

In order to be more explicit, let us consider an AdS *eternal* black hole (whose Penrose diagram

is shown in the two panels of Fig. 1.4) which corresponds to the two sides of a black hole connected by an Einstein-Rosen bridge (sometimes called wormhole)[3]. Within the AdS/CFT correspondence, this geometry is dual to a thermofield double state, which is a state obtained by entangling two copies of a CFT in such a manner that tracing out either copy produces the thermal density matrix with temperature equal to the Hawking temperature of the black hole [139]. In the representation in Fig. 1.4 the two CFTs are assumed to be defined on the two boundaries of the spacetime. Furthermore, the vertical direction of the diagram corresponds to the temporal direction of the CFT parametrised by t.

Consider the spacetime slicing represented in the left panel of Fig. 1.4, where each of the blue curves corresponds to the maximum spatial volume contained in the space-like hypersurface anchored to a given time slice on the two boundaries. The portion of each slice behind the horizon (represented in darker blue) is the instantaneous Einstein-Rosen bridge connecting the two horizons. If we call $V(t)$ the volume of the Einstein-Rosen bridge corresponding to the boundary time t, it has been shown that it grows linearly in time with a rate given by [51]

$$\frac{dV(t)}{dt} \propto G_N S T l_{\text{AdS}} \tag{1.1.17}$$

where G_N is the Newton's constant, S and T are the entropy and the temperature of the black hole respectively and l_{AdS} is a length scale that characterises the AdS spacetime. If we introduce the following geometric quantity [50, 51]

$$\mathcal{C}_{\text{V}} = \frac{V}{G_N l_{\text{AdS}}} \tag{1.1.18}$$

we have

$$\frac{d\mathcal{C}_{\text{V}}}{dt} \propto ST\,. \tag{1.1.19}$$

Passing to the Rindler time $\tau \propto tT$, which, as mentioned before, is expected to correspond to the time of a quantum circuit describing the black hole, we obtain

$$\frac{d\mathcal{C}_{\text{V}}}{d\tau} \propto S \sim K \tag{1.1.20}$$

where we have used that the entropy of the black hole grows as the number of qubits K of the corresponding quantum circuit. Comparing (1.1.20) with (1.1.5), we are immediately led to argue that $\mathcal{C}_{\text{V}}$, which parametrises the growth of the Einstein-Rosen bridge, can be interpreted as a measure of complexity.

Within the context of the AdS/CFT correspondence, whenever we have a gravitational quantity in the AdS bulk, it is natural to look for the dual quantity in the corresponding CFT. The quantity in (1.1.18), which is purely geometric, is conjectured to be dual to the complexity of the CFT state on the boundary of AdS and it is called holographic complexity. More precisely, (1.1.18) is only one of the existing proposals for the holographic complexity, usually called *CV proposal* [50, 51].

The other main prescription is provided by the *CA proposal* and tells that the holographic complexity is given by [56, 57]

$$\mathcal{C}_{\text{A}} = \frac{I_{\text{WDW}}}{\pi} \tag{1.1.21}$$

where I_{WDW} is the gravitational action evaluated on a specific portion of spacetime, called Wheeler-DeWitt patch, which contains all the space-like surfaces in the bulk which terminate on the boundaries at time t (see the blue region in the right panel of Fig. 1.4).

[3]The following argument is not specific of two-sided black holes and can be formulated similarly for the geometry of a single black hole.

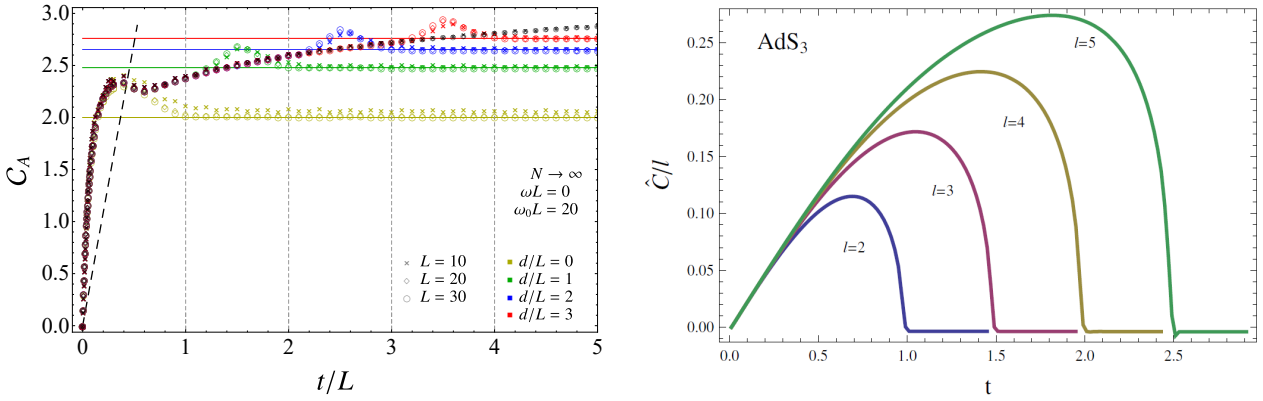

Figure 1.5: Comparison between the temporal evolution of the subsystem complexity of a block of L consecutive sites in harmonic chains (either infinite or semi-infinite) after a global quench of the frequency (left panel, plot taken from [99]) and the one of the holographic subsystem complexity of an interval of length l in the gravitational background given by the Vaidya spacetime (right panel, plot taken from [145]). For more details about this comparison see Sec. 3.5.

Exploiting these two proposals, the holographic complexity has been intensively studied in various spacetimes [50–59,140–144]. It is worth remarking that both the CV and the CA proposals have been adapted to compute the holographic complexity for a *subregion* in a constant time slice of the CFT on the boundary of AdS [55, 59], leading to the notion of holographic subsystem complexity (which is conjectured to be dual to the complexity of reduced density matrices in CFT).

The aforementioned holographic conjectures motivate the study of the complexity of states in CFT (or more generally in quantum field theory), whose properties have not been fully understood yet. Some progresses towards this goal can be found in [35–46, 60–74, 79], but, despite these advances, it remains an interesting open problem that deserves further investigations. In order to understand the circuit complexity in continuum theories, a possible approach consists in exploring the complexity of a process that constructs a quantum state in lattice models whose continuum limit is well understood. For instance, one can consider free theories which are the simplest models. If the underlying field theory is a CFT, it is insightful comparing the results obtained for lattices large enough with the outcomes of the corresponding holographic computations. Let us stress that we do not expect an exact quantitative agreement between these results given that the lattice ones are obtained for free models (with an underlying free CFT), while the holographic ones hold for a strongly interacting CFT [4]. Nevertheless, one can find intriguing qualitative similarities, as the ones that we observe in Fig. 1.5, where the temporal evolution of the subsystem complexity in infinite critical harmonic chains after a global quench (black symbols in the left panel) is compared against the evolution of the holographic subsystem complexity (obtained in [145] through the CV proposal) in the corresponding gravitational background (right panel). Indeed, the initial part of the two evolutions is very similar with a maximum developing after the initial growth followed by a decreasing that ends approximately at the same time in both the panels. For later times, we observe qualitatively different behaviours. More details about the results in the lattice model and about this comparison can be found in Sec. 3.5 (see also [99]). Let us stress that the global quench (detailed in chapter 3), which induces the behaviour shown in Fig. 1.5, provides a different temporal evolution with respect to the one discussed in Sec. 1.1.1 for the simple toy model of K

[4] This is a further reason why it is very important to study the complexity in interacting many-body systems.

qubits. For this reason, we do not compare this result with the one sketched in Fig. 1.2.

1.2 Bipartite entanglement

In this section we review some techniques and results about entanglement in many-body quantum systems and in quantum field theories.

1.2.1 Main definitions

Consider a many-body quantum system on a bipartite spatial domain $A \cup B$. Let us call $\mathcal{H}$ the associated Hilbert space and let us assume that it can be factorised as $\mathcal{H} = \mathcal{H}_A \otimes \mathcal{H}_B$, where $\mathcal{H}_A$ contains the degrees of freedom of the subsystem A and $\mathcal{H}_B$ the degrees of freedom of B [5]. Given a pure state $|\psi\rangle \in \mathcal{H}$, the corresponding density matrix can be written as $\hat{\rho} = |\psi\rangle\langle\psi|$. The key object to study the bipartite entanglement between A and B is the *reduced density matrix* of A, defined as

$$\hat{\rho}_A = \mathrm{Tr}_{\mathcal{H}_B} \hat{\rho} \tag{1.2.1}$$

where the (partial) trace in (1.2.1) has been performed over $\mathcal{H}_B$. Given that $\hat{\rho}_A$ is hermitian, positive semi-definite and normalised to $\mathrm{Tr}_{\mathcal{H}_A} \hat{\rho}_A = 1$, it can be written as

$$\hat{\rho}_A = \frac{e^{-\widehat{K}_A}}{Z} \tag{1.2.2}$$

where the hermitian operator $\widehat{K}_A$ is called entanglement (or modular) Hamiltonian and $Z = \mathrm{Tr}\big(e^{-\widehat{K}_A}\big)$ [155]. Let us remark that, although $|\psi\rangle\langle\psi|$ is the density matrix of a pure state, $\hat{\rho}_A$ in (1.2.1) describes a mixed state unless $|\psi\rangle = |\psi_A\rangle \otimes |\psi_B\rangle$ with $|\psi_A\rangle \in \mathcal{H}_A$ and $|\psi_B\rangle \in \mathcal{H}_B$. If this happens, $\hat{\rho}_A = |\psi_A\rangle\langle\psi_A|$, namely it describes a pure state.

In order to quantify the bipartite entanglement of pure states, we consider the Von Neumann entropy of the reduced density matrix, called *entanglement entropy*, which is defined as

$$S_A = -\mathrm{Tr}\big(\hat{\rho}_A \log \hat{\rho}_A\big) \,. \tag{1.2.3}$$

The entanglement entropy (1.2.3) satisfies all the requirements to be considered a good entanglement measure [156] (an exhaustive list of the properties of this quantity with detailed explanations can be found in [131]). Given two spatial subsystems A_1 and A_2 (not necessarily one the complement of the other), the entanglement entropy satisfies other two important properties, namely the subadditivity

$$S_{A_1 \cup A_2} \leqslant S_{A_1} + S_{A_2} \tag{1.2.4}$$

and the strong subadditivity [6] [164, 165]

$$S_{A_1 \cup A_2} + S_{A_1 \cap A_2} \leqslant S_{A_1} + S_{A_2} \,. \tag{1.2.5}$$

[5] There are cases in which this factorisation is not well defined. The first important example is the one of quantum field theories, where this issue leads to the ultraviolet divergence of the entanglement entropies (see the later discussion in Sec. 1.2.3) [6, 8, 20, 21]. In quantum field theory this problem can be bypassed by introducing a suitable regularisation, as the one discussed in Sec. 1.2.2 [6, 8, 146, 147]. The factorisation of the Hilbert space into two parts associated to two spatial subsystems is ill defined also in models with a gauge symmetry, even if they are defined on a lattice. For these theories, specific treatments have been developed, for instance, in [14, 148–154].

[6] Remarkably, this property is the key ingredient for constructing a c-function [157] from the entanglement entropy in relativistic quantum field theories in $1+1$ dimensions [158–161] and in higher dimensions [162, 163].

The entanglement entropy (1.2.3) is an entanglement measure only if we consider a bipartition of a pure state. Indeed, for a mixed state, the entanglement entropy mixes quantum and classical correlations. For instance, if we consider a bipartition of a state at high temperature, S_A provides the thermal entropy. Some proper measures of entanglement for generic mixed states are the *negativity* [166] (see also [167]), the *entanglement cost*, the *distillable entanglement* and the *entanglement of formation* [131, 168].

We find it worth remarking that, if $|\psi\rangle = |\psi_A\rangle \otimes |\psi_B\rangle$, then $\hat{\rho}_A = |\psi_A\rangle\langle\psi_A|$ and therefore $S_A = 0$, namely A and B are not entangled.

All the considerations done so far could have been applied without loss of generality to $\hat{\rho}_B = \mathrm{Tr}_{\mathcal{H}_A}\hat{\rho}$ and $S_B = -\mathrm{Tr}\big(\hat{\rho}_B \log \hat{\rho}_B\big)$. A reasonable requirement for an entanglement measure is that its value depends only on the bipartition we are considering and not on a single subsystem. Thus, we expect $S_A = S_B$, even if in general $\hat{\rho}_A$ and $\hat{\rho}_B$ act on Hilbert spaces with different dimensionality. A simple proof of $S_A = S_B$ can be obtained exploiting the Hilbert-Schmidt decomposition of the pure state $|\psi\rangle$ [169, 170].

Computing the full reduced density matrix of a generic model, as well as its logarithm, is a very difficult task. It is convenient in this case to focus our attention on the so-called *Rényi entropies*

$$S_A^{(n)} = \frac{1}{1-n} \ln \mathrm{Tr}\hat{\rho}_A^n \,. \tag{1.2.6}$$

The Rényi entropies (1.2.6) are defined for real values of $n > 0$. It is simple to check that

$$S_A = \lim_{n\to 1} S_A^{(n)} \,. \tag{1.2.7}$$

As we are going to see later, in several cases it is much simpler to obtain the Rényi entropies rather than the entanglement entropy. Nonetheless, if one is able to compute $S_A^{(n)}$ for any real value of n, its knowledge leads to S_A through (1.2.7). Let us stress that also the Rényi entropies (1.2.6) are entanglement measures, but, differently from the entanglement entropy, they do not satisfy (1.2.4) and (1.2.5). In the following we use the term *entanglement entropies* for including both the Von Neumann entropy and the Rényi entropies.

Given that the entanglement entropies are defined in terms of traces of functions of the reduced density matrix, they only depend on its spectrum, called *entanglement spectrum* [26]. In particular, if we denote the eigenvalues of $\hat{\rho}_A$ as $0 < \lambda_k < 1$, with $k = 1, \ldots, \dim\mathcal{H}_A$, the Rényi entropies (1.2.6) can be written as

$$S_A^{(n)} = \frac{1}{1-n} \ln \left(\sum_{k=1}^{\dim\mathcal{H}_A} \lambda_k^n \right) . \tag{1.2.8}$$

Thus, the Rényi entropy evaluated in the limit $n \to \infty$ provides the maximum element of the entanglement spectrum as

$$\lambda_{\max} = \lim_{n\to\infty} e^{-S_A^{(n)}} \,. \tag{1.2.9}$$

On the other hand, the reduced density matrix, or equivalently the entanglement Hamiltonian, is not determined only by the entanglement spectrum and therefore it contains the complete information about the entanglement between A and B. For this reason, although they are typically very difficult to study, in the past years many efforts have been done to compute the entanglement Hamiltonians for various systems, either on the lattice or described by continuum theories, and for various bipartitions. Some results we obtained in this direction have been reported in chapters 5, 6 and 7 .

The entanglement entropies (1.2.3) and (1.2.6) do not take into account the spatial structure of the bipartite entanglement inside the subsystem A. For this purpose, the contours for the

entanglement entropies have been introduced [27–29]. Let us partition A into $\mathcal{N}$ cells labeled by an index i [7]. The contour function $s_A^{(n)}(i) : A \to \mathbb{R}$ must satisy the following two conditions

$$S_A^{(n)} = \sum_{i=1}^{\mathcal{N}} s_A^{(n)}(i) \qquad\qquad s_A^{(n)}(i) \geqslant 0\,. \tag{1.2.10}$$

Thus, $s_A^{(n)}(i)$ measures the contribution of the i-th cell to the total n-th Rényi entropy (or, when $n \to 1$, to the total entanglement entropy). Additional requirements have been introduced in [28], but they are not sufficient to determine a unique prescription for computing this quantity. For free fermionic lattices and for harmonic lattices, explicit constructions have been proposed in [28] and [29] respectively. In Appendix A these proposals are reported and the main formulas for determining the entanglement entropies in free fermionic and bosonic lattice models are provided [4, 5, 10]. Let us stress that, like the entanglement Hamiltonian in (1.2.2), also the contour for the entanglement entropies cannot be determined from the entanglement spectrum only.

In chapter 7 we have studied the temporal evolution of the contour for the entanglement entropies after a global quantum quench in a free fermionic chain and in a harmonic chain. A quantitative formula based on the quasi-particle picture introduced in [82] has been obtained and it has been checked against numerical computations.

1.2.2 Entanglement Hamiltonians in quantum field theory

In Sec. 1.2.1 we stressed that the reduced density matrix or its logarithm, namely the entanglement Hamiltonian, provide the complete information about the bipartite entanglement between a subsystem A and its complement. In this subsection we review some results about the entanglement Hamiltonians in quantum field theories and in lattice models. We also focus on the non-trivial task of obtaining from the entanglement Hamiltonian of a given lattice model the corresponding result in the underlying continuum field theory.

In relativistic quantum field theories, there are special cases in which $\widehat{K}_A$ defined in (1.2.2) can be written as an integral over A of the stress-energy tensor $\widehat{T}_{\mu\nu}$ weighted with a suitable function. Consider the ground state of a $d+1$-dimensional quantum field theory (QFT) in Minkowsky spacetime. If the subsystem A is half of the space, namely $A = \{\boldsymbol{x} \equiv (x_1, \dots, x_d) |\, x_1 > 0\}$, the entanglement Hamiltonian reads [171–173]

$$\widehat{K}_A = 2\pi \int_A x_1 \widehat{T}_{00}(\boldsymbol{x}) d^d\boldsymbol{x} \tag{1.2.11}$$

which is the generator of the Lorentz boosts along the x_1 direction restricted to the subsystem A. The result (1.2.11) is known as Bisognano-Wichmann theorem and it has been first proved in the context of Algebraic Quantum Field Theory. In $d+1$-dimensional CFTs, (1.2.11) can be mapped into the case when A is a ball of radius R, leading to [174, 175]

$$\widehat{K}_A = 2\pi \int_A \frac{R^2 - |\boldsymbol{x}|^2}{2R} \widehat{T}_{00}(\boldsymbol{x}) d^d\boldsymbol{x} \tag{1.2.12}$$

where $|\boldsymbol{x}|^2$ is the squared modulus of the position vector $\boldsymbol{x}$. Remarkably, (1.2.11) and (1.2.12) hold in any dimension of the spacetime.

[7] These cells may correspond either to a single site if we are considering a lattice model or to an infinitesimal element $\mathrm{d}^d\boldsymbol{x}$ if we are considering a d-dimensional continuum theory

In a $1+1$-dimensional CFT at equilibrium there are bipartitions where A is an interval such that its entanglement Hamiltonian can be written as

$$\widehat{K}_A \,=\, \ell \int_A \beta(x)\, \widehat{T}_{00}(x)\, dx \tag{1.2.13}$$

where ℓ is the length of A and $\beta(x)$ depends on the bipartition and on the quantum state of the system. The expression (1.2.13) holds, for instance, when we consider a single interval, either in an infinite system in the ground state or at finite temperature, or at zero temperature in a finite system with spatially periodic boundary conditions. Other interesting examples for CFTs in their ground states are when A is an interval at the beginning of a semi-infinite system with one external boundary and when A is at the beginning of a finite interval, as long as the boundary conditions at the two ends are the same. Some of these cases have been discussed in [147,176–179]. A generalisation of (1.2.13) has been obtained in [147] to study also time-dependent settings, as, for instance, the entanglement Hamiltonian of a half infinite line after a quantum quench.

In most cases (1.2.13) is not valid and in some particular examples, where a detailed knowledge of the underlying CFT is available, the entanglement Hamiltonians have been studied finding that the local expression (1.2.13) is modified by the introduction of bi-local and non local contributions [180–184]. Further analyses of entanglement Hamiltonians in free quantum field theories can be found in [185–190].

For the simplest bipartition, where A is a single interval on an infinite line and the CFT is in its ground state, the function $\beta(x)$ is the following parabola [174, 175]

$$\beta(x) = 2\pi\, \frac{x}{\ell} \left(1 - \frac{x}{\ell}\right) . \tag{1.2.14}$$

Let us stress that (1.2.13) with $\beta(x)$ given by (1.2.14) corresponds to (1.2.12) with $d = 1$ once we perform the change of variable $x \to x - R$ and we set $2R = \ell$.

Recovering (1.2.13) and (1.2.14) as continuum limit of the entanglement Hamiltonian of a block made by L consecutive sites in a critical quantum chain turns out to be a non-trivial problem. For free fermions on an infinite chain described by the Hamiltonian

$$\widehat{H} = -\sum_j \left(\hat{c}^\dagger_{j+1}\hat{c}_j + \text{h.c.}\right) \tag{1.2.15}$$

defined in terms of the fermionic creation and annihilation operators $\hat{c}^\dagger_j$ and $\hat{c}_j$ satisfying canonical anti-commutation relations $\{\hat{c}^\dagger_j, \hat{c}_i\} = \delta_{i,j}$, one finds that $\widehat{K}_A$, when the system is in its ground state, can be written as [4, 191]

$$\widehat{K}_A = \sum_{i,j=1}^{L} T_{i,j}\hat{c}^\dagger_i\hat{c}_j\,. \tag{1.2.16}$$

Computing the matrix T through the two-point correlators $\langle\hat{c}^\dagger_i\hat{c}_j\rangle$, with $i, j = 1, \ldots, L$ [4,191], one finds that $\widehat{K}_A$ in (1.2.16) contains nearest-neighbour hopping which does not quite vary parabolically and, in addition, hopping to more distant neighbours with smaller amplitudes [192]. However, it has been shown numerically [193] and also analytically [179] that by properly including the longer-range terms in the continuum limit one recovers the conformal results (1.2.13) and (1.2.14) for $\beta(x)$.

A similar analysis can be performed for a system of coupled oscillators. Indeed, for a d-dimensional harmonic lattice described by the Hamiltonian (1.1.10), when the system is in its

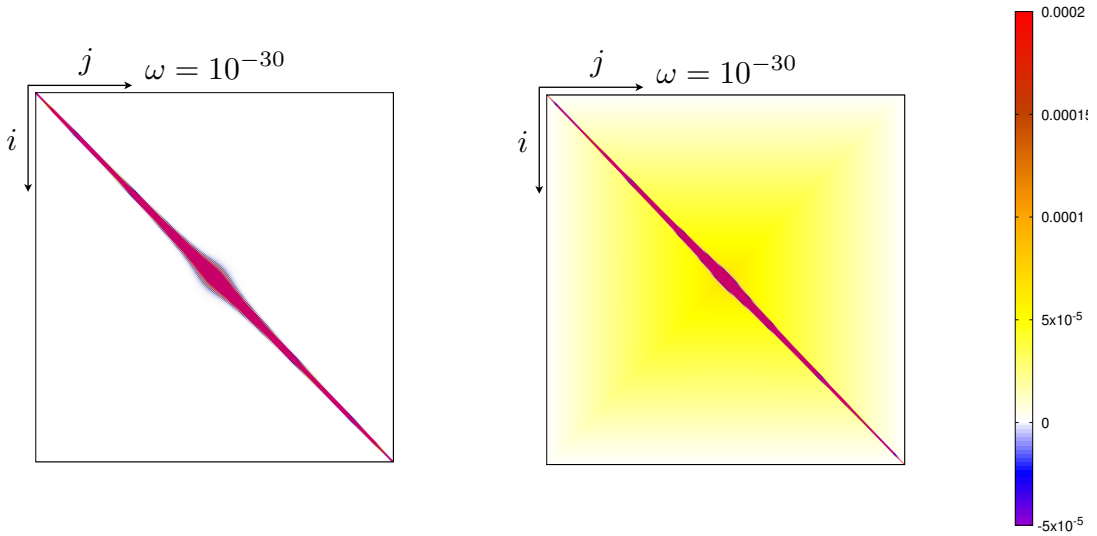

Figure 1.6: Contour plots of the matrices M (left panel) and N (right panel) in (1.2.17) obtained for a block of consecutive $L = 400$ sites in an infinite harmonic chain. Figure adapted from [102].

ground state, the entanglement Hamiltonian of a subsystem made by L sites can be written as [10, 191]

$$\widehat{K}_A = \sum_{i,j=1}^{L} \left(M_{i,j}\, \hat{q}_i\, \hat{q}_j + N_{i,j}\, \hat{p}_i\, \hat{p}_j \right) \tag{1.2.17}$$

where the matrices M and N can be obtained from the restricted correlators $\langle \hat{q}_i \hat{q}_j \rangle$ and $\langle \hat{p}_i \hat{p}_j \rangle$, with $i, j = 1, \dots, L$. Despite the generality of (1.2.17), we consider the case when A is a block made by consecutive sites in an infinite harmonic chain. One finds that the matrices M and N exhibit a highly non-trivial structure which, again, leads to long-range couplings in $\widehat{K}_A$ [101,193]. A detailed discussion of this fact is reported in chapter 5, but an anticipation is shown in Fig. 1.6 where the contour plots of the matrices M (left panel) and N (right panel), obtained for a block made by $L = 400$ sites in an infinite harmonic chain with $\omega = 10^{-30}$, are reported (for infinite harmonic chains the parameter ω cannot be set sharply to zero, as explained, for instance, in chapter 5). These plots suggest that, also for coupled oscillators in one dimension, the long range terms have to be taken into account in computing the continuum limit of the entanglement Hamiltonian. For this purpose, a suitable procedure is developed in chapter 5 (see also [101]), where the CFT results (1.2.13) and (1.2.14) have been recovered from massless harmonic chains through numerical computations. In Fig. 1.7 we show the outcomes of this procedure for studying the continuum limit of the entanglement Hamiltonians. The numerical data (symbols) obtained for a block made by L consecutive sites in an infinite harmonic chain perfectly match the CFT prediction (1.2.14) (red curves).

In chapters 6 and 7 we exploit some lattice results for studying the entanglement Hamiltonians in free fermionic and bosonic models in gapped regimes (chapter 6) and out of equilibrium (chapter 7). Further investigations about the entanglement Hamiltonians in free lattice models can be found in [178,194–201]. Some results also exist for small intervals in interacting fermion systems [202,203].

The entanglement spectrum can be obtained from the eigenvalues of the entanglement Hamiltonian. The gaps in the entanglement spectrum are interesting quantities to study and, in particular,

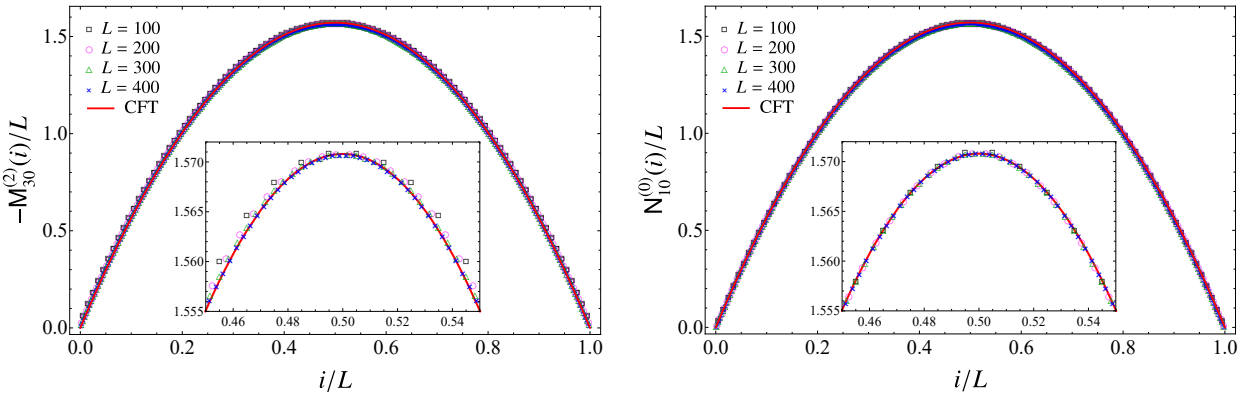

Figure 1.7: Results from the procedure reported in chapter 5 for studying the continuum limit of the entanglement Hamiltonians in massless harmonic chains. The numerical data have been obtained for a block made by L consecutive sites in an infinite chain and the red curves correspond to (1.2.14). Figure taken from [101].

one can consider the gaps with respect to the largest eigenvalue

$$g_k \equiv \log \lambda_{\max} - \log \lambda_k \,. \tag{1.2.18}$$

In a two dimensional QFT in imaginary time, a useful way to regularise the ultraviolet (UV) divergences consists in removing infinitesimal disks whose radius is the UV cutoff around the entangling points of the bipartition [6, 146, 147, 201]. In two-dimensional CFT, this regularisation procedure leads to a Boundary Conformal Field Theory (BCFT) [204–206] if proper conformal boundary conditions are imposed along the boundaries in the euclidean spacetime (both the boundaries given by the physical boundaries of the system and the ones due to this regularisation procedure must be taken into account). If we consider a two-dimensional CFT and one of the bipartitions mentioned below (1.2.13), it has been found that [147]

$$\frac{g_r}{g_1} = \frac{\Delta_r}{\Delta_1} \tag{1.2.19}$$

where $r \geqslant 1$ and $\Delta_r > 0$ are the non vanishing elements of the conformal spectrum (made by conformal dimensions of the primary fields and of their descendants) of the corresponding BCFT. In chapters 5 and 7 we study numerically these quantities for critical lattice models in static and out of equilibrium configurations respectively, in order to get insights about the operator content of their underlying field theories. Further numerical evidences that the conformal spectrum of a BCFT provides the entanglement spectrum have been obtained at equilibrium in [207, 208] and out of equilibrium in [209].

1.2.3 Entanglement entropies in $1+1$-dimensional quantum field theories and symmetry resolution

In the framework of quantum field theory, one of the most powerful theoretical tools to compute the moments of the reduced density matrix is the *path integral approach*. Consider a $1+1$-dimensional quantum field theory, which, after the Wick rotation to imaginary time $t \to \mathrm{i}\tau$, can be formulated as a Euclidean field theory in two dimensions.

We denote by $\{\hat{\phi}_x\}$ a complete set of local commuting observables and by $\{\phi_x\}$ and $|\{\phi_x\}\rangle$ their corresponding eigenvalues and eigenvectors. The elements of the density matrix of this system in

a thermal state at temperature β^{-1} can be written as the following path integral on the imaginary time interval $(0, \beta)$ [9, 11]

$$\langle \{\phi'_x\}|\hat{\rho}|\{\phi_x\}\rangle = Z^{-1} \int \mathcal{D}\phi(y,\tau)\, e^{-\beta S_E} \prod_x \delta\big(\phi(y,0) - \phi_x\big) \prod_{x'} \delta\big(\phi(y,\beta) - \phi_{x'}\big) \tag{1.2.20}$$

where $S_E = \int_0^\beta d\tau \mathcal{L}_E$ is the Euclidean action of the theory and $Z = \mathrm{Tr}\hat{\rho}$ provides the normalisation to one of the matrix in (1.2.20). Taking the limit $\beta \to \infty$, one recovers the density matrix of the theory on an infinite line in its ground state.

In the path integral description, the trace corresponds to identify the field configurations at $\tau = 0$ and $\tau = \beta$. Thus, the reduced density matrix (1.2.1) is obtained by identifying only the points on the edges that do not belong to A and therefore it can be represented as a cylinder (or a plane, in the limit $\beta \to \infty$) with a cut occurring for $\tau = 0 = \beta$ and $x \in A$.

As explained in Sec. 1.2.1, we are interested in $\mathrm{Tr}\hat{\rho}_A^n$. Considering n copies of $\hat{\rho}_A$, the trace we want to compute is obtained by sewing cyclically the different planes along their cuts and identifying the field configurations on A. Let us stress that now n is a positive integer number. Through this procedure we end up with a world-sheet given by a n-sheeted Riemann surface $\mathcal{R}_n$ and $\mathrm{Tr}\hat{\rho}_A^n$ is given by the partition function on $\mathcal{R}_n$, denoted by $Z_n(A)$, as

$$\mathrm{Tr}\hat{\rho}_A^n = \frac{Z_n(A)}{Z^n}\,. \tag{1.2.21}$$

Using (1.2.6), the expression (1.2.21) provides the Rényi entropies for positive integer values of n and, when a unique analytic continuation to complex values of n exists, the entanglement entropy as

$$S_A = -\lim_{n\to 1} \frac{\partial}{\partial n} \frac{Z_n(A)}{Z^n}\,. \tag{1.2.22}$$

This is the *replica trick* for the entanglement entropy [6, 8, 9], which has been also generalised for computing other entanglement-related quantities as the negativity [210,211], the relative entropies [212, 213] and the trace distance [214, 215].

In general, computing the partition function on a n-sheeted Riemann surface can be very complicated. For this reason, in the past years various techniques have been developed and many results have been successfully obtained [9–11,22,216–223]. Among these, we find it worth mentioning here the *twist fields approach* [9,11,216], briefly reviewed in Sec. 8.2, which have been exploited in various two-dimensional QFTs, as, for instance, CFTs, massive field theories [224–227] and integrable field theories [216, 228–230]. In particular, when applied to (1+1) dimensional CFTs in their ground states, the replica trick leads to the famous scaling results [6–9, 11, 231, 232]

$$S_A = \frac{c}{3} \ln \frac{\ell}{\epsilon} \qquad\qquad S_A^{(n)} = \frac{c}{6} \frac{n+1}{n} \ln \frac{\ell}{\epsilon} \tag{1.2.23}$$

when the subsystem A is an interval of length ℓ embedded in an infinite one-dimensional system. In (1.2.23), c is the central charge of the CFT and $\epsilon \ll \ell$ is an ultraviolet cutoff, such that, when $\epsilon \to 0$, the entanglement entropies diverge, as typically happens in quantum field theories [6,8,9,20,21,146, 147]. The results in (1.2.23) can be generalised to CFT either at finite temperature or at finite size by exploiting the conformal invariance of the theory and suitable coordinate transformations [9,11]. Furthermore, results for more complicated bipartitions, like for instance multiple disjoint intervals [180, 217, 233–237], for CFTs in excited states [238, 239] and for inhomogeneous systems [240–242] have been obtained through this approach.

An important arena for studying the entanglement in strongly interacting CFT is provided by the AdS/CFT correspondence. In this context, the gravitational dual of the entanglement

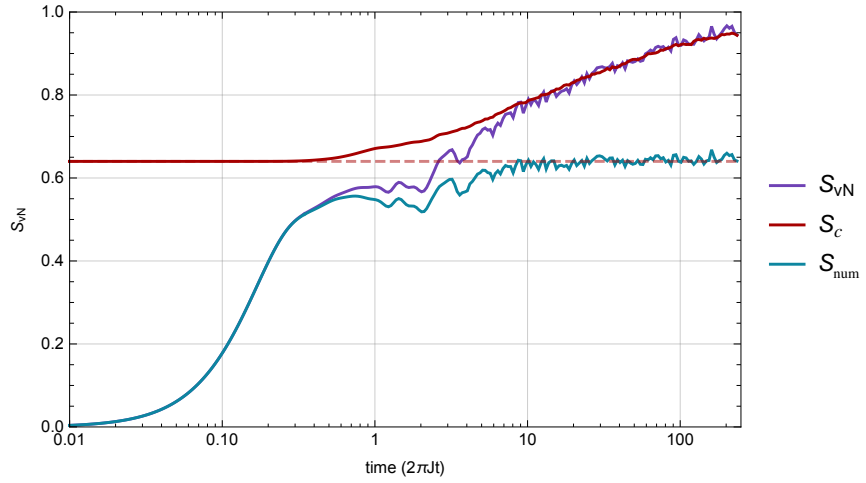

Figure 1.8: The results obtained in [25] for the temporal evolutions of the von Neumann ($S_{\rm vN}$), the configurational (S_c) and the number ($S_{\rm num}$) entanglement entropies for half-system in a one-dimensional interacting bosonic chain with disorder, where J parametrises the interaction strength. The definitions of S_c and $S_{\rm num}$ and their relation with the von Neumann entanglement entropy are given in (1.2.28). For convenience, the configurational entropy is vertically shifted with respect to its vanishing initial value. Figure taken from [25].

entropy (1.2.3) has been conjectured by Ryu and Takayanagi in [48, 49]. Consider a constant time slice of the CFT defined on the d-dimensional boundary of AdS_{d+1} and introduce a spatial bipartition $A\cup B$. The entanglement entropy S_A in the strongly coupled regime of the field theory is obtained by computing the area $\mathcal{A}_A$ of the minimal area surface anchored to the boundary of A and extending into the gravitational bulk. It reads

$$S_A = \frac{\mathcal{A}_A}{4G_N} \tag{1.2.24}$$

where G_N is the Newton's constant. In AdS_3, which is dual to a two dimensional CFT in its ground state, when A is a single interval of length ℓ on its boundary, using (1.2.24) one recovers the result for S_A in (1.2.23) (remind that the holographic computation holds only when $c \gg 1$). In this framework, ϵ is a UV cutoff introduced to regularise the minimal area $\mathcal{A}_A$ which is divergent because the AdS spacetime is non compact.

The formula (1.2.24) is one of the major recent breakthroughs in the context of the AdS/CFT correspondence and it has shown a deep connection between the entanglement and the geometry of the spacetime. In last fifteen years, this result has inspired many attempts to construct a bridge between quantum information and quantum gravity, as for instance the proposals (1.1.18) and (1.1.21) for the holographic complexity.

The covariant generalisation of (1.2.24), which allows to study time dependent gravitational backgrounds, has been proposed in [243]. Various aspects of the holographic entanglement entropy have been studied in the past years, both in static and in time dependent settings (see the reviews [244, 245] and references therein).

In recent times, it became clear the importance of understanding the relation between entanglement and symmetries and in particular how entanglement is shared between the various symmetry sectors of a theory [95, 96]. Consider a system with an internal $U(1)$ symmetry and its usual bipartition into the two subsystems A and B. The charge operator $\widehat{Q}$ is the generator of the symmetry

and we assume it obeys $\widehat{Q}_A \oplus \widehat{Q}_B = \widehat{Q}$, where $\widehat{Q}_i$ is the charge in the subsystem i. If the system described by the density matrix $\hat{\rho}$ is in an eigenstate of $\widehat{Q}$, then $[\hat{\rho}, \widehat{Q}] = 0$. Tracing out the degrees of freedom of B, we obtain the reduced density matrix of A, as in (1.2.1). Hence, taking the trace over B of $[\hat{\rho}, \widehat{Q}] = 0$, we find that $[\hat{\rho}_A, \widehat{Q}_A] = 0$. This means that $\hat{\rho}_A$ has a block-diagonal structure where each block corresponds to an eigenvalue q of $\widehat{Q}_A$. The density matrix $\hat{\rho}_A(q)$ corresponding to an eigenvalue q is obtained by projecting $\hat{\rho}_A$ onto the eigenspace of $\widehat{Q}_A$ with fixed q, as induced by the projector Π_q. Therefore we can write

$$\hat{\rho}_A = \oplus_q p(q)\hat{\rho}_A(q) \tag{1.2.25}$$

where $p(q)$ is the probability of finding q in a measurement of $\widehat{Q}_A$ in the reduced density matrix $\hat{\rho}_A$, i.e. $p(q) = \mathrm{Tr}\Pi_q\hat{\rho}_A$. Within this convention, the density matrices $\hat{\rho}_A(q)$ of different blocks are normalised as $\mathrm{Tr}\hat{\rho}_A(q) = 1$. The amount of entanglement shared by A and B in each symmetry sector can be computed through the *symmetry resolved Rényi entropies*, defined as

$$S_A^{(n)}(q) \equiv \frac{1}{1-n} \ln \mathrm{Tr}\hat{\rho}_A^n(q). \tag{1.2.26}$$

The limit $n \to 1$ gives the *symmetry resolved entanglement entropy*, i.e.

$$S_A(q) \equiv -\mathrm{Tr}\hat{\rho}_A(q) \ln \hat{\rho}_A(q). \tag{1.2.27}$$

The total von Neumann entanglement entropy associated to $\hat{\rho}_A$ in (1.2.25) splits into [170]

$$S_A = \sum_q p(q) S_A(q) - \sum_q p(q) \ln p(q) \equiv S_c + S_{\mathrm{num}}\,. \tag{1.2.28}$$

The two contributions S_c and S_{num} are known as configurational and fluctuation (or number) entanglement entropy [25] and account for the entanglement within symmetry sectors and fluctuations thereof, respectively. The configurational entropy is also related to the operationally accessible entanglement entropy of Refs. [246–248], while the number entropy is the subject of a substantial recent activity [25, 249–252].

There are various physical motivations for shading light on the interplay between symmetry and entanglement. For example, one motivation comes from a recent experiment studying the time evolution of the symmetry resolved entanglement in systems with many-body localisation [25]. In the presence of both disorder and interaction, the dynamics of configurational and number entanglement occur over different time scales: the number entanglement quickly saturates to an asymptotic value while the configurational one exhibits a slow logarithmic growth [25], providing a nice physical explanation of an older finding [12, 253]. This is shown in Fig. 1.8, where a plot with the results of [25] has been reported.

The possibility of measuring some of the quantities introduced above sparked the interest in further studying how the entanglement is related to the internal symmetries of a system, leading to many results concerning critical ones [96, 97, 251, 254–258]. A surprising finding is that conformal invariance forces the entanglement entropy to be equally distributed among the different sectors of a $U(1)$ symmetric theory [97]. It is an open issue to understand whether and when such *equipartition of entanglement* survives away from criticality. The goal of chapters 8 and 9 is to answer this question. More precisely, in chapter 8 we try to understand how the entanglement splits into the different charge sectors of a free massive two dimensional QFT endowed with a $U(1)$ global symmetry. In Fig. 1.9 we have reported some of the results derived in Sec. 8.4 for the symmetry resolved entanglement entropies in a massive Dirac field theory. The solid lines represent the field theoretical predictions which are benchmarked with exact numerical lattice computations

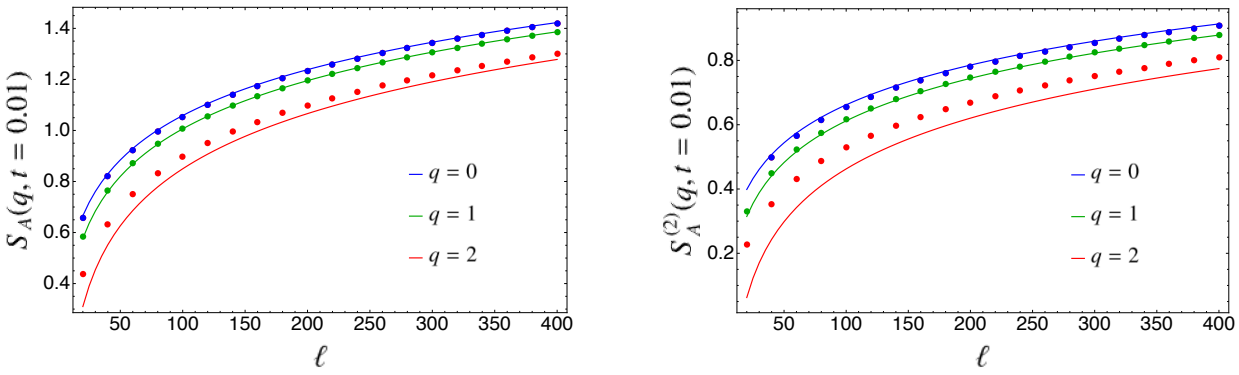

Figure 1.9: Symmetry resolved entanglement entropies of an interval of length ℓ for a massive Dirac field theory with mass $m = t/\ell$ in a sector with charge q. A detailed derivation of these results is reported in Sec. 8.4. Figure taken from [104].

(symbols). In chapter 9 we study the symmetry resolved entanglement in integrable gapped lattice models exploiting corner transfer matrix (CTM) techniques [259–262]. This approach is based on the fact that we can relate the reduced density matrix of a half-infinite integrable quantum chain to the CTM of a corresponding two-dimensional integrable model on a square lattice.

We find it worth stressing that the calculation of the symmetry resolved entropies by the definition (1.2.26) requires the knowledge of the entanglement spectrum of $\hat{\rho}_A$ and its resolution in the charge sectors. However, this is a difficult task, especially for an analytic derivation. In [96], a simple generalisation of the replica trick has been proposed to relate the symmetry resolved quantities to the moments of $\hat{\rho}_A$ on a modified Riemann surface: we refer to them as *charged moments*. We define and employ these quantites in chapter 8 and in Sec. 9.3. Nonetheless, there exist cases where the symmetry resolution of the entanglement spectrum is known analytically [263, 264]. In Sec. 9.4 we exploit such results for the XXZ spin chain to compute the symmetry resolved entanglement entropies.

Part I

Circuit complexity of bosonic mixed Gaussian states

Chapter 2

Complexity from Fisher information geometry

2.1 Introduction

The motivations discussed in Sec. 1.1 sparked the interest in studying the properties of the circuit complexity in many-body quantum systems. The free scalar and the free fermion are the simplest models to consider. For these models, it is worth focussing on the Gaussian states because they provide an interesting arena that includes important states (e.g. the ground state and the thermal states) and that has been largely explored in the literature of quantum information [77,78,265–267].

Various studies have investigated the complexity of quantum circuits made by pure Gaussian states in lattice models [35–44,79]. In these cases the gates implement only unitary transformations of the state. It is important to extend these analyses by considering quantum circuits that involve also mixed states; hence it is impossible to construct them by employing only unitary gates [120].

A method to quantify the complexity of circuits involving mixed states has been recently investigated in [79]. In this approach, the initial mixed state is purified by adding ancillary degrees of freedom and the resulting pure state is obtained by minimising the circuit complexity within the set of pure states.

In this chapter we explore a way to evaluate the complexity of quantum circuits made by mixed states within the framework of the Information Geometry [93, 121, 122]. The method holds for bosonic Gaussian states and it does not require the introduction of ancillary degrees of freedom. It relies on the fact that, whenever the states provide a Riemannian manifold and the available gates allow to reach every point of the manifold, the standard tools of differential geometry can be employed to find the optimal circuit connecting two states. Since the pure states provide a submanifold of this manifold, this analysis also suggests natural quantum circuits to purify a given mixed state.

We focus only on the bosonic Gaussian states occurring in the Hilbert space of harmonic lattices in any number of dimensions. These states are completely characterised by their covariance matrix, a real symmetric and positive definite matrix whose elements can be written in terms of the two point correlators, and by their first moments. In the following we explore the bosonic Gaussian mixed states with vanishing first moments. This set can be described by a proper subset of the Riemann manifold defined by the symmetric and positive definite matrices [124–127,134] equipped with the metric provided by the Fisher information matrix [91–93, 121, 123]. We remark that our analysis considers quantum circuits that are made by Gaussian states only. Despite this important simplifying assumption, the resulting quantum circuits are highly non trivial because non unitary states are involved in the circuit.

The chapter is organised as follows. In Sec. 2.2 we introduce the quantities and the main results employed throughout the chapter: the covariance matrix through the Gaussian Wigner function, the Fisher-Rao distance between covariance matrices and the corresponding geodesics, that provide the optimal circuits. In Sec. 2.3 we provide explicit expressions to evaluate the spectrum complexity and the basis complexity, by employing also the first law of complexity [268, 269]. Moreover, we discuss the purification of a mixed state through particular optimal circuits and some lower and upper bounds on the complexity. In Sec. 2.4 we focus on the circuits that do not contain pure states because they can be also parameterised through the entanglement Hamiltonian matrices. The Gaussian channels underlying the optimal circuits are briefly discussed in Sec. 2.5. In Sec. 2.6 we describe the approach to the complexity of mixed states based on the purification of a mixed state through ancillary degrees of freedom. The last analysis reported in Sec. 2.7 focuses on periodic and infinite harmonic chains in one spatial dimension. Numerical results are reported for the complexity between thermal states and the one between reduced density matrices. Finally, in Sec. 2.8 we summarise our results and discuss future directions.

2.2 Complexity as Fisher-Rao distance and the optimal path

In Sec. 2.2.1 we introduce Gaussian Wigner functions (defined in terms of the covariance matrix and of the first moment) to characterise a generic Gaussian state. The Fisher-Rao distance is defined in Sec. 2.2.2, while in Sec. 2.2.3 we discuss the Williamson's decomposition of the covariance matrix, a crucial tool largely employed throughout the thesis. The optimal circuit in the Fisher information geometry is analysed in Sec. 2.2.4. Finally, the special cases given by pure states and thermal states are explored in Sec. 2.2.5 and Sec. 2.2.6 respectively.

2.2.1 Gaussian states in harmonic lattices

The Hamiltonian of a spatially homogeneous harmonic lattice made by N sites with nearest neighbour spring-like interaction with spring constant κ reads

$$\widehat{H} \,=\, \sum_{i=1}^{N} \left(\frac{1}{2m}\, \hat{p}_i^2 + \frac{m\omega^2}{2}\, \hat{q}_i^2 \right) + \sum_{\langle i,j \rangle} \frac{\kappa}{2} (\hat{q}_i - \hat{q}_j)^2 \,=\, \frac{1}{2}\, \hat{\boldsymbol{r}}^{\mathrm{t}} H^{\mathrm{phys}}\, \hat{\boldsymbol{r}} \tag{2.2.1}$$

where the second sum is performed over the nearest neighbour sites. The position and momentum operators $\hat{q}_i$ and $\hat{p}_i$ are hermitian and satisfy the canonical commutation relations $[\hat{q}_i, \hat{q}_j] = [\hat{p}_i, \hat{p}_j] = 0$ and $[\hat{q}_i, \hat{p}_j] = \mathrm{i}\delta_{ij}$. The boundary conditions do not change the following discussion, although they are crucial to determine the explicit expressions of the correlators. Collecting the position and momentum operators into the vector $\hat{\boldsymbol{r}} \equiv (\hat{q}_1, \dots, \hat{q}_N, \hat{p}_1, \dots, \hat{p}_N)^{\mathrm{t}}$, the canonical commutation relations can be written in the form $[\hat{r}_i, \hat{r}_j] = \mathrm{i} J_{ij}$, where J is the standard symplectic matrix

$$J \equiv \begin{pmatrix} \mathbf{0} & \mathbf{1} \\ -\mathbf{1} & \mathbf{0} \end{pmatrix} \tag{2.2.2}$$

and we have denoted by $\mathbf{1}$ the $N \times N$ identity matrix and $\mathbf{0}$ the matrix with the proper size having all its elements equal to zero. Notice that $J^2 = -\mathbf{1}$ and $J^{\mathrm{t}} = J^{-1} = -J$.

The real symplectic group $\mathrm{Sp}(2N, \mathbb{R})$ is made by the real $2N \times 2N$ matrices S characterising the linear transformations $\hat{\boldsymbol{r}} \to \hat{\boldsymbol{r}}' = S\, \hat{\boldsymbol{r}}$ that preserve the canonical commutation relations [270–274]. This condition is equivalent to $SJS^{\mathrm{t}} = J$. Given $S \in \mathrm{Sp}(2N, \mathbb{R})$, it can be shown that $\det(S) = 1$, $S^{\mathrm{t}} \in \mathrm{Sp}(2N, \mathbb{R})$ and $S^{-1} = JS^{\mathrm{t}}J^{-1}$, hence $S^{-\mathrm{t}} = J^{\mathrm{t}}SJ$ (we have adopted the notation $M^{-\mathrm{t}} \equiv (M^{\mathrm{t}})^{-1}$). The real dimension of $\mathrm{Sp}(2N, \mathbb{R})$ is $N(2N+1)$.

The density matrix $\hat{\rho}$, that characterises a state of the quantum system described by the Hamiltonian (2.2.1), is a positive definite, hermitean operator whose trace is normalised to one. When the state is pure, the operator $\hat{\rho}$ is a projector.

A useful way to characterise a density matrix is based on the Wigner function $w(\boldsymbol{r})$, that depends on the vector $\boldsymbol{r}$ made by $2N$ real components. The Wigner function is defined through the Wigner characteristic function associated to $\hat{\rho}$, that is [77, 78, 267]

$$\chi(\boldsymbol{\xi}) \equiv \mathrm{Tr}\big(\hat{\rho}\, e^{\mathrm{i}\,\hat{\boldsymbol{r}}^{\mathrm{t}}\, J\, \boldsymbol{\xi}}\big) = \mathrm{Tr}\big(\hat{\rho}\, \widehat{D}_{\boldsymbol{\xi}}\big) \qquad\qquad \boldsymbol{\xi} \in \mathbb{R}^{2N} \tag{2.2.3}$$

where in the last step we have introduced the displacement operator as

$$\widehat{D}_{\boldsymbol{a}} \equiv e^{-\mathrm{i}\boldsymbol{a}^{\mathrm{t}}\, J\, \hat{\boldsymbol{r}}} \qquad\qquad \boldsymbol{a} \in \mathbb{R}^{2N}\,. \tag{2.2.4}$$

The Fourier transform of the Wigner characteristic function provides the Wigner function

$$w(\boldsymbol{r}) \equiv \frac{1}{(2\pi)^{2N}} \int \chi(\boldsymbol{\xi})\, e^{-\mathrm{i}\,\boldsymbol{r}^{\mathrm{t}}\, J\, \boldsymbol{\xi}}\, d\boldsymbol{\xi} \tag{2.2.5}$$

where $d\boldsymbol{\xi} = \prod_{i=1}^{2N} d\xi_i$ denotes the integration over the $2N$ real components of $\boldsymbol{\xi}$.

In this chapter we focus on the Gaussian states of the harmonic lattices, which are the states whose Wigner function is Gaussian [5, 77, 266, 275–278]

$$w_{\mathrm{G}}(\boldsymbol{r}; \gamma, \langle \hat{\boldsymbol{r}} \rangle) \equiv \frac{e^{-\frac{1}{2}(\boldsymbol{r}-\langle \hat{\boldsymbol{r}} \rangle)^{\mathrm{t}}\, \gamma^{-1}\, (\boldsymbol{r}-\langle \hat{\boldsymbol{r}} \rangle)}}{(2\pi)^N \sqrt{\det(\gamma)}}\,. \tag{2.2.6}$$

The $2N \times 2N$ real, symmetric and positive definite matrix γ is the covariance matrix of the Gaussian state, whose elements can be defined in terms of the anticommutator of the operators $\hat{r}_i$ as follows

$$\gamma_{i,j} = \frac{1}{2}\langle \{ \hat{r}_i - \langle \hat{r}_i \rangle\,, \hat{r}_j - \langle \hat{r}_j \rangle \} \rangle = \frac{1}{2}\langle \{ \hat{r}_i\,, \hat{r}_j \} \rangle - \langle \hat{r}_i \rangle \langle \hat{r}_j \rangle = \langle \hat{r}_i\, \hat{r}_j \rangle - \langle \hat{r}_i \rangle \langle \hat{r}_j \rangle - \frac{\mathrm{i}}{2}\, J_{i,j}\,. \tag{2.2.7}$$

The covariance matrix γ is determined by $N(2N+1)$ real parameters. The expressions (2.2.6) and (2.2.7) tell us that the Gaussian states are completely characterised by the one-point correlators (first moments) and by the two-points correlators (second moments) of the position and momentum operators collected into the vector $\hat{\boldsymbol{r}}$. It is important to remark that the validity of the uncertainty principle imposes the following condition on the covariance matrix [77, 271]

$$\gamma + \frac{\mathrm{i}}{2}\, J \,\geqslant\, 0\,. \tag{2.2.8}$$

In [126] a real, positive matrix with an even size and satisfying (2.2.8) is called Gaussian matrix. Thus, every symmetric Gaussian matrix provides the covariance matrix of a Gaussian state.

A change of base $\hat{\boldsymbol{r}} \to \hat{\boldsymbol{r}}' = S\, \hat{\boldsymbol{r}}$ characterised by $S \in \mathrm{Sp}(2N, \mathbb{R})$ induces the transformation $\gamma \to \gamma' = S\, \gamma\, S^{\mathrm{t}}$ on the covariance matrix.

In this thesis we mainly consider Gaussian states with vanishing first moments, i.e. having $\langle \hat{r}_i \rangle = 0$. In this case the generic element of covariance matrix (2.2.7) becomes

$$\gamma_{i,j} = \frac{1}{2}\langle \{ \hat{r}_i\,, \hat{r}_j \} \rangle = \mathrm{Re}\big[\langle \hat{r}_i\, \hat{r}_j \rangle\big] \tag{2.2.9}$$

and the Wigner function (2.2.6) slightly simplifies to

$$w_{\mathrm{G}}(\boldsymbol{r}; \gamma) = \frac{e^{-\frac{1}{2}\, \boldsymbol{r}^{\mathrm{t}}\, \gamma^{-1}\, \boldsymbol{r}}}{(2\pi)^N \sqrt{\det(\gamma)}}\,. \tag{2.2.10}$$

where we have lightened the notation with respect to (2.2.6) by setting $w_{\mathrm{G}}(\boldsymbol{r}; \gamma) \equiv w_{\mathrm{G}}(\boldsymbol{r}; \gamma, \boldsymbol{0})$. The quantities introduced above characterise generic mixed Gaussian states. The subclass made by the pure states is discussed in Sec. 2.2.3.

2.2.2 Fisher-Rao distance

The set made by the probability density functions (PDF's) parameterised by the quantities γ is a manifold. In information geometry, the distinguishability between PDF's characterised by two different sets of parameters γ_1 and γ_2 is described through a scalar quantity $D(\gamma_1, \gamma_2)$ called divergence [93, 122], a function such that $D(\gamma_1, \gamma_2) \geqslant 0$ and $D(\gamma_1, \gamma_2) = 0$ if and only if $\gamma_1 = \gamma_2$ and

$$D(\gamma, \gamma + d\gamma) = \frac{1}{2} \sum_{i,j} g_{ij}\, dy_i dy_j + O\big((dy)^3\big) \tag{2.2.11}$$

where g_{ij} is symmetric and positive definite and $\boldsymbol{y}$ denotes the vector collecting the independent parameters that determine $\gamma = \gamma(\boldsymbol{y})$. In general $D(\gamma_1, \gamma_2) \neq D(\gamma_2, \gamma_1)$; nonetheless, notice that the terms that could lead to the loss of this symmetry are subleading in the expansion (2.2.11). Thus, every divergence D introduces a metric tensor g_{ij} that makes $\mathcal{M}$ a Riemannian manifold.

A natural requirement for a measure of distinguishability between states is the information monotonicity [93, 122]. Let us denote by $\boldsymbol{s} = \boldsymbol{s}(\boldsymbol{r})$ a change of variables in the PDF's and by $\bar{D}(\gamma_1, \gamma_2)$ the result obtained from $D(\gamma_1, \gamma_2)$ after this change of variables. If $\boldsymbol{s}(\boldsymbol{r})$ is not invertible, a loss of information occurs because we cannot reconstruct $\boldsymbol{r}$ from $\boldsymbol{s}$. This information loss leads to a less distinguishability between PDF's, namely $\bar{D}(\gamma_1, \gamma_2) < D(\gamma_1, \gamma_2)$. Instead, when $\boldsymbol{s}(\boldsymbol{r})$ is invertible, information is not lost and the distinguishability of the two functions is preserved, i.e. $\bar{D}(\gamma_1, \gamma_2) = D(\gamma_1, \gamma_2)$. Thus, it is naturally to require that any change of variables must lead to [93, 122]

$$\bar{D}(\gamma_1, \gamma_2) \leqslant D(\gamma_1, \gamma_2)\,. \tag{2.2.12}$$

This property is called information monotonicity for the divergence D.

Let us consider a geometric structure on $\mathcal{M}$ induced by a metric tensor g_{ij} associated to a divergence satisfying (2.2.12). An important theorem in information geometry due to Chentsov claims that, considering any set of the PDF's, a unique metric satisfying (2.2.12) exists up to multiplicative constants [93, 121].

The Wigner functions of the bosonic Gaussian states (2.2.6) with vanishing first moments are PDF's that provide a manifold $\mathcal{M}_{\mathrm{G}}$ parameterised by the covariance matrices γ. The Chentsov's theorem for these PDF's leads to introduce the *Fisher information matrix* [91, 93, 121, 123, 279]

$$g_{ij} = \int w_{\mathrm{G}}(\boldsymbol{r}, \gamma)\, \frac{\partial \log[w_{\mathrm{G}}(\boldsymbol{r}; \gamma)]}{\partial y_i}\, \frac{\partial \log[w_{\mathrm{G}}(\boldsymbol{r}; \gamma)]}{\partial y_j}\, d\boldsymbol{r} \tag{2.2.13}$$

which provides the *Fisher-Rao distance* between two bosonic Gaussian states with vanishing first moments. Denoting by γ_1 and γ_2 the covariance matrices of these states, their Fisher-Rao distance reads [92, 124–128]

$$d(\gamma_1, \gamma_2) \,\equiv\, \sqrt{\mathrm{Tr}\big[(\log \Delta)^2\big]} \,\equiv\, \big\| \log\big(\gamma_1^{-1/2}\, \gamma_2\, \gamma_1^{-1/2}\big) \big\|_2 \qquad \Delta \equiv \gamma_2\, \gamma_1^{-1}\,. \tag{2.2.14}$$

This is the main formula employed throughout this chapter and chapters 3 and 4 to study the complexity of Gaussian mixed states.

We remark that (2.2.14) is the Fisher-Rao distance also when the reference state and the target state have the same first moments, that can be non vanishing [92, 128, 280]. Although an explicit expression for the Fisher-Rao distance in the most general case of different covariance matrices and different first moments is not available in the literature, interesting classes of Gaussian PDF's have been identified where explicit expressions for this distance have been found [128, 280–282].

2.2.3 Williamson's decomposition

The *Williamson's theorem* is a very important tool to study Gaussian states [94]: it provides a decomposition for the covariance matrix γ that is crucial throughout our analysis.

The Williamson's theorem holds for any real, symmetric and positive matrix with even size; hence also for the covariance matrices. Given a covariance matrix γ, the Williamson's theorem guarantees that a symplectic matrix $W \in \mathrm{Sp}(2N, \mathbb{R})$ can be constructed such that

$$\gamma = W^{\mathrm{t}}\, \mathcal{D}\, W \tag{2.2.15}$$

where $\mathcal{D} \equiv \mathrm{diag}(\sigma_1, \dots, \sigma_N) \oplus \mathrm{diag}(\sigma_1, \dots, \sigma_N)$ and $\sigma_k > 0$. The set $\{\sigma_k\}$ is the *symplectic spectrum* of γ and its elements are the symplectic eigenvalues (we often call $\mathcal{D}$ the symplectic spectrum throughout this chapter, with a slight abuse of notation). The symplectic spectrum is uniquely determined up to permutations of the symplectic eigenvalues and it is invariant under symplectic transformations. Throughout this thesis we refer to (2.2.15) as the Williamson's decomposition[1] of γ, choosing a decreasing ordering for the symplectic eigenvalues. The real dimension of the set made by the covariance matrices is $N(2N+1)$ [78].

Combining (2.2.8) and (2.2.15), it can be shown that $\sigma_k \geqslant \frac{1}{2}$ [77]. A diagonal matrix is symplectic when it has the form $\Upsilon \oplus \Upsilon^{-1}$. This implies that a generic covariance matrix is not symplectic because of the occurrence of the diagonal matrix $\mathcal{D}$ in the Williamson's decomposition (2.2.15).

Another important tool for our analysis is the *Euler decomposition* of a symplectic matrix S (also known as Bloch-Messiah decomposition) [272]. It reads

$$S = L\, \mathcal{X}\, R \qquad \mathcal{X} = e^{\Lambda} \oplus e^{-\Lambda} \qquad L, R \in K(N) \equiv \mathrm{Sp}(2N, \mathbb{R}) \cap O(2N) \tag{2.2.16}$$

where $\Lambda = \mathrm{diag}(\Lambda_1, \dots, \Lambda_N)$ with $\Lambda_j \geqslant 0$. The non-uniqueness of the decomposition (2.2.16) is due only to the freedom to order the elements along the diagonal of Λ. By employing the Euler decomposition (2.2.16) and that the real dimension of $K(N)$ is N^2, it is straightforward to realise that the real dimension of the symplectic group $\mathrm{Sp}(2N, \mathbb{R})$ is $2N^2 + N$, as already mentioned in Sec. 2.2.1. The simplest case corresponds to the one-mode case, i.e. $N = 1$, where a 2×2 real symplectic matrix can be parameterised by two rotation angles and a squeezing parameter Λ_1.

Covariance matrix of a pure state

A Gaussian state is pure if and only if all the symplectic eigenvalues equal to $\frac{1}{2}$, i.e. $\mathcal{D} = \frac{1}{2}\mathbf{1}$. Thus, the Williamson's decomposition of the covariance matrix characterising a pure state reads

$$\gamma = \frac{1}{2}\, W^{\mathrm{t}}\, W = \frac{1}{2}\, R^{\mathrm{t}}\, \mathcal{X}^2 R \qquad W = L\, \mathcal{X}\, R\,. \tag{2.2.17}$$

The last expression, which has been found by employing the Euler decomposition (2.2.16) for the symplectic matrix W, tells us that the covariance matrix of a pure state can be determined by fixing $N^2 + N$ real parameters.

The covariance matrix of a pure state satisfies the following constraint [283]

$$\big(\mathrm{i}J\gamma\big)^2 = \frac{1}{4}\,\mathbf{1}\,. \tag{2.2.18}$$

After a change of basis characterised by the symplectic matrix S, the covariance matrix (2.2.17) becomes $\gamma' = \frac{1}{2}\, S\, W^{\mathrm{t}}\, W S^{\mathrm{t}}$. Choosing $S = K\, W^{-\mathrm{t}}$, where $K \in K(N)$, the covariance matrix drastically simplifies to $\gamma' = \frac{1}{2}\,\mathbf{1}$.

[1] It is often called normal modes decomposition [78].

2.2.4 Mixed states

Considering the set $\mathbb{P}(N)$ made by the $2N \times 2N$ real and positive definite matrices, the covariance matrices provide the proper subset of $\mathbb{P}(N)$ made by those matrices that also satisfy the inequality (2.2.8).

The set $\mathbb{P}(N)$ equipped with the Fisher-Rao distance is a Riemannian manifold where the length of a generic path $\gamma : [a, b] \to \mathbb{P}(N)$ is given by[2] [123–127]

$$L[\gamma(\tau)] = \int_a^b \sqrt{\mathrm{Tr}\left\{ \left[\gamma(\tau)^{-1}\, \dot{\gamma}(\tau)\right]^2 \right\}}\, d\tau \,. \tag{2.2.19}$$

The unique geodesic connecting two matrices in the manifold $\mathbb{P}(N)$ has been constructed [125]. In our analysis we restrict to the subset made by the covariance matrices γ. Considering the covariance matrix γ_{R} and the covariance matrix γ_{T}, that correspond to the reference state and to the target state respectively, the unique geodesic that connects γ_{R} to γ_{T} is [125]

$$G_s(\gamma_{\mathrm{R}}\,, \gamma_{\mathrm{T}}) \;\equiv\; \gamma_{\mathrm{R}}^{1/2} \Big(\gamma_{\mathrm{R}}^{-1/2}\, \gamma_{\mathrm{T}}\, \gamma_{\mathrm{R}}^{-1/2} \Big)^s \gamma_{\mathrm{R}}^{1/2} \qquad\qquad 0 \leqslant s \leqslant 1 \tag{2.2.20}$$

where s parameterises the generic matrix along the geodesic (we always assume $0 \leqslant s \leqslant 1$ throughout this chapter) and it is straightforward to verify that

$$G_0(\gamma_{\mathrm{R}}\,, \gamma_{\mathrm{T}}) = \gamma_{\mathrm{R}} \qquad\qquad G_1(\gamma_{\mathrm{R}}\,, \gamma_{\mathrm{T}}) = \gamma_{\mathrm{T}} \,. \tag{2.2.21}$$

The geodesic (2.2.20) provides the optimal circuit connecting γ_{R} to γ_{T}. In the mathematical literature, the matrix (2.2.20) is also known as the *s-geometric mean* of γ_{R} and γ_{T}. The matrix associated to $s = 1/2$ provides the *geometric mean* of γ_{R} and γ_{T}. We remark that, since γ_{R} and γ_{T} are symmetric Gaussian matrices, it can be shown that also the matrices belonging to the geodesic (2.2.20) are symmetric and Gaussian [126].

The Fisher-Rao distance between γ_{R} and γ_{T} is the length of the geodesic (2.2.20) evaluated through (2.2.19). It is given by

$$d(\gamma_{\mathrm{R}}, \gamma_{\mathrm{T}}) \;\equiv\; \sqrt{\mathrm{Tr}\big[(\log \Delta_{\mathrm{TR}})^2\big]} \;\equiv\; \big\| \log\big(\gamma_{\mathrm{R}}^{-1/2}\, \gamma_{\mathrm{T}}\, \gamma_{\mathrm{R}}^{-1/2}\big) \big\|_2 \tag{2.2.22}$$

where[3]

$$\Delta_{\mathrm{TR}} \equiv \gamma_{\mathrm{T}}\, \gamma_{\mathrm{R}}^{-1} \,. \tag{2.2.23}$$

This distance provides the following definition of complexity

$$\mathcal{C} \;=\; \frac{1}{2\sqrt{2}}\; d(\gamma_{\mathrm{R}}\,, \gamma_{\mathrm{T}}) \tag{2.2.24}$$

It is straightforward to realise that, in the special case where both γ_{R} and γ_{T} correspond to pure states, the complexity (2.2.24) becomes the result obtained in [40] for the F_2 complexity, based on the F_2 cost function; hence we refer to (2.2.24) also as F_2 complexity in the following. The matching with [40] justifies the introduction of the numerical factor $\frac{1}{2\sqrt{2}}$ in (2.2.24) with respect to the distance (2.2.22). Equivalently, also the $\kappa = 2$ complexity given by $\mathcal{C}_{\kappa=2} \equiv \mathcal{C}^2$ can be considered.

We remark that the complexity (2.2.24) and the optimal circuit (2.2.20) can be applied also for circuits where the reference state and the target state have the same first moments [92, 128, 280].

[2] An explicit computation that relates (2.2.13) to (2.2.19) can be found e.g. in Appendix A of [123].

[3] The expression (2.2.22) cannot be written as $\| \log(\gamma_{\mathrm{T}}\, \gamma_{\mathrm{R}}^{-1}) \|_2$ [98].

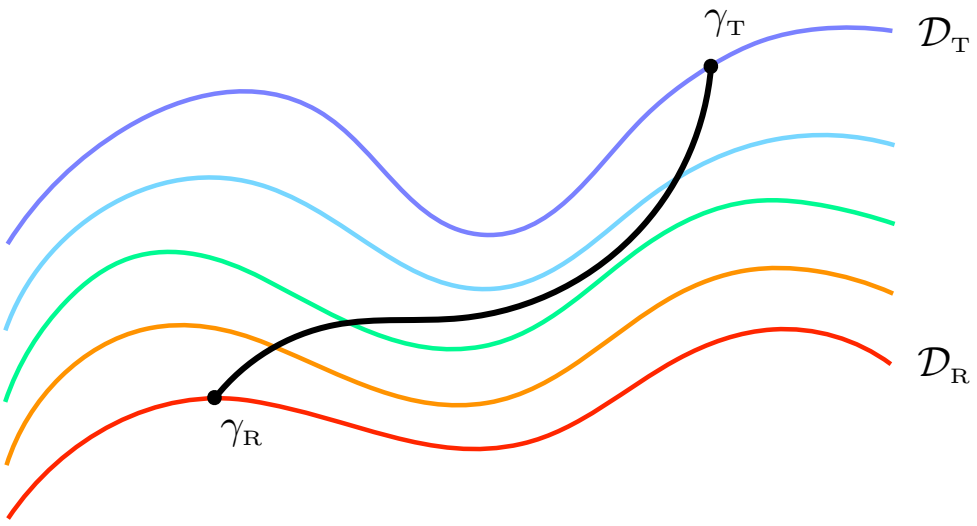

Figure 2.1: Pictorial representation of the optimal circuit (2.2.20) connecting $\gamma_{\rm R}$ to $\gamma_{\rm T}$ (solid black curve). Coloured solid curves represent the sets made by symmetric Gaussian matrices having the same symplectic spectrum. The red curve corresponds to $\mathcal{D}_{\rm R}$ and the blue curve to $\mathcal{D}_{\rm T}$.

The symmetry $d(\gamma_{\rm R}\,,\gamma_{\rm T}) = d(\gamma_{\rm T}\,,\gamma_{\rm R})$, imposed on any proper distance, can be verified for the Fisher-Rao distance (2.2.22) by observing that $\Delta_{\rm TR} \leftrightarrow \Delta_{\rm TR}^{-1}$ under the exchange $\gamma_{\rm R} \leftrightarrow \gamma_{\rm T}$.

Performing a change of basis characterised by the symplectic matrix S, the matrix $\Delta_{\rm TR}$ changes as follows

$$\Delta'_{\rm TR} = \gamma'_{\rm T}(\gamma'_{\rm R})^{-1} = S\,\Delta_{\rm TR}\,S^{-1}\,. \tag{2.2.25}$$

From this expression it is straightforward to observe that the Fisher-Rao distance (2.2.22), and therefore the complexity (2.2.24) as well, is invariant under a change of basis. We remark that (2.2.24) is invariant under any transformation that induces on $\Delta_{\rm TR}$ the transformation (2.2.25) for any matrix S (even complex and not necessarily symplectic).

From the expression (2.2.20) of the geodesic connecting $\gamma_{\rm R}$ to $\gamma_{\rm T}$, one can show that the change $s \to 1-s$ provides the geodesic connecting $\gamma_{\rm T}$ to $\gamma_{\rm R}$; indeed, we have that [125]

$$G_{1-s}(\gamma_{\rm R}\,,\gamma_{\rm T}) \;=\; \gamma_{\rm T}^{1/2}\Big(\gamma_{\rm T}^{-1/2}\,\gamma_{\rm R}\,\gamma_{\rm T}^{-1/2}\Big)^{s}\gamma_{\rm T}^{1/2} \;=\; G_s(\gamma_{\rm T}\,,\gamma_{\rm R})\,. \tag{2.2.26}$$

Remarkably, the geodesic (2.2.20) can be written in the following form

$$G_s(\gamma_{\rm R}\,,\gamma_{\rm T}) \;=\; U_s\,\gamma_{\rm R}\,U_s^{\rm t} \qquad\qquad U_s \equiv \Delta_{\rm TR}^{s/2}\,. \tag{2.2.27}$$

This expression is interesting because the generic matrix of the optimal circuit is written in a form that reminds a symplectic transformation of $\gamma_{\rm R}$ through the U_s. Nonetheless, we remark that in general U_s is not symplectic because the covariance matrices are not symplectic matrices.

It is enlightening to exploit the Williamson's decomposition of the covariance matrices discussed in Sec. 2.2.3 in the expressions for the complexity and for the optimal circuit. The Williamson's decomposition (2.2.15) allows to write $\gamma_{\rm R}$ and $\gamma_{\rm T}$ as follows

$$\gamma_{\rm R} = W_{\rm R}^{\rm t}\,\mathcal{D}_{\rm R}\,W_{\rm R} \qquad \gamma_{\rm T} = W_{\rm T}^{\rm t}\,\mathcal{D}_{\rm T}\,W_{\rm T} \qquad W_{\rm R}\,,W_{\rm T} \in {\rm Sp}(2N,\mathbb{R}) \tag{2.2.28}$$

where $\mathcal{D}_{\rm R}$ and $\mathcal{D}_{\rm T}$ contain the symplectic spectra of $\gamma_{\rm R}$ and $\gamma_{\rm T}$ respectively. Let us introduce also the Williamson's decomposition of the generic matrix along the geodesic (2.2.20), namely

$$G_s(\gamma_{\rm R}\,,\gamma_{\rm T}) = W_s^{\rm t}\,\mathcal{D}_s\,W_s \qquad\qquad W_s \in {\rm Sp}(2N,\mathbb{R})\,. \tag{2.2.29}$$

Later in the thesis we provide analytic expressions for W_s and $\mathcal{D}_s$ in terms of $\gamma_{\rm R}$ and $\gamma_{\rm T}$ for some particular optimal circuits.

In Fig. 2.1 we show a pictorial representation of the optimal circuit (2.2.20), which corresponds to the solid black curve. The figure displays that the symplectic spectrum changes along the geodesic because the black curve crosses solid curves having different colours, which correspond to the sets of matrices having the same symplectic spectrum.

The complexity (2.2.24) can be written in the following convenient form depending on the symplectic spectra and on the symplectic matrices $W_{\rm R}$ and $W_{\rm T}$

$$\mathcal{C} = \frac{1}{2\sqrt{2}}\,\sqrt{{\rm Tr}\left\{\left[\log\!\left(\mathcal{D}_{\rm T}\,W_{\rm TR}\,\mathcal{D}_{\rm R}^{-1}\,W_{\rm TR}^{\rm t}\right)\right]^2\right\}} \tag{2.2.30}$$

where we have introduced the symplectic matrix $W_{\rm TR}$ defined as follows

$$W_{\rm TR} \equiv W_{\rm T}\,W_{\rm R}^{-1}. \tag{2.2.31}$$

Let us conclude this subsection by stressing the main difference between this approach and the one introduced in [79] and reviewed in Sec. 2.6. While the latter requires the introduction of ancillary degrees of freedom to purify the reference and target states before computing the complexity, the one described above provide the optimal circuit and its length directly in the space of mixed states without need of purifications.

2.2.5 Pure states

It is very insightful to specialise the results presented in Sec. 2.2.4 to pure states.

When both the reference state $|\psi_{\rm R}\rangle$ and the target state $|\psi_{\rm T}\rangle$ are pure states, the corresponding density matrices are the projectors $\hat{\rho}_{\rm R} = |\psi_{\rm R}\rangle\langle\psi_{\rm R}|$ and $\hat{\rho}_{\rm T} = |\psi_{\rm T}\rangle\langle\psi_{\rm T}|$ respectively. In this case the symplectic spectra drastically simplify to

$$\mathcal{D}_{\rm R} = \mathcal{D}_{\rm T} = \frac{1}{2}\,\mathbf{1} \tag{2.2.32}$$

where $\mathbf{1}$ is the $2N \times 2N$ identity matrix. This implies that the Williamson's decompositions in (2.2.28) become respectively

$$\gamma_{\rm R} = \frac{1}{2}\,W_{\rm R}^{\rm t}\,W_{\rm R} \qquad\qquad \gamma_{\rm T} = \frac{1}{2}\,W_{\rm T}^{\rm t}\,W_{\rm T}\,. \tag{2.2.33}$$

Let us consider the Euler decomposition (defined in Sec. 2.2.3) of the symplectic matrix $W_{\rm TR}$, namely

$$W_{\rm TR} = L_{\rm TR}\,\mathcal{X}_{\rm TR}\,R_{\rm TR} \tag{2.2.34}$$

where

$$L_{\rm TR}\,,R_{\rm TR} \in K(N) \qquad\qquad \mathcal{X}_{\rm TR} = e^{\Lambda_{\rm TR}} \oplus e^{-\Lambda_{\rm TR}} \in {\rm Sp}(2N,\mathbb{R}) \tag{2.2.35}$$

and $\Lambda_{\rm TR}$ is a diagonal matrix with positive entries.

This decomposition provides the following expression for the complexity of pure states, as obtained in [40]

$$\mathcal{C} = \frac{1}{2\sqrt{2}} \sqrt{\mathrm{Tr}\left\{ \left[\log\left(W_{\mathrm{TR}}\, W_{\mathrm{TR}}^{\mathrm{t}}\right)\right]^2 \right\}} = \frac{1}{2\sqrt{2}} \sqrt{\mathrm{Tr}\left\{ \left[\log\left(\mathcal{X}_{\mathrm{TR}}^2\right)\right]^2 \right\}} = \sqrt{\sum_i (\Lambda_{\mathrm{TR}})_i^2} \qquad (2.2.36)$$

which can be also obtained through the proper choice of the base described below.

As for the optimal circuit (2.2.20), one can obtain

$$G_s(\gamma_{\mathrm{R}}\,, \gamma_{\mathrm{T}}) \;=\; \frac{1}{2}\, W_{\mathrm{R}}^{\mathrm{t}} \left(W_{\mathrm{TR}}^{\mathrm{t}}\, W_{\mathrm{TR}}\right)^s W_{\mathrm{R}}\,. \qquad (2.2.37)$$

We find it instructive also to specialise the expression (2.2.27) for the optimal circuit to pure states. Indeed, in this case Δ_{TR} is symplectic and the result reads

$$G_s(\gamma_{\mathrm{R}}\,, \gamma_{\mathrm{T}}) = \frac{1}{2}\, W_s^{\mathrm{t}}\, W_s \qquad\qquad W_s = W_{\mathrm{R}}\, U_s^{\mathrm{t}} \qquad (2.2.38)$$

This expression provides the Williamson's decomposition of the optimal circuit made by pure states, given that $W_s \in \mathrm{Sp}(2N, \mathbb{R})$.

A proper choice of the basis leads to a simple expression for the optimal circuit. Let us observe that, after a change of basis characterised by the symplectic matrix $S = R_{\mathrm{TR}} W_{\mathrm{R}}^{-\mathrm{t}}$, the covariance matrices γ_{R} and γ_{T} become the following diagonal matrices

$$\gamma'_{\mathrm{R}} = \frac{1}{2}\,\mathbf{1} \qquad\qquad \gamma'_{\mathrm{T}} = \frac{1}{2}\,\mathcal{X}_{\mathrm{TR}}^2\,. \qquad (2.2.39)$$

We remark that this result has been obtained by exploiting the peculiarity of the pure states mentioned in Sec. 2.2.3, namely that, after a change of basis that brings the covariance matrix into the diagonal form $\frac{1}{2}\mathbf{1}$, another change of basis characterised by a symplectic matrix that is also orthogonal leaves the covariance matrix invariant. The occurrence of non trivial symplectic spectra considerably complicates this analysis (see [98] for more details).

Specialising the optimal circuit (2.2.27) to the covariance matrices in (2.2.39), the following simple expression is obtained [40]

$$G_s(\gamma'_{\mathrm{R}}\,, \gamma'_{\mathrm{T}}) = \frac{1}{2}\,\mathcal{X}_{\mathrm{TR}}^{2s}\,. \qquad (2.2.40)$$

This expression tells us that, for pure states, this basis is very convenient because the optimal circuit is determined by the diagonal matrix $\mathcal{X}_{\mathrm{TR}}$.

2.2.6 Thermal states

The thermal states provide an important class of Gaussian mixed states. The density matrix of a thermal state at temperature $T \equiv 1/\beta$ is $\hat{\rho}_{\mathrm{th}} = e^{-\beta \hat{H}}/\mathcal{Z}$, where $\widehat{H}$ is the Hamiltonian (2.2.1) for the harmonic lattices that we are considering and the constant $\mathcal{Z} = \mathrm{Tr}\big(e^{-\beta \hat{H}}\big)$ guarantees the normalisation condition $\mathrm{Tr}\hat{\rho}_{\mathrm{th}} = 1$.

In order to study the Williamson's decomposition of the covariance matrix associated to a thermal state, let us observe the matrix H^{phys} in (2.2.1) can be written as

$$H^{\mathrm{phys}} = Q^{\mathrm{phys}} \oplus P^{\mathrm{phys}} \qquad (2.2.41)$$

where $P^{\mathrm{phys}} = \frac{1}{m}\mathbf{1}$ and Q^{phys} is a $N \times N$ real, symmetric and positive definite matrix whose explicit expression is not important for the subsequent discussion.

Denoting by $\widetilde{V}$ the real orthogonal matrix that diagonalises Q^{phys} (for the special case of the harmonic chain with periodic boundary conditions, $\widetilde{V}$ has been written in (2.7.5) e (2.7.6)), it is straightforward to notice that (2.2.41) can be diagonalised as follows

$$H^{\text{phys}} = V \left[\frac{1}{m} \operatorname{diag}\big((m\Omega)_1^2, \dots, (m\Omega_N)^2, 1, \dots, 1\big) \right] V^{\text{t}} \qquad V \equiv \widetilde{V} \oplus \widetilde{V} \tag{2.2.42}$$

where Ω_k^2 are the real eigenvalues of Q^{phys}/m. It is worth remarking that the $2N \times 2N$ matrix V is symplectic and orthogonal, given that $\widetilde{V}$ is orthogonal. One can show that the r.h.s. of (2.2.42) can be written as

$$H^{\text{phys}} = V\, \mathcal{X}_{\text{phys}} \Big[\operatorname{diag}\big(\Omega_1, \dots, \Omega_N, \Omega_1, \dots, \Omega_N\big) \Big]\, \mathcal{X}_{\text{phys}}\, V^{\text{t}} \tag{2.2.43}$$

where we have introduced the following symplectic and diagonal matrix

$$\mathcal{X}_{\text{phys}} = \operatorname{diag}\Big((m\Omega_1)^{1/2}, \dots, (m\Omega_N)^{1/2}, (m\Omega_1)^{-1/2}, \dots, (m\Omega_N)^{-1/2} \Big)\,. \tag{2.2.44}$$

The expression (2.2.43) provides the Williamson's decomposition of the matrix H^{phys} entering in the Hamiltonian (2.2.1). It reads

$$H^{\text{phys}} \,=\, W_{\text{phys}}^{\text{t}}\, \mathcal{D}_{\text{phys}}\, W_{\text{phys}} \tag{2.2.45}$$

where

$$\mathcal{D}_{\text{phys}} = \operatorname{diag}\big(\Omega_1, \dots, \Omega_N, \Omega_1, \dots, \Omega_N\big) \qquad W_{\text{phys}} = \mathcal{X}_{\text{phys}}\, V^{\text{t}}\,. \tag{2.2.46}$$

The Williamson's decomposition (2.2.45) suggests to write the physical Hamiltonian (2.2.1) in terms of the canonical variables defined through W_{phys}. The result is

$$\widehat{H} = \frac{1}{2}\, \hat{\boldsymbol{s}}^{\text{t}}\, \mathcal{D}_{\text{phys}}\, \hat{\boldsymbol{s}} \qquad \hat{\boldsymbol{s}} \equiv W_{\text{phys}}\, \hat{\boldsymbol{r}} \equiv \begin{pmatrix} \hat{\mathbf{q}} \\ \hat{\mathbf{p}} \end{pmatrix}. \tag{2.2.47}$$

Following the standard quantisation procedure, one introduces the annihilation operators $\hat{\mathfrak{b}}_k$ and the creation operators $\hat{\mathfrak{b}}_k^\dagger$ as

$$\hat{\boldsymbol{b}} \equiv \big(\hat{\mathfrak{b}}_1, \dots, \hat{\mathfrak{b}}_N, \hat{\mathfrak{b}}_1^\dagger, \dots, \hat{\mathfrak{b}}_N^\dagger \big)^{\text{t}} \equiv \Theta^{-1} \hat{\boldsymbol{s}} \qquad \hat{\mathfrak{b}}_k \equiv \frac{\hat{\mathfrak{q}}_k + \mathrm{i}\, \hat{\mathfrak{p}}_k}{\sqrt{2}} \qquad \Theta \equiv \frac{1}{\sqrt{2}} \begin{pmatrix} \mathbf{1} & \mathbf{1} \\ -\mathrm{i}\mathbf{1} & \mathrm{i}\mathbf{1} \end{pmatrix} \tag{2.2.48}$$

which satisfy the well known algebra given by $[\hat{\boldsymbol{b}}_i, \hat{\boldsymbol{b}}_j] = J_{ij}$. In terms of these operators, the Hamiltonian (2.2.47) assumes the standard form

$$\widehat{H} = \sum_{k=1}^{N} \Omega_k \left(\hat{\mathfrak{b}}_k^\dagger\, \hat{\mathfrak{b}}_k + \frac{1}{2} \right). \tag{2.2.49}$$

Thus, the symplectic spectrum in (2.2.46) provides the dispersion relation of the model.

Applying the definition (2.2.9) to the thermal state and exploting standard techniques (see [77, 78]), for the Williamson's decomposition of the covariance matrix of the thermal state one obtains

$$\gamma_{\text{th}} = W_{\text{th}}^{\text{t}}\, \mathcal{D}_{\text{th}}\, W_{\text{th}} \tag{2.2.50}$$

where the symplectic eigenvalues entering in the diagonal matrix $\mathcal{D}_{\text{th}}$ and the symplectic matrix W_{th} are given respectively by

$$\sigma_{\text{th},k} = \frac{1}{2} \coth(\beta\Omega_k/2) \qquad W_{\text{th}} = W_{\text{phys}}^{-\text{t}}\,. \tag{2.2.51}$$

We remark that $W_{\rm th}$ is independent of the temperature.

Taking the zero temperature limit $\beta \to +\infty$ of (2.2.50), one obtains the Williamson's decomposition of the covariance matrix of the ground state. This limit gives $\sigma_{{\rm th},k} \to 1/2$, as expected from the fact that the ground state is a pure state, while $W_{\rm th}$ does not change, being independent of the temperature. Thus, the Williamson's decomposition of the covariance matrix of the ground state reads

$$\gamma_{\rm gs} = \frac{1}{2}\, W_{\rm phys}^{-1}\, W_{\rm phys}^{-{\rm t}} \tag{2.2.52}$$

where $W_{\rm phys}$ has been defined in (2.2.46).

It is worth considering the complexity when the reference state and the target state are thermal states having the same physical Hamiltonian $\widehat{H}$ but different temperatures (we denote respectively by $\beta_{\rm R}$ and $\beta_{\rm T}$ their inverse temperatures). From (2.2.50), we have that the Williamson's decomposition of the covariance matrices of the reference state and the target state read respectively

$$\gamma_{\rm th,R} = W_{\rm th}^{\rm t}\, \mathcal{D}_{\rm th,R}\, W_{\rm th} \qquad\qquad \gamma_{\rm th,T} = W_{\rm th}^{\rm t}\, \mathcal{D}_{\rm th,T}\, W_{\rm th} \tag{2.2.53}$$

where $W_{\rm th}$ is independent of the temperature; hence $W_{\rm R} = W_{\rm T}$. This means that $W_{\rm TR} = \mathbf{1}$ in this case (see (2.2.31)); hence the expression (2.2.30) for the complexity significantly simplifies to

$$\mathcal{C} = \frac{1}{2\sqrt{2}} \sqrt{{\rm Tr}\left\{ \left[\log\!\left(\mathcal{D}_{\rm th,T}\, \mathcal{D}_{\rm th,R}^{-1}\right)\right]^2 \right\}} = \frac{1}{2} \sqrt{\sum_{k=1}^{N} \left\{ \left[\log\!\left(\frac{\coth(\beta_{\rm T}\Omega_k/2)}{\coth(\beta_{\rm R}\Omega_k/2)} \right) \right]^2 \right\}} \,. \tag{2.2.54}$$

The optimal path connecting these particular thermal states is obtained by plugging (2.2.53) into (2.2.27). The Williamson's decomposition of the generic covariance matrix belonging to this optimal path reads

$$G_s(\gamma_{\rm th,R}\,,\gamma_{\rm th,T}) = W_{\rm th}^{\rm t}\, \mathcal{D}_s\, W_{\rm th} \qquad\qquad \mathcal{D}_s = \mathcal{D}_{\rm th,T}^{s}\, \mathcal{D}_{\rm th,R}^{1-s} \qquad\qquad 0 \leqslant s \leqslant 1 \tag{2.2.55}$$

where the same symplectic matrix $W_{\rm th}$ of the reference state and of the target state occurs and only the symplectic spectrum depends on the parameter s labelling the covariance matrices along the optimal path.

It is worth asking whether, for any given value of s, the covariance matrix $G_s(\gamma_{\rm th,R}\,,\gamma_{\rm th,T})$ in (2.2.55) can be associated to a thermal state of the system characterised by the same physical Hamiltonian underlying the reference and the target states. Denoting by $\sigma_{s,k}$ the symplectic eigenvalues of (2.2.55) this means to find a temperature $T_s \equiv \beta_s^{-1}$ such that $\sigma_{s,k} = \frac{1}{2}\coth(\beta_s\Omega_k/2)$. This equation can be written more explicitly as follows

$$\coth(\beta_s\,\Omega_k/2) = \left[\frac{\coth(\beta_{\rm T}\,\Omega_k/2)}{\coth(\beta_{\rm R}\,\Omega_k/2)} \right]^s \coth(\beta_{\rm R}\,\Omega_k/2)\,. \tag{2.2.56}$$

We checked numerically that a solution $T_s = T_s(T_{\rm R}, T_{\rm T})$ for any $1 \leqslant k \leqslant N$ does not exist.

The quantities discussed above are further explored in Sec. 2.7.3, where the thermal states of the harmonic chain are considered. In Appendix B we report a detailed analysis of the complexity of thermofield double (TFD) states for harmonic lattices, which are special cases of purification of thermal states.

2.3 Spectrum complexity and basis complexity

In this section we discuss the spectrum complexity and the basis complexity for mixed Gaussian states in harmonic lattices.

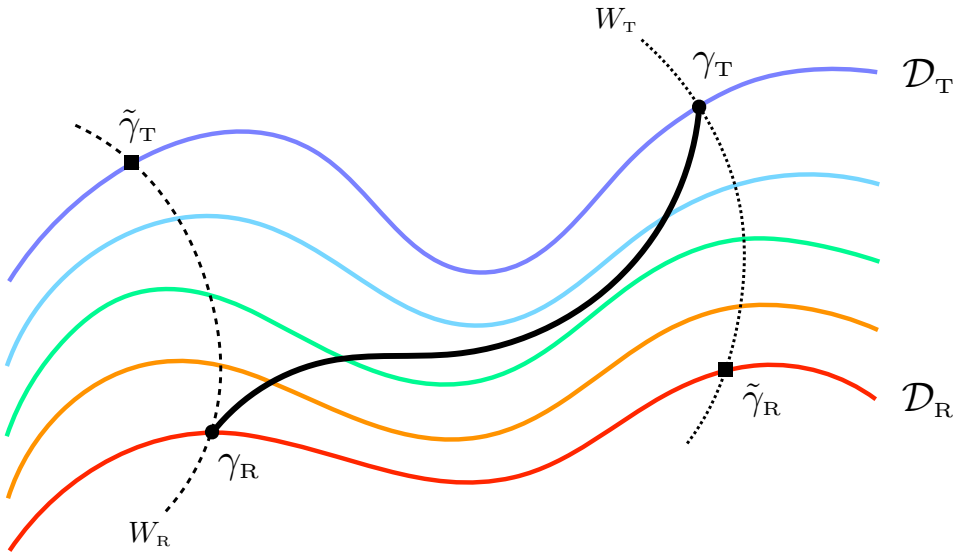

Figure 2.2: The solid black curve and the solid coloured curves have been defined in Fig 2.1. Eq. (2.3.11) tells us that the dashed black curves represent the $W_{\rm R}$ path and the $W_{\rm T}$ path that pass through $\gamma_{\rm R}$ and $\gamma_{\rm T}$ respectively (the auxiliary covariance matrices $\tilde{\gamma}_{\rm R}$ and $\tilde{\gamma}_{\rm T}$ have been defined in (2.3.33)). The arcs of the dashed curves that connect the blue curve to the red curve have the same length given by (2.3.12).

By exploiting the Williamson's decomposition we introduce the W *path* as the optimal circuit connecting two covariance matrices with $W_{\rm R} = W_{\rm T} \equiv W$ and the $\mathcal{D}$ *path* as the optimal circuit connecting two covariance matrices having $\mathcal{D}_{\rm R} = \mathcal{D}_{\rm T} \equiv \mathcal{D}$. In order to study these circuits, in Sec. 2.3.1 we discuss the first law of complexity for the Gaussian states that we are considering. The lengths of a W path and of a $\mathcal{D}$ path are employed to study the spectrum complexity (Sec. 2.3.2) and the basis complexity (Sec. 2.3.3) respectively. In Fig. 2.2 the dashed curves correspond to W paths (see (2.3.11)).

Furthermore, exploiting the W paths and the $\mathcal{D}$ paths, we discuss the purification of mixed states (Sec. 2.3.4) and we provide lower and upper bounds for the complexity (Sec. 2.3.5).

2.3.1 First law of complexity

It is worth investigating the first law of complexity [268, 269] for the states described in Sec. 2.2. The derivations of the results reported below can be found in [98].

Let us consider the following functional

$$S[q(t)] = \int_{t_0}^{t_1} \mathcal{L}[q(t), \dot{q}(t), t]\, dt \tag{2.3.1}$$

where $q_0 = q(t_0)$ and $q_1 = q(t_1)$ are the initial and final configurations respectively.

It is well known that the first variation of (2.3.1) under an infinitesimal change of the boundary conditions $q_i \to q_i + \delta q_i$ for $i = 0, 1$ evaluated on a solution of the equations of motion is

$$\delta S[q(t)] \;=\; \frac{\partial \mathcal{L}}{\partial \dot{q}}\, \delta q \,\Big|_{t_1} - \frac{\partial \mathcal{L}}{\partial \dot{q}}\, \delta q \,\Big|_{t_0} . \tag{2.3.2}$$

The functional we are interested in is the length functional (2.2.19) and the solution of its equations of motion is given by the optimal circuit (2.2.20), that satisfies the boundary conditions (2.2.21). In order to apply (2.3.2), one considers the infinitesimal variations $\gamma_{\rm T} \to \gamma_{\rm T} + \delta\gamma_{\rm T}$ and $\gamma_{\rm R} \to \gamma_{\rm R} + \delta\gamma_{\rm R}$ of the covariance matrices of the reference and of the target states that preserve the properties of these matrices. In other words, these variations are such that also the resulting matrices are covariance matrices.

The length functional (2.2.19) leads to introduce the following cost function

$$F(\gamma, \dot\gamma) \,=\, \sqrt{\mathrm{Tr}\big[\,(\gamma^{-1}\,\dot\gamma)^2\,\big]}\,. \tag{2.3.3}$$

By applying (2.3.2) to the length functional (2.2.19), one obtains the first law of complexity

$$\delta d = \sum_{ij} \frac{\partial F}{\partial \dot\gamma_{ij}}\,\delta\gamma_{ij}\,\Big|_{s=0}^{s=1} \tag{2.3.4}$$

where the r.h.s. is evaluated on the geodesic (2.2.20).

Equivalent expressions for the variation (2.3.4) can be found in [98]. Here, we find it worth providing a formula for (2.3.4) that is based on the Williamson's decompositions (2.2.28). It is given by

$$\begin{aligned} \delta d \;\;=\;\; \frac{1}{d}\,\Big[& 2\,\mathrm{Tr}\Big\{\,\log\big(\gamma_{\rm T}^{-1}\gamma_{\rm R}\big)\,\big(W_{\rm R}^{-1}\,\delta W_{\rm R} - W_{\rm T}^{-1}\,\delta W_{\rm T}\big)\Big\} \\ & + \mathrm{Tr}\Big\{\,\log\big(W_{\rm TR}\,\mathcal{D}_{\rm R}^{-1}\,W_{\rm TR}^{\rm t}\,\mathcal{D}_{\rm T}\big)\,\mathcal{D}_{\rm T}^{-1}\,\delta\mathcal{D}_{\rm T} - \log\big(\mathcal{D}_{\rm R}^{-1}\,W_{\rm TR}^{\rm t}\,\mathcal{D}_{\rm T}\,W_{\rm TR}\big)\,\mathcal{D}_{\rm R}^{-1}\,\delta\mathcal{D}_{\rm R}\,\Big\}\Big]\,. \end{aligned} \tag{2.3.5}$$

The form (2.3.5) for δd tells us that this variation can be written as the sum of four contributions: two terms from the variations $\delta W_{\rm R}$ and $\delta W_{\rm T}$ of the symplectic matrices in (2.2.28) and two terms from the diagonal and non negative variations $\delta\mathcal{D}_{\rm R}$ and $\delta\mathcal{D}_{\rm T}$ of the symplectic spectra.

It is natural to look for relations between $\gamma_{\rm R}$ and $\gamma_{\rm T}$ that lead to $\delta d = 0$ and, in order to find them, let us consider the first law of complexity written in the form (2.3.5). Let us first focus on the variations of $W_{\rm R}$ and $W_{\rm T}$. When $\delta\mathcal{D}_{\rm R} = \delta\mathcal{D}_{\rm T} = \mathbf{0}$ in (2.3.5), the equation $\delta d = 0$ becomes

$$\mathrm{Tr}\Big\{\,\log\big(\gamma_{\rm T}^{-1}\gamma_{\rm R}\big)\,\big(W_{\rm R}^{-1}\,\delta W_{\rm R} - W_{\rm T}^{-1}\,\delta W_{\rm T}\big)\Big\} = 0\,. \tag{2.3.6}$$

Two trivial solutions of this equation are given by

$$W_{\rm R} = W_{\rm T}\,. \tag{2.3.7}$$

and $W_{\rm R} = M\,W_{\rm T}$, where M is a constant symplectic matrix whose elements are just real numbers, i.e. it does not contain parameters to vary. Notice that these two simple solutions require that both $W_{\rm R}$ and $W_{\rm T}$ are allowed to vary.

More generally, $\delta d = 0$ for generic variations of $\gamma_{\rm R}$ and $\gamma_{\rm T}$ when these covariance matrices are related by [98]

$$\gamma_{\rm T} \,=\, \gamma_{\rm R}\,e^{-YJ} \tag{2.3.8}$$

where Y is a real antisymmetric matrix constrained by the conditions that the elements on the diagonals of $W_{\rm T}\,Y\,J\,W_{\rm T}^{-1}$ and $W_{\rm R}\,Y\,J\,W_{\rm R}^{-1}$ vanish.

2.3.2 Spectrum complexity

It is worth exploring the possibility to define the circuit complexity associated to the change of the symplectic spectrum.

Let us consider a reference state and a target state such that in the Williamson's decompositions of their covariance matrices $\gamma_{\rm R}$ and $\gamma_{\rm T}$ (see (2.2.28)) the same symplectic matrix occurs, namely

$$\gamma_{\rm R} = W^{\rm t}\,\mathcal{D}_{\rm R}\,W \qquad\qquad \gamma_{\rm T} = W^{\rm t}\,\mathcal{D}_{\rm T}\,W \qquad\qquad W \in {\rm Sp}(2N,\mathbb{R})\,. \tag{2.3.9}$$

We call W *path* the optimal circuit (2.2.20) connecting these two covariance matrices.

In order to study the Williamson's decomposition of a matrix belonging to a W path, we consider the expression (2.2.27) for the optimal circuit. When (2.3.9) holds, one can find that $\Delta_{\rm TR} = W^{\rm t}\,\mathcal{D}_{\rm T}\,\mathcal{D}_{\rm R}^{-1}\,W^{-{\rm t}}$ and

$$G_s(\gamma_{\rm R}\,,\gamma_{\rm T}) = W^{\rm t}\big(\,\mathcal{D}_{\rm R}^{1-s}\,\mathcal{D}_{\rm T}^{s}\,\big)W \tag{2.3.10}$$

which tells us that the Williamson's decomposition of the matrix along the W path is (2.2.29) with

$$\mathcal{D}_s \;=\; \mathcal{D}_{\rm R}^{1-s}\,\mathcal{D}_{\rm T}^{s} \qquad\qquad W_s = W\,. \tag{2.3.11}$$

It is remarkable that the symplectic matrix W_s is independent of s. This means that in the Williamson's decomposition of a matrix belonging to a W path the same symplectic matrix W occurs. In Fig. 2.2 the dashed curves correspond to the $W_{\rm R}$ path and to the $W_{\rm T}$ path. Considering e.g. the $W_{\rm R}$ path in Fig. 2.2, from (2.3.11) we have that the Williamson's decomposition of a generic matrix γ belonging to this $W_{\rm R}$ path is given by the symplectic matrix $W_{\rm R}$ and by the symplectic spectrum corresponding to the coloured line intersecting the dashed line of the $W_{\rm R}$ path at γ.

An interesting example of W path is given by the thermal states of a given model at different temperatures (see Sec. 2.2.6). Indeed, in the Williamson's decomposition (2.2.50), the symplectic matrix $W_{\rm th}$ is independent of the temperature.

For a W path we have $\delta d = 0$ (see (2.3.7)); hence the W paths provide a preferred way to connect the set of covariance matrices with symplectic spectrum $\mathcal{D}_{\rm R}$ to the set of covariance matrices with symplectic spectrum $\mathcal{D}_{\rm T}$.

We find it natural to define the spectrum complexity as the length of a W path because this quantity is independent of the choice of W. In particular, from (2.3.9), we have that $W_{\rm TR} = \mathbf{1}$, hence (2.2.30) simplifies to

$$d_{\rm spectrum}(\gamma_{\rm R}\,,\gamma_{\rm T}) \equiv \sqrt{{\rm Tr}\Big\{\big[\log\big(\mathcal{D}_{\rm T}\,\mathcal{D}_{\rm R}^{-1}\big)\big]^2\Big\}} = \sqrt{2\sum_{k=1}^{N}\left[\log\left(\frac{\sigma_{{\rm T},k}}{\sigma_{{\rm R},k}}\right)\right]^2} \tag{2.3.12}$$

which is independent of W. This implies that $d_{\rm spectrum}(\gamma_{\rm R}\,,\gamma_{\rm T}) = d_{\rm spectrum}(\mathcal{D}_{\rm R}\,,\mathcal{D}_{\rm T})$. Thus, in Fig. 2.2 the arcs of the dashed curves that connect the blue curve to the red curve have the same length given by (2.3.12).

Another natural definition for the spectrum complexity is the distance between the set of covariance matrices whose symplectic spectrum is $\mathcal{D}_{\rm R}$ (red curve in Fig. 2.2) and the set of covariance matrices whose symplectic spectrum is $\mathcal{D}_{\rm T}$ (blue curve in Fig. 2.2). It reads

$$\tilde{d}_{\rm spectrum}(\mathcal{D}_{\rm R}\,,\mathcal{D}_{\rm T}) \equiv \min\big[\,d\big(W^{\rm t}\,\mathcal{D}_{\rm R}\,W\,,\widetilde{W}^{\rm t}\,\mathcal{D}_{\rm T}\,\widetilde{W}\big)\,\big] \qquad\qquad W,\,\widetilde{W} \in {\rm Sp}(2N,\mathbb{R}) \tag{2.3.13}$$

where the minimisation over the symplectic matrices W and $\widetilde{W}$ is difficult to perform. It is straightforward to realise that $\tilde{d}_{\rm spectrum}(\mathcal{D}_{\rm R}\,,\mathcal{D}_{\rm T}) \leqslant d_{\rm spectrum}(\mathcal{D}_{\rm R}\,,\mathcal{D}_{\rm T})$.

2.3.3 Basis complexity

In order to study the circuit complexity associated to a change of basis, let us consider the Williamson's decompositions of two covariance matrices $\gamma_{\rm R}$ and $\gamma_{\rm T}$ having the same symplectic spectrum, i.e.

$$\gamma_{\rm R} = W_{\rm R}^{\rm t}\,\mathcal{D}\,W_{\rm R} \qquad\qquad \gamma_{\rm T} = W_{\rm T}^{\rm t}\,\mathcal{D}\,W_{\rm T} \tag{2.3.14}$$

that have been obtained by setting $\mathcal{D}_{\rm R} = \mathcal{D}_{\rm T} = \mathcal{D}$ in (2.2.28). An important example is given by states whose density matrices $\hat\rho_{\rm T}$ and $\hat\rho_{\rm R}$ are related through a unitary transformation U, namely $\hat\rho_{\rm T} = U\hat\rho_{\rm R}U^\dagger$. Indeed, this means that the corresponding covariance matrices are related through a symplectic matrix (that does not change the symplectic spectrum) [77, 78].

We denote as $\mathcal{D}$ *path* the optimal circuit connecting the covariance matrices having the same symplectic spectrum, identifying its length as a basis complexity. This basis complexity can be found by specifying (2.2.30) to (2.3.14) and the result is

$$d_{\rm basis}(\gamma_{\rm R}\,,\gamma_{\rm T}) = \sqrt{{\rm Tr}\left\{\left[\log\!\big(\mathcal{D}\,W_{\rm TR}\,\mathcal{D}^{-1}\,W_{\rm TR}^{\rm t}\big)\right]^2\right\}} \tag{2.3.15}$$

where $W_{\rm TR}$ has been defined in (2.2.31). Notice that we have not required that all the matrices along a $\mathcal{D}$ path have the same symplectic spectrum.

We find it reasonable to introduce also another definition of basis complexity as the minimal length of an optimal circuit that connects a covariance matrix whose Williamson's decomposition contains the symplectic matrix $W_{\rm R}$ (i.e. that lies on the dashed curve on the left in Fig. 2.2) to a covariance matrix having the symplectic matrix $W_{\rm T}$ in its Williamson's decomposition (i.e. that belongs to the dashed curve on the right in Fig. 2.2). This basis complexity is defined as follows

$$\tilde d_{\rm basis}(W_{\rm R}\,,W_{\rm T}) \equiv \min\!\big[\, d\big(W_{\rm R}^{\rm t}\,\mathcal{D}\,W_{\rm R}\,,\,W_{\rm T}^{\rm t}\,\widetilde{\mathcal{D}}\,W_{\rm T}\big)\,\big] \qquad\qquad \mathcal{D},\,\widetilde{\mathcal{D}} \in {\rm Diag}(N,\mathbb{R}) \tag{2.3.16}$$

where the minimisation is performed over the set ${\rm Diag}(2N,\mathbb{R})$ made by the diagonal matrices of the form ${\rm diag}(\boldsymbol{\sigma}) \oplus {\rm diag}(\boldsymbol{\sigma})$, with $\boldsymbol{\sigma}$ vector of N real numbers $\sigma_i \geqslant 1/2$. It is immediate to notice that (2.3.16) is a lower bound for (2.3.15), i.e. $\tilde d_{\rm basis}(W_{\rm R}\,,W_{\rm T}) \leqslant d_{\rm basis}(\gamma_{\rm R}\,,\gamma_{\rm T})$.

Specifying the form (2.2.27) for the optimal circuit to (2.3.14), it is straightforward to find that the $\mathcal{D}$ path is given by

$$G_s(\gamma_{\rm R}\,,\gamma_{\rm T}) \,=\, \widetilde{W}_s^{\rm t}\,\mathcal{D}\,\widetilde{W}_s \qquad\qquad \widetilde{W}_s \equiv W_{\rm R}\,U_s^{\rm t} \tag{2.3.17}$$

where we remark that $\widetilde{W}_s$ is not symplectic in general.

It is worth asking when $\widetilde{W}_s$ is symplectic because in these cases (2.3.17) provides the Williamson's decomposition of the $\mathcal{D}$ path. The requirement $U_s \in {\rm Sp}(2N,\mathbb{R})$ leads to

$$\big[\,W_{\rm TR}\,,\mathcal{D}\,\big] \,=\, 0\,. \tag{2.3.18}$$

When this condition holds, (2.3.15) simplifies to the following expression

$$d_{\rm basis}(\gamma_{\rm R}\,,\gamma_{\rm T}) = \sqrt{{\rm Tr}\left\{\left[\log\!\big(W_{\rm TR}\,W_{\rm TR}^{\rm t}\big)\right]^2\right\}} \tag{2.3.19}$$

which is independent of $\mathcal{D}$.

For pure states, which have $\mathcal{D} = \frac{1}{2}\,\mathbf{1}$, the condition (2.3.18) is trivially verified.

When $N > 1$ the condition (2.3.18) is a non trivial requirement. For instance, when $W_{\rm TR}$ is diagonal, (2.3.18) is verified and (2.3.17) holds with $\widetilde{W}_s = \mathcal{X}_{\rm TR}^s W_{\rm R}$. The basis complexity (2.3.15) simplifies to $d^2_{\rm basis}(\gamma_{\rm R}\,,\gamma_{\rm T}) = {\rm Tr}\big\{[\log(\mathcal{X}^2_{\rm TR})]^2\big\}$, that is independent of $\mathcal{D}$.
Writing $W_{\rm TR}$ as a block matrix made by four $N\times N$ matrices, it is straightforward to find that the

condition (2.3.18) holds whenever every block of $W_{\rm TR}$ commutes with $\mathrm{diag}(\sigma_1,\dots,\sigma_N)$. Then, we can exploit the fact that a diagonal matrix with distinct elements commutes with another matrix only when the latter one is diagonal[4]. Thus, if the symplectic spectrum is non degenerate, all the blocks of $W_{\rm TR}$ must be diagonal to fulfil the condition (2.3.18). We remark that the non-degeneracy condition for the symplectic spectrum is not guaranteed; indeed, the symplectic spectrum has some degeneracy in several interesting cases. For instance, for pure states all the symplectic eigenvalues are equal to $\frac{1}{2}$. Another important example is the reduced covariance matrix of an interval in an infinite harmonic chain with non vanishing mass [194].

Let us finally stress that, contrarily to what happens for the W paths (see Sec. 2.3.2), not for all the $\mathcal{D}$ paths we have $\delta d = 0$ (a more detailed analysis can be found in [98]).

2.3.4 Purification through the W path

The purification of a mixed state is a process that provides a pure state starting from a mixed state. This procedure is not unique. Considering the context of the bosonic Gaussian states that we are exploring, in this subsection we discuss the purification of a mixed state by employing the results reported in this section.

Given a mixed state that is not pure and that is characterised by the covariance matrix $\gamma_{\rm R}$, any circuit connecting $\gamma_{\rm R}$ to a pure state provides a *purification path*. A purification path connects the covariance matrices $\gamma_{\rm R}$ to $\gamma_{\rm T}$ whose Williamson's decompositions are given respectively by

$$\gamma_{\rm R} = W_{\rm R}^{\rm t}\,\mathcal{D}\,W_{\rm R} \qquad\qquad \gamma_{\rm T} = \frac{1}{2}\,W_{\rm T}^{\rm t}\,W_{\rm T} \tag{2.3.20}$$

where $W_{\rm R} \in \mathrm{Sp}(2N,\mathbb{R})$ and $\mathcal{D} \neq \frac{1}{2}\,\mathbf{1}$ are assigned, while $W_{\rm T} \in \mathrm{Sp}(2N,\mathbb{R})$ is not. Among all the possible paths, the optimal circuit is obtained by specifying (2.2.20) to (2.3.20). The result is

$$G_s^{(0)}(\gamma_{\rm R},W_{\rm T}) \equiv \frac{1}{2^s}\,\gamma_{\rm R}^{1/2}\Big(\gamma_{\rm R}^{-1/2}\,W_{\rm T}^{\rm t}\,W_{\rm T}\,\gamma_{\rm R}^{-1/2}\Big)^s\gamma_{\rm R}^{1/2} \tag{2.3.21}$$

which depends on the symplectic matrix $W_{\rm T}$ that determines the final pure state. The length of the purification path (2.3.21) can be found by evaluating (2.2.22) for the special case described by (2.3.20). It reads

$$d_0(\gamma_{\rm R},W_{\rm T}) \equiv \sqrt{\mathrm{Tr}\left\{\big[\log\big(2\,\gamma_{\rm R}\,W_{\rm T}^{-1}W_{\rm T}^{-{\rm t}}\big)\big]^2\right\}}\,. \tag{2.3.22}$$

The *optimal purification path* is the purification path with minimal length, which can be found by minimising (2.3.22) as $W_{\rm T} \in \mathrm{Sp}(2N,\mathbb{R})$ varies within the symplectic group. This extremization procedure selects a symplectic matrix W_0 that determines the pure state through its covariance matrix $\frac{1}{2}\,W_0^{\rm t}\,W_0$. The matrix W_0 is obtained by solving $\delta d_0 = 0$, where d_0 is defined in (2.3.22).

In Sec. 2.3.1 we have shown that a W path provides a solution to this equation, namely

$$W_0 = W_{\rm R} \tag{2.3.23}$$

which is the trivial solution corresponding to $\delta W_{\rm R} = \mathbf{0}$. In the following we focus on the purification process based on the W paths. We cannot prove that, among all the solution of $\delta d_0 = 0$, the W path corresponds to the one having minimal length.

[4]Consider the diagonal matrix $\Lambda = \mathrm{diag}(\lambda_1,\dots,\lambda_N)$ with $\lambda_i \neq \lambda_j$ and a matrix M such that $[\Lambda, M] = 0$. The generic element of this relation reads $M_{i,j}\lambda_j = \lambda_i M_{i,j}$, i.e. $M_{i,j}(\lambda_i - \lambda_j) = 0$. Since $\lambda_i \neq \lambda_j$ when $i \neq j$, we have $M_{i,j} = 0$ for $i \neq j$.

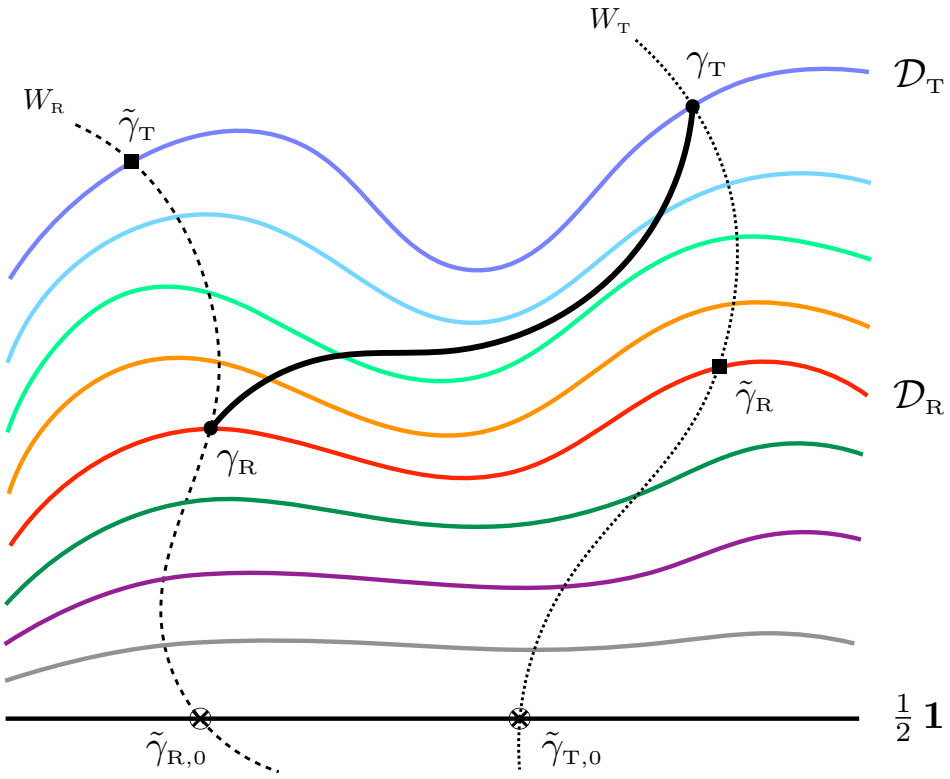

Figure 2.3: The optimal purification paths for $\gamma_{\rm R}$ and $\gamma_{\rm T}$ correspond respectively to the $W_{\rm R}$ path and to the $W_{\rm T}$ path, that are represented through dashed lines. The straight black solid line represent the set of the pure states, whose symplectic spectrum is given by $\mathcal{D} = \frac{1}{2}\mathbf{1}$.

The $W_{\rm R}$ path connects the mixed state $\gamma_{\rm R} = W_{\rm R}^{\rm t}\,\mathcal{D}\,W_{\rm R}$ to the pure state $\gamma_0 = \frac{1}{2}\,W_{\rm R}^{\rm t}\,W_{\rm R}$. By specialising (2.3.10) to $\mathcal{D}_{\rm T} = \frac{1}{2}\,\mathbf{1}$, we find that this $W_{\rm R}$ path is given by

$$G_s(\gamma_{\rm R}\,,\gamma_0) = G_s^{(0)}(\gamma_{\rm R}, W_{\rm R}) = \frac{1}{2^s}\,W_{\rm R}^{\rm t}\,\mathcal{D}^{1-s}\,W_{\rm R} \tag{2.3.24}$$

and its length can be easily obtained by setting $\mathcal{D}_{\rm T} = \frac{1}{2}\,\mathbf{1}$ in (2.3.12), finding an expression that depends only on $\mathcal{D}$

$$d_0(\gamma_{\rm R}, W_{\rm R}) \equiv d_{\rm spectrum}(\gamma_{\rm R}\,,\gamma_0) = \sqrt{{\rm Tr}\Big\{\big[\log\big(2\,\mathcal{D}\big)\big]^2\Big\}} = \sqrt{2\sum_{k=1}^{N}\big[\log(2\,\sigma_k)\big]^2}\,. \tag{2.3.25}$$

The thermal states are interesting examples of mixed states to explore. The Williamson's decomposition of the covariance matrix of a thermal state is given by (2.2.50). By specialising (2.3.24) to this case, we obtain the W path that purifies a thermal state. It reads

$$G_s(\gamma_{\rm th}\,,\gamma_0) = \frac{1}{2^s}\,W_{\rm th}^{\rm t}\,\mathcal{D}_{\rm th}^{1-s}\,W_{\rm th} \tag{2.3.26}$$

where it is worth reminding that the symplectic matrix $W_{\rm th}$, given in (2.2.51), does not depend on the temperature of the thermal state, but only on the parameters occurring in the Hamiltonian.

It is natural to ask whether the $W_{\rm th}$ path (2.3.26) is made by thermal states. This is the case if, for any given $s \in [0,1]$, the symplectic spectrum of (2.3.26) is thermal at some inverse temperature β_s determined by the inverse temperature β of the thermal state that plays the role of the reference state in this purification path. Using (2.2.51), this requirement leads to the following condition

$$\big[\coth(\beta\Omega_k/2)\big]^{1-s} = \coth(\beta_s\Omega_k/2) \tag{2.3.27}$$

which corresponds to (2.2.56) when $\beta_{\rm T} \to \infty$, as expected. This condition depends on the dispersion relation of the model. A straightforward numerical inspection for the periodic chains (see Sec. 2.7.1) shows that (2.3.27) cannot be solved by $\beta_s = \beta_s(\beta)$ for any $1 \leqslant k \leqslant N$; hence we conclude that the purification path (2.3.26) is not entirely made by thermal states.

The W paths provide a natural alternative way to connect two generic mixed states $\gamma_{\rm R}$ and $\gamma_{\rm T}$ by using a path that passes through the set of pure states. In particular, by exploiting the Williamson's decompositions given in (2.2.28), one first considers the $W_{\rm R}$ path that connects $\gamma_{\rm R}$ to the pure state $\tilde{\gamma}_{\rm R,0}$ and the $W_{\rm T}$ path that connects $\gamma_{\rm T}$ to the pure state $\tilde{\gamma}_{\rm T,0}$. From (2.3.24), these W paths are given respectively by

$$G_s(\gamma_{\rm R}\,,\tilde{\gamma}_{\rm R,0}) = \frac{1}{2^s}\, W_{\rm R}^{\rm t}\, \mathcal{D}_{\rm R}^{1-s}\, W_{\rm R} \qquad\qquad G_s(\gamma_{\rm T}\,,\tilde{\gamma}_{\rm T,0}) = \frac{1}{2^s}\, W_{\rm T}^{\rm t}\, \mathcal{D}_{\rm T}^{1-s}\, W_{\rm T} \tag{2.3.28}$$

where

$$\tilde{\gamma}_{\rm R,0} \equiv \frac{1}{2}\, W_{\rm R}^{\rm t}\, W_{\rm R} \qquad\qquad \tilde{\gamma}_{\rm T,0} \equiv \frac{1}{2}\, W_{\rm T}^{\rm t}\, W_{\rm T}\,. \tag{2.3.29}$$

Then, within the set of the pure states, we consider the geodesic connecting $\tilde{\gamma}_{\rm R,0}$ to $\tilde{\gamma}_{\rm T,0}$. Our preferred path to connect $\gamma_{\rm R}$ and $\gamma_{\rm T}$ passing through the set of pure states is obtained by combining these three paths as follows

$$\gamma_{\rm R} \longrightarrow \tilde{\gamma}_{\rm R,0} \longrightarrow \tilde{\gamma}_{\rm T,0} \longrightarrow \gamma_{\rm T} \tag{2.3.30}$$

The length $d_{\rm pur}(\gamma_{\rm R}\,,\gamma_{\rm T})$ of this path can be found by summing the lengths of its three components. From (2.3.15) and (2.3.25), we get

$$d_{\rm pur}(\gamma_{\rm R}\,,\gamma_{\rm T}) \;\equiv\; d_0(\gamma_{\rm R},W_{\rm R}) + d_{\rm basis}(\tilde{\gamma}_{\rm R,0}\,,\tilde{\gamma}_{\rm T,0}) + d_0(\gamma_{\rm T},W_{\rm T}) \tag{2.3.31}$$

which can be written more explicitly as follows

$$d_{\rm pur}(\gamma_{\rm R}\,,\gamma_{\rm T}) \,=\, \sqrt{{\rm Tr}\Big\{\big[\log\big(2\,\mathcal{D}_{\rm R}\big)\big]^2\Big\}} + \sqrt{{\rm Tr}\Big\{\big[\log\big(2\,\mathcal{D}_{\rm T}\big)\big]^2\Big\}} + \sqrt{{\rm Tr}\Big\{\big[\log\big(W_{\rm TR}\,W_{\rm TR}^{\rm t}\big)\big]^2\Big\}}\,. \tag{2.3.32}$$

This expression provides an upper bound $d(\gamma_{\rm R}\,,\gamma_{\rm T}) \leqslant d_{\rm pur}(\gamma_{\rm R}\,,\gamma_{\rm T})$ on (2.2.22).

2.3.5 Bounding complexity

Explicit formulas to evaluate the circuit complexity for mixed states are difficult to obtain; hence it is worth finding calculable expressions which provide either higher or lower bounds to this quantity. In this subsection we construct some bounds in the setup of the bosonic Gaussian states that we are exploring.

The complexity (2.2.24), which holds for states with vanishing first moments, is proportional to the length of the optimal circuit (2.2.20) connecting $\gamma_{\rm R}$ to $\gamma_{\rm T}$; hence it is straightforward to observe that the length of any other path connecting these two covariance matrices provides an upper bound on the complexity. The analysis reported in Sec. 2.3 and in Sec. 2.3.4 naturally leads to consider some particular paths.

The simplest choice is a path made by two geodesics that connect $\gamma_{\rm R}$ and $\gamma_{\rm T}$ to an auxiliary covariance matrix $\gamma_{\rm aux}$ that does not belong to the optimal circuit (2.2.20) (i.e. that does not lie on the black solid curve in Fig. 2.2). Natural candidates for $\gamma_{\rm aux}$ are the covariance matrices whose Williamson's decompositions contain either $\mathcal{D}_{\rm R}$ or $\mathcal{D}_{\rm T}$ or $W_{\rm R}$ or $W_{\rm T}$. For instance, we can choose for $\gamma_{\rm aux}$ a covariance matrix whose symplectic spectrum is $\mathcal{D}_{\rm R}$ or a covariance matrix whose symplectic spectrum is $\mathcal{D}_{\rm T}$ (that lie respectively on the red solid curve and on the blue solid curve in Fig. 2.2). Different choices for $\gamma_{\rm aux}$ lead to different bounds; hence it is worth asking whether a particular choice provides the best bound. The answer depends on the set where $\gamma_{\rm aux}$ is allowed to vary.

Let us consider some natural paths where only a single auxiliary covariance matrix $\gamma_{\rm aux}$ is involved. In Sec. 2.3.1 we have shown that the W paths satisfy the first law of complexity with $\delta d = 0$. Thus, natural candidates to consider for $\gamma_{\rm aux}$ are

$$\tilde{\gamma}_{\rm R} \equiv W_{\rm T}^{\rm t}\, \mathcal{D}_{\rm R} W_{\rm T} \qquad\qquad \tilde{\gamma}_{\rm T} \equiv W_{\rm R}^{\rm t}\, \mathcal{D}_{\rm T} W_{\rm R} \tag{2.3.33}$$

that have been represented by black squares in Fig. 2.2 and Fig. 2.3.

By first applying the triangle inequality for the paths $\gamma_{\rm R} \to \tilde{\gamma}_{\rm R} \to \gamma_{\rm T}$ and $\gamma_{\rm R} \to \tilde{\gamma}_{\rm T} \to \gamma_{\rm T}$, and then picking the one that provides the best constraint between the $\mathcal{D}$ paths, we obtain

$$d(\gamma_{\rm R}\,,\gamma_{\rm T}) \leqslant d_{\rm spectrum}(\gamma_{\rm R}\,,\gamma_{\rm T}) + \min\big[\, d_{\rm basis}(\gamma_{\rm R}\,,\tilde{\gamma}_{\rm R})\,,\, d_{\rm basis}(\tilde{\gamma}_{\rm T}\,,\gamma_{\rm T})\,\big]\,. \tag{2.3.34}$$

Denoting by $\tilde{d}(\gamma_{\rm R}\,,\gamma_{\rm T})$ the r.h.s. of this inequality, we find that

$$\begin{aligned}\tilde{d}(\gamma_{\rm R}\,,\gamma_{\rm T}) \;&=\; \sqrt{{\rm Tr}\Big\{\big[\log\big(\mathcal{D}_{\rm T}\,\mathcal{D}_{\rm R}^{-1}\big)\big]^2\Big\}} \\ &\quad + \min\left[\sqrt{{\rm Tr}\Big\{\big[\log\big(\mathcal{D}_{\rm R}\,W_{\rm TR}\,\mathcal{D}_{\rm R}^{-1}\,W_{\rm TR}^{\rm t}\big)\big]^2\Big\}}\,,\,\sqrt{{\rm Tr}\Big\{\big[\log\big(\mathcal{D}_{\rm T}\,W_{\rm TR}\,\mathcal{D}_{\rm T}^{-1}\,W_{\rm TR}^{\rm t}\big)\big]^2\Big\}}\right].\end{aligned} \tag{2.3.35}$$

The path $\gamma_{\rm R} \to \tilde{\gamma}_{\rm T} \to \gamma_{\rm T}$ corresponds to an explicit realisation of the proposal made in Fig. 6 of [46] within the approach that we are considering, that does not require the addition of ancillary degrees of freedom.

Better bounds could be obtained by constructing paths that involve more auxiliary covariance matrices $\gamma_{\rm aux}$. For instance, one can consider paths $\gamma_{\rm R} \to \gamma_{\rm aux,1} \to \gamma_{\rm aux,2} \to \gamma_{\rm T}$ that involve two auxiliary covariance matrices $\gamma_{\rm aux,1}$ and $\gamma_{\rm aux,2}$. Referring to Fig. 2.2, natural paths to consider within this class are the ones where $\gamma_{\rm aux,1}$ belongs to the $W_{\rm R}$ path and $\gamma_{\rm aux,2}$ to the $W_{\rm T}$ path, or the ones where $\gamma_{\rm aux,1}$ belongs to the red curve (i.e. its symplectic spectrum is $\mathcal{D}_{\rm R}$) and $\gamma_{\rm aux,2}$ belongs to the blue curve (i.e. its symplectic spectrum is $\mathcal{D}_{\rm T}$).

Another interesting path to consider is the one constructed in (2.3.30): it involves the two auxiliary matrices $\gamma_{\rm aux,1} = \tilde{\gamma}_{\rm R,0}$ and $\gamma_{\rm aux,2} = \tilde{\gamma}_{\rm T,0}$ and its length is (2.3.31) (see Fig. 2.3). It is straightforward to observe that $d(\gamma_{\rm R}\,,\gamma_{\rm T}) \leqslant d_{\rm pur}(\gamma_{\rm R}\,,\gamma_{\rm T})$, but it is non trivial to find the best bound between $\tilde{d}(\gamma_{\rm R}\,,\gamma_{\rm T})$ and $d_{\rm pur}(\gamma_{\rm R}\,,\gamma_{\rm T})$ and we cannot provide a general solution to this problem.

2.4 Optimal path for entanglement Hamiltonians

The density matrix of a mixed state can be written as follows

$$\hat{\rho} \,\propto\, e^{-\widehat{K}} \tag{2.4.1}$$

where the proportionality constant determines the normalisation of $\hat{\rho}$. In this chapter, we denote the operator $\widehat{K}$ as *entanglement Hamiltonian*, with a slight abuse of notation. Indeed, as explained

in Sec. 1.2.1, the operator $\widehat{K}$ is the entanglement Hamiltonian when $\hat{\rho} = \hat{\rho}_A = \mathrm{Tr}_{\mathcal{H}_B}\hat{\rho}_{\mathrm{pure}}$ is the reduced density matrix obtained by tracing out the part $\mathcal{H}_B$ of a bipartite Hilbert space $\mathcal{H} = \mathcal{H}_A \otimes \mathcal{H}_B$. Instead, for instance, the thermal states are mixed states that do not correspond to a bipartition of the Hilbert space. For these states $\widehat{K} = \beta\,\widehat{H}$, where $\widehat{H}$ is the Hamiltonian of the system and β the inverse temperature.

For the bosonic Gaussian states that we are considering, the entanglement Hamiltonians are quadratic operators in terms of the position and momentum operators; hence they can be written as follows

$$\widehat{K} = \frac{1}{2}\,\hat{\boldsymbol{r}}^{\mathrm{t}}\,H\,\hat{\boldsymbol{r}} \qquad\qquad \hat{\boldsymbol{r}} = \begin{pmatrix} \hat{\boldsymbol{q}} \\ \hat{\boldsymbol{p}} \end{pmatrix} \tag{2.4.2}$$

where H is a $2N \times 2N$ symmetric and positive definite matrix that characterises the underlying mixed state (see also chapter 5). We denote H as the entanglement Hamiltonian matrix. It can be written in terms of the corresponding covariance matrix γ as follows [10, 101, 191, 195, 201, 284]

$$H = 2\,\mathrm{i}\,J\,\mathrm{arccoth}(2\,\mathrm{i}\gamma\,J) \equiv h(\gamma) \tag{2.4.3}$$

where J is the standard symplectic matrix (2.2.2). The expression (2.4.3) holds for covariance matrices that are not associated to pure states. Thus, in particular, the purification procedure reported in Sec. 2.3.4 cannot be described through the entanglement Hamiltonian matrices H defined by (2.4.2).

Since the matrix H is symmetric and positive definite, we can adapt to the entanglement Hamiltonian matrices many results reported in the previous discussions for the covariance matrices.

Given the matrices H_{R} and H_{T} corresponding to the reference state γ_{R} and to the target state γ_{T} respectively, we can consider the optimal path connecting H_{R} to H_{T}, namely

$$\widetilde{G}_s(H_{\mathrm{R}}\,, H_{\mathrm{T}}) \;\equiv\; H_{\mathrm{R}}^{1/2}\Big(H_{\mathrm{R}}^{-1/2}\,H_{\mathrm{T}}\,H_{\mathrm{R}}^{-1/2}\Big)^{s}\,H_{\mathrm{R}}^{1/2} \qquad\qquad 0 \leqslant s \leqslant 1 \tag{2.4.4}$$

whose boundary conditions are given by $\widetilde{G}_0(H_{\mathrm{R}}\,, H_{\mathrm{T}}) = H_{\mathrm{R}}$ and $\widetilde{G}_1(H_{\mathrm{R}}\,, H_{\mathrm{T}}) = H_{\mathrm{T}}$. The length of the geodesic (2.4.4) measured through the Fisher-Rao metric reads

$$d(H_{\mathrm{R}}, H_{\mathrm{T}}) \equiv \sqrt{\mathrm{Tr}\left\{\big[\log\big(H_{\mathrm{T}}\,H_{\mathrm{R}}^{-1}\big)\big]^2\right\}}\,. \tag{2.4.5}$$

The Williamson's decomposition of the entanglement Hamiltonian matrix H is given by

$$H = \widetilde{W}^{\mathrm{t}}\,\mathcal{E}\,\widetilde{W} \tag{2.4.6}$$

where $\mathcal{E} \equiv \mathrm{diag}(\varepsilon_1, \dots, \varepsilon_N) \oplus \mathrm{diag}(\varepsilon_1, \dots, \varepsilon_N)$ with $\varepsilon_k > 0$. The symplectic spectrum of H can be determined from the symplectic spectrum of γ as follows [191, 195, 201]

$$\mathcal{E} = 2\,\mathrm{arccoth}(2\,\mathcal{D}) = \log\left(\frac{\mathcal{D} + 1/2}{\mathcal{D} - 1/2}\right). \tag{2.4.7}$$

This formula cannot be applied for pure states, which have $\mathcal{D} = \frac{1}{2}\mathbf{1}$. The symplectic matrices W and $\widetilde{W}$, introduced in (2.2.15) and (2.4.6) respectively, are related as follows [101, 284]

$$\widetilde{W} \equiv J^{\mathrm{t}}\,W\,J = W^{-\mathrm{t}}\,. \tag{2.4.8}$$

We find it worth expressing the distance (2.4.5) in terms of the matrices occurring in the Williamson's decompositions of H_{R} and H_{T}, as done in Sec. 2.2.4 for the covariance matrices. These decompositions read

$$H_{\mathrm{R}} = \widetilde{W}_{\mathrm{R}}^{\mathrm{t}}\,\mathcal{E}_{\mathrm{R}}\,\widetilde{W}_{\mathrm{R}} \qquad\qquad H_{\mathrm{T}} = \widetilde{W}_{\mathrm{T}}^{\mathrm{t}}\,\mathcal{E}_{\mathrm{T}}\,\widetilde{W}_{\mathrm{T}} \tag{2.4.9}$$

where $\widetilde{W}_{\rm R}$ and $\widetilde{W}_{\rm T}$ are related respectively to $W_{\rm R}$ and $W_{\rm T}$ through (2.4.8) and therefore we can write the distance (2.4.5) as

$$d(H_{\rm R}, H_{\rm T}) = \sqrt{\mathrm{Tr}\left\{ \left[\log\left(\mathcal{E}_{\rm T}\, W_{\rm TR}\, \mathcal{E}_{\rm R}^{-1}\, W_{\rm TR}^{\rm t} \right) \right]^2 \right\}} \,. \tag{2.4.10}$$

The expression (2.4.3) (or equivalently (2.4.7) and (2.4.8)) provides a highly non trivial relation between the set made by the covariance matrices γ that are associated to the mixed states that are not pure states and the set of the entanglement Hamiltonian matrices H. The map h in (2.4.3) is not an isometry, hence the distances are not preserved and geodesics are not sent into geodesics. Thus, we find it worth comparing the distance $d(\gamma_{\rm R}, \gamma_{\rm T}) = d(h^{-1}(H_{\rm R}), h^{-1}(H_{\rm T}))$ from (2.2.30) and the distance $d(H_{\rm R}, H_{\rm T})$ in (2.4.10).

For the sake of simplicity, let us explore the case in which $W_{\rm T} = W_{\rm R}$, i.e. $W_{\rm TR} = \mathbf{1}$ (this includes the thermal states originating from the same physical Hamiltonian), the distance (2.4.10) simplifies to

$$d(H_{\rm R}, H_{\rm T}) = \sqrt{\mathrm{Tr}\left\{ \left[\log\left(\mathcal{E}_{\rm T}\, \mathcal{E}_{\rm R}^{-1} \right) \right]^2 \right\}} = \sqrt{2 \sum_{k=1}^{N} \left[\log\left(\frac{\varepsilon_{{\rm T},k}}{\varepsilon_{{\rm R},k}} \right) \right]^2} \tag{2.4.11}$$

while $d(\gamma_{\rm R}, \gamma_{\rm T})$ is given by (2.3.12). One can verify that $[\log(\sigma_{{\rm T},k}/\sigma_{{\rm R},k})]^2 \leqslant [\log(\varepsilon_{{\rm T},k}/\varepsilon_{{\rm R},k})]^2$ for any given k; hence $d(\gamma_{\rm R}, \gamma_{\rm T})^2 \leqslant d(H_{\rm R}, H_{\rm T})^2$ is obtained after summing over the modes.

By using the decompositions (2.4.9), one can draw a pictorial representation similar to Fig. 2.1 and Fig. 2.2 also for the entanglement Hamiltonian matrices H, just by replacing each γ with the corresponding H, each W with the corresponding $\widetilde{W}$ and where the solid coloured lines are labelled by the corresponding symplectic spectra $\mathcal{E}$.

We find it worth discussing further the set of thermal states through the approach based on the entanglement Hamiltonian matrices because the simplicity of these matrices in this case allows to write analytic results. For a thermal state $H = \beta H^{\rm phys}$, where $H^{\rm phys}$ is the matrix characterising the physical Hamiltonian (2.2.1) and β is the inverse temperature. This implies that the symplectic eigenvalues of H are $\varepsilon_{{\rm th},k} = \beta\, \sigma_{{\rm phys},k}$, where $\sigma_{{\rm phys},k}$ are the symplectic eigenvalues of $H^{\rm phys}$.

We denote by $\beta_{\rm R}$ and $\beta_{\rm T}$ the inverse temperatures of the reference state and of the target state respectively. An interesting special case is given by thermal states of the same system, which have the same $H^{\rm phys}$. In this case $H_{\rm T} H_{\rm R}^{-1} = (\beta_{\rm T}/\beta_{\rm R})\, \mathbf{1}$; hence (2.4.5) simplifies to

$$d(H_{\rm R}, H_{\rm T}) = \big| \log(\beta_{\rm T}/\beta_{\rm R}) \big| \sqrt{2V} \tag{2.4.12}$$

where V is the number of sites in the harmonic lattice. Furthermore, from (2.4.4) it is straightforward to observe that in this case the entire optimal circuit is made by thermal states having the same $H^{\rm phys}$. The optimal circuit (2.4.4) significantly simplifies to

$$\widetilde{G}_s(H_{\rm R}\,, H_{\rm T}) = \beta_s\, H^{\rm phys} \qquad \beta_s \equiv \beta_{\rm R} \left(\frac{\beta_{\rm T}}{\beta_{\rm R}} \right)^s \qquad 0 \leqslant s \leqslant 1 \,. \tag{2.4.13}$$

The Williamson's decomposition of this optimal circuit reads

$$\widetilde{G}_s(H_{\rm R}\,, H_{\rm T}) \;=\; W_{\rm phys}^{\rm t}\, \mathcal{D}_s\, W_{\rm phys} \qquad \mathcal{D}_s = \beta_s\, \mathcal{D}_{\rm phys} \qquad 0 \leqslant s \leqslant 1 \tag{2.4.14}$$

where $W_{\rm phys}$ is independent of s. Thus, (2.4.13) tells us that β_s is the inverse temperature of the thermal state labelled by s along this optimal circuit.

In Sec. 2.7.3 the above results are applied to the thermal states of the harmonic chain with periodic boundary conditions.

2.5 Gaussian channels

Quantum operations are described by completely positive operators acting on a quantum state, which can be either pure or mixed, and they are classified in *quantum channels* and *quantum measurements* [131, 285]. The quantum channels are trace preserving quantum operations, while quantum measurements are not trace preserving [286].

The output $\Theta(\hat{\rho})$ of a quantum channel applied to the density matrix $\hat{\rho}$ of a system is obtained by first extending the system through an ancillary system (the environment) in a pure state $|\Phi_E\rangle$, then by allowing an interaction characterised by a unitary transformation U and finally by tracing out the degrees of freedom of the environment [77, 132, 287], namely

$$\Theta(\hat{\rho}) = \mathrm{Tr}_E\big[\, U^\dagger \big(\hat{\rho} \otimes |\Phi_E\rangle\langle\Phi_E|\big)\, U \,\big] \,. \tag{2.5.1}$$

While within the set of the pure states the unitary transformations are the only operations that allow to pass from a state to another, within the general set of mixed states also non unitary operations must be taken into account.

In this section we consider circuits in the space made by quantum Gaussian states; hence only quantum operations between Gaussian states (also called Gaussian operations) can be considered [286]. The quantum channels and the quantum measurements restricted to the set of the Gaussian states are often called Gaussian channels [77, 283] and Gaussian measurements [267] respectively.

In the following we focus only on the Gaussian channels. A Gaussian state with vanishing first moments is completely described by its covariance matrix; hence the action of a Gaussian channel on a Gaussian state can be defined through its effect on the covariance matrix of the Gaussian state. This effect can be studied by introducing two real matrices T and N as [283]

$$\gamma \,\to\, T\,\gamma\,T^{\mathrm{t}} + N \qquad\qquad N = N^{\mathrm{t}} \qquad\qquad N + \mathrm{i}\,\frac{J}{2} - \mathrm{i}\,T\,\frac{J}{2}\,T^{\mathrm{t}} \geqslant 0 \tag{2.5.2}$$

where T is unconstrained and the last inequality corresponds to the complete positivity condition. The Gaussian unitary transformations are the Gaussian channels with $N = 0$ and symplectic T. In this case the inequality in (2.5.2) is saturated. Further interesting results for Gaussian operations have been reported e.g. in [267, 288].

We find it worth asking whether a matrix along the optimal circuit (2.2.20) can be obtained by acting with a Gaussian channel on the reference state. This means finding T_s and N_s that fulfil (2.5.2) for any $0 \leqslant s \leqslant 1$ and such that

$$G_s(\gamma_{\mathrm{R}}\,,\gamma_{\mathrm{T}}) \,=\, U_s\,\gamma_{\mathrm{R}}\,U_s^{\mathrm{t}} \,=\, T_s\,\gamma_{\mathrm{R}}\,T_s^{\mathrm{t}} + N_s \qquad\qquad 0 \leqslant s \leqslant 1 \tag{2.5.3}$$

where U_s is defined in (2.2.27). Unfortunately, we are not able to determine T_s and N_s as functions of U_s in full generality. In the following we provide some simple particular solutions.

A simple possibility reads

$$T_s = 0 \qquad\qquad N_s = G_s \tag{2.5.4}$$

which satisfies the inequality in (2.5.2), since G_s is a symmetric Gaussian matrix (see Sec. 2.2.4).

Another, less trivial, solution is given by

$$T_s = U_s \qquad\qquad N_s = \mathbf{0} \tag{2.5.5}$$

where the complete positivity condition in (2.5.2) becomes $\mathrm{i}\,\frac{J}{2} - \mathrm{i}\,T_s\,\frac{J}{2}\,T_s^{\mathrm{t}} \geqslant 0$. We have considered numerically some cases, finding that U_s satisfies the complete positivity condition only when it is symplectic (in this case the complete positivity inequality is saturated).

An explicit example belonging to the class identified by (2.5.5) can be constructed by considering a particular $\mathcal{D}$ path where $W_{\rm T} = \mathcal{X}_{\rm TR} W_{\rm R}$ (see Sec. 2.3.3). In this case (2.5.5) is realised with

$$T_s = U_s = W_{\rm R}^{\rm t}\, \mathcal{X}_{\rm TR}^{s}\, W_{\rm R}^{-{\rm t}}\,. \tag{2.5.6}$$

A more general solution where both T_s and N_s can be non vanishing is obtained by imposing the following relation

$$T_s \,=\, \big[\big(G_s - N_s\big)\,\gamma_{\rm R}^{-1}\big]^{1/2} \tag{2.5.7}$$

which solves (2.5.3) for any symmetric N_s. The solution (2.5.4) is recovered from (2.5.7) with $T_s = 0$. Plugging (2.5.7) into the complete positivity condition in (2.5.2), we obtain

$$N_s + {\rm i}\,\frac{J}{2} - {\rm i}\,\big[\big(G_s - N_s\big)\,\gamma_{\rm R}^{-1}\big]^{1/2}\,\frac{J}{2}\,\big[\gamma_{\rm R}^{-1}\,\big(G_s - N_s\big)\big]^{1/2} \,\geqslant\, 0 \tag{2.5.8}$$

Thus, for any N_s fulfilling this inequality, by using (2.5.7) we can implement our optimal circuit (2.2.20) through Gaussian channels. It would be interesting to find explicit cases of Gaussian channels where the inequality (2.5.8) is not saturated.

2.6 Complexity of mixed states through ancillae

In this section we discuss the approach to the complexity of mixed states explored in [79], which is based on the introduction of ancillary degrees of freedom.

Consider a quantum system in a mixed state characterised by the density matrix $\hat\rho$. A pure state can be always constructed from $\hat\rho$ by adding ancillary degrees of freedom. This purification procedure consists in first extending the Hilbert space of the system to a larger Hilbert space $\mathcal{H}_{\rm extended} \equiv \mathcal{H} \otimes \mathcal{H}_{\rm anc}$ through an auxiliary Hilbert space $\mathcal{H}_{\rm anc}$, and then finding a pure state $|\Omega\rangle \in \mathcal{H}_{\rm extended}$ such that the original mixed state is obtained as the reduced density matrix given by

$$\hat\rho \,=\, {\rm Tr}_{\mathcal{H}_{\rm anc}} |\Omega\rangle\langle\Omega| \tag{2.6.1}$$

where the ancillary degrees of freedom have been traced out. In Sec. 2.6.1, employing a covariance matrix analysis, we review some properties of the purifications through ancillae. We remark that the purifications discussed in Sec. 2.3.4 do not involve ancillary degrees of freedom.

There are infinitely many ways to construct $\mathcal{H}_{\rm extended}$ and $|\Omega\rangle$ such that (2.6.1) is satisfied; hence a purification criterion must be introduced. In Sec. 2.6.2 we survey some of the purification criteria which have been considered in the literature to study different quantities. An important example is the entanglement of purification [289–292]. In this section we are interested in the purification complexity [46], that has been employed in [79] to study the complexity of mixed states.

2.6.1 Covariance matrix of the extended system

We are interested in a generic harmonic lattice made by N sites in the Gaussian mixed state characterised by the covariance matrix γ and by vanishing first moments. The covariance matrix γ can be decomposed in blocks as follows

$$\gamma \equiv \begin{pmatrix} Q & M \\ M^{\rm t} & P \end{pmatrix} \tag{2.6.2}$$

where Q and P are $N \times N$ symmetric matrices, while M is a generic $N \times N$ real matrix; hence $N(2N+1)$ real parameters must be fixed to determine γ.

We consider a simplification of the purification process by focussing only on Gaussian purifications. This means that a mixed state characterised by the covariance matrix (2.6.2) is purified by introducing ancillary degrees of freedom and construcing a $2N_{\rm ext} \times 2N_{\rm ext}$ covariance matrix $\gamma_{\rm ext}$ that corresponds to a Gaussian pure state $|\Omega\rangle$ for the extended lattice having $N_{\rm ext} \equiv N + N_{\rm anc}$ sites. For the sake of simplicity, we assume also that $|\Omega\rangle$ has vanishing first moments, i.e. $\langle\Omega|\hat{\boldsymbol{r}}_{\rm ext}|\Omega\rangle = 0$, where $\hat{\boldsymbol{r}}^{\rm t}_{\rm ext} \equiv (\hat{\boldsymbol{q}}^{\rm t}, \hat{\boldsymbol{q}}^{\rm t}_{\rm anc}, \hat{\boldsymbol{p}}^{\rm t}, \hat{\boldsymbol{p}}^{\rm t}_{\rm anc})$ and we have separated the ancillary degrees of freedom from the ones associated to the physical system.

By writing also $\gamma_{\rm ext}$ through the block decomposition (2.6.2) we have

$$\gamma_{\rm ext} \equiv \begin{pmatrix} Q_{\rm ext} & M_{\rm ext} \\ M^{\rm t}_{\rm ext} & P_{\rm ext} \end{pmatrix} \tag{2.6.3}$$

where $Q_{\rm ext}$ and $P_{\rm ext}$ are $N_{\rm ext} \times N_{\rm ext}$ symmetric matrices. Since the covariance matrix (2.6.3) corresponds to a pure state, the condition (2.2.18) must hold. This tells us that the blocks occurring in (2.6.3) are related by the following constraints

$$Q_{\rm ext}\, P_{\rm ext} - M^2_{\rm ext} = \frac{1}{4}\,\mathbf{1} \qquad M_{\rm ext}\, Q_{\rm ext} = Q_{\rm ext}\, M^{\rm t}_{\rm ext} \qquad P_{\rm ext}\, M_{\rm ext} = M^{\rm t}_{\rm ext}\, P_{\rm ext}\,. \tag{2.6.4}$$

The first relation tells us that $M_{\rm ext}$ is determined by the product $Q_{\rm ext}\, P_{\rm ext}$, while the remaining two relations mean that $M_{\rm ext}\, Q_{\rm ext}$ and $P_{\rm ext}\, M_{\rm ext}$ are symmetric. Thus, (2.6.3) is determined by the symmetric matrices $Q_{\rm ext}$ and $P_{\rm ext}$, that depend on $2\,\frac{N_{\rm ext}(N_{\rm ext}+1)}{2}$ real parameters, as expected also from Sec. 2.2.3.

We can impose that $\gamma_{\rm ext}$ is the covariance matrix of a pure state also by using (2.2.17), i.e. by requiring that the Williamson's decomposition of (2.6.3) reads

$$\gamma_{\rm ext} = \frac{1}{2}\, W^{\rm t}_{\rm ext} W_{\rm ext} = \frac{1}{2}\, R^{\rm t}_{\rm ext}\, \mathcal{X}^2_{\rm ext}\, R_{\rm ext} \tag{2.6.5}$$

where $W_{\rm ext} \in {\rm Sp}(2N_{\rm ext}, \mathbb{R})$ and the last expression has been obtained from the Euler decomposition (2.2.16) of $W_{\rm ext}$, that includes $R_{\rm ext} \in K(N_{\rm ext})$. The symplectic matrix $W_{\rm ext}$ can be partitioned through $N_{\rm ext} \times N_{\rm ext}$ matrices as follows

$$W_{\rm ext} = \begin{pmatrix} U_{\rm ext} & Y_{\rm ext} \\ Z_{\rm ext} & V_{\rm ext} \end{pmatrix} \qquad \begin{cases} U_{\rm ext} Y^{\rm t}_{\rm ext} \text{ and } V_{\rm ext} Z^{\rm t}_{\rm ext} \text{ are symmetric} \\ U_{\rm ext} V^{\rm t}_{\rm ext} - Y_{\rm ext} Z^{\rm t}_{\rm ext} = \mathbf{1}\,. \end{cases} \tag{2.6.6}$$

The relation (2.6.5) provides the blocks in (2.6.3) through to the ones in (2.6.6). The result reads

$$Q_{\rm ext} = \frac{1}{2}\big(U^{\rm t}_{\rm ext} U_{\rm ext} + Z^{\rm t}_{\rm ext} Z_{\rm ext}\big) \qquad P_{\rm ext} = \frac{1}{2}\big(V^{\rm t}_{\rm ext} V_{\rm ext} + Y^{\rm t}_{\rm ext} Y_{\rm ext}\big) \qquad M_{\rm ext} = \frac{1}{2}\big(U^{\rm t}_{\rm ext} Y_{\rm ext} + Z^{\rm t}_{\rm ext} V_{\rm ext}\big)\,. \tag{2.6.7}$$

In order to relate γ in (2.6.2) to $\gamma_{\rm ext}$ in (2.6.3), one observes that, since $\hat{\boldsymbol{r}}^{\rm t}_{\rm ext} \equiv (\hat{\boldsymbol{q}}^{\rm t}, \hat{\boldsymbol{q}}^{\rm t}_{\rm anc}, \hat{\boldsymbol{p}}^{\rm t}, \hat{\boldsymbol{p}}^{\rm t}_{\rm anc})$, we have that the $N_{\rm ext} \times N_{\rm ext}$ blocks occurring in (2.6.3) can be partitioned in blocks as follows

$$Q_{\rm ext} \equiv \begin{pmatrix} Q & \Gamma_Q \\ \Gamma^{\rm t}_Q & Q_{\rm anc} \end{pmatrix} \qquad P_{\rm ext} \equiv \begin{pmatrix} P & \Gamma_P \\ \Gamma^{\rm t}_P & P_{\rm anc} \end{pmatrix} \qquad M_{\rm ext} \equiv \begin{pmatrix} M & \Gamma_M \\ \widetilde{\Gamma}^{\rm t}_M & M_{\rm anc} \end{pmatrix} \tag{2.6.8}$$

where Q, P and M are the $N \times N$ blocks of γ in (2.6.2), while $Q_{\rm anc}$ and $P_{\rm anc}$ are $N_{\rm anc} \times N_{\rm anc}$ symmetric matrices. Instead, $M_{\rm anc}$ is a generic $N_{\rm anc} \times N_{\rm anc}$ real matrix. Indeed, by plugging (2.6.8) into (2.6.3), it is straightforward to observe that the covariance matrix (2.6.2) is obtained by restricting $\gamma_{\rm ext}$ to the sites corresponding to the original degrees of freedom. Instead, by restricting $\gamma_{\rm ext}$ to the ancillary sites, one gets the following $2N_{\rm anc} \times 2N_{\rm anc}$ symmetric matrix

$$\gamma_{\rm anc} \equiv \begin{pmatrix} Q_{\rm anc} & M_{\rm anc} \\ M^{\rm t}_{\rm anc} & P_{\rm anc} \end{pmatrix}. \tag{2.6.9}$$

By changing the order of the rows and the columns, the matrix in (2.6.3) becomes

$$\begin{pmatrix} \gamma & \Gamma \\ \Gamma^{\mathrm{t}} & \gamma_{\mathrm{anc}} \end{pmatrix} \tag{2.6.10}$$

where γ is the covariance matrix (2.6.2), γ_{anc} is the symmetric matrix defined in (2.6.9) and

$$\Gamma \equiv \begin{pmatrix} \Gamma_Q & \Gamma_M \\ \widetilde{\Gamma}_M & \Gamma_P \end{pmatrix} \tag{2.6.11}$$

By using that (2.6.10) is positive definite, it can be shown that also γ_{anc} is positive definite[5]; hence γ_{anc} can be interpreted as the covariance matrix of the ancillary system made by N_{anc} sites.

There are many ways to construct the pure state $|\Omega\rangle$. They correspond to the freedom to fix N_{anc} first and then to choose e.g. the blocks in (2.6.8) that are different from Q, P and M, provided that the constraints (2.6.4) are satisfied.

One-mode mixed states

We find it instructive to consider explicitly the simplest case of a one-mode mixed state, i.e. $N = 1$. The minimal choice for the number of ancillae is $N_{\mathrm{anc}} = 1$.

When $N = 1$, only a non trivial symplectic eigenvalue σ occurs; hence the Williamson's decomposition (2.2.15) and the Euler decomposition (2.2.16) of a symplectic matrix provide the 2×2 covariance matrix given by

$$\gamma = \sigma\, W^{\mathrm{t}}\, W = \sigma\, R^{\mathrm{t}} \eta^2 R = R^{\mathrm{t}}\, \mathrm{diag}\big(\sigma e^{2\lambda}, \sigma e^{-2\lambda}\big) R = \begin{pmatrix} Q & M \\ M & P \end{pmatrix} \tag{2.6.13}$$

where λ is the squeezing parameter and R is a 2×2 rotation matrix, which is completely fixed by the rotation angle θ. Notice that Q, P and M are real parameters in (2.6.13). Le us remark that the pure state condition (2.2.18) for (2.6.13) gives $1 - 4d_\gamma = 0$, where we have introduced $d_\gamma \equiv \det(\gamma) = QP - M^2$. This implies that $1 - 4d_\gamma \neq 0$ for the covariance matrices (2.6.13) that correspond to the mixed states that are not pure.

When $N_{\mathrm{anc}} = 1$, the covariance matrix (2.6.5) of the pure state for the extended system reads

$$\gamma_{\mathrm{ext}} = \frac{1}{2}\, W_{\mathrm{ext}}^{\mathrm{t}} W_{\mathrm{ext}} = \frac{1}{2}\, R_{\mathrm{ext}}^{\mathrm{t}}\, \eta_{\mathrm{ext}}^2\, R_{\mathrm{ext}} = \frac{1}{2}\, R_{\mathrm{ext}}^{\mathrm{t}}\, \mathrm{diag}\big(e^{2\lambda_1}, e^{2\lambda_2}, e^{-2\lambda_1}, e^{-2\lambda_2}\big) R_{\mathrm{ext}}\,. \tag{2.6.14}$$

This 4×4 covariance matrix corresponds to a pure state, hence it depends on $N_{\mathrm{ext}}(N_{\mathrm{ext}} + 1) = 6$ real parameters (2^2 from R_{ext} and two squeezing parameters λ_i), since $N_{\mathrm{ext}} = 2$. Writing the 4×4 covariance matrix γ_{ext} in the form (2.6.3), it is straightforward to realise that 3 elements are given by the real parameters Q, P and M. Thus, we are left with three real parameters to construct the pure state for the extended system.

We find it instructive to write explicit expressions for the elements of the covariance matrix γ_{ext}. The constraints (2.6.4) for the 2×2 matrices Q_{ext}, P_{ext} and M_{ext} provide six equations: four

[5]By employing the following formula for the determinant of a block matrix

$$\det\begin{pmatrix} A & B \\ C & D \end{pmatrix} = \det(A - B\, D^{-1} C)\, \det(D) \tag{2.6.12}$$

where it is assumed that D is invertible, one finds that the eigenvalues of γ_{anc} are also eigenvalues of γ_{ext}. If A is invertible, a formula similar to (2.6.12) can be written where $\det(A)$ is factorised and this result can be used to show that the eigenvalues of γ are eigenvalues of γ_{ext} as well.

from the first relation and one from each one of the other two relations (that can be written in the form $X = 0$, where X is a 2×2 antisymmetric matrix).

When $\Gamma_M \neq 0$, the solution of this system can be written in terms of Γ_Q, Γ_P and Γ_M as

$$\begin{aligned}
Q_{\text{anc}} &= -\frac{1-4d_\gamma}{4\Gamma_M^2}\left(Q + \frac{8\Gamma_Q(M\,\Gamma_M - Q\,\Gamma_P)}{1-4d_\gamma} + \frac{16\Gamma_Q^2\big[P\,\Gamma_M^2 - \Gamma_P(2M\,\Gamma_M - Q\,\Gamma_P)\big]}{(1-4d_\gamma)^2}\right) \\
M_{\text{anc}} &= -\frac{1}{\Gamma_M}\left(M\,\Gamma_M - Q\,\Gamma_P + \frac{4\Gamma_Q\big[P\,\Gamma_M^2 - \Gamma_P(2M\,\Gamma_M - Q\,\Gamma_P)\big]}{1-4d_\gamma}\right) \\
P_{\text{anc}} &= -\frac{4\big[P\,\Gamma_M^2 - \Gamma_P(2M\,\Gamma_M - Q\,\Gamma_P)\big]}{1-4d_\gamma} \\
\widetilde{\Gamma}_M &= \frac{4\Gamma_Q\,\Gamma_P + 4d_\gamma - 1}{4\Gamma_M}\,.
\end{aligned} \tag{2.6.15}$$

When $\Gamma_M = 0$ and $\Gamma_P \neq 0$, we find

$$\begin{aligned}
Q_{\text{anc}} &= \frac{P(4d_\gamma - 1)}{4\Gamma_P^2} + \frac{2M\,\widetilde{\Gamma}_M}{\Gamma_P} - \frac{4Q\,\widetilde{\Gamma}_M^2}{1-4d_\gamma} & \Gamma_Q &= \frac{1-4d_\gamma}{4\Gamma_P} \\
P_{\text{anc}} &= -\frac{4Q\,\Gamma_P^2}{1-4d_\gamma} & M_{\text{anc}} &= M - \frac{4Q\,\Gamma_P\,\widetilde{\Gamma}_M}{1-4d_\gamma}
\end{aligned} \tag{2.6.16}$$

while a solution does not exist for $\Gamma_M = \Gamma_P = 0$. Notice that $1 - 4d_\gamma \neq 0$ in these expressions because γ does not corresponds to a pure state.

Block diagonal covariance matrices

Many interesting mixed states are described by a block diagonal covariance matrix $\gamma = Q \oplus P$. In this cases $M = \mathbf{0}$ in (2.6.2).

It is worth considering a pure state for the extended system such that $M_{\text{ext}} = \mathbf{0}$ in the corresponding covariance matrix (2.6.3). In this case (2.6.4) reduce to

$$Q_{\text{ext}}\,P_{\text{ext}} = \frac{1}{4}\,\mathbf{1} \qquad \Longleftrightarrow \qquad \begin{cases} Q\,P = \dfrac{1}{4}\,\mathbf{1} - \Gamma_Q\,\Gamma_P^{\text{t}} \\ Q_{\text{anc}}\,P_{\text{anc}} = \dfrac{1}{4}\,\mathbf{1} - \Gamma_Q^{\text{t}}\,\Gamma_P \\ Q\,\Gamma_P + \Gamma_Q\,P_{\text{anc}} = \mathbf{0} \\ P\,\Gamma_Q + \Gamma_P\,Q_{\text{anc}} = \mathbf{0} \end{cases} \tag{2.6.17}$$

where $\Gamma_Q\,\Gamma_P^{\text{t}} \neq \mathbf{0}$ and $\gamma = Q \oplus P$ is the covariance matrix of a state that is not pure.

A common choice consists in considering purifications where the extended system has twice the degrees of freedom occurring in the original one, namely $N_{\text{anc}} = N$. In these cases Γ_Q, Γ_P and Γ_M are $N \times N$ matrices.

Considering the purifications with $N_{\text{anc}} = N$, a drastic simplification corresponds to require that $\gamma = \gamma_{\text{anc}}$, which is equivalent to impose that $Q = Q_{\text{anc}}$ and $P = P_{\text{anc}}$. In this case, a solution is given by symmetric and commuting matrices Γ_Q and Γ_P that can be related through the last two equations in (2.6.17), which give

$$Q = -\,\Gamma_Q\,P\,\Gamma_P^{-1} \qquad \Gamma_Q\,P\,\Gamma_P^{-1} = \Gamma_P^{-1}\,P\,\Gamma_Q\,. \tag{2.6.18}$$

Setting $\Gamma_P = \alpha\,\Gamma_Q^{-1}$ with $\alpha \in \mathbb{R}$, the last equality is solved while the remaining relation $Q = -\frac{1}{\alpha}\,\Gamma_Q\,P\,\Gamma_Q$, whose validity is not guaranteed, provides Γ_Q.

A different solution for the matrix equations in (2.6.18) can be written when Q and P can be decomposed through three real matrices A, B and Λ as follows

$$Q = A\,\Lambda\,B^{-1} \qquad\qquad P = B\,\Lambda\,A^{-1}\,. \tag{2.6.19}$$

In this case, we can construct Γ_Q and Γ_P as

$$\Gamma_Q = A\,\tilde{\Lambda}\,B^{-1} \qquad\qquad \Gamma_P = -\,B\,\tilde{\Lambda}\,A^{-1} \qquad\qquad \big[\,\tilde{\Lambda}\,,\Lambda\,\big] = 0 \tag{2.6.20}$$

where a new matrix $\tilde{\Lambda}$ that commutes with Λ has been introduced.

It is straightforward to check that (2.6.19) and (2.6.20) satisfy the matrix equations in (2.6.18). Notice that Γ_P is not proportional to Γ_Q^{-1} in (2.6.20).

An important example where $N_{\rm anc} = N$ and $\gamma = \gamma_{\rm anc}$ is the thermofield double state (TFD). In Appendix B a detailed analysis for this pure state for harmonic lattices is reported. The relations (B.1.25) and (B.1.26) tell us that the TFD corresponds to a special case[6] of (2.6.19) and (2.6.20).

The simplest case corresponds to $N = N_{\rm anc} = 1$, which has been discussed in Sec. 2.6.1 in the most general setting. Solving the system (2.6.17) for this case, one finds

$$Q_{\rm anc} = -\frac{(1-4QP)P}{4\Gamma_P^2} \qquad P_{\rm anc} = \frac{4Q\Gamma_P^2}{4QP-1} \qquad \Gamma_Q = \frac{1-4QP}{4\Gamma_P}\,. \tag{2.6.21}$$

When $M = 0$, the observation in the text below (2.6.13) tells us that $4QP - 1 \neq 0$ in order to have a mixed state that is not pure to purify. Notice also that, by setting $M = \widetilde{\Gamma}_M = 0$ in (2.6.16), that holds for $\Gamma_M = 0$, one finds (2.6.21) and $M_{\rm anc} = 0$. Thus, when $M_{\rm ext} = \mathbf{0}$ and $N = N_{\rm anc} = 1$ we can parameterise the pure state of the extended system through a single parameter. This is consistent with the analysis reported in [79]. As final remark about the purifications having $N = N_{\rm anc} = 1$, let us observe that the second equation in (2.6.18) is trivially satisfied, while the first one is obtained by setting $Q = Q_{\rm anc}$ and $P = P_{\rm anc}$ in (2.6.21).

2.6.2 Selection criterion for the pure state

In the previous discussion we have explored the constraints guaranteeing that the covariance matrix $\gamma_{\rm ext}$ corresponds to a pure state under the condition that $\gamma_{\rm ext}$ provides the covariance matrix γ of the given mixed state once the ancillary degrees of freedom have been traced out.

These constraints identify the parameter space of the pure states allowed by γ for a given value of $N_{\rm anc}$. Within this space of parameters, it is natural to introduce a quantity $\mathcal{F}$ whose minimisation provides a particular pure state with certain properties. Thus, $\mathcal{F}$ characterises the criterion to select the pure state provided by the purification procedure as follows

$$\widetilde{\mathcal{F}}(\gamma) \,\equiv\, \min_{\gamma_{\rm ext}} \big[\mathcal{F}(\gamma_{\rm ext})\big] \tag{2.6.22}$$

where $\gamma_{\rm ext}$ is the covariance matrix for the extended system, that is constrained as described in Sec. 2.6.1, and $\widetilde{\mathcal{F}}$ denotes the minimal value of $\mathcal{F}$ as $\gamma_{\rm ext}$ spans all the pure states allowed by γ. For the bosonic Gaussian states that we are considering, the calculations can be performed by employing either the wave functions or the covariance matrices.

[6] In particular, Λ and $\tilde{\Lambda}$ are the diagonal matrices in (B.1.13), while $A = \widetilde{V}\,\mathcal{S}^{-1}$ and $B = \widetilde{V}\,\mathcal{S}$, in terms of the matrices $\widetilde{V}$ and $\mathcal{S}$ introduced in the Appendix B.

For instance, the entanglement of purification for a bipartite mixed state [289–292] is (2.6.22), with $\mathcal{F}$ given by the entanglement entropy of a particular bipartition of $\mathcal{H}_{\text{extended}}$.

In [46, 79], the purification complexity has been introduced to quantify the complexity of a mixed state. The definition of purification complexity is given by (2.6.22) in the special case where $\mathcal{F}$ is the complexity of the pure state corresponding to γ_{ext} with respect to a given fixed pure state in $\mathcal{H}_{\text{extended}}$, whose covariance matrix is denoted by $\gamma_{\text{ext},0}$. This definition of purification complexity requires the choice of a cost function. The purification complexity explored in [79] reads

$$\widetilde{\mathcal{C}}_r(\gamma) \equiv \min_{\gamma_{\text{ext}}} \big[\mathcal{C}_r(\gamma_{\text{ext}}, \gamma_{\text{ext},0}) \big] \tag{2.6.23}$$

where either $r = 1$ or $r = 2$, depending on whether the F_1 cost function or the F_2 cost function is adopted. In [79] the purification complexity based on the F_1 cost function has been mainly studied because, for the pure states, the divergence structure of the complexity evaluated through the F_1 cost function is closer to the one obtained from holographic calculations [35, 63]. The complexity defined through the F_1 cost function depends on the choice of the underlying basis, while the F_2 cost function leads to a complexity that is independent of this choice.

This approach to the complexity of mixed states is different from the one considered in this thesis. The main difference is due to the fact that in the purification procedure described in Sec. 2.3.4 ancillary degrees of freedom have not been introduced. Moreover, the purification complexity defined in (2.6.23) depends on the choice of the pure state corresponding to $\gamma_{\text{ext},0}$. Furthermore, in the evaluation of the complexity of a mixed state through (2.6.23), no cost is assigned to the purification process of extending the system through ancillary degrees of freedom, given that the circuit considered in (2.6.23) is entirely made by pure states in $\mathcal{H}_{\text{extended}}$.

Explicit computations through (2.6.23) are technically involved; we refer the interested reader to the detailed analysis performed in [79]. Focussing on the simple case of one-mode thermal states, in Sec. 2.7.6 we compare the complexity evaluated through the Fisher-Rao distance in chapter 2 with the results found in [79] for the complexity of mixed states based on the purification complexity.

2.7 Harmonic chains

In this section we further study some of the quantities discussed in the previous sections by focussing on the one-dimensional case of the harmonic chain, either on the circle (i.e. with periodic boundary conditions) or on the infinite line. In this case we obtain analytic expressions in terms of the parameters of the circuit for some quantities and provide numerical results for the quantities that are more difficult to address analytically. After a brief discussion of the model in Sec. 2.7.1, circuits whose reference and target states are either pure or thermal are considered in Sec. 2.7.2 and Sec. 2.7.3 respectively. Numerical results for the complexity and the mutual complexity associated to subregions are presented in Sec. 2.7.4 and Sec. 2.7.5. Finally, in Sec. 2.7.6 we consider a simple comparison between the complexity for mixed states discussed in this chapter and the one based on the purification complexity proposed in [79]. In Appendix C we report the two-point functions of harmonic chains in various configurations. In particular, the correlators employed in this section for ground states and thermal states of periodic and infinite harmonic chains have been reported in Appendix C.1.

In this section we consider only examples that involve states whose covariance matrices are block diagonal. We remark that the results discussed in the previous sections hold also for states characterised by covariance matrices that are not block diagonal. For instance, these states typically occur in the out-of-equilibrium dynamics of the harmonic lattices, as discussed in chapters 3

and 4 (see also [101, 293–295]).

2.7.1 Hamiltonian

The Hamiltonian of the periodic harmonic chain made by N sites, with frequency ω, mass m and elastic constant κ reads

$$\widehat{H} = \sum_{i=1}^{N} \left(\frac{1}{2m}\,\hat{p}_i^2 + \frac{m\omega^2}{2}\,\hat{q}_i^2 + \frac{\kappa}{2}(\hat{q}_{i+1} - \hat{q}_i)^2 \right) \tag{2.7.1}$$

where $\hat{\boldsymbol{r}} \equiv (\hat{q}_1, \dots, \hat{q}_N, \hat{p}_1, \dots, \hat{p}_N)^{\mathrm{t}}$ collects the position and momentum operators and the periodic boundary conditions $\hat{q}_{N+1} = \hat{q}_1$ and $\hat{p}_{N+1} = \hat{p}_1$ are imposed.

Assuming that both κ and m are non-vanishing, the canonical transformation given by $\hat{q}_i \to \hat{q}_i / \sqrt[4]{m\kappa}$ and $\hat{p}_i \to \sqrt[4]{m\kappa}\,\hat{p}_i$ allows to write (2.7.1) as follows

$$\widehat{H} = \frac{\sqrt{\kappa/m}}{2} \sum_{i=1}^{N} \left(\hat{p}_i^2 + \frac{\omega^2}{\kappa/m}\,\hat{q}_i^2 + (\hat{q}_{i+1} - \hat{q}_i)^2 \right) \equiv \frac{1}{2}\,\hat{\boldsymbol{r}}^{\mathrm{t}} H^{\mathrm{phys}}\,\hat{\boldsymbol{r}} \tag{2.7.2}$$

where

$$H^{\mathrm{phys}} = \sqrt{\kappa/m}\,\Big(\big[(\tilde{\omega}^2 + 2)\mathbf{1} - T \big] \oplus \mathbf{1} \Big) \tag{2.7.3}$$

and we are naturally led to introduce the dimensionless parameter

$$\tilde{\omega}^2 = \frac{\omega^2}{\kappa/m}\,. \tag{2.7.4}$$

The non vanishing elements of the symmetric matrix T in (2.7.3) are $T_{i,i+1} = T_{i+1,i} = 1$ with $1 \leqslant i \leqslant N-1$ and $T_{1,N} = T_{N,1} = 1$.

Let us introduce the $N \times N$ real and orthogonal matrix $\widetilde{V}$, whose generic element for even N is given by

$$\widetilde{V}_{i,k} \equiv \begin{cases} \sqrt{2/N}\,\cos(2\pi i\,k/N) & 1 \leqslant k < N/2 \\ (-1)^i/\sqrt{N} & k = N/2 \\ \sqrt{2/N}\,\sin(2\pi i\,k/N) & N/2+1 \leqslant k < N-1 \\ 1/\sqrt{N} & k = N \end{cases} \tag{2.7.5}$$

and for odd N by

$$\widetilde{V}_{i,k} \equiv \begin{cases} \sqrt{2/N}\,\cos(2\pi i\,k/N) & 1 \leqslant k < (N-1)/2 \\ \sqrt{2/N}\,\sin(2\pi i\,k/N) & (N-1)/2+1 \leqslant k < N-1 \\ 1/\sqrt{N} & k = N\,. \end{cases} \tag{2.7.6}$$

The matrix $\widetilde{V}$ diagonalises both T and $\mathbf{1}$ in (2.7.3); hence, by introducing the orthogonal matrix $V \equiv \widetilde{V} \oplus \widetilde{V}$, that is also symplectic, we have [78]

$$H^{\mathrm{phys}} = V \left[\sqrt{\kappa/m}\,\mathrm{diag}\big(\Omega_1^2, \dots, \Omega_N^2, 1, \dots, 1\big) \right] V^{-1} \tag{2.7.7}$$

where Ω_k provides the dispersion relation, which depends on the parameter $\tilde{\omega}$ defined in (2.7.4) as follows

$$\Omega_k \equiv \sqrt{\tilde{\omega}^2 + 4\,(\sin[\pi k/N])^2} \qquad k = 1, \dots, N\,. \tag{2.7.8}$$

Adapting the computation reported in Sec. 2.2.6 to this case, one obtains the Williamson's decomposition (2.2.45) with the symplectic eigenvalues given by

$$\sigma_{\text{phys},k} = \sqrt{\kappa/m}\,\Omega_k \tag{2.7.9}$$

and the symplectic matrix W_{phys} by

$$W_{\text{phys}} = \mathcal{X}_{\text{phys}}\, V^t \qquad \mathcal{X}_{\text{phys}} \equiv \text{diag}\big(\sqrt{\Omega_1},\dots,\sqrt{\Omega_N},1/\sqrt{\Omega_1},\dots,1/\sqrt{\Omega_N}\,\big)\,. \tag{2.7.10}$$

In these expressions the zero mode corresponds to $k = N$ and its occurrence is due to the invariance of the system under translations. The comparison between the expressions reported throughout this section and the corresponding ones in Sec. 2.2.6 can be done once the canonical transformation above (2.7.2) has been taken into account[7].

It is worth remarking that the canonical transformation that brings (2.7.1) into (2.7.2) cannot be defined when $\kappa = 0$. This implies, for instance, that, in order to employ the unentangled product state of the harmonic chain as reference state (this is often the case in the recent literature on the circuit complexity [35, 36, 40, 67, 79]), our analysis must be adapted to the Hamiltonian (2.7.1).

2.7.2 Pure states

In this subsection we study the circuit complexity for pure states that are the ground states of periodic harmonic chains having different frequencies [35].

Covariance matrix

The two-point correlators $\langle \hat{q}_i \hat{q}_j \rangle$ and $\langle \hat{p}_i \hat{p}_j \rangle$ in the ground state of the Hamiltonian (2.7.2), where periodic boundary conditions are imposed, are given by (C.1.1) and determine the elements of the correlation matrices Q_{gs} and P_{gs} respectively. These matrices provide the block diagonal covariance matrix $\gamma_{\text{gs}} = Q_{\text{gs}} \oplus P_{\text{gs}}$. One can show that

$$\gamma_{\text{gs}} = V\big(\mathcal{Q}_{\text{gs}} \oplus \mathcal{P}_{\text{gs}}\big)\, V^{\text{t}} = V\big(\mathcal{Q}_{\text{gs}} \oplus \mathcal{P}_{\text{gs}}\big)\, V^{-1}\,. \tag{2.7.11}$$

where $\mathcal{Q}_{\text{gs}}$ and $\mathcal{P}_{\text{gs}}$ are diagonal matrices whose elements read

$$(\mathcal{Q}_{\text{gs}})_{k,k} = \frac{1}{2\,\Omega_k} \qquad (\mathcal{P}_{\text{gs}})_{k,k} = \frac{1}{2}\,\Omega_k \qquad k = 1,\dots,N\,. \tag{2.7.12}$$

The relation (2.7.11) tells us that the orthogonal matrix V introduced in Sec. 2.7.1 diagonalises the symmetric matrix γ_{gs}. Let us remark that V depends only on the number of sites N of the harmonic chain. Moreover we have that

$$\mathcal{Q}_{\text{gs}} \oplus \mathcal{P}_{\text{gs}} = \frac{1}{2}\,\mathcal{X}_{\text{C}}^2\,. \tag{2.7.13}$$

where

$$\mathcal{X}_{\text{C}} \,\equiv\, \text{diag}\big(1/\sqrt{\Omega_1},\dots,1/\sqrt{\Omega_N},\sqrt{\Omega_1},\dots,\sqrt{\Omega_N}\,\big) = J^{\text{t}}\,\mathcal{X}_{\text{phys}}\,J \tag{2.7.14}$$

and $\mathcal{X}_{\text{phys}}$ has been introduced in (2.7.10). By introducing the symplectic matrix

$$W_{\text{C}} \,\equiv\, \mathcal{X}_{\text{C}}\, V^{\text{t}} \tag{2.7.15}$$

we have that the Williamson's decomposition of γ_{gs} reads

$$\gamma_{\text{gs}} = \frac{1}{2}\, W_{\text{C}}^{\text{t}}\, W_{\text{C}}\,. \tag{2.7.16}$$

Notice that the symplectic matrices W_{phys} and W_{C}, defined in (2.7.10) and (2.7.15) respectively, are related as $W_{\text{C}} = W_{\text{phys}}^{-\text{t}}$.

[7] This canonical transformation is responsible e.g. for the different definitions of Ω_k in (2.7.8) and in Sec. 2.2.6 and also for the factor between (2.7.9) and (2.2.46), which is the same prefactor occurring in the Hamiltonian (2.7.2).

Complexity

We consider the circuit complexity where the reference state and the target state are the ground states of periodic harmonic chains whose Hamiltonians are characterised by the parameters $(\omega_{\rm R}, \kappa_{\rm R}, m_{\rm R})$ and $(\omega_{\rm T}, \kappa_{\rm T}, m_{\rm T})$ respectively.

For the sake of simplicity, in our analysis we set $\kappa_{\rm R} = \kappa_{\rm T} \equiv \kappa$ and $m_{\rm R} = m_{\rm T} \equiv m$; hence only the parameter $\tilde{\omega}$ distinguishes the reference and the target states.

In this case it is straightforward to find that (2.2.23) becomes

$$\Delta_{\rm TR} = V\big(\mathcal{Q}_{\rm gs,T}\,\mathcal{Q}^{-1}_{\rm gs,R} \oplus \mathcal{P}_{\rm gs,T}\,\mathcal{P}^{-1}_{\rm gs,R}\big)\,V^{-1} \tag{2.7.17}$$

where the diagonal matrices $\mathcal{Q}_{\rm gs,R}$, $\mathcal{Q}_{\rm gs,T}$, $\mathcal{P}_{\rm gs,R}$ and $\mathcal{P}_{\rm gs,T}$ can be easily obtained by writing (2.7.12) for the reference and for the target state. Thus, the complexity given by (2.2.22) and (2.2.24) simplifies to [35]

$$\mathcal{C} = \frac{1}{2\sqrt{2}}\sqrt{\mathrm{Tr}\Big\{\big[\log\big(\mathcal{Q}_{\rm gs,T}\,\mathcal{Q}^{-1}_{\rm gs,R} \oplus \mathcal{P}_{\rm gs,T}\,\mathcal{P}^{-1}_{\rm gs,R}\big)\big]^2\Big\}} = \frac{1}{2}\sqrt{\sum_{k=1}^{N}\Big(\log\big[\Omega_{{\rm T},k}/\Omega_{{\rm R},k}\big]\Big)^2} \tag{2.7.18}$$

where

$$\Omega_{{\rm S},k} \equiv \sqrt{\tilde{\omega}_{\rm S}^2 + 4\,(\sin[\pi k/N])^2} \qquad\qquad k = 1, \dots, N \qquad\qquad {\rm S} \in \big\{{\rm R}, {\rm T}\big\}\,. \tag{2.7.19}$$

Notice that the complexity (2.7.18) depends on m and κ only through the dimensionless parameters $\tilde{\omega}_{\rm R}$ and $\tilde{\omega}_{\rm T}$.

In the thermodynamic limit $N \to \infty$, the expression (2.7.18) for the complexity becomes [35]

$$\mathcal{C} = a(\tilde{\omega}_{\rm T}, \tilde{\omega}_{\rm R})\,\sqrt{N} + \dots \qquad\qquad \tilde{\omega}_{\rm R} \neq \tilde{\omega}_{\rm T} \qquad\qquad N \to \infty \tag{2.7.20}$$

where the subleading terms have been neglected and the coefficient of the leading term reads

$$a(\tilde{\omega}_{\rm T}, \tilde{\omega}_{\rm R}) \equiv \frac{1}{2}\sqrt{\frac{1}{\pi}\int_0^\pi \Big(\log\big[\Omega_{{\rm T},\theta}/\Omega_{{\rm R},\theta}\big]\Big)^2 d\theta} \qquad\qquad \Omega_{\rm R} \neq \Omega_{\rm T} \tag{2.7.21}$$

with

$$\Omega_{{\rm S},\theta} \equiv \sqrt{\tilde{\omega}_{\rm S}^2 + 4\,(\sin\theta)^2} \qquad\qquad \theta \in (0, \pi) \tag{2.7.22}$$

which can be easily obtained from (2.7.19). As consistency check, notice that $a(\tilde{\omega}_{\rm R}, \tilde{\omega}_{\rm R}) = 0$, as expected.

We find it interesting to observe that, once the limit $N \to \infty$ has been taken, either $\tilde{\omega}_{\rm R}$ or $\tilde{\omega}_{\rm T}$ can be set to zero. For instance, setting $\tilde{\omega}_{\rm T} = 0$ in (2.7.21) gives the following finite result

$$a(\tilde{\omega}_{\rm R}, \tilde{\omega}_{\rm T} = 0)^2 = \frac{1}{16\pi}\int_0^\pi \left(2\log[\sin\theta] - \log\left[\frac{\tilde{\omega}_{\rm R}^2}{4} + (\sin\theta)^2\right]\right)^2 d\theta\,. \tag{2.7.23}$$

On the other hand, it is well known that the correlators $\langle \hat{q}_i \hat{q}_j \rangle$ in (C.1.1) diverge when the frequency of the chain vanishes because of the occurrence of the zero mode; hence we cannot evaluate $\mathcal{C}$ for a finite chain when either $\tilde{\omega}_{\rm T} = 0$ or $\tilde{\omega}_{\rm R} = 0$. This tells us that the limits $N \to \infty$ and $\tilde{\omega}_{\rm T} \to 0$ do not commute.

In Fig. 2.4 we show the complexity $\mathcal{C}$ as function of the size N of the periodic chain. The numerical results discussed in this chapter have been obtained for $\kappa = 1$ and $m = 1$, unless otherwise specified; hence $\tilde{\omega}_{\rm R} = \omega_{\rm R}$ and $\tilde{\omega}_{\rm T} = \omega_{\rm T}$. In the left and right panels of Fig. 2.4 we

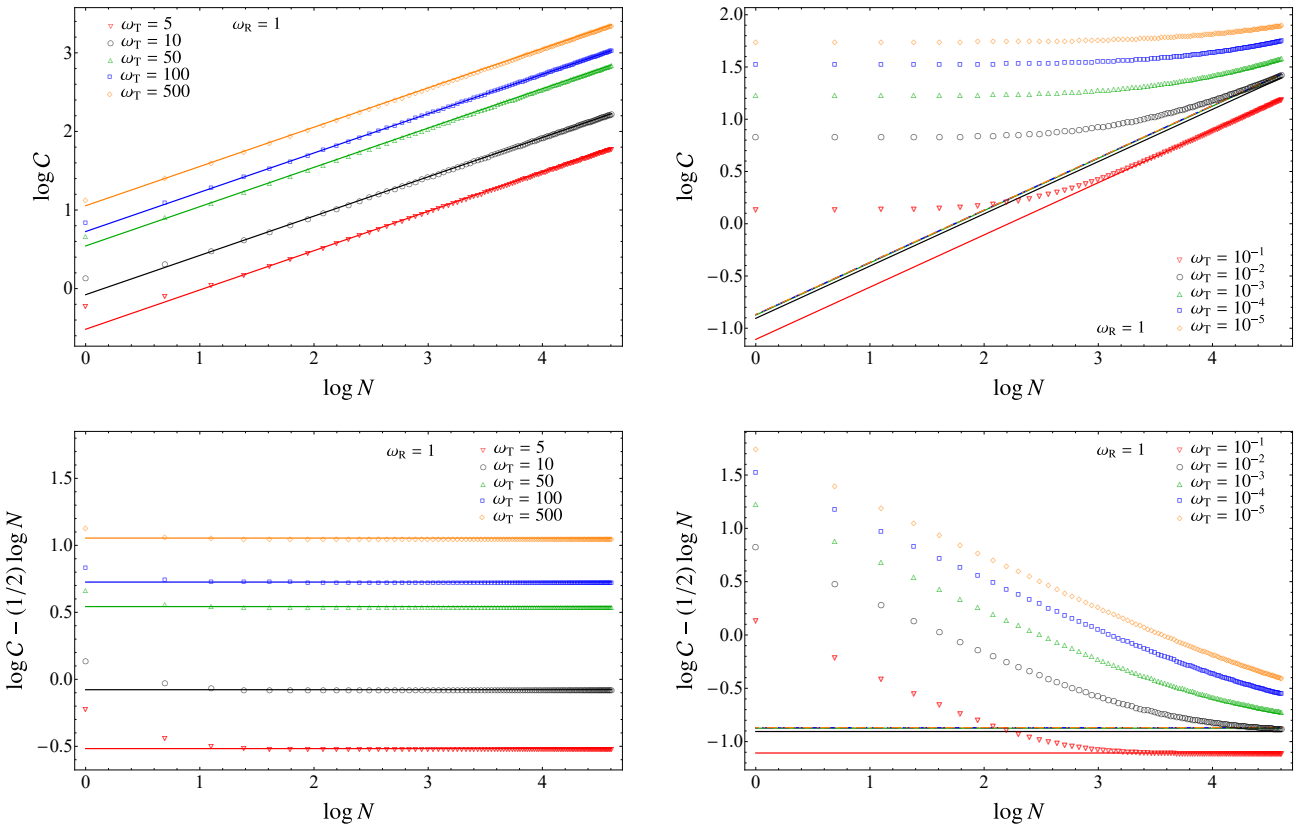

Figure 2.4: The complexity $\mathcal{C}$ in terms of the size N of the periodic harmonic chain. The reference and the target states are the ground states with $\omega = \omega_{\rm R}$ and $\omega = \omega_{\rm T}$ respectively (here $\kappa = 1$ and $m = 1$). The data reported correspond to $\omega_{\rm R} = 1$ and different $\omega_{\rm T}$. The solid lines in the top panels represent (2.7.20), while the horizontal solid lines in the bottom panels correspond to the constant values of $a(\tilde{\omega}_{\rm T}, \tilde{\omega}_{\rm R})$ obtained from (2.7.21).

have $\omega_{\rm T} > \omega_{\rm R}$ and $\omega_{\rm T} < \omega_{\rm R}$ respectively (notice that $\omega_{\rm R} = 1$ for all the panels). In the top panels the numerical data are compared against the expression (2.7.20) (solid lines) obtained in the thermodynamic limit: while in the top left panel the agreement is very good at large N, from the top right panel we conclude that larger values of N are needed to observe a reasonable agreement as $\tilde{\omega}_{\rm T} \to 0$. In the bottom panels of Fig. 2.4 we consider the subleading term in (2.7.20): while in the bottom left panel the data agree with the horizontal lines corresponding to $a(\tilde{\omega}_{\rm T}, \tilde{\omega}_{\rm R})$ given by (2.7.21), in the bottom right panel the agreement gets worse as $\tilde{\omega}_{\rm T} \to 0$. Notice that the solid lines in the right panels of Fig. 2.4 accumulate on a limiting line as $\omega_{\rm T} \to 0$. This line can be found by plugging (2.7.23) with $\omega_{\rm R} = 1$ into (2.7.20).

2.7.3 Thermal states

The thermal states are the most natural mixed states to consider. In the following we evaluate the complexity (2.2.24) when both the reference and the target states are thermal states of the harmonic chain.

Covariance matrix

The two-point correlators $\langle \hat{q}_i \hat{q}_j \rangle$ and $\langle \hat{p}_i \hat{p}_j \rangle$ of a periodic chain in a thermal state at temperature T are given by (C.1.3) and (C.1.4) and provide the generic elements of the correlation matrices $Q_{\rm th}$ and $P_{\rm th}$ respectively. These matrices are the non vanishing blocks of the covariance matrix $\gamma_{\rm th} = Q_{\rm th} \oplus P_{\rm th}$ of the thermal state.

One can show that

$$\gamma_{\rm th} = V \big(\mathcal{Q}_{\rm th} \oplus \mathcal{P}_{\rm th} \big) V^{\rm t} = V \big(\mathcal{Q}_{\rm th} \oplus \mathcal{P}_{\rm th} \big) V^{-1} \tag{2.7.24}$$

where V is the same symplectic and orthogonal matrix introduced through (2.7.5) and (2.7.6) for the ground state. The matrices $\mathcal{Q}_{\rm th}$ and $\mathcal{P}_{\rm th}$ are diagonal and have elements given respectively by [296]

$$(\mathcal{Q}_{\rm th})_{k,k} = \frac{\coth\big[\Omega_k/(2\widetilde{T})\big]}{2\,\Omega_k} \qquad (\mathcal{P}_{\rm th})_{k,k} = \frac{1}{2}\,\Omega_k \coth\big[\Omega_k/(2\widetilde{T})\big] \qquad k = 1, \dots, N\,. \tag{2.7.25}$$

where we have introduced the dimensionless parameter

$$\widetilde{T} \equiv \frac{T}{\sqrt{\kappa/m}}\,. \tag{2.7.26}$$

It is straightforward to check that (2.7.25) becomes (2.7.12) as $T \to 0$ and therefore, in the same regime, (2.7.24) reduces to (2.7.11), as expected.

By employing the results obtained in Sec. 2.7.2 for the covariance matrix of the ground state, it is not difficult to find that the Williamson's decomposition of the covariance matrix $\gamma_{\rm th}$ of the thermal state reads

$$\gamma_{\rm th} = W_{\rm C}^{\rm t}\, \mathcal{D}_{\rm th}\, W_{\rm C}\,. \tag{2.7.27}$$

The matrix $W_{\rm C}$ is the symplectic matrix (2.7.15) occurring in the Williamson's decomposition (2.7.16) of the ground state and $\mathcal{D}_{\rm th} \equiv {\rm diag}(\sigma_{{\rm th},1}, \dots, \sigma_{{\rm th},N}) \oplus {\rm diag}(\sigma_{{\rm th},1}, \dots, \sigma_{{\rm th},N})$, with the symplectic eigenvalues given by [267]

$$\sigma_{{\rm th},k} = \frac{1}{2}\,\coth\big[\Omega_k/(2\widetilde{T})\big] = \frac{1}{2}\,\coth\big[\sigma_{{\rm phys},k}/(2T)\big] \qquad k = 1, \dots, N\,. \tag{2.7.28}$$

Complexity

In order to explore the complexity of two thermal states of a periodic chain, let us consider a reference state characterised by frequency $\omega_{\rm R}$ and temperature $T_{\rm R}$ and a target state characterised by frequency $\omega_{\rm T}$ and temperature $T_{\rm T}$, assuming again that $\kappa_{\rm R} = \kappa_{\rm T} = \kappa$ and $m_{\rm R} = m_{\rm T} = m$. Like (2.7.11), we have that also (2.7.17) can be adapted to this case, simply by replacing $\mathcal{Q}_{\rm gs,M}$ with $\mathcal{Q}_{\rm th,M}$ and $\mathcal{P}_{\rm gs,M}$ with $\mathcal{P}_{\rm th,M}$ taken from (2.7.25), with ${\rm M} \in \{{\rm R}, {\rm T}\}$. Thus, the complexity given by (2.2.24) and (2.2.22) for these thermals states becomes

$$\mathcal{C} = \frac{1}{2\sqrt{2}} \sqrt{{\rm Tr}\Big\{ \big[\log\big(\mathcal{Q}_{\rm th,T}\, \mathcal{Q}_{\rm th,R}^{-1} \oplus \mathcal{P}_{\rm th,T}\, \mathcal{P}_{\rm th,R}^{-1} \big) \big]^2 \Big\}} \tag{2.7.29}$$

$$= \frac{1}{2\sqrt{2}} \sqrt{\sum_{k=1}^{N} \left\{ \left[\log\left(\frac{\Omega_{{\rm R,T},k}}{\Omega_{{\rm T,R},k}} \right) \right]^2 + \left[\log\left(\frac{\Omega_{{\rm T,T},k}}{\Omega_{{\rm R,R},k}} \right) \right]^2 \right\}} \tag{2.7.30}$$

where we have introduced

$$\Omega_{{\rm M,N},k} \equiv \Omega_{{\rm M},k} \coth\big(\Omega_{{\rm N},k}/(2\widetilde{T}_{\rm N}) \big) \qquad {\rm M, N} \in \big\{ {\rm R}\,, {\rm T} \big\} \tag{2.7.31}$$

with $\Omega_{\mathrm{S},k}$ given in (2.7.19). Notice that $\Omega_{\mathrm{M,N},k} \to \Omega_{\mathrm{M},k}$ as $T_{\mathrm{N}} \to 0$; hence in the limit given by $\widetilde{T}_{\mathrm{R}} \to 0$ and $\widetilde{T}_{\mathrm{T}} \to 0$, the expected expression (2.7.18) for pure states is recovered. Notice that the complexity (2.7.30) depends on the dimensionless parameters $\tilde{\omega}_{\mathrm{R}}$, $\tilde{\omega}_{\mathrm{T}}$, $\tilde{T}_{\mathrm{R}}$ and $\tilde{T}_{\mathrm{T}}$.

An interesting application of (2.7.30) is the computation of the mutual complexity of the thermofield double states, as discussed in Appendix B.3 (see (B.3.4)).

In the special case where $\tilde{\omega}_{\mathrm{R}} = \tilde{\omega}_{\mathrm{T}} \equiv \tilde{\omega}$, the expression (2.7.30) simplifies to

$$\mathcal{C} \,=\, \frac{1}{2}\sqrt{\sum_{k=1}^{N}\left[\log\left(\frac{\coth(\Omega_k/(2\widetilde{T}_{\mathrm{T}}))}{\coth(\Omega_k/(2\widetilde{T}_{\mathrm{R}}))}\right)\right]^2} \,=\, \frac{1}{2\sqrt{2}}\,\sqrt{\mathrm{Tr}\left\{\left[\log\left(\mathcal{D}_{\mathrm{th,T}}\,\mathcal{D}_{\mathrm{th,R}}^{-1}\right)\right]^2\right\}}\,. \tag{2.7.32}$$

This result is consistent with the general expression (2.2.30) for the complexity in the special case where $W_{\mathrm{TR}} = \mathbf{1}$.

In the special case of $\tilde{\omega}_{\mathrm{R}} = \tilde{\omega}_{\mathrm{T}}$, from (2.7.27) and (2.7.15) we have that $W_{\mathrm{T}} = W_{\mathrm{R}}$, hence (2.7.32) provides the length of the W path connecting the reference and the target state that we are considering (see Sec. 2.3.2). Indeed it is proportional to the proposal (2.3.12) for the spectrum complexity.

As for the basis complexity, from (2.7.28), one observes that, for a generic number of modes larger than one, the requirement $\mathcal{D}_{\mathrm{R}} = \mathcal{D}_{\mathrm{T}}$ leads to $\tilde{\omega}_{\mathrm{R}} = \tilde{\omega}_{\mathrm{T}}$ and $\tilde{T}_{\mathrm{R}} = \tilde{T}_{\mathrm{T}}$. This implies $W_{\mathrm{R}} = W_{\mathrm{T}}$, as just remarked above, hence $\gamma_{\mathrm{R}} = \gamma_{\mathrm{T}}$ and the basis complexity (2.3.15) vanishes for the thermal states. Also the corresponding basis complexity (2.3.16) vanishes because it is bounded from above by (2.3.15). We expect that this is a peculiar feature due to the simplicity of the model. Notice that, for pure states, the constraint $\mathcal{D}_{\mathrm{R}} = \mathcal{D}_{\mathrm{T}}$ does not imply that $\gamma_{\mathrm{R}} = \gamma_{\mathrm{T}}$, hence a non vanishing basis complexity is obtained.

In the thermodynamic limit $N \to \infty$, for the complexity (2.7.30) we find

$$\mathcal{C} = \sqrt{N}\; a\big(\tilde{\omega}_{\mathrm{R}}, \tilde{\omega}_{\mathrm{T}}, \widetilde{T}_{\mathrm{R}}, \widetilde{T}_{\mathrm{T}}\big) + \dots \tag{2.7.33}$$

where

$$a(\tilde{\omega}_{\mathrm{R}}, \tilde{\omega}_{\mathrm{T}}, \widetilde{T}_{\mathrm{R}}, \widetilde{T}_{\mathrm{T}}) \,\equiv\, \frac{1}{2\sqrt{2}}\,\sqrt{\int_0^{\pi}\left\{\left[\log\left(\frac{\Omega_{\mathrm{R,T},\theta}}{\Omega_{\mathrm{T,R},\theta}}\right)\right]^2 + \left[\log\left(\frac{\Omega_{\mathrm{T,T},\theta}}{\Omega_{\mathrm{R,R},\theta}}\right)\right]^2\right\}\frac{d\theta}{\pi}} \tag{2.7.34}$$

and $\Omega_{\mathrm{M,N},\theta} \equiv \Omega_{\mathrm{M},\theta}\coth\big(\Omega_{\mathrm{N},\theta}/(2\widetilde{T}_{\mathrm{N}})\big)$, with $\mathrm{M},\mathrm{N} \in \{\mathrm{R},\mathrm{T}\}$ (see (2.7.31)), written in terms of the dispersion relation $\Omega_{\mathrm{S},\theta}$ given by (2.7.22). Notice that $a(\tilde{\omega}_{\mathrm{R}}, \tilde{\omega}_{\mathrm{T}}, \widetilde{T}_{\mathrm{R}}, \widetilde{T}_{\mathrm{T}}) \to a(\tilde{\omega}_{\mathrm{R}}, \tilde{\omega}_{\mathrm{T}})$ when $\widetilde{T}_{\mathrm{R}} \to 0$ and $\widetilde{T}_{\mathrm{T}} \to 0$, where $a(\tilde{\omega}_{\mathrm{R}}, \tilde{\omega}_{\mathrm{T}})$ has been defined in (2.7.21).

In Sec. 2.7.2 we have observed that the massless limit of the coefficient of the leading term of the complexity of pure states is finite (see (2.7.23)). This happens also for thermal states. Indeed, by setting $\tilde{\omega}_{\mathrm{R}} = \tilde{\omega}_{\mathrm{T}} = 0$ in (2.7.34), we find

$$a\big(\tilde{\omega}_{\mathrm{R}} = 0, \tilde{\omega}_{\mathrm{T}} = 0, \widetilde{T}_{\mathrm{R}}, \widetilde{T}_{\mathrm{T}}\big) \,=\, \frac{1}{2}\,\sqrt{\int_0^{\pi}\left[\log\left(\frac{\coth((\sin\theta)/\widetilde{T}_{\mathrm{T}})}{\coth((\sin\theta)/\widetilde{T}_{\mathrm{R}})}\right)\right]^2\frac{d\theta}{\pi}}\,. \tag{2.7.35}$$

In Fig. 2.5 and Fig. 2.6 we report some numerical results for the complexity (2.2.24) between thermal states with different temperatures and $\omega_{\mathrm{R}} = \omega_{\mathrm{T}} \equiv \omega$. The data have been taken for $\kappa = m = 1$, hence $\widetilde{T}_{\mathrm{R}} = T_{\mathrm{R}}$ and $\widetilde{T}_{\mathrm{T}} = T_{\mathrm{T}}$. Notice that these numerical results display an example of spectrum complexity for thermal states, as discussed in the text below (2.7.32).

In Fig. 2.5 we consider the complexity as function of the length N of the periodic harmonic chain. For the sake of simplicity, the reference state is the ground state (i.e. $T_{\mathrm{R}} = 0$) and the target

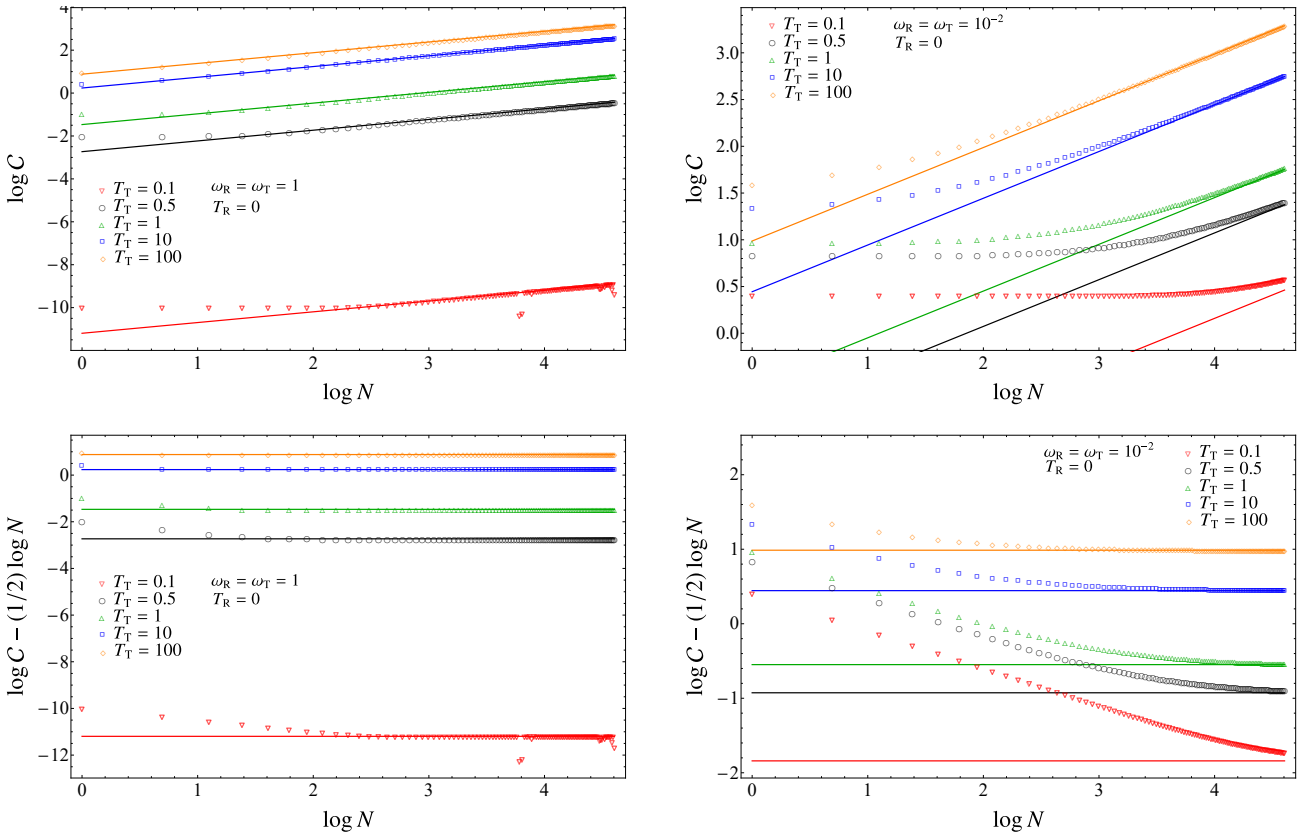

Figure 2.5: The complexity $\mathcal{C}$ for thermal states as function of the size N of the periodic harmonic chain. Here $\kappa = 1$ and $m = 1$; hence $\tilde{\omega}_R = \omega_R$, $\tilde{\omega}_T = \omega_T$, $\widetilde{T}_R = T_R$ and $\widetilde{T}_T = T_T$. In all the panels $T_R = 0$ and various values of T_T are considered. Top panels: $\omega_R = \omega_T = 1$ (left) and $\omega_R = \omega_T = 10^{-2}$ (right). The solid lines correspond to (2.7.33). Bottom panels: subleading term $\log \mathcal{C} - \frac{1}{2} \log N$ as function of $\log N$, for $T_R = 0$ and various values of T_T. In the left panel $\omega_R = \omega_T = 1$ and $\omega_R = \omega_T = 10^{-2}$ in the right panel. The horizontal solid lines correspond to the constant values obtained from (2.7.34).

state is a thermal state with temperature T_T. In the left panels $\omega = 1$, while in the right panels $\omega = 10^{-2}$. In the top panels the data are compared against the expression (2.7.33) (solid lines), while in the bottom panels the subleading term of the same expression is considered (horizontal solid lines). The data having $\omega = 1$ agree very well with the predictions, while for the ones with $\omega \ll 1$ the agreement is worse because in these cases the values of N considered are not large enough.

In Fig. 2.6 the same quantity considered in Fig. 2.5 is shown as function of T_T. The increasing behaviour of the curves tells us that the distance between the states increases with T_T, as expected. In the left panel we test numerically the analytic expression (2.7.30) for $N = 50$ and different values of ω. Instead, in the right panel we test numerically the formula (2.7.34), obtained in the thermodynamic limit $N \to \infty$: the agreement is very good when $\omega \gtrsim 1$, while it gets worse when $\omega \ll 1$. Thus, when ω is very small, larger values of N should be explored to observe the expected agreement between the numerical data and the curve (2.7.34). When $T_R = 0$, in the latter case the curves for (2.7.34) collapse onto the limiting curve (2.7.35), obtained by setting $\omega_R = \omega_T = 0$.

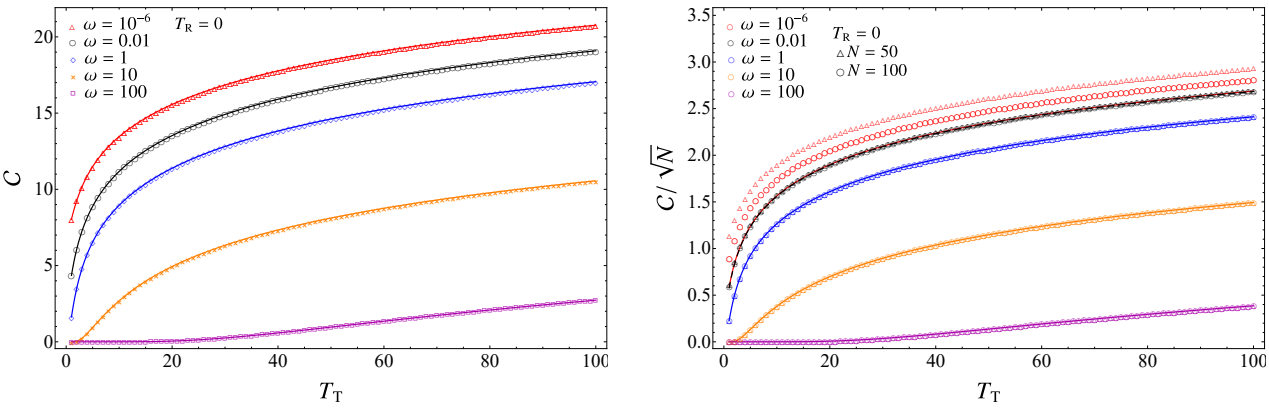

Figure 2.6: The complexity $\mathcal{C}$ for thermal states when $T_R = 0$. Left panel: $\mathcal{C}$ for a chain of length $N = 50$ as function of T_T, reported for different values of $\omega_R = \omega_T = \omega$. The solid lines correspond to (2.7.30). Right panel: $\mathcal{C}/\sqrt{N}$ as function of T_T for different values of $\omega_R = \omega_T = \omega$ and two values of N. The solid lines correspond to (2.7.34). The dashed black line and the solid red line are collapsed on the curve (2.7.35).

Optimal path for entanglement Hamiltonians and its complexity

In Sec. 2.4 we have discussed the map that provides the entanglement Hamiltonian in terms of the covariance matrix of a mixed state. In the following we explore further the optimal path of entanglement Hamiltonian matrices for the periodic harmonic chain in the special case where both the reference and the target states are thermal states.

The entanglement Hamiltonian matrices H_R and H_T of a reference state and of a target state that are both thermal can be obtained by applying the map (2.4.3) to the covariance matrix $\gamma_{th} = Q_{th} \oplus P_{th}$ introduced in Sec. 2.7.3, whose Williamson's decomposition is (2.7.27). The symplectic spectrum of the entanglement Hamiltonian matrix of a thermal state can be easily obtained by plugging (2.7.28) into (2.4.7), finding

$$\varepsilon_{th,k} = \frac{\Omega_k}{\widetilde{T}} = \beta \sigma_{phys,k} \qquad k = 1, \dots, N\,. \tag{2.7.36}$$

where $\sigma_{phys,k}$ is defined in (2.7.9). This provides the elements of the diagonal matrix $\mathcal{E}_{th}$ entering in the Williamson's decomposition (2.4.6) for the thermal state.

As for the distance (2.4.10) between H_R and H_T, we find

$$d(H_R, H_T) = \sqrt{\sum_{k=1}^{N} \left\{ \left[\log\left(\frac{T_R}{T_T}\right) \right]^2 + \left[\log\left(\frac{T_R\, \Omega_{T,k}}{T_T\, \Omega_{R,k}}\right) \right]^2 \right\}} \tag{2.7.37}$$

In the special case of $\widetilde{\omega}_R = \widetilde{\omega}_T$, the summation in (2.7.37) can be easily performed, finding

$$d(H_R, H_T) = \sqrt{2N}\, \left| \log(\beta_T/\beta_R) \right| \tag{2.7.38}$$

which corresponds to (2.4.12) specified to the one-dimensional harmonic chain.

In the periodic harmonic chain the Williamson's decomposition of the optimal circuit connecting H_R and H_T is given by (2.4.14), with the symplectic eigenvalues (2.7.9) and the symplectic

matrix (2.7.10). Thus, the symplectic eigenvalues for the matrix labeled by $s \in [0,1]$ along this optimal circuit are

$$\sigma_{k,s} = \beta_{\rm T}^{s}\, \beta_{\rm R}^{1-s}\, \sqrt{\kappa/m}\, \Omega_k \tag{2.7.39}$$

where Ω_k is the dispersion relation (2.7.8). This means that the optimal circuit is made by the entanglement Hamiltonian matrices of thermal states, as also discussed in Sec. 2.4. This is not a feature of the optimal circuit connecting the covariance matrices of two thermal states, as discussed in Sec. 2.2.6. This discrepancy is consistent with the fact that the map (2.4.3) does not send geodesics into geodesics.

2.7.4 Reduced density matrices

Important mixed states to explore are the reduced density matrices of a subsystem A.

Consider the density matrix $\hat{\rho}_{\rm R}$ and $\hat{\rho}_{\rm T}$ of the reference and of the target states respectively and introduce a spatial bipartition $A \cup B$ of the system that induces a factorisation of the Hilbert space, as already discussed in Sec. 2.4. For the Gaussian states that we are interested in, let us denote by $\gamma_{{\rm R},A}$ and $\gamma_{{\rm T},A}$ the reduced covariance matrices corresponding to the subsystem A, that characterise the reduced density matrices $\hat{\rho}_{{\rm R},A} \equiv {\rm Tr}_B \hat{\rho}_{\rm R}$ and $\hat{\rho}_{{\rm T},A} \equiv {\rm Tr}_B \hat{\rho}_{\rm T}$ respectively. We remark that, whenever $B \neq \emptyset$, the reduced density matrices $\hat{\rho}_{{\rm R},A}$ and $\hat{\rho}_{{\rm T},A}$ are mixed states, even when $\hat{\rho}_{\rm R}$ and $\hat{\rho}_{\rm T}$ are pure states. The reduced covariance matrix γ_A is obtained by just restricting the indices of the covariance matrix of the entire system to the ranges identifying the subsystem A.

By applying (2.2.24) to these mixed states, one obtains the subsystem complexity

$$\mathcal{C}_A \,=\, \frac{1}{2\sqrt{2}} \sqrt{{\rm Tr}\left\{ \left[\log\!\big(\gamma_{{\rm T},A}\, \gamma_{{\rm R},A}^{-1}\big) \right]^2 \right\}}\,. \tag{2.7.40}$$

In the context of the gauge/gravity correspondence, the subsystem complexity has been studied e.g. in [46, 55, 297, 298].

In the following we provide numerical results of this complexity only for the simplest case where A is an interval in an infinite harmonic chain and for some convenient reference and target states. In order to construct the reduced covariance matrices, in this case we need the two-point correlators of the harmonic chain in the thermodynamic limit. For a thermal state, they are given by (C.1.7) and (C.1.8). The limit $\widetilde{T} \to 0$ of these expressions provides the two-point correlators in the ground state reported in (C.1.5) and (C.1.6). Let us stress that, in principle, we should apply to (C.1.5), (C.1.6), (C.1.7) and (C.1.8) the canonical transformation reported above (2.7.2). Actually, this is not strictly necessary given that all the results reported in the following are obtained for $m = 1$ and $\kappa = 1$ and, in this case, the aforementioned canonical transformation reduces to the identity.

In Fig. 2.7 we consider the subsystem complexity for a block made by L consecutive sites in an infinite harmonic chain when the entire system is in its ground state and $\omega_{\rm R} \neq \omega_{\rm T}$. The data reported in Fig. 2.7, where we have fixed $\omega_{\rm R} = 1$, allow to conclude that

$$\log \mathcal{C}_A = \frac{1}{2} \log L + O(1) \qquad\qquad L \to \infty \tag{2.7.41}$$

where the additive constant depends on $\omega_{\rm T}$. Comparing the left panels and the right panels, we observe that larger values for L are needed to reach the behaviour (2.7.41) for these choices of $\omega_{\rm R} > \omega_{\rm T}$. We checked numerically that, when $\omega_{\rm R} \neq 1$, (2.7.41) holds with a subleading term that depends also on $\omega_{\rm R}$.

In Fig. 2.8 we have reported the subsystem complexity for a block made by L consecutive sites in an infinite harmonic chain when the entire system is in a thermal state and $\omega_{\rm R} = \omega_{\rm T}$.

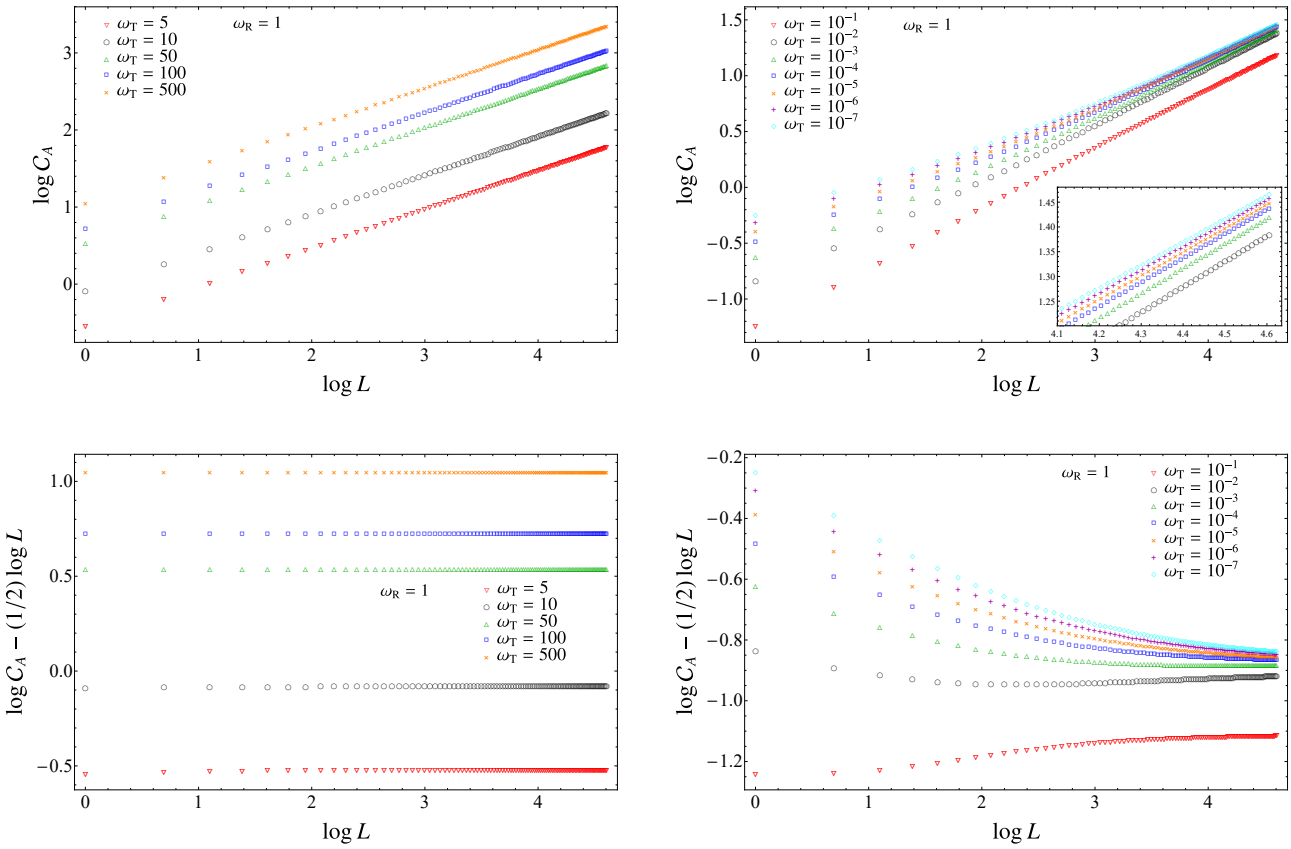

Figure 2.7: Subsystem complexity $\mathcal{C}_A$ for an interval made by L sites in an infinite harmonic chain as function of L. The chain is in its ground state and $\omega_R \neq \omega_T$. Here $\kappa = 1$ and $m = 1$; hence $\tilde{\omega}_R = \omega_R$ and $\tilde{\omega}_T = \omega_T$. We fix $\omega_R = 1$, considering various values for ω_T: $\omega_T > \omega_R$ in the left panels and $\omega_T < \omega_R$ in the right panels. The subsystem complexity $\mathcal{C}_A$ is reported in the top panels, while its subleading term is studied in the bottom panels.

In particular, we have chosen $T_R = 0$ and various values of $T_T > 0$. In the left panels we have considered $\omega_T = \omega_R = 1$, finding a reasonable agreement with (2.7.41), where the subleading constant term depends on T_T. In the right panels we have fixed $\omega_T = \omega_R = 10^{-6}$, finding that the behaviour (2.7.41) is more difficult to observe as $T_T \to 0$ because larger values for L are needed.

2.7.5 Mutual complexity of reduced density matrices

The complexity of the ground states and of the thermal states, considered in Sec. 2.7.2 and Sec. 2.7.3 respectively, grow like $\sqrt{N}$ as $N \to \infty$, where N is the number of sites composing the entire periodic chain. Furthermore, considering an interval made by L sites in an infinite harmonic chain, the numerical results reported in Sec. 2.7.4 tell us that the subsystem complexity for this interval grows like $\sqrt{L}$ as $L \to \infty$.

Given a spatial subregion A and the density matrices $\hat{\rho}_R$ and $\hat{\rho}_T$, which can correspond to pure or mixed states, let us denote by $\mathcal{C}_{R,T}(A)$ the subsystem complexity between the reduced density matrices $\hat{\rho}_{R,A}$ and $\hat{\rho}_{T,A}$ introduced in Sec. 2.7.4. This notation, which differs from the one introduced in (2.7.40), makes explicit the dependence of the subsystem complexity on the choice

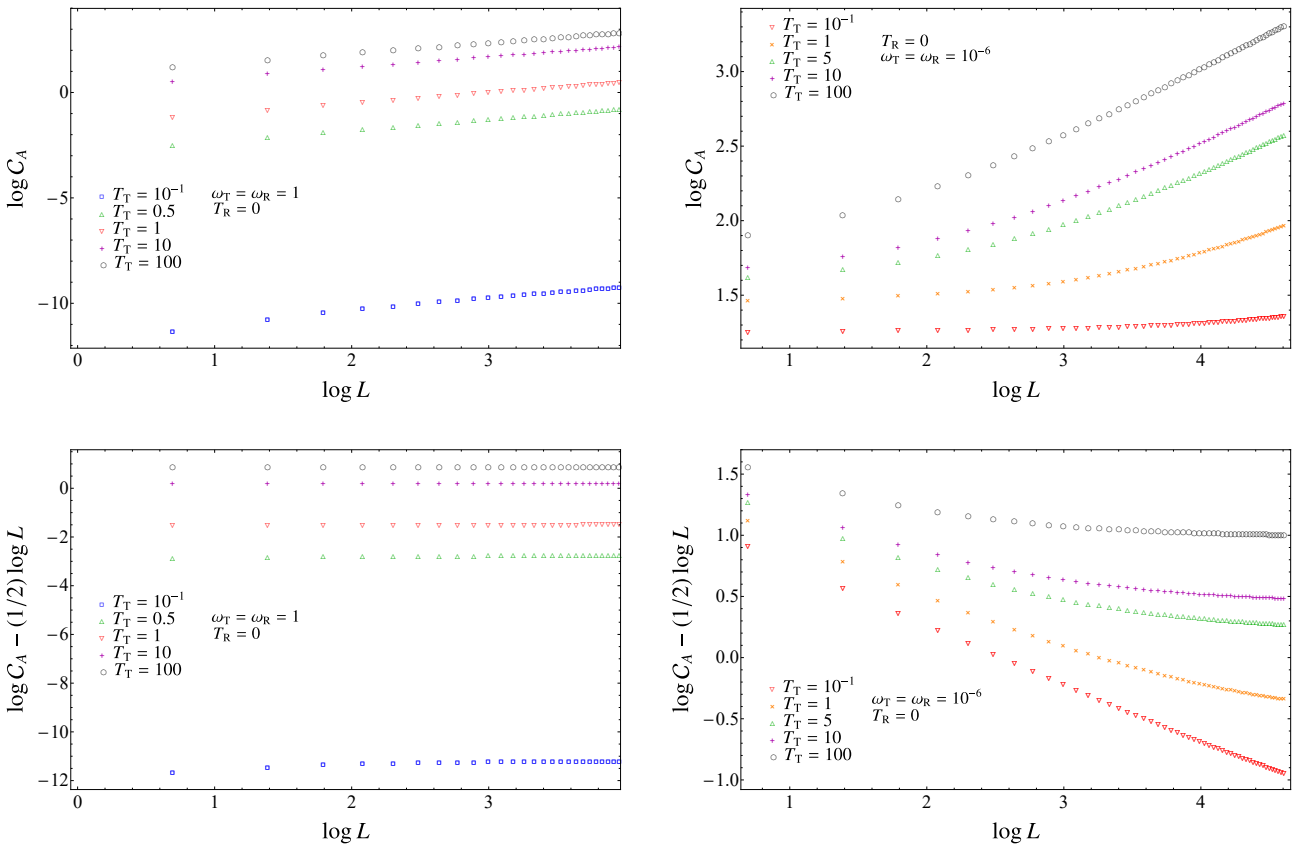

Figure 2.8: Subsystem complexity $\mathcal{C}_A$ for an interval made by L sites in an infinite harmonic chain as function of L. The infinite harmonic chain is in a thermal state and $T_R \neq T_T$. Here $\kappa = m = 1$; hence $\tilde{\omega}_R = \omega_R$, $\tilde{\omega}_T = \omega_T$, $\tilde{T}_R = T_R$ and $\tilde{T}_T = T_T$. We fix $T_R = 0$, considering various values for T_T. We set $\omega_T = \omega_R = 1$ in the left panels and $\omega_T = \omega_R = 10^{-6}$ in the right panels. The subsystem complexity $\mathcal{C}_A$ is reported in the top panels, while its subleading term is studied in the bottom panels.

of the reference and the target states.

In this subsection we consider the cases where the spatial subsystem A is bipartite into two complementary spatial subregions A_1 and A_2 such that $A = A_1 \cup A_2$. For this spatial configuration, various entanglement quantifiers like the entanglement entropies [233–237, 299] (see e.g. [300–303] for related calculations in the gauge/gravity correspondence) and the entanglement negativity [210, 211, 304–308] have been studied.

The subregions A_1 and A_2 can be either disjoint or have a non vanishing intersection. Since $\mathcal{C}_{R,T}(A)^2$ grows with the volume of A as the number of sites in A diverges, we are naturally led to introduce the mutual complexity for subregions as follows [79, 297]

$$\mathcal{M}_{R,T}(A_1, A_2) \equiv \mathcal{C}_{R,T}(A_1)^2 + \mathcal{C}_{R,T}(A_2)^2 - \mathcal{C}_{R,T}(A_1 \cup A_2)^2 - \mathcal{C}_{R,T}(A_1 \cap A_2)^2 \tag{2.7.42}$$

which is finite as the number of sites in A_1 and A_2 diverges.

In an infinite chain, let us consider the mutual complexity when A_1 and A_2 are two equal and disjoint intervals made by L sites and separated by d sites. In Fig. 2.9 we report the numerical

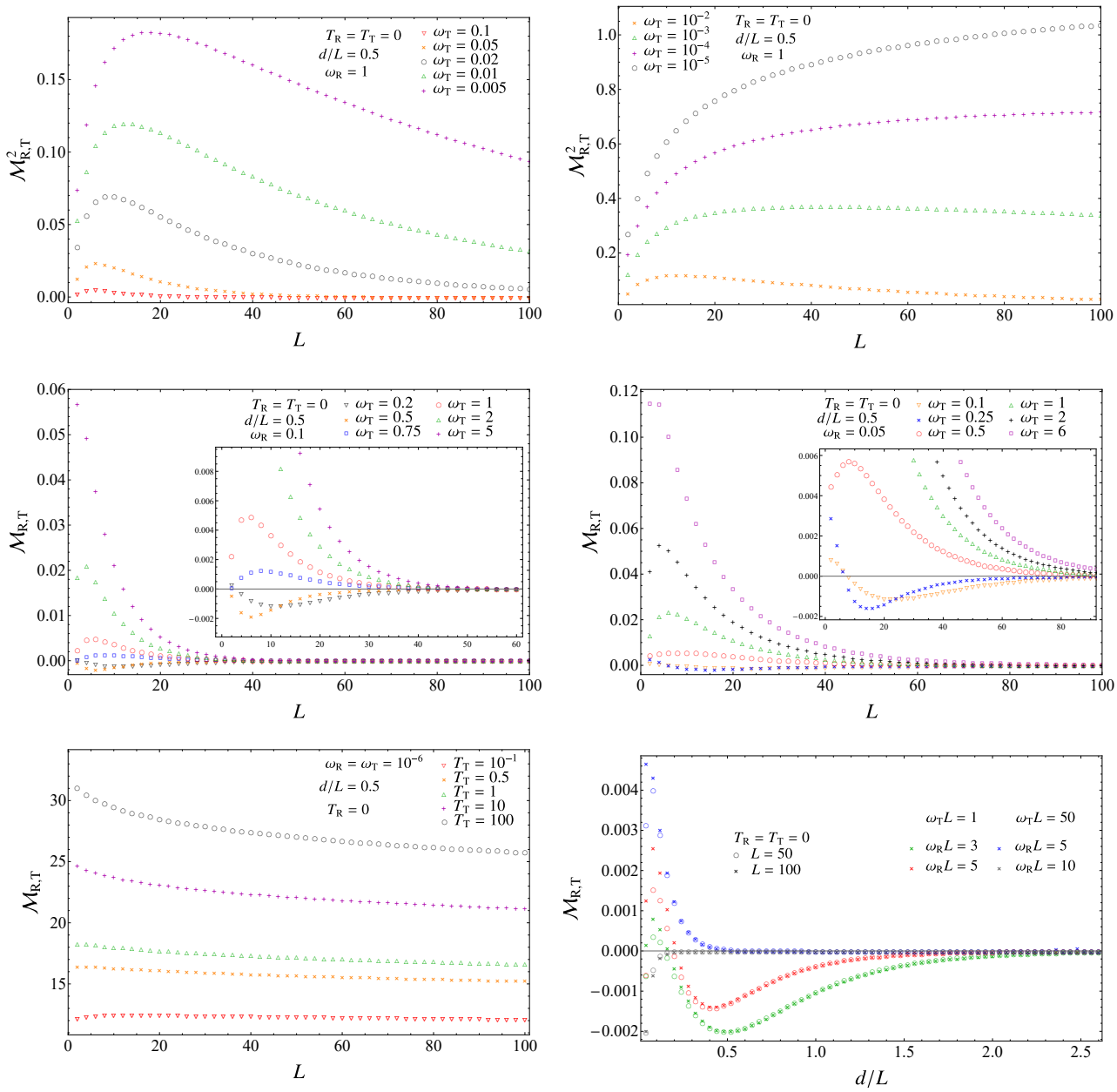

Figure 2.9: The mutual complexity $\mathcal{M}_{\mathrm{R,T}}$ for two disjoint equal intervals made by L sites and separated by d sites in an infinite harmonic chain. Here $\kappa = m = 1$, hence $\tilde{\omega}_{\mathrm{R}} = \omega_{\mathrm{R}}$, $\tilde{\omega}_{\mathrm{T}} = \omega_{\mathrm{T}}$, $\widetilde{T}_{\mathrm{R}} = T_{\mathrm{R}}$ and $\widetilde{T}_{\mathrm{T}} = T_{\mathrm{T}}$. In the top panels, in the middle panels and in the bottom right panel the chain is in its ground state and $\omega_{\mathrm{R}} \neq \omega_{\mathrm{T}}$: both $\omega_{\mathrm{T}} < \omega_{\mathrm{R}}$ (top panels) and $\omega_{\mathrm{T}} > \omega_{\mathrm{R}}$ (middle panels) are considered. In the bottom left panel, a case involving thermal states with $T_{\mathrm{R}} = 0$ and various $T_{\mathrm{T}} > 0$ is explored. The ratio d/L is kept fixed, except in the bottom right panel, where $\mathcal{M}_{\mathrm{R,T}}$ is shown as function of d/L.

results of the mutual complexity for this configuration as function of L, while d/L is kept fixed ($d/L = 1/2$ for the data in the figure).

In the top and middle panels of Fig. 2.9, the reference state and the target state are the ground states of the chains characterised by ω_{R} and ω_{T} respectively. The mutual complexity is shown as

function of L: for the data shown in each panel $\omega_{\rm R}$ is fixed and the different curves are associated to different values of $\omega_{\rm T}$. When $\omega_{\rm T} < \omega_{\rm R}$ (top panels) the numerical curves for small values of L are increasing until they reach a maximum at a value of L that depends on $\omega_{\rm T}$ (top left panel). After the maximum, the mutual complexity decreases with L, but for many values of $\omega_{\rm T}$ we cannot appreciate the finite asymptotic limit as $L \to \infty$ because larger values of L are needed. In the top right panel, for small enough values of $\omega_{\rm T}$, the values of L that we consider are too small to appreciate the occurrence of a maximum.

When $\omega_{\rm T} > \omega_{\rm R}$ (middle panels) a similar behaviour is observed: also in these cases the position of the maximum of the curve depends on $\omega_{\rm T}$. In these cases we observe that, as $L \to \infty$, the mutual complexity decreases until the zero value is reached. By comparing the two panels in the middle, one observes that the value of L where the data vanish increases when $\omega_{\rm R}$ decreases. Furthermore, from the middle panels we can appreciate also the fact that the sign of $\mathcal{M}_{\rm R,T}$ is not definite: it is mainly positive, but for some values of the parameters ($\omega_{\rm T}$ close to $\omega_{\rm R}$ and L sufficiently small) the curve is negative.

In the bottom left panel of Fig. 2.9, the reference state is a ground state again, while $\hat{\rho}_{\rm T}$ is a thermal state at temperature $T_{\rm T} > 0$. The curves corresponding to different values of $T_{\rm T} > 0$ decrease with L and the asymptotic value depends on $T_{\rm T}$.

In the bottom right panel of Fig. 2.9, the dependence of the mutual complexity on the ratio d/L is considered, when the chain is in its ground state and $\omega_{\rm R} \neq \omega_{\rm T}$. We observe an interesting collapse for data corresponding to fixed values of $\omega_{\rm R}L$ and $\omega_{\rm T}L$, while L changes. Furthermore, the resulting curve vanishes after a critical value of d/L. This critical ratio increases as either $\omega_{\rm R}L$ or $\omega_{\rm T}L$ decreases.

2.7.6 A comparison with the approach based on the purification complexity

We find it worth comparing our results of Sec. 2.7.3 for the complexity of thermal states with the corresponding ones obtained in [79] through the approach based on the purification complexity, that has been discussed in Sec. 2.6.2.

The results from [79] that we consider have been obtained using both the F_1 the F_2 cost functions, while the complexity (2.2.24) is based on the F_2 cost function. These different cost functions lead to a different scaling with the total size L of the chain. In particular, the F_1 cost function provides a complexity that diverges with L, while the F_2 cost function leads to the milder divergence given by $\sqrt{L}$. This feature, which has been observed already in [35] for pure states, holds also for thermal states, as remarked in [79] for the F_1 cost function and in (2.7.33) for our approach, that is based on the F_2 cost function. Because of this different scaling, a meaningful comparison between these two approaches can be done only for one-mode mixed states, where $L = 1$. When both the reference and the target states are pure and $L = 1$, both the F_1 cost function and the F_2 cost function provide the same complexity [35].

Let us consider the circuit made by one-mode mixed states where the reference state is the ground state with frequency $\omega_{\rm R}$ and the target state is a thermal state at inverse temperature β with frequency $\omega_{\rm T}$.

Specialising the complexity in (2.7.30) to this case and for $m = \kappa = 1$ we obtain

$$\mathcal{C} = \frac{1}{2\sqrt{2}} \sqrt{\left[\log\left(\frac{\omega_{\rm R}}{\omega_{\rm T}} \coth\frac{\beta\omega_{\rm T}}{2}\right)\right]^2 + \left[\log\left(\frac{\omega_{\rm T}}{\omega_{\rm R}} \coth\frac{\beta\omega_{\rm T}}{2}\right)\right]^2} \,. \tag{2.7.43}$$

In this simple case, analytical results have been found in [79] also through the approach based on the purification complexity. The results for the $\mathcal{C}_1$ complexity, which is defined through the F_1 cost function, are basis dependent. In [79] two particular bases have been considered, which have

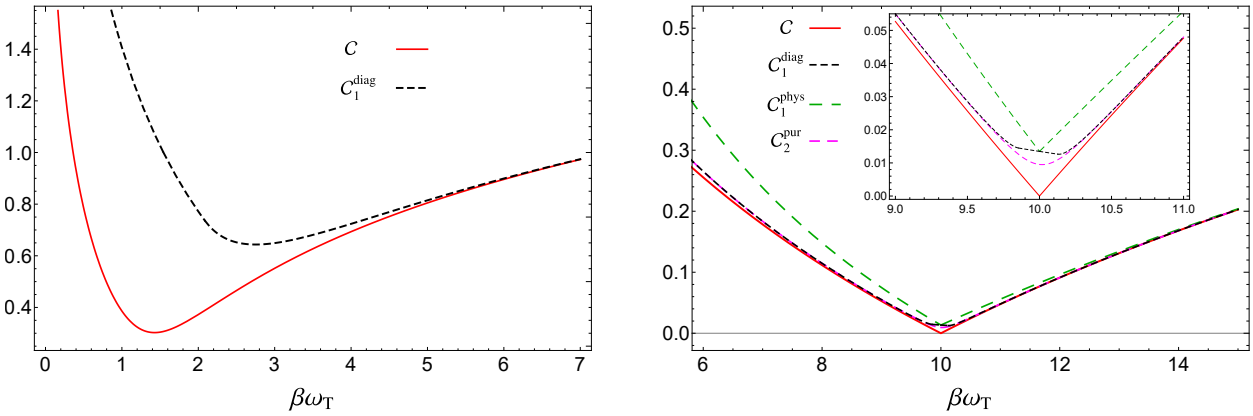

Figure 2.10: One-mode mixed states: the complexity $\mathcal{C}$ from (2.7.43) (red solid line) and the complexities $\mathcal{C}_1$ and $\mathcal{C}_2^{\rm pur}$ based on the purification complexity, as functions of $\beta\omega_{\rm T}$. The complexity $\mathcal{C}_1$ is evaluated for the diagonal basis from (2.7.44) (black dashed line) and for the physical basis from (2.7.45) (green dashed line). The complexity $\mathcal{C}_2^{\rm pur}$ from (2.7.46) is independent on the basis (magenta dashed line). In the left panel $\beta\omega_{\rm R}=1$, while in the right panel $\beta\omega_{\rm R}=10$, hence also $\mathcal{C}_1^{\rm phys}$ and $\mathcal{C}_2^{\rm pur}$ are shown.

been called physical basis and diagonal basis (see [79] for their definitions). In the diagonal basis, the analytic result found in [79] for this case reads

$$\mathcal{C}_1^{\rm diag}=\begin{cases}\dfrac{1}{2}\log\left(\dfrac{\omega_{\rm R}}{\omega_{\rm T}}\right)+\dfrac{1}{2}\log\left(\dfrac{\frac{\omega_{\rm R}}{\omega_{\rm T}}\coth\left(\beta\omega_{\rm T}/2\right)-1}{\frac{\omega_{\rm R}}{\omega_{\rm T}}-\coth\left(\beta\omega_{\rm T}/2\right)}\right) & \coth\left(\dfrac{\beta\omega_{\rm T}}{4}\right)\leqslant\dfrac{\omega_{\rm R}}{\omega_{\rm T}}\\ \log\left[\coth\left(\beta\omega_{\rm T}/4\right)\right] & \tanh\left(\dfrac{\beta\omega_{\rm T}}{4}\right)\leqslant\dfrac{\omega_{\rm R}}{\omega_{\rm T}}\leqslant\coth\left(\dfrac{\beta\omega_{\rm T}}{4}\right)\\ \dfrac{1}{2}\log\left(\dfrac{\omega_{\rm T}}{\omega_{\rm R}}\right)+\dfrac{1}{2}\log\left(\dfrac{\frac{\omega_{\rm T}}{\omega_{\rm R}}\coth\left(\beta\omega_{\rm T}/2\right)-1}{\frac{\omega_{\rm T}}{\omega_{\rm R}}-\coth\left(\beta\omega_{\rm T}/2\right)}\right) & \tanh\left(\dfrac{\beta\omega_{\rm T}}{4}\right)\geqslant\dfrac{\omega_{\rm R}}{\omega_{\rm T}}\,.\end{cases}\tag{2.7.44}$$

For the physical basis analytic results are not available. In the regime $\beta\omega_{\rm T}\gg 1$, the following perturbative expansion has been found [79]

$$\mathcal{C}_1^{\rm phys}=\frac{1}{2}\left|\log(\omega_{\rm R}/\omega_{\rm T})\right|+\frac{\log\left[\coth\left(\beta\omega_{\rm T}/4\right)\right]\log(\omega_{\rm R}/\omega_{\rm T})}{\sqrt{\omega_{\rm R}/\omega_{\rm T}}-\sqrt{\omega_{\rm T}/\omega_{\rm R}}}+O(e^{-\beta\omega_{\rm T}})\,.\tag{2.7.45}$$

As for the F_2 purification complexity, an analytic result valid in the entire range of the parameter is not available in the literature. However, in the regime where $\beta\omega_{\rm T}\gg 1$, it has been found [79]

$$\mathcal{C}_2^{\rm pur}=\frac{1}{2}\sqrt{\log\left(\omega_{\rm R}/\omega_{\rm T}\right)\left[\log\left(\omega_{\rm R}/\omega_{\rm T}\right)+\left[\log\left(\coth\left(\beta\omega_{\rm T}/4\right)\right)\right]^2\left(\frac{\omega_{\rm R}/\omega_{\rm T}+1}{\omega_{\rm R}/\omega_{\rm T}-1}\right)\right]}+O\left(e^{-\beta\omega_{\rm T}}\right)\tag{2.7.46}$$

The expressions for the complexity in (2.7.43), (2.7.44), (2.7.45) and (2.7.46) depend only on $\beta\omega_{\rm T}$ and on the ratio $\omega_{\rm R}/\omega_{\rm T}$. As consistency check, we notice that in the limit $\beta\omega_{\rm T}\to\infty$, where the circuit is made by pure states, all the expressions in (2.7.43), (2.7.44), (2.7.45) and (2.7.46) become $\frac{1}{2}|\log(\omega_{\rm R}/\omega_{\rm T})|$, as expected from [35].

In Fig. 2.10 we show the expressions for the complexity in (2.7.43), (2.7.44), (2.7.45) and (2.7.46) in terms of $\beta\omega_{\rm T}$ for a fixed value of $\beta\omega_{\rm R}$ (we choose $\beta\omega_{\rm R}=1$ in the left panel and $\beta\omega_{\rm R}=10$ in the

right panel). The curves for $\mathcal{C}_1^{\rm phys}$ ad $\mathcal{C}_2^{\rm pur}$ occur only in the right panel because they exist only in the regime of $\beta\omega_{\rm T} \gg 1$. We find it worth remarking that the curves for $\mathcal{C}$ always lie below the curves corresponding to the complexity evaluated through the purification complexity. Furthermore, as $\beta\omega_{\rm T}$ growths, all the curves collapse on the same curve, as expected from the above observation, since $\beta\omega_{\rm T} \to \infty$ corresponds to the limit where the circuit is made by pure states. In the right panel one also notices that $\mathcal{C}_2^{\rm pur}$ is smaller than the complexity $\mathcal{C}_1$ in the diagonal basis, which in turn is smaller than $\mathcal{C}_1$ in the physical basis, as already remarked in [79].

2.7.7 A comparison with holography

In the context of the gauge/gravity correspondence, the procedures introduced for the gravitational dual of the circuit complexity are known as "complexity = volume" proposal (CV) [50, 51], "complexity = action" proposal (CA) [56, 57] and "complexity = spacetime volume" proposal (CV2.0) [309] (see Sec. 1.1.3 for a brief discussion of the CV and CA proposals).

The subsystem holographic complexity corresponding to these three proposals have been also explored [55, 59, 79]. Considering a subregion A in the constant time slice of the d-dimensional Conformal Field Theory (CFT) on the boundary of AdS_{d+1}, it has been found that the leading divergence of the holographic complexity is proportional to $V(A)/\epsilon^{d-1}$, where $V(A)$ is the volume of A and ϵ is the UV cutoff. This divergence suggests that the holographic results should be compared with the square of the complexity $\mathcal{C}$ mainly explored in this chapter.

Denoting by $\mathcal{C}_{\rm AdS}$ the holographic complexity evaluated through one of the proposals mentioned above and by the $\mathcal{C}_{\rm AdS}(A)$ the corresponding subregion holographic complexity, $\mathcal{C}_{\rm AdS}$ is superadditive when, given two disjoint subregions A and B on the boundary of the AdS space, the following inequality holds [46]

$$\mathcal{C}_{\rm AdS}(A) + \mathcal{C}_{\rm AdS}(B) \leqslant \mathcal{C}_{\rm AdS}(A \cup B) \tag{2.7.47}$$

while $\mathcal{C}_{\rm AdS}$ is subadditive when the opposite inequality holds. Equivalently, in terms of the holographic mutual complexity [297]

$$\mathcal{M}_{\rm AdS}(A, B) = \mathcal{C}_{\rm AdS}(A) + \mathcal{C}_{\rm AdS}(B) - \mathcal{C}_{\rm AdS}(A \cup B) \tag{2.7.48}$$

which should be the gravitational dual of (2.7.42), the holographic complexity is superadditive when $\mathcal{M}_{\rm AdS}(A, B) \leqslant 0$ for any choice of the regions A and B.

When the dual CFT is in its ground state (hence its gravitational dual is the empty AdS spacetime) and a spatial subregion is considered, for AdS_3 it has been shown that the holographic mutual complexity (2.7.48) is negative for all the three proposals [55, 59, 79]. This qualitatively disagrees with the results reported in Sec. 2.7.5 because we do not observe a definite sign for the mutual complexity (2.7.42) (see e.g. Fig. 2.9).

2.8 Discussion

In this chapter we have studied the circuit complexity of the mixed bosonic Gaussian states occurring in the Hilbert space of harmonic lattices in any number of dimensions by employing the Fisher-Rao distance between Gaussian Wigner functions.

Considering mixed states with vanishing first moments, by applying a known result for the symmetric and positive definite matrices [124–127, 134] to the covariance matrices of the model, we have provided the optimal circuit (2.2.20), which holds when the set of the allowed gates provides circuits made only by Gaussian states. The length (2.2.22) of this optimal circuit in the

geometry determined by the Fisher information matrix is identified with the circuit complexity (2.2.24) to obtain a target state from a given reference state (the tolerance is zero for these circuits). In the special case of pure states, the known results of [35, 40] for the $\mathcal{C}_2$ complexity (namely the complexity based on the F_2 cost function) have been recovered. For thermal states originating from the same Hamiltonian, the expression (2.2.54) has been obtained.

The Williamson's decomposition of the covariance matrix (see Sec. 2.2.3) is the main tool employed throughout our analysis. This decomposition leads to natural ways to introduce the spectrum complexity and the basis complexity for mixed bosonic Gaussian states (see Sec. 2.3.2 and Sec. 2.3.3). This provides an explicit realisation of the proposal made in [46].

The optimal circuits described in this chapter allow us to study the purification of mixed states without ancillae. Motivated by the first law of complexity, in Sec. 2.3.4 we have mainly considered the purification of a given mixed state through the W path (2.3.24).

The Gaussian mixed states that are not pure in harmonic lattices can be characterised also through their entanglement Hamiltonian matrices. The optimal circuit and the corresponding complexity in terms of the entanglement Hamiltonian matrices have been investigated in Sec. 2.4.

A detailed analysis has been carried out in the simplest case of the harmonic chain either on the circle or on the infinite line (see Sec. 2.7). Analytic or numerical results have been reported. In particular, for the mixed states given by reduced density matrices, we have studied the circuit complexity for an interval in the infinite line and the mutual complexity of two disjoint intervals (see Sec. 2.7.5).

The circuit complexity of mixed states is a challenging task deserving many future studies.

One of the main motivations of our work is to provide some tools to study complexity in quantum field theories. Evaluating complexity of mixed states in quantum field theories remains an important challenge. The complexity of pure states in quantum field theories has been explored in various studies [39, 60–63, 65–74] and it would be instructive to extend these analyses to mixed states.

Let us remark that our analysis has been performed by assuming that all the states of the quantum circuits are Gaussian. It is important to go beyond this limitation by exploring the complexity of circuits involving mixed states that are not Gaussian.

Finally, we remind that the results reported in this chapter have been obtained in the ideal situation where the maximal freedom is allowed in the choice of the gates. Typically, only a limited number of gates can be employed in the construction of quantum circuits. It is worth trying to adapt our analysis to more realistic cases by introducing a tolerance and various kinds of restrictions in the set of the allowed gates [30, 31].

Chapter 3

Complexity after a global quantum quench

3.1 Introduction

Quantum quenches are insightful ways to explore the dynamics of isolated quantum systems out of equilibrium (see [80, 81] for recent reviews). Given a quantum system prepared in the ground state $|\psi_0\rangle$ of the Hamiltonian $\widehat{H}_0$, at $t = 0$ a sudden change is performed such that the evolution Hamiltonian of the initial state $|\psi_0\rangle$ becomes $\widehat{H} \neq \widehat{H}_0$. Since $\widehat{H}$ and $\widehat{H}_0$ do not commute in general, the unitary evolution $|\psi(t)\rangle = e^{-\mathrm{i}\widehat{H}t}|\psi_0\rangle$ for $t > 0$ is highly non trivial. In the typical global quench, a parameter occurring in the Hamiltonian is suddenly changed from its value ω_0 in $\widehat{H}_0$ to the value ω in $\widehat{H}$ [80, 82–84]. Insightful results have been obtained about the asymptotic regime $t \to \infty$ of this unitary evolution by employing the generalised Gibbs ensemble (GGE) (see the reviews [89, 90, 310]).

It is worth studying the circuit complexity with the target state given by the time-evolved pure state of a certain unitary evolution and the reference state by another pure state along the same evolution [40, 67, 311–315]. In particular, considering a global quench protocol, we are interested in the optimal circuit and in the corresponding complexity where $|\psi(t)\rangle$ and $|\psi_0\rangle$ are respectively the target and the reference states. Moreover, exploiting an approach for the complexity of mixed states (as, for instance, the one discussed in chapter 2), it is interesting to investigate the evolution of the subsystem complexity after this quench protocol.

Within the gauge/gravity correspondence, the temporal evolution of complexity for pure states has been explored in [140–142], while the one of the subsystem complexity (given by the volume identified by the extremal hypersurface anchored to the boundary of the subsystem occurring in the covariant proposal for the holographic entanglement entropy [243]) has been evaluated in [145, 316–318].

In this chapter we study the temporal evolution of the subsystem complexity after a global quantum quench in harmonic lattices where the mass parameter is suddenly changed from ω_0 to ω. Considering a ground state as the initial state, the Gaussian nature of the state is preserved during the temporal evolution. In these bosonic systems, the reduced density matrices are characterised by the corresponding reduced covariance matrices [77]. By employing the approach to the complexity of bosonic mixed Gaussian states based on the Fisher information geometry introduced in chapter 2, we evaluate numerically the subsystem complexity for one-dimensional harmonic lattices (i.e. harmonic chains) and subsystems A given by blocks of consecutive sites. We consider harmonic chains where either periodic boundary conditions (PBC) or Dirichlet boundary conditions (DBC) are imposed. This allows to study the role of the zero mode. The temporal evolution of the

subsystem complexity at a generic time after the global quench w.r.t. the initial state is compared with the temporal evolution of the corresponding increment of the entanglement entropy, which has been investigated through various methods in [81, 243, 295, 319–321] (see also [28, 29, 103, 147, 209, 294, 322] for the evolution of other entanglement quantifiers after a global quench).

This chapter is organised as follows. In Sec. 3.2 we introduce the main expressions to evaluate the circuit complexity after the global quench of the mass parameter through the covariance matrices of the reference and the target states for harmonic lattices in a generic number of dimensions. In Sec. 3.3 we specify this analysis to harmonic chains with either PBC or DBC. The main results of this chapter are discussed in Sec. 3.4 and Sec. 3.5, where the temporal evolution of the subsystem complexity for a block of consecutive sites is investigated. In Sec. 3.4, finite harmonic chains with either PBC or DBC are studied, while in Sec. 3.5 we consider infinite harmonic chains either on the line or on the semi-infinite line with DBC at the origin. In the cases of infinite chains, we employ known results about the GGE to determine the asymptotic regime of the subsystem complexity. In Sec. 3.6 we draw some conclusions.

3.2 Complexity from the covariance matrix after the quench

In this section we discuss the expressions that allow to evaluate the temporal evolution of the circuit complexity based on the Fisher-Rao geometry for the harmonic lattices in a generic number of spatial dimensions when both the reference and the target states are pure. Analytic expressions that bound this temporal evolution are also derived.

3.2.1 Covariance matrix after the quench

The Hamiltonian of the harmonic lattice made by N sites with nearest neighbour spring-like interaction is given by (2.2.1). In the Heisenberg picture, the unitary temporal evolution of the position and the momentum operators $\hat{q}_j(t)$ and $\hat{p}_j(t)$ through the evolution Hamiltonian $\widehat{H}$ in (2.2.1) reads

$$\hat{q}_j(t) = e^{\mathrm{i}\widehat{H}t}\hat{q}_j(0)e^{-\mathrm{i}\widehat{H}t} \qquad \hat{p}_j(t) = e^{\mathrm{i}\widehat{H}t}\hat{p}_j(0)e^{-\mathrm{i}\widehat{H}t}\,. \tag{3.2.1}$$

In order to study the temporal evolution of the harmonic lattices after the global quantum quench of the mass parameter that we are considering, we need to introduce the $N \times N$ correlation matrices for operators (3.2.1) whose elements read

$$\begin{aligned} Q_{i,j}(t) &\equiv \langle\psi_0|\, \hat{q}_i(t)\, \hat{q}_j(t)\, |\psi_0\rangle \\ P_{i,j}(t) &\equiv \langle\psi_0|\, \hat{p}_i(t)\, \hat{p}_j(t)\, |\psi_0\rangle \\ M_{i,j}(t) &\equiv \mathrm{Re}\big[\langle\psi_0|\, \hat{q}_i(t)\, \hat{p}_j(t)\, |\psi_0\rangle\big] \end{aligned} \tag{3.2.2}$$

where $|\psi_0\rangle$ is the ground state of the Hamiltonian $\widehat{H}_0$, defined by (2.2.1) with ω replaced by ω_0.

At any time $t > 0$ after the quench, the system is completely characterised by its covariance matrix $\gamma(t)$, which is the following $2N \times 2N$ real, symmetric and positive definite matrix

$$\gamma(t) = \begin{pmatrix} Q(t) & M(t) \\ M(t)^{\mathrm{t}} & P(t) \end{pmatrix} \tag{3.2.3}$$

where the elements of the $N \times N$ block matrices are given by (3.2.2). This covariance matrix has been already used to study the entanglement dynamics e.g. in [294, 295, 319].

The blocks of the covariance matrix (3.2.3) can be decomposed as

$$Q(t) = \widetilde{V}\, \mathcal{Q}(t)\, \widetilde{V}^{\mathrm{t}} \qquad P(t) = \widetilde{V}\, \mathcal{P}(t)\, \widetilde{V}^{\mathrm{t}} \qquad M(t) = \widetilde{V}\, \mathcal{M}(t)\, \widetilde{V}^{\mathrm{t}} \tag{3.2.4}$$

where $\widetilde{V}$ is the real orthogonal $N \times N$ matrix introduced in Sec. 2.2.6, while $\mathcal{Q}(t)$, $\mathcal{P}(t)$ and $\mathcal{M}(t)$ are $N \times N$ diagonal matrices whose k-th element along the diagonal is [84]

$$\begin{aligned}
Q_k(t) \equiv \mathcal{Q}_{k,k}(t) &= \frac{1}{2m\Omega_k} \left(\frac{\Omega_k}{\Omega_{0,k}} \left[\cos(\Omega_k t)\right]^2 + \frac{\Omega_{0,k}}{\Omega_k} \left[\sin(\Omega_k t)\right]^2 \right) \\
P_k(t) \equiv \mathcal{P}_{k,k}(t) &= \frac{m\Omega_k}{2} \left(\frac{\Omega_k}{\Omega_{0,k}} \left[\sin(\Omega_k t)\right]^2 + \frac{\Omega_{0,k}}{\Omega_k} \left[\cos(\Omega_k t)\right]^2 \right) \\
M_k(t) \equiv \mathcal{M}_{k,k}(t) &= \frac{1}{2} \left(\frac{\Omega_{0,k}}{\Omega_k} - \frac{\Omega_k}{\Omega_{0,k}} \right) \sin(\Omega_k t) \cos(\Omega_k t)
\end{aligned} \tag{3.2.5}$$

in terms of the dispersion relations $\Omega_{0,k}$ and Ω_k of the Hamiltonians $\widehat{H}_0$ and $\widehat{H}$ respectively, which depend both on the dimensionality of the lattice and on the boundary conditions.

At $t = 0$, the expressions in (3.2.5) simplify respectively to

$$Q_k(0) = \frac{1}{2m\,\Omega_{0,k}} \qquad P_k(0) = \frac{m\,\Omega_{0,k}}{2} \qquad M_k(0) = 0\,. \tag{3.2.6}$$

From the above discussion, one realises that $\gamma(t)$ is a function of t determined by the set of parameters given by $\{m, \kappa, \omega, \omega_0\}$.

When the dispersion relation vanishes for certain value of k, e.g. $k = N$, the corresponding mode is a zero mode. The relations (3.2.5) and (3.2.6) are well defined when $\Omega_{0,k}$ does not vanish; hence Ω_k can have a zero mode, while $\Omega_{0,k}$ cannot. This highlights the asymmetric role of $\Omega_{0,k}$ and Ω_k.

3.2.2 Complexity for the system

The circuit complexity is proportional to the length of the optimal quantum circuit that creates a target state from a reference state. In this chapter we evaluate the complexity (2.2.24) between two bosonic Gaussian states with vanishing first moments. This approach allows to study also the circuits made by mixed states. In the following discussion and in Sec. 3.3 we consider first the case where both the reference and the target states are pure states, while in Sec. 3.4 and Sec. 3.5 we study the case where both the reference and the target states are mixed states.

Denoting by t_{R} and t_{T} the values of t corresponding to the reference state and to the target state respectively, let us adopt the following notation

$$\gamma_{\mathrm{R}} = \gamma(t_{\mathrm{R}}) \qquad \gamma_{\mathrm{T}} = \gamma(t_{\mathrm{T}})\,. \tag{3.2.7}$$

In the most general setup, γ_{R} is a function of t_{R} characterised by the set of parameters $\{m_{\mathrm{R}}, \kappa_{\mathrm{R}}, \omega_{\mathrm{R}}, \omega_{0,\mathrm{R}}\}$, while γ_{T} is a function of t_{T} parameterised by $\{m_{\mathrm{T}}, \kappa_{\mathrm{T}}, \omega_{\mathrm{T}}, \omega_{0,\mathrm{T}}\}$. This means that the reference and target states are obtained as the time-evolved states at $t = t_{\mathrm{R}} \geqslant 0$ and $t = t_{\mathrm{T}} \geqslant t_{\mathrm{R}}$ respectively, through two different global quenches determined by $\{\kappa_{\mathrm{R}}, m_{\mathrm{R}}, \omega_{\mathrm{R}}, \omega_{0,\mathrm{R}}\}$ and $\{\kappa_{\mathrm{T}}, m_{\mathrm{T}}, \omega_{\mathrm{T}}, \omega_{0,\mathrm{T}}\}$ respectively.

The covariance matrix (3.2.3) at a generic value of t can be written as follows

$$\gamma(t) = V^{\mathrm{t}}\, \Gamma(t)\, V \qquad V = \widetilde{V} \oplus \widetilde{V} \tag{3.2.8}$$

where V is the orthogonal and symplectic matrix introduced in (2.2.42) and the block decomposition of $\Gamma(t)$ reads

$$\Gamma(t) = \begin{pmatrix} \mathcal{Q}(t) & \mathcal{M}(t) \\ \mathcal{M}(t) & \mathcal{P}(t) \end{pmatrix} \tag{3.2.9}$$

in terms of the diagonal matrices whose elements have been defined in (3.2.5).

Hereafter we enlighten the expressions by avoiding to indicate explicitly the dependence on t, wherever this is possible. The inverse of (3.2.9) is

$$\Gamma^{-1} = \big(\mathcal{Q}\,\mathcal{P} - \mathcal{M}^2\big)^{-1} \begin{pmatrix} \mathcal{P} & -\mathcal{M} \\ -\mathcal{M} & \mathcal{Q} \end{pmatrix} = 4 \begin{pmatrix} \mathcal{P} & -\mathcal{M} \\ -\mathcal{M} & \mathcal{Q} \end{pmatrix}. \tag{3.2.10}$$

where in the last step we have used that, since γ in (3.2.3) describes a pure state, the blocks $\mathcal{Q}$, $\mathcal{P}$ and $\mathcal{M}$ are constrained by

$$\mathcal{Q}\,\mathcal{P} - \mathcal{M}^2 = \frac{1}{4}\,\mathbf{1} \qquad \Longleftrightarrow \qquad Q_k P_k - M_k^2 = \frac{1}{4} \qquad 1 \leqslant k \leqslant N\,. \tag{3.2.11}$$

In this chapter we restrict to cases where a symplectic matrix V exists such that

$$\gamma_{\mathrm{R}} = V^{\mathrm{t}}\,\Gamma_{\mathrm{R}}\,V \qquad\qquad \gamma_{\mathrm{T}} = V^{\mathrm{t}}\,\Gamma_{\mathrm{T}}\,V \tag{3.2.12}$$

where both Γ_{R} and Γ_{T} have the form (3.2.9), in terms of the corresponding diagonal matrices. When (3.2.12) holds, the matrix occurring in the argument of the logarithm in (2.2.24) becomes

$$\gamma_{\mathrm{T}}\,\gamma_{\mathrm{R}}^{-1} = V^{\mathrm{t}}\,\Gamma_{\mathrm{T}}\,\Gamma_{\mathrm{R}}^{-1}\,V^{-\mathrm{t}} \tag{3.2.13}$$

which tells us that the complexity (2.2.24) is provided by the eigenvalues of $\Gamma_{\mathrm{T}}\,\Gamma_{\mathrm{R}}^{-1}$. Thus, the matrix V does not influence the temporal evolution of the complexity after the global quench when both the reference and the target states are pure states. Instead, they play a crucial role for the temporal evolution of the subsystem complexity discussed in Sec. 3.4 and Sec. 3.5.

By using (3.2.9) for Γ_{T} and (3.2.10) for Γ_{R}^{-1}, we obtain the following block matrix

$$\Gamma_{\mathrm{T}}\,\Gamma_{\mathrm{R}}^{-1} = 4 \begin{pmatrix} \mathcal{P}_{\mathrm{R}}\mathcal{Q}_{\mathrm{T}} - \mathcal{M}_{\mathrm{R}}\mathcal{M}_{\mathrm{T}} & \mathcal{Q}_{\mathrm{R}}\mathcal{M}_{\mathrm{T}} - \mathcal{M}_{\mathrm{R}}\mathcal{Q}_{\mathrm{T}} \\ \mathcal{P}_{\mathrm{R}}\mathcal{M}_{\mathrm{T}} - \mathcal{M}_{\mathrm{R}}\mathcal{P}_{\mathrm{T}} & \mathcal{Q}_{\mathrm{R}}\mathcal{P}_{\mathrm{T}} - \mathcal{M}_{\mathrm{R}}\mathcal{M}_{\mathrm{T}} \end{pmatrix} \tag{3.2.14}$$

whose blocks are diagonal matrices. For the eigenvalues of (3.2.14) we find

$$\begin{aligned} g^{(\pm)}_{\mathrm{TR},k} \;\equiv\; 2\Big(& P_{\mathrm{R},k}Q_{\mathrm{T},k} + Q_{\mathrm{R},k}P_{\mathrm{T},k} - 2M_{\mathrm{R},k}M_{\mathrm{T},k} \\ & \pm \sqrt{\big(P_{\mathrm{R},k}Q_{\mathrm{T},k} - Q_{\mathrm{R},k}P_{\mathrm{T},k}\big)^2 + 4\big(Q_{\mathrm{R},k}M_{\mathrm{T},k} - M_{\mathrm{R},k}Q_{\mathrm{T},k}\big)\big(P_{\mathrm{R},k}M_{\mathrm{T},k} - M_{\mathrm{R},k}P_{\mathrm{T},k}\big)} \Big) \end{aligned} \tag{3.2.15}$$

labelled by $1 \leqslant k \leqslant N$, which can be written as

$$g^{(\pm)}_{\mathrm{TR},k} = C_{\mathrm{TR},k} \pm \sqrt{C^2_{\mathrm{TR},k} - 1} \tag{3.2.16}$$

where

$$C_{\mathrm{TR},k} \equiv 2\big(Q_{\mathrm{T},k}\,P_{\mathrm{R},k} + P_{\mathrm{T},k}\,Q_{\mathrm{R},k} - 2\,M_{\mathrm{T},k}\,M_{\mathrm{R},k}\big) \tag{3.2.17}$$

in terms of the expressions in (3.2.5) specialised to the reference and the target states.

Let us observe that

$$g^{(+)}_{\mathrm{TR},k}\,g^{(-)}_{\mathrm{TR},k} = 16\big(Q_{\mathrm{R},k}P_{\mathrm{R},k} - M^2_{\mathrm{R},k}\big)\big(Q_{\mathrm{T},k}P_{\mathrm{T},k} - M^2_{\mathrm{T},k}\big)\,. \tag{3.2.18}$$

By employing (3.2.11) in this result, we find $g^{(+)}_{\mathrm{TR},k} = 1/g^{(-)}_{\mathrm{TR},k}$ for pure states, for any $1 \leqslant k \leqslant N$.

Thus, for the complexity (2.2.24) one obtains

$$\mathcal{C} \,=\, \frac{1}{2}\sqrt{\sum_{k=1}^{N}\big[\log(g^{(+)}_{\mathrm{TR},k})\big]^2} \,=\, \frac{1}{2}\sqrt{\sum_{k=1}^{N}\big[\log(g^{(-)}_{\mathrm{TR},k})\big]^2} \,=\, \frac{1}{2}\sqrt{\sum_{k=1}^{N}\big[\operatorname{arccosh}(C_{\mathrm{TR},k})\big]^2}\,. \tag{3.2.19}$$

In the most general setup described below (4.3.1), the complexity can be found by writing (3.2.5) for the reference and the target states first and then and plugging the results into (3.2.17) and (3.2.19). The final result is a complicated expressions which can be seen as a function of t_{R} and t_{T} parameterised by $\{\kappa_{\mathrm{R}}, m_{\mathrm{R}}, \omega_{\mathrm{R}}, \omega_{0,\mathrm{R}}\}$ and $\{\kappa_{\mathrm{T}}, m_{\mathrm{T}}, \omega_{\mathrm{T}}, \omega_{0,\mathrm{T}}\}$. We remark that (3.2.19) can be employed when (3.2.12) holds. Furthermore, we consider only cases where the matrix V in (3.2.12) depends on the geometric parameters of the system and of the subsystem but it is independent of the physical parameters occurring in the Hamiltonians (see Sec. 3.3.1).

A remarkable simplification occurs when the reference and the target states are pure states along the time evolution of a given quench. In this case, the parameters to fix in (3.2.5) are $m_{\mathrm{R}} = m_{\mathrm{T}} = m$, $\kappa_{\mathrm{R}} = \kappa_{\mathrm{T}} = \kappa$, $\omega_{\mathrm{R}} = \omega_{\mathrm{T}} = \omega$, and $\omega_{0,\mathrm{R}} = \omega_{0,\mathrm{T}} = \omega_0$; hence (3.2.17) simplifies to

$$C_{\mathrm{TR},k} = 1 + \frac{1}{2}\left(\frac{\Omega_k^2 - \Omega_{0,k}^2}{\Omega_k\,\Omega_{0,k}}\,\sin[\Omega_k(t_{\mathrm{R}} - t_{\mathrm{T}})]\right)^2 \tag{3.2.20}$$

which must be plugged into (3.2.19) to get the complexity of pure states after the global quench. Notice that (3.2.20) is not invariant under the exchange $\Omega_k \leftrightarrow \Omega_{0,k}$ for a given k. We remark that (3.2.20) and the corresponding complexity depend on $|t_{\mathrm{R}} - t_{\mathrm{T}}|$. This is not the case for the most generic choice of the parameters.

3.2.3 Complexity with respect to the initial state

A very natural choice for the reference state is the initial state $|\psi_0\rangle$, which is a crucial ingredient of the quench protocol. This corresponds to choose $t_{\mathrm{R}} = 0$ in (4.3.1). In this case, we have that $\mathcal{M}_{\mathrm{R}} = \mathbf{0}$ and $\mathcal{Q}_{\mathrm{R}}\mathcal{P}_{\mathrm{R}} = \frac{1}{4}\mathbf{1}$, which allow to write (3.2.17) as

$$C_{\mathrm{TR},k} \,\equiv\, \frac{1}{2}\left(\frac{Q_{\mathrm{T},k}}{Q_{\mathrm{R},k}} + \frac{P_{\mathrm{T},k}}{P_{\mathrm{R},k}}\right). \tag{3.2.21}$$

Setting $m_{\mathrm{R}} = m_{\mathrm{T}} = m$ for simplicity and $t_{\mathrm{T}} = t$ and $t_{\mathrm{R}} = 0$ in the most general setup described below (4.3.1), this expression becomes

$$C_{\mathrm{TR},k} = \frac{\big(\Omega^2_{0,\mathrm{T},k} + \Omega^2_{0,\mathrm{R},k}\big)\,\Omega^2_{\mathrm{T},k}\,[\cos(\Omega_{\mathrm{T},k}t)]^2 + \big(\Omega^4_{\mathrm{T},k} + \Omega^2_{0,\mathrm{T},k}\,\Omega^2_{0,\mathrm{R},k}\big)[\sin(\Omega_{\mathrm{T},k}t)]^2}{2\,\Omega^2_{\mathrm{T},k}\,\Omega_{0,\mathrm{R},k}\,\Omega_{0,\mathrm{T},k}} \tag{3.2.22}$$

in terms of the dispersion relations $\Omega_{0,\mathrm{S},k}$ (with $\mathrm{S} \in \{\mathrm{R},\mathrm{T}\}$) before the quenches providing the reference and the target states and of the dispersion relations $\Omega_{\mathrm{T},k}$ after the quench ($\Omega_{\mathrm{R},k}$ does not occur because $t_{\mathrm{R}} = 0$, hence (3.2.6) must be employed).

The expression (3.2.21) is consistent with the result reported in [67], where the temporal evolution of the complexity of this free bosonic system has been also studied through a different quench profile that does not include the quench protocol that we are considering. In many studies the reference state is the unentangled product state [35,36,40,311]. Given that we are considering a different reference state, in this thesis we do not directly compare their results with our findings.

When the same quench is employed to construct the reference and the target states $\Omega_{0,\mathrm{R},k} = \Omega_{0,\mathrm{T},k} = \Omega_{0,k}$ for any k and (3.2.22) simplifies. This choice corresponds to evaluate the complexity

between the initial state and the state at time t after the quench. Specialising (3.2.22) to this case and renaming $\Omega_{\mathrm{T},k} \equiv \Omega_k$, we obtain

$$C_{\mathrm{TR},k} = 1 + \frac{1}{2}\left(\frac{\Omega_k^2 - \Omega_{0,k}^2}{\Omega_k\,\Omega_{0,k}}\,\sin(\Omega_k t)\right)^2 \tag{3.2.23}$$

which coincides with (3.2.20) for $t_{\mathrm{R}} = 0$ and $t_{\mathrm{T}} = t$, as expected. Plugging (3.2.23) into (3.2.19) and using the identity $|\mathrm{arccosh}(1 + x^2/2)| = 2\,|\mathrm{arcsinh}(x/2)|$, one finds

$$\mathcal{C} \,=\, \sqrt{\sum_{k=1}^{N}\left[\mathrm{arcsinh}\left(\frac{\Omega_k^2 - \Omega_{0,k}^2}{2\,\Omega_k\,\Omega_{0,k}}\,\sin(\Omega_k t)\right)\right]^2}\,. \tag{3.2.24}$$

In this expression the dispersion relations Ω_k and $\Omega_{0,k}$ (which depend on the number of spatial dimensions and on the boundary conditions of the lattice) do not occur in a symmetric way.

We find it worth highlighting the contribution of the N-th mode by denoting

$$c_0 \equiv \left[\mathrm{arcsinh}\left(\frac{\Omega_N^2 - \Omega_{0,N}^2}{2\,\Omega_N\,\Omega_{0,N}}\,\sin(\Omega_N t)\right)\right]^2 \qquad \mathcal{C}_0^2 \equiv \sum_{k=1}^{N-1}\left[\mathrm{arcsinh}\left(\frac{\Omega_k^2 - \Omega_{0,k}^2}{2\,\Omega_k\,\Omega_{0,k}}\,\sin(\Omega_k t)\right)\right]^2 \tag{3.2.25}$$

which lead to write (3.2.24) as

$$\mathcal{C}^2 = \eta\, c_0 + \mathcal{C}_0^2 \tag{3.2.26}$$

where either $\eta = 1$ or $\eta = 0$, depending on whether the N-th mode plays a particular role, as one can read from the dispersion relation. This is the case e.g. for the zero mode in the harmonic lattices that are invariant under spatial translations, which is briefly discussed also at the end of Sec. 3.2.1; hence hereafter we refer to c_0 as the zero mode contribution. For instance, $\eta = 1$ in the harmonic chains with PBC, while $\eta = 0$ when DBC are imposed, as discussed later in Sec. 3.3.1. The result (3.2.24), which can be applied for harmonic lattices in generic number of dimensions and for diverse boundary conditions, has been already reported in [312] for harmonic chains with PBC.

It is interesting to determine the initial growth of the complexity by considering the series expansion of (3.2.24) as $t \to 0$. The function $\mathcal{C}^2$ obtained from (3.2.24) is an even function of t, hence its expansion for $t \to 0$ contains only even powers of t. Since $\mathcal{C}|_{t=0} = 0$, we have

$$\mathcal{C}^2 = b_1\,t^2 + b_2\,t^4 + b_3\,t^6 + O(t^8) \quad \Longrightarrow \quad \mathcal{C} = \sqrt{b_1}\;t\left(1 + \frac{b_2}{2b_1}\,t^2 + \frac{4\,b_1 b_3 - b_2^2}{8b_1^2}\,t^4 + O(t^6)\right) \tag{3.2.27}$$

where the coefficients b_1, b_2 and b_3 are

$$b_1 = \frac{1}{4}\sum_{k=1}^{N}\left(\frac{\Omega_k^2 - \Omega_{0,k}^2}{\Omega_{0,k}}\right)^2 \qquad b_2 = -\frac{1}{48}\sum_{k=1}^{N}\left(\frac{\Omega_k^4 - \Omega_{0,k}^4}{\Omega_{0,k}^2}\right)^2 \tag{3.2.28}$$

and

$$b_3 = \frac{1}{360}\sum_{k=1}^{N}\frac{(\Omega_k^4 - \Omega_{0,k}^4)^2(\Omega_k^4 + \Omega_{0,k}^4 - \Omega_k^2\,\Omega_{0,k}^2)}{\Omega_{0,k}^6}\,. \tag{3.2.29}$$

Since $b_1 > 0$, the expansion (3.2.27) tells us that the initial growth of the complexity (3.2.24) is linear in t.

The temporal evolution of the circuit complexity for a bosonic system after a global quench has been studied also in [311], by employing a smooth quench and the unentangled product state as the reference state. This smooth quench becomes the one that we are considering in the limit of sudden quench but it is different from the quench considered in [67].

Bounds and the zero mode contribution

We find it worth studying some bounds for the complexity with respect to the initial state. From (3.2.24), it is straightforward to observe that $\eta\, c_0 \leqslant \mathcal{C}^2 \leqslant \widetilde{\mathcal{C}}^2$, where c_0 is the time dependent expression defined in (3.2.25) and

$$\widetilde{\mathcal{C}}^2 \equiv \eta\, c_0 + \sum_{k=1}^{N-1} \left[\operatorname{arcsinh}\left(\frac{\Omega_k^2 - \Omega_{0,k}^2}{2\,\Omega_k\,\Omega_{0,k}} \right) \right]^2 \tag{3.2.30}$$

hence for the complexity (3.2.24) we find

$$\sqrt{\eta\, c_0} \leqslant \mathcal{C} \leqslant \widetilde{\mathcal{C}}\,. \tag{3.2.31}$$

The zero mode contribution determines the behaviour of these bounds for large t.
The occurrence of a zero mode in the dispersion relation Ω_k e.g. for $k = N$ means that $\Omega_N = 0$. In the absence of a zero mode, Ω_k is non vanishing for any value of k; hence c_0 and $\widetilde{\mathcal{C}}$ are finite for any t and (3.2.31) tells us that the complexity (3.2.24) is always finite after the quench. Instead, when a zero mode for $k = N$ occurs, the time dependent zero mode contribution c_0 in (3.2.25) becomes

$$c_0 = \big[\operatorname{arcsinh}(\Omega_{0,N}\, t/2)\big]^2 \tag{3.2.32}$$

which diverges at large t because $\operatorname{arcsinh}(x) \sim \log(2x)$ as $x \to +\infty$. The terms labelled by $1 \leqslant k \leqslant N-1$ in the sum in (3.2.30) are bounded functions of t because Ω_k is non vanishing. Thus, in the presence of a zero mode, the bounds (3.2.31) tell us that the complexity for pure states in (3.2.24) diverges logarithmically when $t \to \infty$.

The bounds (3.2.31) can be significantly improved by employing the decomposition (3.2.26) which leads to the following bounds for the complexity (3.2.24)

$$\mathcal{C}_{\mathrm{L}}^2 \leqslant \mathcal{C}^2 \leqslant \mathcal{C}_{\mathrm{U}}^2 \tag{3.2.33}$$

where we have introduced

$$\mathcal{C}_{\mathrm{B}}^2 \equiv \eta\, c_0 + \sum_{k=1}^{N-1} f_{\mathrm{B}}(\tilde{x}_k) \big[\sin(\Omega_k t)\big]^2 = \left(\eta\, c_0 + \frac{1}{2} \sum_{k=1}^{N-1} f_{\mathrm{B}}(\tilde{x}_k) \right) - \frac{1}{2} \sum_{k=1}^{N-1} f_{\mathrm{B}}(\tilde{x}_k) \cos(2\Omega_k\, t) \tag{3.2.34}$$

with $\mathrm{B} \in \{\mathrm{L}, \mathrm{U}\}$ and

$$f_{\mathrm{L}}(x) = \big[\operatorname{arcsinh}(x)\big]^2 \qquad f_{\mathrm{U}}(x) = x^2 \tag{3.2.35}$$

in terms of $\tilde{x}_k \equiv (\Omega_k^2 - \Omega_{0,k}^2)/(2\,\Omega_k\,\Omega_{0,k})$, of the time dependent zero mode contribution c_0 introduced in (3.2.25) and of the parameter η, which is either $\eta = 1$ or $\eta = 0$, depending on whether the zero mode contribution occurs or not respectively.

The bounds (3.2.33) can be employed to improve the bounds reported in (3.2.31). Indeed, in the presence of a zero mode, $\mathcal{C}_{\mathrm{L}}^2 \geqslant c_0$ and therefore $\mathcal{C}_{\mathrm{L}}^2$ provides a better lower bound than (3.2.25). Instead, the relation between $\mathcal{C}_{\mathrm{U}}^2$ in (3.2.34) and $\widetilde{\mathcal{C}}^2$ in (3.2.30) depends on the parameters; hence the optimal upper bound is given by $\min\big[\mathcal{C}_{\mathrm{U}}(t)^2, \widetilde{\mathcal{C}}(t)^2\big]$.

3.3 Complexity for harmonic chains

In this section we apply the results discussed in Sec. 3.2 to the harmonic chains where either PBC or DBC are imposed. The numerical data reported in all the figures of the chapter have been obtained by setting $\kappa = 1$ and $m = 1$.

3.3.1 Complexity

The Hamiltonian of the harmonic chain made by N oscillators with the same frequency ω, the same mass m and coupled through the elastic constant κ is (2.7.1). Imposing PBC means that $\hat{q}_{N+1} = \hat{q}_1$ and $\hat{p}_{N+1} = \hat{p}_1$, while DBC are satisfied when $\hat{q}_0 = \hat{q}_N = \hat{q}_{N+1} = 0$ and $\hat{p}_0 = \hat{p}_N = 0$.

When PBC hold, the orthogonal matrix $\widetilde{V}$ defined in (3.2.4) is given in (2.7.5), when N is even and in (2.7.6), when N is odd. The dispersion relations of $\hat{H}_0$ and $\hat{H}$ for PBC are respectively

$$\Omega_{0,k} = \sqrt{\omega_0^2 + \frac{4\kappa}{m}[\sin(\pi k/N)]^2} \qquad \Omega_k = \sqrt{\omega^2 + \frac{4\kappa}{m}[\sin(\pi k/N)]^2} \qquad 1 \leqslant k \leqslant N\,. \tag{3.3.1}$$

When DBC hold, only $N-1$ sites display some dynamics because the ones labelled by $i = 0$ and $i = N$ are fixed by the boundary conditions; hence the covariance matrix $\gamma(t)$ is the $(2N-2)\times(2N-2)$ symmetric matrix given by (3.2.3), where Q, P and R are $(N-1)\times(N-1)$ matrices. For DBC and independently of the parity of N, the matrix $\widetilde{V}$ defined in (3.2.4) becomes

$$\widetilde{V}_{i,k} = \sqrt{\frac{2}{N}}\,\sin(i\,k\,\pi/N) \qquad 1 \leqslant i,k \leqslant N-1\,. \tag{3.3.2}$$

The dispersion relations of $\hat{H}_0$ and $\hat{H}$ for DBC read respectively

$$\Omega_{0,k} = \sqrt{\omega_0^2 + \frac{4\kappa}{m}\,[\sin(\pi k/(2N))]^2} \qquad \Omega_k = \sqrt{\omega^2 + \frac{4\kappa}{m}\,[\sin(\pi k/(2N))]^2} \qquad 1 \leqslant k \leqslant N-1\,. \tag{3.3.3}$$

We remark that, both for PBC and DBC, the matrix $V = \widetilde{V} \oplus \widetilde{V}$ defined in (3.2.8) depends only on N; hence the corresponding harmonic chains can be studied as special cases of the harmonic lattices considered in Sec. 3.2.2 because the condition (3.2.12) is satisfied. Since $\eta = 1$ for PBC and $\eta = 0$ for DBC, the complexity (3.2.24) for these harmonic chains becomes

$$\begin{aligned} \mathcal{C} &= \sqrt{\sum_{k=1}^{N-1+\eta}\left[\operatorname{arcsinh}\left(\frac{\omega^2-\omega_0^2}{2\,\Omega_k\,\Omega_{0,k}}\,\sin(\Omega_k t)\right)\right]^2} \qquad (3.3.4)\\ &= \sqrt{\eta\left[\operatorname{arcsinh}\left(\frac{\omega^2-\omega_0^2}{2\,\omega\,\omega_0}\,\sin(\omega t)\right)\right]^2 + \sum_{k=1}^{N-1}\left[\operatorname{arcsinh}\left(\frac{\omega^2-\omega_0^2}{2\,\Omega_k\,\Omega_{0,k}}\,\sin(\Omega_k t)\right)\right]^2} \end{aligned}$$

where the dispersion relations $\Omega_{0,k}$ and Ω_k are given by (3.3.1) for PBC and by (3.3.3) for DBC.

When PBC are imposed, the first term under the square root in the last expression of (3.3.4) comes from the zero mode $k = N$ and it does not occur for DBC. This crucial difference between the two models leads to different qualitative behaviours for the complexity.

The dispersion relations of the harmonic chain with PBC given in (3.3.1) are invariant under the exchange $k \leftrightarrow N-k$. This symmetry leads to an expression for the complexity which is simpler to evaluate numerically. Indeed, by introducing

$$c_0 \equiv \left[\operatorname{arcsinh}\left(\frac{\omega^2-\omega_0^2}{2\,\omega\,\omega_0}\,\sin(\omega t)\right)\right]^2 \tag{3.3.5}$$

and

$$c_{N/2} \equiv \begin{cases} \left[\operatorname{arcsinh}\left(\dfrac{\omega^2-\omega_0^2}{2\,\Omega_{N/2}\,\Omega_{0,N/2}}\,\sin(\Omega_{N/2}\,t)\right)\right]^2 & \text{even } N \\ 0 & \text{odd } N \end{cases} \tag{3.3.6}$$

one observes that (3.3.4) for PBC can be written as

$$\mathcal{C} \,=\, \sqrt{c_0 + 2\sum_{k=1}^{\lfloor \frac{N-1}{2} \rfloor} \Big[\operatorname{arcsinh}\Big(\frac{\omega^2-\omega_0^2}{2\,\Omega_k\,\Omega_{0,k}}\,\sin(\Omega_k t)\Big)\Big]^2 + c_{N/2}} \tag{3.3.7}$$

where $\lfloor x \rfloor$ denotes the integer part of x. Notice that $c_{N/2}$ in (3.3.6), as function of t, is bounded by a constant.

3.3.2 Critical evolution

An important case that we find worth emphasising is the global quench where the evolution Hamiltonian is gapless, i.e. when $\omega = 0$.

When PBC are imposed, by specialising (3.2.23) and (3.3.1) to $\omega = 0$, we obtain

$$C_{\mathrm{TR},k} \,=\, 1 + \frac{\omega_0^4\,\big[\sin\big(2\sqrt{\kappa/m}\;t\;\sin(\pi k/N)\big)\big]^2}{8\,(\kappa/m)\,[\sin(\pi k/N)]^2\,\big(\omega_0^2 + 4(\kappa/m)[\sin(\pi k/N)]^2\big)} \tag{3.3.8}$$

which satisfies the following bounds

$$1 \,<\, C_{\mathrm{TR},k} \,<\, 1 + \frac{\omega_0^4}{8\,(\kappa/m)\,[\sin(\pi k/N)]^2\,\big(\omega_0^2 + 4(\kappa/m)[\sin(\pi k/N)]^2\big)} \qquad 1 \leqslant k \leqslant N-1\,. \tag{3.3.9}$$

For $k = N$, the expression (3.3.8) simplifies to $C_{\mathrm{TR},N} = 1 + \frac{\omega_0^2}{2}\,t^2$, which diverges as $t \to \infty$.

Instead, when DBC hold and therefore the zero mode does not occur, by using (3.3.3) and (3.2.23) with $\omega = 0$, we obtain

$$C_{\mathrm{TR},k} \,=\, 1 + \frac{\omega_0^4\,\big[\sin\big(2\sqrt{\kappa/m}\,t\,\sin(\pi k/(2N))\big)\big]^2}{8\,(\kappa/m)[\sin(\pi k/(2N))]^2\,\big(\omega_0^2 + 4\kappa/m[\sin(\pi k/(2N))]^2\big)} \tag{3.3.10}$$

which is finite when $t \to \infty$, for any allowed value of k.

Plugging the expressions discussed above for $C_{\mathrm{TR},k}$ into (3.2.19), we find that, when the evolution Hamiltonian is critical, the complexity of the pure state at time t with respect to the initial state can be written by highlighting the zero mode contribution as follows

$$\mathcal{C}^2 \,=\, \frac{\eta}{4}\left[\log\left(1 + \frac{(\omega_0\,t)^2}{2} + \frac{\omega_0\,t}{2}\,\sqrt{(\omega_0\,t)^2+4}\right)\right]^2 + \frac{1}{4}\sum_{k=1}^{N-1}\big[\operatorname{arccosh}\big(C_{\mathrm{TR},k}\big)\big]^2 \tag{3.3.11}$$

where either $\eta = 1$ for PBC or $\eta = 0$ for DBC (see the text above (3.3.4)) and $C_{\mathrm{TR},k}$ is given by (3.3.8) for PBC and by (3.3.10) for DBC. In particular, (3.3.11) tells us that, for PBC and finite N, the complexity diverges logarithmically as $t \to \infty$ because of the zero mode contribution. Instead, for DBC (i.e. $\eta = 0$) and finite N, all the terms in (3.3.11) are finite as $t \to \infty$.

In Fig. 3.1 we show the temporal evolution of the complexity (3.3.11) for various ω_0's, when either PBC (left panels) or DBC (right panels) are imposed. Since N is finite, the revivals already studied in the temporal evolutions of other quantities [323] are observed also in the temporal evolution of the complexity, with a period given by $N/2$ for PBC and by N for DBC. The most important qualitative difference between PBC and DBC is the overall growth observed for PBC, which does not occur for DBC. This growth is due to the zero mode contribution occurring in the complexity (3.3.11) for PBC. Indeed, when the corresponding term is subtracted, as done in

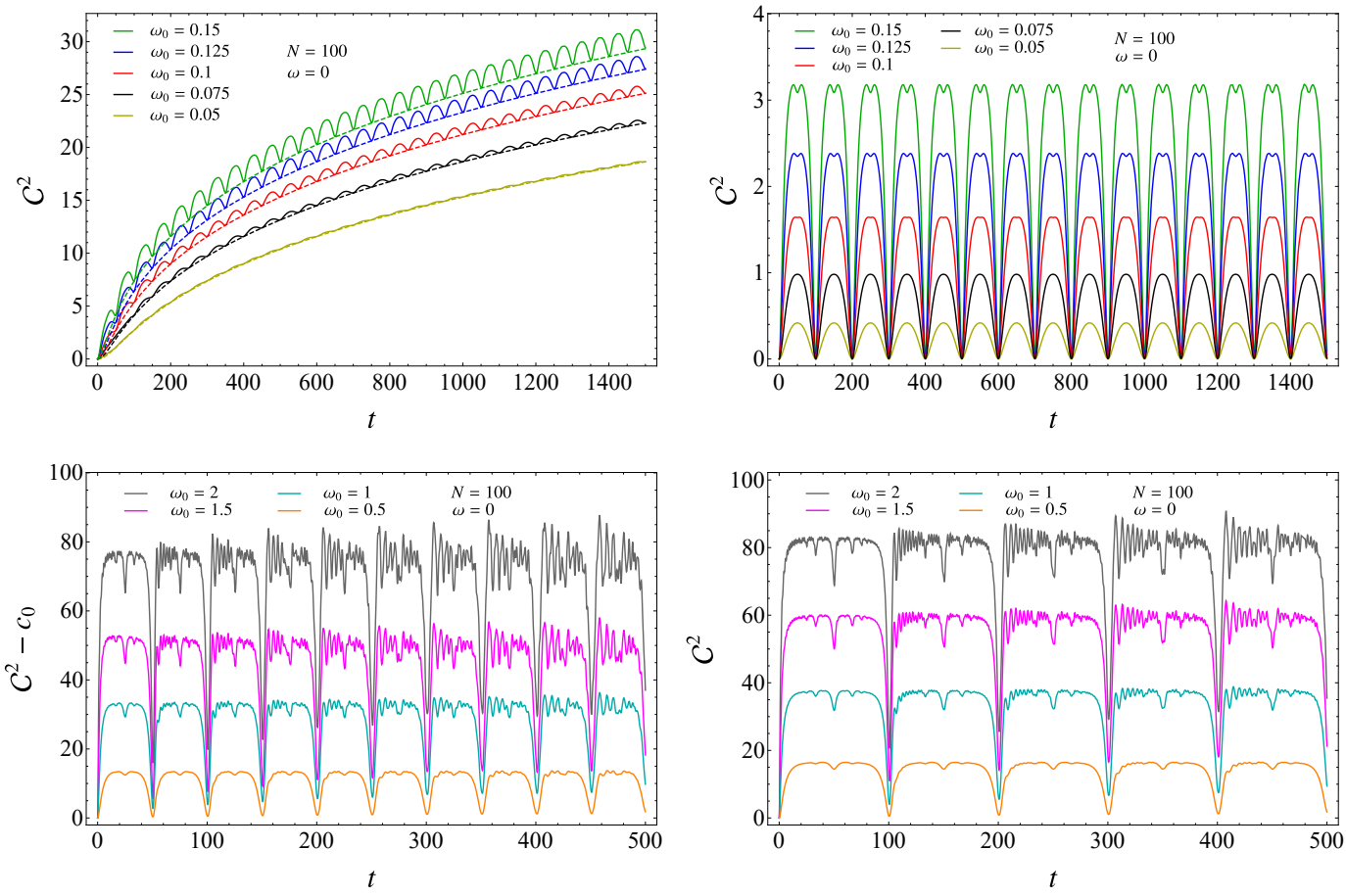

Figure 3.1: Temporal evolution of the complexity after the global quench w.r.t. the initial state at $t = 0$ for harmonic chains with either PBC (left panels) or DBC (right panels) made by $N = 100$ sites. The solid lines correspond to the complexity (3.3.11). In the top left panel, the dashed lines show the zero mode term c_0 (i.e. the expression multiplyed by η in (3.3.11), which has been subtracted to obtain the bottom left panel), with the same colour code for the corresponding value of ω_0.

the bottom left panel of Fig. 3.1, the resulting curve is similar to the temporal evolution of the complexity when DBC hold.

Finally, let us remark that the effect of the decoherence as t increases is more evident for higher values of ω_0. For PBC this is observed once the zero mode contribution has been subtracted (see the bottom left panel of Fig. 3.1).

In [40] the temporal evolution of the complexity of a thermofield double state is considered by taking the unentangled product state as the reference state (in this setup, the choice $\omega = 0$ is not allowed). Despite this temporal evolution is different from the one investigated in this chapter, it also exhibits an overall logarithmic growth due to the zero mode contribution.

3.3.3 Bounds

It is instructive to discuss further the bounds for the complexity introduced in Sec. 3.2.3 in the special cases of the harmonic chains with either PBC or DBC.

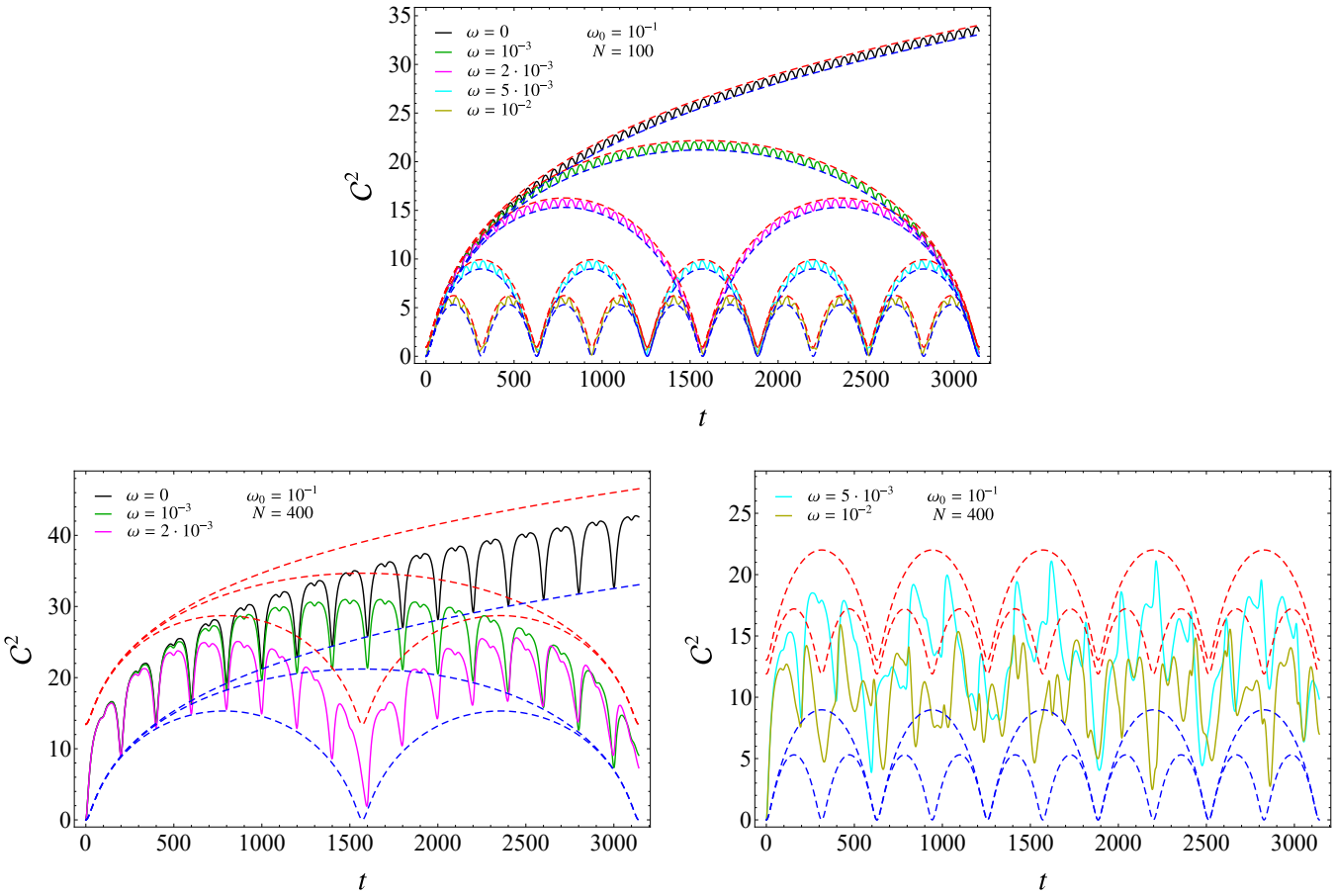

Figure 3.2: Temporal evolution of the complexity (3.3.4) (solid lines) and of the corresponding bounds in (3.2.31) for PBC. The blue and red dashed lines show the lower and the upper bounds, from (3.2.25) and (3.2.30) respectively.

In Fig. 3.2 we show the complexity (3.3.4) and the corresponding bounds (3.2.31) for harmonic chains with PBC. In this case the zero mode term influences the bounds in a crucial way. In Fig. 3.2, the bounds (3.2.31) correspond to the red and blue dashed lines, while in the top left panel of Fig. 3.1, where $\omega = 0$, the lower bound in (3.2.31) is shown through the dashed curves.

In the temporal evolutions of the complexity for PBC displayed in the top panel of Fig. 3.2, we can identify two periods approximatively given by π/ω and $N/2$. Considering also the bottom panels of Fig. 3.2, the revivals observed for the critical evolution in Fig. 3.1 for PBC and $\omega = 0$ occur also when $\omega > 0$ whenever $\frac{\pi}{\omega} \gg \frac{N}{2}$. The bottom panels in Fig. 3.2 highlight that the revivals are not observed when ω is large enough with respect to $1/N$.

For PBC, by comparing the top panel with the bottom ones in Fig. 3.2, which differ for the size N of the chain, we notice that the bounds (3.2.31) are very efficient when $\frac{\pi}{\omega} \gg \frac{N}{2}$, while they become not useful away from this regime. In our numerical investigations we have also observed that the bounds (3.2.31) are not useful when $\omega > \omega_0$.

When DBC hold, the lower bound in (3.2.31) is trivial and the upper bound is a constant.

The bounds (3.2.33) can be written explicitly for the harmonic chains that we are considering by setting either $\eta = 1$ or $\eta = 0$ and employing either (3.3.1) or (3.3.3) for the dispersion relations when either PBC or DBC respectively are imposed. The resulting expressions for these bounds

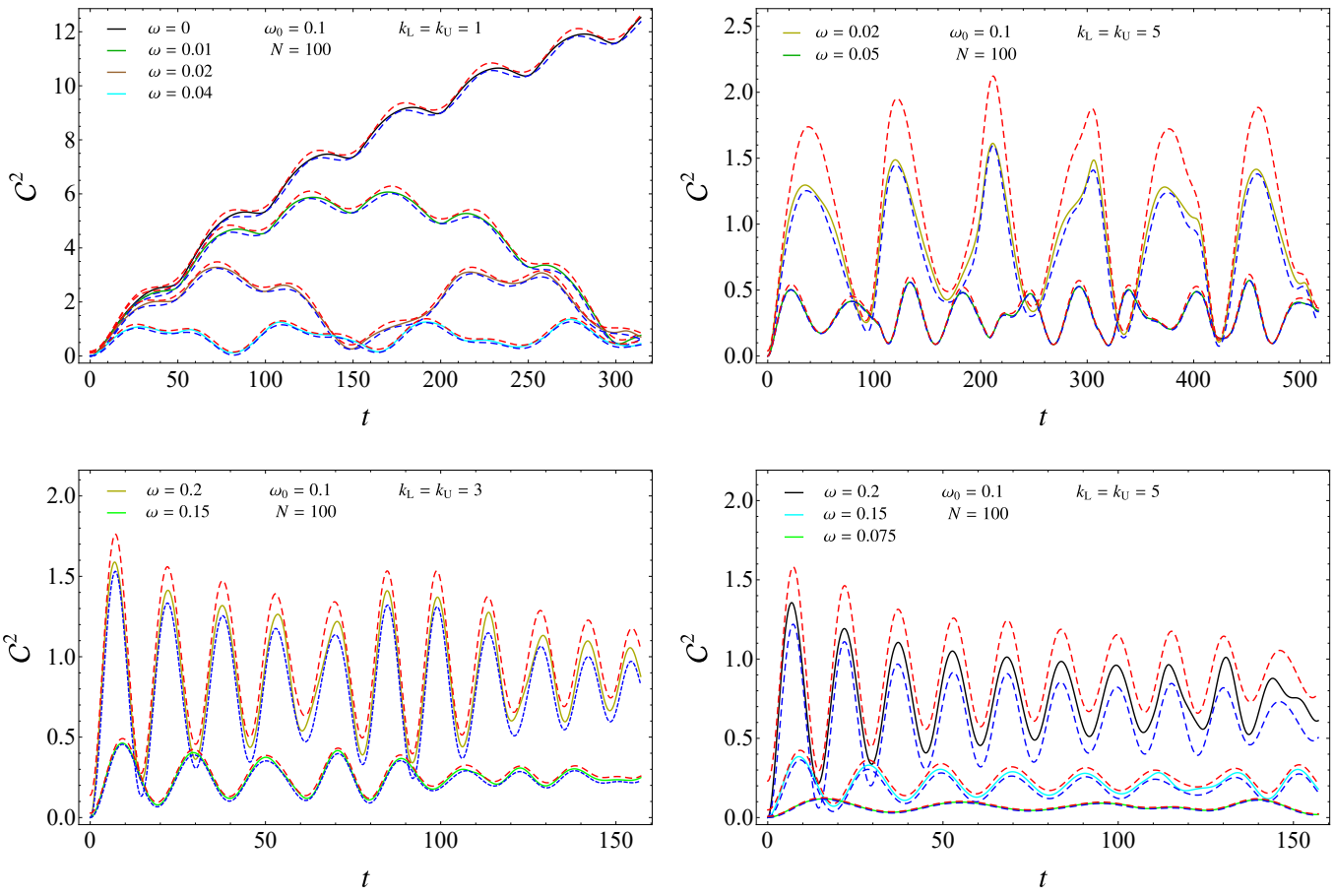

Figure 3.3: Temporal evolution of the complexity (3.3.4) (solid lines) and of the corresponding bounds in (3.3.12) for harmonic chains with either PBC (left panels) or DBC (right panels) and $N = 100$. The blue (red) dashed lines correspond to the lower (upper) bound (see (3.3.14) and (3.3.13) for the left panels and (3.3.15) for the right panels). In all the panels $\omega_0 = 0.1$.

require to sum either N or $N-1$ terms and we can obtain less constraining but still insightful bounds by keeping only few terms in these sums, i.e.

$$\mathcal{C}^2_{\mathrm{L},k_\mathrm{L}} \leqslant \mathcal{C}^2 \leqslant \mathcal{C}^2_{\mathrm{U},k_\mathrm{U}} \tag{3.3.12}$$

where k_L and k_U are independent parameters related to the number of terms in the sum kept to define the corresponding bound. Since the explicit expressions of the dispersion relations are important to write explicitly the bounds in (3.3.12), the cases of PBC and DBC must be studied separately.

Considering PBC first, we find

$$\mathcal{C}^2_{\mathrm{L},k_\mathrm{L}} = c_0 + 2\sum_{k=1}^{k_\mathrm{L}} f_\mathrm{L}(\tilde{x}_k)\,[\sin(\Omega_k t)]^2\,. \tag{3.3.13}$$

$$\mathcal{C}^2_{\mathrm{U},k_\mathrm{U}} = c_0 + 2\sum_{k=1}^{k_\mathrm{U}} f_\mathrm{U}(\tilde{x}_k)\,[\sin(\Omega_k t)]^2 + \sum_{k=k_\mathrm{U}+1}^{\lfloor\frac{N-1}{2}\rfloor} 2\,f_\mathrm{U}(\tilde{x}_k) + f_\mathrm{U}(\tilde{x}_{N/2})\,\big|\cos(\pi N/2)\big|\,. \tag{3.3.14}$$

where $f_{\rm L}(\tilde{x}_k)$ as function of k is constructed from (3.2.35) and (3.3.1)). The bounds (3.2.33) are recovered when $k_{\rm L} = k_{\rm U} = \lfloor \frac{N-1}{2} \rfloor$, by setting to zero the second sum in the r.h.s. of (3.3.14) and by restoring the time dependence in the term having $k = N/2$ when N is even, both in (3.3.13) and (3.3.14).

When DBC are imposed, we have

$$\mathcal{C}^2_{{\rm L},k_{\rm L}} \equiv \sum_{k=1}^{k_{\rm L}} f_{\rm L}(\tilde{x}_k) \, [\sin(\Omega_k t)]^2 \qquad \mathcal{C}^2_{{\rm U},k_{\rm U}} \equiv \sum_{k=1}^{k_{\rm U}} f_{\rm U}(\tilde{x}_k) \, [\sin(\Omega_k t)]^2 + \sum_{k=k_{\rm U}+1}^{N-1} f_{\rm U}(\tilde{x}_k) \tag{3.3.15}$$

where $1 \leqslant k_{\rm L}, k_{\rm U} \leqslant N-1$. In order to recover (3.2.33) from (3.3.12), we have to choose $k_{\rm L} = k_{\rm U} = N-1$ and set to zero the last sum in the second expression of (3.3.15).

By construction, we have $\mathcal{C}^2_{{\rm L},k_{\rm L}} \leqslant \mathcal{C}^2_{\rm L}$ and $\mathcal{C}^2_{{\rm U},k_{\rm U}} \geqslant \mathcal{C}^2_{\rm U}$, but $\mathcal{C}^2_{{\rm L},k_{\rm L}}$ and $\mathcal{C}^2_{{\rm U},k_{\rm U}}$ contain less terms than $\mathcal{C}^2_{\rm L}$ and $\mathcal{C}^2_{\rm U}$ respectively, hence they are easier to evaluate and to study analytically. For both PBC and DBC, considering either the lower or the upper bound in (3.3.12), it improves as either $k_{\rm L}$ or $k_{\rm U}$ respectively increases.

In Fig. 3.3 we show the bounds (3.3.12) when either PBC (left panels) or DBC (right panels) are imposed and small values of $k_{\rm L}$ and $k_{\rm U}$ are considered. For given values of $k_{\rm L}$ and $k_{\rm U}$, the agreement between the bounds and the exact curve improves as $|\omega_0 - \omega|$ decreases. Notice that higher values of $k_{\rm L}$ and $k_{\rm U}$ are needed for DBC to reach an agreement with the exact curve comparable with the one obtained for PBC.

3.3.4 Large N

It is important to study approximate expressions for the temporal evolution of the complexity when large values of N are considered.

In our numerical analysis, we noticed that, for finite but large enough values of $N \gtrsim 10$ the complexity (3.3.4) is well described by a function of ωN, $\omega_0 N$ and t/N. This function, which depends on whether PBC or DBC are imposed, can be written by introducing the approximation $\sin(x) \simeq x$ into the dispersion relations and keeping only the leading term. For PBC we find

$$\mathcal{C}_{\rm approx} = \sqrt{c_0(t) + 2 \sum_{k=1}^{\lfloor \frac{N-1}{2} \rfloor} \left[\operatorname{arcsinh}\left(\frac{(\omega N)^2 - (\omega_0 N)^2}{2\, \widetilde{\Omega}^{(\rm P)}_k \, \widetilde{\Omega}^{(\rm P)}_{0,k}} \, \sin\!\big(\widetilde{\Omega}^{(\rm P)}_k t/N\big) \right) \right]^2} \tag{3.3.16}$$

where $c_0(t)$ is (3.3.5); while for DBC we get

$$\mathcal{C}_{\rm approx} = \sqrt{\sum_{k=1}^{N-1} \left[\operatorname{arcsinh}\left(\frac{(\omega N)^2 - (\omega_0 N)^2}{2\, \widetilde{\Omega}^{(\rm D)}_k \widetilde{\Omega}^{(\rm D)}_{0,k}} \, \sin\!\big(\widetilde{\Omega}^{(\rm D)}_k t/N\big) \right) \right]^2} \tag{3.3.17}$$

where

$$\widetilde{\Omega}^{(\rm P)}_k = \sqrt{(\omega N)^2 + \frac{4\pi^2 \kappa}{m} \, k^2} \qquad \widetilde{\Omega}^{(\rm D)}_k = \sqrt{(\omega N)^2 + \frac{\pi^2 \kappa}{m} \, k^2} \tag{3.3.18}$$

while $\widetilde{\Omega}^{(\rm P)}_{0,k}$ and $\widetilde{\Omega}^{(\rm D)}_{0,k}$ are obtained by replacing ω with ω_0 in these expressions. Notice that both (3.3.16) and (3.3.17) depend on ωN, $\omega_0 N$ and t/N. These approximate expressions have been used to plot the dashed light grey curves in the top panels of Fig. 3.4, which nicely agree with the corresponding solid coloured curves.

The thermodynamic limit $N \to \infty$ of the complexity can be studied through the standard procedure. Introducing $\theta \equiv \pi k/N$ and substituting $\sum_k \to \frac{N}{\pi}\int_0^\pi d\theta$ in (3.3.4), at the leading order we find

$$\mathcal{C}_{\text{TD}} = \sqrt{\frac{N}{\pi}} \sqrt{\int_0^\pi \left[\text{arcsinh}\Big(\frac{\omega^2 - \omega_0^2}{2\,\Omega_\theta\,\Omega_{0,\theta}}\, \sin(\Omega_\theta\, t)\Big)\right]^2 d\theta} \tag{3.3.19}$$

where the dispersion relations become

$$\Omega_{0,\theta} = \sqrt{\omega_0^2 + \frac{4\kappa}{m}\,(\sin\theta)^2} \qquad \Omega_\theta = \sqrt{\omega^2 + \frac{4\kappa}{m}\,(\sin\theta)^2} \tag{3.3.20}$$

Notice that, for PBC, the zero mode does not contribute because $c_0/N \to 0$ as $N \to \infty$. Let us stress that (3.3.19) with (3.3.20) holds for both PBC and DBC. Thus, the leading order of this limit is independent of the boundary conditions. This means that the complexity does not distinguish the boundary conditions in this regime. Indeed, in the left and right panels of Fig. 3.4, the same function (just described) has been used to plot the dashed black curves.

The boundary conditions become crucial in the subleading term of the expansion of (3.3.4) as $N \to \infty$, which can be studied through the Euler-Maclaurin formula [324]. The final result is

$$\mathcal{C}^2 - \mathcal{C}_{\text{TD}}^2 = R_{1,\infty}^{(\text{B})} \qquad \text{B} \in \big\{\text{P}, \text{D}\big\} \qquad R_{1,\infty}^{(\text{B})} = \begin{cases} R_{1,\infty}^{(\text{P})} & \text{PBC} \\ R_{1,\infty}^{(\text{D})} = \dfrac{R_{1,\infty}^{(\text{P})}}{2} + \zeta & \text{DBC} \end{cases} \tag{3.3.21}$$

where

$$\zeta = \frac{1}{2}\left\{ \left[\text{arcsinh}\Big(\frac{(\omega^2 - \omega_0^2)\, \sin\big(\sqrt{\omega^2 + 4\kappa/m}\; t\,\big)}{2\sqrt{\omega^2 + 4\kappa/m}\,\sqrt{\omega_0^2 + 4\kappa/m}}\Big)\right]^2 - \left[\text{arcsinh}\Big(\frac{\omega^2 - \omega_0^2}{2\,\omega\,\omega_0}\, \sin(\omega t)\Big)\right]^2 \right\} \tag{3.3.22}$$

and $R_{1,\infty}^{(\text{P})}$ is the time-dependent remainder for which we do not have an exact expression. Numerical checks for these results are shown in Fig. 3.4. In the top panels of this figure we have displayed also $\mathcal{C}_{\text{approx}}/N$ from (3.3.16) (left panel) and $(\mathcal{C}_{\text{approx}} - \zeta)/N$ from (3.3.17) (right panel) through dashed light grey lines.

In the continuum limit, $N \to \infty$ and the lattice spacing $a \equiv \sqrt{m/\kappa} \to 0$ is vanishing while $Na \equiv \ell$ is kept fixed. In this limit, the expression (3.3.4) for the complexity (which holds for both PBC and DBC) becomes

$$\mathcal{C}_{\text{cont}} = \sqrt{\frac{\ell}{2\pi}} \sqrt{\int_{-\infty}^{\infty} \left[\text{arcsinh}\Big(\frac{\omega^2 - \omega_0^2}{2\,\Omega_p\,\Omega_{0,p}}\, \sin(\Omega_p t)\Big)\right]^2 dp} \tag{3.3.23}$$

where

$$\Omega_{0,p} = \sqrt{\omega_0^2 + p^2} \qquad \Omega_p = \sqrt{\omega^2 + p^2}\,. \tag{3.3.24}$$

Since $\Omega_p \simeq p$ when $p \gg \omega$, the vanishing of the integrand in (3.3.23) as $p \to \pm\infty$ is such that the complexity is UV finite.

3.3.5 Initial growth

It is worth discussing the initial growth of the complexity for the harmonic chains that we are considering. Since the complexity (3.3.4) is a special case of (3.2.24), its expansion as $t \to 0$ can be found by specialising the expansion (3.2.27) and its coefficients (3.2.28) and (3.2.29) to the harmonic chains with either PBC or DBC. For the sake of simplicity, in the following we discuss

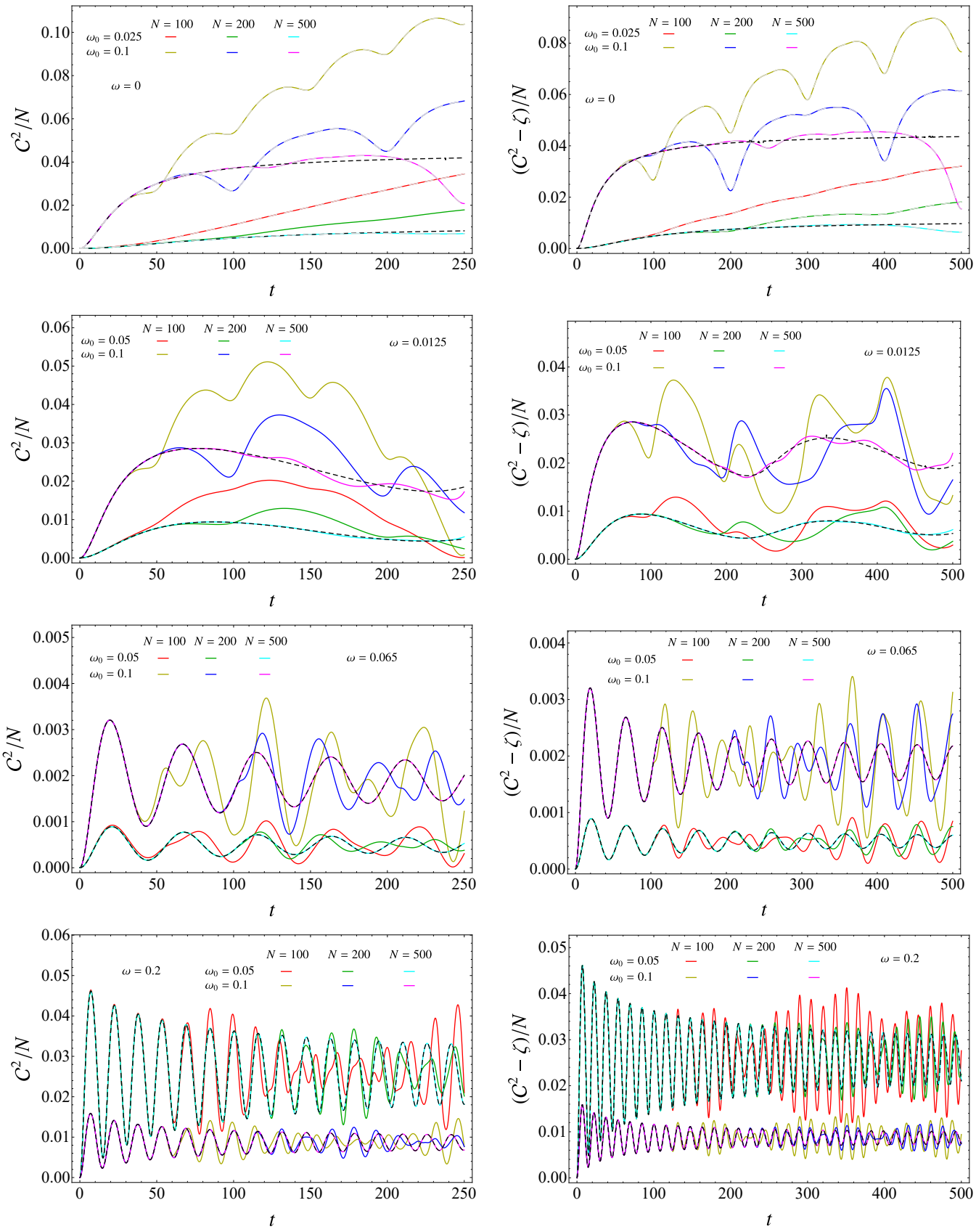

Figure 3.4: Temporal evolutions of the complexity for harmonic chains with either PBC (left panels) or DBC (right panels). The solid lines show $\mathcal{C}^2/N$ for PBC and $(\mathcal{C}^2-\zeta)/N$ for DBC, with $\mathcal{C}$ given by (3.3.4) and ζ by (3.3.22). The dashed black lines represent $\mathcal{C}^2_{\rm TD}/N$, from (3.3.19).

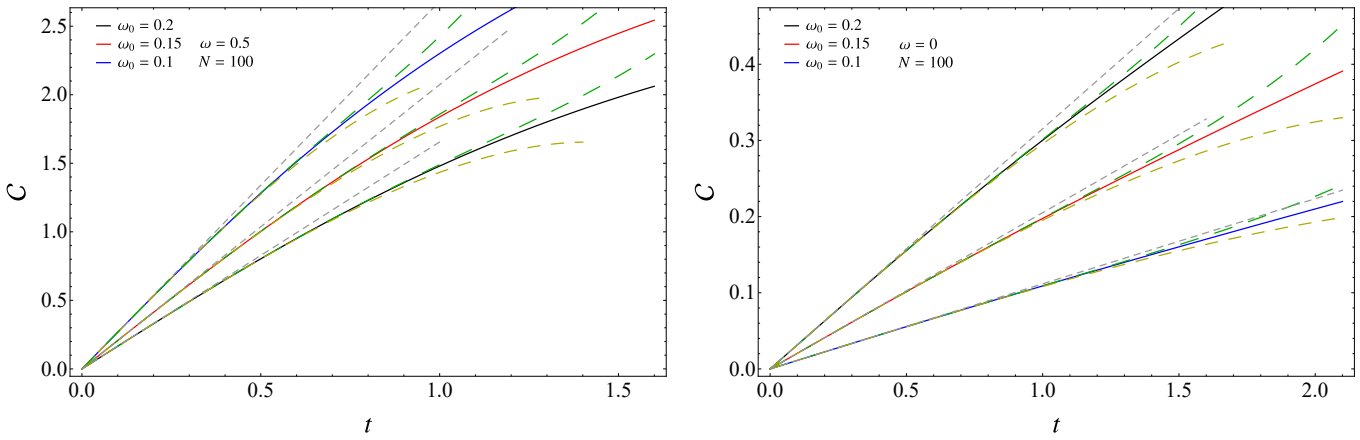

Figure 3.5: Initial growth of the complexity for harmonic chains with PBC and $N = 100$. The evolution Hamiltonian is either massive (left panel) or massless (right panel), for three values ω_0. The solid lines show the complexity (3.3.4) (with (3.3.1)) and the dashed lines represent its expansion (3.2.27) up to the $O(t)$ (grey), $O(t^3)$ (yellow) and $O(t^5)$ (green) term included.

only the leading term (i.e. only the coefficient b_1 in (3.2.28)), which provides the linear growth, but a similar analysis can be applied straightforwardly to the coefficients of the higher order terms in the $t \to 0$ expansion.

For the harmonic chains with either PBC or DBC, the linear growth in (3.2.27) becomes

$$\mathcal{C} = \frac{|\omega^2 - \omega_0^2|}{2} \left(\sum_{k=1}^{N-1+\eta} \Omega_{0,k}^{-2} \right)^{1/2} t + O(t^3) \tag{3.3.25}$$

where $\eta = 1$ and (3.3.1) must be used for PBC, while $\eta = 0$ and (3.3.3) must be employed for DBC. We remark that the slope of the initial linear growth in (3.3.25) is proportional to $|\omega - \omega_0|$.

In Fig. 3.5, we consider the initial growth of the complexity (3.3.4) when PBC are imposed, comparing the exact curve against its expansion (3.2.27). The corresponding analysis for DBC provides curves that are very similar to the ones displayed in Fig. 3.5; hence it has not been reported in this thesis.

Let us conclude our discussion about the temporal evolution of the complexity of pure states with a brief qualitative comparison between the results discussed above and the corresponding ones for the temporal evolution of the holographic complexity [51–53, 56, 57, 140–142].

The Vaidya spacetimes are the typical backgrounds employed as the gravitational duals of global quantum quenches in the conformal field theory on their boundary. They describe the formation of a black hole through the collapse of a matter shell. In Vaidya spacetimes, the temporal evolution of the holographic entanglement entropy has been largely studied [243, 321, 325–330] and the temporal evolutions of the holographic complexity for the entire spatial section of the conformal field theory on the boundary has been investigated in [140–142, 331]. Considering the temporal evolution of the rate $\frac{d\mathcal{C}}{dt}$ allows to avoid the problem of choosing the reference state, which deserves further clarifications for the holographic complexity, even for static gravitational backgrounds. The analysis of $\frac{d\mathcal{C}}{dt}$ in Vaidya spacetimes, both for the CV and for the CA prescriptions, shows that these temporal evolutions are linear in time both at very early and at late time [140, 141]. While also the initial growth of the complexity that we have explored is linear (see (3.3.25)), the late time growth is at most logarithmic. This disagreement, which deserves further analysis, has

been discussed in [40].

We find it worth observing also that the coefficient of the initial growth (3.3.25) is proportional to $|\omega^2 - \omega_0^2|$ and that the corresponding coefficient for the holographic complexity is proportional to the mass of the final black hole [140, 141].

3.4 Subsystem complexity in finite harmonic chains

In this section we study the temporal evolution of the subsystem complexity after a global quench. The reference and the target states are the reduced density matrices associated to a given subsystem. We focus on the simple cases where the subsystem A is a block made by consecutive sites in harmonic chains with either PBC or DBC.

3.4.1 Subsystem complexity

In the harmonic lattices that we are considering, the reduced density matrix associated to A characterises a Gaussian state which can be described equivalently through its reduced covariance matrix γ_A. This matrix is constructed by considering the reduced correlation matrices Q_A, P_A and M_A, whose elements are respectively given by $(Q_A)_{i,j} = \langle\psi_0|\,\hat{q}_i(t)\,\hat{q}_j(t)\,|\psi_0\rangle$, $(P_A)_{i,j} = \langle\psi_0|\,\hat{p}_i(t)\,\hat{p}_j(t)\,|\psi_0\rangle$ and $(M_A)_{i,j} = \mathrm{Re}\big[\langle\psi_0|\,\hat{q}_i(t)\,\hat{p}_j(t)\,|\psi_0\rangle\big]$ with $i, j \in A$, which depend also on the time after the global quench. These matrices provide the following block decomposition of the reduced covariance matrix

$$\gamma_A(t) = \begin{pmatrix} Q_A(t) & M_A(t) \\ M_A(t)^{\mathrm{t}} & P_A(t) \end{pmatrix}. \tag{3.4.1}$$

For the harmonic chains with either PBC or DBC introduced in Sec. 3.3 and A made by L consecutive sites, Q_A and P_A are $L \times L$ symmetric matrices and γ_A is a real, symmetric and positive definite $2L \times 2L$ matrix. The temporal evolution of $(Q_A)_{i,j}$, $(P_A)_{i,j}$ and $(M_A)_{i,j}$ after a global quench is reported in Appendix C.2 for finite chains with either PBC or DBC and for their thermodynamic limit.

Adapting the analysis made in Sec. 3.3 for pure states to the mixed states described by the reduced covariance matrices $\gamma_A(t)$, we have that the reference state is given by the reduced density matrix for the interval A at time $t_{\mathrm{R}} \geqslant 0$ obtained through the quench protocol characterised by $\big(\kappa_{\mathrm{R}}, m_{\mathrm{R}}, \omega_{\mathrm{R}}, \omega_{0,\mathrm{R}}\big)$ and the target state by the reduced density matrix for the same interval at time $t_{\mathrm{T}} \geqslant t_{\mathrm{R}}$ constructed through the quench protocol described by $\big(\kappa_{\mathrm{T}}, m_{\mathrm{T}}, \omega_{\mathrm{T}}, \omega_{0,\mathrm{T}}\big)$. The corresponding reduced covariance matrices are denoted by $\gamma_{\mathrm{R},A}(t_{\mathrm{R}})$ and $\gamma_{\mathrm{T},A}(t_{\mathrm{T}})$ respectively. These reduced covariance matrices are decomposed in terms of the correlation matrices of the subsystem like in (3.4.1).

The approach to the circuit complexity of mixed states based on the Fisher information geometry discussed in chapter 2 allows to construct the optimal circuit between $\gamma_{\mathrm{R},A}(t_{\mathrm{R}})$ and $\gamma_{\mathrm{T},A}(t_{\mathrm{T}})$. The covariance matrices along this optimal circuit are

$$G_s(\gamma_{\mathrm{R},A}(t_{\mathrm{R}})\,, \gamma_{\mathrm{T},A}(t_{\mathrm{T}})) \,\equiv\, \gamma_{\mathrm{R},A}(t_{\mathrm{R}})^{1/2}\Big(\gamma_{\mathrm{R},A}(t_{\mathrm{R}})^{-1/2}\,\gamma_{\mathrm{T},A}(t_{\mathrm{T}})\,\gamma_{\mathrm{R},A}(t_{\mathrm{R}})^{-1/2}\Big)^{s}\gamma_{\mathrm{R},A}(t_{\mathrm{R}})^{1/2} \tag{3.4.2}$$

where $0 \leqslant s \leqslant 1$ parameterises the optimal circuit. The length of this optimal circuit is proportional to its complexity

$$\mathcal{C}_A \,=\, \frac{1}{2\sqrt{2}}\,\sqrt{\mathrm{Tr}\,\Big\{\big[\log\big(\gamma_{\mathrm{T},A}(t_{\mathrm{T}})\,\gamma_{\mathrm{R},A}(t_{\mathrm{R}})^{-1}\big)\big]^2\Big\}}\,. \tag{3.4.3}$$

The reduced covariance matrices $\gamma_{\mathrm{R},A}(t_{\mathrm{R}})$ and $\gamma_{\mathrm{T},A}(t_{\mathrm{T}})$ for the block A providing the optimal circuit (3.4.2) and its complexity (3.4.3) are constructed as in (3.4.1), through the reduced correlation matrices Q_A, P_A and M_A, obtained by restricting to $i, j \in A$ the indices of the correlation matrices whose elements are given in (C.2.1) for PBC and (C.2.2) for DBC.

We remark that the matrix $\widetilde{V}$ in (3.2.4) (given in (2.7.5) or (2.7.6) for PBC and in (3.3.2) for DBC) is crucial to write (C.2.1) and (C.2.2); hence it enters in a highly non-trivial way in the evaluation of the subsystem complexity. Instead, it does not affect the complexity for the entire system, where both the reference and the target states are pure states, as remarked below (3.2.13).

The temporal evolution of the subsystem complexity after a global quench in harmonic chains made by two sites has been explored in [67,315] through other approaches, including the one based on the purification complexity.

3.4.2 Numerical results

Considering the global quench that we are exploring, in the following we discuss some numerical results for the temporal evolution of the subsystem complexity of a block A made by L consecutive sites in harmonic chains made by N sites, where either PBC or DBC are imposed. We focus on the simplest setup where the reference state is the initial state (hence $t_{\mathrm{R}} = 0$) and the target state corresponds to a generic value of $t_{\mathrm{T}} = t \geqslant 0$ after the quench. The remaining parameters are fixed to $\omega_{0,\mathrm{R}} = \omega_{0,\mathrm{T}} \equiv \omega_0$, $\omega_{\mathrm{R}} = \omega_{\mathrm{T}} \equiv \omega$, $\kappa_{\mathrm{R}} = \kappa_{\mathrm{T}} = 1$ and $m_{\mathrm{R}} = m_{\mathrm{T}} = 1$. In the case of DBC, we consider both A adjacent to the boundary and separated from it.

In this setup, the subsystem complexity (3.4.3) can be written as

$$\mathcal{C}_A \,=\, \frac{1}{2\sqrt{2}} \sqrt{\mathrm{Tr}\left\{ \left[\log\!\big(\gamma_A(t)\, \gamma_A(0)^{-1}\big) \right]^2 \right\}} \,. \tag{3.4.4}$$

It is natural to introduce also the entanglement entropy $S_A(t)$ and its initial value $S_A(0)$, which lead to define the increment of the entanglement entropy w.r.t. its initial value, i.e.

$$\Delta S_A \equiv S_A(t) - S_A(0) \tag{3.4.5}$$

where $S_A(t)$ and $S_A(0)$ can be evaluated from the symplectic spectrum of $\gamma_A(t)$ and of $\gamma_A(0)$ respectively, as discussed in Appendix A.1(see (A.1.3)).

In all the figures discussed in this section we show the temporal evolutions of the subsystem complexity $\mathcal{C}_A$ in (3.4.4) or of the increment ΔS_A of the entanglement entropy in (3.4.5) after the global quench. In particular, we show numerical results corresponding to $N = 100$ and $N = 200$, finding nice collapses of the data when L/N, $\omega_0 N$ and ωN are kept fixed, independently of the boundary conditions. The data reported in all the left panels have been obtained in harmonic chains with PBC, whose dispersion relations are (3.3.1), while the ones in all the right panels correspond to a block adjacent to a boundary of harmonic chains where DBC are imposed, whose dispersion relations are (3.3.3), if not otherwise indicated (like in Fig.3.12). The evolution Hamiltonian is gapless in Fig. 3.6, Fig. 3.7, Fig. 3.8 and Fig. 3.12, while it is gapped in Fig. 3.9 and Fig. 3.10, with $\omega N = 5$. In Fig. 3.11, where the initial growth is explored, both gapless and gapped evolution Hamiltonians have been employed. When $L = N$, the complexity (3.3.4) for pure states has been evaluated with either $N = 100$ (black solid lines) or $N = 200$ (dashed green lines).

In Fig. 3.6, Fig. 3.7 and Fig. 3.8 all the data have been obtained with $\omega N = 0$ and either $\omega_0 N = 20$ (Fig. 3.6 and Fig. 3.8) or $\omega_0 N = 100$ (Fig. 3.7). Revivals are observed and the different cycles correspond to $p < 2t/N < p + 1$ for PBC and to $p < t/N < p + 1$ for DBC, where p is a non-negative integer.

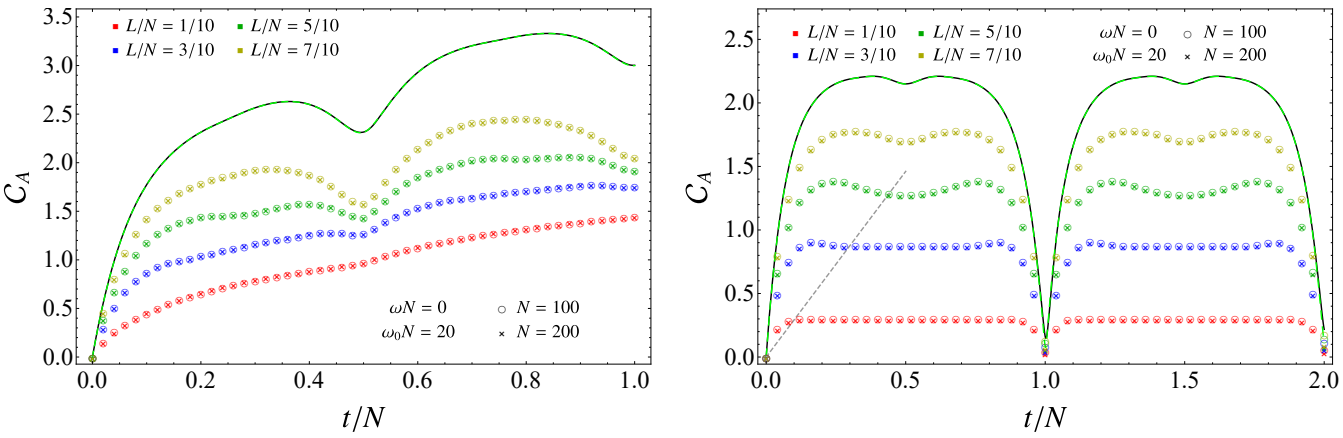

Figure 3.6: Temporal evolution of $\mathcal{C}_A$ in (3.4.4) after the global quench with gapless evolution Hamiltonian and $\omega_0 N = 20$, for a block A made by L consecutive sites in harmonic chains with either PBC (left panels) or DBC (right panels) made by N sites (in the latter case A is adjacent to a boundary). When $L = N$, the complexity (3.3.4) is shown for $N = 100$ (solid black lines) and $N = 200$ (dashed green lines).

The qualitative behaviour of the temporal evolution of the subsystem complexity crucially depends on the boundary conditions of the harmonic chain. For DBC, considering the data having $L/N < 1/2$ when $t/N < 1/2$, we can identify three regimes: an initial growth until a local maximum is reached, a decrease and then a thermalisation regime after certain value of t/N, where the subsystem complexity remains constant. For PBC and $L/N < 1/2$, the latter regime is not observed and $\mathcal{C}_A$ keeps growing. Comparing the right panel in Fig. 3.6 with the top right panel in Fig. 3.7, one realises that, for DBC, the height of the plateaux increases as either L/N or $\omega_0 N$ increases, as expected. The absence of thermalisation regimes for PBC could be related to the occurrence of the zero mode, as suggested by the fact that, for pure states, the zero mode contribution provides the logarithmic growth of the complexity (3.3.11). However, we are not able to identify explicitly the zero mode contribution in the subsystem complexity, hence we cannot subtract it as done in the bottom left panel of Fig. 3.1 for the temporal evolution of the complexity of pure states.

For DBC, the plateau in the thermalisation regime is not observed when $L/N \geqslant 1/2$ and, considering the interval $t/N \in [\nu, \nu + 1]$ with $\nu = \{0, 1\}$, it approximately begins at $t - \nu N \simeq L$ and ends at $t - \nu N \simeq N - L + 1$. The straight dashed grey lines approximatively indicate the beginning of the plateaux for different $L/N < 1/2$ (in particular, they are obtained by joining the origin with the point of the curve made by the blue data points at $t/N = 0.3$).

We remark that the temporal evolution of $\mathcal{C}_A$ in infinite chains is made by the three regimes mentioned above (see Fig. 3.14, Fig. 3.15 and Fig. 3.16), as largely discussed in Sec. 3.5.

Comparing the temporal evolutions of $\mathcal{C}_A$ and ΔS_A for the same quench protocol and the same subsystem in Fig. 3.7, we observe that the initial growth of $\mathcal{C}_A$ in the first revival is faster than the linear initial growth of ΔS_A, as highlighted by the straight dashed black lines in Fig. 3.7. Within the first revival, we do not observe a long range of t/N where the evolution of $\mathcal{C}_A$ is linear. Nonetheless, the straight line characterising the initial growth of ΔS_A intersects the first local maximum corresponding to the end of the initial growth of $\mathcal{C}_A$ when $L/N < 1/2$. Considering the data points for $L/N < 1/2$ and the initial regime of t/N corresponding to half of the first revival, we

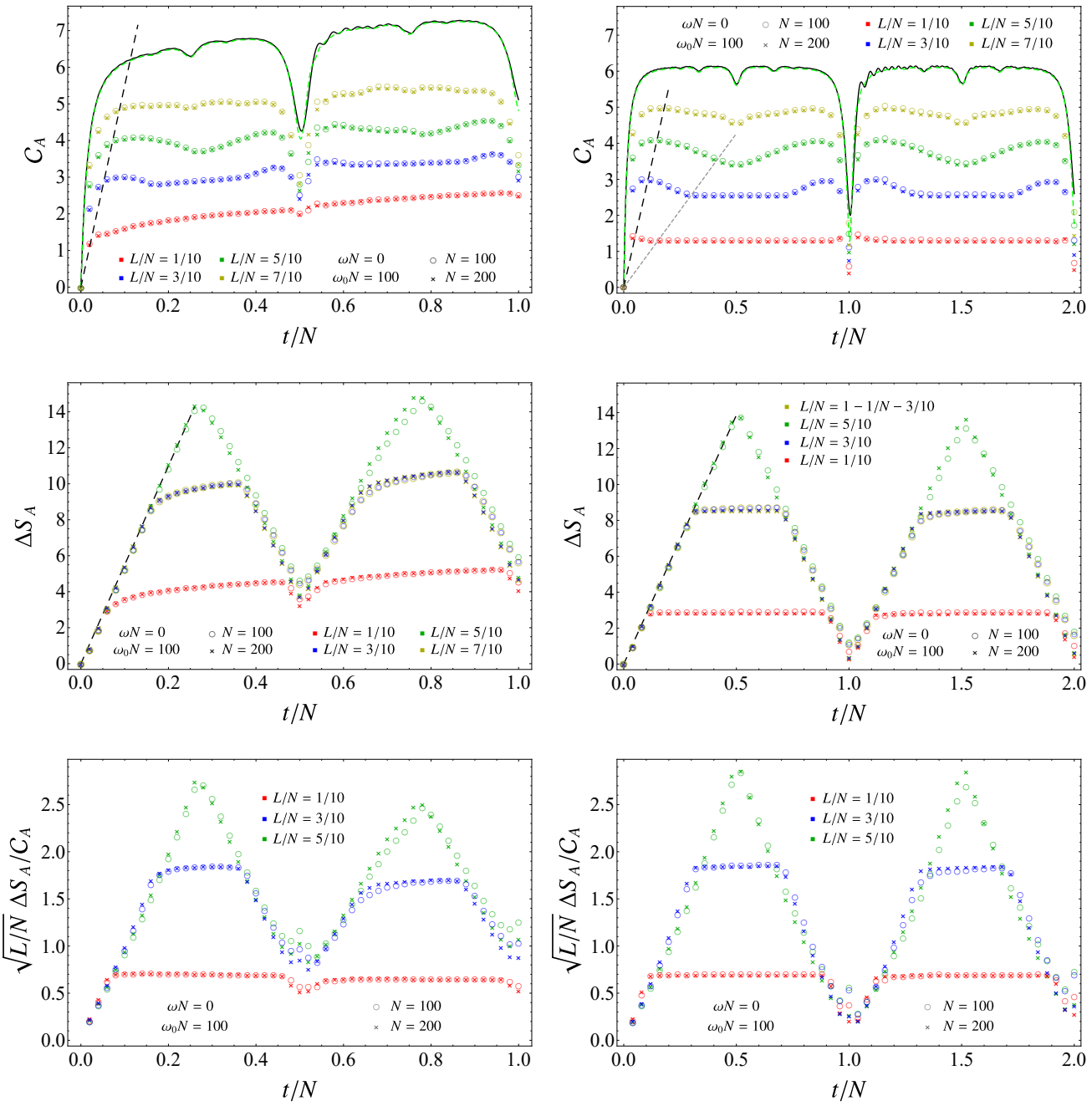

Figure 3.7: Temporal evolution of $\mathcal{C}_A$ in (3.4.4) (top panels), of ΔS_A in (3.4.5) (middle panels) and of $\sqrt{L/N}\,\Delta S_A/\mathcal{C}_A$ (bottom panels) after the global quench with gapless evolution Hamiltonian and $\omega_0 N = 100$, for a block A made by L consecutive sites in a harmonic chains with either PBC (left panels) or DBC (right panels) made by N sites (in the latter case A is adjacent to a boundary). When $L = N$ the complexity (3.3.4) is shown for $N = 100$ (solid black lines) and $N = 200$ (dashed green lines).

notice that, while the temporal evolution of ΔS_A displays a linear growth followed by a saturation regime, the temporal evolution of $\mathcal{C}_A$ is characterised by the three regimes described above. The saturation regimes of $\mathcal{C}_A$ and ΔS_A are qualitatively very similar and begin approximatively at the

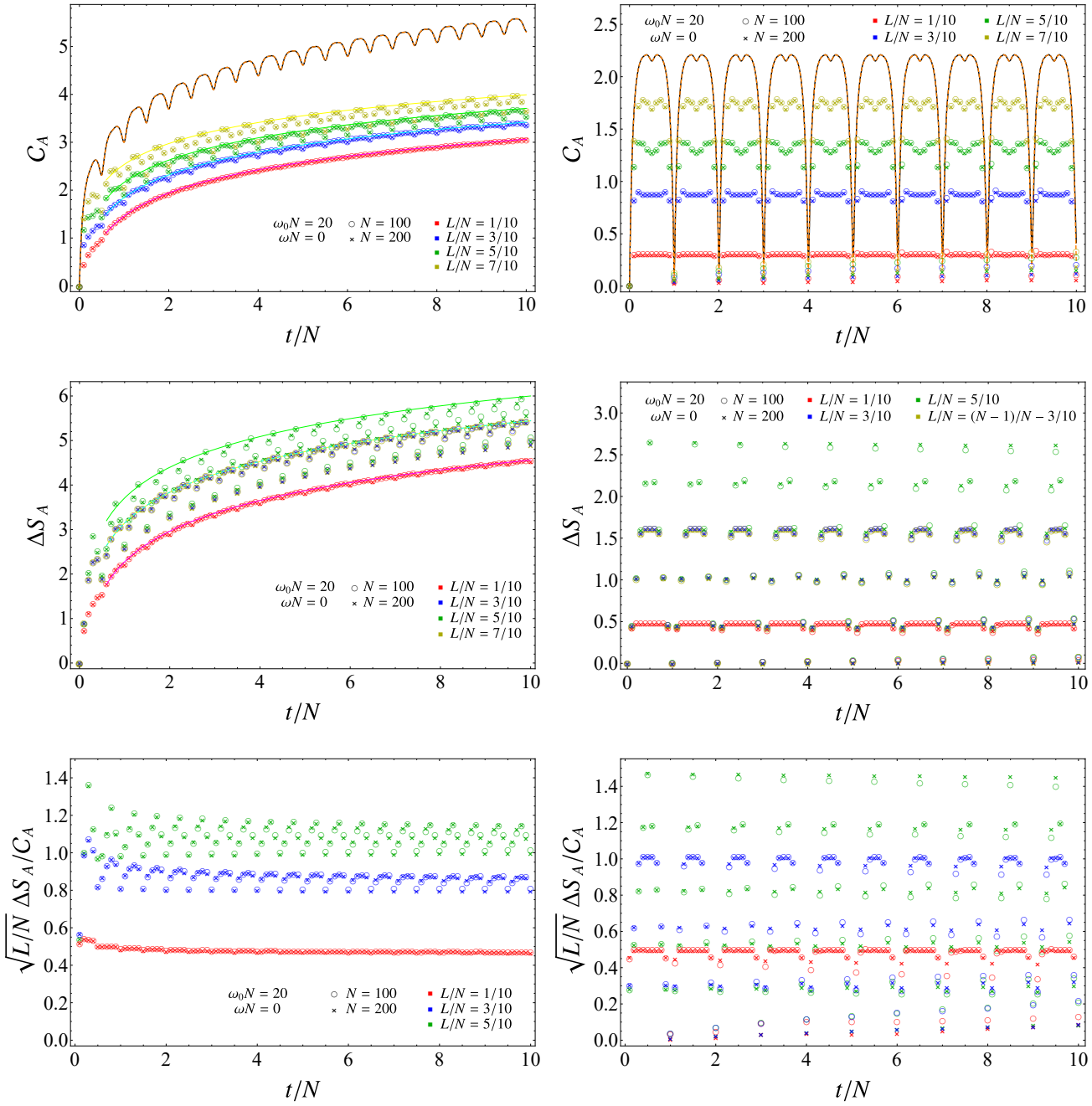

Figure 3.8: Temporal evolution of $\mathcal{C}_A$ in (3.4.4) (top panels), of ΔS_A in (3.4.5) (middle panels) and of $\sqrt{L/N}\,\Delta S_A/\mathcal{C}_A$ (bottom panels) after the global quench with a gapless evolution Hamiltonian and $\omega_0 N = 20$, for harmonic chains with either PBC (left panels) or DBC (right panels), in the same setups of Fig. 3.6 are considered.

same value of t/N. Notice that the amplitude of the decrease of $\mathcal{C}_A$ at the end of the first revival is smaller than the one of ΔS_A.

The temporal evolutions of $\mathcal{C}_A$ and ΔS_A can be compared for $L/N \leqslant 1/2$. Indeed, for a bipartite system in a pure state the entanglement entropy of a subsystem is equal to the entanglement entropy of the complementary subsystem. This property, which does not hold for $\mathcal{C}_A$, implies the

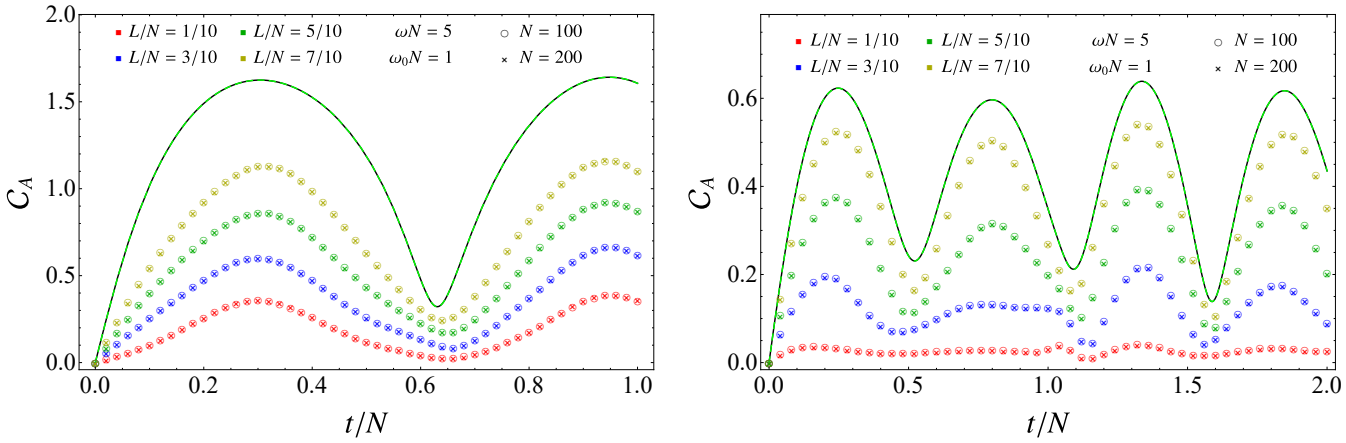

Figure 3.9: Temporal evolution of $\mathcal{C}_A$ in (3.4.4) after the global quench with a gapped evolution Hamiltonian for a block A made by L consecutive sites in harmonic chains with either PBC (left panels) or DBC (right panels) made by N sites (in the latter case A is adjacent to a boundary of the segment). When $L = N$ the complexity (3.3.4) is shown for $N = 100$ (solid black lines) and $N = 200$ (dashed green lines).

overlap between the data for ΔS_A corresponding to $L/N = 3/10$ and to $L/N = 7/10$. Furthermore, $\Delta S_A = 0$ identically when $L = N$.

In the bottom panels of Fig. 3.7 we have reported the temporal evolutions of the ratio $\Delta S_A/\mathcal{C}_A$ for the data reported in the other panels of the figure. The curves of $\Delta S_A/\mathcal{C}_A$ corresponding to PBC (left panel) and DBC (right panel) are very similar. For instance, the curves for $\sqrt{L/N}\,\Delta S_A/\mathcal{C}_A$ have the same initial growth for different values of L/N. However, we remark that a mild logarithmic decrease occurs in the thermalisation regime for PBC.

In Fig. 3.8 the range $0 \leqslant t/N \leqslant 10$ is considered, which is made by 20 revivals for PBC and by 10 cycles for DBC. The temporal evolutions of $\mathcal{C}_A$ in the top panels show that, up to oscillations due to the revivals, after the initial growth $\mathcal{C}_A$ keeps growing logarithmically for PBC (the solid coloured lines in the top left panel are two-parameter fits through the function $a + b\log(t/N)$ of the corresponding data), while it remains constant for DBC. This feature is observed also in the corresponding temporal evolutions of ΔS_A (middle panels of Fig. 3.8). These two logarithmic growths for PBC are very similar, as shown by the temporal evolution of $\Delta S_A/\mathcal{C}_A$ displayed in the bottom left panel of Fig. 3.8.

In Fig. 3.9 and Fig. 3.10 we show some temporal evolutions of $\mathcal{C}_A$ when the evolution Hamiltonian is massive ($\omega_0 < \omega$ in Fig. 3.9 and $\omega_0 > \omega$ in Fig. 3.10, with $\omega N = 5$ in both the figures). In these temporal evolutions one observes that the local extrema of the curves for $\mathcal{C}_A$ having different L/N roughly occur at the same values of t/N. It is insightful to compare these temporal evolutions with the corresponding ones characterised by $\omega = 0$ in Fig. 3.6 and Fig. 3.7. For PBC, the underlying growth observed when $\omega = 0$ does not occur if $\omega > 0$. For DBC, the plateaux observed in the saturation regime when $\omega = 0$ are replaced by oscillatory behaviours if $\omega > 0$.

In Fig. 3.10, we report the temporal evolutions of $\mathcal{C}_A$, of ΔS_A and of $\Delta S_A/\mathcal{C}_A$ for the same global quench. The evolutions of $\mathcal{C}_A$ and of ΔS_A are qualitatively similar when $L/N < 1/2$. An important difference is the initial growth at very small values of t/N: for $\mathcal{C}_A$ is linear (see also Fig. 3.11 and the corresponding discussion), while for ΔS_A is quadratic, as highlighted in the insets of the middle panels (the coefficient of this quadratic growth for PBC is twice the one obtained for

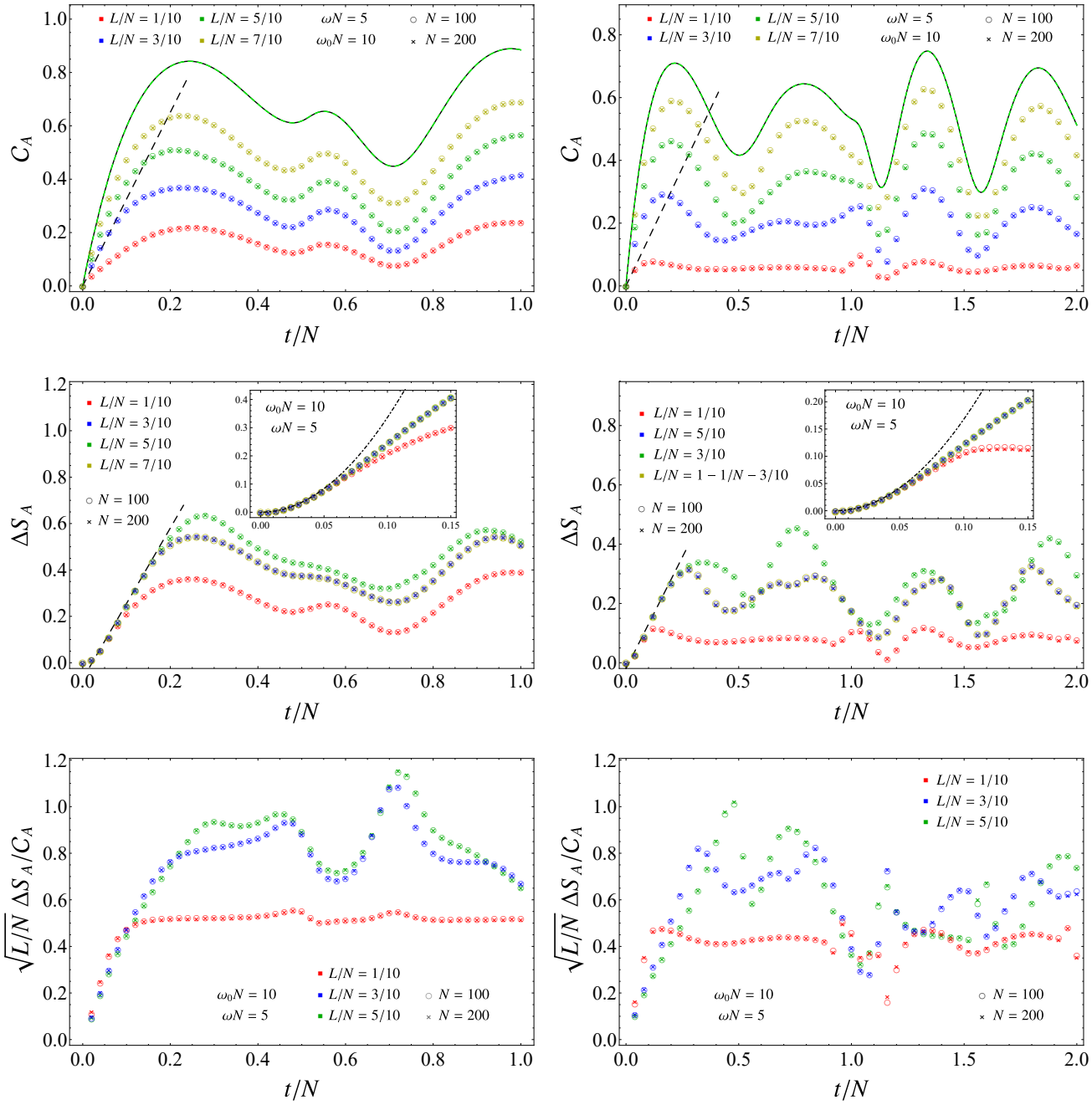

Figure 3.10: Temporal evolution after the global quench with a gapped evolution Hamiltonian of $\mathcal{C}_A$ in (3.4.4) (top panels), of ΔS_A in (3.4.5) (middle panels) and of $\sqrt{L/N}\,\Delta S_A/\mathcal{C}_A$ (bottom panels) for a block A made by L consecutive sites in harmonic chains with either PBC (left panels) or DBC (right panels) made by N sites (in the latter case A is adjacent to a boundary of the segment). When $L = N$, the complexity (3.3.4) is shown for $N = 100$ (solid black lines) and $N = 200$ (dashed green lines).

DBC) and also observed in [329, 332–334]. Comparing the bottom panels of Fig. 3.10 against the bottom panels of Fig. 3.7, one notices that the similarity observed for PBC and DBC when $\omega = 0$ does not occur when $\omega \neq 0$. It is important to perform a systematic analysis considering many

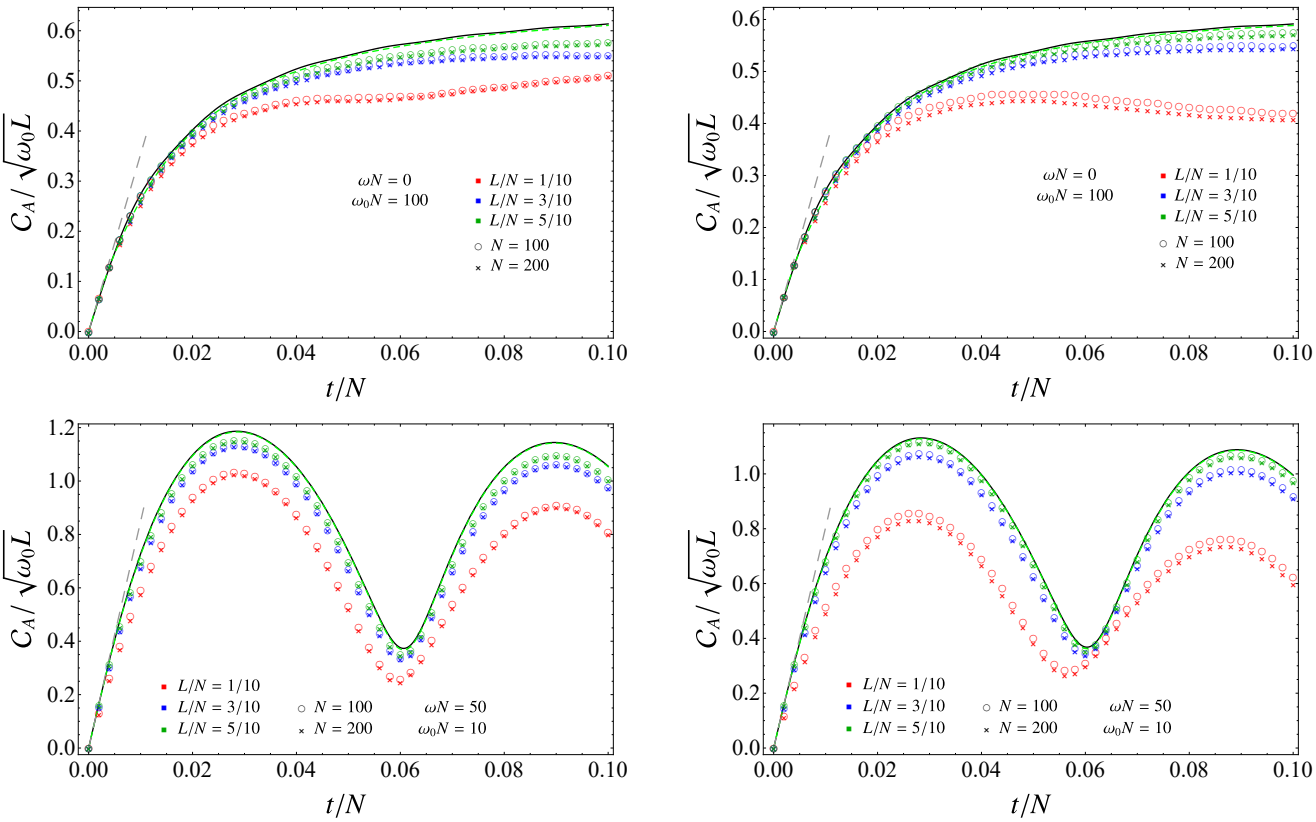

Figure 3.11: Initial growth of $\mathcal{C}_A$ in (3.4.4) for a block A made by L consecutive sites in harmonic chains with either PBC (left panels) or DBC (right panels) made by N sites (in the latter case A is adjacent to a boundary). When $L = N$, the complexity (3.3.4) is shown for $N = 100$ (solid black lines) and $N = 200$ (dashed green lines).

other values of ωN and $\omega_0 N$, in order to understand the effect of a gapped evolution Hamiltonian in the temporal evolution of $\mathcal{C}_A$.

In Fig. 3.11 we consider the initial regime of the temporal evolution of $\mathcal{C}_A$ w.r.t. the initial state for various choices of $\omega_0 N$ and ωN (in particular, $\omega = 0$ in the top panels, while $\omega > 0$ in the bottom ones). Very early values of t are considered with respect to the ones explored in the previous figures. In this regime, data collapses are observed for different values of L/N when $\mathcal{C}_A/\sqrt{\omega_0 L}$ is reported as function of t/N. In the special case of $L = N$, the complexity of pure states (3.3.4) discussed in Sec. 3.3 is recovered, as shown in Fig. 3.11 by the black solid lines ($N = 100$) and by the green dashed lines ($N = 200$).

Each panel on the left in Fig. 3.11 is characterised by the same $\omega_0 N$ and ωN of the corresponding one on the right. From their comparison, one realises that the qualitative behaviour of the initial growth at very early times is not influenced by the choice of the boundary conditions. Moreover, the linear growth of $\mathcal{C}_A/\sqrt{\omega_0 L}$ is independent of L/N for very small values of t/N; hence the slope of the initial growth can be found by considering the case $L = N$ (discussed in Sec. 3.3) and the approximation described in Sec. 3.3.4. From these observations, we obtain the initial linear growth $a_{(\mathrm{B})}\, t/N + \dots$ where the dots represent higher order in t/N and the slope

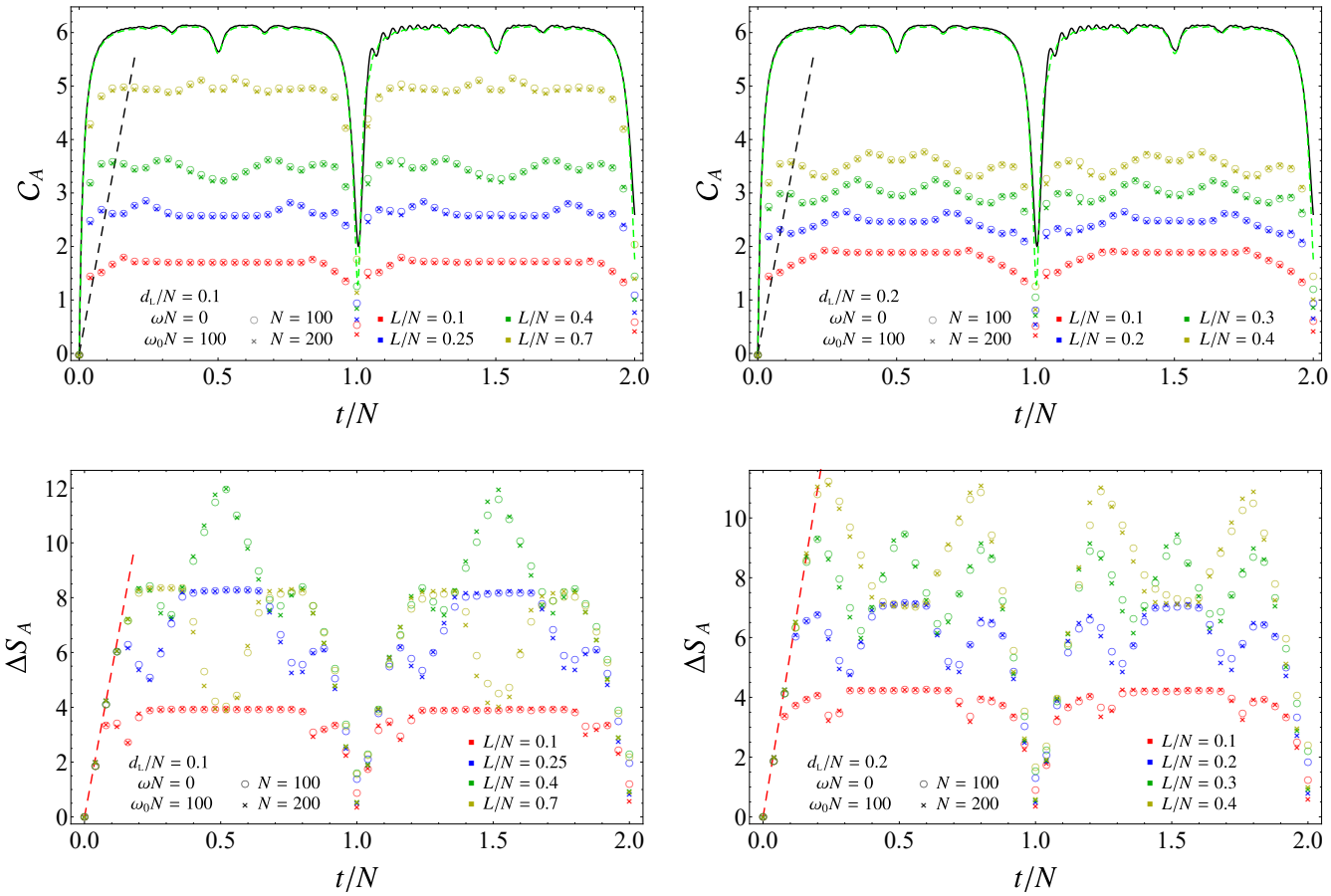

Figure 3.12: Temporal evolution after the global quench with a gapless evolution Hamiltonian of $\mathcal{C}_A$ in (3.4.4) (top panels) and of ΔS_A in (3.4.5) (bottom panels) for a block A made by L consecutive sites and separated by $d_{\rm L}$ sites from the left boundary of harmonic chains with DBC made by N sites. When $L = N$, the complexity (3.3.4) is shown for $N = 100$ (solid black lines) and $N = 200$ (dashed green lines).

depends on the boundary conditions labelled by $\mathrm{B} \in \{\mathrm{P}, \mathrm{D}\}$ as follows

$$a_{(\mathrm{P})} = \frac{\left|(\omega N)^2 - (\omega_0 N)^2\right|}{2\omega_0 N} \sqrt{\sqrt{\frac{m}{4\kappa}}\,\omega_0 N \coth\left(\sqrt{\frac{m}{4\kappa}}\,\omega_0 N\right)} \tag{3.4.6}$$

$$a_{(\mathrm{D})} = \frac{\left|(\omega N)^2 - (\omega_0 N)^2\right|}{2\sqrt{2}\omega_0 N} \sqrt{\sqrt{\frac{m}{\kappa}}\,\omega_0 N \coth\left(\sqrt{\frac{m}{\kappa}}\,\omega_0 N\right) - 1}\,. \tag{3.4.7}$$

The grey dashed lines in Fig. 3.11 represent $a_{(\mathrm{P})}\, t/N$ (left panels) and $a_{(\mathrm{D})}\, t/N$ (right panels).

Since for DBC and $\omega = 0$ the temporal evolution of $\mathcal{C}_A$ displays a thermalisation regime after the initial growth and the subsequent decrease when the block A with $L/N < 1/2$ is adjacent to a boundary, we find it worth investigating also the case where A is separated from the boundary. Denoting by $d_{\rm L}$ the number of sites separating A from the left boundary of the chain (hence $d_{\rm R} = N - L - d_{\rm L}$ sites occur between A and the right boundary), $\mathcal{C}_A$ must be invariant under a

spatial reflection w.r.t. the center of the chain, i.e. when $d_{\rm L}$ and $d_{\rm R}$ are replaced by $d_{\rm R}-1$ and $d_{\rm L}+1$ respectively.

In Fig. 3.12 we show the temporal evolutions of $\mathcal{C}_A$ and of ΔS_A for this bipartition of the segment when the evolution Hamiltonian is gapless and $\omega_0 N = 100$, for four different values of L/N and fixed values of $d_{\rm L}/N$ given by $d_{\rm L}/N = 0.1$ (left panels) or $d_{\rm L}/N = 0.2$ (right panels). Once these parameters have been chosen, the data points corresponding to $N = 100$ and $N = 200$ nicely collapse on the same curve.

When $d_{\rm L} \neq 0$, a thermalisation regime where both the curves of $\mathcal{C}_A$ and ΔS_A are constant occurs if $b/N < 1/2$, with $b = \min[d_{\rm L} + L, d_{\rm R} + L - 1]$ (see the red and blue curves in Fig. 3.12). The plateau is observed approximatively for $t/N \in [b/N, 1 - b/N]$ and its height depends on $\omega_0 L$, on L/N and also on $d_{\rm L}/N$. A remarkable feature of the temporal evolution of $\mathcal{C}_A$ when $d_{\rm L} > 0$ is the occurrence of two local maxima for $t/N < 1/2$, while only one maximum is observed when $d_{\rm L} = 0$ for $t/N < 1/2$ (see the top panels in Fig. 3.7). For any given value of $L/N \leqslant 1/2$ in the top panels of Fig. 3.12, the subsystem complexity grows in the temporal regime between the two local maxima, for $t/N < 1/2$. The occurrence of two local maxima in the temporal evolution of $\mathcal{C}_A$ when A is separated from the boundary is observed also when $N \to \infty$. This is shown in Fig. 3.14 and Fig. 3.16, where we also highlight the logarithmic nature of the growth of $\mathcal{C}_A$ in the temporal regime between the two local maxima, which can be compared with a logarithmic growth occurring in ΔS_A (see e.g. Fig. 3.15).

Comparing each top panel with the corresponding bottom panel in Fig. 3.12, we observe that the black dashed straight line (it is the same in the two top panels) captures the first local maximum of $\mathcal{C}_A$. The slope of this line is twice the slope of the red dashed straight line in the bottom panels, which identifies the initial linear growth of ΔS_A.

3.5 Subsystem complexity and the generalised Gibbs ensemble

In this section we consider infinite harmonic chains, either on the infinite line or on the semi-infinite line with DBC at the origin, and discuss that the asymptotic value of $\mathcal{C}_A$ for a block made by consecutive sites can be found through the generalised Gibbs ensemble (GGE).

3.5.1 Complexity of the GGE

An isolated system prepared in a pure state and then suddenly driven out of equilibrium through a global quench does not relax. Instead, relaxation occurs for a subsystem [335–337] (see also the review [80] and the references therein).

Consider a spatial bipartition of a generic harmonic chain given by a finite subsystem A and its complement. Denoting by $\hat{\rho}(t)$ the density matrix of the entire system and by $\hat{\rho}_A(t)$ the reduced density matrix of A, a quantum system relaxes locally to a stationary state if the limit $\lim_{t\to\infty}\lim_{N\to\infty}\hat{\rho}_A(t) \equiv \hat{\rho}_A(t=\infty)$ exists for any A, where N is the number of sites in the harmonic chain. This stationary state is described by the time independent density matrix $\hat{\rho}_{\rm E}$ describing a statistical ensemble if $\lim_{N\to\infty}\hat{\rho}_{{\rm E},A} = \hat{\rho}_A(t=\infty)$, for any A, where $\hat{\rho}_{{\rm E},A}$ is obtained by tracing $\hat{\rho}_{\rm E}$ over the degrees of freedom of the complement of A. For the global quench of the mass parameter that we are investigating in infinite harmonic chains, the stationary state is described by a GGE [89, 310, 338, 339] (see the review [90] for an extensive list of references).

In terms of the creation and annihilation operators (2.2.48), the evolution Hamiltonian reads

$$\widehat{H} = \sum_{k=1}^{N} \Omega_k \left(\hat{\mathfrak{b}}_k^\dagger \, \hat{\mathfrak{b}}_k + \frac{1}{2} \right). \tag{3.5.1}$$

The GGE that provides the stationary state reads [84]

$$\hat{\rho}_{\text{GGE}} = \frac{e^{-\sum_{k=1}^{N}\lambda_k \hat{\mathfrak{b}}_k^\dagger \hat{\mathfrak{b}}_k}}{\mathcal{Z}_{\text{GGE}}} \qquad \mathcal{Z}_{\text{GGE}} = \text{Tr}(\hat{\rho}_{\text{GGE}}) = \prod_{k=1}^{N} \frac{1}{1-e^{-\lambda_k}} \tag{3.5.2}$$

where $\hat{\rho}_{\text{GGE}}$ is normalised through the condition $\text{Tr}(\hat{\rho}_{\text{GGE}}) = 1$. The conservation of the number operators $\hat{\mathfrak{b}}_k^\dagger \hat{\mathfrak{b}}_k$ tells us that the relation between their expectation values and λ_k reads [84]

$$n_k \equiv \text{Tr}\big(\hat{\mathfrak{b}}_k^\dagger \, \hat{\mathfrak{b}}_k \, \hat{\rho}_{\text{GGE}}\big) = \frac{1}{e^{\lambda_k}-1} = \langle\psi_0|\, \hat{\mathfrak{b}}_k^\dagger \, \hat{\mathfrak{b}}_k \, |\psi_0\rangle \tag{3.5.3}$$

which is strictly positive because $\lambda_k > 0$ for any value of k.

Since the GGE in (3.5.2) is a bosonic Gaussian state, it is characterised by its covariance matrix γ_{GGE}, which can be decomposed as follows

$$\gamma_{\text{GGE}} = \begin{pmatrix} Q_{\text{GGE}} & M_{\text{GGE}} \\ M_{\text{GGE}}^{\text{t}} & P_{\text{GGE}} \end{pmatrix} \tag{3.5.4}$$

where (see Appendix C.2.2)

$$(Q_{\text{GGE}})_{i,j} = \text{Tr}\big(\hat{q}_i \, \hat{q}_j \, \hat{\rho}_{\text{GGE}}\big) \qquad (P_{\text{GGE}})_{i,j} = \text{Tr}\big(\hat{p}_i \, \hat{p}_j \, \hat{\rho}_{\text{GGE}}\big) \qquad (M_{\text{GGE}})_{i,j} = \text{Re}\big[\text{Tr}\big(\hat{q}_i \, \hat{p}_j \, \hat{\rho}_{\text{GGE}}\big)\big] \,. \tag{3.5.5}$$

One can find that

$$Q_{\text{GGE}} = \widetilde{V} \, \mathcal{Q}_{\text{GGE}} \, \widetilde{V}^{\text{t}} \qquad P_{\text{GGE}} = \widetilde{V} \, \mathcal{P}_{\text{GGE}} \, \widetilde{V}^{\text{t}} \qquad M_{\text{GGE}} = \mathbf{0} \tag{3.5.6}$$

where $\widetilde{V}$ is defined below (3.2.4) and

$$\mathcal{Q}_{\text{GGE}} \equiv \text{diag}\Big\{Q_{\text{GGE},k}\,; 1 \leqslant k \leqslant N\Big\} \qquad \mathcal{P}_{\text{GGE}} \equiv \text{diag}\Big\{P_{\text{GGE},k}\,; 1 \leqslant k \leqslant N\Big\} \tag{3.5.7}$$

with

$$Q_{\text{GGE},k} \equiv \frac{1+2n_k}{2m\,\Omega_k} \qquad P_{\text{GGE},k} \equiv \frac{m\,\Omega_k}{2}\,(1+2n_k)\,. \tag{3.5.8}$$

Thus, the covariance matrix (3.5.4) simplifies to $\gamma_{\text{GGE}} = Q_{\text{GGE}} \oplus P_{\text{GGE}}$, where Q_{GGE} and P_{GGE} are given by (3.5.6).

We find it worth writing the Williamson's decomposition of γ_{GGE}, namely

$$\gamma_{\text{GGE}} = W_{\text{GGE}}^{\text{t}} \, \mathcal{D}_{\text{GGE}} \, W_{\text{GGE}} \qquad W_{\text{GGE}} = \mathcal{X}_{\text{GGE}} \, V^{\text{t}} \tag{3.5.9}$$

where the symplectic spectrum is given by

$$\mathcal{D}_{\text{GGE}} = \frac{1}{2}\,\mathbf{1} + \text{diag}\Big\{n_1, \ldots, n_N, n_1, \ldots, n_N\Big\} \tag{3.5.10}$$

and, like for the $2N \times 2N$ symplectic matrix W_{GGE}, we have $V = \widetilde{V} \oplus \widetilde{V}$ and that the diagonal matrix $\mathcal{X}_{\text{GGE}} = \mathcal{X}_{\text{phys}}^{-1}$ is the inverse of $\mathcal{X}_{\text{phys}}$ defined in (2.2.44). We emphasise that γ_{GGE} does not describe a pure state. Indeed, since $n_k \geqslant 0$ for any k, from (3.5.10) we have that the symplectic eigenvalues of γ_{GGE} are greater than $1/2$, as expected for a mixed bosonic Gaussian state.

For the global quench in the harmonic chains that we considering, n_k in (3.5.3) can be computed from the expectation value of $\hat{\mathfrak{b}}_k^\dagger \hat{\mathfrak{b}}_k$ on the initial state obtaining [84]

$$n_k = \frac{1}{4}\bigg(\frac{\Omega_k}{\Omega_{0,k}} + \frac{\Omega_{0,k}}{\Omega_k}\bigg) - \frac{1}{2} \tag{3.5.11}$$

where $\Omega_{0,k}$ and Ω_k are the dispersion relations of the Hamiltonian defining the initial state and of the evolution Hamiltonian respectively. Notice that (3.5.11) is symmetric under the exchange $\Omega_k \leftrightarrow \Omega_{0,k}$. We recall that the boundary conditions defining the harmonic chain influence both the dispersion relations and the matrix V.

By introducing the reduced covariance matrix $\gamma_{\text{GGE},A}$ for A, obtained from (3.5.4) in the usual way, the entanglement entropy

$$S_{\text{GGE},A} \equiv -\text{Tr}(\hat{\rho}_{\text{GGE},A} \log \hat{\rho}_{\text{GGE},A}) \tag{3.5.12}$$

can be evaluated from the symplectic spectrum of $\gamma_{\text{GGE},A}$ through standard methods [4, 191].

The asymptotic value of the increment of the entanglement entropy ΔS_A when $t \to \infty$ can be computed as follows

$$\lim_{L\to\infty} \frac{\lim_{t\to\infty} \lim_{N\to\infty} \Delta S_A}{L} = \lim_{L\to\infty} \frac{\lim_{N\to\infty} S_{\text{GGE},A}}{L} = \lim_{N\to\infty} \frac{S_{\text{GGE}}}{N} \tag{3.5.13}$$

where the order of the limits is important and in the last step we used that S_{GGE} is an extensive quantity (see the review [340] and the references therein).

For the global quench in the harmonic chains that we are considering, the asymptotic value (3.5.13) for the entanglement entropy reads [320]

$$\lim_{N\to\infty} \frac{S_{\text{GGE}}}{N} = \int_0^\pi \Big[(n_\theta + 1)\log(n_\theta + 1) - n_\theta \log n_\theta\Big] \frac{d\theta}{\pi} \tag{3.5.14}$$

$$= \int_0^\pi \left\{ \left[\frac{1}{4}\left(\frac{\Omega_\theta}{\Omega_{0,\theta}} + \frac{\Omega_{0,\theta}}{\Omega_\theta}\right) + \frac{1}{2}\right] \log\left[\frac{1}{4}\left(\frac{\Omega_\theta}{\Omega_{0,\theta}} + \frac{\Omega_{0,\theta}}{\Omega_\theta}\right) + \frac{1}{2}\right] \right. \tag{3.5.15}$$

$$\left. - \left[\frac{1}{4}\left(\frac{\Omega_\theta}{\Omega_{0,\theta}} + \frac{\Omega_{0,\theta}}{\Omega_\theta}\right) - \frac{1}{2}\right] \log\left[\frac{1}{4}\left(\frac{\Omega_\theta}{\Omega_{0,\theta}} + \frac{\Omega_{0,\theta}}{\Omega_\theta}\right) - \frac{1}{2}\right] \right\} \frac{d\theta}{\pi}$$

in terms of n_θ given in (3.5.11), where the dispersion relations to employ are (3.3.20). Let us stress that (3.5.15) holds both for PBC and DBC and is finite for any choice of the parameter (including $\omega = 0$), for both the boundary conditions. It is also symmetric under the exchange $\Omega_\theta \leftrightarrow \Omega_{0,\theta}$; hence under $\omega \leftrightarrow \omega_0$ as well.

We study the circuit complexity to construct the GGE (which is a mixed state) starting from the (pure) initial state at $t = 0$, by employing the approach based on the Fisher information geometry developed in chapter 2. The optimal circuit to get γ_{GGE} from the initial covariance matrix $\gamma(0)$ at $t = 0$ reads [125]

$$G_s(\gamma(0), \gamma_{\text{GGE}}) \equiv \gamma(0)^{1/2} \Big(\gamma(0)^{-1/2}\, \gamma_{\text{GGE}}\, \gamma(0)^{-1/2}\Big)^s \gamma(0)^{1/2} \tag{3.5.16}$$

where $0 \leqslant s \leqslant 1$ parameterises the covariance matrix along the circuit. The length of the optimal circuit (3.5.16) provides the circuit complexity

$$\mathcal{C}_{\text{GGE}} = \frac{1}{2\sqrt{2}} \sqrt{\text{Tr}\Big\{\big[\log\big(\gamma_{\text{GGE}}\, \gamma(0)^{-1}\big)\big]^2\Big\}}\,. \tag{3.5.17}$$

Since $M_{\text{GGE}} = M(0) = \mathbf{0}$, we have

$$\gamma_{\text{GGE}} = V\big[\mathcal{Q}_{\text{GGE}} \oplus \mathcal{P}_{\text{GGE}}\big]V^{\text{t}} \qquad \gamma(0) = V\big[\mathcal{Q}(0) \oplus \mathcal{P}(0)\big]V^{\text{t}}\,. \tag{3.5.18}$$

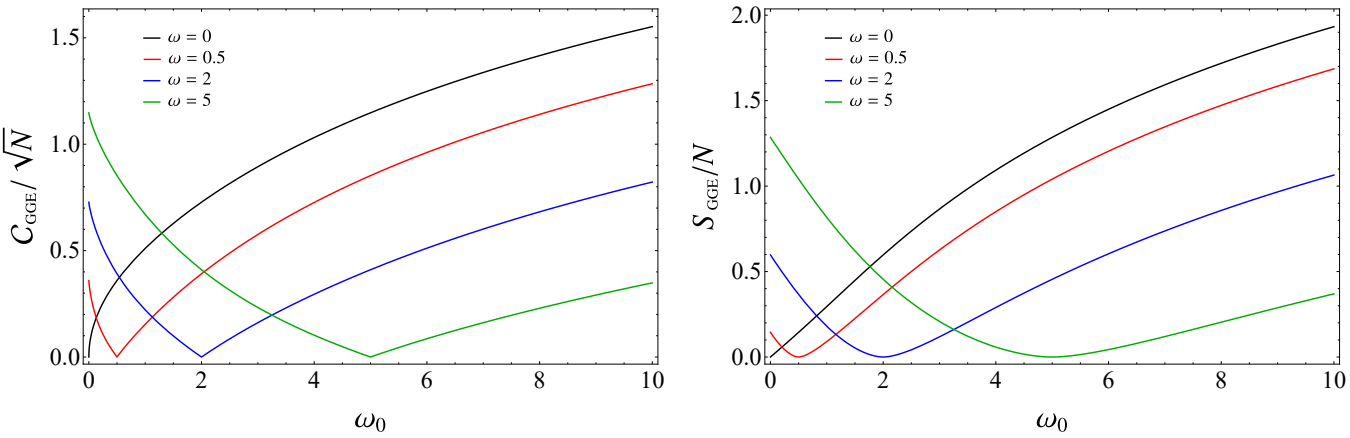

Figure 3.13: Asymptotic value of $\mathcal{C}_{\rm GGE}/\sqrt{N}$ from (3.5.22) (left panel) and of $S_{\rm GGE}/N$ from (3.5.14) (right panel) as functions of ω_0, for some values of ω.

and therefore the complexity (3.5.17) reads

$$\mathcal{C}_{\rm GGE} = \frac{1}{2\sqrt{2}} \sqrt{\sum_{k=1}^{N} \left\{ \left[\log\left(\frac{Q_{{\rm GGE},k}}{Q_k(0)} \right) \right]^2 + \left[\log\left(\frac{P_{{\rm GGE},k}}{P_k(0)} \right) \right]^2 \right\}} \tag{3.5.19}$$

$$= \frac{1}{2\sqrt{2}} \sqrt{\sum_{k=1}^{N} \left\{ \left[\log\left(\frac{\Omega_{0,k}}{\Omega_k} (1+2n_k) \right) \right]^2 + \left[\log\left(\frac{\Omega_k}{\Omega_{0,k}} (1+2n_k) \right) \right]^2 \right\}} \,. \tag{3.5.20}$$

By using (3.5.11), this expression becomes

$$\mathcal{C}_{\rm GGE} = \frac{1}{2\sqrt{2}} \sqrt{\sum_{k=1}^{N} \left\{ \left[\log\left(\frac{\Omega_{0,k}^2}{2\,\Omega_k^2} + \frac{1}{2} \right) \right]^2 + \left[\log\left(\frac{\Omega_k^2}{2\,\Omega_{0,k}^2} + \frac{1}{2} \right) \right]^2 \right\}} \tag{3.5.21}$$

which is symmetric under the exchange $\Omega_k \leftrightarrow \Omega_{0,k}$, hence under $\omega \leftrightarrow \omega_0$ as well.

The leading order of this expression as $N \to \infty$ is given by

$$\mathcal{C}_{\rm GGE} = \frac{\sqrt{N}}{2\sqrt{2\pi}} \sqrt{\int_0^\pi \left\{ \left[\log\left(\frac{\Omega_{0,\theta}^2}{2\,\Omega_\theta^2} + \frac{1}{2} \right) \right]^2 + \left[\log\left(\frac{\Omega_\theta^2}{2\,\Omega_{0,\theta}^2} + \frac{1}{2} \right) \right]^2 \right\} d\theta} \tag{3.5.22}$$

where $\Omega_{0,\theta}$ and Ω_θ are thermodynamic limits of the dispersion relations associated to the Hamiltonians before and after the quench respectively. By repeating the argument reported below (3.3.19), one finds that (3.5.22) with (3.3.20) can be employed for both PBC and DBC. Moreover, the resulting expression for $\mathcal{C}_{\rm GGE}/\sqrt{N}$ is finite for any choice of the parameters (including for $\omega = 0$).

In Fig. 3.13 we show $\mathcal{C}_{\rm GGE}/\sqrt{N}$ from (3.5.22) and $S_{\rm GGE}/N$ from (3.5.14) as functions of ω_0, for some values of ω. The resulting curves are qualitatively similar. At $\omega_0 = \omega$ they both vanish, but $\mathcal{C}_{\rm GGE}/\sqrt{N}$ is singular at this point, while $S_{\rm GGE}/N$ is smooth.

The reduced covariance matrix $\gamma_{{\rm GGE},A}$ associated to any finite subsystem A is obtained by selecting the rows and the columns in (3.5.4) corresponding to A. The results of chapter 2 can be applied again to write the optimal circuit that provides $\gamma_{{\rm GGE},A}$ from the initial mixed state

characterised by the reduced covariance matrix $\gamma_A(0)$ at $t = 0$, obtained from $\gamma(0)$ through the usual reduction procedure. This optimal circuit reads

$$G_s(\gamma_A(0)\,,\gamma_{\rm GGE,A}) \,\equiv\, \gamma_A(0)^{1/2}\Big(\gamma_A(0)^{-1/2}\,\gamma_{\rm GGE,A}\,\gamma_A(0)^{-1/2}\Big)^s\,\gamma_A(0)^{1/2} \tag{3.5.23}$$

where $0 \leqslant s \leqslant 1$ parametrises the covariance matrix along the optimal circuit. Its length corresponds to the subsystem complexity of the GGE w.r.t. the initial state

$$\mathcal{C}_{\rm GGE,A} \,=\, \frac{1}{2\sqrt{2}}\,\sqrt{{\rm Tr}\,\Big\{\big[\log\big(\gamma_{\rm GGE,A}\,\gamma_A(0)^{-1}\big)\big]^2\Big\}}\,. \tag{3.5.24}$$

Since the harmonic chain relaxes locally to the GGE after the quantum quench, for the subsystem complexity of any finite subsystem A we expect

$$\lim_{t\to\infty}\lim_{N\to\infty}\mathcal{C}_A = \lim_{N\to\infty}\mathcal{C}_{\rm GGE,A} \tag{3.5.25}$$

which is confirmed by the numerical results in Fig. 3.14 and Fig. 3.16.

A numerical analysis shows that (3.5.25) grows like $\sqrt{L}$ as $L \to \infty$ for fixed values of ω and ω_0; hence, by adapting (3.5.13) to the subsystem complexity, we expect

$$\lim_{L\to\infty}\frac{\lim_{t\to\infty}\lim_{N\to\infty}\mathcal{C}_A}{\sqrt{L}} = \lim_{L\to\infty}\frac{\lim_{N\to\infty}\mathcal{C}_{\rm GGE,A}}{\sqrt{L}} = \lim_{N\to\infty}\frac{\mathcal{C}_{\rm GGE}}{\sqrt{N}} \tag{3.5.26}$$

where $\mathcal{C}_{\rm GGE}$ is given in (3.5.22) and the order of the limits is important.

In the following numerical analysis we show that, for the harmonic chains that we are exploring, the asymptotic limit for $t \to \infty$ of the reduced density matrix after the global quench is the reduced density matrix obtained from the GGE. This result has been already discussed for a fermionic chain in [341], where, considering a global quench of the magnetic field in the transverse-field Ising chain and the subsystem given by a finite block made by consecutive sites in an infinite chain on the line, it has been found that a properly defined distance between the reduced density matrix at a generic value of time along the evolution and the asymptotic one obtained from the GGE vanishes as $t \to \infty$.

3.5.2 Numerical results

In order to test (3.5.24), infinite harmonic chains must be considered. The reference and the target states have been described in Sec. 3.4. In this section we study harmonic chains both on the line and on the semi-infinite line with DBC imposed at its origin. In the latter case, the block A made by L consecutive sites is either adjacent to the origin or separated from it.

The correlators to employ in the numerical analysis are given by (C.2.3) for the infinite harmonic chain on the line and by (C.2.4) for the harmonic chain on the semi-infinite line with DBC. The reduced correlation matrices Q_A, P_A and M_A are the blocks providing the reduced covariance matrix (3.4.1). These matrices are obtained by restricting the indices of the proper correlators to $i, j = 1, \ldots, L$ when A is on the infinite line and to $i, j = 1 + d, \ldots, L + d$ when A is on the semi-infinite line, where d corresponds to its separation from the origin

In the following we discuss numerical data sets obtained for infinite harmonic chains, either on the infinite line or on the semi-infinite line, where ωL and $\omega_0 L$ are kept fixed.

In Fig. 3.14 and Fig. 3.15 we show the temporal evolutions of $\mathcal{C}_A$, of ΔS_A and of $\Delta S_A/\mathcal{C}_A$ after the quench with $\omega_0 L = 20$ and $\omega L = 0$. In Fig. 3.16 we display the temporal evolution of $\mathcal{C}_A$ with $\omega_0 L = 100$ and $\omega L = 0$. The subsystem A is a block made by L consecutive sites either on a

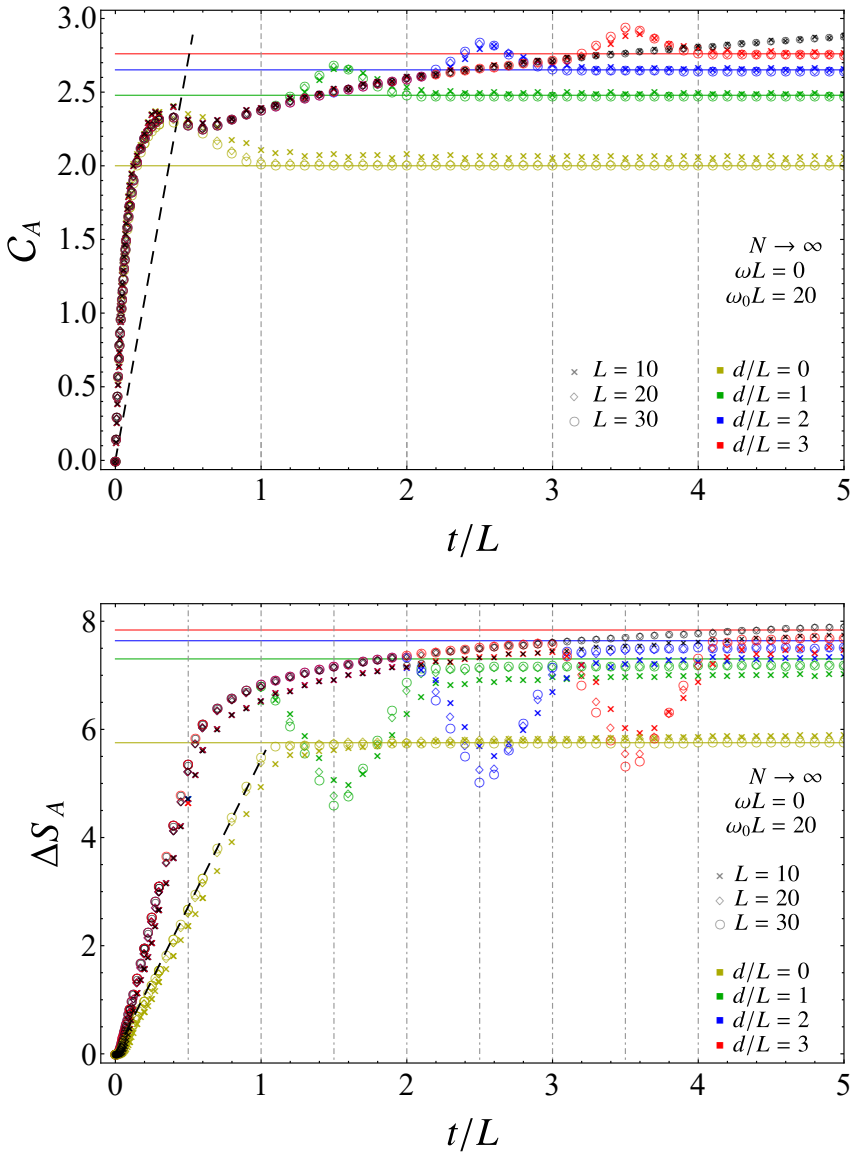

Figure 3.14: Temporal evolution of $\mathcal{C}_A$ (top panel) and of ΔS_A (bottom panel) after a global quantum quench with a gapless evolution Hamiltonian and $\omega_0 L = 20$. The subsystem is a block A made by L consecutive sites either on the infinite line (black data points) or on the semi-infinite line, separated by d sites from the origin where DBC hold (coloured data points). The dashed black straight line is the same in both panels.

semi-infinite line, separated by d sites from the origin where DBC are imposed (coloured symbols), or on the infinite line (black symbols). The black and coloured data points for $\mathcal{C}_A$ have been found through (3.4.4) with the reduced correlators obtained from either (C.2.3) or (C.2.4) respectively. The coloured horizontal solid lines correspond to either (3.5.24) or (3.5.12), with the reduced correlators from (C.2.11) for the target state and from (C.2.4) at $t = 0$ for the reference state, with $L = 50$. Notice that a black horizontal solid line does not occur because the corresponding value is divergent, as indicated also by the left panel in Fig. 3.17.

Considering the block on the semi-infinite line, in Fig. 3.14 and Fig. 3.16 we observe that the

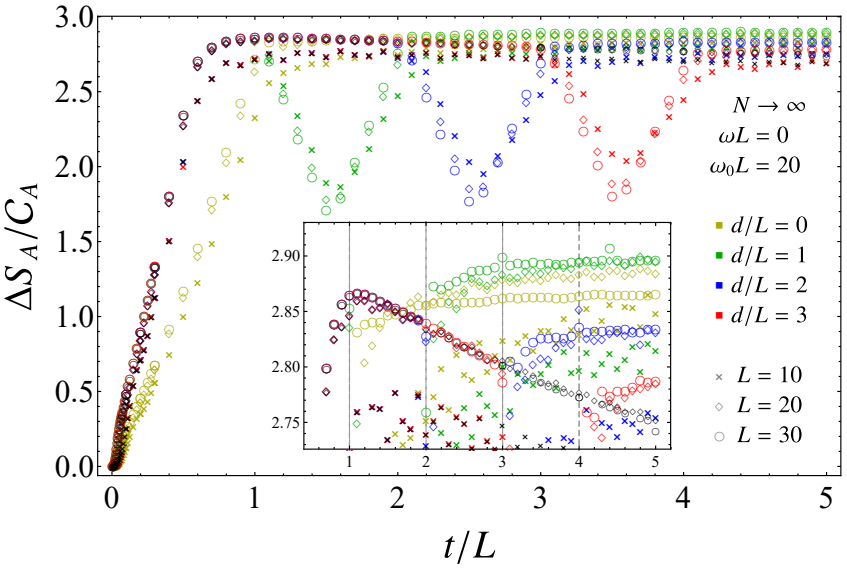

Figure 3.15: Temporal evolution of $\Delta S_A/\mathcal{C}_A$ for the data reported in Fig. 3.14. The inset zooms in to highlight the data points having $t/L > 1$.

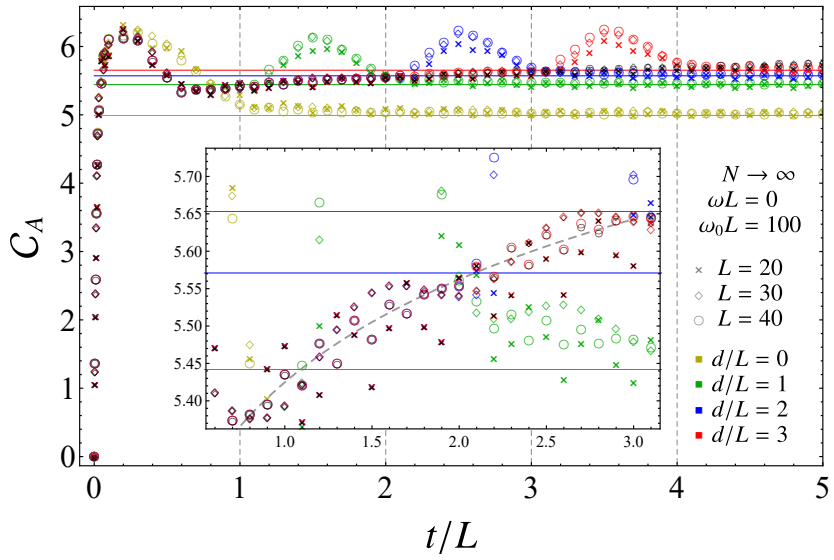

Figure 3.16: Temporal evolution of $\mathcal{C}_A$ after a global quantum quench with a gapless evolution Hamiltonian and $\omega_0 L = 100$, in the same setups of Fig. 3.14. The inset zooms in on the intermediate temporal regime between the two local maxima for the data having $d/L = 3$.

initial growth of $\mathcal{C}_A$ is the same until the first local maximum, for all the values of d/L. After the first local maximum, the temporal evolution of $\mathcal{C}_A$ depends on whether the block is adjacent to the boundary. If $d/L = 0$ the curve decreases until it reaches the saturation value. Instead, when $d/L > 0$, first $\mathcal{C}_A$ decreases along a different curve (see e.g. Fig. 3.16) until a local minimum; then we observe an intermediate growth, followed by a second local maximum and finally by the saturation regime. A fitting procedure shows that the intermediate growth between the two local maxima is logarithmic (in the inset of Fig. 3.16 the grey dashed curve has been found by fitting

the data having $L = 40$ and $d/L = 3$ through a logarithm and a constant). Its temporal duration is approximatively $d/L - 1/2$, for the three values of non vanishing d/L considered in Fig. 3.14 and Fig. 3.16. Fitting the intermediate growth in Fig. 3.14 and Fig. 3.16, one observes that the coefficient of the logarithmic growth decreases as $\omega_0 L$ increases. The first local maximum in the temporal evolution of $\mathcal{C}_A$ occurs for $0 < t/L < 1$. When $d > 0$, the second maximum occurs for $d/L < t/L < (d+1)/L$. Notice that these two local maxima can be seen also in the top panels of Fig. 3.12 for $t/N < 1/2$.

In Fig. 3.14, Fig. 3.15 and Fig. 3.16, the data points represented through black symbols have been obtained for a block in the infinite line. These data overlap with the ones corresponding to the block on the semi-infinite line with $d > 0$ until the latter ones display the development of the second local maximum. For the temporal evolution of $\mathcal{C}_A$ on the infinte line only one local maximum occurs and the intermediate logarithmic growth mentioned above does not finish within the temporal regime that we have considered. This agreement tells us that the second local maximum in the temporal evolution of $\mathcal{C}_A$ is due to the presence of the boundary.

The temporal evolutions of ΔS_A in the bottom panel of Fig. 3.14 can be explained by employing the quasi-particle picture [82], which provides the different temporal regimes and the corresponding qualitative behaviour of ΔS_A (for the subsystems where a boundary occurs, the quasi-particle picture has been described e.g. in [209]). The different regimes identified by this analysis correspond to the vertical dot-dashed lines in the bottom panel of Fig. 3.14. Instead, the vertical dashed grey lines in the top panel of Fig. 3.14 correspond to $t/L = 1 + d/L$. For $d > 0$, when $t/L > 1/2$ we observe a regime of logarithmic growth for ΔS_A whose duration depends on d/L according to the quasi-particle picture, until the beginning of a linear decreases. Considering two sets of data points of ΔS_A having different d/L, they collapse until the first linear decrease is reached.

The initial growths of $\mathcal{C}_A$ and of ΔS_A in Fig. 3.14 are very different. For instance, the growth of $\mathcal{C}_A$ is the same for all the data sets, while for ΔS_A it depends on whether d vanishes. Moreover, while the growth of ΔS_A is linear for $t/L < 1$ when $d = 0$ and for $t/L < 1/2$ when $d > 0$, the growth of $\mathcal{C}_A$ is linear only at the very beginning of the temporal evolution and it clearly deviates from linearity within the regime of t/L where ΔS_A grows linearly. The dashed black straight line passing through the origin in Fig. 3.14 describes the linear growth of ΔS_A when $d = 0$ and it is the same in both the panels. This straight line intersects the first local maximum of $\mathcal{C}_A$. This has been highlighted also for finite systems in Fig. 3.7 and Fig. 3.12.

In Fig. 3.15 we show the ratio $\Delta S_A/\mathcal{C}_A$ for the data reported in Fig. 3.14. We remark that the two logarithmic growths occurring in ΔS_A and in $\mathcal{C}_A$ almost cancel in the ratio; indeed, a mild logarithmic decreasing is observed when $t/L > 1$ for the data obtained on the infinite line (black symbols) and when $1 < t/L < 3$ for the data obtained on the semi-infinite line with $d/L = 3$ (red symbols) that are already collapsed.

The curves in Fig. 3.16 must be compared with the corresponding ones in top panel in Fig. 3.14 in order to explore the effect of $\omega_0 L$. The height of the first local maximum in the temporal evolution of $\mathcal{C}_A$ and also the saturation values for the data obtained on the semi-infinite line increase as $\omega_0 L$ increases. Instead, the coefficient of the logarithmic growth after the first local maximum decreases as $\omega_0 L$ increases, as already remarked above. Notice that higher values of L are needed to observe data collapse as $\omega_0 L$ increases.

From the numerical results reported in the previous figures, we conclude that (3.5.24) provides the asymptotic value of the subsystem complexity as $t \to \infty$; hence it is worth studying the dependence of this expression on the subsystem size and on the parameters of the quench protocol.

In Fig. 3.17 we show numerical results for (3.5.24), obtained by using the reduced correlators from (C.2.8) and (C.2.11) for the target state and the reduced correlators from (C.2.3) and (C.2.4) at $t = 0$ for the reference state.

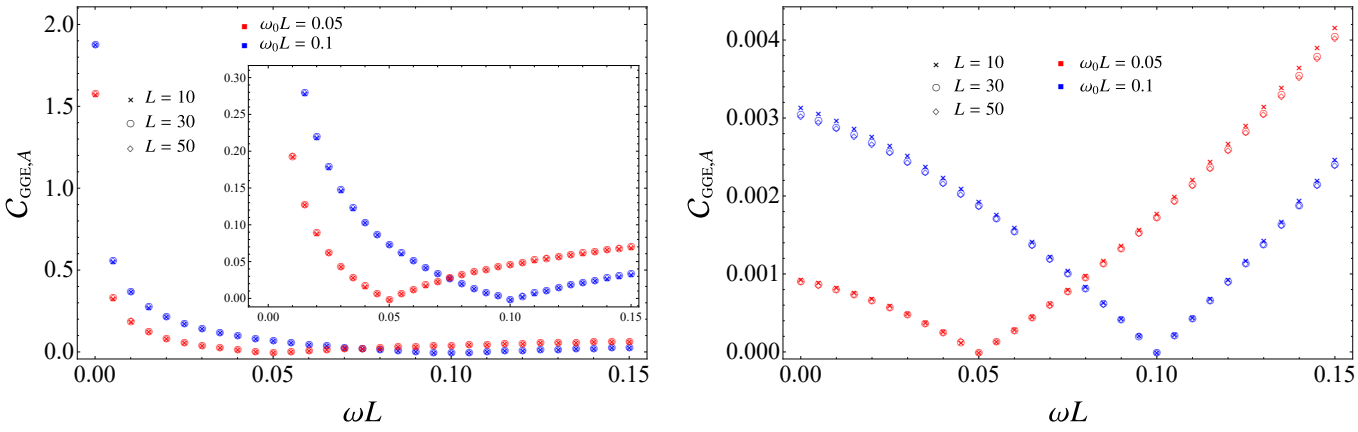

Figure 3.17: Asymptotic value of $\mathcal{C}_{\mathrm{GGE},A}$ in (3.5.24) for a block A made by L consecutive sites in infinite chains in terms of ωL. The block is either in an infinite chain (left panel) or adjacent to the origin of the semi-infinite line with DBC (right panel).

In Fig. 3.17 we show (3.5.24) as function of ωL when the block is either in the infinite line (left panel) or at the beginning of the semi-infinite line with DBC (right panel). The main difference between the two panels of Fig. 3.17 is that the limit $\omega L \to 0$ is finite for the semi-infinite line while it diverges for the infinite line (the correlators (C.2.8) are well defined for $\omega \neq 0$). This is consistent with the results displayed through the black symbols in the top panel of Fig. 3.14 and in Fig. 3.16.

Within the context of the gauge/gravity correspondence, the temporal evolution of the holographic subsystem complexity in the gravitational backgrounds given by Vaidya spacetimes has been studied numerically through the CV proposal [145, 316–318].

We find it worth remarking that the qualitative behaviour of the temporal evolution of $\mathcal{C}_A$ for an interval in the infinite line shown by the black data points in Fig. 3.14 and Fig. 3.16 is in agreement with the results for the temporal evolution of the holographic subsystem complexity reported in [145, 316]. The change of regime occurs at $t/L \simeq 1/2$ for both these quantities and their qualitative behaviour in the initial regime given by $0 < t/L < 1/2$ is very similar.

For $t/L > 1/2$ we observe a logarithmic growth whose coefficient depends on $\omega_0 L$ in Fig. 3.14 and Fig. 3.16, while the holographic subsystem complexity remains constant. However, a similar issue occurs in the corresponding comparison for the entanglement entropy.

3.6 Discussion

In this chapter we studied the temporal evolution of the subsystem complexity after a global quench of the mass parameter in harmonic lattices, focussing our analysis on harmonic chains with either PBC or DBC and on subsystems given by blocks of consecutive sites. The initial state is mainly chosen as the reference state of the circuit. The circuit complexity of the mixed states described by the reduced density matrices has been evaluated by employing the approach based on the Fisher information geometry introduced in chapter 2, which provides also the optimal circuit (see (3.4.2) and (3.4.3)).

When the entire system is considered (see Sec. 3.2.2, Sec. 3.2.3 and Sec. 3.3) and when the reference and the target states are pure states along the time evolution of a given quench, the optimal

circuit is made by pure states [35, 40] and for the temporal evolution of the circuit complexity after the global quench one obtains the expression given by (3.2.19) and (3.2.20), which holds in a generic number of dimensions. Specialising the latter result to the harmonic chains where either PBC or DBC are imposed, one obtains (3.3.4), where the contribution of the zero mode for PBC is highlighted. The occurrence of the zero mode provides the logarithmic growth of the complexity when the evolution is critical (see (3.3.11) and Fig. 3.1).

In Sec. 3.4 and Sec. 3.5 we investigate the temporal evolution of the subsystem complexity $\mathcal{C}_A$ after a global quench. For a gapless evolution Hamiltonian, our main results are shown in Fig. 3.6, Fig. 3.7, Fig. 3.8 and Fig. 3.12 for finite chains and in Fig. 3.14, Fig. 3.15, and Fig. 3.16 for infinite chains. In some cases, also the temporal evolutions for the corresponding increment of the entanglement entropy ΔS_A are reported, in order to highlight the similar features and the main differences. This comparison allows to observe that the initial growths of $\mathcal{C}_A$ and ΔS_A are very different, while the behaviours in the saturation regime are similar, as highlighted in Fig. 3.7, Fig. 3.8 and Fig. 3.15. An important difference between the temporal evolution of $\mathcal{C}_A$ and of ΔS_A is that $\mathcal{C}_A$ displays a local maximum before the saturation regime (within a revival for finite systems). Interestingly, within the framework of the gauge/gravity correspondence, this feature has been observed also in the temporal evolution of holographic subsystem complexity in Vaidya gravitational backgrounds [145, 316].

For the infinite harmonic chains that we have considered the asymptotic regime is described by a GGE; hence in Sec. 3.5 we have argued that the asymptotic value of the temporal evolution of $\mathcal{C}_A$ is given by (3.5.24). This result has been checked for $\omega = 0$ (see Fig. 3.14and Fig. 3.16).

In the future research, it would be interesting to investigate the subsystem complexity and its temporal evolution after a quench in fermionic systems, in circuits involving non-Gaussian states and in interacting systems. The analysis reported in this chapter can be extended straightforwardly in various directions. For instance, we find it worth exploring the dependence of the temporal evolution on the reference state (e.g. by considering the unentangled product state as the reference state) and the temporal evolution for higher dimensional harmonic lattices. In Sec. 2.4 the subsystem complexity has been studied also by employing the entanglement Hamiltonians [4, 10, 101, 102, 177–179, 192]; hence one can consider the possibility to explore also its temporal evolution through these entanglement quantifiers.

It would be interesting to study the temporal evolutions of the subsystem complexity by employing other ways to evaluate the complexity of mixed states, e.g. through other distances between bosonic Gaussian states [129] or the approach based on the purification complexity [79, 130]. The cost function plays an important role in the evaluation of the circuit complexity [35]; hence it is worth studying its effect on the temporal evolution of the subsystem complexity.

Finally, it is important to keep exploring the temporal evolutions of the subsystem complexity through holographic calculations in order to find qualitative features that are observed in lattice models. They would be crucial tests for quantum field theory methods to evaluate the subsystem complexity.

Chapter 4

Complexity after a local quantum quench

4.1 Introduction

The global quench discussed in chapter 3 is not the only interesting protocol for studying the dynamics of a quantum system out of equilibrium. Given a system prepared in a state $|\psi_0\rangle$, if we consider a sudden change at $t = 0$ (that provides the time-evolved state $|\psi(t)\rangle = e^{-\mathrm{i}\widehat{H}t}|\psi_0\rangle$ for $t > 0$) occurring only at a point, we have the so-called local quench. For instance, local quenches where either two systems are joined together [85, 86] or a local operator is inserted at some point [87, 88] have been explored and the entanglement entropy S_A after these quenches has been studied [198, 342, 343]. It is worth investigating the temporal evolutions of the circuit complexity for the entire system and of the subsystem complexity after a local quench.

The temporal evolution of the holographic entanglement entropy after a local quench has been explored in [344–350]. For the local quench corresponding to an operator insertion the temporal evolution of the holographic subsystem complexity has been considered [143, 144], while for the local quench where two systems are joined together only the holographic entanglement entropy has been studied [345, 349].

In this chapter, we are interested in the temporal evolution of the circuit complexity after a local quench. We consider the local quench described by Eisler and Zimborás in [293], where two harmonic chains containing rN and $(1-r)N$ sites are joined at $t = 0$ (here r is a rational number $0 \leqslant r \leqslant 1$), as shown in the top panel in Fig. 4.1. We focus on circuits made only by Gaussian states. First we study the temporal evolution of the complexity for the entire chain; then we investigate the temporal evolution of the subsystem complexity $\mathcal{C}_A$ for the subsystem A given by a block of L consecutive sites (the spatial bipartitions considered in the chapter are shown in the bottom panels of Fig. 4.1), by employing the complexity for mixed states based on the Fisher information geometry and discussed in chapter 2 (see also [98]).

The outline of this chapter is as follows. In Sec. 4.2 we describe the local quench protocol, introducing the covariance matrices characterising the states involved in the construction of the optimal circuit. In Sec. 4.3 we evaluate numerically the temporal evolution of the circuit complexity for the entire chain, choosing the (pure) initial state at $t = 0$ as the reference state and the (pure) state at generic time $t > 0$ after the local quench as the target state. In Sec. 4.4 we discuss our numerical analysis of the temporal evolutions of the subsystem complexity for a block of consecutive sites. Some conclusions and open questions are drawn in Sec. 4.5.

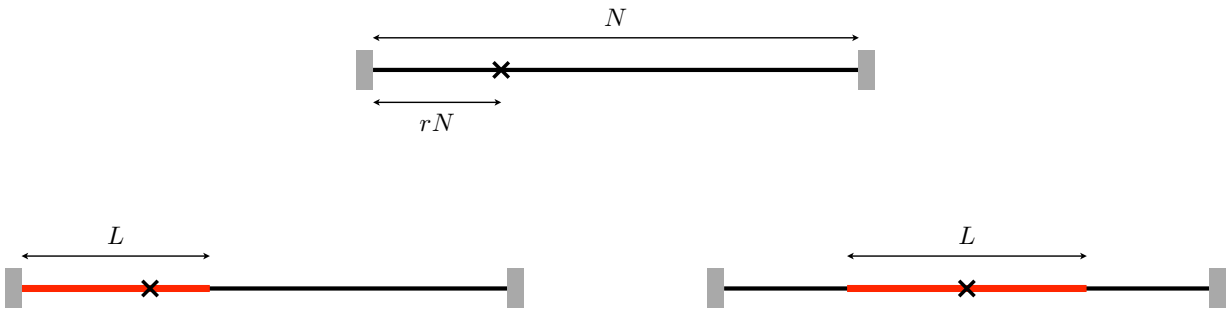

Figure 4.1: The local quench considered in this chapter: two harmonic chains containing $N_{\rm l} = rN$ and $N_{\rm r} = (1-r)N$ sites are joined together at $t = 0$ into a single chain made by $N \equiv N_{\rm l} + N_{\rm r}$ sites (top panel). The subsystem A is a block of L consecutive sites (red segment), either adjacent to the left boundary (bottom left panel) or centered at the midpoint of the chain, when $r = 1/2$ (bottom right panel).

4.2 Covariance matrix after the quench

The Hamiltonian of the harmonic chain made by N sites (we set $\hbar = 1$) is given by

$$\widehat{H} = \sum_{i=0}^{N} \left(\frac{1}{2m}\, \hat{p}_i^2 + \frac{m\omega^2}{2}\, \hat{q}_i^2 + \frac{\kappa}{2}(\hat{q}_{i+1} - \hat{q}_i)^2 \right) \tag{4.2.1}$$

where the position and the momentum operators $\hat{q}_i$ and $\hat{p}_i$ are hermitean operators satisfying the canonical commutation relations $[\hat{q}_i, \hat{q}_j] = [\hat{p}_i, \hat{p}_j] = 0$ and $[\hat{q}_i, \hat{p}_j] = \mathrm{i}\delta_{i,j}$. The Dirichlet boundary conditions (DBC) $\hat{q}_0 = \hat{q}_{N+1} = 0$ and $\hat{p}_0 = \hat{p}_{N+1} = 0$ are imposed at the endpoints.

The initial state is given by the following pure state

$$|\Psi_0^{(\mathrm{l,r})}\rangle \equiv |\psi_{\rm l}\rangle \otimes |\psi_{\rm r}\rangle \tag{4.2.2}$$

where $|\psi_{\rm l}\rangle$ is the ground state of the Hamiltonian $\widehat{H}_{\rm l}$, defined by (4.2.1) for the sites labelled by $1 \leqslant i \leqslant N_{\rm l}$, with the physical parameters $m_{\rm l}$, $\omega_{\rm l}$ and $\kappa_{\rm l}$ and DBC imposed at $i = N_{\rm l} + 1$. Similarly, $|\psi_{\rm r}\rangle$ is the ground state of the Hamiltonian $\widehat{H}_{\rm r}$ in (4.2.1) for the chain made by the sites labelled by $N_{\rm l} + 1 \leqslant i \leqslant N_{\rm l} + N_{\rm r} + 1$, with parameters $m_{\rm r}$, $\omega_{\rm r}$ and $\kappa_{\rm r}$ and DBC imposed at $i = N_{\rm l} + N_{\rm r} + 1$. Thus, the initial state (4.2.2) depends on $N_{\rm l}$, $m_{\rm l}$, $\omega_{\rm l}$, $\kappa_{\rm l}$, $N_{\rm r}$, $m_{\rm r}$, $\omega_{\rm r}$ and $\kappa_{\rm r}$. The total number of sites is $N \equiv N_{\rm l} + N_{\rm r}$. Equivalently, we can describe the initial state in terms of N and of the position parameter $0 \leqslant r \leqslant 1$ (in unit of N), that determines the separation between the left and the right chain; indeed $N_{\rm l} = Nr$ and $N_{\rm r} = N(1-r)$.

Given the state (4.2.2) at $t = 0$, the time evolved state at $t > 0$ through (4.2.1) is

$$|\Psi^{(\mathrm{l,r})}(t)\rangle = e^{-\mathrm{i}\widehat{H}t} |\Psi_0^{(\mathrm{l,r})}\rangle\,. \tag{4.2.3}$$

This setup describes different quantum quenches. A global quench can be obtained by setting $N_{\rm l} = N$ and $N_{\rm r} = 0$ (or viceversa, equivalently), $\kappa_{\rm l} = \kappa_{\rm r} \equiv \kappa_0$, $m_{\rm l} = m_{\rm r} \equiv m_0$ and $\omega_{\rm l} = \omega_{\rm r} \equiv \omega_0$. In this case the initial state is the ground state of a single chain made by N sites. If $\kappa_0 \neq \kappa$, $m_0 \neq m$ and $\omega_0 \neq \omega$, the global quench involves all the parameters occurring in the Hamiltonian (4.2.1). An important special case is the global quench of the frequency parameter [83].

In this chapter we consider the local quench described in [293], where two disconnected harmonic chains, containing $N_{\rm l} = rN$ and $N_{\rm r} = (1-r)N$ sites, are joined at $t = 0$, as represented pictorially in the top panel of Fig. 4.1. This quench protocol corresponds to $m_{\rm r} = m_{\rm l} = m$, $\kappa_{\rm r} = \kappa_{\rm l} = \kappa$ and $\omega_{\rm r} = \omega_{\rm l} = \omega$.

The bosonic Gaussian states in harmonic lattices are fully characterised by their covariance matrix [77, 78]. In the quench protocol that we are considering [293], the initial state (4.2.2) is Gaussian and the time evolution generated by (4.2.1) preserves its Gaussian nature; hence (4.2.3) is Gaussian too, for any $t > 0$. The time evolved state (4.2.3) is completely characterised by the $2N \times 2N$ covariance matrix $\gamma^{(\mathrm{l,r})}(t)$, whose generic element is defined as

$$\gamma^{(\mathrm{l,r})}_{i,j}(t) \,=\, \mathrm{Re}\big[\langle \hat{r}_i(t)\, \hat{r}_j(t) \rangle\big] \qquad\qquad \hat{\boldsymbol{r}}(t) \equiv \big(\hat{q}_1(t), \dots, \hat{q}_N(t), \hat{p}_1(t), \dots, \hat{p}_N(t)\big)^{\mathrm{t}} . \tag{4.2.4}$$

The covariance matrix of the initial state (4.2.2) at $t = 0$ reads [293]

$$\gamma^{(\mathrm{l,r})}_0 \,=\, V_0^{\mathrm{t}}\, \Gamma_0\, V_0 \tag{4.2.5}$$

where the superscript indicates that this covariance matrix corresponds to an initial configuration made by two disjoint chains, containing $N_{\rm l}$ and $N_{\rm r}$ sites respectively, and

$$\Gamma_0 \,=\, \mathcal{Q}_0 \oplus \mathcal{P}_0 \qquad\qquad \mathcal{Q}_0 \,=\, \frac{1}{2}\, \mathcal{T}_0^{-1} \qquad\qquad \mathcal{P}_0 \,=\, \frac{1}{2}\, \mathcal{T}_0 \tag{4.2.6}$$

with $\mathcal{T}_0$ being the following diagonal matrix

$$\mathcal{T}_0 \,\equiv\, \mathrm{diag}\Big(m_{\rm l}\, \Omega^{(\mathrm{l})}_1, \dots, m_{\rm l}\, \Omega^{(\mathrm{l})}_{N_{\rm l}}, m_{\rm r}\, \Omega^{(\mathrm{r})}_1, \dots, m_{\rm r}\, \Omega^{(\mathrm{r})}_{N_{\rm r}}\Big) \tag{4.2.7}$$

written in terms of the dispersion relations

$$\Omega^{(\mathrm{s})}_k = \sqrt{\omega_{\rm s}^2 + \frac{4\kappa_{\rm s}}{m_{\rm s}} \bigg[\sin\bigg(\frac{\pi k}{2(N_{\rm s}+1)} \bigg) \bigg]^2} \qquad\qquad 1 \leqslant k \leqslant N_{\rm s} \qquad\qquad \mathrm{s} \in \big\{ \mathrm{l}, \mathrm{r} \big\} . \tag{4.2.8}$$

The matrix V_0 in (4.2.5) is block diagonal too and it can be written as

$$V_0 \,\equiv\, \widetilde{V}_0 \oplus \widetilde{V}_0 \qquad\qquad \widetilde{V}_0 = \widetilde{V}_{N_{\rm l}} \oplus \widetilde{V}_{N_{\rm r}} \tag{4.2.9}$$

where the elements of the $\widetilde{V}_{N_{\rm l}}$ and $\widetilde{V}_{N_{\rm r}}$ are given by

$$\big(\widetilde{V}_{N_{\rm s}}\big)_{j,k} \,=\, \sqrt{\frac{2}{N_{\rm s}+1}}\, \sin\bigg(\frac{\pi j k}{N_{\rm s}+1} \bigg) \qquad\qquad 1 \leqslant j, k \leqslant N_{\rm s} \qquad\qquad \mathrm{s} \in \big\{ \mathrm{l}, \mathrm{r} \big\} . \tag{4.2.10}$$

Notice that, since the matrices $\widetilde{V}_{N_{\rm s}}$ defined by (4.2.10) are orthogonal, $\widetilde{V}_0$ is symplectic and orthogonal. Thus, also V_0 in (4.2.9) is symplectic and orthogonal.

We find it worth remarking that, in the expression (4.2.5) for $\gamma^{(\mathrm{l,r})}_0$, the parameters $m_{\rm l}$, $\omega_{\rm l}$, $\kappa_{\rm l}$, $m_{\rm r}$, $\omega_{\rm r}$ and $\kappa_{\rm r}$ occur in $\mathcal{Q}_0$ and $\mathcal{P}_0$, while V_0 depends only on $N_{\rm l}$ and $N_{\rm r}$.

The covariance matrix (4.2.4) of the pure state (4.2.3) at any $t > 0$ after the quench is written in terms of the covariance matrix of the initial state (4.2.5) as [293]

$$\gamma^{(\mathrm{l,r})}(t) \,=\, E(t)\, \gamma^{(\mathrm{l,r})}_0\, E(t)^{\mathrm{t}} \tag{4.2.11}$$

where the time dependence occurs only through the matrix $E(t)$.

As done also for the covariance matrix after a global quench in Sec. 3.2.1, a convenient block decomposition of (4.2.11), which is employed in Sec. 4.4.1, reads

$$\gamma^{(\mathrm{l,r})}(t) = \begin{pmatrix} Q(t) & M(t) \\ M(t)^{\mathrm{t}} & P(t) \end{pmatrix} \tag{4.2.12}$$

where $Q(t)$, $P(t)$ and $M(t)$ are the $N \times N$ correlation matrices whose elements are given by (3.2.2).

An insightful decomposition for the matrix $E(t)$ in (4.2.11) is [293]

$$E(t) \,=\, V^{\mathrm{t}}\, \mathcal{E}(t)\, V \qquad\qquad V = \widetilde{V}_N \oplus \widetilde{V}_N \tag{4.2.13}$$

in terms of the matrix $\widetilde{V}_N$, whose generic element is given by (4.2.10) with N_{s} replaced by N, and of the matrix $\mathcal{E}(t)$, whose block decomposition reads

$$\mathcal{E}(t) \equiv \begin{pmatrix} \mathcal{D}(t) & \mathcal{A}(t) \\ \mathcal{B}(t) & \mathcal{D}(t) \end{pmatrix} \tag{4.2.14}$$

with $\mathcal{D}$, $\mathcal{A}$ and $\mathcal{B}$ being diagonal matrices whose elements are respectively

$$\mathcal{D}_k(t) \,\equiv\, \cos\bigl(\Omega_k t\bigr) \qquad \mathcal{A}_k(t) \,\equiv\, \frac{\sin\bigl(\Omega_k t\bigr)}{m\,\Omega_k} \qquad \mathcal{B}_k(t) \,\equiv\, -\,m\,\Omega_k \sin\bigl(\Omega_k t\bigr) \tag{4.2.15}$$

where Ω_k is the dispersion relation given by (3.3.1) Since $\widetilde{V}_N$ is orthogonal, V is symplectic and orthogonal. This observation and the fact that $\mathcal{E}(t=0) = \mathbf{1}$ lead to $E(t=0) = \mathbf{1}$; hence, from (4.2.11), we have that $\gamma^{(\mathrm{l,r})}(t=0) = \gamma_0^{(\mathrm{l,r})}$, as expected. Notice that, by using (4.2.15), one finds that $\mathcal{E}(t)$ in (4.2.14) is symplectic; hence, since V is symplectic too, we conclude that $E(t)$ in (4.2.13) is symplectic. Thus, $E(t)$ implements on the initial covariance matrix the unitary transformation on the initial state given in (4.2.3).

4.3 Complexity for the harmonic chain

In this section we discuss the temporal evolution of the complexity for the entire chain after the local quench defined in Sec. 4.2; hence both the reference and the target states are pure. We focus on the simplified setup where the quantum circuits are made only by bosonic Gaussian states with vanishing first moments.

4.3.1 Optimal circuit and complexity

The reference and the target states are fully characterised by their covariance matrices, which are γ_{R} and γ_{T} respectively. The circuit complexity obtained from the Fisher-Rao distance between γ_{R} and γ_{T} is given by (2.2.24), which is, as detailed in Sec. 2.2.4, proportional to the length of the optimal circuit that allows to construct γ_{T} from γ_{R} (see (2.2.20)).

Denoting by t_{R} and t_{T} the values of time t corresponding to the reference and to the target states respectively, for their covariance matrices we have

$$\gamma_{\mathrm{R}} = \gamma^{(\mathrm{l,r})}(t_{\mathrm{R}}) \qquad\qquad \gamma_{\mathrm{T}} = \gamma^{(\mathrm{l,r})}(t_{\mathrm{T}})\,. \tag{4.3.1}$$

In the most general setup, these matrices depend on the sets of parameters given by $\mathcal{Y}_{\mathrm{S}} \equiv \{m_{\mathrm{l,S}}, \kappa_{\mathrm{l,S}}, \omega_{\mathrm{l,S}}, m_{\mathrm{r,S}}, \kappa_{\mathrm{r,S}}, \omega_{\mathrm{r,S}}, m_{\mathrm{S}}, \kappa_{\mathrm{S}}, \omega_{\mathrm{S}}\}$, with S = R and S = T for the reference and the target state respectively. The corresponding states can be interpreted as the states obtained through

the time evolutions at $t = t_{\rm R} \geqslant 0$ and $t = t_{\rm T} \geqslant t_{\rm R}$ respectively, through two different quenches determined by the parameters $\mathcal{Y}_{\rm R}$ and $\mathcal{Y}_{\rm T}$ respectively, as described in Sec. 4.2.

The circuit complexity (2.2.24) can be evaluated by finding the eigenvalues of $\gamma_{\rm T}\,\gamma_{\rm R}^{-1}$.

For the reference and the target states (where V is orthogonal) with $\mathcal{E}_{\rm R} \equiv \mathcal{E}(t_{\rm R})$ and $\mathcal{E}_{\rm T} \equiv \mathcal{E}(t_{\rm T})$, we find

$$\begin{aligned}\gamma_{\rm T}\,\gamma_{\rm R}^{-1} &= \big(V^{\rm t}\,\mathcal{E}_{\rm T}\,V\big)\big(V_0^{\rm t}\,\Gamma_{0,{\rm T}}\,V_0\big)\big(V^{\rm t}\,\mathcal{E}_{\rm T}^{\rm t}\,V\big)\big(V^{\rm t}\,\mathcal{E}_{\rm R}^{-{\rm t}}\,V\big)\big(V_0^{\rm t}\,\Gamma_{0,{\rm R}}^{-1}\,V_0\big)\big(V^{\rm t}\,\mathcal{E}_{\rm R}^{-1}\,V\big) \\ &= V^{\rm t}\,\mathcal{E}_{\rm T}\,V\,V_0^{\rm t}\,\Gamma_{0,{\rm T}}\,V_0\,V^{\rm t}\,\mathcal{E}_{\rm T}^{\rm t}\,\mathcal{E}_{\rm R}^{-{\rm t}}\,V\,V_0^{\rm t}\,\Gamma_{0,{\rm R}}^{-1}\,V_0\,V^{\rm t}\,\mathcal{E}_{\rm R}^{-1}\,V\,. \end{aligned} \tag{4.3.2}$$

This expression is difficult to deal with mainly because of $V\,V_0^{\rm t}$, which encodes the spatial geometries before and after the local quench.

Notice that, when $t_{\rm R} = t_{\rm T} = 0$ (corresponding to a static configuration), $m_{\rm l,R} = m_{\rm l,T}$, $m_{\rm r,R} = m_{\rm r,T}$ and either $N_{\rm l} = 0$ or $N_{\rm r} = 0$, the result obtained in [35] can be recovered.

The above results can be employed to study the temporal evolution of the complexity after a global quench. In particular, choosing the parameters as mentioned in Sec. 4.2, one can show that the analysis of [293] allows to recover the correlators obtained in [84], which have been employed in chapter 3 to evaluate the temporal evolutions both of the complexity of the entire chain (see also [312]) and of the subsystem complexity after this kind of global quench.

In this chapter we are interested in circuits whose reference and the target states are pure states along the time evolution of a given local quench at different times $t_{\rm R}$ and $t_{\rm T}$. This can be done by choosing the parameters introduced in Sec. 4.2 as follows

$$\begin{aligned} &m \equiv m_{\rm l,R} = m_{\rm l,T} = m_{\rm r,R} = m_{\rm r,T} = m_{\rm R} = m_{\rm T} \\ &\kappa \equiv \kappa_{\rm l,R} = \kappa_{\rm l,T} = \kappa_{\rm r,R} = \kappa_{\rm r,T} = \kappa_{\rm R} = \kappa_{\rm T} \\ &\omega \equiv \omega_{\rm l,R} = \omega_{\rm l,T} = \omega_{\rm r,R} = \omega_{\rm r,T} = \omega_{\rm R} = \omega_{\rm T}\,. \end{aligned} \tag{4.3.3}$$

From (4.2.6), we have that $\Gamma_{0,{\rm T}}$ and $\Gamma_{0,{\rm R}}$ do not depend on time and the setting given by (4.3.3) leads to $\Gamma_{0,{\rm T}} = \Gamma_{0,{\rm R}} \equiv \Gamma_0$. Thus, (4.3.2) simplifies to

$$\gamma_{\rm T}\,\gamma_{\rm R}^{-1} \;=\; V^{\rm t}\,\mathcal{E}_{\rm T}\,V\,V_0^{\rm t}\,\Gamma_0\,V_0\,V^{\rm t}\,\mathcal{E}_{\rm T}^{\rm t}\,\mathcal{E}_{\rm R}^{-{\rm t}}\,V\,V_0^{\rm t}\,\Gamma_0^{-1}\,V_0\,V^{\rm t}\,\mathcal{E}_{\rm R}^{-1}\,V\,. \tag{4.3.4}$$

In our analysis we mainly consider the initial state (4.2.2) as the reference state. This choice corresponds to set $t_{\rm R} = 0$ in (4.3.1) and $\gamma_{\rm R} = \gamma_0^{({\rm l,r})}$ given by (4.2.5). In this case one finds that $\mathcal{E}_{\rm R} = \mathcal{E}(t=0) = \mathbf{1}$ and that (4.3.4) simplifies to

$$\gamma_{\rm T}\,\gamma_{\rm R}^{-1} = V^{\rm t}\,\mathcal{E}\,V\,V_0^{\rm t}\,\Gamma_0\,V_0\,V^{\rm t}\,\mathcal{E}^{\rm t}\,V\,V_0^{\rm t}\,\Gamma_0^{-1}\,V_0 \tag{4.3.5}$$

where the notation $\mathcal{E}_{\rm T} = \mathcal{E}$ has been introduced. Finding the eigenvalues of (4.3.5) analytically is complicated; hence we study them numerically.

4.3.2 Initial growth

It is worth exploring the leading term of the initial growth of the temporal evolution of the complexity (2.2.24) for the entire chain when the reference state is the initial state (i.e. $\gamma_{\rm R} = \gamma_0^{({\rm l,r})}$ in (4.2.5)) and the target state is the state at time t after the local quench that we are exploring (i.e. $\gamma_{\rm T} = \gamma^{({\rm l,r})}(t)$ in (4.2.11)).

By expanding $\mathcal{E}(t)$ in (4.2.14) as $t \to 0$, one finds

$$\mathcal{E}(t) = \begin{pmatrix} \mathbf{1} & \frac{t}{m}\mathbf{1} \\ t\,\mathcal{N} & \mathbf{1} \end{pmatrix} + O\big(t^2\big) \qquad\qquad \mathcal{N} \equiv -\,m\,{\rm diag}\Big(\Omega_1^2, \dots, \Omega_N^2\Big) \tag{4.3.6}$$

where Ω_k is given in (3.3.1). This leads to the following expansion for (4.2.13)

$$E(t) = \mathbf{1} + t\, E_{(1)} + O\big(t^2\big) \qquad E_{(1)} = \begin{pmatrix} \mathbf{0} & \frac{1}{m}\mathbf{1} \\ \widetilde{V}_N^{\mathrm{t}}\, \mathcal{N}\, \widetilde{V}_N & \mathbf{0} \end{pmatrix} \tag{4.3.7}$$

where the $N \times N$ matrix $\widetilde{V}_N^{\mathrm{t}}\, \mathcal{N}\, \widetilde{V}_N$ is not diagonal. By using the expansion (4.3.7), for the covariance matrix (4.2.11) we find

$$\gamma^{(\mathrm{l,r})}(t) \,=\, \gamma_0^{(\mathrm{l,r})} + \Big((E_{(1)} \gamma_0^{(\mathrm{l,r})} + \gamma_0^{(\mathrm{l,r})} E_{(1)}^{\mathrm{t}} \Big)\, t + O\big(t^2\big) \tag{4.3.8}$$

where the $O(t)$ term is symmetric, as expected. This straightforwardly leads to

$$\gamma_{\mathrm{T}}\, \gamma_{\mathrm{R}}^{-1} = \mathbf{1} + \Big[\, E_{(1)} + \gamma_0^{(\mathrm{l,r})} E_{(1)}^{\mathrm{t}} \big(\gamma_0^{(\mathrm{l,r})}\big)^{-1} \Big]\, t + O\big(t^2\big)\,. \tag{4.3.9}$$

This expansion provides the following linear growth for the complexity (2.2.24)

$$\mathcal{C} \,=\, c_1\, t + O\big(t^2\big) \tag{4.3.10}$$

where for the coefficient c_1 we find

$$\begin{aligned} c_1^2 \;\;=\;\; \frac{1}{4} \Bigg\{ & \sum_{k=1}^{N_{\mathrm{l}}} \big[\Omega_k^{(\mathrm{l})}\big]^2 + \sum_{k=1}^{N_{\mathrm{r}}} \big[\Omega_k^{(\mathrm{r})}\big]^2 - 2 \sum_{k=1}^{N} \Omega_k^2 \\ & + \mathrm{Tr}\Big[\widetilde{V}_N^{\mathrm{t}}\, \mathcal{N}\, \widetilde{V}_N\, \widetilde{V}_0^{\mathrm{t}}\, \mathcal{Q}_0\, \widetilde{V}_0\, \widetilde{V}_N^{\mathrm{t}}\, \mathcal{N}\, \widetilde{V}_N\, \widetilde{V}_0^{\mathrm{t}}\, \mathcal{P}_0^{-1}\, \widetilde{V}_0 \Big] \Bigg\}\,. \end{aligned} \tag{4.3.11}$$

Simplifying further the last term in this expression is complicated, hence we evaluate it numerically, as done in the bottom panel of Fig. 4.4 to determine the dashed straight line.

As a consistency check for (4.3.11), let us consider the trivial case where the quench does not occur, which corresponds to set $N_{\mathrm{l}} = N$ and $N_{\mathrm{r}} = 0$ (or viceversa), implying that $\widetilde{V}_0 = \widetilde{V}_N$. One finds that the last term in (4.3.11) simplifies to $\sum_{k=1}^{N} \Omega_k^2$. Then, since $N_{\mathrm{r}} = 0$, the second sum in (4.3.11) does not occur and therefore $c_1 = 0$, as expected, consistently with the fact that the initial state does not evolve.

4.3.3 Numerical results

In this section we discuss some temporal evolutions of the complexity for the entire chain after a local quench where two chains are joined (see Sec. 4.2), evaluated numerically through (2.2.24). The reference and the target states are respectively the initial state ($t_{\mathrm{R}} = 0$) and the pure state corresponding to a generic value of $t_{\mathrm{T}} \equiv t \geqslant 0$ along the evolution after the quench. The parameters of this quench protocol are set as in (4.3.3). The data points reported in all the figures shown in the main text have been obtained for $m = 1$ and $\kappa = 1$.

In Fig. 4.2 and Fig. 4.3, the temporal evolutions corresponding to critical Hamiltonians are considered; i.e. $\omega = 0$. Since the volume is kept finite, revivals are observed, as already discussed for the temporal evolutions of other quantities [323]. The different cycles correspond to $p < t/(2N+2) < p+1$, with p being a non-negative integer. This approximate periodic behaviour is observed also in the correlators providing the covariance matrix. For instance, in Fig. 4.2 the cycles corresponding to $p = 0$ and $p = 1$ are displayed.

Within each cycle we can identify three temporal regimes: (I) $p < t/(2N+2) < p+r$, characterised by an initial growth, a local maximum and a subsequent decrease; (II) $p+r < t/(2N+2) < p+1-r$,

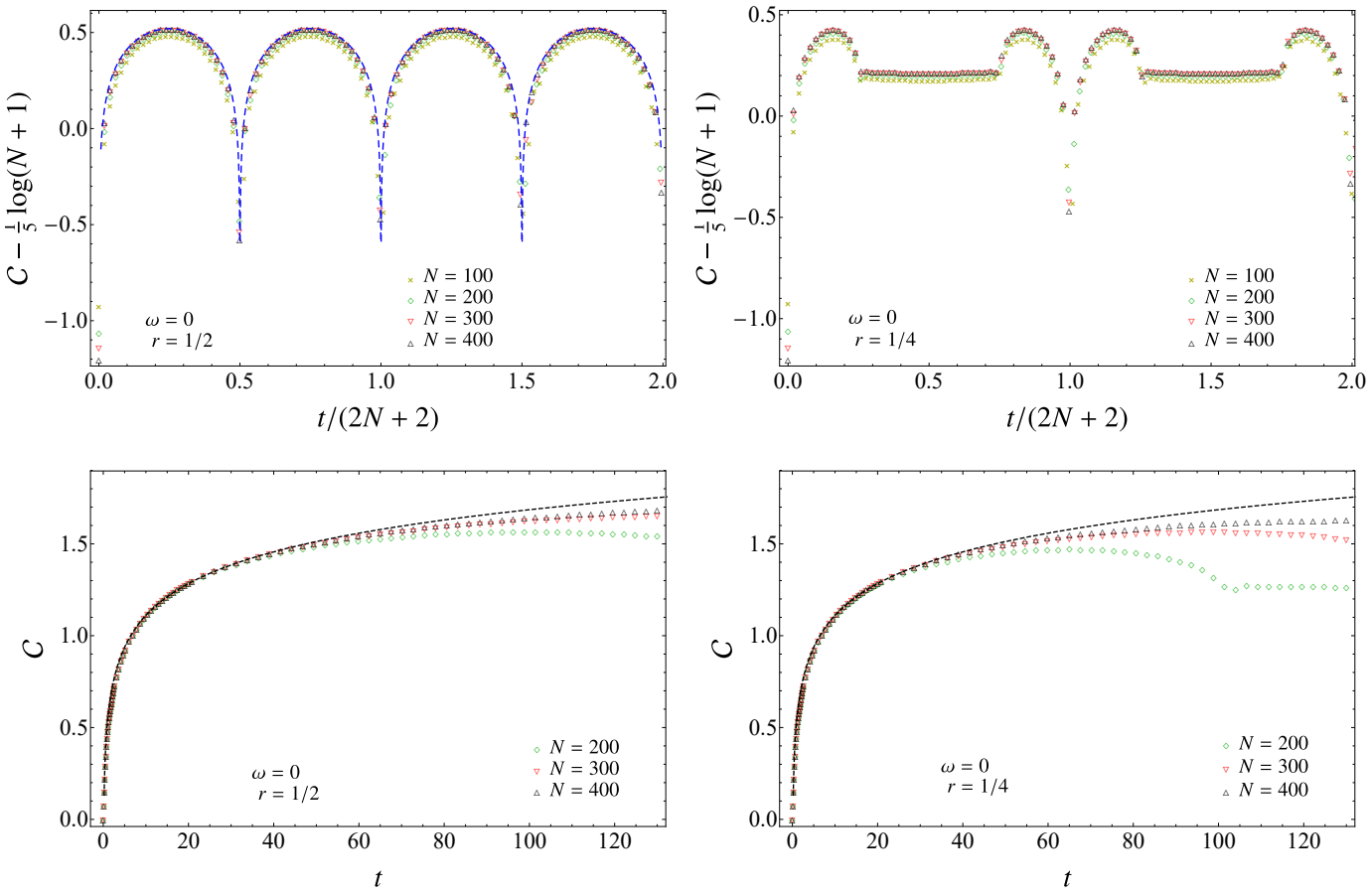

Figure 4.2: Temporal evolution of the complexity $\mathcal{C}$ in (2.2.24) for the entire chain (made by N sites) after a local quench with $\omega = 0$ w.r.t. the initial state at $t = 0$. Here either $r = 1/2$ (left panels) or $r = 1/4$ (right panels). The dashed curve in the top left panel corresponds to (4.3.12), while the ones in the bottom panels are obtained from (4.3.13).

where the evolution is almost stationary (a slight convexity of the curves is observed by zooming in); (III) $p + 1 - r < t/(2N + 2) < p + 1$, characterised by a growth until a local maximum is reached and a subsequent decrease. The last regime is very similar the first one, after a time reversal; indeed, the curve of $\mathcal{C}(t)$ within each cycle remains roughly invariant after a reflection with respect to the value of t corresponding to the center of the cycle.

In the special case of $r = 1/2$ (see the top left panel of Fig. 4.2 and the black symbols in Fig. 4.3), the second regime does not occur; hence the cycles correspond to $p < t/(N+1) < p+1$, with p being a non-negative integer.

In the top panels of Fig. 4.2, the temporal evolutions of $\mathcal{C} - \frac{1}{5}\log(N+1)$ are displayed for $r = 1/2$ (left panel) and $r = 1/4$ (right panel). When N is large enough, the data for different values of N nicely collapse, except for the beginning and the end of each cycle, as discussed below. In the top left panel of Fig. 4.2, where $r = 1/2$, also the following curve is shown

$$\mathcal{C}(t) \;=\; \frac{1}{5}\,\log\left\{\left(\frac{N+1}{\pi}\right)\left|\sin\left(\frac{\pi\, t}{N+1}\right)\right|\right\} \;+\; \text{const} \tag{4.3.12}$$

which nicely agrees with the data points in the middle of each cycle $p < t/(N+1) < p+1$, when

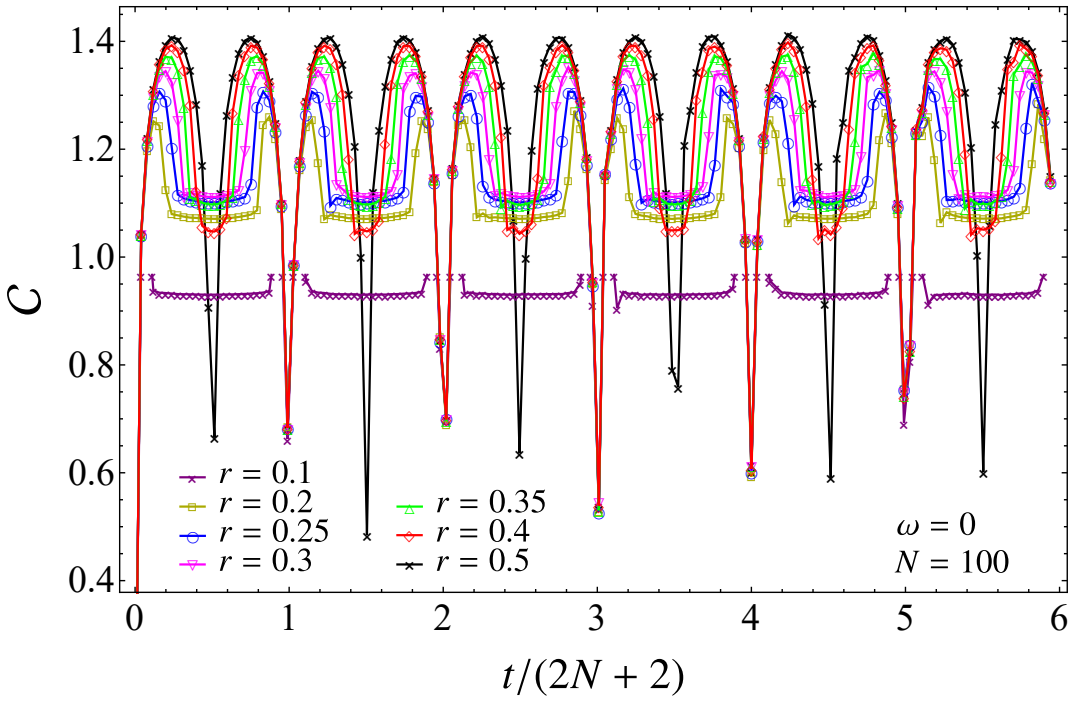

Figure 4.3: Temporal evolution of the complexity $\mathcal{C}$ in (2.2.24) for the chain with $N = 100$ after a local quench with $\omega = 0$ w.r.t. the initial state, for various positions of the joining point (see the top panel of Fig. 4.1).

N is large enough.

In the bottom panels of Fig. 4.2, we consider the temporal regime of initial growth for $\mathcal{C}$ subsequent to the early linear growth (4.3.10). We find that the data corresponding to different values of N nicely collapse on the curve given by

$$\mathcal{C} \;=\; \frac{1}{4}\log(t) + \text{const} \tag{4.3.13}$$

with const $\simeq 0.5346$ within a temporal regime whose width increases with N. Notice that (4.3.13) does not correspond to the leading term of (4.3.12) when $t/(N+1) \to 0$ because the coefficients multiplying the logarithms are different. This is consistent with the fact that the data in the top panels of Fig. 4.2 do not collapse at the beginning and at the end of each cycle. Taking $t/(2N+2)$ instead of t as the independent variable in the bottom panels of Fig. 4.2, the data collapse is observed for $\mathcal{C} - \frac{1}{4}\log(N+1)$ and not for $\mathcal{C} - \frac{1}{5}\log(N+1)$, which is plotted in the top panels of the same figure. This is consistent with the data corresponding to the black symbols in the right panels Figs. 4.5 and 4.7 and in the left panels of Fig. 4.9, which describe the complexity of the entire chain. Let us anticipate that also for the subsystem complexity $\mathcal{C}_A$ different temporal regimes occur where the data points for $\mathcal{C}_A - \alpha\log(N+1)$ corresponding to increasing values of N collapse, with different values of α in the different regimes (see Sec. 4.4). By comparing the two bottom panels in Fig. 4.2, we observe that the initial growth of the complexity is independent of the value of r.

In Fig. 4.3 we consider a longer range of t, in order to include more cycles and to highlight the fact that the approximate periodicity persists, for various values of r. Notice that the values of the local maximum within each cycle increases with r until $r = 1/2$. Furthermore, the height of the

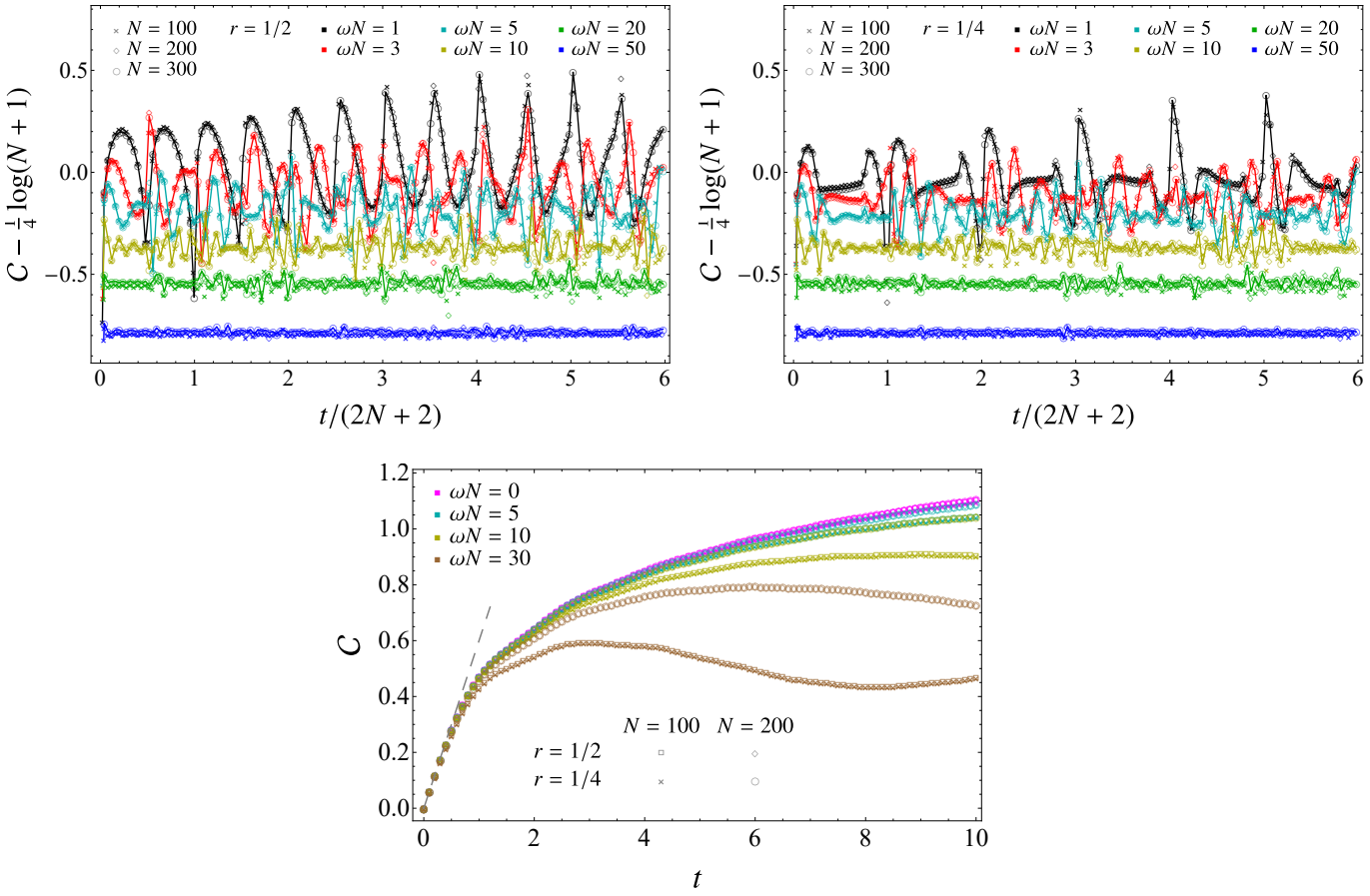

Figure 4.4: Temporal evolution of the complexity $\mathcal{C}$ in (2.2.24) for the entire chain after local quenches characterised by various $\omega > 0$ w.r.t. the initial state (the data corresponding to $N = 300$ have been joined through a piecewise line), with either $r = 1/2$ (top left panel) or $r = 1/4$ (top right panel). The initial growth is shown in the bottom panel, where the dashed grey line corresponds to (4.3.10) and (4.3.11) with $\omega = 0$, $r = 1/2$ and $N = 200$.

plateaux characterising the second temporal regime within each cycle grows with r until certain value r_* (from Fig. 4.3, we have $0.25 < r_* < 0.35$), then it decreases. Instead, the duration of this plateaux is always decreasing for $0 < r \leqslant 1/2$ and vanishes at $r = 1/2$. The symmetry of the problem straightforwardly leads to realise that the temporal evolution of the complexity for a given r is equal to the one corresponding to $1 - r$, for the same choice of all the other parameters. We have obtained numerical data for the temporal evolutions of the complexity displayed in Fig. 4.3 also for $N = 200$, finding that the data points of $\mathcal{C} - \frac{1}{5}\log(N + 1)$ for $N = 100$ and $N = 200$ approximatively collapse (see also the top panels of Fig. 4.2). In Fig. 4.3 we have reported only the numerical curves for $N = 100$ in order to display in a clear way the qualitative changes in the temporal evolutions corresponding to different r.

Some temporal evolutions of the complexity determined by gapped Hamiltonians after the local quench are shown in Fig. 4.4, where the different coloured curves correspond to different values of $\omega N \leqslant 50$.

In the top panels of Fig. 4.4, we show that the curves for $\mathcal{C} - \frac{1}{4}\log(N + 1)$ corresponding to different values of N collapse. We remind that this collapse has been observed for $\mathcal{C} - \frac{1}{5}\log(N+1)$

when $\omega = 0$ (see the top panels of Fig. 4.2). It would be interesting to understand this numerical observation. Furthermore, by comparing the temporal evolutions in the top panels of Fig. 4.4 with the ones in Fig. 4.3, we notice that the periodicity highlighted for $\omega = 0$ does not occur when $\omega N > 0$ in general.

When $\omega N \lesssim 1$, the initial part of the temporal evolution is similar to the one observed in the case of $\omega = 0$ (see Fig. 4.2), as one realises from the curves corresponding to $\omega N = 1$ in the top panels of Fig. 4.4. For large values of $\omega N \gtrsim 10$, the temporal evolution of $\mathcal{C} - \frac{1}{4}\log(N+1)$ is roughly described by a complicated oscillation about a constant value. This constant value decreases with ωN and, when ωN is large enough, is independent of r. Also the amplitude of the oscillations about this constant value decreases as ωN increases.

The bottom panel of Fig. 4.4 focuses on the initial growth of $\mathcal{C}$; hence it is instructive to compare it against the bottom panels of Fig. 4.2 where $\omega = 0$. In the temporal regime considered in the bottom panel of Fig. 4.4, the curves corresponding to different values of N nicely collapse. Furthermore, for small values of ωN a collapse is observed for different values of r (see also the bottom panels of Fig. 4.2), while they are clearly different for $\omega N = 30$, after a certain time. For $t \lesssim 1/2$, all the numerical curves displayed in the panel collapse on the same approximate dashed gray line, which has been obtained by setting $\omega = 0$, $r = 1/2$ and $N = 200$ in (4.3.10) and (4.3.11). Although the lines corresponding to the other values of ω, r and N are different, they roughly overlap with the only one that we have displayed.

We find it worth mentioning some results about the temporal evolution of the complexity evaluated within the gauge/gravity correspondence.

The temporal evolution of the holographic complexity in the Vaidya gravitational spacetimes, which model the formation of a black hole through the collapse of a shell and have been exploited to study the gravitational duals of global quenches [243,321], has been studied in [51–53,56,57,140–142]. Qualitative comparisons between these results and the temporal evolution of the complexity in harmonic chains have been discussed at the end of Sec. 3.3.5 (see also [67,311]).

A gravitational background dual to the local quench obtained through the insertion of a local operator [87,88] has been proposed in [344]. The temporal evolution of the holographic complexity in this spacetime has been studied in [143,144]. However, this local quench is very different from the one considered in this chapter, where two systems initially disconnected are glued together at some point. A gravitational dual for this local quench has been studied e.g. in [345,346,349] by employing the AdS/BCFT setup discussed in [351,352]. It would be interesting to investigate the temporal evolution of the holographic complexity for the entire system in this spacetime.

4.4 Subsystem complexity

In this section we investigate the temporal evolution of the subsystem complexity $\mathcal{C}_A$ after the local quench introduced in Sec. 4.2, when the reference and the target states are the reduced density matrices of the block A in the configurations shown in the bottom panels of Fig. 4.1.

4.4.1 Optimal circuit and subsystem complexity

As discussed in Sec. 3.4.1, in the harmonic lattices in the pure states that we are considering, the reduced density matrix associated to a spatial subsystem A characterises a mixed Gaussian state which can be fully described through its reduced covariance matrix γ_A [5,77,191], defined as the $2L \times 2L$ real, symmetric and positive definite matrix (L denotes the number of sites in A). Its expression is given by (3.4.1), where, in the case of the quench protocol considered in this chapter,

$Q_A(t)$, $P_A(t)$ and $M_A(t)$ are the reduced correlation matrices, obtained by selecting the rows and the columns corresponding to A in (4.2.12), namely $Q(t)_{i,j}$, $P(t)_{i,j}$ and $M(t)_{i,j}$, with $i, j \in A$.

In this section we study the circuit complexity when both the reference and the target states are mixed states corresponding to a subsystem A. In particular, we apply to the local quench that we are investigating the results for the circuit complexity of mixed states based on the Fisher information geometry discussed in chapter 2, as done in chapter 3 for a global quench.

We consider the reference state given by the reduced density matrix for the subsystem A at time $t_{\rm R} \geqslant 0$ obtained through the local quench protocol characterised by $\{m_{\rm R}, \kappa_{\rm R}, \omega_{\rm R}\}$ and the target state given by the reduced density matrix of the same subsystem at time $t_{\rm T} \geqslant t_{\rm R}$, constructed through the quench protocol described by $\{m_{\rm T}, \kappa_{\rm T}, \omega_{\rm T}\}$ (see Sec. 4.3.1). The corresponding reduced covariance matrices, denoted by $\gamma_{{\rm R},A}(t_{\rm R})$ and $\gamma_{{\rm T},A}(t_{\rm T})$ respectively, can be decomposed as done in (3.4.1).

The approach to the circuit complexity of mixed states based on the Fisher information geometry provides also the optimal circuit connecting $\gamma_{{\rm R},A}(t_{\rm R})$ to $\gamma_{{\rm T},A}(t_{\rm T})$ given by (3.4.2). The length of the optimal circuit (3.4.2) is proportional to its complexity (3.4.3).

For the quench protocol studied in this chapter, both the reduced covariance matrices in (3.4.3) have the form (3.4.1), obtained by restricting to A the covariance matrix $\gamma(t)$ in (4.2.11), as discussed above.

In our analysis we consider the simplest setup where the reference state is the initial state (i.e. $t_{\rm R} = 0$) and the target state corresponds to a generic value of $t_{\rm T} = t \geqslant 0$ after the local quench. The remaining parameters are fixed to $\omega_{\rm R} = \omega_{\rm T} \equiv \omega$, $\kappa_{\rm R} = \kappa_{\rm T} \equiv \kappa$ and $m_{\rm R} = m_{\rm T} \equiv m$. In this case the subsystem complexity (3.4.3) reads

$$\mathcal{C}_A \,=\, \frac{1}{2\sqrt{2}} \sqrt{{\rm Tr}\Big\{\big[\log\big(\gamma_A(t)\,\gamma_A(0)^{-1}\big)\big]^2\Big\}}\,. \tag{4.4.1}$$

It is instructive to compare the temporal evolution of $\mathcal{C}_A$ against the temporal evolution of the entanglement entropy S_A after the same local quench, which can be evaluated from the symplectic spectrum of $\gamma_A(t)$ as discussed in Appendix A.1 (see (A.1.3) and (A.1.4) and also [4, 10, 275, 277]). The considerations above can be easily adapted to harmonic lattices in any number of spatial dimensions.

4.4.2 Numerical results

In the following we discuss some numerical results for the temporal evolution after a local quench of the subsystem complexity (4.4.1) in the case where the subsystem A is a block made by L consecutive sites in harmonic chains made by N sites. Let us remind that the reference state is the initial state ($t_{\rm R} = 0$) and the target state corresponds to the state at the generic value $t_{\rm T} \equiv t \geqslant 0$ after the local quench, whose protocol is specified by the values of the parameters in (4.3.3) with $m = 1$ and $\kappa = 1$. In this thesis we report only the numerical results obtained when $\omega = 0$, namely when the evolution Hamiltonian after the local quench is critical. A preliminary analysis of the massive case can be found in [100], but this issue deserves future investigations. For a given local quench, we display both the temporal evolution of the subsystem complexity $\mathcal{C}_A$ and of the entanglement entropy S_A.

The temporal evolutions in Figs. 4.5, 4.6, 4.7 and 4.8 correspond to blocks A adjacent to the left boundary of the chain (as shown pictorially in the bottom left panel of Fig. 4.1) and for this bipartition the joining point is outside the subsystem whenever $L < rN$. The temporal evolutions in Fig. 4.9 correspond to blocks A whose midpoint coincides with the joining point (see Fig. 4.1, bottom right panel).

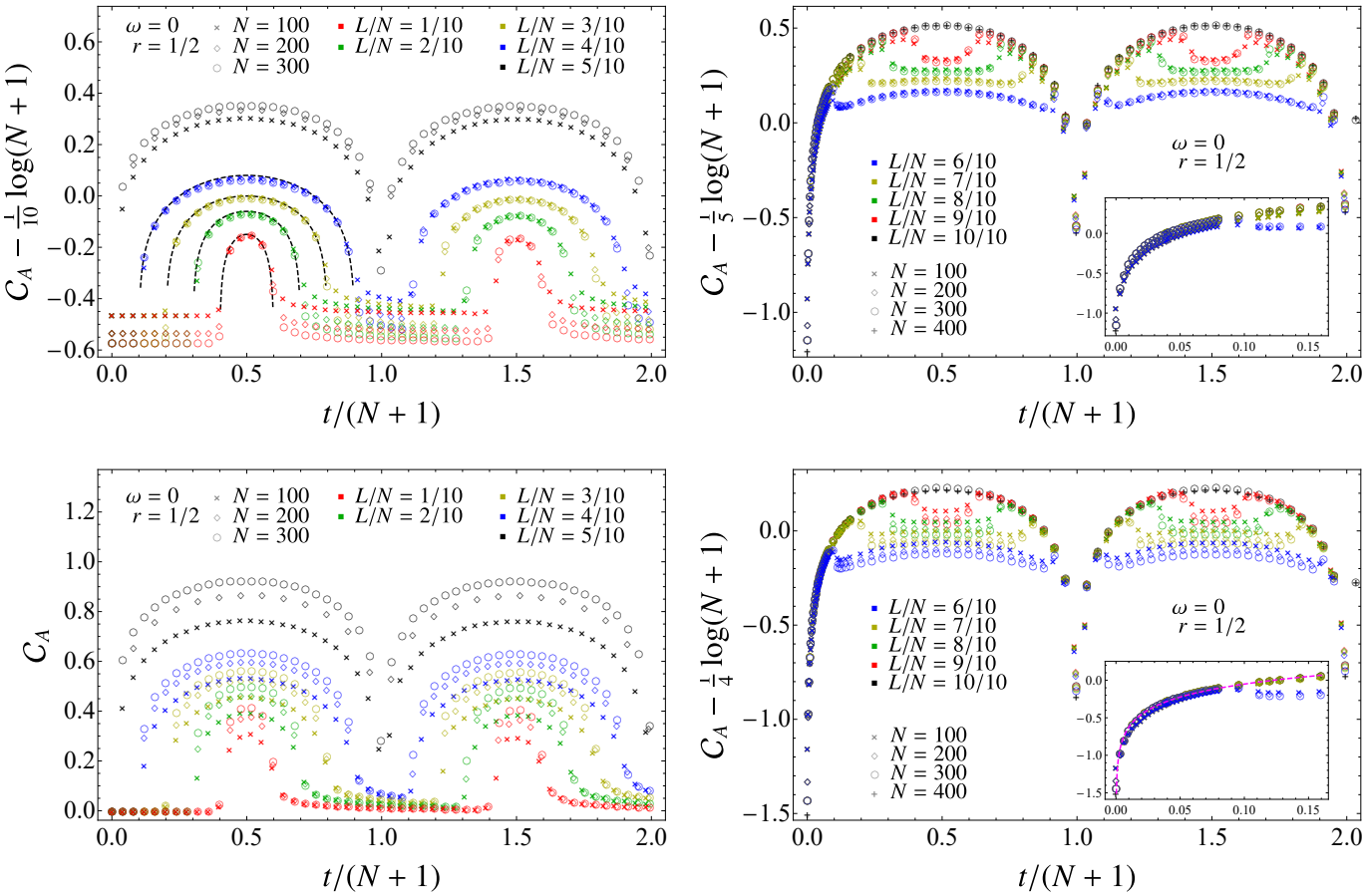

Figure 4.5: Temporal evolution of the subsystem complexity $\mathcal{C}_A$ in (4.4.1) for a block A made by L consecutive sites adjacent to the left boundary of harmonic chains made by N sites (see Fig. 4.1, bottom left panel) after a local quench with $\omega = 0$ and $r = 1/2$. The size of the blocks is $L \leqslant Nr$ in the left panels and $L > Nr$ in the right panels. The black dashed curves in the top left panel correspond to (4.4.3). The insets zoom in on the initial growth (the dashed curve in the bottom right panel corresponds to (4.3.13)). The data points corresponding to $L/N = 1$ in the right panels are also reported in the top left panel of Fig. 4.2.

Let us consider first subsystems A given by blocks adjacent to the left boundary of the chain (see the bottom left panel of Fig. 4.1) The corresponding temporal evolutions for $\mathcal{C}_A$ and S_A are shown respectively in Fig. 4.5 and Fig. 4.6 when $r = 1/2$ and respectively in Fig. 4.7 and Fig. 4.8 when $r = 1/4$.

Both the temporal evolutions of $\mathcal{C}_A$ and S_A exhibit revivals because our system has finite volume. For a generic values of r, the cycles correspond to $p < t/(2N + 2) < p + 1$, with p non negative integer (see Fig. 4.7 and Fig. 4.8), while only for $r = 1/2$ they correspond to $p < t/(N + 1) < p + 1$ (see Fig. 4.5 and Fig. 4.6) because of the symmetry provided by the fact that the joining point coincides with the midpoint of the chain [323, 353].

Focussing on the temporal evolution during a single cycle, as N and L increase with L/N kept fixed, two different scalings are observed: one at the beginning and at the end of the cycle and another one in its central part. In these two temporal regimes, the curves obtained for different values of N collapse when the time independent quantity $\alpha \log(N+1)$ is subtracted, with different

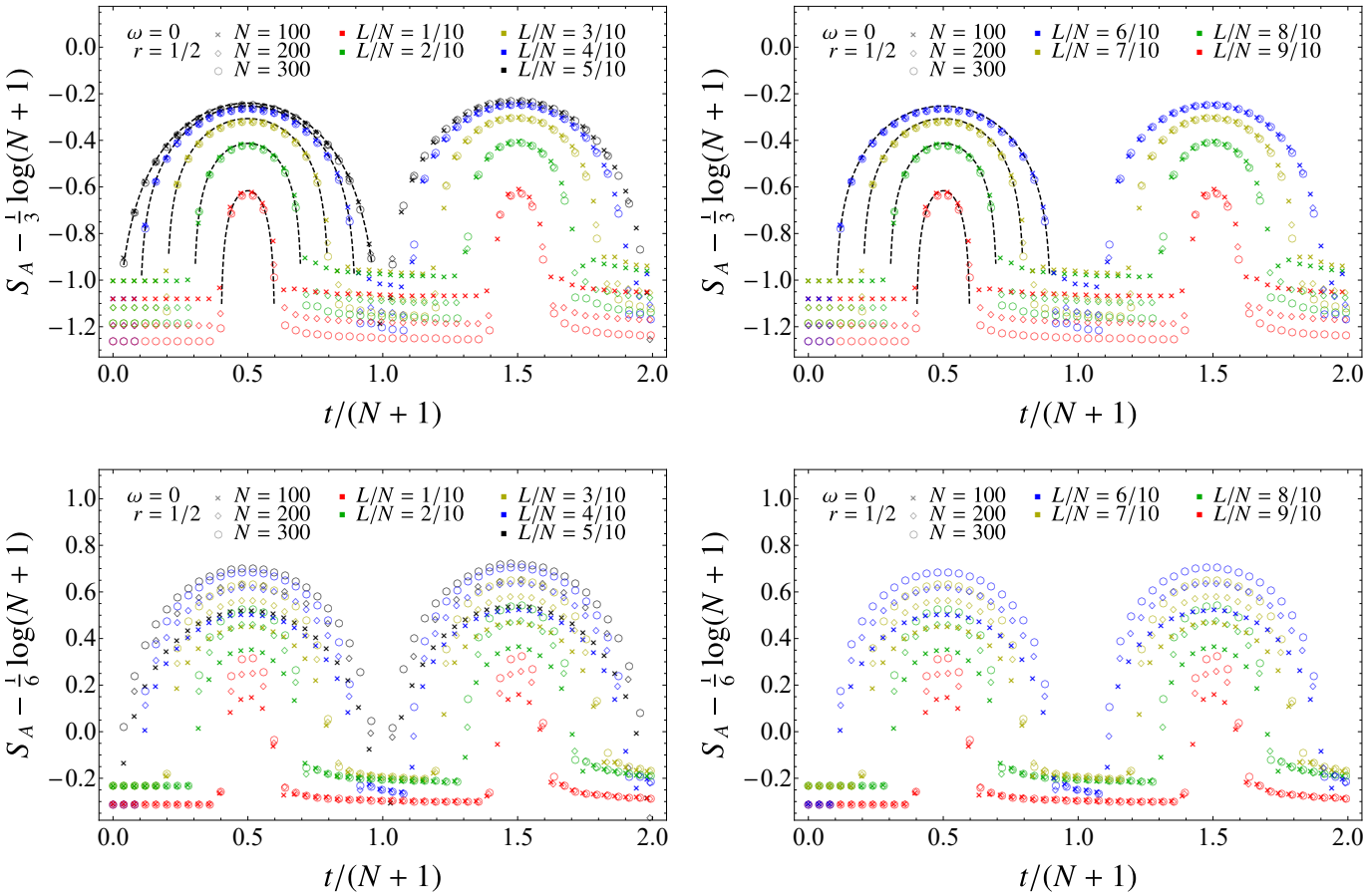

Figure 4.6: Temporal evolution of the entanglement entropy S_A in the same setup described for Fig. 4.5. The size of the blocks is $L \leqslant Nr$ in the left panels and $L > Nr$ in the right panels. The black dashed curves in the top panels correspond to (4.4.2).

values of α.

In Fig. 4.5 and Fig. 4.7 we show some temporal evolutions of $\mathcal{C}_A - \alpha \log(N+1)$ when $r = 1/2$ and $r = 1/4$ respectively. We find that α depends on (a) whether the joining point is outside ($L < rN$) or inside ($L > rN$) the subsystem; (b) the temporal regime within the cycle where the collapse of the data is observed (either the central part of the cycle or its extremal parts).

When the entangling point coincides with the joining point, i.e. $L = rN$, the collapses of the data in the different temporal regimes is observed for values of α that are slightly different from the ones adopted in the vertical axes of the panels in Fig. 4.5 and Fig. 4.7. In particular, when $\mathcal{C}_A$ is not constant, the black curves in the left panels of these figures collapse with $\alpha \simeq 1/7$, otherwise the data collapse is observed with $\alpha \simeq 1/10$ (see Fig. 4.7, left panels).

The different scalings in the diverse temporal regimes within each cycle pointed out in (b) occur also for the temporal evolution of S_A after a local quench [85, 86, 342]. Numerical results for the temporal evolution of S_A after the same quench and for the same bipartition considered above (see the bottom left panel of Fig. 4.1) are reported in Fig. 4.6 and Fig. 4.8 for $r = 1/2$ and $r = 1/4$ respectively. In the case of $r = 1/2$, these numerical outcomes for S_A are well described by the

analytic curve discussed in [342], namely[1]

$$S_A(t) = \begin{cases} \frac{1}{6}\log(N+1) + a & \frac{t}{N+1} \in T_0 \\ \frac{1}{6}\log\left\{\left(\frac{N+1}{\pi}\right)^2\left[\left(\sin\left(\frac{\pi t}{N+1}\right)\right)^2 - \left(\sin(\pi d)\right)^2\right]\right\} + \tilde{a} & \frac{t}{N+1} \in T_1 \end{cases} \tag{4.4.2}$$

(see the black dashed curves in Fig. 4.6) within the first cycle (then extended periodically to the subsequent cycles), where $d \equiv \frac{1}{2} - \frac{L}{N+1}$ parameterises the distance between the entangling point and the joining point and we have introduced the temporal regimes $T_0 \equiv (0,d) \cup (1-d\,,1)$ and $T_1 \equiv (d\,,1-d)$. The expression (4.4.2) holds only when $r = 1/2$ and the interval A is adjacent to one of the boundaries of the segment. The different scalings corresponding to the two different regimes within the cycle, which lead to subtract $\alpha \log(N+1)$ with either $\alpha = 1/3$ (top panels) or $\alpha = 1/6$ (bottom panels), agree with (4.4.2). We remark that, since $r = 1/2$, the numerical curves in the left panels of Fig. 4.6 are identical to the ones in the right panels characterised by the same coloured marker: this is because the entanglement entropy of a subsystem is equal to the entanglement entropy of its complement when the entire state is in a pure state (this is the case for any $t > 0$ after the local quench that we are exploring).

As for the temporal evolution of the subsystem complexity $\mathcal{C}_A$, when $r = 1/2$ and $L < N/2$, hence the joining point is outside the subsystem (see the left panels of Fig. 4.5), we find that it is qualitatively similar to the temporal evolution of S_A. Combining this observation with the different scalings obtained numerically, we are led to consider the following ansatz

$$\mathcal{C}_A(t) = \begin{cases} 0 & \frac{t}{N+1} \in T_0 \\ \frac{1}{10}\log\left\{\left(\frac{N+1}{\pi}\right)^2\left[\left(\sin\left(\frac{\pi t}{N+1}\right)\right)^2 - \left(\sin(\pi d)\right)^2\right]\right\} + \tilde{b} & \frac{t}{N+1} \in T_1 \end{cases} \tag{4.4.3}$$

within the first cycle (the parameter d and the temporal regimes are introduced in (4.4.2)), which is then extended periodically to any value of $t > 0$. In the top left panel of Fig. 4.5, a remarkable agreement is observed between the numerical data and the ansatz (4.4.3), which corresponds to the black dashed curves.

Considering also the right panels of Fig. 4.5, where $r = 1/2$ again but $L > N/2$, we find that the temporal evolutions of $\mathcal{C}_A$ for blocks that include the joining point are qualitatively different from the ones corresponding to blocks that do not contain the joining point. Indeed, in the right panels of Fig. 4.5, focussing e.g. on the first cycle and considering $t/(N+1) < 1/2$ (the regime $t/(N+1) > 1/2$ is obtained straightforwardly through a time reversal), we observe three regimes: an initial growth until a local maximum, followed by a fast decrease and then another growth, milder than the previous one (it becomes almost flat as L/N increases).

When $r \neq 1/2$, the symmetry under a spatial reflection with respect to the midpoint of the chain does not occur and more regimes are observed within a cycle, for both $\mathcal{C}_A$ and S_A.

The same quantities considered in Fig. 4.5 and Fig. 4.6, where $r = 1/2$, are shown in Fig. 4.7 and Fig. 4.8 for $r = 1/4$. Notice the different periodicity with respect to the case of $r = 1/2$, as already mentioned above. The main feature to highlight is the qualitative difference between the temporal evolutions of $\mathcal{C}_A$ when the joining point lies outside A (see Fig. 4.7, left panels) and the ones corresponding to blocks that include the joining point (see Fig. 4.7, right panels). Furthermore,

[1] See Eq. (39) of [342] with $c = 1$ and $v_{\rm F} = 1$.

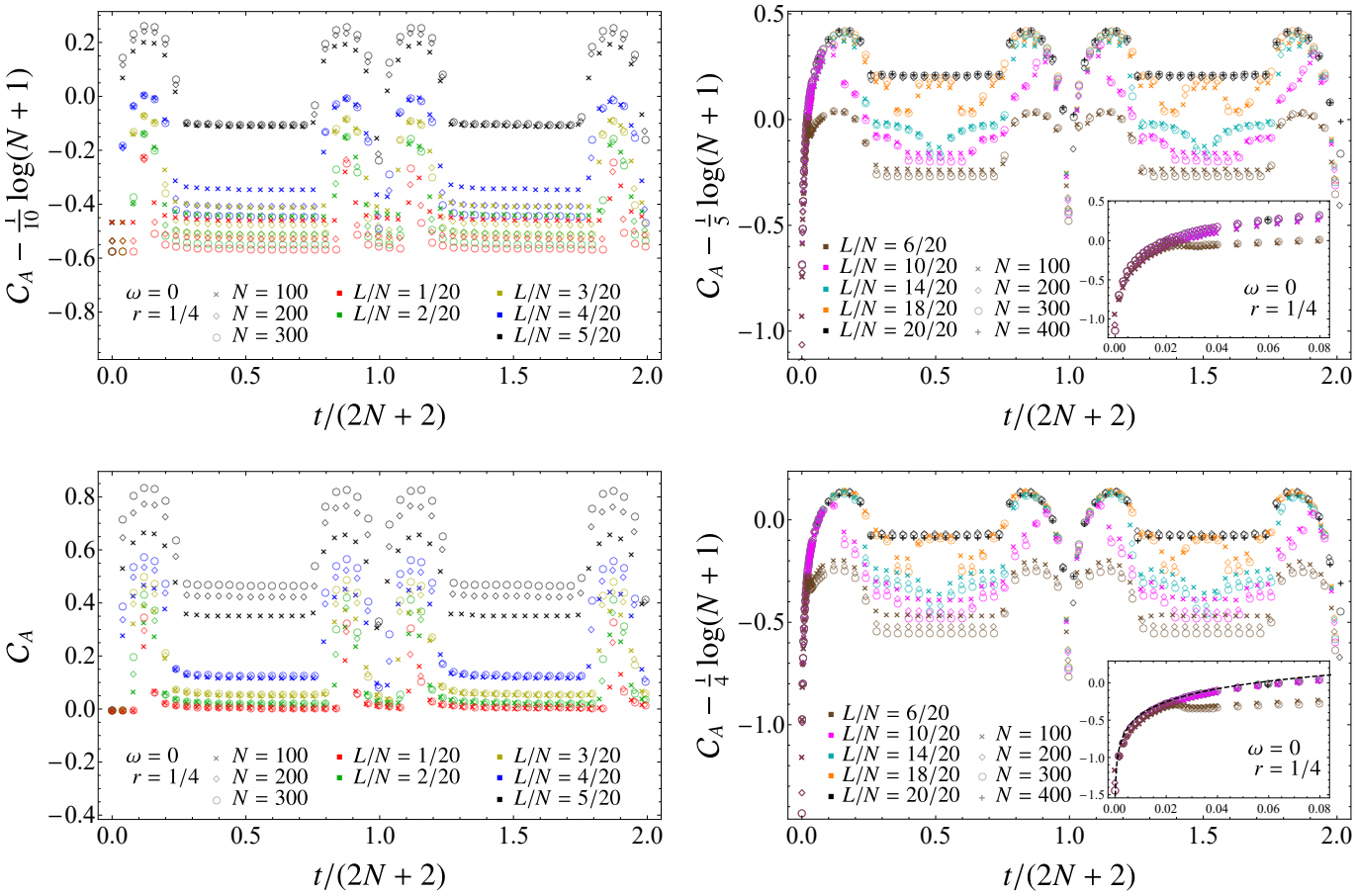

Figure 4.7: Temporal evolution of the subsystem complexity $\mathcal{C}_A$ in (4.4.1) for a block A made by L consecutive sites adjacent to the left boundary of harmonic chains made by N sites (see Fig. 4.1, bottom left panel) after a local quench with $\omega = 0$ and $r = 1/4$. The size of the blocks is $L \leqslant Nr$ in the left panels and $L > Nr$ in the right panels. The insets zoom in on the initial growth (the dashed curve in the bottom right panel corresponds to (4.3.13)). The data points corresponding to $L/N = 1$ in the right panels are also reported in the top right panel of Fig. 4.2.

the temporal evolution of $\mathcal{C}_A$ when the joining point lies outside A is also qualitatively similar to the one of the corresponding S_A (see Fig. 4.8, left panels).

When $L < rN$, focussing on the temporal evolutions in the first half of the first cycle (i.e. $0 < \frac{t}{2N+2} < 1/2$), for both $\mathcal{C}_A$ and S_A we observe three regimes (left panels of Fig. 4.7 and Fig. 4.8): first a flat curve, then a growth followed by a decrease and finally another regime where the evolution is almost constant. This means that, when $L < rN$, for the temporal evolutions within the first cycle we identify five regimes. The values of $\frac{t}{2N+2}$ at which the changes of regime occur are given by $rN - L$, $L + rN$, $2N - L - rN$ and $2N - rN + L$, whose time ordering depends on the explicit values of N, r and L. In the special case of $r = 1/2$, we have only three regimes within the first cycle (first a flat regime, then a growth/decrease regime and finally another flat regime), as one can observe from Fig. 4.5 and Fig. 4.6, but also from the analytic expressions in (4.4.2) and (4.4.3).

When $L > rN$ and therefore the joining point is inside the subsystem, by comparing the right panels of Fig. 4.7 against the right panels of Fig. 4.8, it is straightforward to realise that the

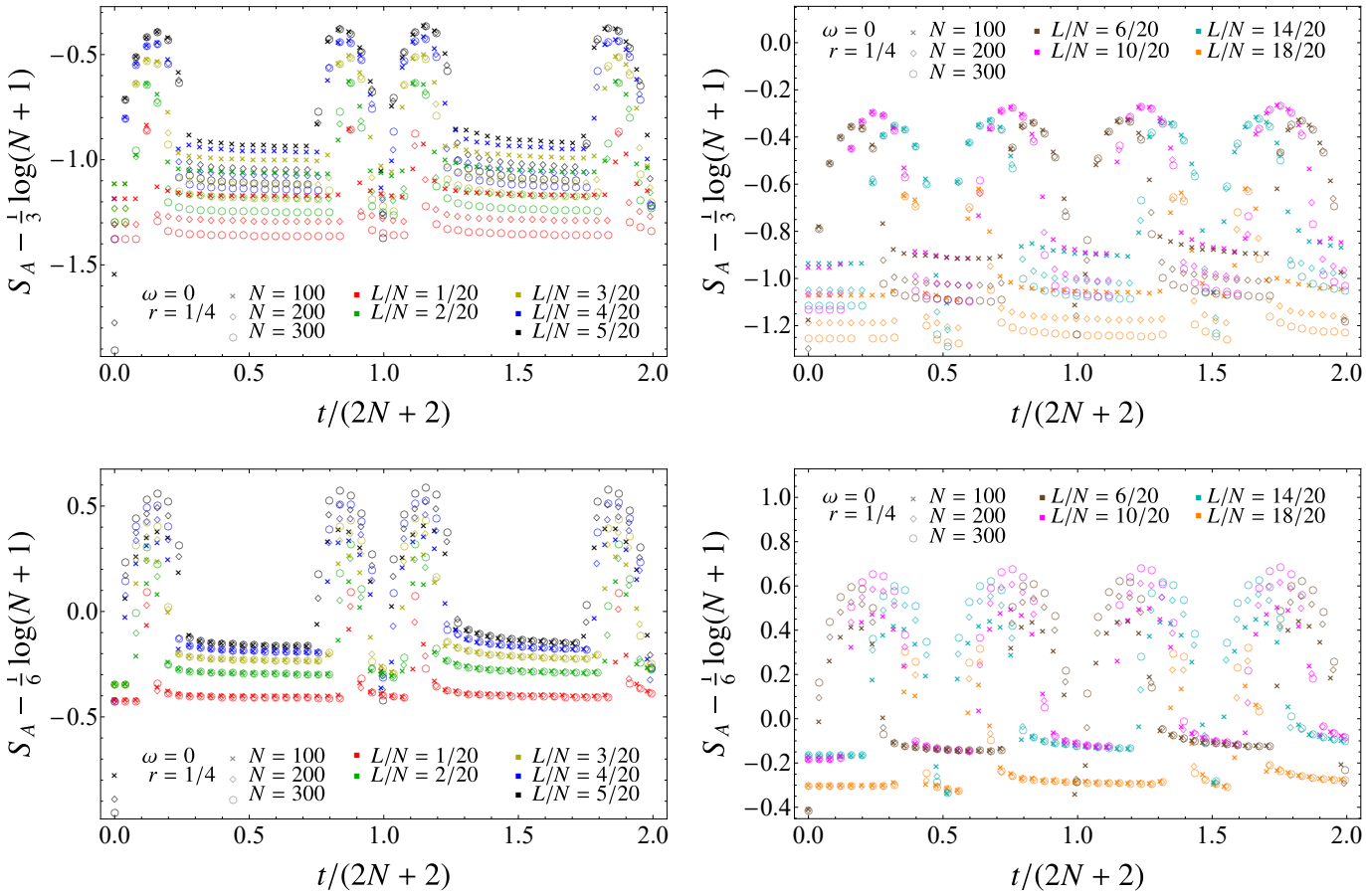

Figure 4.8: Temporal evolution of the entanglement entropy S_A in the same setup described for Fig. 4.7. The size of the blocks is $L \leqslant rN$ in the left panels and $L > rN$ in the right panels.

temporal evolutions of $\mathcal{C}_A$ and S_A are qualitatively very different. In particular, while the temporal evolutions of S_A in the right panels of Fig. 4.8 are similar to the ones displayed in the left panels of the same figure (e.g. the same five regimes mentioned above), as expected from the fact that $S_A = S_B$ for the spatial bipartition $A \cup B$ of the system in a pure state (the qualitative difference is only due to the asymmetric position of the joining point), the temporal evolutions of $\mathcal{C}_A$ in the right panels of Fig. 4.7 are more complicated than the ones in the left panels of the same figure, which correspond to blocks that do not include the joining point. For instance, considering the temporal evolution of $\mathcal{C}_A$ immediately after the quench, a rapid initial growth is observed when $L > rN$ (highlighted in the insets in the right panels of Fig. 4.7), while it remains stationary when $L < rN$. We remind that, whenever $L \neq rN$, also the temporal evolution of S_A right after the quench remains stationary (see Fig. 4.6 and Fig. 4.8). As for initial growth of $\mathcal{C}_A$ when $L > rN$, an interesting numerical observation that we find it worth remarking is the fact that the logarithmic curve (4.3.13), which has been first employed in the bottom panels of Fig. 4.2 to describe the logarithmic growth for the complexity of the entire chain, occurs also in the temporal evolution of the subsystem complexity; indeed it corresponds also to the dashed lines displayed in the bottom right panels of Fig. 4.5 and Fig. 4.7. Notice that, when the joining point is outside the subsystem (see the left panels of Fig. 4.5 and Fig. 4.7), a logarithmic growth right after the stationary regime is observed, but in this case the coefficient of the logarithm is different from the one in (4.3.13),

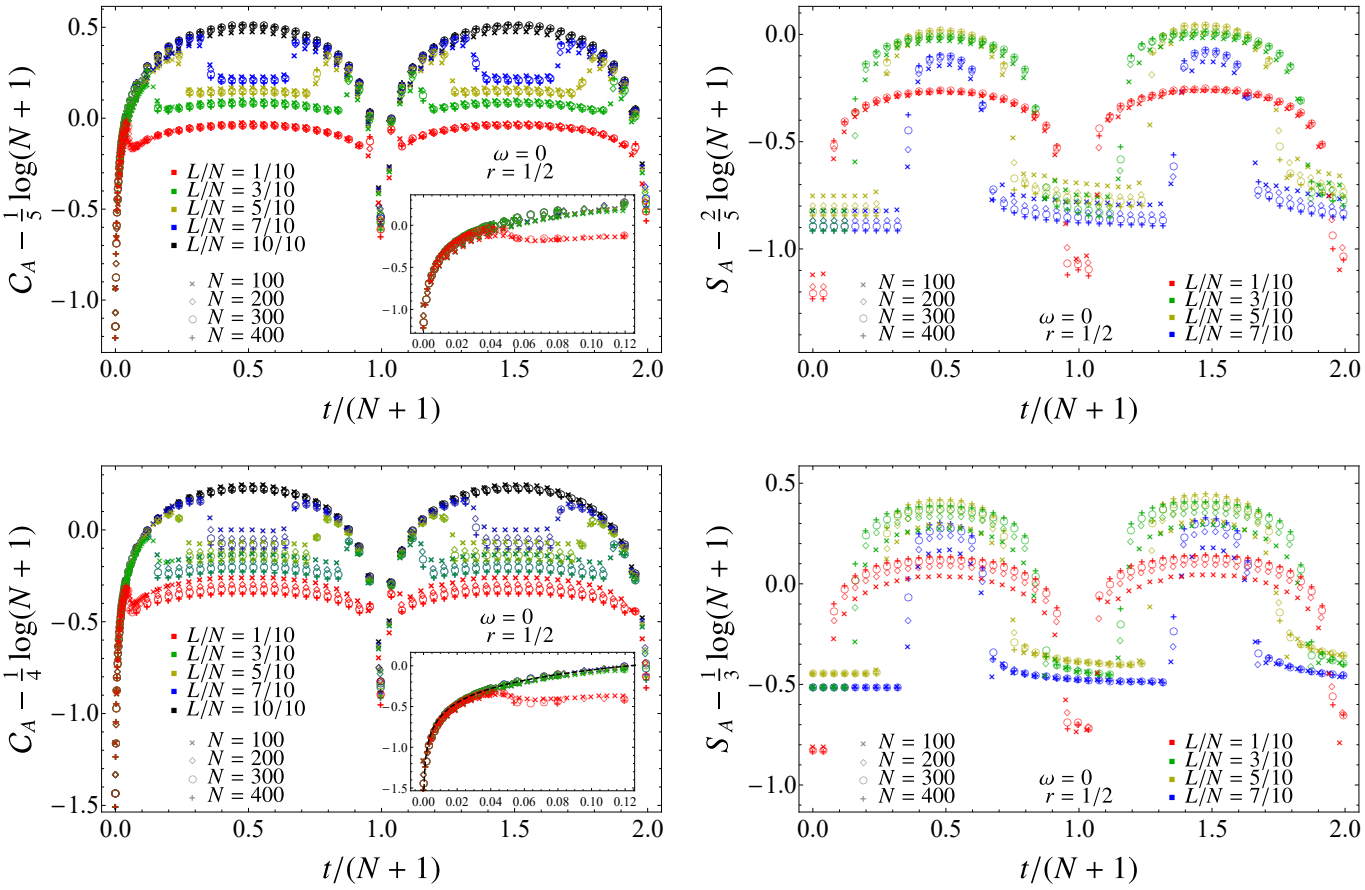

Figure 4.9: Temporal evolution of the subsystem complexity $\mathcal{C}_A$ (left panels) and entanglement entropy S_A (right panels) for a block A made by L sites whose midpoint is given by the joining point at $r = 1/2$ (see Fig. 4.1, bottom right panel) after a local quench with $\omega = 0$. The insets zoom in on the initial growth (the dashed curve in the bottom left panel is given by (4.3.13)).

as one can infer from the second line of (4.4.3) when $r = 1/2$ and $t/(N+1) \simeq d$.

Comparing the left and the right panels in Fig. 4.7, it is straightforward to observe that the qualitative behaviour of temporal evolutions of $\mathcal{C}_A$ is more complicated when the joining point lies inside A, as anticipated above. For instance, focussing on $t/(2N+2) < 1/2$ for the magenta and the cyan curves, after the first local maximum two subsequent temporal regimes occur where the curves decrease before becoming constant. Furthermore, when $L/N > 1-r$ (see the orange curves) and considering again only $t/(2N+2) < 1/2$, after the first local maximum, the two decreases and the flat regime mentioned above, we observe another growth followed by a regime where $\mathcal{C}_A$ becomes constant again (at a higher value w.r.t. the previous flat regime). We remark that, when $L/N \gtrsim r$ (see the brown curves), two local maxima occur in the temporal evolution of $\mathcal{C}_A$ for $\frac{t}{2N+2} < \frac{1}{2}$ (the first one is highlighted in the insets). A more systematic analysis is needed to determine the values of $t/(2N+2)$ that identify the various regimes occurring in these temporal evolutions.

While in Figs. 4.5, 4.6, 4.7 and 4.8 the block A is adjacent to a boundary (see Fig. 4.1, bottom left panel) and therefore only one entangling point occurs, in Fig. 4.9 we consider some temporal evolutions of $\mathcal{C}_A$ and S_A when $r = 1/2$ and the joining point coincides with the midpoint of A

(see Fig. 4.1, bottom right panel), hence two entangling points separate A from its complement B, which is made by two disjoint intervals adjacent to different boundaries. By construction, for this configuration the joining point is always inside the subsystem. The blocks providing the reduced covariance matrix (3.4.1) for this bipartition are obtained by restricting the indices of the matrices Q, P and M in (4.2.12) to $i, j \in \{\frac{N}{2} - \frac{L}{2} + 1, \dots, \frac{N}{2} + \frac{L}{2}\}$.

The numerical results shown in Fig. 4.9 for some temporal evolutions of $\mathcal{C}_A$ (left panels) and S_A (right panels) after local quenches correspond to critical evolution Hamiltonians, i.e. with $\omega = 0$. Also in this numerical analysis we subtract $\alpha \log(N+1)$ with the proper value of α, in order to observe collapses of data sets corresponding to the same L/N when N is large enough, finding that α depends both on the quantity (either $\mathcal{C}_A$ or S_A) and on the temporal regime within the cycle where the data collapses are observed (either the central regime or the initial and final regimes). Interestingly, by comparing the left panels of Fig. 4.9 against the right panels of Fig. 4.5, we observe that, when the joining point is inside the subsystem A, the temporal evolutions of $\mathcal{C}_A$ are qualitatively very similar, despite the fact that the number of entangling points is different in the two figures. Moreover, the values of α employed are the same, which are therefore independent of the number of the entangling points. Instead, let us remind that the values of α to employ for S_A depend on the number of the entangling points, as one realises by comparing the right panels of Fig. 4.9 against the right panels of Fig. 4.6.

Focussing on bipartitions where the joining point lies inside the subsystem, by comparing the left and the right panels of Fig. 4.9, one notices that, while S_A is constant at the beginning of its evolution, $\mathcal{C}_A$ increases immediately. This feature has been highlighted also during the comparison of the right panels of Fig. 4.5 and Fig. 4.7 against the right panels of Fig. 4.6 and Fig. 4.8, where only one entangling point occurs.

Another interesting difference between the temporal evolutions corresponding to the two bottom panels in Fig. 4.1 is that the first local minimum occurs at $\frac{t}{N+1} \simeq \frac{L}{N} - \frac{1}{2}$ in the right panels of Fig. 4.5 (one entangling point) and at $\frac{t}{N+1} \simeq \frac{L}{2N}$ in the left panels of Fig. 4.9 (two entangling points).

In the Vaidya gravitational spacetimes, the temporal evolution of the holographic subsystem complexity has been studied through the prescription based on the volume of a particular spacetime slice [145, 316], finding curves that qualitatively agree with the temporal evolution of the subsystem complexity after a global quench of the mass parameter in the harmonic chains discussed in Sec. 3.5.2.

It would be interesting to perform a comparison between the qualitative behaviour of the temporal evolutions of the subsystem complexity discussed in this chapter and the one of the temporal evolutions of the holographic subsystem complexity in the spacetime describing the gravitational dual of the joining local quench [345, 349].

4.5 Discussion

We studied the temporal evolutions of the circuit complexity and of the subsystem complexity after a local quench by considering harmonic chains in a segment with Dirichlet boundary conditions and the local quench where two finite chains made by rN and $(1-r)N$ sites (with $0 < r < 1$) are joined at $t = 0$ [293]. The subsystem complexity $\mathcal{C}_A$ in (4.4.1) has been evaluated by employing the complexity of mixed bosonic Gaussian states based on the Fisher information geometry introduced in chapter 2.

In Sec. 4.3 we have evaluated some temporal evolutions of the circuit complexity for the entire harmonic chain. For any value $\omega \geqslant 0$ of the mass occurring in the evolution Hamiltonian, we found that the initial growth of the complexity immediately after the quench is linear (see (4.3.10)) with

a slope given by (4.3.11), which can be evaluated numerically, as done in the bottom panel of Fig. 4.4. When the evolution Hamiltonian is critical (i.e. $\omega = 0$), after the above mentioned initial growth we observe a logarithmic growth independent of r (see (4.3.13) and the bottom panels of Fig. 4.2). We expect to observe this feature also when the system is infinite. The temporal evolutions of the complexity for finite systems and $\omega = 0$ display revivals, independently of r. Three temporal regimes are observed within the first half of the temporal interval containing a single revival. When $\omega > 0$, the temporal evolutions of the complexity are more complicated (see Fig. 4.4 and its discussion). Importantly, we have identified different temporal regimes where different scaling behaviours are observed as N increases. It would be interesting to explain these scalings through quantum field theory methods.

In Sec. 4.4 we have explored the temporal evolutions of $\mathcal{C}_A$ when $\omega = 0$ for the bipartitions shown in the bottom panels of Fig. 4.1, where either one entangling point or two entangling points occur. One of our main results is given by the numerical evidences that the qualitative behaviour of the temporal evolutions of $\mathcal{C}_A$ depends on whether the block A contains the joining point. In the case of the spatial bipartition shown in the bottom left panel of Fig. 4.1, where one entangling point occurs, this qualitative difference is evident once the left panels are compared against the corresponding right panels both in Fig. 4.5 and Fig. 4.7. When the joining point is inside the block, during the initial regime of the temporal evolution of $\mathcal{C}_A$ we observe the same logarithmic growth (4.3.13) occurring in the temporal evolution of the complexity of the entire chain. Furthermore, in the case of $r = 1/2$ and when the joining point lies outside the block, we find that the analytic expression (4.4.3) for the temporal evolution of $\mathcal{C}_A$ nicely reproduces the behaviour of the numerical data.

It is very instructive to compare a temporal evolution of $\mathcal{C}_A$ against the corresponding temporal evolution of S_A, obtained for the same bipartition and the same quench protocol. We remark that, whenever the block A does not contain the joining point, the temporal evolutions of $\mathcal{C}_A$ and of S_A are qualitatively similar (for instance, both these quantities do not evolve immediately after the quench whenever $L \neq rN$). Instead, they are qualitatively very different when the joining point is inside the subsystem; indeed, for instance, when $L \neq rN$ we find that $\mathcal{C}_A$ rapidly grows immediately after the quench, while S_A remains constant for a while.

As for the local quench considered in this chapter, it would be interesting to explore systematically the temporal evolutions of the subsystem complexity when $\omega > 0$ or for asymmetric bipartitions involving two or even more entangling points, to obtain analytic results in the thermodynamic limit, to find bounds that still describe some essential features of the temporal evolution of the subsystem complexity and also to study the thermalisation of the subsystem complexity, as done in chapter 3 for a global quench of the mass parameter.

The Gaussian states can be employed to investigate the temporal evolution of the subsystem complexity after some local quenches in higher dimensions and also in free fermionic lattice models.

In this chapter we have compared the temporal evolutions of the subsystem complexity against the ones of the corresponding entanglement entropy, but it could be interesting to perform analogue comparisons against the temporal evolutions of other entanglement quantifiers like the entanglement negativity [166, 167, 210, 211, 293, 294, 308, 354, 355], the entanglement contours [28, 29] and the relative entropies [356].

We remark that investigating the temporal evolutions of the subsystem complexity after various quantum quenches through lattice methods and quantum field theory techniques in interacting models is a very challenging task that deserves future studies. Interesting analyses have been performed [60, 62, 63, 65, 66, 68–70, 73–76, 268, 269] and it would be interesting to employ these methods to explore also the out-of-equilibrium dynamics of the circuit complexity.

Part II

Entanglement Hamiltonians in free systems

Chapter 5

Entanglement Hamiltonians in massless systems

5.1 Introduction

The fundamental theorem (1.2.11) proved by Bisognano and Wichmann [171,172], which holds for any relativistic Quantum Field Theory (QFT) in $d+1$ dimensions in its vacuum state, provides the entanglement Hamiltonian of the spatial bipartition where A corresponds to half space and the entangling hypersurface is the flat hyperplane.

As explained in Sec. 1.2.2, when the QFT is a Conformal Field Theory (CFT), the conformal symmetry allows to write the analytic expressions (1.2.12) and, in $1+1$ dimensional CFTs, (1.2.13) for the entanglement Hamiltonians for simple spatial bipartitions.

In a $1+1$ dimensional CFT at equilibrium in its vacuum state, we consider bipartitions where A is an interval of length ℓ and such that its entanglement Hamiltonian can be written as (1.2.13). In this chapter we focus on the bipartitions shown in Fig. 5.1. For an interval in the infinite line (left panel in Fig. 5.1), the weight function in (1.2.13) is the following parabola [174, 175]

$$\beta(x) = 2\pi \, \frac{x}{\ell} \left(1 - \frac{x}{\ell}\right). \tag{5.1.1}$$

When A is an interval at the beginning of a semi-infinite line (right panel in Fig. 5.1), the weight function in (1.2.13) is the half parabola given by [147]

$$\beta(x) = \pi \left(\frac{x}{\ell} + 1\right) \left(1 - \frac{x}{\ell}\right) \tag{5.1.2}$$

independently of the boundary conditions imposed at the beginning of the semi-infinite line. It is interesting to explore the procedure that allows to obtain these entanglement Hamiltonians in CFT as the continuum limit of the corresponding entanglement Hamiltonians in the lattice models providing a discretisation of the CFT.

Entanglement Hamiltonians in free lattice models at equilibrium in their ground state have been studied in [4, 10, 178, 179, 191–201]. A detailed analysis of the continuum limit has been recently carried out for an interval in an infinite chain of free fermions [179], by employing the analytic results obtained by Eisler and Peschel in [192]. In this chapter we study the continuum limit of the entanglement Hamiltonians of a block of consecutive sites in massless harmonic chains by following the approach of [179], which is based on the observation that, in this limit, the proper combinations of all the diagonals of the matrices determining the entanglement Hamiltonian on the lattice must be considered [193].

Figure 5.1: The spatial bipartitions considered in this chapter: an interval A in the infinite line (left) and an interval A at the beginning of the semi-infinite line (right).

The eigenvalues of the entanglement Hamiltonian provide the entanglement spectrum, which contains relevant physical information [26]. It is worth studying the gaps g_r with respect to the largest eigenvalue defined in (1.2.18) and also their ratios g_r/g_1 with respect to the smallest gap g_1. We remark that these ratios are not influenced by a global shift and a rescaling of the entire spectrum. For the class of systems which includes the ones we are interested in, the ratios g_r/g_1 are related to the conformal dimensions of the underlying BCFT as reported in (1.2.18) [147].

In this chapter we focus on massless harmonic chains and perform a numerical analysis of the continuum limit of two entanglement Hamiltonians of an interval A and of the corresponding entanglement spectra. We consider a massless harmonic chain both on the infinite line and on the semi-infinite line with Dirichlet boundary conditions imposed at its origin. The continuum limit of these lattice models is the CFT given by the massless scalar field Φ, whose central charge is $c = 1$. By introducing the canonical momentum field $\Pi = -\partial_t \Phi$, the energy density on the infinite line reads

$$T_{00}(x) = \frac{1}{2}\Big[\,\Pi(x)^2 + \big(\partial_x \Phi(x)\big)^2\,\Big] \tag{5.1.3}$$

and on the semi-infinite line is given by [357]

$$T_{00}(x) = \frac{1}{2}\Big[\,\Pi(x)^2 - \Phi(x)\,\partial_x^2 \Phi(x)\,\Big]\,. \tag{5.1.4}$$

We study the spatial bipartitions shown in Fig. 5.1, whose entanglement Hamiltonians predicted by CFT are given by (1.2.13), (5.1.1) and (5.1.3) for the interval in the infinite line and by (1.2.13), (5.1.2) and (5.1.4) for the interval at the beginning of the semi-infinite line. Our numerical analysis is based on the procedure described in [179, 192] to study the continuum limit of the entanglement Hamiltonian of an interval in an infinite chain of free fermions. We study also the entanglement spectra of these entanglement Hamiltonians, finding that the CFT prediction (1.2.18) holds, once Neumann boundary conditions are imposed along the boundaries introduced by the regularisation procedure.

This chapter is organised as follows. In Sec. 5.2 we report the entanglement Hamiltonian of an interval in harmonic chains in terms of the two-point correlators. In Sec. 5.3 we study the continuum limit of the entanglement Hamiltonian of an interval in the infinite line and in Sec. 5.4 this analysis is performed for an interval at the beginning of the semi-infinite line with Dirichlet boundary conditions. In Sec. 5.5 we draw some conclusions.

Notations: following [101], in this chapter we adopt different notations for the operators in the lattice model and the corresponding ones in the continuum limit; the former ones are denoted by the hat, while the latter ones are not.

5.2 Entanglement Hamiltonians in the harmonic chain

In this section we report the expression of the entanglement Hamiltonian of a subsystem in harmonic chains in terms of the two-point correlators [10], discussing also some decompositions that will be employed throughout the chapter.

The Hamiltonian of the harmonic chain with nearest neighbour spring-like interaction on an infinite line reads

$$\widehat{H} = \sum_i \left(\frac{1}{2m}\, \hat{p}_i^2 + \frac{m\omega^2}{2}\, \hat{q}_i^2 + \frac{\kappa}{2}(\hat{q}_{i+1} - \hat{q}_i)^2 \right) \tag{5.2.1}$$

where the position and the momentum operators $\hat{q}_i$ and $\hat{p}_i$ are hermitean operators satisfying the canonical commutation relations $[\hat{q}_i, \hat{q}_j] = [\hat{p}_i, \hat{p}_j] = 0$ and $[\hat{q}_i, \hat{q}_j] = \mathrm{i}\delta_{i,j}$. In our numerical analysis we set $\kappa = m = 1$.

The Hamiltonian (5.2.1) is the discretization of the Hamiltonian of a massive scalar field in the continuum, whose massless regime given by $\omega = 0$ is a CFT with central charge $c = 1$. The range of the index i in (5.2.1) depends on the spatial domain supporting the harmonic chain: in this chapter we consider either the infinite line ($i \in \mathbb{Z}$) or the semi-infinite line (integer $i \geqslant 0$). When (5.2.1) is defined on the semi-infinite line, it is crucial to specify also the boundary condition imposed at the beginning of the semi-infinite line (i.e. at $i = 0$) and in our analysis we consider the case of Dirichlet boundary conditions. The two-point correlators $Q_{ij} = \langle \hat{q}_i\, \hat{q}_j \rangle$ and $P_{ij} = \langle \hat{p}_i\, \hat{p}_j \rangle$ provide the generic elements of the correlation matrices Q and P respectively.

Let us consider harmonic chains (5.2.1) in their ground state $|0\rangle$ and introduce the bipartition of the chain into a spatial domain A made by L sites and its complement B, assuming that the Hilbert space can be bipartite accordingly as $\mathcal{H} = \mathcal{H}_A \otimes \mathcal{H}_B$. Since for these quantum systems the reduced density matrix $\rho_A \equiv \mathrm{Tr}_{\mathcal{H}_B}(|0\rangle\langle 0|)$ remains Gaussian, independently of the choice of the bipartition, the corresponding entanglement Hamiltonian $\widehat{K}_A$ is a quadratic hermitian operator, which can be written as follows [10, 178, 191–201]

$$\widehat{K}_A = \frac{1}{2}\, \hat{\boldsymbol{r}}^{\mathrm{t}} H_A\, \hat{\boldsymbol{r}} \qquad\qquad \hat{\boldsymbol{r}} = \begin{pmatrix} \hat{\boldsymbol{q}} \\ \hat{\boldsymbol{p}} \end{pmatrix} \tag{5.2.2}$$

where the $2L$ dimensional vector $\hat{\boldsymbol{r}}$ collects the position and the momentum operators $\hat{q}_i$ and $\hat{p}_i$ with $i \in A$. The matrix H_A is real, symmetric and positive definite; hence $\widehat{K}_A$ is hermitian. In terms of the reduced correlation matrices Q_A and P_A, obtained by restricting Q and P to the subsystem A, the matrix H_A can be evaluated as follows [10]

$$\begin{aligned} H_A = M \oplus N &\equiv \Big(h\big(\sqrt{P_A Q_A}\,\big) \oplus h\big(\sqrt{Q_A P_A}\,\big) \Big) \big(P_A \oplus Q_A\big) \\ &= \big(P_A \oplus Q_A\big) \Big(h\big(\sqrt{Q_A P_A}\,\big) \oplus h\big(\sqrt{P_A Q_A}\,\big) \Big) \end{aligned} \tag{5.2.3}$$

where

$$h(y) \equiv \frac{1}{y}\, \log\!\left(\frac{y + 1/2}{y - 1/2} \right). \tag{5.2.4}$$

In this chapter we study entanglement Hamiltonians $\widehat{K}_A$ when the entire chain is at equilibrium in its ground state and when the subsystem A is a block of L consecutive sites either in the infinite line or at the beginning of the semi-infinite line where Dirichlet boundary conditions are imposed (see Fig. 5.1). In these two cases, the matrix H_A is block diagonal. The off-diagonal blocks of H_A can be non vanishing e.g. for the time dependent entanglement Hamiltonians after a global quantum quench (see chapter 7).

The matrix H_A can be constructed numerically through (5.2.3) and (5.2.4). In order to employ these formulas, the eigenvalues of the matrix $\sqrt{Q_A P_A}$ must be strictly larger than $1/2$. In our numerical analysis many eigenvalues very close to $1/2$ occur and the software automatically approximates them to $1/2$ whenever a low numerical precision is set throughout the numerical analysis. This forces us to work with very high numerical precisions. In particular we have employed precisions up to 6500 digits, depending on the specific calculation. We observe that higher precision is required as L and ω increase.

The expressions (5.2.2) and (5.2.3) naturally lead to write the entanglement Hamiltonian in terms of the symmetric matrices M and N as follows

$$\widehat{K}_A = \frac{\widehat{H}_M + \widehat{H}_N}{2} \tag{5.2.5}$$

where

$$\widehat{H}_M \equiv \sum_{i,j=1}^{L} M_{i,j}\, \hat{q}_i\, \hat{q}_j \qquad\qquad \widehat{H}_N \equiv \sum_{i,j=1}^{L} N_{i,j}\, \hat{p}_i\, \hat{p}_j\,. \tag{5.2.6}$$

These sums can be organised in different ways. For instance, by writing the symmetric matrices M and N as sums of a diagonal matrix, an upper triangular matrix and a lower triangular matrix, it is straightforward to obtain

$$\widehat{H}_M \;=\; L\sum_{i=1}^{L}\left(\frac{M_{i,i}}{L}\,\hat{q}_i^2 + 2\sum_{k=1}^{L-i}\frac{M_{i,i+k}}{L}\,\hat{q}_i\,\hat{q}_{i+k}\right) \tag{5.2.7}$$

$$\widehat{H}_N \;=\; L\sum_{i=1}^{L}\left(\frac{N_{i,i}}{L}\,\hat{p}_i^2 + 2\sum_{k=1}^{L-i}\frac{N_{i,i+k}}{L}\,\hat{p}_i\,\hat{p}_{i+k}\right). \tag{5.2.8}$$

In [193] the sums (5.2.6) have been rewritten by decomposing the contribution coming from the i-th row of the matrices M and N, and this leads to

$$\widehat{H}_M \;=\; L\sum_{i=1}^{L}\left(\frac{M_{i,i}}{L}\,\hat{q}_i^2 + \sum_{k=1}^{L-i}\frac{M_{i,i+k}}{L}\,\hat{q}_i\,\hat{q}_{i+k} + \sum_{k=1}^{i-1}\frac{M_{i,i-k}}{L}\,\hat{q}_i\,\hat{q}_{i-k}\right) \tag{5.2.9}$$

$$\widehat{H}_N \;=\; L\sum_{i=1}^{L}\left(\frac{N_{i,i}}{L}\,\hat{p}_i^2 + \sum_{k=1}^{L-i}\frac{N_{i,i+k}}{L}\,\hat{p}_i\,\hat{p}_{i+k} + \sum_{k=1}^{i-1}\frac{N_{i,i-k}}{L}\,\hat{p}_i\,\hat{p}_{i-k}\right). \tag{5.2.10}$$

We find it convenient to introduce also the following decomposition

$$\widehat{H}_M = L\left[\sum_{i=1}^{L/2}\left(\frac{M_{i,i}}{L}\,\hat{q}_i^2 + 2\sum_{k=1}^{L-2i+1}\frac{M_{i,i+k}}{L}\,\hat{q}_i\,\hat{q}_{i+k}\right) + \sum_{i=L/2+1}^{L}\left(\frac{M_{i,i}}{L}\,\hat{q}_i^2 + 2\sum_{k=1}^{2i-L-2}\frac{M_{i-k,i}}{L}\,\hat{q}_i\,\hat{q}_{i-k}\right)\right] \tag{5.2.11}$$

$$\widehat{H}_N = L\left[\sum_{i=1}^{L/2}\left(\frac{N_{i,i}}{L}\,\hat{p}_i^2 + 2\sum_{k=1}^{L-2i+1}\frac{N_{i,i+k}}{L}\,\hat{p}_i\,\hat{p}_{i+k}\right) + \sum_{i=L/2+1}^{L}\left(\frac{N_{i,i}}{L}\,\hat{p}_i^2 + 2\sum_{k=1}^{2i-L-2}\frac{N_{i-k,i}}{L}\,\hat{p}_i\,\hat{p}_{i-k}\right)\right] \tag{5.2.12}$$

where the contribution of the counter diagonal has been included into the summation over $1 \leqslant i \leqslant L/2$. This choice leads to an inconsistency in the range of k of the last double sum when $i = L/2 + 1$, which can be easily fixed by imposing the vanishing of this term.

The analytic results for the entanglement Hamiltonian of an interval in the infinite chain of free fermions found in [179, 192] and the decompositions introduced above for the operators $\widehat{H}_M$ and $\widehat{H}_N$ suggest to introduce the following limits

$$\lim_{L\to\infty} \frac{M_{i,i+k}}{L} \equiv \mu_k(x_k) \qquad \lim_{L\to\infty} \frac{N_{i,i+k}}{L} \equiv \nu_k(x_k) \qquad x_k \equiv \frac{1}{L}\left(i+\frac{k}{2}\right) \tag{5.2.13}$$

where $i+k/2$ is the midpoint between the i-th and the $(i+k)$-th site. The existence of the functions μ_k and ν_k is a crucial assumption in the subsequent derivations of the CFT predictions for the entanglement Hamiltonians.

5.3 Interval in the infinite line

In this section we consider the harmonic chain on the infinite line and perform a numerical analysis to study the continuum limit of the entanglement Hamiltonian of an interval. We follow the procedure discussed in [179, 192] for the continuum limit of the entanglement Hamiltonian of an interval in the infinite chain of free fermions. In Sec. 5.3.1 we report the main analysis, which leads to the CFT prediction (1.2.13), with the weight function (5.1.1) and the energy density (5.1.3). The entanglement spectrum is explored in Sec. 5.3.2.

5.3.1 Entanglement Hamiltonian

The entanglement Hamiltonian of a block made by L consecutive sites in the infinite line, when the entire harmonic chain is in its ground state, is the operator constructed as explained in Sec. 5.2. Considering the massless regime, we study the procedure to obtain the CFT prediction (1.2.13), with $\beta(x)$ and $T_{00}(x)$ given by (5.1.1) and (5.1.3) respectively, through a numerical analysis of the continuum limit.

The reduced correlation matrices Q_A and P_A are obtained by restricting the indices i and j of the correlators (C.1.5) and (C.1.6) to the interval A, i.e. to the integer values in $[1, L]$. By employing these reduced correlation matrices into (5.2.3), one finds the entanglement Hamiltonian matrix H_A. The entanglement Hamiltonian of the interval in the infinite line is obtained by plugging the matrix H_A into (5.2.2). The translation invariance of the entire system prevents us from setting $\omega = 0$ in our numerical analysis (see Appendix C.1.1). The data reported in all the figures discussed in this subsection have been obtained for $\omega L = 10^{-500}$.

In Fig. 5.2 and Fig. 5.3 we show the data for the diagonals $M_{i,i+k}/L$ and $N_{i,i+k}/L$ with $0 \leqslant k \leqslant 7$ for some values of L. This numerical results lead to conclude that the limits in (5.2.13) provide well defined functions. Furthermore, these functions have a well defined sign given by the parity of k, are symmetric under reflection with respect to the center of the interval (we checked numerically that this symmetry holds also for the data points, i.e. that $M_{i,i+p} = M_{L-i-p+1,L-i+1}$ and $N_{i,i+p} = N_{L-i-p+1,L-i+1}$) and the absolute value of their maximum significantly decreases as k increases. It would be interesting to find analytic expressions for the functions defined through the limits (5.2.13), as done in [192] for the interval in the infinite chain of free fermions.

Assuming that the functions μ_k and ν_k introduced in (5.2.13) are well defined, let us study the continuum limit of the entanglement Hamiltonian (5.2.5), where the quadratic operators $\widehat{H}_M$ and $\widehat{H}_N$ have been introduced in (5.2.6). In the following we adapt the procedure discussed in [179] for the entanglement Hamiltonian of an interval in the infinite chain of free fermions. The quadratic operators $\widehat{H}_M$ and $\widehat{H}_N$ can be decomposed in different ways, as discussed in Sec. 5.2. For the sake of simplicity, in the following we describe the continuum limit for the decomposition given

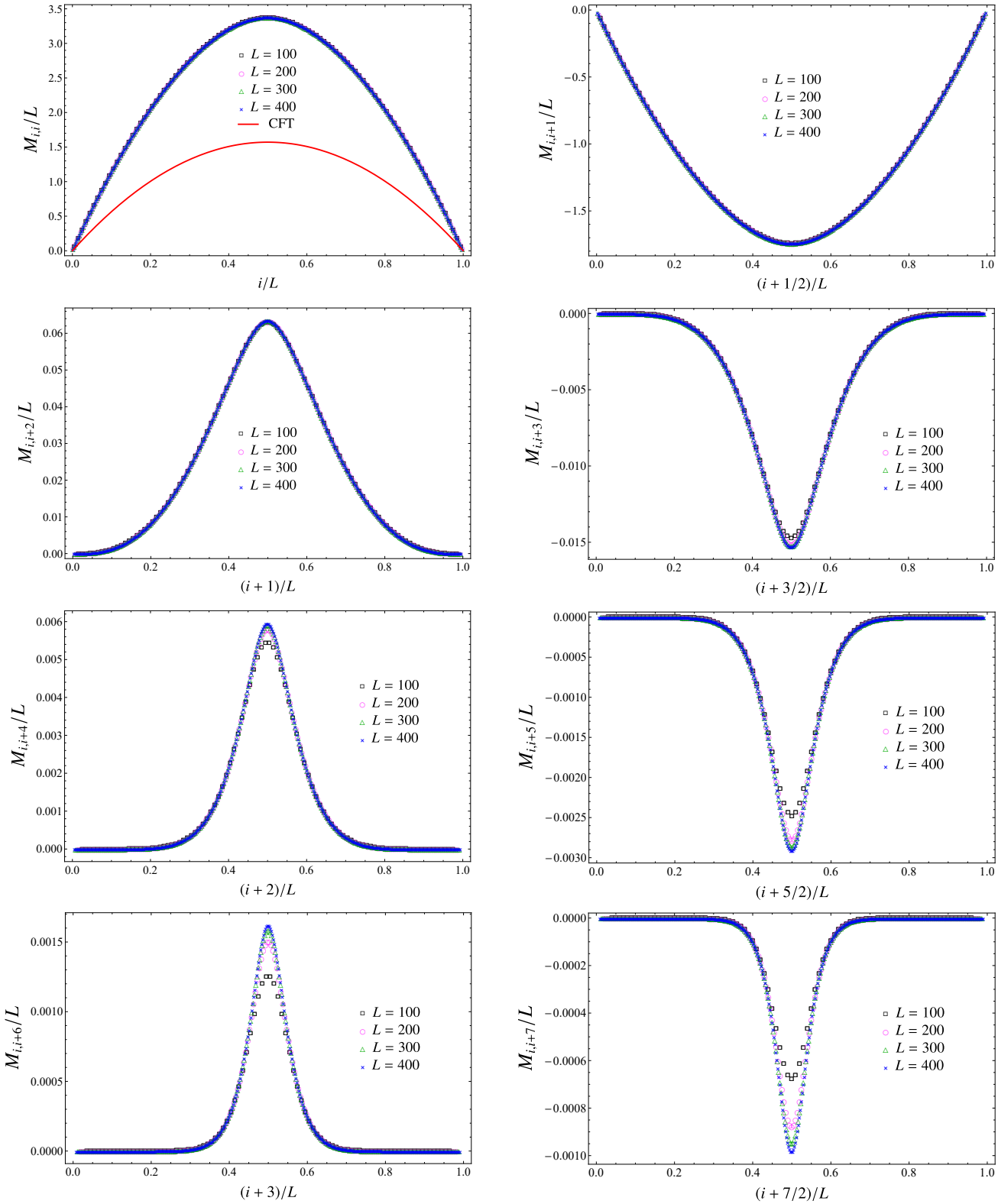

Figure 5.2: Diagonals of the matrix M (see (5.2.13)) when the subsystem is an interval made by L sites in the infinite line and $\omega L = 10^{-500}$. The red solid curve is the parabola (5.1.1).

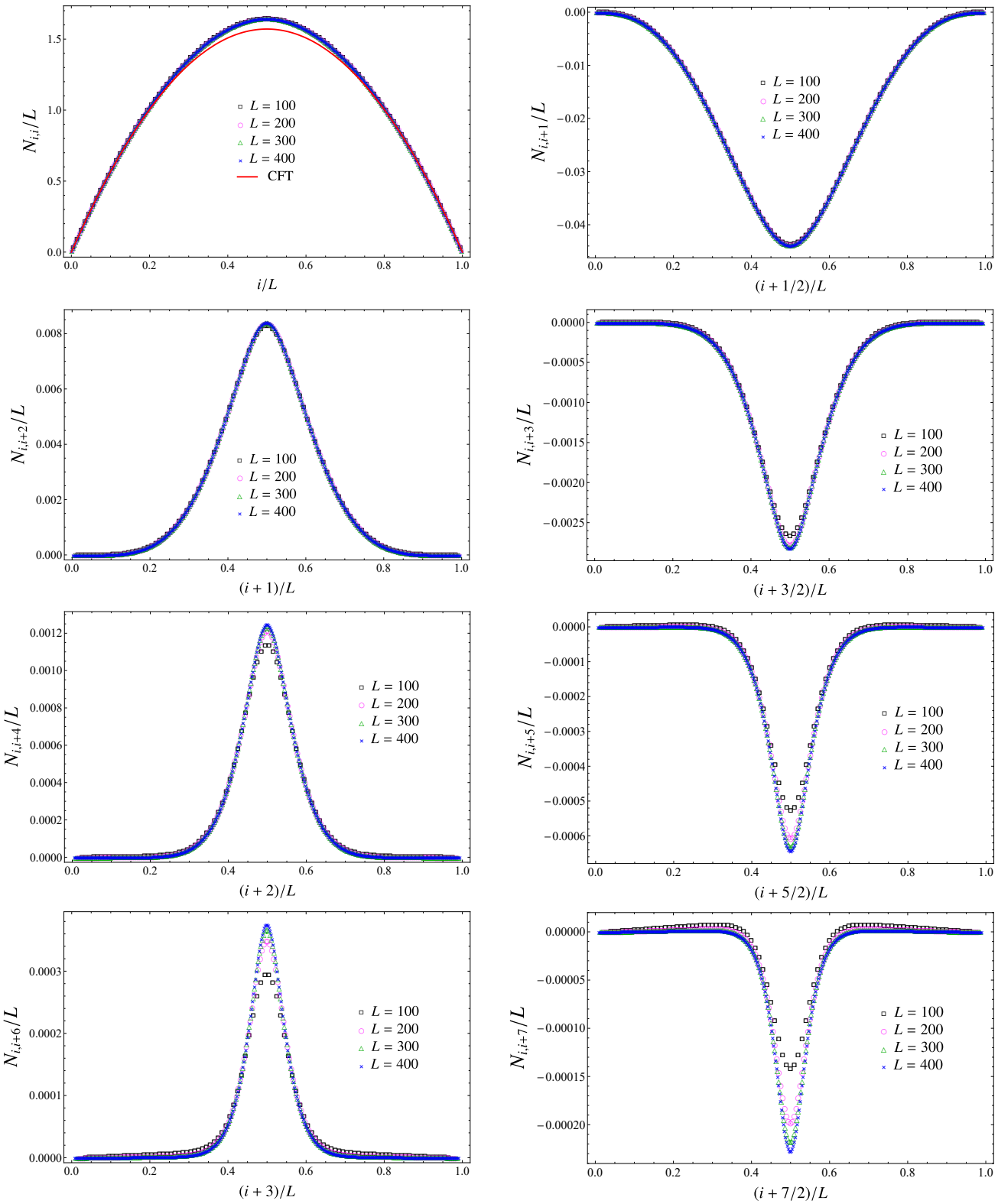

Figure 5.3: Diagonals of the matrix N (see (5.2.13)) when the subsystem is an interval made by L sites in the infinite line and $\omega L = 10^{-500}$. The red solid curve is the parabola (5.1.1).

by (5.2.7) and (5.2.8), but the procedure can be easily adapted to the ones given by (5.2.9) and (5.2.10) or by (5.2.11) and (5.2.12).

The continuum limit is defined through the infinitesimal ultraviolet (UV) cutoff a: it corresponds to take $a \to 0$ and $L \to \infty$ while $La = \ell$ is kept constant. The position within the interval is labelled by $x = ia$ with $0 < x < \ell$. This leads to write the independent variable in (5.2.13) as follows

$$x_k = \frac{x}{La} + \frac{ka/2}{La} \tag{5.3.1}$$

which tells that $\mu_k = \mu_k(x + ka/2)$ and $\nu_k = \nu_k(x + ka/2)$.

In the continuum limit, the fields $\Phi(x)$ and $\Pi(x)$ are introduced through the position and momentum operators as follows [296]

$$\hat{q}_i \;\longrightarrow\; \Phi(x) \qquad\qquad \hat{p}_i \;\longrightarrow\; a\,\Pi(x) \tag{5.3.2}$$

where the UV cutoff guarantees that these fields satisfy the canonical commutation relations in the continuum limit, where the delta function occurs. The operators $\hat{q}_{i+k}$ and $\hat{p}_{i+k}$ in (5.2.7) and (5.2.8) lead to fields whose argument is properly shifted. By employing (5.3.2) and the Taylor expansion as $a \to 0$, in the continuum limit it is straightforward to obtain that

$$\hat{q}_{i+k} \;\longrightarrow\; \Phi(x + ka) = \sum_{p \geqslant 0} \frac{(ka)^p}{p!}\, \partial_x^p \Phi(x) \tag{5.3.3}$$

and

$$\hat{p}_{i+k} \;\longrightarrow\; a\,\Pi(x + ka) = a \sum_{p \geqslant 0} \frac{(ka)^p}{p!}\, \partial_x^p \Pi(x)\,. \tag{5.3.4}$$

In (5.2.7) and (5.2.8) we find it convenient to insert the UV cutoff into the sums by writing them as $L\sum_{i=1}^{L}(\dots) = \frac{(La)}{a^2}\sum_{i=1}^{L}(\dots)a$ because $\sum_{i=1}^{L}(\dots)a \longrightarrow \int_0^\ell(\dots)dx$ in the continuum limit and the divergent factor L provides the factor ℓ. From (5.3.2), (5.3.3) and (5.3.4), for the operators (5.2.7) and (5.2.8) it is straightforward to obtain $\widehat{H}_M \longrightarrow H_M$ and $\widehat{H}_N \longrightarrow H_N$ respectively in the continuum limit, where

$$H_M = \frac{\ell}{a^2}\int_0^\ell \Big(\mu_0(x)\,\Phi(x)^2 + 2\sum_{k=1}^{k_{\max}} \mu_k(x + ka/2)\,\Phi(x)\,\Phi(x+ka) \Big) dx \tag{5.3.5}$$

$$H_N = \ell\int_0^\ell \Big(\nu_0(x)\,\Pi(x)^2 + 2\sum_{k=1}^{k_{\max}} \nu_k(x + ka/2)\,\Pi(x)\,\Pi(x+ka) \Big) dx \tag{5.3.6}$$

being $k_{\max}$ the number of diagonals to include in the sums occurring in these expressions.

In our numerical analysis the parameter $k_{\max}$ plays a crucial role which is discussed below in this subsection. Since $k_{\max} \to \infty$ in the continuum limit (see (5.3.3) and (5.3.4)), increasing values of $k_{\max}$ are considered. We find it worth remarking that the limit $L \to \infty$ in (5.2.13) is taken before the limit $k_{\max} \to \infty$. This implies that we have to consider the regime given by $k_{\max} \ll L$ in our numerical studies, where both L and $k_{\max}$ are finite.

Since $a \to 0$ in the continuum limit, we expand the integrands in (5.3.5) and (5.3.6) by keeping only the terms that could provide a non vanishing contribution after the limit. For (5.3.5) we obtain

$$\begin{aligned} H_M = \frac{\ell}{a^2}\int_0^\ell \Big\{ \mathcal{M}^{(0)}_{k_{\max}}(x)\,\Phi(x)^2 + a\sum_{k=1}^{k_{\max}} k\Big[\,\mu_k'(x)\,\Phi(x) + 2\,\mu_k(x)\,\Phi(x)'\,\Big]\Phi(x) \\ + a^2\sum_{k=1}^{k_{\max}} k^2\,\Big[\,\frac{1}{4}\,\mu_k''(x)\,\Phi(x) + \partial_x\Big(\mu_k(x)\,\Phi'(x)\Big)\,\Big]\,\Phi(x)\Big\}\,dx + O(a) \end{aligned} \tag{5.3.7}$$

where we have introduced the function

$$\mathcal{M}^{(0)}_{k_{\max}}(x) \equiv \lim_{L\to\infty} \frac{\mathsf{M}^{(0)}_{k_{\max}}(i)}{L} = \mu_0(x) + 2\sum_{k=1}^{k_{\max}} \mu_k(x) \tag{5.3.8}$$

defined by combining the diagonals of the symmetric matrix M as follows

$$\mathsf{M}^{(0)}_{k_{\max}}(i) \equiv M_{i,i} + 2\sum_{k=1}^{k_{\max}} M_{i,i+k}\,. \tag{5.3.9}$$

While the expansion (5.3.7) contains terms that are divergent if the corresponding weight functions are non vanishing, it is straightforward to notice that (5.3.6) is finite as $a \to 0$. Indeed, its Taylor expansion reads

$$H_N \;=\; \ell \int_0^\ell \mathcal{N}^{(0)}_{k_{\max}}(x)\, \Pi(x)^2\, dx + O(a) \tag{5.3.10}$$

where the function $\mathcal{N}^{(0)}_{k_{\max}}(x)$ is the combination of the functions $\nu_k(x)$ in (5.2.13) given by

$$\mathcal{N}^{(0)}_{k_{\max}}(x) \equiv \lim_{L\to\infty} \frac{\mathsf{N}^{(0)}_{k_{\max}}(i)}{L} = \nu_0(x) + 2\sum_{k=1}^{k_{\max}} \nu_k(x) \tag{5.3.11}$$

being $\mathsf{N}^{(0)}_{k_{\max}}(i)$ the same combination of the corresponding diagonals of the symmetric matrix N, namely

$$\mathsf{N}^{(0)}_{k_{\max}}(i) \equiv N_{i,i} + 2\sum_{k=1}^{k_{\max}} N_{i,i+k}\,. \tag{5.3.12}$$

Assuming that the integral and the discrete sums can be exchanged in the expression (5.3.7) for H_M, one notices that the integrand of the $O(1/a)$ term is the total derivative $\partial_x[\mu_k(x)\,\Phi(x)^2]$; hence its integration provides the boundary terms $[\mu_k(x)\,\Phi(x)^2]|_{x=0}^{x=\ell}$. These boundary terms vanish because $\mu_k(0) = \mu_k(\ell) = 0$ for the interval in the infinite line (see Fig. 5.2). As for the $O(1)$ term in (5.3.7), an integration by parts can be performed for the term whose integrand is $\Phi(x)\,\partial_x[\mu_k(x)\,\Phi(x)']$, and the resulting boundary terms vanish, again because $\mu_k(0) = \mu_k(\ell) = 0$. By employing these observations and discarding the $O(a)$ terms, the expression (5.3.7) can be written as follows

$$H_M = \frac{\ell}{a^2}\int_0^\ell \left\{ \mathcal{M}^{(0)}_{k_{\max}}(x)\,\Phi(x)^2 + a^2 \sum_{k=1}^{k_{\max}} k^2 \left[\frac{1}{4}\,\mu_k''(x)\,\Phi(x)^2 - \mu_k(x)\left(\Phi'(x)\right)^2 \right] \right\} dx\,. \tag{5.3.13}$$

Considering the integral whose integrand is $\mu_k(x)[\Phi'(x)]^2$ from the $O(1)$ term of this expression, we find it worth defining

$$\mathcal{M}^{(2)}_{k_{\max}}(x) \equiv \lim_{L\to\infty} \frac{\mathsf{M}^{(2)}_{k_{\max}}(i)}{L} \equiv \sum_{k=1}^{k_{\max}} k^2 \mu_k(x_k) \tag{5.3.14}$$

where, by using (5.2.13), we have introduced the following combination of diagonals of the symmetric matrix M

$$\mathsf{M}^{(2)}_{k_{\max}}(i) \equiv \sum_{k=1}^{k_{\max}} k^2 M_{i,i+k}\,. \tag{5.3.15}$$

As for the integral whose integrand is $\mu_k''(x)\,\Phi(x)^2$ in (5.3.13), we approximate the functions $\mu_k''(x)$ through finite differences because the analytic expressions of the functions $\mu_k(x)$ are not available. Thus, we have

$$a^2\mu_k''(x) = \mu_k(x+a) - 2\,\mu_k(x) + \mu_k(x-a)\,. \tag{5.3.16}$$

This expression and (5.2.13) naturally lead us to introduce

$$\mathcal{M}^{(2)}_{2,k_{\max}}(x) \equiv \lim_{L\to\infty} \frac{\mathsf{M}^{(2)}_{2,k_{\max}}(i)}{L} \equiv \sum_{k=1}^{k_{\max}} k^2 \mu_{2,k}(x_k) \tag{5.3.17}$$

where the subindex 2 indicates that these quantities are related to the second derivative of $\mu_k(x)$. In (5.3.17) we have defined the functions $\mu_{2,k}(x_k)$ as follows

$$\lim_{L\to\infty} \frac{M_{i+1,i+1+k} - 2M_{i,i+k} + M_{i-1,i-1+k}}{L} \equiv \mu_{2,k}(x_k) \tag{5.3.18}$$

and the combinations of matrix elements of M given by

$$\mathsf{M}^{(2)}_{2,k_{\max}}(i) \equiv \sum_{k=1}^{k_{\max}} k^2 \big(M_{i+1,i+1+k} - 2M_{i,i+k} + M_{i-1,i-1+k}\big)\,. \tag{5.3.19}$$

In the continuum limit $k_{\max}\to\infty$; hence we introduce the weight functions obtained by taking this limit in (5.3.8), (5.3.11), (5.3.14) and (5.3.17), namely

$$\mathcal{M}^{(0)}_{k_{\max}}(x) \;\longrightarrow\; \mathcal{M}^{(0)}_{\infty}(x) \qquad\qquad \mathcal{N}^{(0)}_{k_{\max}}(x) \;\longrightarrow\; \mathcal{N}^{(0)}_{\infty}(x) \tag{5.3.20}$$

and

$$\mathcal{M}^{(2)}_{k_{\max}}(x) \;\longrightarrow\; \mathcal{M}^{(2)}_{\infty}(x) \qquad\qquad \mathcal{M}^{(2)}_{2,k_{\max}}(x) \;\longrightarrow\; \mathcal{M}^{(2)}_{2,\infty}(x)\,. \tag{5.3.21}$$

Summarising, the continuum limit of the entanglement Hamiltonian (5.2.5) obtained from (5.2.7) and (5.2.8) is found by taking the limit $k_{\max}\to\infty$ of half of the sum of (5.3.10) and (5.3.13). By employing the functions introduced in (5.3.20) and (5.3.21), for the continuum limit of the entanglement Hamiltonian (5.2.5) we find

$$\begin{aligned}\frac{H_M + H_N}{2} \;=\; & \frac{\ell}{a^2}\int_0^\ell \frac{1}{2}\left[\,\mathcal{M}^{(0)}_{\infty}(x) + \frac{1}{4}\,\mathcal{M}^{(2)}_{2,\infty}(x)\right]\Phi(x)^2\,dx \\ & + \ell\int_0^\ell \frac{1}{2}\Big[\,\mathcal{N}^{(0)}_{\infty}(x)\,\Pi(x)^2 - \mathcal{M}^{(2)}_{\infty}(x)\big(\Phi'(x)\big)^2\,\Big]dx + O(a)\,.\end{aligned} \tag{5.3.22}$$

Since analytic results for the functions μ_k and ν_k are not available, we study the weight functions $\mathcal{M}^{(0)}_{\infty}(x)$, $\mathcal{M}^{(2)}_{2,\infty}(x)$, $\mathcal{N}^{(0)}_{\infty}(x)$ and $\mathcal{M}^{(2)}_{\infty}(x)$ in (5.3.22) by performing a numerical analysis of the combinations of the matrix elements of M and N defining them, which are given respectively by (5.3.9), (5.3.19), (5.3.12) and (5.3.15). These combinations depend on the number of sites L in the interval and on the parameter $k_{\max}$ labelling the number of diagonals to include in the sums. As already remarked above, we study the continuum limit by taking $L\to\infty$ first, in order to guarantee that the functions μ_k and ν_k in (5.2.13) are well defined, and then $k_{\max}\to\infty$. This means that we must keep $k_{\max}\ll L$ in our numerical analysis. If we had analytic expressions for the functions μ_k and ν_k, we could check whether they vanish fast enough as $k\to\infty$ to find convergence in the infinite sums defining the weight functions in (5.3.20) and (5.3.21), which occur in (5.3.22).

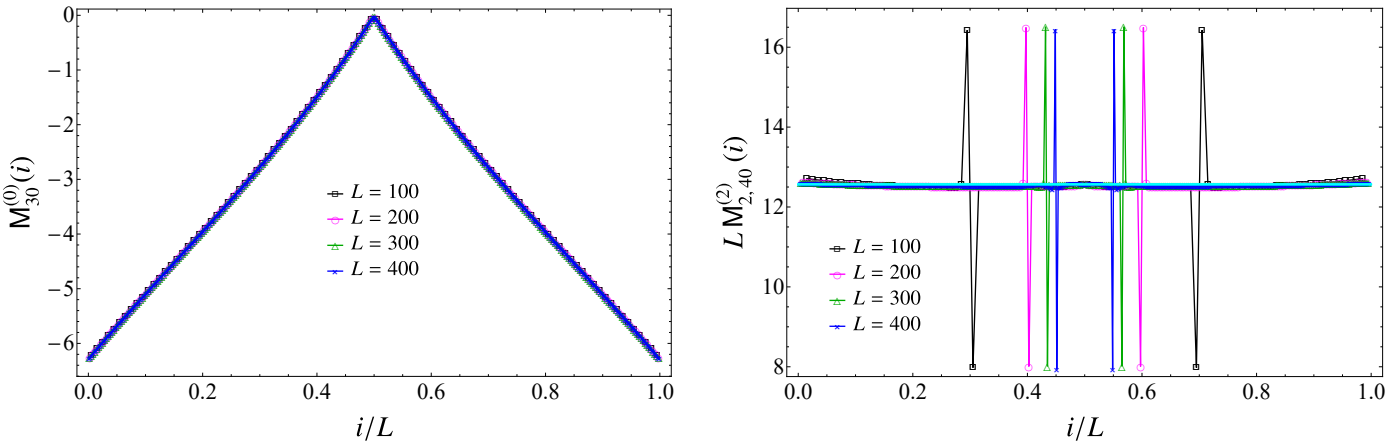

Figure 5.4: The combinations (5.3.23) (left) and (5.3.26) (right) when the subsystem is an interval made by L sites in the infinite line and $\omega L = 10^{-500}$. The cyan horizontal line in the right panel corresponds to 4π. The collapses of the data points for increasing values of L support (5.3.27).

It is important to observe that, since (5.3.9), (5.3.12), (5.3.19) and (5.3.15) can be evaluated only in the spatial range given by $1 \leqslant i \leqslant L - k_{\max}$, these combinations are not defined on the whole interval for finite values of L and $k_{\max}$. The numerical results for these combinations do not provide symmetric curves with respect to the center of the interval, as expected from the symmetry of the configuration, and they do not capture the CFT curve close to the right endpoint of the interval. This motivates us to employ decompositions of the operators $\widehat{H}_M$ and $\widehat{H}_N$ given in (5.2.11) and (5.2.12).

The procedure explained above to study the continuum limit of the entanglement Hamiltonian can be adapted straightforwardly to the case where the decompositions (5.2.11) and (5.2.12) are employed. The result is again (5.3.22), with the weight functions given by (5.3.20) and (5.3.21). The crucial difference with respect to the previous analysis is that, as $L \to \infty$, in (5.3.20) we have $\mathsf{M}^{(0)}_{k_{\max}}(i)/L \to \mathcal{M}^{(0)}_{k_{\max}}(x)$ with

$$\mathsf{M}^{(0)}_{k_{\max}}(i) \;=\; \begin{cases} M_{i,i} + 2\sum_{k=1}^{k_{\max}} M_{i,i+k} & 1 \leqslant i \leqslant L/2 \\ M_{i,i} + 2\sum_{k=1}^{k_{\max}} M_{i-k,i} & L/2+1 \leqslant i \leqslant L \end{cases} \tag{5.3.23}$$

and $\mathsf{N}^{(0)}_{k_{\max}}(i)/L \to \mathcal{N}^{(0)}_{k_{\max}}(x)$ with

$$\mathsf{N}^{(0)}_{k_{\max}}(i) \;=\; \begin{cases} N_{i,i} + 2\sum_{k=1}^{k_{\max}} N_{i,i+k} & 1 \leqslant i \leqslant L/2 \\ N_{i,i} + 2\sum_{k=1}^{k_{\max}} N_{i-k,i} & L/2+1 \leqslant i \leqslant L \end{cases} \tag{5.3.24}$$

while in (5.3.21) we have $\mathsf{M}^{(2)}_{k_{\max}}(i)/L \to \mathcal{M}^{(2)}_{k_{\max}}(x)$ with

$$\mathsf{M}^{(2)}_{k_{\max}}(i) = \begin{cases} \sum_{k=1}^{k_{\max}} k^2 M_{i,i+k} & 1 \leqslant i \leqslant L/2 \\ \sum_{k=1}^{k_{\max}} k^2 M_{i-k,i} & L/2+1 \leqslant i \leqslant L \end{cases} \tag{5.3.25}$$

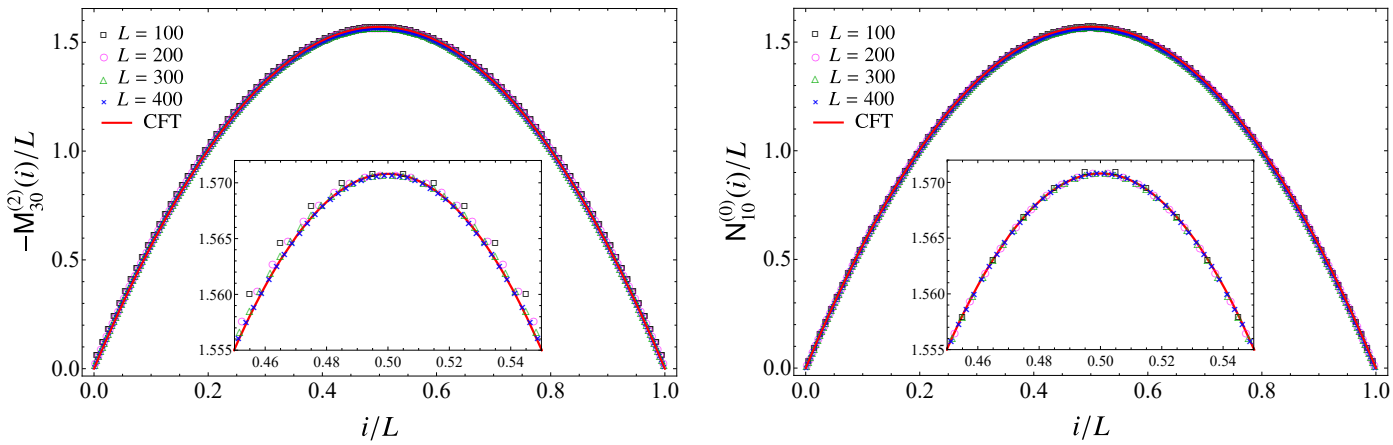

Figure 5.5: The combinations (5.3.25) (left) and (5.3.24) (right) when the subsystem is an interval made by L sites in the infinite line and $\omega L = 10^{-500}$. The collapses of the data points corresponding to increasing values of L support (5.3.28), with $\beta(x)$ given by the parabola (5.1.1) (red solid curve).

and $\mathsf{M}^{(2)}_{2,k_{\max}}(i)/L \to \mathcal{M}^{(2)}_{2,k_{\max}}(x)$ with

$$\mathsf{M}^{(2)}_{2,k_{\max}}(i) = \begin{cases} \sum_{k=1}^{k_{\max}} k^2 \big(M_{i+1,i+1+k} - 2M_{i,i+k} + M_{i-1,i-1+k}\big) & 1 \leqslant i \leqslant L/2 \\ \sum_{k=1}^{k_{\max}} k^2 \big(M_{i-k+1,i+1} - 2M_{i-k,i} + M_{i-k-1,i-1}\big) & L/2+1 \leqslant i \leqslant L\,. \end{cases} \tag{5.3.26}$$

The occurrence of two branches in these functions of the spatial index i (which originates from the splitting of the range $1 \leqslant i \leqslant L$ in (5.2.11) and (5.2.12)) guarantees that they are well defined on the entire interval for finite values of $k_{\max} \ll L$. The combinations of diagonals in (5.3.23), (5.3.24), (5.3.25) and (5.3.26) display the symmetry under reflection with respect to the center of the interval, which has been observed also for the diagonals of M and N (see Fig. 5.2 and Fig. 5.3).

In Fig. 5.4 we show some numerical results for the combinations in (5.3.23) and (5.3.26). From the left panel we observe that, when $k_{\max}$ is large enough, $\mathsf{M}^{(0)}_{k_{\max}}$ converges to a well defined function of $x/\ell \in (0,1)$. This observation allows to conclude that $\mathsf{M}^{(0)}_{k_{\max}}/L \to 0$ as $L \to \infty$ at any given value of $x/\ell \in (0,1)$. Similarly, the data reported in the right panel of Fig. 5.4 show that, when $k_{\max}$ is large enough, the product $L\,\mathsf{M}^{(2)}_{2,k_{\max}}$ for increasing values of L collapses on the horizontal line corresponding to 4π except for four isolated and finite picks in each curve, whose positions depend on L and whose heights are independent of L. The positions of these picks are symmetric with respect to the center of the interval and they move towards the center of the interval as L increases. These observations allow to conclude that $\mathsf{M}^{(2)}_{2,k_{\max}}/L \to 0$ as $L \to \infty$. Thus, the collapses of the data points observed in Fig. 5.4 for increasing values of L lead to conclude that for the weight functions occurring in the $O(1/a^2)$ term of (5.3.22) we should have

$$\mathcal{M}^{(0)}_{\infty}(x) = 0 \qquad \mathcal{M}^{(2)}_{2,\infty}(x) = 0\,. \tag{5.3.27}$$

The curves in Fig. 5.4 are obtained through the decompositions (5.2.11) and (5.2.12).

In Fig. 5.5 and Fig. 5.6 we report numerical results for the combinations in (5.3.24) and (5.3.25). Comparing these two figures, it is straightforward to conclude that the agreement between the numerical data and the CFT prediction $\beta(x)$ given by the parabola (5.1.1) (red solid curve) improves as $k_{\max} \ll L$ increases, i.e. by including more diagonals in the sums occurring in (5.3.24) and (5.3.25). The data reported in Fig. 5.4 and Fig. 5.5 correspond to the optimal values of $k_{\max}$, when

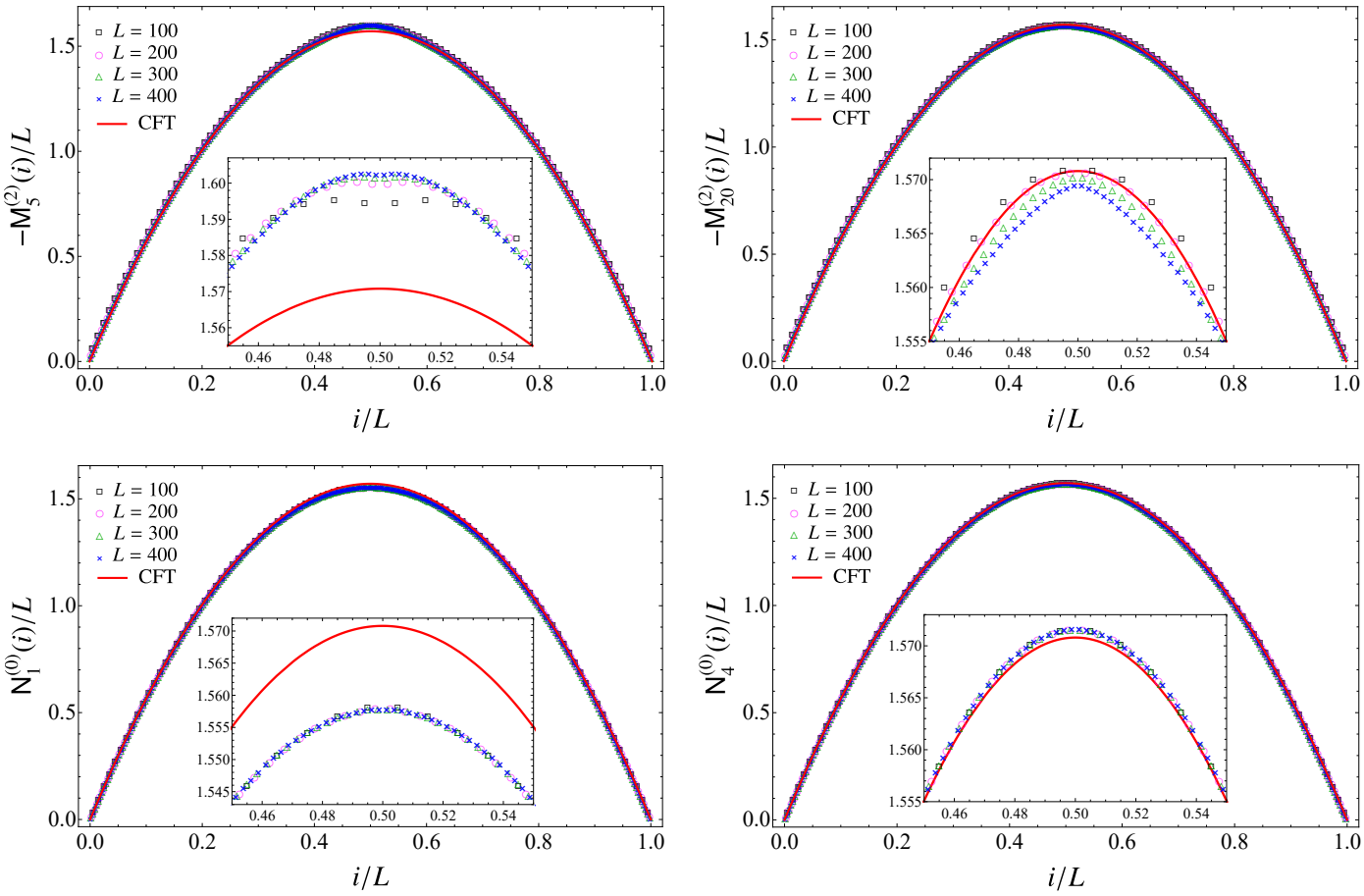

Figure 5.6: Role of the parameter $k_{\max}$ in the combinations (5.3.25) (top panels) and (5.3.24) (bottom panels) when the subsystem is an interval made by L sites in the infinite line and $\omega L = 10^{-500}$. The insets, which zoom in on the central part of the interval, show that the agreement with the CFT prediction given by the parabola (5.1.1) (red solid curve) improves as $k_{\max}$ increases.

the behaviours of the data become stable. These optimal values are different for the combinations involving M and N. From Fig. 5.6 we also observe a parity effect in k: the asymptotic curve for a given $k_{\max}$ is either above or below the CFT curve, depending on the parity of $k_{\max}$, and the distances between these curve decrease as $k_{\max}$ increases until the optimal value is reached. This parity effect in $k_{\max}$ is due to the fact that the k-th diagonals of M and N (i.e. $M_{i,i+k}$ and $N_{i,i+k}$ for a given k) have a definite sign determined by the parity of k (see Fig. 5.2 and Fig. 5.3) and that $\mathsf{M}^{(2)}_{k_{\max}}$ and $\mathsf{N}^{(0)}_{k_{\max}}$ are linear combinations of these diagonals through positive coefficients.

We remark that the data points reported in Fig. 5.4, Fig. 5.5 and Fig. 5.6 probe the entire interval A, including the neighbourhoods of the endpoints. Furthermore, the resulting curves are symmetric under reflection with respect to the center of the interval, as expected for this bipartition. These features support our choice to employ the combinations (5.3.23), (5.3.24), (5.3.25) and (5.3.26).

The collapses of the data points in Fig. 5.5 for increasing values of L lead to conjecture that the weight functions occurring in the finite term of (5.3.22) are

$$\mathcal{M}^{(2)}_{\infty}(x) = -\,\beta(x) \qquad\qquad \mathcal{N}^{(0)}_{\infty}(x) = \beta(x)\,. \tag{5.3.28}$$

Thus, by employing the numerical results (5.3.27) and (5.3.28) into the expression (5.3.22)

for the entanglement Hamiltonian of an interval in the infinite line, we find the CFT prediction (1.2.13) with $\beta(x)$ given by (5.1.1) and the energy density by (5.1.3).

We find it worth remarking that the height of the cyan horizontal line in the right panel of Fig. 5.4 corresponds to $4\pi = -\ell^2\beta(x)''$, being $\beta(x)$ the weight function (5.1.1) predicted by CFT. A naive explanation of this observation comes from the fact that $\mathsf{M}^{(2)}_{2,k_{\max}}$ is a combination obtained through a finite differences approximation of $\mu_k''(x)$ (see (5.3.19)) and that the combination $\mathsf{M}^{(2)}_{k_{\max}}$ of $\mu_k(x)$ provides $-\beta(x)$ in the continuum limit (see (5.3.28)). Nonetheless, an exchange of the second derivate of $\mu_k(x)$ with the discrete sum over k in (5.3.7) would provide an unexpected term containing Φ^2 multiplied by a constant weight function in the entanglement Hamiltonian. This leads us to conclude that exchanges between derivatives with respect to x and discrete sums over k are not allowed.

5.3.2 Entanglement spectrum

In a two dimensional CFT, the entanglement spectra of an interval for the bipartitions shown in Fig. 5.1 have been studied in [147] through methods of Boundary Conformal Field Theory (BCFT) [204–206,358–360] (see the brief discussion in Sec. 1.2.2). In the imaginary time description of the two dimensional spacetime underlying the bipartitions shown in Fig. 5.1, the UV cutoff ϵ can be introduced by removing an infinitesimal disk of radius ϵ around each entangling point [6,146,147,201]. For the interval in the infinite line (left panel of Fig. 5.1), the remaining spacetime has two boundaries which encircle the two endpoints of the interval A; hence it can be mapped into an annulus through a conformal transformation. Given the symmetry of this bipartition with respect to the center of the interval, the same conformal boundary condition must be imposed on the two boundaries.

For harmonic chains in Gaussian states, standard techniques allow to evaluate the entanglement spectrum in terms of the single particle entanglement energies ε_r, which are obtained from the symplectic spectrum of the reduced covariance matrix of the subsystem [4,10,103,178,191–201,361]. More precisely, given the elements σ_k, with $k = 1, \dots, L$, of the symplectic spectrum of $\gamma_A = Q_A \oplus P_A$, the single particle entanglement energies are obtained from (see also (2.4.7))

$$\varepsilon_k = 2\,\mathrm{arccoth}(2\,\sigma_k) = \log\left(\frac{\sigma_k + 1/2}{\sigma_k - 1/2}\right). \tag{5.3.29}$$

Once the single particle entanglement energies have been ordered as $\varepsilon_1 \leqslant \varepsilon_2 \leqslant \cdots \leqslant \varepsilon_L$, the gaps g_r introduced in (1.2.18) can be written as linear combinations $\sum_{k=1}^{L} n_k\,\varepsilon_k$ with non negative integer coefficients n_k.

In the top left panel of Fig. 5.7, we report some numerical results for ε_1. For a given finite value of L, we observe that $\varepsilon_1 \to 0$ as $\omega L \to 0$, while this does not happen for ε_r with $r > 1$. This leads us to assume that ε_1 vanishes in the comparison of the numerical data with the CFT predictions in the bottom panel of Fig. 5.7. In the top right panel of Fig. 5.7 we show the single particle entanglement energies ε_k/L in terms of k/L for some values of L and, if L is large enough, we find that the data having different L collapse on a well defined curve, that would be interesting to obtain analytically. Given the above assumption about ε_1, in the bottom panel of Fig. 5.7 we show the numerical data for the ratios g_r/g_1 of the gaps with respect to the first gap as functions of $\log L$. It is remarkable to observe that, as L increases, the values of g_r/g_1 with $1 \leqslant r \leqslant 29$ collapse on all the integers n with $1 \leqslant n \leqslant 6$ (we checked that $g_r/g_1 > 6.5$ when $r \geqslant 30$ for the largest value of L at our disposal). This originates from the fact that the single particle entanglement energies in the low-lying part of the spectrum are equally separated by a multiple integer of ε_2.

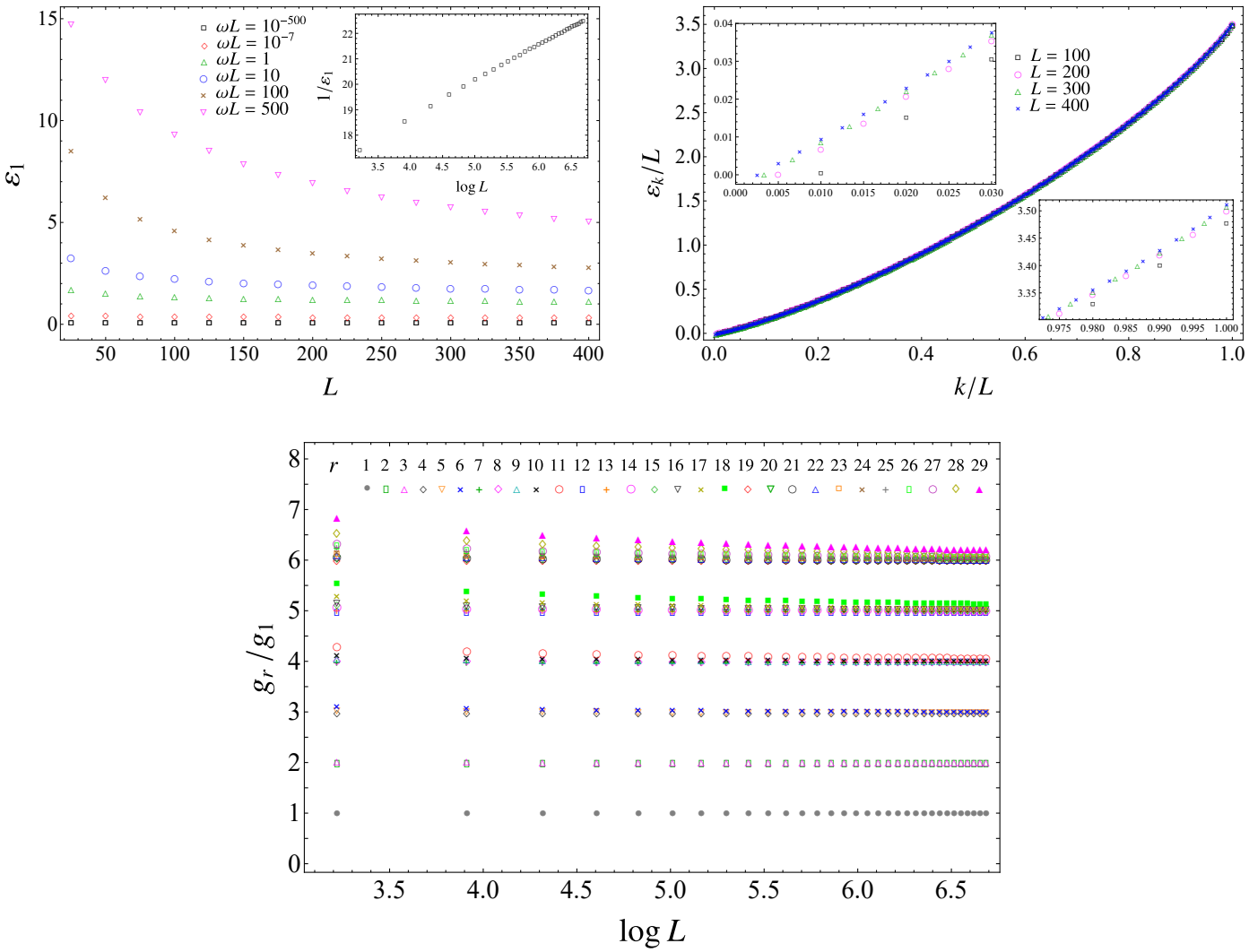

Figure 5.7: Entanglement spectrum for an interval in the infinite line. Top left: The smallest single particle entanglement energy ε_1 as function of the number of sites L of the interval, for increasing values of ωL. Top right: The single particle entanglement energies ε_k for different values of L (the insets zoom in on the lowest and on the highest values of k). Bottom: The ratios of the gaps g_r in the entanglement spectrum as functions of $\log L$ in the massless regime, i.e. when $\omega L = 10^{-500}$.

Furthermore, the degeneracy of the n-th level is given by the number of possible ways to partition the integer n.

These numerical results for g_r/g_1 are compatible with the conformal spectrum of the BCFT given by a free massless scalar field on the segment with either Dirichlet or Neumann boundary conditions imposed on both the endpoints of the segment [360, 362], but they cannot discriminate between these two possibilities. As discussed e.g. in [360], when the same boundary conditions is imposed on both the boundaries, the Laurent expansion of the holomorphic part of primary field $\partial_z\Phi(z)$ reads $\partial_z\Phi(z) = \sum_{n\in\mathbb{Z}} j_n\, J_n(z)$, being z the complex variable in Euclidean signature and where it is worth remarking that the index of the sum runs over the integer numbers. The functions $J_n(z)$ form an orthonormal basis and their explicit expressions depend on whether Neumann or Dirichlet boundary conditions are imposed. Since the Laurent modes satisfy the algebra $[j_m, j_n] =$

$m\,\delta_{m+n,0}$ in the proper normalisation, the ground state $|0\rangle$ can be introduced in such a way that $j_n|0\rangle = 0$ for $n \geqslant 0$ and the Hilbert space can be constructed by acting with j_n, with $n < 0$ on the ground state. The conformal dimension of the field associated to the state $j_{-n_1} \dots j_{-n_k}|0\rangle$ is $\sum_{l=1}^{k} n_l$ and this implies that the conformal spectrum contains the non negative integer numbers and the degeneracy of the level with dimension n is given by the number of ways to write n as a sum of integers.

The ambiguity between Neumann and Dirichlet boundary conditions can be resolved by considering the entanglement spectrum of an interval at the beginning of a semi-infinite line with Dirichlet boundary conditions, that will be discussed in Sec. 5.4.2. In terms of the primary fields and of their descendants, we observe the towers of the identity and of $\partial\Phi$.

The agreement found above with the spectrum of the BCFT of the free massless scalar field is expected only for the low-lying part of the entanglement spectrum.

5.4 Interval at the beginning of the semi-infinite line with Dirichlet b.c.

In this section we study the continuum limit of the entanglement Hamiltonian of L consecutive sites at the beginning of the massless harmonic chain on the semi-infinite line with Dirichlet boundary conditions at its endpoint. Focussing on the massless regime, in Sec. 5.4.1 we adapt the procedure explained in Sec. 5.3 to this case, finding the CFT prediction (1.2.13), with the weight function (5.1.2) and the energy density (5.1.4). The continuum limit of the entanglement spectrum is discussed in Sec. 5.4.2.

5.4.1 Entanglement Hamiltonian

We are interested in the bipartition of the semi-infinite line whose origin coincides with the left endpoint of the interval A made by L sites (see the right panel of Fig. 5.1), when the entire system is in its ground state. The entanglement entropy of this bipartition has been studied for various systems e.g. in [9, 363]. In the massless harmonic chain with Dirichlet boundary conditions, the entanglement Hamiltonian $\widehat{K}_A = (\widehat{H}_M + \widehat{H}_N)/2$ of this interval is given by (5.2.2) and (5.2.3), where the $L \times L$ matrices Q_A and P_A are the reduced correlation matrices introduced by restricting the indices i and j of the correlators (C.1.15) and (C.1.16) to the interval A at the beginning of the semi-infinite line (see the right panel of Fig. 5.1), i.e. to the integer values in $[1, L]$. The result for the continuum limit predicted by CFT is (1.2.13), with the weight function $\beta(x)$ given by (5.1.2) and the energy density (5.1.4) [357]. In the following we discuss a numerical procedure to obtain this CFT result.

The decompositions of the operators $\widehat{H}_M$ and $\widehat{H}_N$ introduced in Sec. 5.2 naturally lead to consider the k-th diagonals of the symmetric matrices M and N, like in the case of the interval in the infinite line discussed in Sec. 5.3.1. In the massless regime, we find numerical evidence that the limiting procedures defined in (5.2.13) provide well defined functions for any given value of k. This is shown in Fig. 5.8 and Fig. 5.9 for the k-th diagonal of the matrices M and N respectively, with $0 \leqslant k \leqslant 7$. Notice that, while the functions μ_k and ν_k vanish at the entangling point that separates A and B, they are non vanishing at the beginning of the semi-infinite line, where the Dirichlet boundary condition is imposed. It would be interesting to find analytic expressions for these functions. Like for the interval in the infinite line, these functions have a well defined sign given by the parity of k and the absolute value of their maximum significantly decreases as k increases.

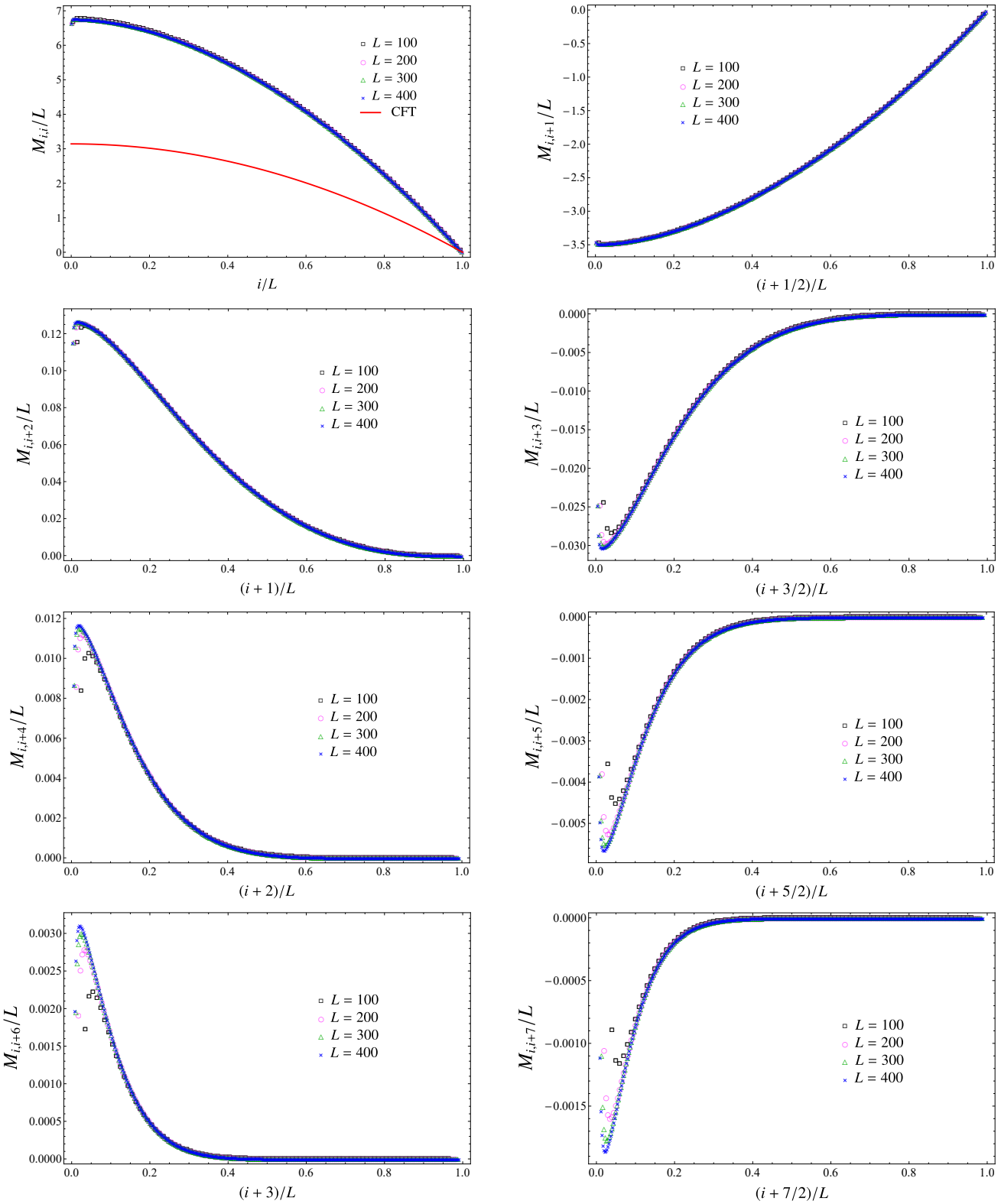

Figure 5.8: Diagonals of the matrix M (see (5.2.13)) when A is an interval with L sites at the beginning of the semi-infinite line and $\omega = 0$. The red solid curve is the half parabola (5.1.2).

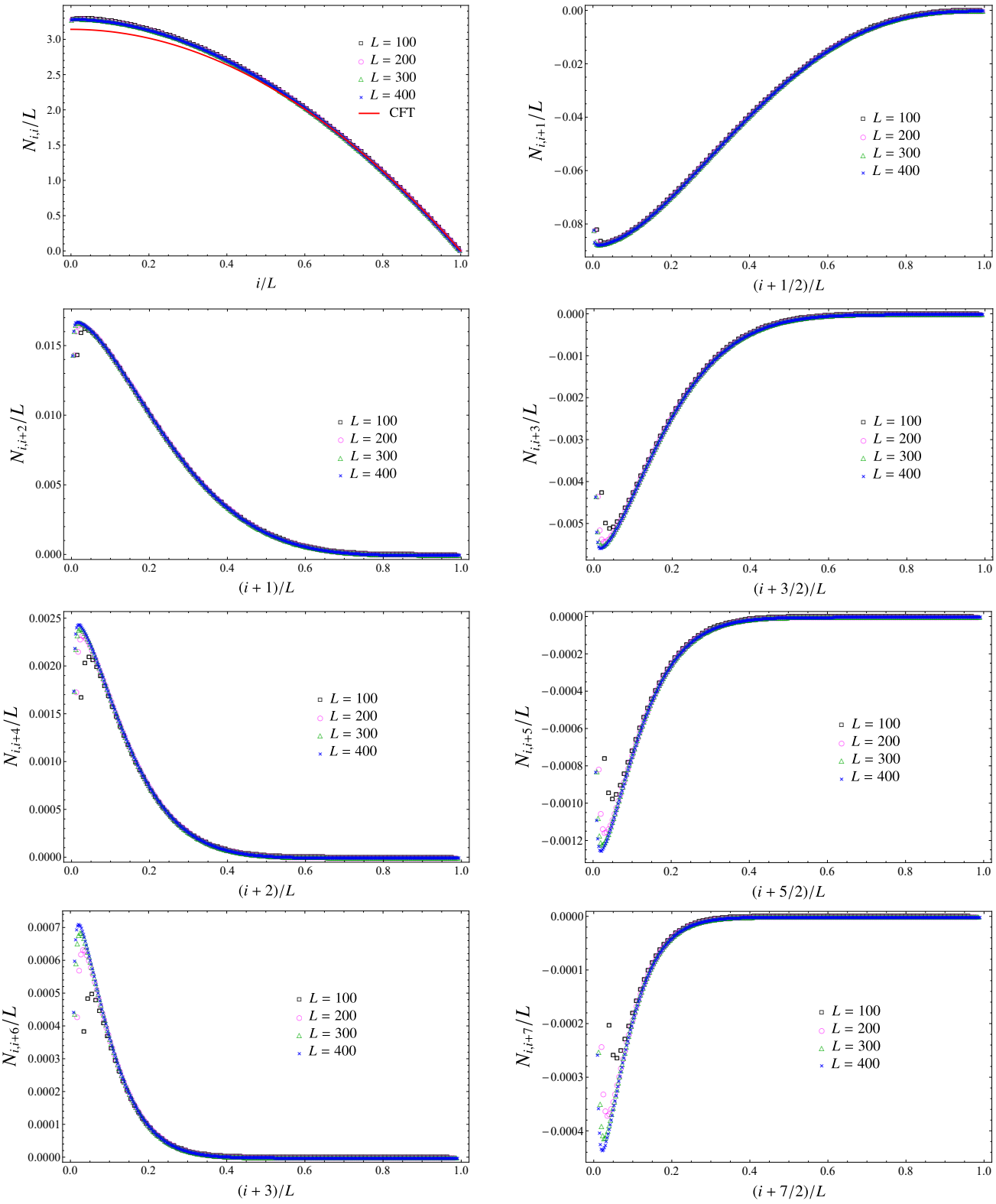

Figure 5.9: Diagonals of the matrix N (see (5.2.13)) when A is an interval with L sites at the beginning of the semi-infinite line and $\omega = 0$. The red solid curve is the half parabola (5.1.2).

Assuming the existence of the functions μ_k and ν_k defined in (5.2.13), the continuum limit of the entanglement Hamiltonian (5.2.5) can be studied by adapting to the bipartition that we are considering the procedure described in Sec. 5.3. Special care must be devoted to the boundary terms due to the integrations of a total derivative or to the integrations by parts. In particular, in (5.3.7) the integrand of the $O(1/a)$ term is the total derivative $\partial_x[\mu_k(x)\,\Phi(x)^2]$, whose integral over the interval gives the boundary terms $[\mu_k(x)\,\Phi(x)^2]|_{x=0}^{x=\ell}$. These boundary terms vanish because $\mu_k(\ell) = 0$ at the entangling point and the Dirichlet boundary condition $\Phi(0) = 0$ is imposed at the beginning of the semi-infinite line, where $\mu_k(0) \neq 0$. The remaining expression reads

$$H_M = \frac{\ell}{a^2} \int_0^\ell \mathcal{M}^{(0)}_{k_{\max}}(x)\,\Phi(x)^2\,dx \qquad (5.4.1)$$
$$+\,\ell \int_0^\ell \sum_{k=1}^{k_{\max}} k^2 \left[\frac{1}{4}\,\mu_k''(x)\,\Phi(x) + \mu_k'(x)\,\Phi'(x) + \mu_k(x)\,\Phi''(x) \right] \Phi(x)\,dx$$

where $O(a)$ terms have been discarded and $\mathcal{M}^{(0)}_{k_{\max}}(x)$ has been introduced in (5.3.8).

The $O(1)$ term in (5.4.1) is similar to the $O(1)$ term in (5.3.7) and the terms containing $\mu_k''(x)$ and $\mu_k(x)$ can be treated as discussed in Sec. 5.3.1. As for the term whose integrand is $\mu_k'(x)\,\Phi'(x)\,\Phi(x)$, we approximate $\mu_k'(x)$ through finite differences by writing $\mu_k'(x) = [\mu_k(x+a) - \mu_k(x)]/a$ because analytic expressions for $\mu_k(x)$ are not known. Combining this approximation with (5.2.13) and (5.4.1), we are naturally led to introduce

$$\mathsf{M}^{(2)}_{1,k_{\max}}(i) \equiv \sum_{k=1}^{k_{\max}} k^2 \big(M_{i+1,i+1+k} - M_{i,i+k} \big) \qquad (5.4.2)$$

and

$$\mathcal{M}^{(2)}_{1,k_{\max}}(x) \equiv \lim_{L\to\infty} \frac{\mathsf{M}^{(2)}_{1,k_{\max}}(i)}{L} \equiv \sum_{k=1}^{k_{\max}} k^2 \mu_{1,k}(x_k) \qquad (5.4.3)$$

being

$$\lim_{L\to\infty} \frac{M_{i+1,i+1+k} - M_{i,i+k}}{L} \equiv \mu_{1,k}(x_k) \qquad (5.4.4)$$

where the subindex 1 means that these quantities are related to the first derivative of the functions $\mu_k(x)$. Taking $k_{\max} \to \infty$ in (5.4.3), we find

$$\mathcal{M}^{(2)}_{1,k_{\max}}(x) \;\longrightarrow\; \mathcal{M}^{(2)}_{1,\infty}(x)\,. \qquad (5.4.5)$$

Notice that we can also follow the steps performed in Sec. 5.3.1 combining the last two terms within the square brackets in (5.4.1) into $\partial_x[\mu_k(x)\,\Phi(x)']$ and integrating by parts the corresponding integral, which provides the boundary terms $[\mu_k(x)\,\Phi'(x)\,\Phi(x)]|_{x=0}^{x=\ell}$. These terms do not contribute because $\mu_k(\ell) = 0$ at the entangling point and the Dirichlet boundary condition $\Phi(0) = 0$ holds at the beginning of the semi-infinite line.

Taking the limit $k_{\max} \to \infty$ in (5.4.1) and employing the weight functions introduced in (5.3.20), (5.3.21) and (5.4.5), for the non vanishing contributions to the continuum limit of the entanglement Hamiltonian we find

$$\frac{H_M + H_N}{2} = \frac{\ell}{a^2} \int_0^\ell \frac{1}{2} \left[\mathcal{M}^{(0)}_{\infty}(x) + \frac{1}{4}\,\mathcal{M}^{(2)}_{2,\infty}(x) \right] \Phi(x)^2\,dx \qquad (5.4.6)$$
$$+\,\ell \int_0^\ell \frac{1}{2} \Big[\mathcal{N}^{(0)}_{\infty}(x)\,\Pi(x)^2 + \mathcal{M}^{(2)}_{1,\infty}(x)\,\Phi'(x)\,\Phi(x) + \mathcal{M}^{(2)}_{\infty}(x)\,\Phi''(x)\,\Phi(x) \Big] dx\,.$$

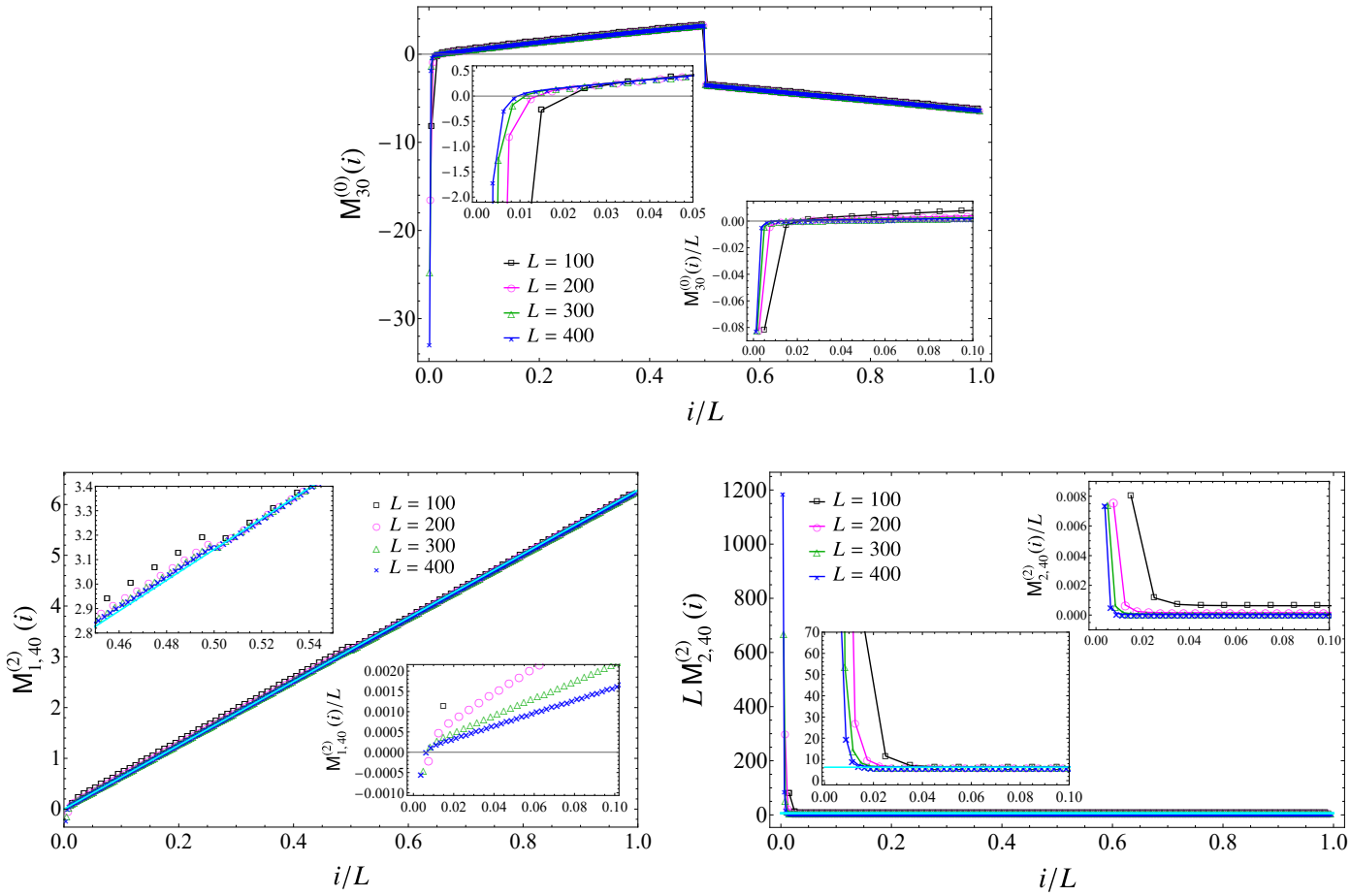

Figure 5.10: The combinations (5.3.23) (top), (5.4.7) (bottom left) and (5.3.26) (bottom right) when the subsystem is an interval made by L sites at the beginning of the semi-infinite line and $\omega = 0$. The cyan line in the bottom left panel corresponds to $2\pi(i/L)$, while the cyan horizontal line in the bottom right panel corresponds to 2π. The collapses of the data points for increasing values of L support (5.4.8).

We remark that, although some formal expressions occur also in the case of the interval in the infinite line in Sec. 5.3.1, their values depend on the system that we are exploring through the correlators (C.1.15) and (C.1.16).

For the interval at the beginning of the semi-infinite line, we also need the combination of the matrix elements of M for $\mathsf{M}^{(2)}_{1,k_{\max}}$ and it is not difficult to find that it reads

$$\mathsf{M}^{(2)}_{1,k_{\max}} = \begin{cases} \sum_{k=1}^{k_{\max}} k^2 \big(M_{i+1,i+1+k} - M_{i,i+k}\big) & 1 \leqslant i \leqslant L/2 \\ \sum_{k=1}^{k_{\max}} k^2 \big(M_{i-k+1,i+1} - M_{i-k,i}\big) & L/2+1 \leqslant i \leqslant L\,. \end{cases} \tag{5.4.7}$$

Like for the interval in the infinite line, the occurrence of two branches in (5.3.23), (5.3.24), (5.3.25) (5.3.26) and (5.4.7) allows to probe the entire interval. This cannot be done when the decompositions (5.2.7) and (5.2.8) are employed. Notice that, in contrast with Sec. 5.3.1, in this case the reflection symmetry with respect to the center of the interval is not expected.

In Fig. 5.10 we observe that the numerical data for $\mathsf{M}^{(0)}_{k_{\max}}(i)$, $\mathsf{M}^{(2)}_{1,k_{\max}}(i)$ and $L\,\mathsf{M}^{(2)}_{2,k_{\max}}(i)$ with $i \neq 1$ collapse on well defined curves when L increases. As for some of the weight functions

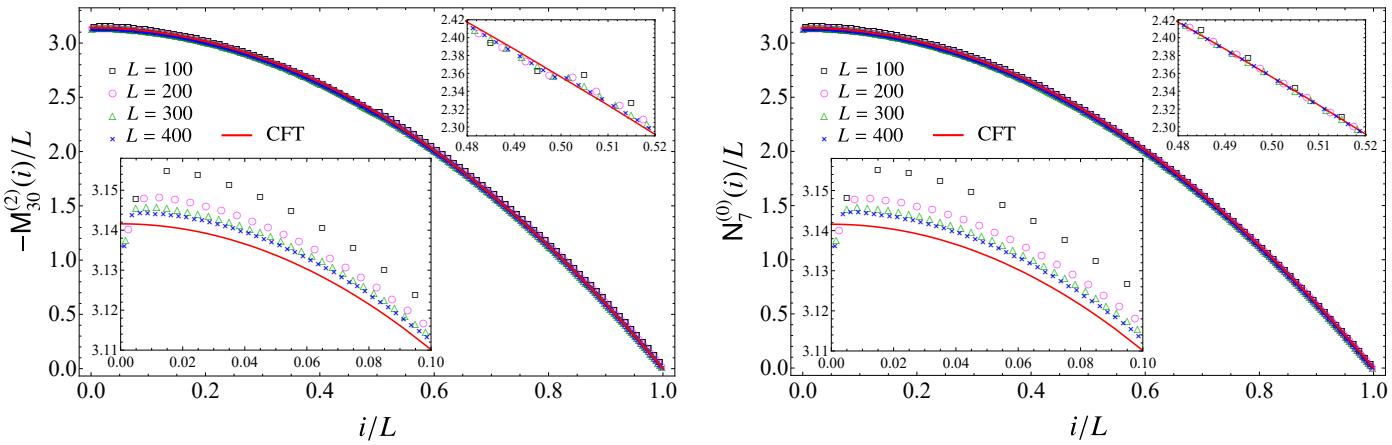

Figure 5.11: The combinations (5.3.25) (left) and (5.3.24) (right) when the subsystem is an interval made by L sites at the beginning of the semi-infinite line and $\omega = 0$. The collapses of the data points shown support (5.4.9), with $\beta(x)$ given by the half parabola (5.1.2) (red solid curve).

occurring in (5.4.6), these collapses support the following conjecture

$$\mathcal{M}^{(0)}_{\infty}(x) = 0 \qquad \mathcal{M}^{(2)}_{1,\infty}(x) = 0 \qquad \mathcal{M}^{(2)}_{2,\infty}(x) = 0 \tag{5.4.8}$$

for any fixed value of $x \in A$ such that $x \neq 0$. The insets on the right in all the panels of Fig. 5.10 highlight that the values of $\mathsf{M}^{(0)}_{k_{\max}}(i)/L$, $\mathsf{M}^{(2)}_{1,k_{\max}}(i)/L$ and $\mathsf{M}^{(2)}_{2,k_{\max}}(i)/L$ for $i = 1$ seem to converge to finite non vanishing constants. Since $\mathcal{M}^{(0)}_{\infty}(0)$, $\mathcal{M}^{(2)}_{1,\infty}(0)$ and $\mathcal{M}^{(2)}_{2,\infty}(0)$ are multiplied by $\Phi(0)$ in (5.4.6), the Dirichlet boundary condition $\Phi(0) = 0$ implies that this feature does not provide a non vanishing term in the continuum limit of the entanglement Hamiltonian. In the top panel of Fig. 5.10, the discontinuity in the center of the interval is due to the fact that $\mathsf{M}^{(0)}_{k_{\max}}$ in (5.3.23) is defined through two branches. This discontinuity is not observed if different decompositions for the operators $\widehat{H}_M$ and $\widehat{H}_N$ in (5.2.6) are adopted (see [], where these auxiliary analyses are reported).

In Fig. 5.11 we show $-\mathsf{M}^{(2)}_{k_{\max}}/L$ (left panel) and $\mathsf{N}^{(0)}_{k_{\max}}/L$ (right panel) for increasing values of L and an optimal value of $k_{\max}$ which guarantee certain stability of the numerical results. The collapses of the data points naturally lead to conjecture that

$$\mathcal{M}^{(2)}_{\infty}(x) = -\,\beta(x) \qquad\qquad \mathcal{N}^{(0)}_{\infty}(x) = \beta(x) \tag{5.4.9}$$

where $\beta(x)$ is the half parabola (5.1.2) predicted by the CFT. Comparing these results with the corresponding ones for the interval in the infinite line (see Fig. 5.5), we observe that larger values of L are needed in this case to reach the CFT curve in the neighbourhood of the beginning of the semi-infinite line, which is sensible to the boundary conditions.

In the bottom panels of Fig. 5.10, the data points for $\mathsf{M}^{(2)}_{1,k_{\max}}$ and $L\,\mathsf{M}^{(2)}_{2,k_{\max}}(i)$ with $i \neq 1$ collapse on the cyan straight lines, which correspond respectively to $2\pi\, x/\ell = -\ell\beta'(x)$ and to $2\pi = -\ell^2\beta''(x)$ when L is large enough. Similarly to the case of the interval in the infinite line (see the final remarks of Sec. 5.3.1), we can roughly justify this behaviour by noticing that $\mathsf{M}^{(2)}_{1,k_{\max}}$ and $\mathsf{M}^{(2)}_{2,k_{\max}}$ are obtained through finite differences approximations of $\mu'_k(x)$ and $\mu''_k(x)$ respectively; hence, from (5.4.9), one expects to find respectively $-\beta(x)'$ and $-\beta(x)''$. Also in this case exchanging the derivatives with respect to x with the discrete sums over k leads to wrong results, as already discussed in the final part of Sec. 5.3.1 for the interval in the infinite line.

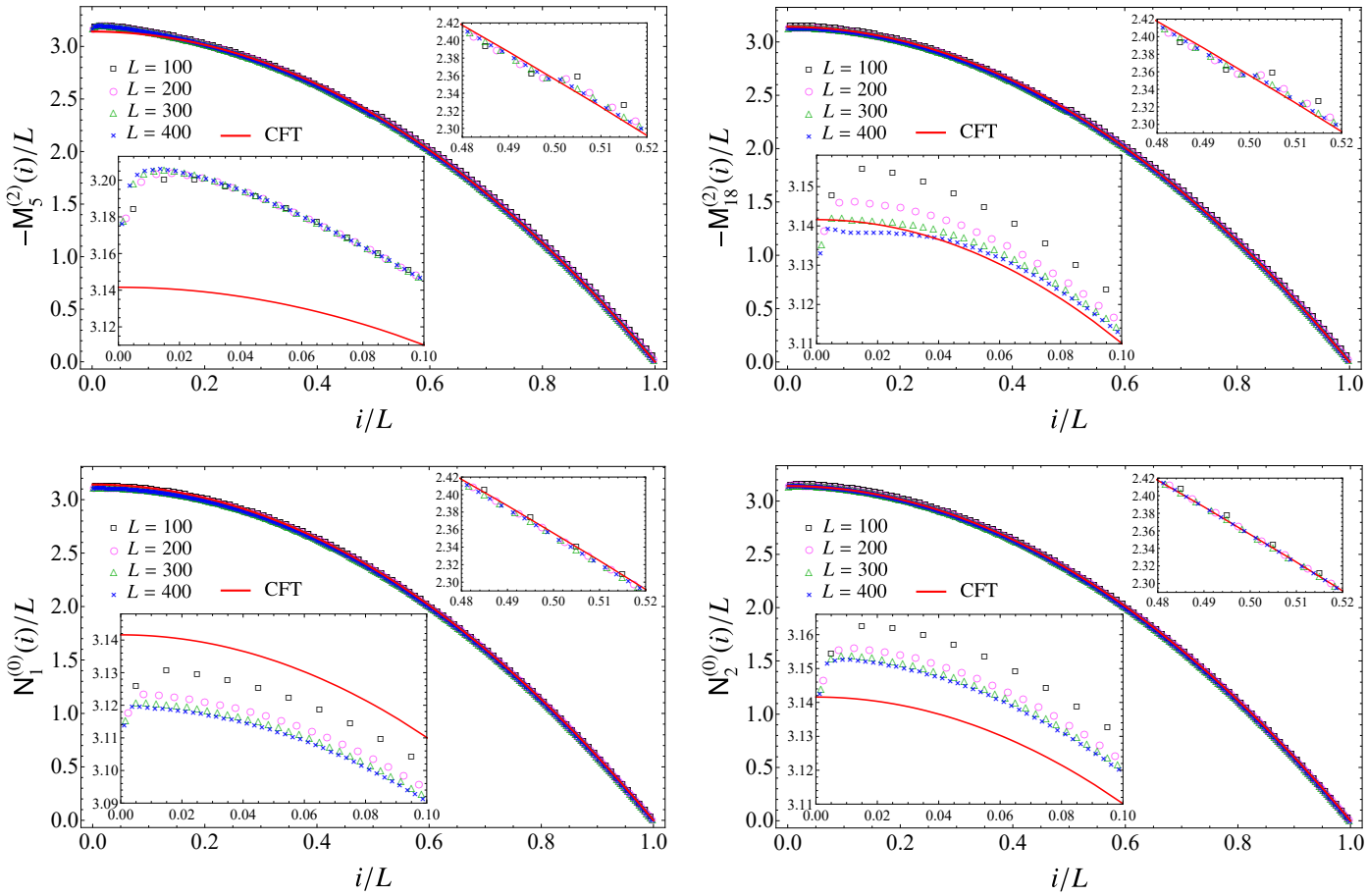

Figure 5.12: Role of the parameter $k_{\max}$ in the combinations (5.3.25) (top panels) and (5.3.24) (bottom panels) when the subsystem is an interval made by L sites at the beginning of the semi-infinite line and $\omega = 0$. The insets, which zoom in on the left endpoint and on the central part of the interval, show that the agreement with the CFT prediction given by the half parabola (5.1.2) (red solid curve) improves as $k_{\max}$ increases.

In Fig. 5.12 we show again $-\mathsf{M}^{(2)}_{k_{\max}}/L$ and $\mathsf{N}^{(0)}_{k_{\max}}/L$, but for lower values of $k_{\max}$ in order to highlight the fact that the collapse of the numerical data onto the CFT curve improves as $k_{\max}$ increases. This behaviour is stabilised around optimal values for $k_{\max}$ that correspond to the data reported in Fig. 5.11. Furthermore, we encounter the same parity effect observed in Fig. 5.6 and mentioned in Sec. 5.3.1, which is due also in this case to the fact that the k-th diagonals of M and N have a definite sign related to the parity of k (see Fig. 5.8 and Fig. 5.9).

5.4.2 Entanglement spectrum

The BCFT analysis of the entanglement spectrum presented in [147], where (1.2.18) has been derived, includes the case that we are considering, given by the entire system in its ground state and the interval A at the beginning of the semi-infinite line. In this bipartition only one entangling point occurs; hence the UV cutoff ϵ is introduced by removing only a disk of radius ϵ around the entangling point. The resulting euclidean spacetime has the topology of the annulus and in this case different conformal boundary conditions are allowed at the two boundaries. In our analysis we impose Dirichlet boundary conditions along the boundary corresponding to the beginning of

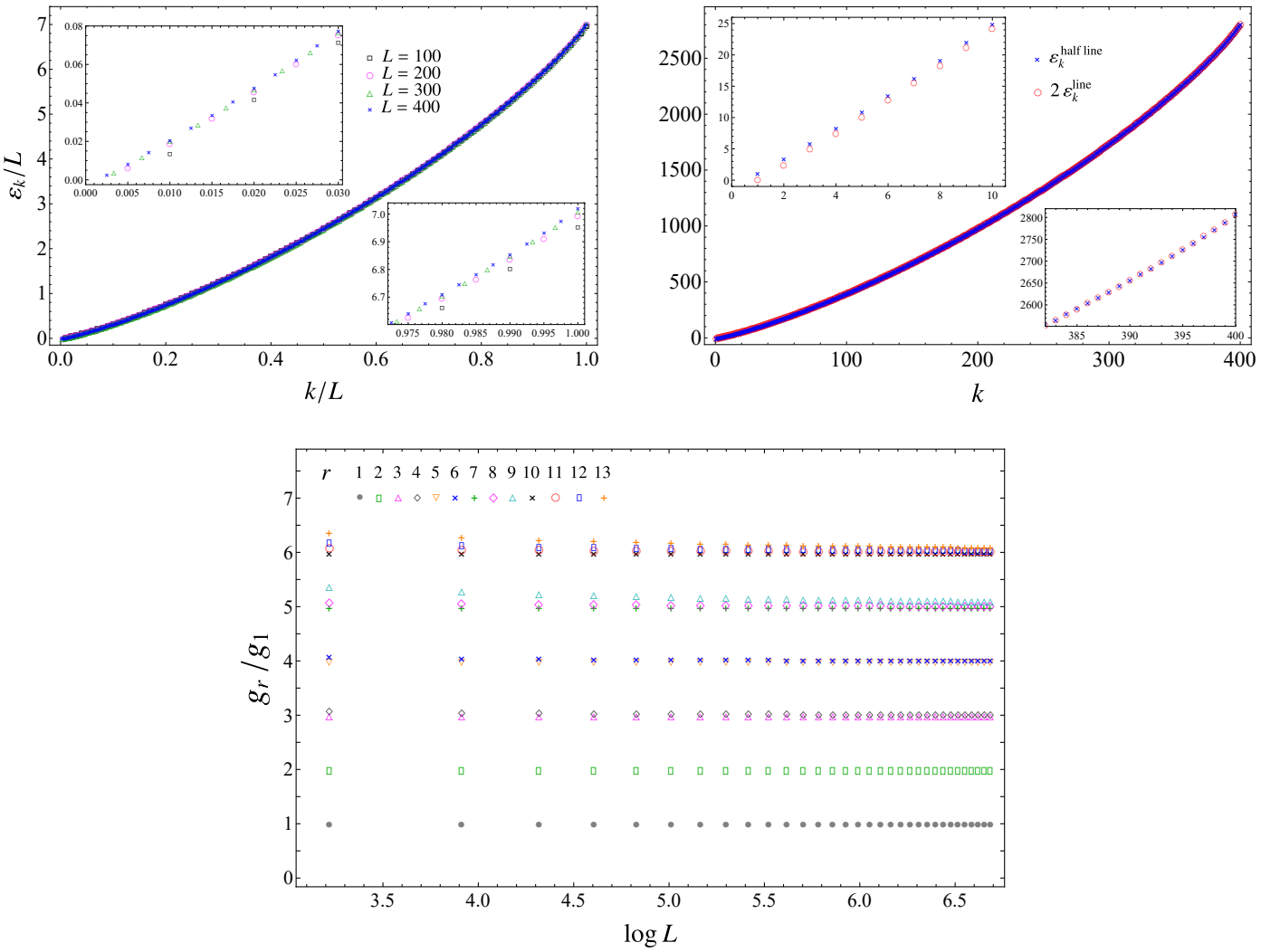

Figure 5.13: Entanglement spectrum for an interval at the beginning of the semi-infinite line with Dirichlet boundary conditions. Top left: The single particle entanglement energies ε_k for different values of L (the insets zoom in on the lowest and on the highest values of k). Top right: Comparison between the single particle entanglement energies ε_k for an interval with $L = 400$ sites at the beginning of the semi-infinite line with Dirichlet boundary conditions (see the top left panel) and the ones for an interval with $L = 400$ sites in the infinite line (see the top right panel of Fig. 5.7). Bottom: The ratios of the gaps in the entanglement spectrum as functions of $\log L$ when $\omega = 0$.

the semi-infinite line.

The numerical analysis of the entanglement spectrum is performed like in Sec. 5.3.2 and the crucial difference with respect to the interval in the infinite line is that the massless regime given by $\omega = 0$ is well defined. In this regime we observe that the lowest single particle entanglement energy ε_1 is non vanishing, in contrast with the case of the interval in the infinite line.

In the top left panel of Fig. 5.13 we show the numerical results for the single particle entanglement energies ε_k/L in terms of k/L corresponding to some values of L, finding that they nicely collapse on a well defined curve when L is large enough, like in the case of the interval in the infinite line (see the top right panel of Fig. 5.7). The curves obtained for these two spatial bipar-

titions are compared in the top right panel of Fig. 5.13, finding that they basically overlap, once the curve for the interval in the infinite line is multiplied by a factor of 2 (the insets highlight that this agreement is very good in the highest part of the spectrum and gets worse in the lowest part of the spectrum).

In the bottom panel of Fig. 5.13 we show the ratios g_r/g_1 between the generic gap g_r and the smallest gap g_1 in the entanglement spectrum as functions of $\log L$, for $1 \leqslant r \leqslant 13$. These ratios take all the integer values between 1 and 6 included (we checked that $g_r/g_1 > 6.5$ for $r > 13$ for the largest value of L at our disposal). This feature originates from the fact that in the low-lying part of the single particle entanglement spectrum the eigenvalues are equally separated by an integer multiple of ε_1 (see also Sec. 5.3.2). Comparing Fig. 5.13 and Fig. 5.7, it is straightforward to notice that g_r/g_1 take all the integer values for both the bipartitions, but the corresponding degeneracies are very different in the two cases. In particular, for the low-lying part of the single particle entanglement spectrum the ratios $\varepsilon_r/\varepsilon_1$ take the integer odd numbers $1, 3, 5, 7 \dots$ (see e.g. the top inset in the top right panel of Fig. 5.13). Plugging these values into the relation between ε_r and g_r, we find that g_r/g_1 take strictly positive integer values n whose the degeneracy is given by the number of ways to write n as a sum of positive integers that are not repeated (see the bottom panel of Fig. 5.13).

The degeneracy observed in Fig. 5.13 is compatible with the conformal spectrum of the BCFT given by the free massless scalar on a segment with mixed boundary conditions, namely with Dirichlet boundary conditions imposed at one endpoint and Neumann boundary conditions at the other endpoint [360, 362]. As discussed e.g. in [360], in this case the Laurent expansion that we need is given by $\partial_z \Phi(z) = \sum_{n \in \mathbb{Z}+\frac{1}{2}} j_n \tilde{J}_n(z)$, where the functions $\tilde{J}_n$ form an orthonormal basis different from the one mentioned in Sec. 5.3.2 and it is worth remarking that the index of the sum runs over half-integers. By constructing the Hilbert space as discussed in Sec. 5.3.2, now we have that the conformal dimensions associated to the different states can take both integer or half-integer values. Thus, by writing strictly positive integer or half-integer numbers as sums of half-integers, one finds that g_r/g_1 take strictly positive integer values n whose degeneracy is the number of ways to decompose n as a sum of non repeated strictly positive integers.

Since in our analysis Dirichlet boundary conditions are imposed at the beginning of the semi-infinite line, we can conclude that Neumann boundary conditions must be imposed at the boundary introduced by the regularisation procedure around the entangling point. This allows to fix the ambiguity found in Sec. 5.3.2, concluding that the numerical results for the entanglement spectrum of the interval in the infinite line in the continuum limit agree with the conformal spectrum of the BCFT given by the free massless scalar on a segment with Neumann boundary conditions imposed on both the boundaries encircling the endpoints of the interval in the euclidean spacetime. Also for this bipartition we expect that the agreement with the conformal spectrum of the BCFT holds only for the low-lying part of the entanglement spectrum.

5.5 Discussion

In this chapter we have performed a numerical analysis of the continuum limit of the entanglement Hamiltonians of a block made by L consecutive sites in massless harmonic chains, in the two cases where the subsystem is an interval in the infinite line or an interval at the beginning of the semi-infinite line with Dirichlet boundary conditions imposed at its endpoint. The procedure is based on the method introduced in [179, 192] for chains of free fermions, which has been adapted here to harmonic chains.

We have obtained the analytic expression (1.2.13) predicted by CFT, with the weight function $\beta(x)$ and the energy density $T_{00}(x)$ respectively given by (5.1.1) and (5.1.3) for the interval in the

infinite line and by (5.1.2) and (5.1.4) for the interval at the beginning of a semi-infinite line. A remarkable agreement between the data points and the weight functions $\beta(x)$ predicted by CFT is observed (see Fig. 5.5 and Fig. 5.11). It would be instructive to support our numerical results with analytic computations, by first finding analytic expressions for the functions $\mu_k(x)$ and $\nu_k(x)$ (see Fig. 5.2, Fig. 5.3 for the interval in the infinite line and Fig. 5.8 and Fig. 5.9 for the interval at the beginning of the semi-infinite line) and then by performing analytically the sums involving these functions and their derivatives which provide continuum limit of the entanglement Hamiltonians, as done in [179, 192] for the interval in the infinite chain of free fermions.

We have also explored the continuum limit of the entanglement spectra of these entanglement Hamiltonians, finding that the ratios of the low-lying gaps provide the ratios of the conformal dimensions of the BCFT given by the massless scalar on the annulus with the proper conformal boundary conditions, as predicted in [147] (see Fig. 5.7 and Fig. 5.13). The numerical results indicate that Neumann boundary conditions must be imposed along the boundaries introduced by the regularisation procedure. This is in agreement with a similar numerical analysis performed in lattice spin models [207], where it has been found that the numerical results for the entanglement spectra are compatible with the conformal spectra of BCFT with free boundary conditions imposed along the boundaries around the entangling points. This has been confirmed also by numerical studies out of equilibrium [209].

The results reported in this chapter can be extended in various directions. In massless harmonic chains, the entanglement Hamiltonians of an interval in a circle when the system is in its ground state or in the infinite line when the system is at finite temperature should be studied because in these cases (1.2.13) still holds and the weight functions $\beta(x)$ are known from CFT [147, 176, 178, 179]. It is also natural to explore the entanglement Hamiltonians for bipartitions involving disjoint intervals [180–182, 233–237, 299, 364–367], spatially inhomogeneous chains [177, 240, 368] and higher dimensional quantum systems [175]. It is important to find explicit expressions for the entanglement Hamiltonians in interacting lattice models, both through analytic and numerical methods [185–190, 202, 203, 260–262, 369]. Also the analysis of the entanglement spectra [207, 263, 361, 370–373] and of the contour for the entanglement entropies [27–29], which is a quantity strictly related to the entanglement Hamiltonian, deserves further analysis. It is useful also to study operators on the lattice that provides efficient approximations of the entanglement Hamiltonians [177, 374, 375].

Chapter 6

Entanglement Hamiltonians in gapped systems

6.1 Introduction

The entanglement Hamiltonians in free massive quantum field theories have still to be fully understood, even for simple bipartitions. For relativistic theories, the Bisognano-Wichmann theorem (1.2.11) holds even in presence of mass terms, but, when the subsystem A is not the half space, the lack of conformal invariance makes difficult obtaining results as the ones available for conformal field theories (CFTs) (see Sec. 1.2.2). Some analyses on the entanglement Hamiltonians in massive theories can be found, for instance, in [193, 200].

The goal of the present chapter is to characterise the entanglement Hamiltonian for an interval in chains *away* from criticality, and we do this by studying two free-particle models, namely a massive harmonic chain and a gapped fermionic chain. For the bosons, the frequency ω of each single oscillator is kept finite, while for the fermions a dimerization is introduced via alternating hopping matrix elements $t(1 \pm \delta)$. This corresponds to the Su-Schrieffer-Heeger model for polyacetylene in the absence of interactions [376, 377]. In both cases, the ground states have Gaussian nature and $\widehat{K}_A$ is a free-particle Hamiltonian which can be determined from the correlation functions of the chains [4, 191]. This is done with high-precision numerics which allows to treat large intervals. Both chains can also be related to integrable two-dimensional models which leads to explicit formulae for $\widehat{K}_A$ if the interval is half-infinite [4, 259, 262, 378].

We find that the basic pattern is always similar to the critical case: there are some dominant terms in $\widehat{K}_A$ whereas all others are much smaller. In the bosonic case, these are the diagonal matrix elements in the kinetic and in the potential energy (characterised by the matrices with entries given by $N_{i,j}$ and $M_{i,j}$ respectively) and the nearest-neighbour coupling in the latter, while in the fermionic model at half filling, it is the nearest-neighbour hopping. These quantities vanish linearly at the ends of the interval, and the linear behaviour extends more and more into the interior, as one moves away from criticality. In the end, the curves approach a triangular form instead of a parabola. This corresponds to a combination of the effects from the two boundaries, and the slopes are given correctly by the corner transfer matrix (CTM) results for the half-infinite subsystem [4,262]. Defining an approximate entanglement Hamiltonian with these dominant terms, one finds that, except at the upper end, its spectrum is identical to that of the true one. Therefore, it also gives the same entanglement entropy except very close to criticality. These features are completely analogous to those found for critical chains with a parabolic variation of the couplings in $\widehat{K}_A$ [375, 379, 380].

In the fermionic case, there is an additional feature due to the dimerization: the dimerization

pattern of the physical Hamiltonian is found again in the entanglement Hamiltonian, as already noted in [381]. The even and odd bonds differ, and this is particularly marked in the centre, but both show a trend towards a triangular variation as the dimerization increases.

The behaviour of the small matrix elements, which describe longer-range couplings, is more complex. They show spatial oscillations which are absent at criticality and can vanish outside a region around the middle of the interval. A particular subset corresponds to couplings across the centre. The region where they have relatively large values has its maximal extent when the correlation length is comparable to the size of the interval. Because of these features we were not able to obtain a consistent continuum picture near the critical point.

The layout of the chapter is as follows. In section 6.2, we describe the setting and give the basic formulae, in particular for the elements of the correlation functions. Section 6.3 presents explicit expressions for the entanglement Hamiltonians of half-infinite subsystems, which serve as points of reference for the case of an interval. In section 6.4, the numerical results for the elements in $\widehat{K}_A$ are presented for intervals in strongly non-critical oscillator chains and a simplified version of $\widehat{K}_A$ is discussed. In section 6.5, the same is done for the dimerized hopping chain. Section 6.6 is devoted to the general features of $\widehat{K}_A$ in the non-critical region, including long-range couplings across the middle of the interval, while section 6.7 sums up our findings and also addresses the question of a continuum limit.

Notations: in this chapter we follow the notations of [102], denoting by N the number of sites belonging to the subsystem A of the infinite chains that we study. This notation differs from the one employed in chapter 5, where the size of the subsystem A was denoted by L.

6.2 Setting

In this section, we describe the two chains we shall study and give the formulae from which the entanglement Hamiltonian $\widehat{K}_A$ of a subsystem A follows. If A is a subsystem made by N sites, the diagonal form of $\widehat{K}_A$ reads

$$\widehat{K}_A = \sum_{l=1}^{N} \varepsilon_l \, \hat{f}_l^\dagger \hat{f}_l \tag{6.2.1}$$

where $\hat{f}_l^\dagger$ and $\hat{f}_l$ are either bosonic or fermionic creation and annihilation operators and ε_l denote the single-particle eigenvalues. They are determined via elementary correlation matrices restricted to the given segment in the quantum chain at hand, with the relation depending on the particle statistics (for harmonic chains this has been reported in 5.3.29). In order to obtain the entanglement Hamiltonian in real space, the operators $\hat{f}_l^\dagger$ and $\hat{f}_l$ have to be transformed back into the original variables, which is again model dependent. In the following we present the two cases separately.

6.2.1 Harmonic chain

The harmonic chain on an infinite line is defined by the Hamiltonian (5.2.1). For simplicity, in our numerical calculations we shall set $\kappa = 1$ and $m = 1$, in (5.2.1), leaving a single parameter ω to be varied. As discussed in chapters 2 and 5, the ground state of the harmonic chain can be fully characterized by the correlation functions of positions and momenta. They can be obtained by standard computations and they have been reported in (C.1.5) and (C.1.6) respectively.

The procedure to compute the entanglement Hamiltonian has been discussed in Sec. 5.2. In particular, let us recall that $\widehat{K}_A$ can be written in the original position and momentum basis as

in (5.2.2). The matrix H_A in (5.2.2) can be decomposed into two blocks N and M which can be computed numerically through (5.2.3) in terms of the reduced correlation matrices Q_A and P_A. Moreover, the single-particle spectrum in (6.2.1) is obtained from [191]

$$(4P_AQ_A)\,\phi_l = \coth^2\left(\frac{\varepsilon_l}{2}\right)\phi_l\,, \qquad (4Q_AP_A)\,\psi_l = \coth^2\left(\frac{\varepsilon_l}{2}\right)\psi_l \tag{6.2.2}$$

where ϕ_l and ψ_l are respectively the right and left eigenvectors of the nonsymmetric matrix P_AQ_A. Let us stress that the single-particle spectrum can be equivalently obtained as discussed Sec. 5.3.2.

6.2.2 Dimerized hopping model

Our second model is a fermionic chain with dimerized hopping, given by the Hamiltonian

$$\hat{H} = -t\sum_{m=-\infty}^{\infty}\left(\frac{1-\delta}{2}\,\hat{c}^\dagger_{2m-1}\hat{c}_{2m} + \frac{1+\delta}{2}\,\hat{c}^\dagger_{2m}\hat{c}_{2m+1} + \text{h.c.}\right) \tag{6.2.3}$$

where $\hat{c}^\dagger_m$ and $\hat{c}_m$ are now fermionic creation and annihilation operators, satisfying canonical anti-commutation relations $\{\hat{c}_m, \hat{c}^\dagger_n\} = \delta_{m,n}$. The dimerization is governed by the parameter δ, where $\delta = 0$ corresponds to the homogeneous chain while $\delta = \pm 1$ is the fully dimerized limit, with every second hopping being zero. We set the overall hopping amplitude to $t = 1$. The Hamiltonian is two-site shift invariant and can be diagonalized after introducing Fourier modes on the two sublattices. This leads to a two-band structure of the dispersion $\omega_q = \pm\sqrt{\cos^2 q + \delta^2 \sin^2 q}$ within a reduced Brillouin zone $q \in [-\pi/2, \pi/2]$, with the excitation gap given by $2|\delta|$.

The half-filled ground state can be fully characterized in terms of the fermionic correlation matrix $\langle \hat{c}^\dagger_m \hat{c}_n\rangle$ which has a checkerboard structure. In particular, the only nonvanishing matrix elements beyond the diagonal $\langle \hat{c}^\dagger_m \hat{c}_m\rangle = 1/2$ are given by

$$\langle \hat{c}^\dagger_{2m-1}\hat{c}_{2n}\rangle = \mathcal{C}_r - \delta\,\mathcal{S}_r, \qquad \langle \hat{c}^\dagger_{2m}\hat{c}_{2n+1}\rangle = \mathcal{C}_r + \delta\,\mathcal{S}_r \tag{6.2.4}$$

where $r = 2n + 1 - 2m$ and we defined the integrals

$$\mathcal{C}_r = \int_{-\pi/2}^{\pi/2}\frac{dq}{2\pi}\frac{\cos qr\cos q}{\sqrt{\cos^2 q + \delta^2\sin^2 q}}\,, \qquad \mathcal{S}_r = \int_{-\pi/2}^{\pi/2}\frac{dq}{2\pi}\frac{\sin qr\sin q}{\sqrt{\cos^2 q + \delta^2\sin^2 q}}\,. \tag{6.2.5}$$

A closed form expression can also be found for the dimerized chain and reads for $n \geq m$ [382]

$$\langle \hat{c}^\dagger_{2m-1}\hat{c}_{2n}\rangle = k^{1/2}\mathcal{J}_{n-m}(k) + k^{-1/2}\mathcal{J}_{n-m+1}(k) \tag{6.2.6}$$

$$\langle \hat{c}^\dagger_{2m}\hat{c}_{2n+1}\rangle = k^{-1/2}\mathcal{J}_{n-m}(k) + k^{1/2}\mathcal{J}_{n-m+1}(k) \tag{6.2.7}$$

where we assumed $\delta > 0$ and introduced

$$\mathcal{J}_r(k) = (-1)^r\frac{k^{r+1/2}}{2}\,\frac{\Gamma(r+1/2)}{\Gamma(1/2)\,\Gamma(r+1)}\,{}_2F_1\big(1/2\,, r+1/2\,, r+1\,, k^2\,\big) \tag{6.2.8}$$

and the parameter k is now given by

$$k \equiv \frac{1-\delta}{1+\delta}\,. \tag{6.2.9}$$

The correlations thus depend on the dimerization only via the parameter $0 < k < 1$, which is related to the correlation length as $\xi^{-1} = -\ln k$.

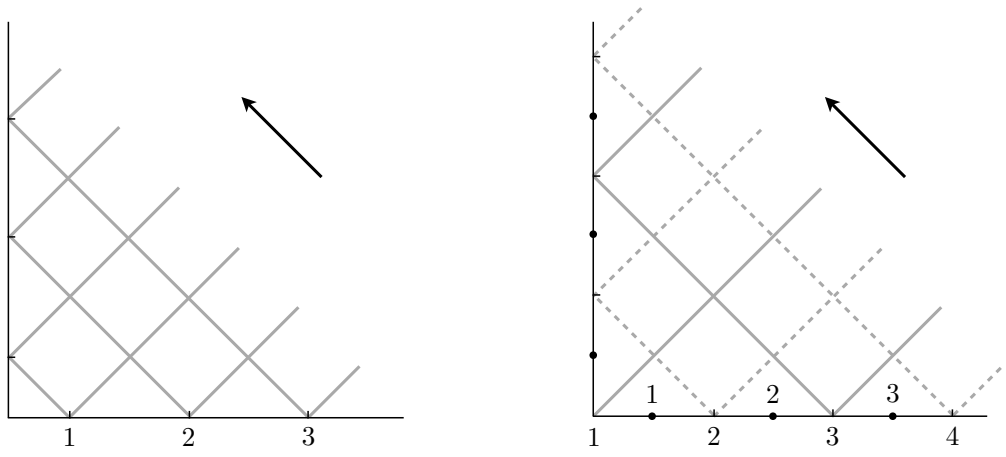

Figure 6.1: Corner transfer matrix geometries. Left: Gaussian model related to the oscillator chain. Right: Interpenetrating Ising models related to the dimerized hopping chain. Full circles show the location of the dual variables. The arrows indicate the direction of transfer.

The single-particle spectrum in (6.2.1) follows from the eigenvalues of the reduced correlation matrix C_A as [191]

$$(1 - 2C_A)\,\phi_l = \tanh\left(\frac{\varepsilon_l}{2}\right)\phi_l \tag{6.2.10}$$

which is the expression analogous to the bosonic case (6.2.2). Writing the entanglement Hamiltonian in the local fermionic basis

$$\widehat{K}_A = \sum_{i,j=1}^{N} H_{i,j}\,\hat{c}_i^\dagger \hat{c}_j \tag{6.2.11}$$

the matrix H follows as

$$H_{i,j} = \sum_{l=1}^{N} \phi_l(i)\;\varepsilon_l\;\phi_l(j) \tag{6.2.12}$$

where ϕ_l is the eigenvector corresponding to ε_l from (6.2.10).

6.3 Half-infinite subsystem

In this case, there are explicit expressions for the entanglement Hamiltonians which result from the relation of the chain problem to an integrable two-dimensional lattice model and the use of (infinite-size) corner transfer matrices in the latter. This provides a point of reference for the later treatment of finite subsystems and will therefore be discussed first.

6.3.1 Harmonic chain

The harmonic chain can be related to a Gaussian model on a square lattice as described in [194]. The necessary CTM was studied before in [383] and is shown in Fig. 6.1 on the left (see chapter 9 for an application of the CTM techniques to the study of the symmetry resolved entanglement). This leads to the following expression for the entanglement Hamiltonian of the half chain with

sites $i \geq 1$ if one chooses $m = 1$, $\kappa = \zeta$ and $\omega = 1 - \zeta$ in (5.2.1)

$$\widehat{K}_{\rm half} \,=\, 2I(\zeta') \sum_{i=1}^{\infty} \frac{1}{2} \Big[\,(2i-1)\,\hat{p}_i^2 + (2i-1)(1-\zeta)^2\,\hat{q}_i^2 + 2i\,\zeta\,\big(\hat{q}_{i+1} - \hat{q}_i\big)^2 \,\Big] \tag{6.3.1}$$

where $\zeta' = \sqrt{1-\zeta^2}$ and $I(\zeta)$ is the complete elliptic integral of the first kind which arises from the elliptic parametrisation of the couplings in the Gaussian model.

To get the result in the parametrisation $\kappa = 1$ with ω being independent, one needs to carry out the canonical transformation $\hat{p}_n \to (m\kappa)^{1/4}\,\hat{p}_n$ and $\hat{q}_n \to (m\kappa)^{-1/4}\,\hat{q}_n$. In terms of the rescaled variables one has

$$\widehat{K}_{\rm half} \,=\, 2I(\zeta')\,\sqrt{\zeta} \sum_{i=1}^{\infty} \frac{1}{2} \Big[\,(2i-1)\,\hat{p}_i^2 + (2i-1)\,\omega^2\,\hat{q}_i^2 + 2i\,\big(\hat{q}_{i+1} - \hat{q}_i\big)^2 \,\Big] \tag{6.3.2}$$

where the rescaled frequency reads

$$\omega^2 = (1-\zeta)^2/\zeta\,. \tag{6.3.3}$$

Note that since ω is now the free parameter of the Hamiltonian, the relation (6.3.3) must be inverted to get the elliptic parameter $\zeta(\omega)$. It is easy to see that the solution is given by

$$\zeta \equiv \frac{1}{4}\big(\sqrt{\omega^2+4} - \omega\,\big)^2. \tag{6.3.4}$$

Note that $0 < \zeta < 1$. In particular, $\zeta \to 1$ yields the critical point corresponding to the choice $\omega \to 0$.

The operator (6.3.2) has thus the same structure as the physical Hamiltonian, but the coefficients of the terms increase linearly as one moves into the subsystem. The matrices $N_{i,j}$ and $M_{i,j}$ introduced in (5.2.2) can be read off the expression, and the only non-zero elements are

$$N_{i,i} = b(\zeta)\,(2i-1)\,, \quad M_{i,i} = b(\zeta)\,(2i-1)\,(\omega^2+2)\,, \quad M_{i,i+1} = -b(\zeta)\,2i \tag{6.3.5}$$

with $b(\zeta) = 2I(\zeta')\sqrt{\zeta}$ and ζ given by (6.3.4) in terms of ω.

Finally, the bosonic single-particle eigenvalues ε_l are given by [194]

$$\varepsilon_l = \varepsilon\,(2l-1)\,, \qquad \varepsilon = \pi\frac{I(\zeta')}{I(\zeta)}\,, \quad l = 1,2,3,\ldots\,. \tag{6.3.6}$$

This result can be checked in the limit $\kappa \to 0$, where the last term in (6.3.1) vanishes and $\widehat{K}_{\rm half}$ becomes the sum of independent oscillators multiplied by factors $(2i-1)$.

6.3.2 Dimerized hopping chain

The entanglement Hamiltonian for this case has not been given before, but it can be obtained from known results for the transverse Ising (TI) chain. The reason is that the dimerized chain is an XX model in spin language which corresponds to two interlacing transverse Ising chains [384]. Consider the two TI Hamiltonians defined on odd resp. even lattice sites

$$\hat{H}_1 \;=\; -\sum_m \big(h_{2m-1}\,\hat{\sigma}^x_{2m-1} + \lambda_{2m-1}\hat{\sigma}^z_{2m-1}\hat{\sigma}^z_{2m+1}\big) \tag{6.3.7}$$

$$\hat{H}_2 \;=\; -\sum_m \big(h_{2m}\,\hat{\sigma}^x_{2m} + \lambda_{2m}\,\hat{\sigma}^z_{2m}\hat{\sigma}^z_{2m+2}\big) \tag{6.3.8}$$

where $\hat{\sigma}^x_n, \hat{\sigma}^z_n$ are Pauli matrices. Then, going over to dual variables via

$$\hat{\sigma}^z_m \hat{\sigma}^z_{m+1} = \hat{\tau}^z_m\,, \quad \hat{\sigma}^x_m = \hat{\tau}^x_{m-1}\hat{\tau}^x_m \tag{6.3.9}$$

the total Hamiltonian $\hat{H} = \hat{H}_1 + \hat{H}_2$ becomes

$$\hat{H} = -\sum_m \Big[(h_{2m}\hat{\tau}^x_{2m-1}\hat{\tau}^x_{2m} + \lambda_{2m-1}\hat{\tau}^z_{2m-1}\hat{\tau}^z_{2m}) + (h_{2m+1}\hat{\tau}^x_{2m}\hat{\tau}^x_{2m+1} + \lambda_{2m}\hat{\tau}^z_{2m}\hat{\tau}^z_{2m+1})\Big]. \tag{6.3.10}$$

Therefore one can make the interaction isotropic by choosing

$$h_{2m} = \lambda_{2m-1}, \quad h_{2m+1} = \lambda_{2m} \tag{6.3.11}$$

which means that the fields in one chain are the couplings in the other one and vice versa. With a rotation $\hat{\tau}^z \to \hat{\tau}^y$, the Hamiltonian assumes the form

$$\hat{H} = -\sum_m \Big[\lambda_{2m-1}(\hat{\tau}^x_{2m-1}\hat{\tau}^x_{2m} + \hat{\tau}^y_{2m-1}\hat{\tau}^y_{2m}) + \lambda_{2m}(\hat{\tau}^x_{2m}\hat{\tau}^x_{2m+1} + \hat{\tau}^y_{2m}\hat{\tau}^y_{2m+1})\Big] \tag{6.3.12}$$

and describes an inhomogeneous XX chain. The special choice

$$\lambda_{2m-1} = (1-\delta)\,, \qquad \lambda_{2m} = (1+\delta) \tag{6.3.13}$$

then leads to the operator (6.2.3) if one writes (6.3.12) in terms of fermions. The two TI chains involved are homogeneous but with interchanged parameters.

Now, a *single* TI chain with field h and coupling λ, is related to an isotropic two-dimensional Ising model on a square lattice with coupling K if $\lambda/h = \mathrm{sh}^2(2K)$, and the entanglement Hamiltonian follows from the appropriate CTM as in the bosonic case [262]. The operator $\widehat{K}_{\rm half}$ describes again a TI chain and differs somewhat for $\lambda/h < 1$ (disordered region) and $\lambda/h > 1$ (ordered region), see [385]. In the disordered region, it is

$$\widehat{K}_{\rm half} = -\,2I(k')\,\frac{1}{2}\sum_{i\geq 1}\Big[(2i-1)\,\hat{\sigma}^x_i + k\,2i\,\hat{\sigma}^z_i\hat{\sigma}^z_{i+1}\Big] \tag{6.3.14}$$

where $k = \lambda/h$ and $I(k)$ is the same quantity as before. In the ordered region, $k = h/\lambda$, and k appears in front of the first term in the brackets.

In the present case, one has two interpenetrating Ising lattices, one in the ordered and one in the disordered region. This leads to two interpenetrating CTMs, one with a tip and one without a tip, as shown in Fig. 6.1 on the right, see also [386]. As a result, the two operators in the exponent satisfy the condition (6.3.11) and after the dual transformation one has

$$\widehat{K}_{\rm half} = -\,2I(k')\,\frac{1}{2}\sum_{i\geq 1}\Big[\,k\,(2i-1)\,(\hat{\tau}^x_{2i-1}\hat{\tau}^x_{2i} + \hat{\tau}^y_{2i-1}\hat{\tau}^y_{2i}) + 2i\,(\hat{\tau}^x_{2i}\hat{\tau}^x_{2i+1} + \hat{\tau}^y_{2i}\hat{\tau}^y_{2i+1})\Big] \tag{6.3.15}$$

where now, using (6.3.13), the parameter k is given by $k = (1-\delta)/(1+\delta)$ as in (6.2.9). Writing this in terms of fermions, one arrives at the final result for a half-chain with sites $i \geq 1$

$$\widehat{K}_{\rm half} = -\,2I(k')\sum_{i\geq 1}\Big[\,k\,(2i-1)\,(\hat{c}^\dagger_{2i-1}\hat{c}_{2i} + \text{h.c.}) + 2i\,(\hat{c}^\dagger_{2i}\hat{c}_{2i+1} + \text{h.c.})\Big]. \tag{6.3.16}$$

This is a hopping model with hopping amplitudes which increase linearly and, in addition, alternate between 1 and k in exactly the same way as in the physical Hamiltonian (6.2.3) (if one divides $\hat{H}$ by $(1+\delta)$). Thus the pattern of strong and weak bonds reappears in the entanglement Hamiltonian,

as found in earlier numerical calculations [381]. Note that $\widehat{K}_{\rm half}$ in (6.3.16) starts with a weak bond between $i = 1$ and $i = 2$, i.e. the chain is divided at a strong bond. If one wants to consider the opposite situation, the factor k has to be moved to the other term in the bracket.

The fermionic single-particle eigenvalues ε_l of $\widehat{K}_{\rm half}$ are given by an expression as for a single TI chain and analogous to the bosonic case

$$\varepsilon_l = \varepsilon\, 2l\,, \qquad \varepsilon = \pi \frac{I(k')}{I(k)}\,, \quad l = 0, \pm 1, \pm 2, \pm 3, \ldots \tag{6.3.17}$$

where the factor $2l$ can be checked by taking the limit $k \to 0$ in (6.3.15) or (6.3.16). The pairs $(\varepsilon_l, \varepsilon_{-l})$ arise from the two TI operators in the original representation and the state with $l = 0$ is the analogue of the surface state one finds in the Hamiltonian $\hat{H}$ if the chain is actually cut at the strong bond. For a chain divided at a weak bond, one has to move the factor k as mentioned above, and this changes $2l$ into $2l - 1$ in the formula.

6.4 Interval in the harmonic chain

In this section we consider a finite block made by N consecutive sites in the harmonic chain and calculate the entanglement Hamiltonian numerically from the correlation matrices via (5.2.3). As mentioned earlier, we set $m = 1$ and $\kappa = 1$ in (5.2.1) so that only the oscillator frequency ω remains, from which ζ can be obtained via (6.3.4). The numerical data shown in Fig. 6.2, where $N = 200$ and $\omega = 1$, have been obtained through a numerical precision given by 800 digits, while for Fig. 6.3, where $N = 100$ and $\omega = 10$, we have employed 1000 digits. In general, we have observed that higher precision is required as N or ω increase.

In Fig. 6.2 the elements $N_{i,j}$ and $M_{i,j}$ in and near the diagonals of the matrices are shown for $\omega = 1$, which corresponds to $\zeta = 0.383$. From previous investigations [101] (see also chapter 5) one expects $\widehat{K}_A$ to be extensive, therefore the matrix elements are divided by N. Dividing also the site indices by N, one finds a perfect collapse of the data for $N = 100$ and $N = 200$ and thus a well-defined limiting behaviour.

In the kinetic energy, only the diagonal elements $N_{i,i}$ are large and show a variation with i which lies somewhere between a parabola and a triangular form. The next elements $N_{i,i+1}$ have a sharp cusp in the middle of the interval and are already an order of magnitude smaller. This cusp remains in the following elements which are still smaller and, in addition, develop more and more structures, including zeros which do not occur in the case of a critical chain, as shown in chapter 5 (see also [101]).

In the potential energy, the diagonal elements $M_{i,i}$ are again the largest ones, with a shape similar to that of $N_{i,i}$. However, here the nearest-neighbour terms $M_{i,i+1}$ are also large, negative and show a kind of plateau in the centre. Only the terms describing the interactions with more distant neighbours are much smaller and show structures resembling those in the kinetic terms. Note that we have plotted $-M_{i,i+r}$ for $r > 0$. These are the spring constants if one rewrites the potential energy properly and therefore typically positive.

A particular feature is that the structures in the small matrix elements only appear in a certain region in the centre of the subsystem, while the quantities are zero in the rest of the interval. This region is the same for all quantities and its width becomes smaller and approaches zero as ω increases, i.e. as the coupling between the oscillators in the chain becomes less important (see also Fig. 6.10).

In Fig. 6.3 we look at the three dominant matrix elements $N_{i,i}$, $M_{i,i}$ and $M_{i,i+1}$ in more detail. They are shown there for relatively large values of ω, ranging from $\omega = 1$ ($\zeta = 0.38$) to $\omega = 10$ ($\zeta = 0.01$) and one sees that all approach a triangular shape as ω increases. The dashed lines are

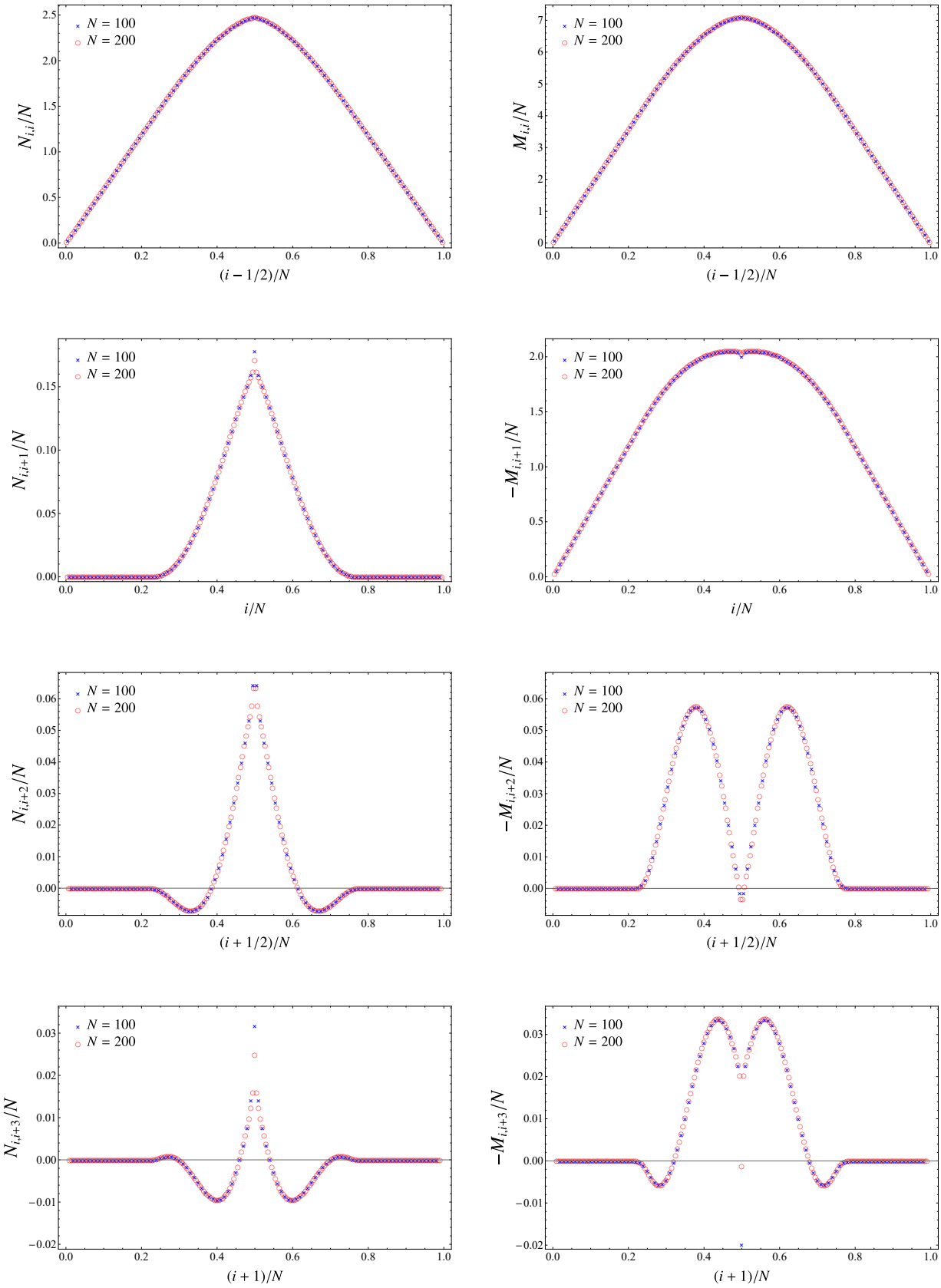

Figure 6.2: Short-range couplings $N_{i,j}$ (left panels) and $M_{i,j}$ (right panels) for $\omega = 1$ and two segment sizes. Note the different vertical scales.

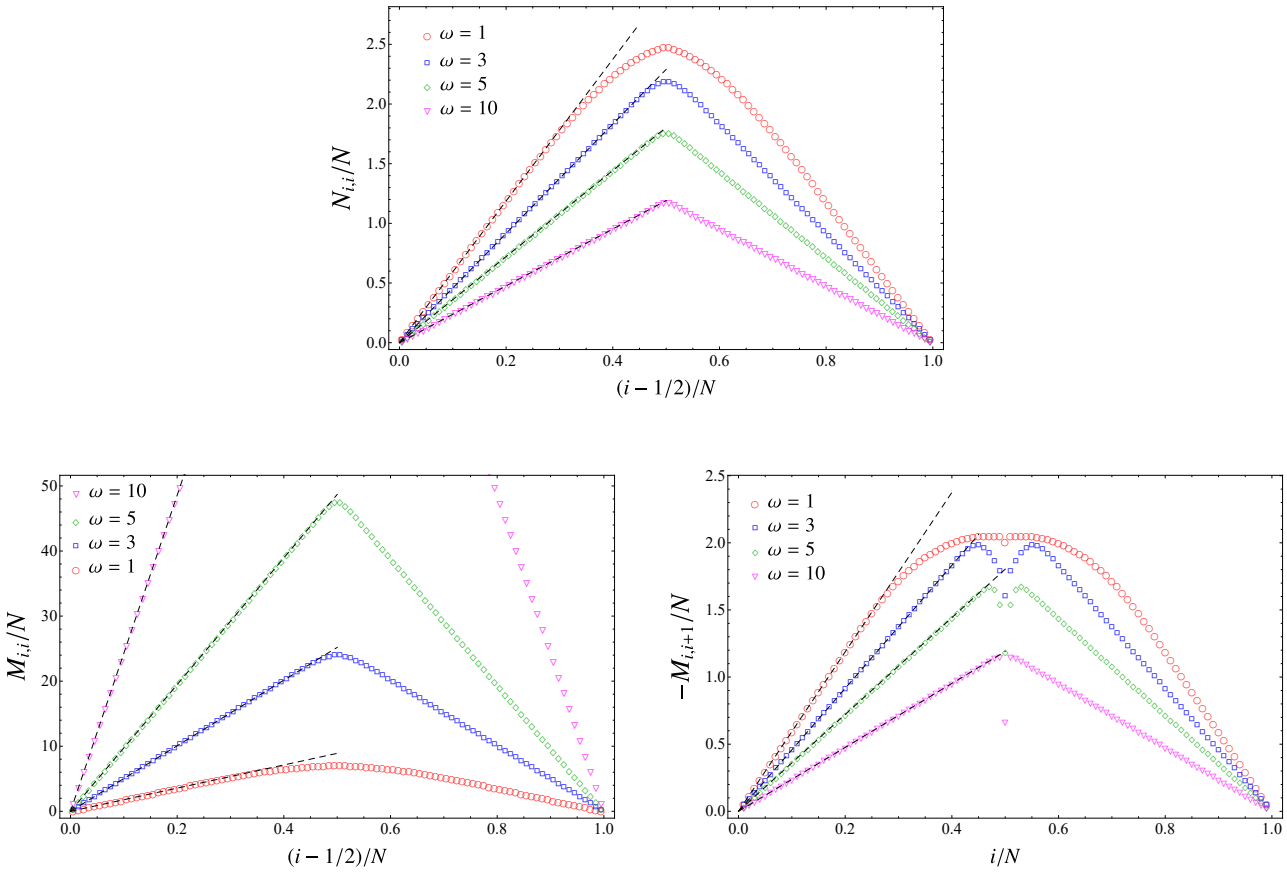

Figure 6.3: Dominant matrix elements $N_{i,j}$ and $M_{i,j}$ for $N = 100$ and various values of ω. The black dashed lines correspond to the three-diagonals approximation (6.4.1) and (6.4.2).

the slopes found in (6.3.5) for the half-infinite subsystem and describe the results very well. This suggests an approximation which consists in keeping only these elements and setting

$$\frac{N_{i,i}}{N} = 2\,b(\zeta)\,\Delta((i-1/2)/N) \tag{6.4.1}$$

and

$$\frac{M_{i,i}}{N} = 2\big(\omega^2+2\big)\,b(\zeta)\,\Delta((i-1/2)/N)\,, \qquad \frac{M_{i,i+1}}{N} = -\,2\,b(\zeta)\,\Delta(i/N) \tag{6.4.2}$$

with the "triangular" function

$$\Delta(x) \equiv \frac{1}{2} - \left|x-\frac{1}{2}\right| = \begin{cases} x & 0 \le x \le 1/2 \\ 1-x & 1/2 \le x \le 1 \end{cases} \tag{6.4.3}$$

replacing the simple linear behaviour in (6.3.5). In physical terms, this three-diagonals approximation models the entanglement Hamiltonian $\widehat{K}_A$ of the interval by glueing the half-infinite ones attached to the endpoints together. This should be good for small correlation lengths and the analytical expressions allow to predict how the slopes vary with ω. Since ζ decreases as ω becomes larger, $b(\zeta)$ also decreases while $\omega^2\,b(\zeta)$ increases.

While this approximation describes $\widehat{K}_A$ quite well, it neglects the structure in the nearest-neighbour coupling $M_{i,i+1}$ in the middle of the subsystem. This probably has to be seen together with the features in the small longer-distance couplings.

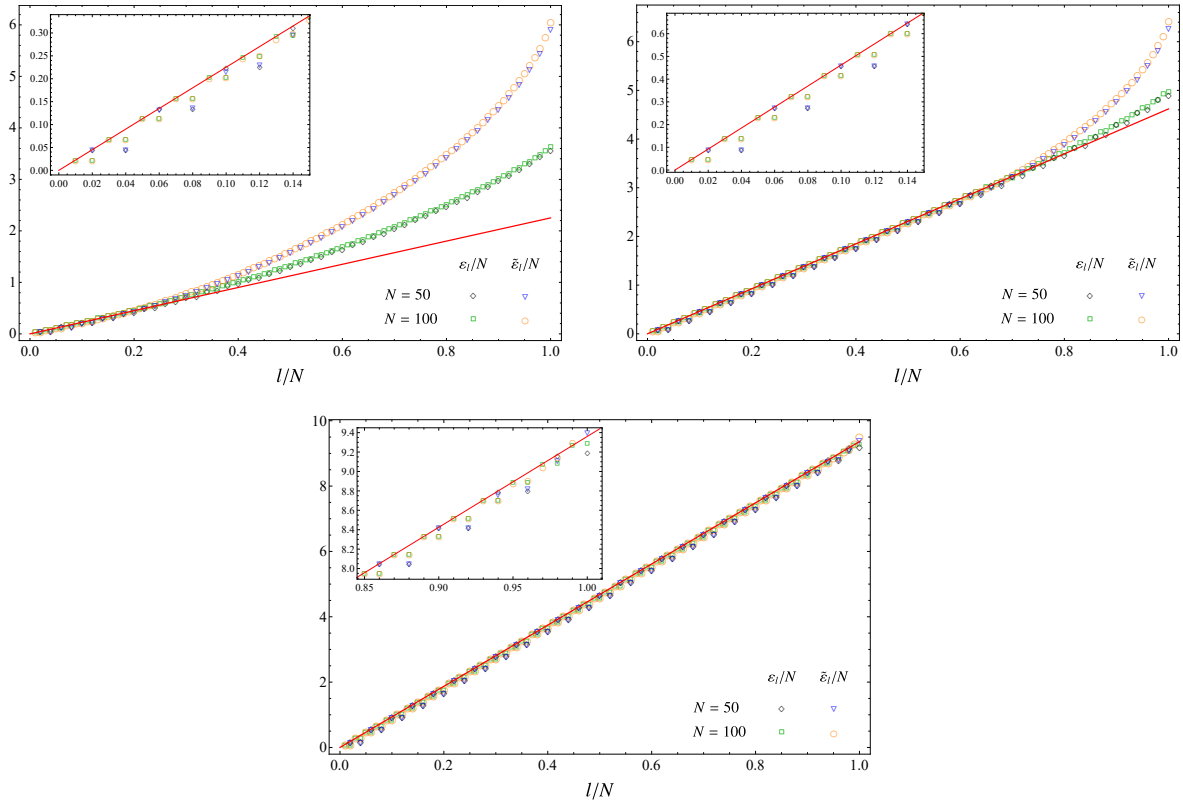

Figure 6.4: Exact ε_l and approximate $\tilde{\varepsilon}_l$ single-particle entanglement eigenvalues for $\omega = 0.1$ (top left), $\omega = 1$ (top right) and $\omega = 5$ (bottom). The slope of the red solid straight line is given by ε in (6.3.6).

Finally, we turn to the single-particle spectra ε_l which follow from the eigenvalues of the matrix $P_A Q_A$ according to (6.2.2). They are shown in Fig. 6.4 for three typical values of ω. As $\widehat{K}_A$ scales with N, so do the ε_l, and a plot ε_l/N vs. l/N gives a universal curve for large N. Basically, the ε_l increase at first linearly with l, but for large l there is an upward bend. This sets in early for small ω and late for larger ω. Already for $\omega = 5$ the behaviour is just linear. The full lines are the results of (6.3.6) and are seen to describe the (initial) slope very well. A closer look at the smaller eigenvalues for $\omega = 0.1$ and $\omega = 1$ is provided by the insets and shows that they are doubly degenerate, as one would expect if one associates them with the two boundaries. The degenerate levels are described by the half-chain formula (6.3.6). As the dispersion bends, the degeneracy is also lost.

In Fig. 6.4 the eigenvalues $\tilde{\varepsilon}_l$ result from the entanglement Hamiltonian based on the three-diagonals approximation (6.4.1) and (6.4.2). For large ω, a perfect agreement between the two sets is observed up to the largest few eigenvalues, as shown in the inset for $\omega = 5$. In contrast, for smaller values of ω the $\tilde{\varepsilon}_l$ lie above the ε_l at the upper end of the spectrum. This is quite reasonable since the triangular form in (6.4.1) and (6.4.2) overestimates the largest matrix elements in the middle of the interval which mainly determine the largest eigenvalues, since the eigenfunctions are concentrated there. By contrast, there is always agreement between $\tilde{\varepsilon}_l$ and ε_l at the lower end.

With the eigenvalues ε_l, the entanglement entropy is given by

$$S = \sum_{l=1}^{N} \left(\frac{\varepsilon_l}{e^{\varepsilon_l} - 1} - \log(1 - e^{-\varepsilon_l}) \right) \tag{6.4.4}$$

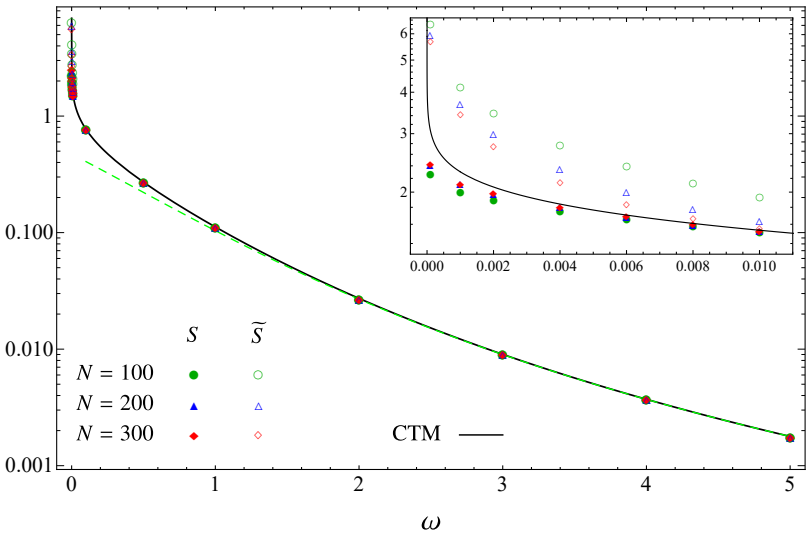

Figure 6.5: Entanglement entropy as function of ω: S is obtained through the exact formula (6.4.4), $\widetilde{S}$ through the three-diagonals approximation and the solid black curve corresponds to (6.4.5). The green dashed line shows the approximation (6.4.7) for $\omega \gg 1$, while the inset shows the behaviour for $\omega \ll 1$.

and the result of the numerical calculation is shown in Fig. 6.5 where S is plotted as a function of ω. For $\omega > 1$ one can safely use the spectrum of the half-infinite subsystem given in (6.3.6) plus the two-fold degeneracy. A closed formula for the entropy can be found as

$$S = -\frac{1}{12}\left[\ln\left(\frac{16\zeta'^4}{\zeta^2}\right) - (1+\zeta^2)\frac{4I(\zeta)I(\zeta')}{\pi}\right]. \tag{6.4.5}$$

It differs by a factor 2 from the one reported in [4] for the half-infinite chain, reflecting the contributions from the two endpoints of the interval. The result (6.4.5) is shown by the solid black line in Fig. 6.5, which perfectly agrees with the numerical data.

This agreement actually extends to much smaller ω as shown in the inset, where deviations occur only below $\omega = 0.01$. The same holds for the entropy $\widetilde{S}$ calculated with the eigenvalues $\tilde{\varepsilon}_l$, because S is determined essentially by the low end of the spectrum.

For $\zeta \to 1$, i.e. near criticality, the entropy (6.4.5) diverges and, using $I(\zeta) \simeq \ln(4/\zeta')$, one has for the interval

$$S \simeq \frac{1}{3}\ln\left(\frac{1}{1-\zeta}\right) \tag{6.4.6}$$

while for $\zeta \to 0$ it goes to zero as

$$S \simeq \frac{1}{4}\zeta^2(-\ln\zeta + 1/2 + \ln 4) \tag{6.4.7}$$

because the coupling of the oscillators vanishes. The expression (6.4.7) in the regime $\omega \gg 1$, that corresponds to $\zeta \to 0$ from (6.3.4), is shown by the green dashed line in Fig. 6.5.

6.5 Interval in the dimerized chain

The study of the dimerized hopping chain is somewhat simpler as one has only the matrix H to consider. The corresponding matrix elements are given by (6.2.12) via the eigenvalue equation

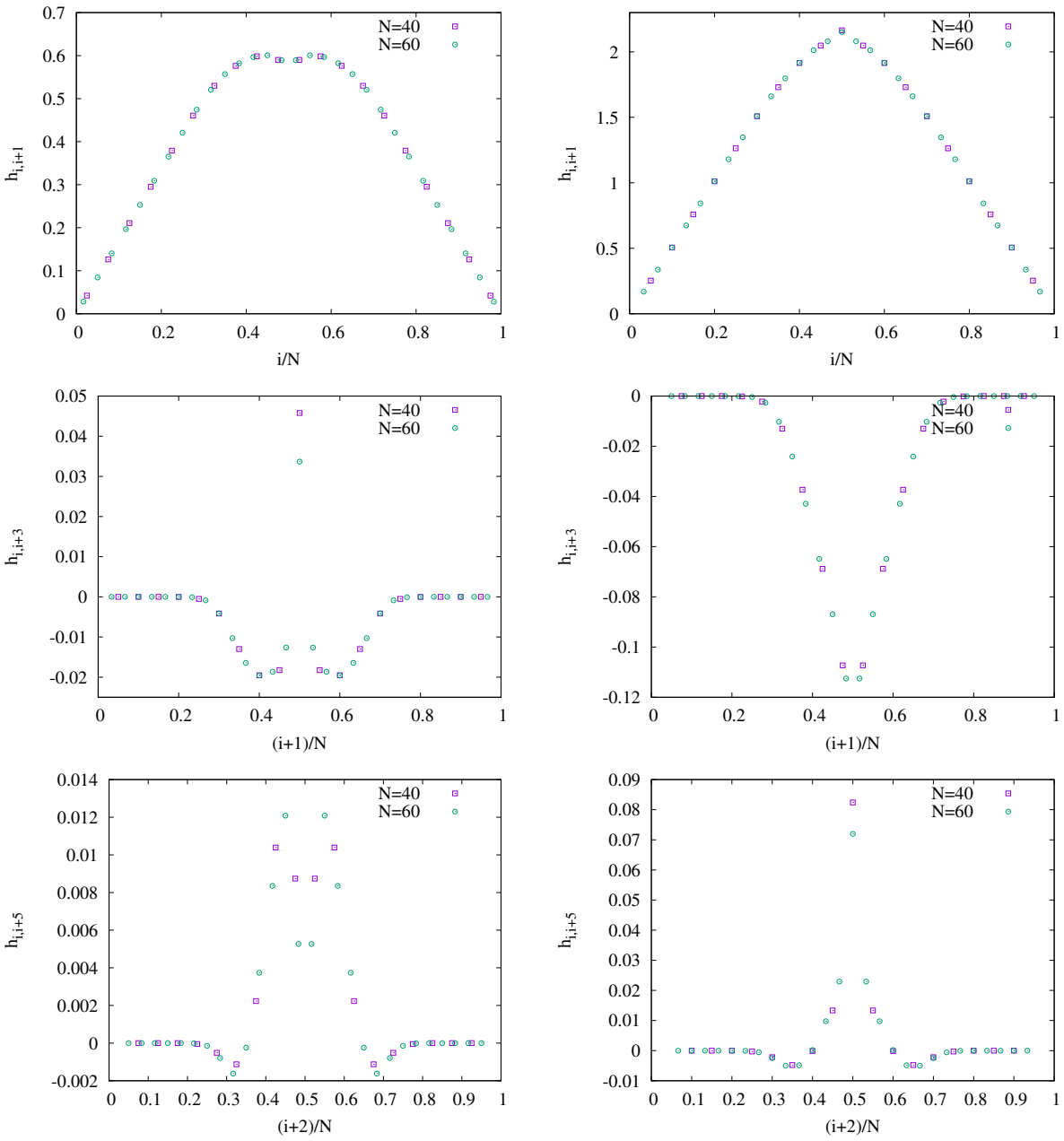

Figure 6.6: First-, third- and fifth-neighbour hopping in H for odd (left) and even (right) bonds, with dimerization $\delta = 0.5$ and for two segment sizes. Note the different vertical scales.

(6.2.10) of the reduced correlation matrix. Similarly to the bosonic case, this requires the matrix elements of C_A to be calculated with a high precision via the analytic expressions in (6.2.6)-(6.2.8). Due to the particle-hole symmetry, the nonvanishing entries $H_{i,j}$ are hopping terms over an odd distance $|j-i| = 2p+1$ and it is useful to define their density as

$$h_{i,j} = -\frac{H_{i,j}}{N}\,. \tag{6.5.1}$$

To get an overall impression on the structure of the entanglement Hamiltonian, in Fig. 6.6 we plot the scaled hopping amplitudes in (6.5.1) along the diagonals up to the fifth-neighbour terms,

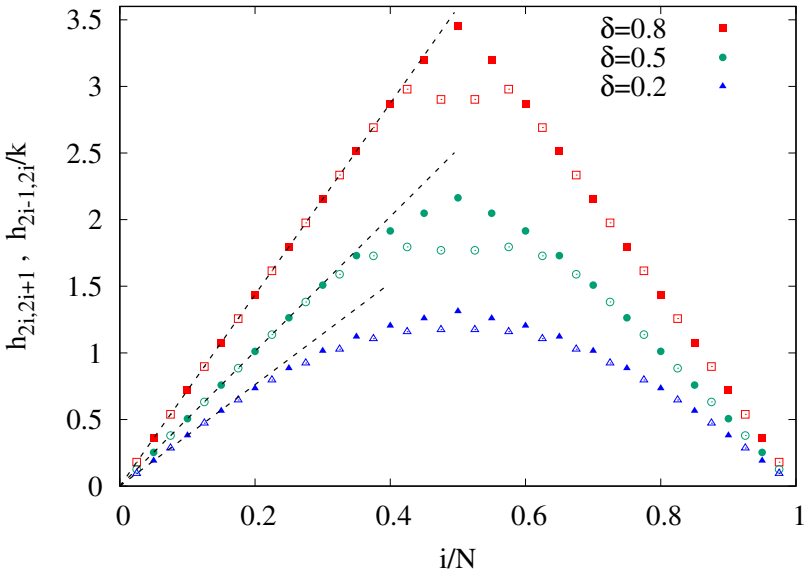

Figure 6.7: Nearest-neighbour hopping in the entanglement Hamiltonian of the dimerized chain for various δ and $N = 40$. The hopping across odd bonds (empty symbols) are divided by a factor of k. The dashed lines have slopes $2I(k')$ corresponding to the result for the half-infinite subsystem in (6.3.16).

for a dimerization parameter $\delta = 0.5$. The hopping amplitudes $h_{i,i+2p+1}$ depend on the scaling variable $(i + p)/N$ as is clear from the data collapse for two different segment sizes. The hopping matrix is dominated by the nearest-neighbour terms ($p = 0$), similarly to the homogeneous chain ($\delta = 0$). However, the dimerization induces a strong variation of the hopping across even and odd bonds, shown by the left and right columns in Fig. 6.6. The third- and fifth-neighbour hopping ($p = 1, 2$) is an order of magnitude smaller and has a nontrivial structure, developing sharp peaks in the center, which is reminiscent of the behaviour seen for the oscillator chain in Fig. 6.2. Note also that, in contrast to the homogeneous case where $h_{i,i+2p+1} > 0$ for all p, the amplitudes $h_{i,i+3}$ are dominantly negative for the dimerized case. We checked numerically that this sign change occurs gradually as one moves towards $\delta \to 0$.

We shall now focus on the nearest-neighbour hopping and use the exact results for the half-infinite chain in Sec. 6.3 to obtain an approximate understanding for the segment. Our main physical argument is that in a non-critical system with correlation length $\xi \ll N$, the segment should effectively behave like a half-infinite system around both of its boundaries. Hence, the result in Eq. (6.3.16) predicts a linear increase of the hopping with a slope $2I(k')$, multiplied by a factor of 1 or k for the strong (even) and weak (odd) bonds. To check this prediction, we have plotted in Fig. 6.7 the hopping profiles $h_{2i,2i+1}$ and $h_{2i-1,2i}/k$, and compared them to the half-infinite result shown by the dashed lines. The linear approximation works perfectly around the boundary of the segment, with the agreement improving towards the center for larger δ. One should remark that all the δ values in Fig. 6.7 correspond to very short correlation lengths, in particular one has $\xi \approx 2.5$ for $\delta = 0.2$. Nevertheless, the deviation from the wedge profile for this value is more pronounced. Clearly, in the limit $\delta \to 0$ one has to recover the result for the critical case [192], which is roughly parabolic with a slope $2I(0) = \pi$ at the boundaries. Note also that the odd hopping profile develops a dip around the center, in contrast to the even profile which has a marked peak.

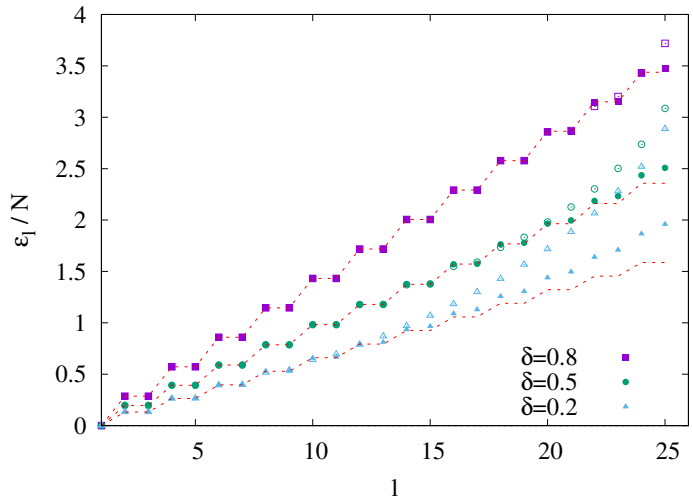

Figure 6.8: Comparison of the scaled single-particle entanglement spectra ε_l/N (full symbols) to those $\tilde{\varepsilon}_l/N$ (empty symbols) calculated from $\tilde{h}$ for $N = 50$ and various δ. The dashed red lines show the half-infinite result in Eq. (6.3.17) with double degeneracy. Only positive eigenvalues are shown.

Despite the systematic deviations, one expects that a simple nearest-neighbour entanglement Hamiltonian $\tilde{h}_{i,j}$ with wedge-like hopping amplitudes would give a very good approximation $\tilde{\rho}$ of the actual reduced density matrix $\hat{\rho}$. In fact, in the critical case $\delta = 0$, it has recently been shown that such an approximation with a *parabolic* hopping profile yields a vanishing distance between $\tilde{\rho}$ and ρ as $N \to \infty$ [380]. For the dimerized chain we assume, analogously to the oscillator chain in (6.4.1) and (6.4.2), a *triangular* profile for the nearest-neighbour hopping

$$\tilde{h}_{2i-1,2i} = 2I(k')\, k\, \Delta((2i-1)/N)\,, \qquad \tilde{h}_{2i,2i+1} = 2I(k')\, \Delta(2i/N) \tag{6.5.2}$$

where the function $\Delta(x)$ was defined in (6.4.3), and we set $\tilde{h}_{i,i+2p+1} = 0$ for all i and $p > 0$. To check the feasibility of such an approximation, in Fig. 6.8 we compare the spectra $\tilde{\varepsilon}_l$ calculated from $\tilde{h}$ to the actual spectrum ε_l, studied previously in Ref. [387]. Note that due to particle-hole symmetry, the eigenvalues come in pairs with opposite signs, and we show only the positive part of the spectra for better visibility. Clearly, the low-lying part of the spectrum is perfectly reproduced, while the larger eigenvalues ε_l tend to be overestimated by $\tilde{\varepsilon}_l$. The agreement of the high-energy spectrum improves for larger dimerizations, and for $\delta = 0.8$ it already becomes perfect up to the last few eigenvalues. Note also that the low-lying spectra are doubly degenerate, corresponding to contributions from the two boundaries, and the levels are given by the CTM result (6.3.17) for the half-infinite chain, shown by the dashed lines in Fig. 6.8. The observed features are completely analogous to those shown in Fig. 6.4 for the oscillator chain.

It is instructive to have a look also at the entanglement entropy, given by

$$S = \sum_{l=1}^{N} \left(\frac{\varepsilon_l}{e^{\varepsilon_l} + 1} + \log(1 + e^{-\varepsilon_l}) \right). \tag{6.5.3}$$

The quantity $\tilde{S}$ calculated via $\tilde{\varepsilon}_l$ is defined analogously. As only the low-lying ε_l have a significant contribution, it is already clear from Fig. 6.8 that $\tilde{S}$ would give a perfect approximation of the entropy for the δ values shown. Therefore we now focus on smaller dimerizations $|\delta| < 0.1$, corresponding to larger correlation lengths, with the results for $N = 50$ shown in Fig. 6.9. Remarkably,

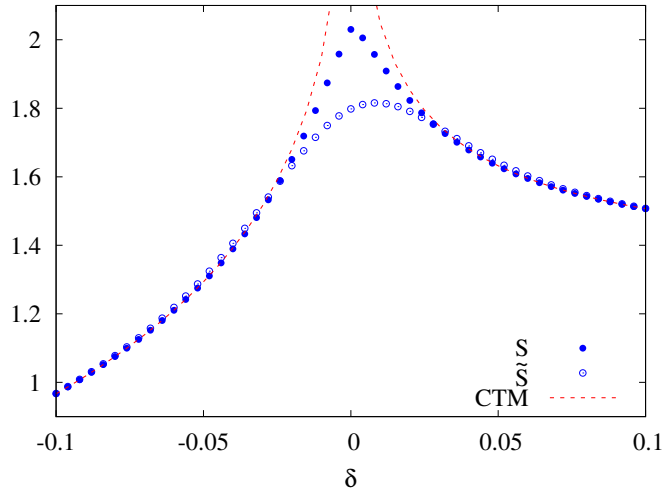

Figure 6.9: Entanglement entropy S and its approximation $\tilde{S}$ as a function of the dimerization strength for $N = 50$. The red dashed lines show the CTM result in Eq. (6.5.4).

the agreement between S and $\tilde{S}$ remains very good down to $|\delta| \approx 0.025$ corresponding to $\xi \approx 20$. For even smaller $|\delta|$ the correlation length exceeds the half-length of the segment, and the ansatz (6.5.2) built from the contributions of two independent boundaries gradually breaks down. The same is true for the doubled CTM result which, using the formulas for the TI chain [4, 388], can be written as

$$S = \begin{cases} \frac{1}{3}\left[\ln\left(\frac{k^2}{16k'}\right) + \left(1-\frac{k^2}{2}\right)\frac{4I(k)I(k')}{\pi}\right] + 2\ln 2 & \delta > 0 \\ \frac{1}{6}\left[\ln\left(\frac{16}{k^2k'^2}\right) + (k^2-k'^2)\frac{4I(k)I(k')}{\pi}\right] & \delta < 0 \end{cases} \tag{6.5.4}$$

where for $\delta < 0$ one has to use $|\delta|$ in the definition (6.2.9) such that $k < 1$. In particular, for $\delta \to 0$ ($k \to 1$) the CTM result diverges logarithmically. In contrast, the entropy $\tilde{S}$ was found to scale as $\tilde{S} = 1/3 \ln N + \text{const}$, reproducing the correct prefactor but not the proper constant in S. Although the correct ansatz for the hopping is a parabola for $\delta = 0$, the triangular profile has the same slope at the boundaries and thus reproduces the proper logarithmic scaling of the entropy.

6.6 General features of the non-critical regime

In the last two sections, we focussed on strongly non-critical systems with a correlation length of the order of the lattice constant and thus much smaller than the length of the interval. Here we want to outline the situation in the whole non-critical region.

For the dominant matrix elements, this was done to some extent already in Figs. 6.2 and 6.3 (see Figs. 6.6 and 6.7 for the fermionic chain), where a transition from parabolic to triangular profiles could be observed as ω increased. The properties of all others are collected in the form of contour plots in Fig. 6.10 for the case of the oscillator chain, where the elements $N_{i,j}/N$ and $M_{i,j}/N$ for $N = 400$ and six different values of ω are shown. The size of the elements is given by a colour code where white represents values smaller than 10^{-5}. The case $\omega = 10^{-30}$ corresponds to a system which is essentially critical and this was studied in detail in chapter 5 (see also [101]). The finite value of ω only serves to avoid a zero mode in the chain. The cases $\omega = 1$ and

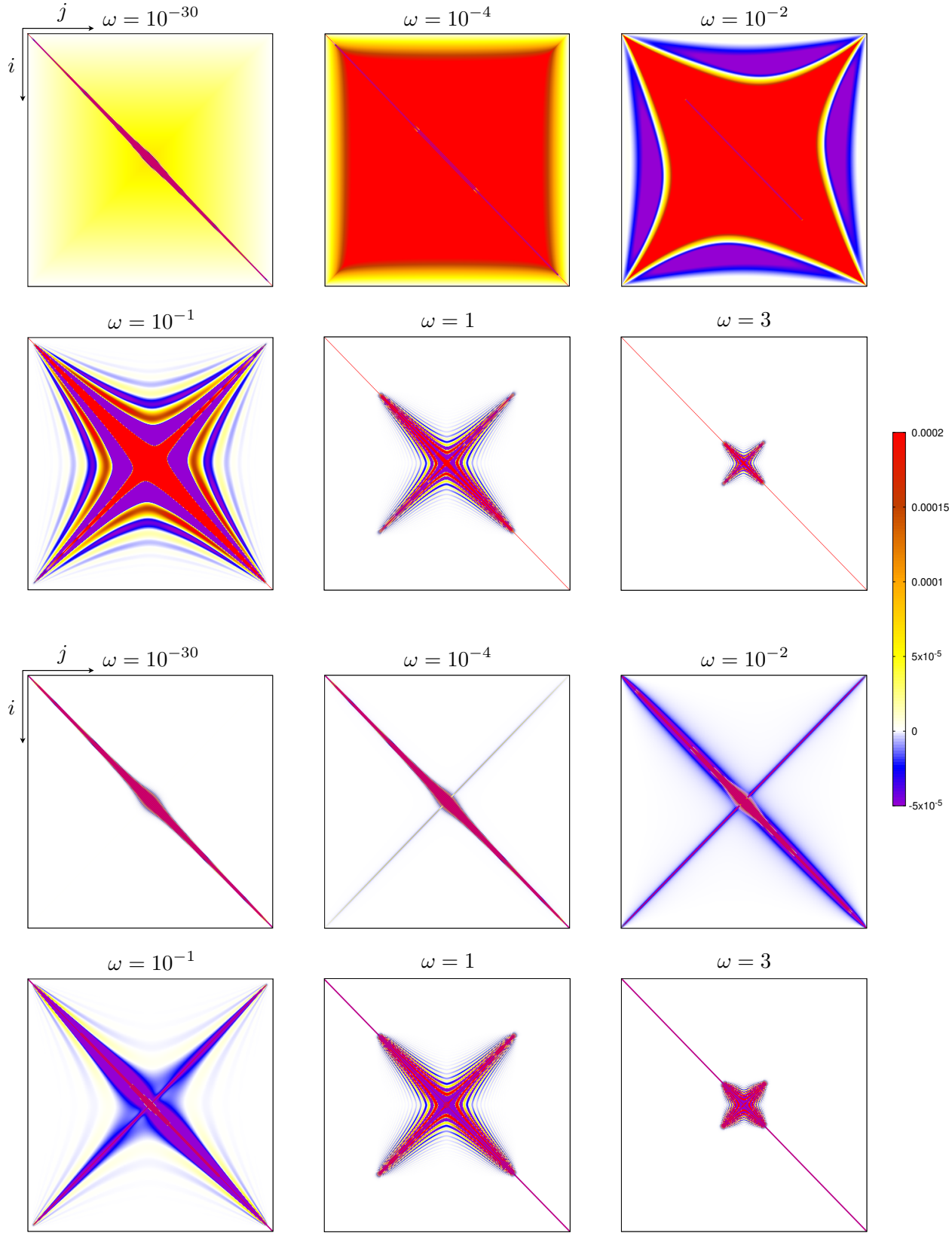

Figure 6.10: Contour plots of $N_{i,j}/N$ (top) and $M_{i,j}/N$ (bottom) for $N = 400$ and six values of ω.

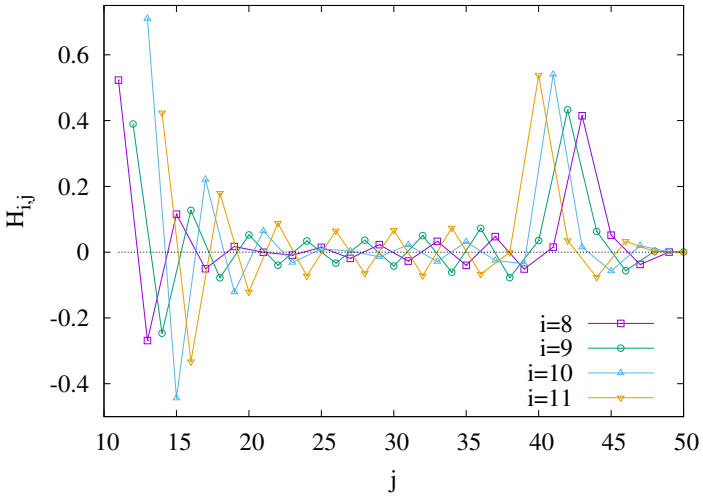

Figure 6.11: Hopping amplitudes $H_{i,j}$ along a fixed row i in the dimerized chain. The data are shown for $N = 50$ as a function of $j > i + 1$, omitting the dominant nearest-neighbour term.

$\omega = 3$ correspond to the situation considered in section 6.4. One sees that in both limits the matrices have somewhat larger elements only near the main diagonal. Physically, these are short-range couplings. As one moves away from criticality, larger regions of the squares become filled (in particular for $N_{i,j}$), a cross-shaped structure develops in the middle and then shrinks again. Calculations for larger ω show that it vanishes around $\omega = 100$. Its finite extent in the direction of the main diagonal was already encountered in Fig. 6.2, where the matrix elements $M_{i,i+r}$ for small r were seen to vanish beyond a certain distance from the centre. The elements in the other arm of the cross correspond to longer-range couplings near and across the centre, and a particular case is the sharp "antidiagonal" in the matrix of the potential energy, formed by the elements $M_{i,N+1-i}$ which connect points symmetric with respect to the middle of the interval. In particular $i = 1$ corresponds to a coupling across the whole subsystem. This structure was already observed in [193].

For the dimerized hopping model, an analogous plot of $H_{i,j}/N$ shows similar features and resembles the picture for $\omega = 10^{-2}$ in Fig. 6.10. The structure is always cross-like and a sharp antidiagonal exists. In Fig. 6.11 we present this feature in more detail by showing horizontal cuts through the matrix, plotting the elements $H_{i,j}$ for fixed i as function of the column index j. One sees not only a sharp spike right at $j = N + 1 - i$, but already an increase of the values as the antidiagonal is approached while they are initially decreasing with j. This behaviour can also be inferred from the contour plots, but is clearer in the direct plot. As to the values along the antidiagonal, these are shown in Fig. 6.12 for several dimerizations δ. While close to criticality, they are small and decrease only slowly with i, they become larger in the centre for stronger dimerization but also decrease faster, approaching zero at some finite point. Remarkably, plotted against i/N and away from the centre, the amplitudes $H_{i,N+1-i}$ along the antidiagonal collapse on the same curve for various N and are thus nonextensive, in sharp contrast to the short-range hopping in Fig. 6.6. This is similar to the situation for the central structure in the oscillator chain. In that case, one finds a similar profile along the antidiagonals, but the alternations of the dimerized chain are absent.

The phenomenon of the antidiagonals is somewhat intriguing but does not seem to have a simple interpretation. In [193] it was shown to arise in a perturbative calculation around the critical point, where it comes from the logarithmic oscillations of the critical eigenfunctions, but

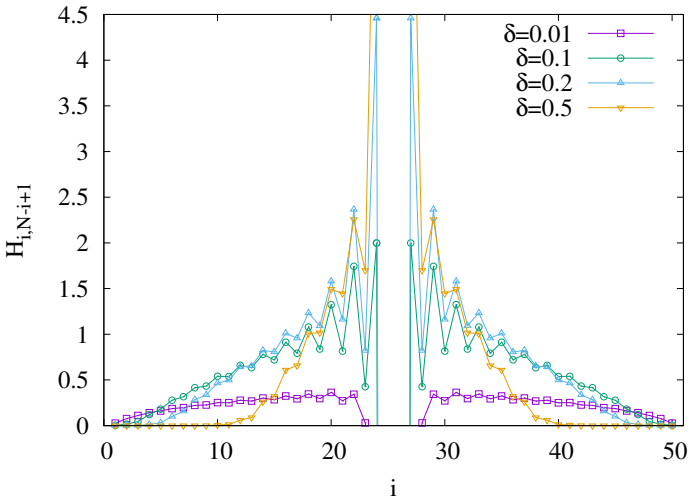

Figure 6.12: Hopping amplitudes $H_{i,N-i+1}$ along the antidiagonal for $N = 50$ and various δ, omitting the dominant nearest-neighbour terms in the middle.

this is more a formal argument.

Altogether these results show that the structure of the matrices, as far as the small entries are concerned, is most complex in the transition region where $\xi \sim N$. This is not unexpected, since there the effects from both ends of the interval start to mix, but it will be seen below to cause problems in a continuum limit.

6.7 Discussion

We have determined the entanglement Hamiltonian of an interval in a non-critical chain for two systems which allow for an explicit calculation, one bosonic and one fermionic. In both cases, one had to resort to numerics, but the analytical results for the infinite interval provided a strong guidance. Quite generally, the matrices describing the quadratic Hamiltonian $\widehat{K}_A$ in real space contain couplings over arbitrary distances. However, as in the critical cases studied before, only those with short range are large, whereas all others are significantly smaller. In this sense, the situation is simple, and an obvious approximate treatment consists in keeping only the large elements. Using in addition the analytical results for them then leads to a Hamiltonian with a triangular variation of the terms along the interval. This was seen to reproduce the low-lying single-particle eigenvalues very accurately over most of the parameter space. As a consequence, also the resulting entanglement entropies are correct except in a small region around the critical point. This is a variant of the "corner Hamiltonian" approach [374, 389] in which one replaces the true entanglement Hamiltonian by one with linearly varying couplings.

All our considerations were for lattice systems, but one can ask about a possible continuum limit in the vicinity of the critical point, by introducing a lattice spacing a and taking $a \to 0$. In fact, for the half-infinite interval this limit can easily be taken and leads to the Bisognano-Wichmann result (1.2.11). For the finite interval, one knows that the small longer-range couplings on the lattice should be included properly. This leads to sums along horizontal cuts of the corresponding matrices. For example, the mass parameter $m(x)$ in the continuum description, with $x = ia$, is given in the oscillator chain by

$$m(x) = \sum_r M_{i,i+r} \tag{6.7.1}$$

whereas the local velocity is

$$v(x) = \sum_r r^2 \, M_{i,i+r} \tag{6.7.2}$$

and a similar expression holds for the local Fermi velocity $v_F(x)$ in the dimerized chain. It turns out that, in contrast to the situation at criticality, one may need a large number of terms in order to obtain convergence of the sums, for example 30 terms for $v_F(x)$ if $\delta = 0.05$ and $N = 100$. Then $v_F(x)$ shows a triangular profile, but the better converging $m(x)$ looks roughly parabolic with an additional structure in the centre. However, further increasing the cutoff in the sums, the numerical results for the velocity and mass parameter become unstable, and even more severe irregularities tend to occur also for the oscillators. Here, the particular features of the matrices including the antidiagonals enter. Altogether, we were not able to obtain well-defined general results in the massive regime by fixing N/ξ and increasing N. This hints toward the possibility that the naive continuum limit, that perfectly reproduces the CFT results in the massless case as discussed in chapter 5 (see also [101, 179]), might not be valid away from criticality and that $\widehat{K}_A$ remains non-local also in the continuum [193].

Chapter 7

Entanglement Hamiltonians after a global quench

7.1 Introduction

The bipartite entanglement has been studied during the last decade also to explore the out of equilibrium dynamics of quantum systems. The global quantum quench discussed in chapter 3 is an insightful process for this purpose. The temporal evolutions of various quantities after global quantum quenches and also other kinds of quenches have been studied in quantum field theories, in many-body systems on the lattice [82–86, 89, 294, 295, 310, 319, 320, 339, 341, 390–396] and also in quantum gravity through the gauge/gravity correspondence [243, 321, 325–329, 332, 344] (see the reviews [80, 81, 90] for an extensive list of references).

In this chapter we study the temporal evolution of the entanglement Hamiltonian and of a contour for the entanglement entropy after a global quantum quench in free lattice models. Also the temporal evolution of the gaps in the entanglement spectrum (1.2.18) is discussed. For simplicity, we consider, in one spatial dimension, a harmonic chain and a chain of free fermions. In the harmonic chain, we explore a quench of the frequency parameter such that the unitary evolution is governed by the massless Hamiltonian. In the chain of free fermions, we consider the global quench introduced in [4, 85], where the system is prepared in the ground state of a fully dimerised chain while the evolution Hamiltonian is fully homogeneous.

The rest of the chapter is organised as follows. In Sec. 7.2 we provide a naive formula for the contour function obtained through results of Conformal Field Theory (CFT). The numerical results for the harmonic chain and for the chain of free fermions are described in Sec. 7.3 and Sec .7.4 respectively. In Sec. 7.5 we draw some conclusions.

Notations: in this chapter we follow the notations of [103], denoting by ℓ the number of sites in the subsystem A of the infinite chains that we study. Let us stress that this notation is different from the ones employed in chapters 5 and 6. Furthermore, the correlation matrix with entries given by $\mathrm{Re}\langle \hat{q}_i \hat{p}_j \rangle$ in the harmonic chain has been denoted by R, instead of M as in chapters 2, 3 and 4. This is done for distinguishing the correlation matrix from one of the blocks of the entanglement Hamiltonian matrix indicated by M, as in [182, 193, 200].

7.2 Insights from CFT

In this section we employ the analytic results obtained for the entanglement Hamiltonian of a semi-infinite line after a global quench in CFT [147] to get some insights about the qualitative

behaviour of the entanglement spectrum and of the contour for the entanglement entropies.

The CFT analysis performed in [82] (see also the recent review [81]) leads to the following linear growth of the entanglement entropies before the saturation

$$S_A^{(n)} \simeq \frac{\pi c}{3\tau_0}\left(1+\frac{1}{n}\right) t \qquad\qquad t/\ell < 1/2 \tag{7.2.1}$$

(comparing the notation with [81], we have $\tau_0 = 4\tau_{0,\text{there}}$), where c is the central charge of the model. This gives $S_A \simeq 2\pi c\, t/(3\tau_0)$ for the entanglement entropy and, by fitting this linear growth, we can get τ_0 numerically. A slight dependence on n has been observed in τ_0 (see e.g. [294]). We find it worth remarking that a factor of 2 in (7.2.1) is due to the fact that the interval has two endpoints. Taking the limit $n \to \infty$ in (7.2.1) one obtains $-\log \lambda_{\max} \simeq \pi c\, t/(3\tau_0)$. The parameter τ_0 encodes some features of the initial state (we refer to [390] for a complete discussion).

The temporal evolution of the entanglement Hamiltonian of a semi-infinite line after a global quantum quench in CFT has been studied in [147] by employing methods and results of CFT with boundaries [204–206, 397, 398]. This analysis provides also the entanglement spectrum and, in particular, the above linear growth for $-\log \lambda_{\max}$ is recovered up to a factor of 2, which is due to the fact that the semi-infinite line has only one endpoint. This result suggests to explore the qualitative behaviour of the entanglement spectrum before the saturation at $t/\ell \simeq 1/2$ by taking the analytic CFT expressions for the semi-infinite line and introducing properly a factor of 2 to take into account the occurrence of two endpoints. As for the gaps in the entanglement spectrum (1.2.18), from [147] we obtain

$$g_{a,0} \simeq \frac{\pi \tau_0\, \Delta_a}{2\, t} \qquad\qquad t/\ell < 1/2 \tag{7.2.2}$$

which is 1/2 of the corresponding quantity for the semi-infinite line. In (7.2.2), the coefficients Δ_a are the non vanishing conformal dimensions (including also the ones of the descendants) of a boundary CFT with the proper boundary condition, as discussed in [147]. We find it worth considering also the ratios $g_{b,0}/g_{a,0} = \Delta_b/\Delta_a$ because they are independent of τ_0. From (7.2.1) and (7.2.2) it is straightforward to construct another expression where τ_0 does not occur, namely

$$g_{a,0}\, S_A^{(n)} \simeq \frac{\pi^2 c}{6}\left(1+\frac{1}{n}\right) \Delta_a \qquad\qquad t/\ell < 1/2\,. \tag{7.2.3}$$

The temporal evolutions of (7.2.2), of (7.2.3) and of the ratios of the entanglement gaps with respect to the first one after the global quenches that we consider in this chapter are shown in Fig. 7.6 and Fig. 7.17. From these data we notice that the best agreement with CFT is observed for the ratios of the entanglement gaps.

The above analysis can be easily adapted to the temporal evolution after a local quantum quenches [86] by employing the corresponding results of [147]. The crucial difference is that logarithmic growths occur in these cases. For instance, for local quenches (7.2.2) has $\log t$ instead of t in the denominator. Instead, (7.2.3) holds also for local quenches.

In the remaining part of this section we exploit the CFT results for the entanglement Hamiltonian of the semi-infinite line after a global quench [147] to get insights about the temporal evolution of the contour function for the entanglement entropies of an interval.

For a continuous theory in one spatial dimension, the properties (1.2.10) for the contour functions become

$$S_A^{(n)} = \int_{x\in A} s_A^{(n)}(x)\, dx \qquad\qquad s_A^{(n)}(x) \geqslant 0 \tag{7.2.4}$$

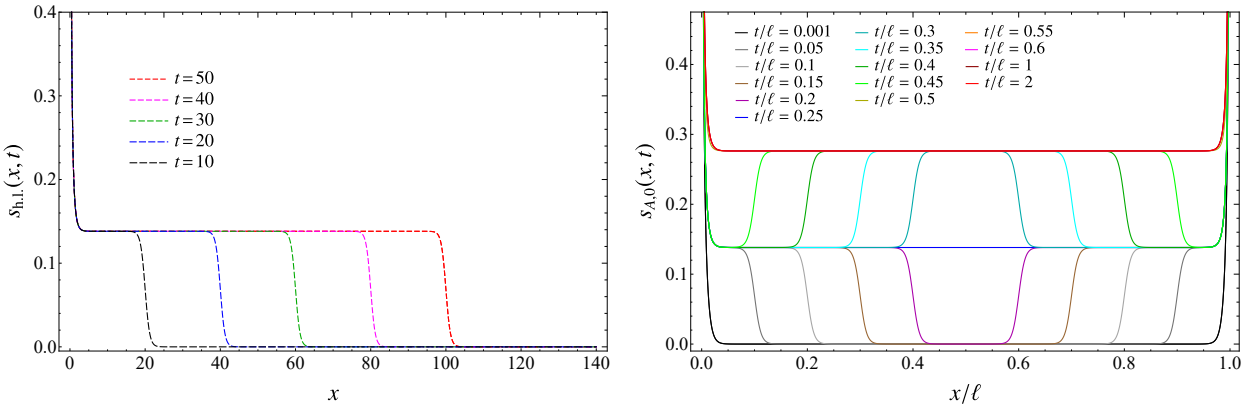

Figure 7.1: The contour function for the entanglement entropy of half line (left panel) from (7.2.5) and of an interval (right panel) from the naive formula (7.2.8). In these plots $c = 1$ and $\tau_0 = 3.7905$.

where $s_A^{(n)}(x)$ is now a function of the position inside the subsystem A. For some particular spatial bipartitions at equilibrium (e.g. an interval in the infinite line at zero and finite temperature, or in a finite periodic system for the ground state) a natural candidate for the contour function for the entanglement entropies in CFT can be obtained from the weight function occurring in the entanglement Hamiltonian [29]. By applying this idea to the half line after a global quench, one finds the following CFT ansatz for the contour function [147]

$$s_{\rm h.l.}^{(n)}(x,t) = \frac{c}{12}\left(1+\frac{1}{n}\right)\mathcal{F}_{\rm h.l.}(x,t) \tag{7.2.5}$$

where $n \geqslant 1$ and

$$\mathcal{F}_{\rm h.l.}(x,t) \equiv \frac{2\pi\,[\cosh(2\pi t/\tau_0)]^2\coth(\pi x/\tau_0)}{\tau_0\,[\cosh(4\pi t/\tau_0)+\cosh(2\pi x/\tau_0)]}\,. \tag{7.2.6}$$

It is straightforward to observe that $\tau_0\, s_{\rm h.l.}^{(n)}(x,t)$ depends on x/τ_0, t/τ_0 and the central charge c. Furthermore, $\mathcal{F}_{\rm h.l.}(x,t) = 1/x + O(1)$ as $x \to 0^+$, independently of time. This implies that the expected logarithmic divergence of $S_A^{(n)}$ as the UV cutoff $\epsilon \to 0$ is independent of time as well. Indeed, this divergence can be obtained by removing an infinitesimal disk around the endpoint of the half line and integrating the contour function (7.2.5) from ϵ to some point inside the half line. Instead, by integrating (7.2.5) in the entire half line $(\epsilon, +\infty)$ with $\epsilon/\tau_0 \ll 1$, one obtains [147]

$$\int_\epsilon^\infty s_{\rm h.l.}^{(n)}(x,t)\,dx = \frac{c}{12}\left(1+\frac{1}{n}\right)\log\!\left(\frac{\tau_0}{\pi\epsilon}\,\cosh(2\pi t/\tau_0)\right) + O(\epsilon^2) \tag{7.2.7}$$

that gives the linear growth found in [82], namely $\frac{\pi c}{3\tau_0}t$ when $t \gg \tau_0$. The r.h.s. of (7.2.7) provides only the leading term of the entanglement entropy as $\epsilon \to 0$. A subleading $O(1)$ term comes from the contribution of the conformal boundary states introduced through the regularisation procedure [146, 147] (see [29] for a discussion on this term in relation to the contour function at equilibrium).

Considering t/τ_0 fixed in (7.2.5), we find that $s_{\rm h.l.}^{(n)}(x,t) \sim e^{-2\pi x/\tau_0}$ as $x \to +\infty$ and that the height of the horizontal plateau is given by $\frac{\pi\, c}{12\tau_0}(1+\frac{1}{n})$ (this can be done by taking $t \to \infty$ first and then $x \to +\infty$).

A typical temporal evolution of the contour function for the entanglement entropy $s_{\rm h.l.}(x,t) \equiv s_{\rm h.l.}^{(1)}(x,t)$ is shown in the left panel of Fig. 7.1. The linear divergence as $x \to 0^+$ and the exponential

decay as $x \to +\infty$ are independent of time. These two regimes are connected for the intermediate values of x by a smooth step at $x \simeq 2t$ whose height is $\frac{\pi\, c}{6\,\tau_0}$. The occurrence of this step moving in time has been first observed in the numerical analysis performed in [28].

We focus our attention on the contour function for the entanglement entropies of an interval A of length ℓ in the infinite line after a global quantum quench. A CFT analysis for this case is not available in the literature. Hence, let us consider the naive contour function obtained by superposing the two contour functions (7.2.5) associated to the half lines $(0, +\infty)$ and $(-\infty, \ell)$, namely

$$s^{(n)}_{A,0}(x,t) \equiv s^{(n)}_{\text{h.l.}}(x,t) + s^{(n)}_{\text{h.l.}}(\ell - x, t) = \frac{c}{12}\left(1 + \frac{1}{n}\right)\big[\mathcal{F}_{\text{h.l.}}(x,t) + \mathcal{F}_{\text{h.l.}}(\ell - x, t)\big] \tag{7.2.8}$$

with $\mathcal{F}_{\text{h.l.}}(x,t)$ given by (7.2.6). The observations made above about $\mathcal{F}_{\text{h.l.}}(x,t)$ lead to notice that $\tau_0\, s^{(n)}_{A,0}(x,t)$ obtained from (7.2.8) is a function of t/ℓ, x/ℓ and τ_0/ℓ; and that $s^{(n)}_{A,0}(x,t)$ displays a linear divergence for $x \to 0^+$ and for $x \to \ell^-$, with the same time independent coefficient. For $t = 0$, the naive analytic result (7.2.8) gives

$$s^{(n)}_{A,0}(x,0) = \frac{\pi c}{6\tau_0}\left(1 + \frac{1}{n}\right)\left[\frac{1}{\sinh(2\pi x/\tau_0)} + \frac{1}{\sinh(2\pi(\ell - x)/\tau_0)}\right] \tag{7.2.9}$$

and in the asymptotic regime of long time we find

$$\lim_{t\to\infty} s^{(n)}_{A,0}(x,t) = \frac{\pi c}{12\,\tau_0}\left(1 + \frac{1}{n}\right)\Big[\coth(\pi x/\tau_0) + \coth(\pi(\ell - x)/\tau_0)\Big]\,. \tag{7.2.10}$$

The naive contour function for the entanglement entropy is given by (7.2.8) with $n = 1$ and its typical temporal evolution is shown in the right panel of Fig. 7.1. This evolution can be explained qualitatively in terms of two fronts with height $\frac{\pi c}{6\tau_0}$ that start at the two different endpoints of the interval and then propagate in opposite directions with velocity equal to 2. The two fronts cross and superpose at $t/\ell \simeq 1/4$ and each front takes $t \simeq \ell/2$ to travel across the entire interval. This qualitative features have been first observed in [28] by analysing the numerical data obtained in a chain of free fermions. Further numerical data supporting this picture are presented in Sec. 7.3 and Sec. 7.4.

Given two points $0 < x_1 < x_2 < \ell$ inside the interval A, let us integrate the naive contour function (7.2.8) in the interval (x_1, x_2). The result reads

$$\begin{aligned}\mathcal{S}^{(n)}_{A,0}(x_1, x_2; t) &\equiv \int_{x_1}^{x_2} s^{(n)}_{A,0}(x,t)\, dx \\ &= \frac{c}{24}\left(1 + \frac{1}{n}\right)\log\left(\frac{\big[\cosh(4\pi t/\tau_0) + \cosh(2\pi(\ell - x)/\tau_0)\big]\big(\sinh(\pi x/\tau_0)\big)^2}{\big[\cosh(4\pi t/\tau_0) + \cosh(2\pi x/\tau_0)\big]\big(\sinh(\pi(\ell - x)/\tau_0)\big)^2}\right)\Bigg|_{x_1}^{x_2}\end{aligned} \tag{7.2.11}$$

which is a function of t/ℓ, x_1/ℓ, x_2/ℓ and τ_0/ℓ. Subtracting to (7.2.11) its value at $t = 0$, one finds

$$\Delta\mathcal{S}^{(n)}_{A,0}(x_1, x_2; t) \equiv \mathcal{S}^{(n)}_{A,0}(x_1, x_2; t) - \mathcal{S}^{(n)}_{A,0}(x_1, x_2; 0) = \frac{c}{24}\left(1 + \frac{1}{n}\right)\log\left(\frac{\eta(x_2; t)}{\eta(x_1; t)}\right) \tag{7.2.12}$$

where we have introduced the following function

$$\eta(x;t) \equiv \frac{\cosh(\pi(2t - \ell + x)/\tau_0)\, \cosh(\pi(2t + \ell - x)/\tau_0)\, [\cosh(\pi x/\tau_0)]^2}{\cosh(\pi(2t - x)/\tau_0)\, \cosh(\pi(2t + x)/\tau_0)\, [\cosh(\pi(\ell - x)/\tau_0)]^2}\,. \tag{7.2.13}$$

In Fig. 7.10 and Fig. 7.19 this formula (where the value of τ_0 is obtained by fitting the linear growth of the entanglement entropy) gives the grey dashed-dotted curves, that can be compared against numerical data corresponding to particular quenches in a harmonic chain (see Sec .7.3) and in a chain of free fermions (see Sec .7.4) respectively.

The expression in (7.2.12) provides the entanglement entropies when $(x_1, x_2) = (\epsilon, \ell - \epsilon)$. In this case, we have

$$\Delta\mathcal{S}^{(n)}_{A,0}(0,\ell;t) = \lim_{\epsilon\to 0} \Delta\mathcal{S}^{(n)}_{A,0}(\epsilon,\ell-\epsilon;t) \,=\, \frac{c}{12}\left(1+\frac{1}{n}\right)\log\left(\frac{2\left[\cosh(\pi\ell/\tau_0)\cosh(2\pi t/\tau_0)\right]^2}{\cosh(2\pi\ell/\tau_0)+\cosh(4\pi t/\tau_0)}\right). \tag{7.2.14}$$

Taking $t \gg \tau_0$ and $\ell \gg \tau_0$ first, and then considering the regimes $t \ll \ell/2$ and $t \gg \ell/2$, this expression simplifies respectively to

$$\Delta\mathcal{S}^{(n)}_{A,0}(0,\ell;t) \simeq \frac{\pi c}{3\tau_0}\left(1+\frac{1}{n}\right) t \qquad\qquad \Delta\mathcal{S}^{(n)}_{A,0}(0,\ell;t) \simeq \frac{\pi c}{3\tau_0}\left(1+\frac{1}{n}\right)\frac{\ell}{2} \tag{7.2.15}$$

in agreement with [82].

Let us remark that the results reported above have been obtained by employing in a naive way the CFT analytic expressions of [147] corresponding to the half line to study the case of a finite interval, assuming that the dynamics before the thermalisation at $t/\ell \simeq 1/2$ is governed by a neighbourhood of the endpoints, where the interval is indistinguishable from the half line.

7.3 Interval in a harmonic chain

In this section we study the temporal evolution of the entanglement Hamiltonian matrix H_A of an interval A in an infinite harmonic chain, described by the Hamiltonian (5.2.1), after a global quench of the frequency parameter. This quench protocol has been already discussed in details in chapter 3.

7.3.1 Numerical results for the entanglement Hamiltonian matrix

We are interested in the temporal evolution of the entanglement Hamiltonian matrix $H_A(t)$ defined in (5.2.2) corresponding to an interval A made by ℓ sites after the global quench of the frequency parameter. The reduced covariance matrix $\gamma_A(t)$ and the entanglement Hamiltonian matrix $H_A(t)$ can be partitioned into $\ell \times \ell$ blocks that depend on $t > 0$, namely

$$\gamma_A(t) = \begin{pmatrix} Q(t) & R(t) \\ R(t)^{\mathrm{t}} & P(t) \end{pmatrix} \qquad H_A(t) = \begin{pmatrix} M(t) & E(t) \\ E(t)^{\mathrm{t}} & N(t) \end{pmatrix}. \tag{7.3.1}$$

The entanglement Hamiltonian matrix $H_A(t)$ can be evaluated, once the reduced covariance matrix $\gamma_A(t)$ is known, as (see also (2.4.3)) [284]

$$H_A = 2\,\mathrm{i}\,J\,\mathrm{arccoth}(2\,\mathrm{i}\gamma_A\,J) \tag{7.3.2}$$

where J is the standard symplectic matrix defined in (2.2.2).

In our numerical analysis, the entanglement Hamiltonian matrix $H_A(t)$ has been constructed by employing the Williamson's decomposition for H_A, which reads

$$H_A = \widetilde{W}^{\mathrm{t}}\,\mathcal{E}\,\widetilde{W} \qquad\qquad \widetilde{W} \equiv J^{\mathrm{t}}\,W\,J = W^{-\mathrm{t}}\,. \tag{7.3.3}$$

where W is the symplectic matrix entering in the Williamson's decomposition for γ_A (2.2.15) and the symplectic eigenvalues of $H_A(t)$ given by the diagonal matrix $\mathcal{E}$ have been found from

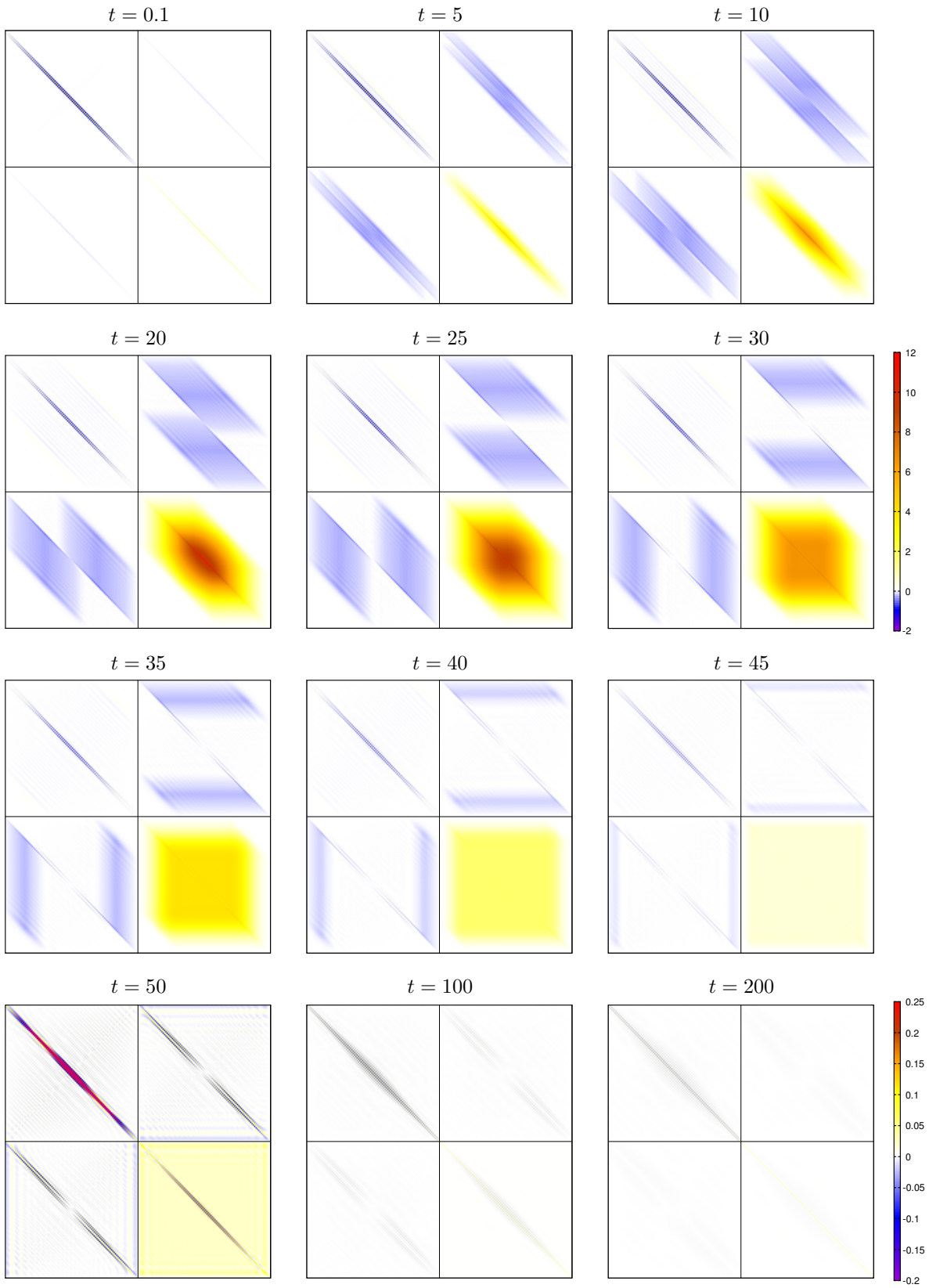

Figure 7.2: Entanglement Hamiltonian matrix $H_A(t)$ in (7.3.1) for an interval having $\ell = 100$ sites in the infinite harmonic chain after the global quench given by $\omega_0 = 1$ and $\omega = 0$.

the symplectic spectrum of γ_A through the relation (2.4.7). Let us stress that the entanglement Hamiltonian depends both on the symplectic spectrum of γ_A and on the matrix W, while the entanglement entropies and the entanglement spectrum only depends on the symplectic eigenvalues of the reduced covariance matrix (see Sec. 7.3.2 and Appendix A.1).

The reduced covariance matrix $\gamma_A(t)$ can be constructed exploiting the correlators given by (C.2.3) (once the notations have been adapted to the ones of this chapter, reported at the end of Sec. 7.1), as discussed in Sec. 3.4.1 (see (3.4.1)) for the computation of the subsystem complexity after a global quench.

In this section we mainly consider the global quench of the frequency parameter described above with $\omega_0 = 1$ and $\omega = 0$. Some data corresponding to an initial state having $\omega_0 = 5$ are also provided.

The relation (2.4.7), that provides the symplectic spectrum of H_A in terms of the one of γ_A, requires $\sigma_k > 1/2$. Since many elements of the symplectic spectrum of γ_A are very close to $1/2$, the software approximates them to $1/2$, spoiling the applicability of (2.4.7) to get the symplectic spectrum of H_A. This forces to obtain σ_k's with very high numerical precision. The number of digits depends on various parameters of the configuration like ℓ and t. In our numerical analysis for the harmonic chain we worked with precisions between 200 and 1000 digits.

In Fig. 7.2 we show the temporal evolution of the entanglement Hamiltonian matrix $H_A(t)$ after the global quench written in the form (7.3.1), i.e. in terms of its $\ell \times \ell$ blocks. The main feature to highlight with respect to the entanglement Hamiltonian matrices corresponding to static configurations (as the ones treated in chapters 5 and 6) is that the off diagonal block E is not vanishing and therefore it contributes in a non trivial way to determine the out of equilibrium dynamics. The magnitudes of the elements of $H_A(t)$ become very small for long time. Indeed, a smaller scale has been chosen in the three bottom panels of Fig. 7.2 to show the structure of the non vanishing elements. At early times only the diagonal blocks are non vanishing and mostly around their main diagonals. As time evolves, also the off diagonal elements of the blocks become relevant. The most evident feature that can be observed from the time evolution in Fig. 7.2 is the occurrence of bands in the different blocks of $H_A(t)$ whose widths increase with time. We consider these widths in more detail below, during the discussion of Fig. 7.4, Fig. 7.5.

The reflection symmetry of the configuration with respect to the center of the interval leads to a corresponding reflection symmetry with respect to the center in any given diagonal of the blocks $M(t)$ and $N(t)$ at any fixed time. More explicitly, we checked numerically that $M_{i,i} = M_{\ell-i+1,\ell-i+1}$ and $N_{i,i} = N_{\ell-i+1,\ell-i+1}$ with $1 \leqslant i \leqslant \ell$ for the main diagonals and that $M_{i,i+p} = M_{\ell-p-i+1,\ell-i+1}$ and $N_{i,i+p} = N_{\ell-p-i+1,\ell-i+1}$ along the p-th diagonal, with $p > 0$ and $1 \leqslant i \leqslant \ell - p$. As for the off diagonal block $E(t)$, we observe a symmetry with respect to the center of the block, namely $E_{i,j} = E_{\ell-i+1,\ell-j+1}$ for $1 \leqslant i, j \leqslant \ell$.

The temporal evolution of the blocks composing $H_A(t)$ is qualitatively different. As for the symmetric $\ell \times \ell$ matrix $M(t)$ in (7.3.1), the largest contributions come from the main diagonal, that decrease as time evolves and remain positive during all the evolution, reaching a stationary curve for long times (see the top left panel of Fig. 7.3). The first diagonals are mostly negative and in some point become positive at some time (see the top right panel of Fig. 7.3 and the corresponding inset). In the top left panel of Fig. 7.4 we show the antidiagonal of $M(t)$, that displays oscillations around zero.

Interesting features can be observed also for the temporal evolution of the symmetric block $N(t)$ in (7.3.1). The diagonal of $N(t)$ is shown in the middle left panel of Fig. 7.3: first it grows until a maximal curve and then it relaxes to a positive curve for long time. The elements of $N(t)$ are mostly positive but some of them become negative for large times (see e.g. the inset of the top right panel in Fig. 7.4 and the one of the middle right panel in Fig. 7.3). The block $N(t)$ is

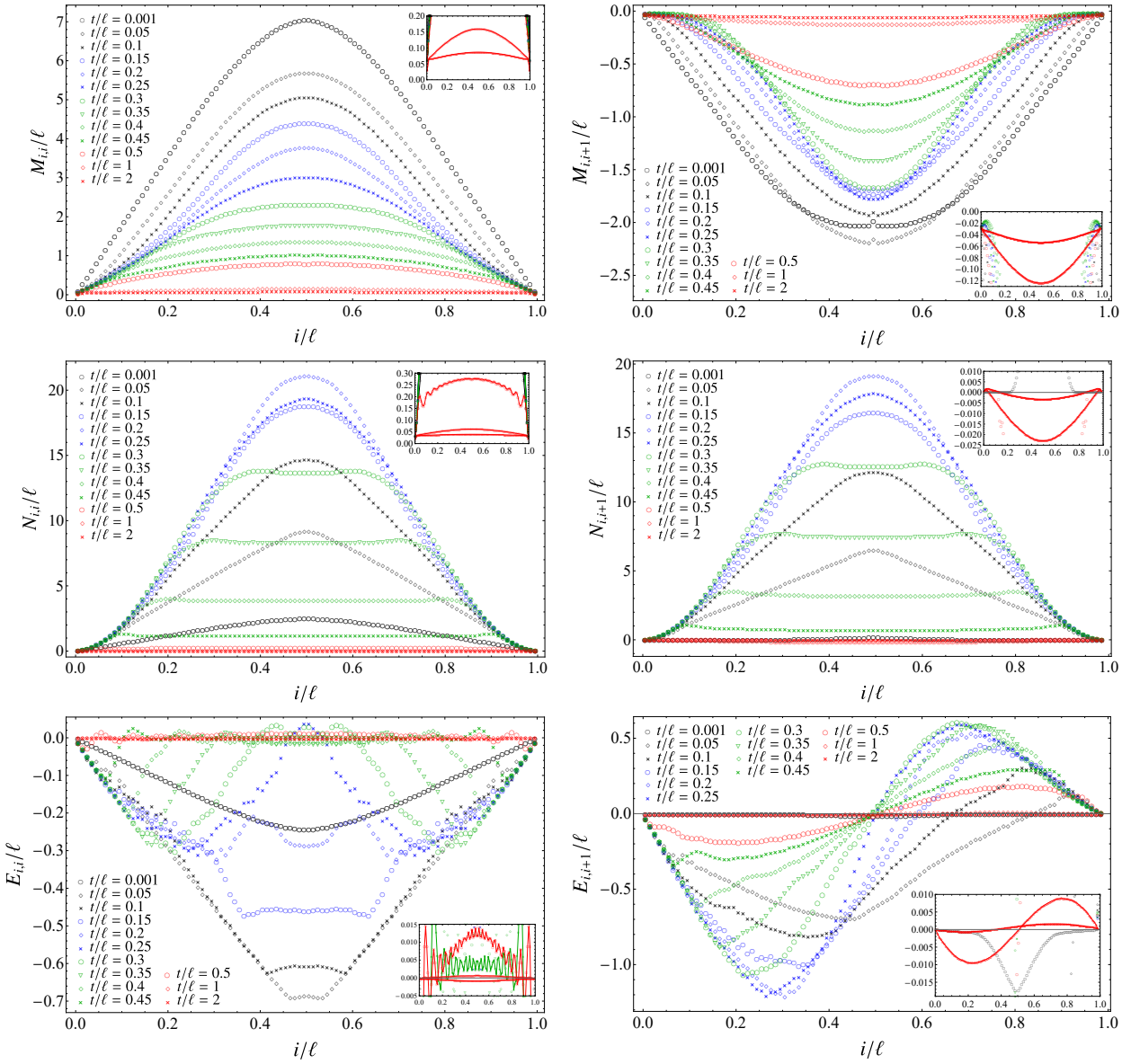

Figure 7.3: Harmonic chain: Temporal evolution of the main diagonals (left panels) and of the first diagonals (right panels) composing the $\ell \times \ell$ blocks of the entanglement Hamiltonian matrix $H_A(t)$ in (7.3.1) for an interval with $\ell = 100$ sites. The insets zoom in on small values, in order to show the curves for large times. This figure, that is complementary to Fig. 7.2 and Fig. 7.4, has been discussed in Sec .7.3.1.

the only one where the evolution of the main diagonal and of the first diagonal are qualitatively similar: a smooth positive wedge grows from the center of the interval until $t/\ell \simeq 0.2$, then its tip decreases and gets smooth forming a plateau whose height decreases in time.

The evolution of the block $E(t)$ is qualitatively different from the one of $M(t)$ and $N(t)$ because this matrix is not symmetric. Furthermore, it vanishes for $t = 0$ and it seems that its contribution is zero also for long times. The elements of this block are mostly negative but without a definite sign for all the times (see e.g. its first diagonal in the bottom right panel of Fig. 7.3). From Fig. 7.2, we observe the formation of two mostly negative bands close to the diagonal for small

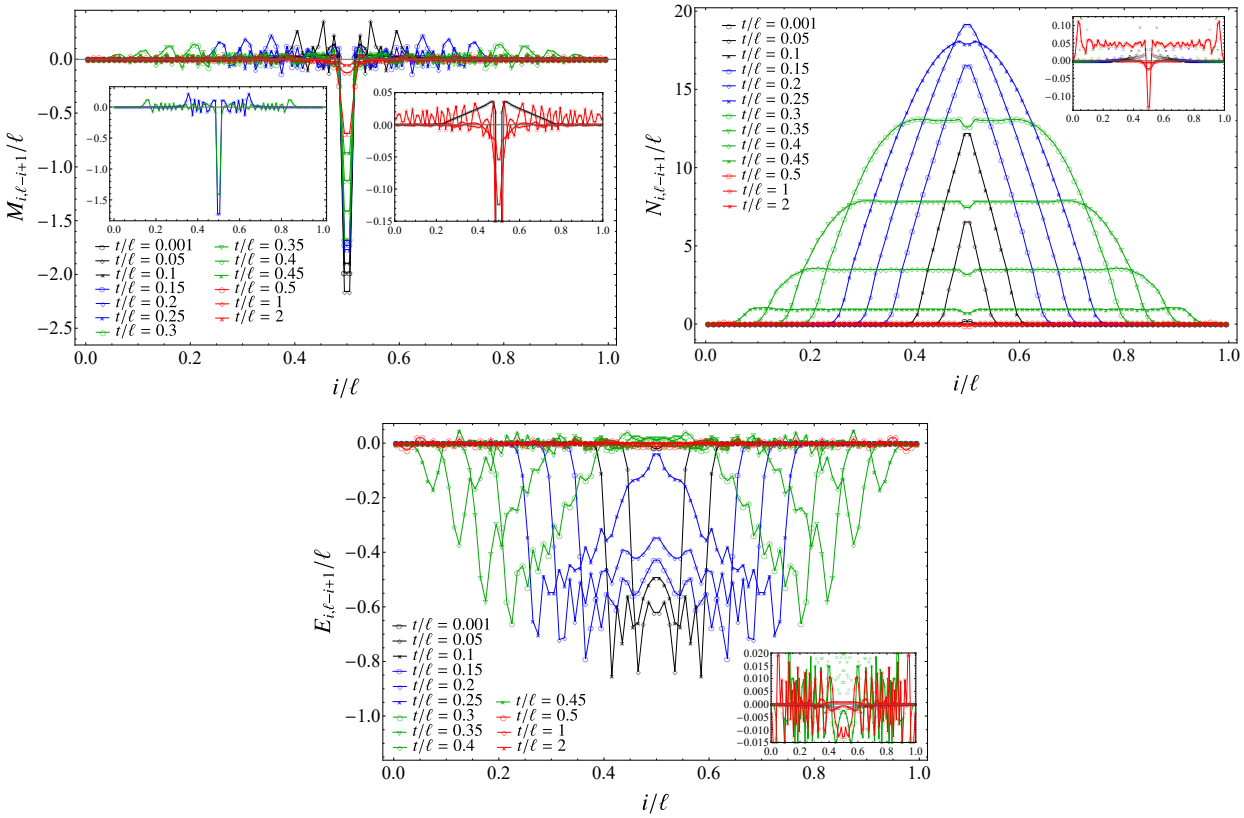

Figure 7.4: Harmonic chain: Temporal evolution of the antidiagonals of the $\ell \times \ell$ blocks composing the entanglement Hamiltonian matrix $H_A(t)$ in (7.3.1) for an interval with $\ell = 100$ sites. The insets containing red curves zoom in on small values, in order to show the curves for large times. In the second zoom of the top left panel we show only two curves to highlight the fact that the antidiagonals are very small for $|i/\ell - 1/2| \gtrsim t/\ell$. A similar behaviour occurs in the other panels, as shown in Fig. 7.5.

times having the shape of two parallelograms (see also the top right panel in Fig. 7.16) whose height along the antidiagonal increases in time until $t/\ell \simeq 0.5$, when they vanish. As for the main diagonal of $E(t)$, a smooth negative wedge develops until it reached a minimum value; then it goes back to zero in a peculiar way; indeed a small plateau is formed whose width increases and then decreases, leading to two fronts that move in the opposite directions towards the endpoints of the interval (see the bottom left panel of Fig. 7.3).

In Fig. 7.4 we show the temporal evolution of the antidiagonals of the blocks composing the entanglement Hamiltonian matrix $H_A(t)$ in (7.3.1). Although the temporal evolutions of the antidiagonals in the three blocks look quite different, the main common feature is the fact that at a fixed time they become very small (and not vanishing) around the same points. The distance $2d_0$ between these points provides the total width of the bands occurring at any given time in each block (see Fig. 7.2). The width d_0 increases linearly in time with velocity equal to one, as shown in the top left panel of Fig. 7.16. This feature has been highlighted in Fig. 7.5, where each panel shows all the three antidiagonals together at a given time.

As for the block $M(t)$, its main diagonal (top left panel of Fig. 7.3) is not captured in the top left panel of Fig. 7.4 because ℓ is even. In $N(t)$ both the temporal evolutions of the diagonal (middle left panel in Fig. 7.3) and of the antidiagonal (top right panel in Fig. 7.4) display a plateau

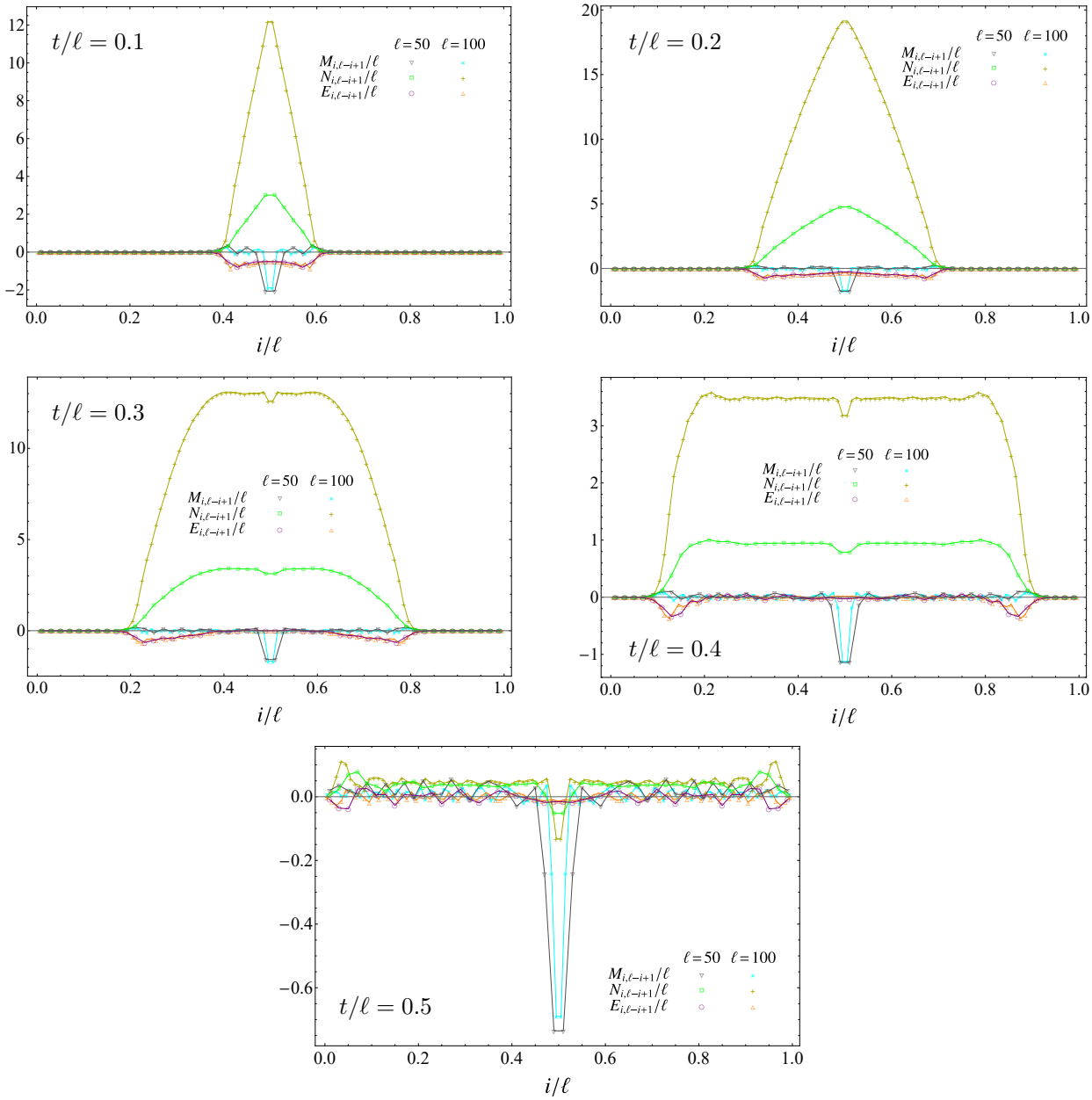

Figure 7.5: Harmonic chain: Antidiagonals of the blocks in the entanglement Hamiltonian matrix (7.3.1) for various times and two values for ℓ. The points where all these antidiagonals become very small evolve linearly in opposite direction travelling from the center towards the endpoints of the interval with velocity equal to one (see top panels in Fig. 7.16, where $2d_0$ denotes the width of the curves shown here).

but we remark that the behaviour before the formation of this plateau is very different.

As first quantitative check, we have compared the linear growth of the entanglement entropy obtained from our numerical data for the harmonic chain with the CFT formula $S_A \simeq 2\pi c\, t/(3\tau_0)$ [81,82] (see also Sec .7.2) with $c = 1$, finding $\tau_0 \simeq 3.79$ (which agrees e.g. with the numerical value obtained in [29]).

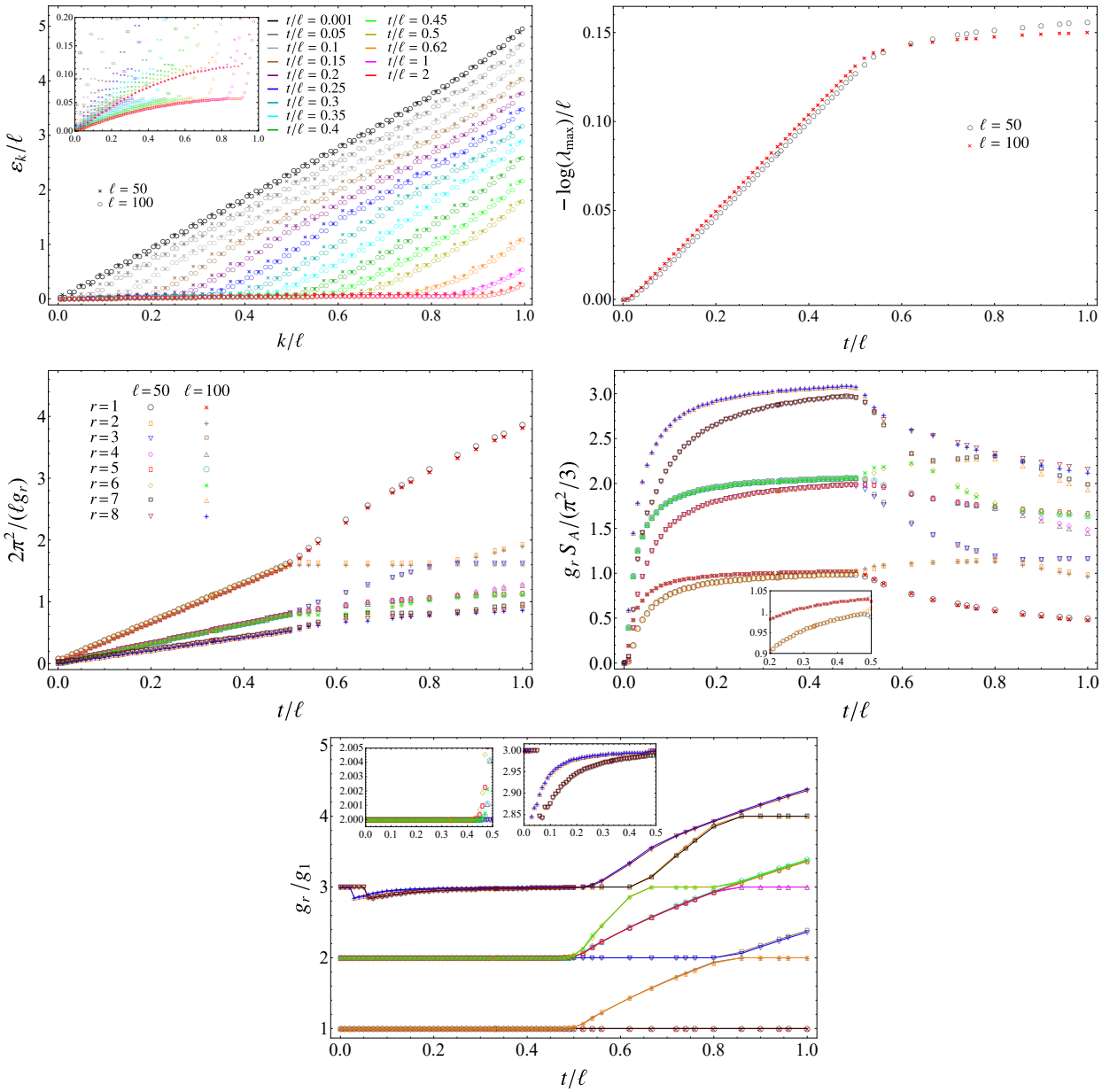

Figure 7.6: Harmonic chain: Entanglement spectrum for an interval of length ℓ after the quench of the frequency parameter given by $\omega_0 = 1$ and $\omega = 0$. Top left: Single particle entanglement spectrum (see (2.4.7)). Top right: Temporal evolution of the largest eigenvalue of the entanglement spectrum. Middle left: Temporal evolution of the first gaps in the entanglement spectrum. The legenda of this panel holds also in the remaining ones. Middle right: Temporal evolution of $g_r S_A$ (the inset zooms in on the lowest plateau, showing that the data having $\ell = 50$ and $\ell = 100$ do not overlap). Bottom: Temporal evolution of the ratios g_r/g_1 between the gaps in the entanglement spectrum (the insets zoom in on the two higher plateaux).

7.3.2 Entanglement spectrum

A numerical analysis for some quantities related to the entanglement spectrum has been reported in Fig. 7.6. The top left panel shows the symplectic spectrum of H_A (see (2.4.7)) for various times and two different values of ℓ. For the low-lying part of this spectrum, i.e. small k's, we have

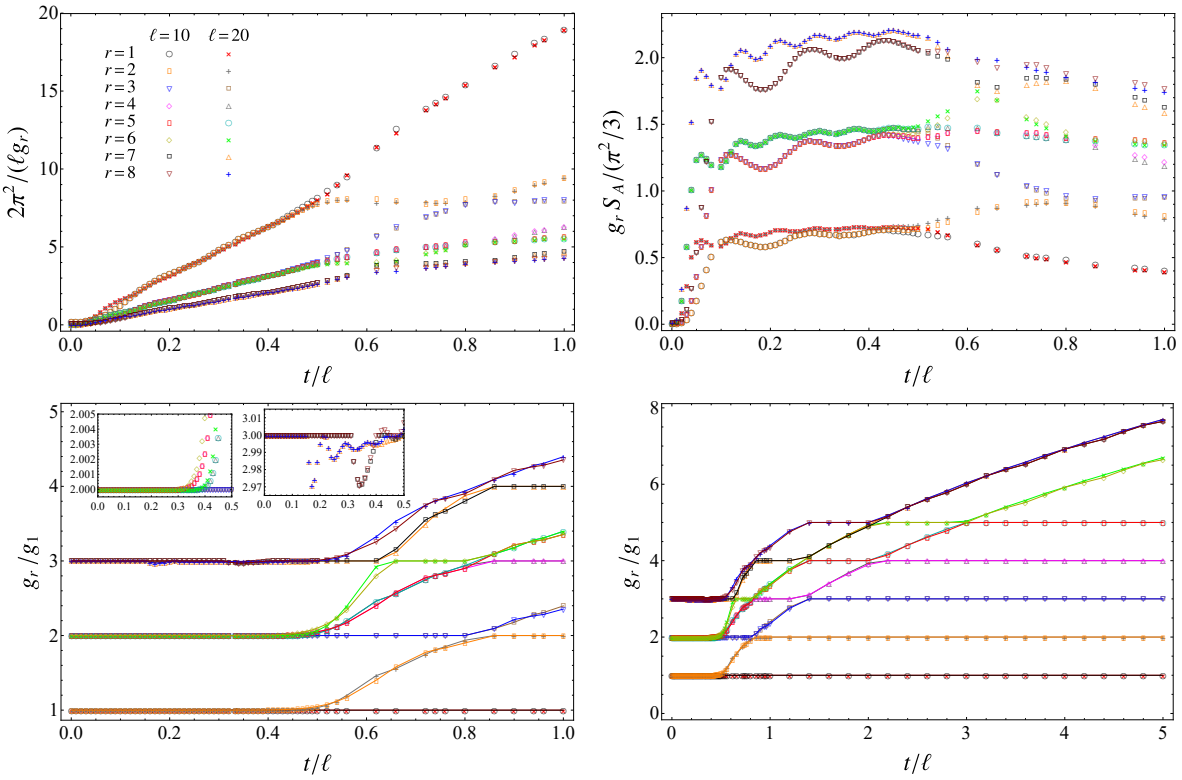

Figure 7.7: Harmonic chain: Temporal evolution of the gaps in the entanglement spectrum for an interval of length ℓ after the quench of the frequency parameter given by $\omega_0 = 5$ and $\omega = 0$ (see also the corresponding panels in Fig. 7.6). Top left: Temporal evolution of the first gaps in the entanglement spectrum. The legenda of this panel holds also for the other ones. Top right: Temporal evolution of $g_r S_A$. Bottom: Temporal evolution of the ratios g_r/g_1 between the gaps in the entanglement spectrum. The panel on the left focuses on the regime $t/\ell < 1$ (the insets zoom in on the two higher plateaux), while the panel on the right highlights the behaviour for long times. The curves in the left panel are very similar to the ones in the bottom panel of Fig. 7.6.

$\varepsilon_k \simeq \varepsilon_{k+1}$ and this degeneracy disappears for high values of k. At small times, ε_k is linear in terms of k while for long time the curve of ε_k bends towards zero, although it never vanishes. It would be interesting to consider ε_k/ℓ in the limit of large values of ℓ. In the top right panel of Fig. 7.6 we consider the temporal evolution of the largest eigenvalue of the entanglement spectrum, which, in terms of the symplectic spectrum of H_A, is given by $\prod_{k=1}^{\ell}(1-e^{-\varepsilon_k})$. Since $S_A^{(n)} \to -\log\lambda_{\max}$ as $n \to \infty$, this curve can be compared with the CFT results for the Rényi entropies [81, 82] and a good agreement is found. Fitting the linear growth of $-\log\lambda_{\max}$ we get a slope of $\frac{1}{2.1}$ times the slope of the entanglement entropy, while the one predicted by (7.2.1) is $\frac{1}{2}$.

In the remaining panels of Fig. 7.6 we explore the temporal evolutions of the gaps in the entanglement spectrum. For the harmonic chain and the bipartition that we are considering here, each element $\lambda_{\boldsymbol{n}}$ of the entanglement spectrum is labeled by a ℓ-dimensional vector $\boldsymbol{n}$, whose entries n_k are non-negative integers [266]. Explicitly, it reads

$$\lambda_{\boldsymbol{n}} = \prod_{k=1}^{\ell} \left[\left(1-e^{-\varepsilon_k}\right) e^{-n_k \varepsilon_k} \right] . \tag{7.3.4}$$

The gaps between the largest eigenvalue and $\lambda_{\boldsymbol{n}}$ can be written as $\log\lambda_{\max} - \log\lambda_{\boldsymbol{n}} = \sum_{k=1}^{\ell} \varepsilon_k\, n_k$.

Let us arrange the symplectic spectrum of H_A in increasing order $\varepsilon_1 \leqslant \varepsilon_2 \leqslant \cdots \leqslant \varepsilon_\ell$. In order to find the gaps $0 < g_1 < g_2 < \dots$ with respect to the largest eigenvalue, one can first introduce $\mathcal{B}_p^{(r)} \equiv \big\{ \sum_{j=1}^{p} \varepsilon_{k_j} \, , 1 \leqslant k_j \leqslant r \big\}$ for $r \geqslant 1$ and then compute the r-th gap as $g_r = \min[(\cup_{p=1}^{r} \mathcal{B}_p^{(r)}) \setminus \{g_j, 1 \leqslant j \leqslant r-1\}]$. This procedure is not optimal, but it allows to get g_r easily also for high values of r. The smallest gaps are given by $g_1 = \varepsilon_1$, $g_2 = \min\{2\varepsilon_1, \varepsilon_2\}$ and $g_3 = \min\big\{3\varepsilon_1, \max\{2\varepsilon_1, \varepsilon_2\}, \varepsilon_3\big\}$.

The data about the evolution of the gaps display two distinct temporal regimes separated by $t/\ell \simeq 1/2$. For $t/\ell < 1/2$, the CFT result (7.2.2), obtained from the analysis of [147] for the semi-infinite line, predicts linear growths in time for the inverse of the gaps with slopes proportional to the conformal spectrum (including also the dimensions of the descendants) allowed by the proper conformal boundary conditions. The numerical data in the middle left panel of Fig. 7.6 display these linear growths for $t/\ell < 1/2$. By fitting the slopes of these linear growths through (7.2.2) with $\tau_0 \simeq 3.79$ obtained above from the linear growth of the entanglement entropy, we find $\Delta_1 = 1.022$, $\Delta_2 = 2.045$ and $\Delta_3 = 3.058$. In order to reduce the influence of the initial state encoded in τ_0, in the middle right panel and in the bottom panel of Fig. 7.6 we consider the temporal evolutions of $g_r S_A$ and the ratios g_r/g_1 respectively, which should be independent of τ_0 according to (7.2.1) and (7.2.2). As for $g_r S_A$, it is evident that curves corresponding to different values of ℓ do not collapse; hence more values of ℓ (possibly also larger than the ones considered here) are needed in order to make comparisons with CFT results.

The temporal evolutions of the ratios g_r/g_1 of the entanglement gaps in the bottom panel of Fig. 7.6 display interesting features. For $t/\ell < 1/2$ the curves having different ℓ's collapse forming plateaux whose heights are given by strictly positive integers. This result agrees with the fact that the underlying CFT contains the primary $\partial_z \phi$ and its descendants.

In Fig. 7.7 we show numerical data for the temporal evolution of the gaps in the entanglement spectrum when the initial state has $\omega_0 = 5$, in order to explore the robustness of the observations made above under changes of the initial state. For this ω_0 we consider small values of ℓ such that the product $\omega_0 \ell$ gets the same values corresponding to the data shown in Fig. 7.6. The qualitative behaviour of $1/g_r$ is the same one observed in Fig. 7.6 (the slopes of the linear growths are different, as expected, being (7.2.2) dependent on the initial state through τ_0). In the temporal evolution of $g_r S_A$ we observe oscillations that are due to the small values of ℓ (indeed, they do not occur in the middle right panel of Fig. 7.6). Interestingly, the temporal evolutions of the ratios g_r/g_1 coincide with the ones reported in Fig. 7.6, meaning that this quantity displays some independence on the initial state. It would be instructive to consider other values of ω_0 and higher gaps in order to understand better how much the temporal evolutions of g_r/g_1 are robust under modifications of the initial state. In the bottom right panel of Fig. 7.7 we have considered also long times and from these data we can identify two regimes: $t/\ell \leqslant 1/2$ and the long time regime. In both these temporal regimes we observe plateaux having the same heights. Thus, the ratios in the CFT spectrum can be read also from the long time regime.

7.3.3 A contour function from the quasi-particle picture

In this subsection we study the temporal evolution of the contour for the entanglement entropies (1.2.10) in harmonic chains after a global quantum quench.

If we consider a subsystem A made by ℓ sites of a given lattice, the contour function for the entanglement entropies $s_A^{(n)} : A \to \mathbb{R}$ has to satisfy the following properties

$$S_A^{(n)} = \sum_{i=1}^{\ell} s_A^{(n)}(i) \qquad\qquad s_A^{(n)}(i) \geqslant 0 \, . \tag{7.3.5}$$

In this subsection we exploit the prescription from [29], which has been detailed in Appendix A.1, for computing the contour functions in harmonic lattices.

We find it natural to consider also the contribution to the entanglement entropies given by an interval $(i_1, i_2) \subset A$, namely

$$\mathcal{S}_A^{(n)}(i_1, i_2) = \sum_{i=i_1}^{i_2} s_A^{(n)}(i) \qquad i_1, i_2 \in A\,. \tag{7.3.6}$$

The entanglement entropies $S_A^{(n)}$ correspond to the special case where i_1 and i_2 are the sites at the boundary of A.

We are interested in the temporal evolution of the above quantities after a global quench and it is often useful to study their increments with respect to their initial value. In particular, for $\mathcal{S}_A^{(n)}(i_1, i_2; t)$ given by (7.3.6), let us introduce

$$\Delta\mathcal{S}_A^{(n)}(i_1, i_2; t) \equiv \mathcal{S}_A^{(n)}(i_1, i_2; t) - \mathcal{S}_A^{(n)}(i_1, i_2; 0)\,. \tag{7.3.7}$$

In [82] a quasi-particle picture has been introduced to explain the temporal evolution of the entanglement entropy after a global quantum quench. The underlying idea is based on the fact that the initial state has very high energy with respect to the ground state of the Hamiltonian governing the temporal evolution; hence it can be seen as a source of quasi-particle excitations. In particular, in one spatial dimension, it is assumed that at $t = 0$ each point of the space emits two quasi-particles with opposite momenta p and $-p$ according to certain probability distribution that depends on both the initial state and the evolution Hamiltonian. Only the particles emitted at the same point are entangled and all the points of the space emit the quasi-particles in the same way. For $t > 0$, the positions of the quasi-particles emitted at the same point x are $x + v_p t$ and $x - v_p t$, being $v_p > 0$ and $v_{-p} = -v_p$ for $p > 0$.

Considering a spatial bipartition $A \cup B$ and two points $x_1 \in A$ and $x_2 \in B$; at time t they are entangled only if they are reached simultaneously by two quasi-particle emitted from the same point x at $t = 0$. The bipartite entanglement between A and B is obtained by summing the contributions of all the points x fulfilling this condition. In particular, for the entanglement entropy we have [82]

$$S_A(t) \approx \int_{x_1\in A} dx_1 \int_{x_2\in B} dx_2 \int_{-\infty}^{\infty} dx \int dp\; \delta(x_1 - x - v_p t)\, \delta(x_2 - x + v_p t)\, \tilde{s}(p) \tag{7.3.8}$$

where $\tilde{s}(p)$ is obtained by multiplying the momentum distribution function and the contribution of the pair of quasi-particles with momenta p and $-p$ to the entanglement entropy. The integration domain of the allowed momenta is model dependent. Performing the spatial integrals in (7.3.8), one finds

$$S_A(t) \approx\; 2\,t \int_{2|v_p|t<\ell} dp\, \tilde{s}(p)\, v_p \;+ \ell \int_{2|v_p|t>\ell} dp\, \tilde{s}(p)\,. \tag{7.3.9}$$

When a maximum velocity $v_{\max}$ exists, S_A grows linearly in time for $v_{\max} t \leqslant \ell/2$, while $S_A \propto \ell$ for $v_{\max} t \gg \ell/2$. In a CFT we have $|v_p| = v_{\max} = 1$ for all p [81, 82]. Notice that (7.3.9) does not take into account the initial value of the entanglement entropy.

The expression (7.3.9) of the entanglement entropy obtained from this quasi-particle picture provides some functions $s_A(x, t)$ such that $S_A(t) = \int_A s_A(x, t) dx$. Let us introduce three positive functions $f_0(x)$, $f_1(x, p, t)$ and $f_2(x, p, t)$ fulfilling the following conditions

$$\int_A f_0(x)\, dx = S_A\big|_{t=0} \qquad \int_A f_1(x, p, t)\, dx = 2 v_p\, t \qquad \int_A f_2(x, p, t)\, dx = \ell\,. \tag{7.3.10}$$

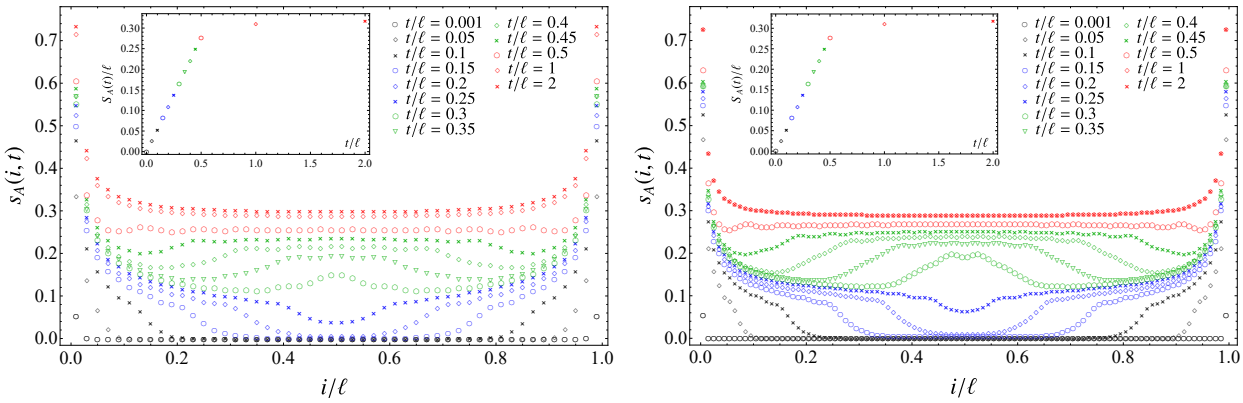

Figure 7.8: Temporal evolution of the contour for the entanglement entropy of an interval made by ℓ sites in the periodic harmonic chain, evaluated from (A.1.8) and (A.1.11). Left: $\ell = 50$. Right: $\ell = 100$. The insets show the temporal evolution of the entanglement entropy obtained through the contour function (see (7.3.5) for $n = 1$).

Taking into account the initial value $S_A|_{t=0}$ in (7.3.9) and employing the constraints (7.3.10), it is straightforward to write the entanglement entropy as $S_A(t) = \int_A s_A(x,t)\,dx$ with

$$s_A(x,t) = \int_{2|v_p|t<\ell} dp\, f_1(x,p,t)\,\tilde{s}(p) + \int_{2|v_p|t>\ell} dp\, f_2(x,p,t)\,\tilde{s}(p) + f_0(x)\,. \tag{7.3.11}$$

Since our configuration is symmetric with respect to the center of the interval, it is natural to require that $f_0(x) = f_0(\ell - x)$ and $f_i(x,p,t) = f_i(\ell - x,p,t)$ for $i = 1,2$. As mentioned above, (7.3.8) is obtained by assuming that the emission of the quasi-particles is spatially homogeneous, and this assumption provides a significant restriction to the form of the functions in (7.3.11).

Let us consider the infinitesimal contribution to the entanglement entropy $dS_A(t) = s_A(x,t)dx$ provided by an infinitesimal interval $(x - dx/2, x + dx/2)$ centered in a point $x \in A$. At $t > 0$, this quantity is proportional to the number of quasi-particles (i) that are in this infinitesimal interval (ii) whose entangled quasi-particle is in B. The quasi-particles fulfilling these conditions have been emitted at $t = 0$ from the position $x - |v_p|t$ or from $x + |v_p|t$. For $v_p\, t \leq \ell/2$, the quasi-particles emitted at $x - |v_p|t$ contribute when $2|v_p|\, t > x$, while the ones emitted at $x + |v_p|t$ matter when $2|v_p|\, t > \ell - x$. Instead, for $v_p\, t > \ell/2$ the quasi-particles coming from both $x - |v_p|t$ and $x + |v_p|t$ contribute. These considerations lead to the following expressions

$$f_1(x,p,t) = \frac{1}{2}\Big[\varphi_1(x)\,\Theta(2|v_p|\,t - x) + \varphi_1(\ell - x)\,\Theta(2|v_p|\,t - \ell + x)\Big] \qquad f_2(x,p,t) = \varphi_2(x) \tag{7.3.12}$$

where φ_j are non negative, $\varphi_2(\ell - x) = \varphi_2(x)$ and Θ is the Heaviside step function. The spatial homogeneity in the quasi-particle production leads to drastic simplifications given by $\varphi_1(x) = \varphi_2(x) = 1$ identically.

The functions in (7.3.12) fulfil (7.3.10) and the symmetry conditions introduced in the text below (7.3.11). Thus, the contour function (7.3.11) becomes

$$s_A(x,t) = \frac{1}{2}\left[\int_{x<2|v_p|t<\ell} \tilde{s}(p)\,dp + \int_{\ell-x<2|v_p|t<\ell} \tilde{s}(p)\,dp\right] + \int_{2|v_p|t>\ell} \tilde{s}(p)\,dp + f_0(x) \tag{7.3.13}$$

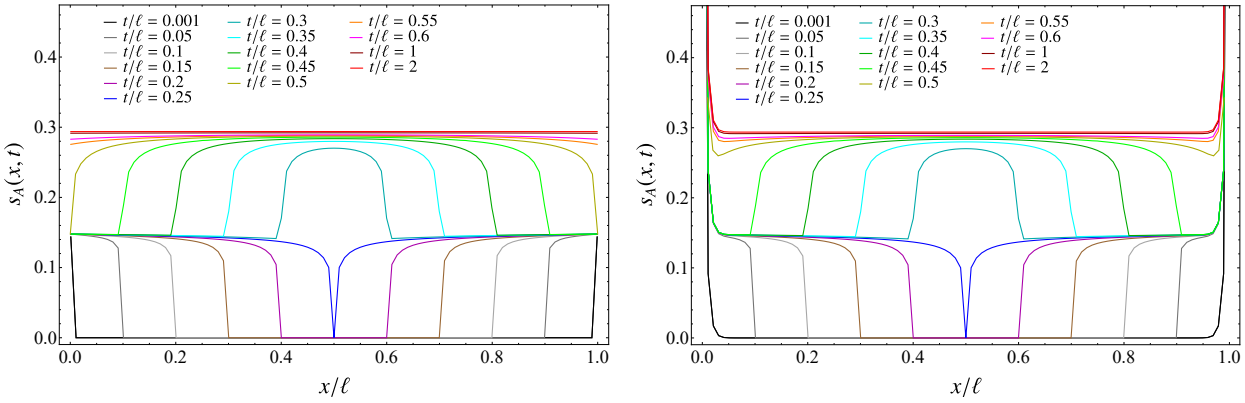

Figure 7.9: Temporal evolution of the contour for the entanglement entropy of an interval of length ℓ in the periodic harmonic chain according to (7.3.13), obtained through the quasi-particle picture (see Sec .7.3.3). Left: $f_0(x) = 0$ identically. Right: $f_0(x) = s^{(1)}_{A,0}(x, 0)$ defined in (7.2.9) has been used in (7.3.13) in order to capture the linear divergence close to the endpoints.

Integrating this expression between two generic points $0 < x_1 < x_2 < \ell$, we obtain

$$\mathcal{S}_A(x_1, x_2; t) = \frac{x_2 - x_1}{2}\left[2\int_{2|v_p|t>\ell} \tilde{s}(p)\, dp + \int_{\ell - x_1 < 2|v_p|t < \ell} \tilde{s}(p)\, dp + \int_{x_2 < 2|v_p|t < \ell} \tilde{s}(p)\, dp\right] \tag{7.3.14}$$

$$+\frac{1}{2}\left[\int_{\ell - x_2 < 2|v_p|t < \ell - x_1} \tilde{s}(p)\,(2|v_p|t + x_2 - \ell)\, dp + \int_{x_1 < 2|v_p|t < x_2} (2|v_p|t - x_1)\,\tilde{s}(p)\, dp\right] + \int_{x_1}^{x_2} f_0(x)\, dx\,.$$

The function $\tilde{s}(p)$ can be computed by employing the fact that the density of thermodynamic entropy in the stationary state coincides with the one of the entanglement entropy in (7.3.9) [320].

As already discussed in Sec. 3.5, for the global quench in the harmonic chain, the stationary values of local observables can be described by a Generalised Gibbs Ensemble. The velocity v_p of the quasi-particles can be computed as $v_p = \partial_p \Omega_p$, where Ω_p the dispersion relation of the model after the quench. For the harmonic chain, in [84, 320] it has been found that

$$\tilde{s}(p) = \frac{1}{2\pi}\big[(n_p + 1)\log(n_p + 1) - n_p \log n_p\big] \qquad n_p = \frac{1}{4}\left(\frac{\omega_p}{\omega_{0,p}} + \frac{\omega_{0,p}}{\omega_p}\right) - \frac{1}{2} \tag{7.3.15}$$

where n_p is given by (3.5.11). The dispersion relation (3.3.20) provides the velocity of each momentum mode as follows

$$v_p \equiv \frac{\partial \Omega_p}{\partial p} = \frac{(\kappa/m)\sin(2p)}{\sqrt{\omega^2 + (4\kappa/m)\sin^2(p)}} \tag{7.3.16}$$

Let us remark that the above results based on the quasi-particle picture hold for any value of the frequencies ω_0 and ω, while in our numerical analysis $\omega_0 = 1$ and $\omega = 0$.

In Fig. 7.8 we show the temporal evolution of the contour for the entanglement entropy evaluated through the prescription of [29] discussed in Appendix A.1. This qualitative behaviour, which has been observed also in [28] for fermionic chains after a global quench, has been obtained through the naive analysis performed in Sec .7.2 by employing the CFT formulas of [147] (see the right panel of Fig. 7.1). The curves in Fig. 7.8 can be interpreted in terms of two fronts starting from the endpoints and travelling in the opposite directions towards the center of the interval. Each front has a plateau, that is not exactly horizontal in the numerical data. Since the two fronts

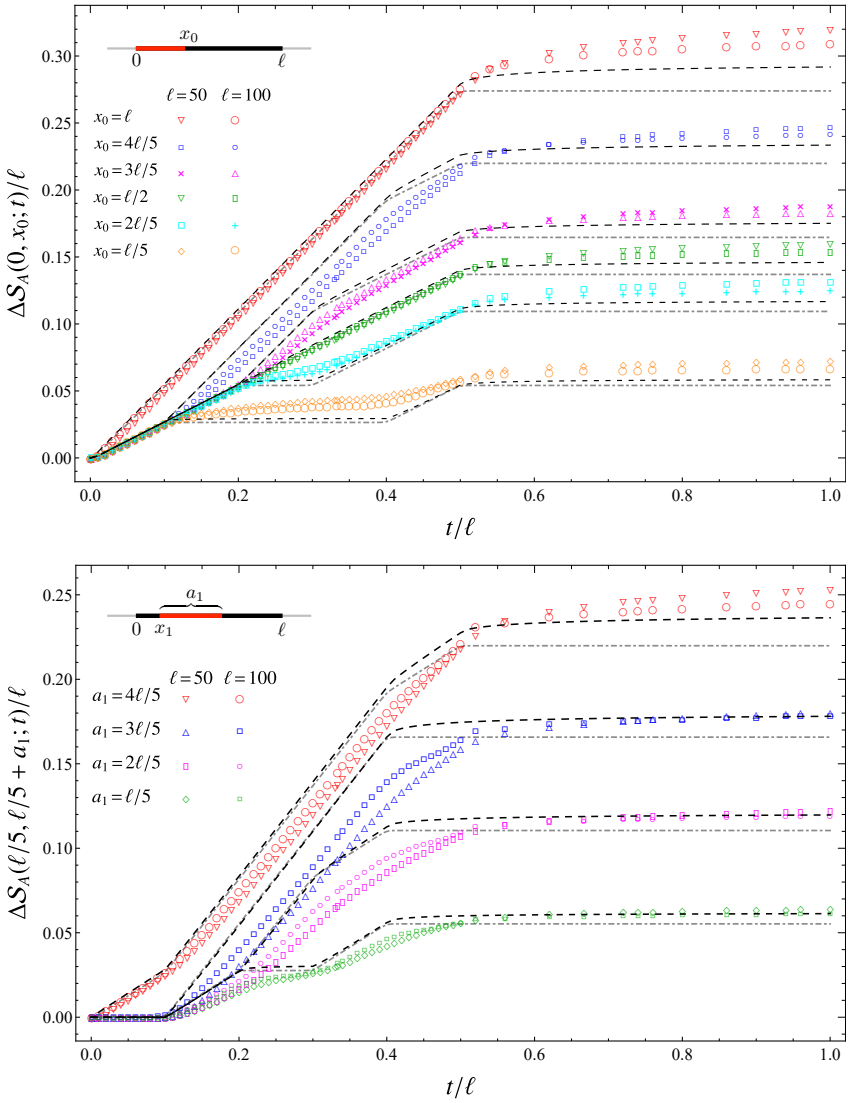

Figure 7.10: Harmonic chain: Temporal evolution of (7.3.7) for $n = 1$.

have velocity equal to 2 (see also Sec .7.2), they cross each other around $t/\ell \simeq 1/4$ and superpose until they reach the opposite endpoint around $t/\ell \simeq 1/2$. Notice that the data shown in the two panels of Fig. 7.8 do not overlap, meaning that larger values of ℓ are needed to obtain a prediction for this curve in the limit of large ℓ. This prediction can be done from the data obtained for the global quench in the chain of free fermions considered in Sec .7.4 (see Fig. 7.18). We remark that the data in Fig. 7.8 display a divergence close to the endpoints of the interval that is independent of time.

The contour function for the entanglement entropy obtained through the quasi-particle picture (namely by employing (7.3.13), (7.3.15) and (7.3.16)) is shown in Fig. 7.9, where in the left panel $f_0(x) = 0$ identically, while $f_0(x) = s^{(1)}_{A,0}(x, 0)$ in (7.2.9) has been chosen in the right panel. The latter choice leads to reproduce also the linear divergencies of the contour function for the entanglement entropy near the endpoints of the interval. The quasi-particle picture formula (7.3.13) captures in a better way some features of the numerical data with respect to the corresponding CFT expression (7.2.8). For instance, the curve in Fig. 7.9 having $t/\ell = 1/4$ is not flat in the

middle of the interval and that the local maximum of the curve having $1/4 < t/\ell < 1$ increases with time, while in the right panel of Fig. 7.1 it is constant and equal to half of its asymptotic value for $t \to \infty$.

In Fig. 7.10 we consider the quantity introduced in (7.3.7) with $n = 1$ for two different choices of (i_1, i_2): the case with $i_1 = 0$ (top panel) and the case with fixed $0 < i_1 < \ell/2$ and i_2 variable (middle panel). The data points (obtained through (A.1.8), (7.3.6), (7.3.7) and (A.1.11)) are compared against the corresponding formula coming from the quasi-particle picture expression (7.3.14) (black dashed curves), where the terms containing f_0 cancel, and also against the naive CFT expression (7.2.12) (grey dashed-dotted curves). Notice that the CFT curves and the ones obtained from the quasi-particle picture change slope at the same values of t/ℓ. At the beginning of the evolution, $\Delta\mathcal{S}_A$ grows linearly with a slope that depends on whether (i_1, i_2) contains one or two endpoints of A (notice that the red curves in the top and bottom panels correspond to the entanglement entropy), while it vanishes whenever the endpoints of A do not belong to (i_1, i_2). For $t/\ell > 1/2$ all the pairs of quasi-particles have contributed and the curves reach a constant value proportional to the size of the interval (i_1, i_2).

For $t/\ell < 1/2$, all the curves in Fig. 7.10 exhibit a piecewise linear behaviour and, for a given configuration, the slope changes at most four times in correspondence to values of t/ℓ that depend on (i_1, i_2) and that are captured both by the naive CFT expression (7.2.12) and by the quasi-particle picture expression (7.3.14). In the top panel of Fig. 7.10 the changes of slope occur at $t/\ell = x_0/(2\ell)$, $t/\ell = (\ell - x_0)/(2\ell)$ and $t/\ell = 1/2$; and in the bottom panel at $t/\ell = x_1/2$, $t/\ell = (a_1 + x_1)/(2\ell)$, $t/\ell = (\ell - a_1 - x_1)/(2\ell)$ and $t/\ell = (\ell - x_1)/(2\ell)$ (in the data shown correspond to $x_1 = \ell/5$). First we observe that the segments composing any piecewise linear curve are horizontal or have a positive slope that can take two values such that one is twice the other one. The quasi-particles can entangle (i_1, i_2) with B by crossing one or both the endpoints of A. Denoting by $\mathfrak{n}_R$ ($\mathfrak{n}_L$) the number of particles entangling (i_1, i_2) with B across the right (left) endpoint of A, we have that the segment is horizontal whenever both $\mathfrak{n}_R$ and $\mathfrak{n}_L$ are constant in time. Instead, when only either $\mathfrak{n}_R$ or $\mathfrak{n}_L$ is increasing in time, the corresponding segment has a positive slope, that becomes twice this value whenever both $\mathfrak{n}_R$ and $\mathfrak{n}_L$ are increasing in time. By adapting these considerations to the configurations for (i_1, i_2) considered in the two panels of Fig. 7.10, one obtains the above values of t/ℓ corresponding to the changes in the slope of the piecewise linear curves.

7.4 Interval in a chain of free fermions

In this section we study the temporal evolution of the entanglement Hamiltonian matrix after the global quench in a chain of free fermions introduced in [4, 85].

Let us consider the following inhomogeneous Hamiltonian written in terms of the fermionic creation and annihilation operators $\hat{c}_n$ and $\hat{c}_n^\dagger$, (that satisfy the standard anticommutation relations $\{\hat{c}_n^\dagger, \hat{c}_m^\dagger\} = \{\hat{c}_n, \hat{c}_m\} = 0$ and $\{\hat{c}_n, \hat{c}_m^\dagger\} = \delta_{m,n}$) [85]

$$\widehat{H}_0 = -\frac{1}{2} \sum_{n=-\infty}^{+\infty} t_n \big(\hat{c}_n^\dagger \, \hat{c}_{n+1} + \hat{c}_{n+1}^\dagger \, \hat{c}_n\big) \tag{7.4.1}$$

where $t_{2n} = 1$ and $t_{2n+1} = 0$, namely only pairs of sites are coupled (dimerized chain). The system is half filled and prepared in the ground state $|\psi_0\rangle$ of H_0.

At $t = 0$ the inhomogeneity is removed and the unitary time evolution of $|\psi_0\rangle$ is governed by

the translation invariant hopping Hamiltonian given by

$$\widehat{H} = -\frac{1}{2}\sum_{n=-\infty}^{+\infty} \big(\hat{c}_n^\dagger\, \hat{c}_{n+1} + \hat{c}_{n+1}^\dagger\, \hat{c}_n\big) \tag{7.4.2}$$

which is also known as the tight binding model at half filling.

In [85] the analytic expression of the correlation matrix after the global quench has been computed. Its generic element $C_{i,j}(t) \equiv \langle \hat{c}_i^\dagger(t)\, \hat{c}_j(t)\rangle$ reads

$$C_{i,j}(t) = C_{i,j}^{(\infty)} + \mathrm{i}\,\frac{i-j}{4t} e^{-\mathrm{i}\frac{\pi}{2}(i+j)} J_{i-j}(2t) \tag{7.4.3}$$

where $J_\nu(x)$ is the Bessel function of the first kind and

$$C_{i,j}^{(\infty)} \equiv \frac{1}{2}\left[\delta_{i,j} + \frac{1}{2}\big(\delta_{i,j+1} + \delta_{i,j-1}\big)\right]. \tag{7.4.4}$$

By employing that $J_{-\nu}(x) = (-1)^\nu J_\nu(x)$, we have that $\mathrm{Re}[C_{i,j}(t)]$ is symmetric and that $\mathrm{Im}[C_{i,j}(t)]$ is antisymmetric. Furthermore, we remark that $C_{i,j}(t) \to C_{i,j}^{(\infty)}$ as $t \to +\infty$; hence the correlation matrix is real in the asymptotic regime of long time.

7.4.1 Entanglement Hamiltonian matrix

Considering an interval A containing ℓ sites labelled by $1 \leqslant i \leqslant \ell$, the generic element of the $\ell \times \ell$ correlation matrix $C_A(t)$ is obtained by just restricting to the rows and columns corresponding to the sites in A, namely $C_A(t)_{i,j} = C(t)_{i,j}$ in (7.4.3) with $1 \leqslant i, j \leqslant \ell$. The entanglement Hamiltonian of A after this global quench is

$$\widehat{K}_A = \sum_{i,j=1}^{\ell} T_{i,j} \hat{c}_i^\dagger \hat{c}_j \tag{7.4.5}$$

with $\hat{c}_i$ and $\hat{c}_i^\dagger$ the fermionic creation and annihilation operators appearing in the Hamiltonians (7.4.1) and (7.4.2) and the matrix T given by [191]

$$T^{\mathrm{t}} = \log\big(C_A(t)^{-1} - \mathbf{1}\big)\,. \tag{7.4.6}$$

If we call η_k the eigenvalues of T and ζ_k the eigenvalues of C_A, we have $\eta_k = \log(1/\zeta_k - 1)$. For a generic value of t, the entanglement Hamiltonian matrix T in (7.4.6) is a complex $\ell \times \ell$ matrix. Since T is hermitian at any t, its real part is symmetric and its imaginary part is antisymmetric. Thus, we can focus on the p-th diagonal of these two matrices with $p \geqslant 0$.

The eigenvalues $\zeta_k \in (0, 1)$ and many of them lie exponentially close to 0 and 1. This forces us to work with very high precision in order to get finite results for (7.4.6). In particular, the largest interval we considered has $\ell = 600$ sites and we employed between 900 and 2500 digits, depending on the value of t. The needed working precision decreases as time increases.

Also for this global quench, the configuration given by an interval in the infinite line is symmetric with respect to the center of the interval and this leads to a symmetry in the elements of the p-th diagonal. In particular, the odd diagonals of T are symmetric, while the even ones are antisymmetric, namely $T_{i,i+p} = T_{\ell-i-p+1,\ell-i-p+1}$ for odd p and $T_{i,i+p} = -T_{\ell-i-p+1,\ell-i-p+1}$ for even p. The main diagonal vanishes identically.

In Fig. 7.11 and Fig. 7.12 we show respectively the real part of T and the imaginary part of T of an interval with $\ell = 400$ for nine values of t. For $t \to \infty$ the imaginary part of T vanishes (a

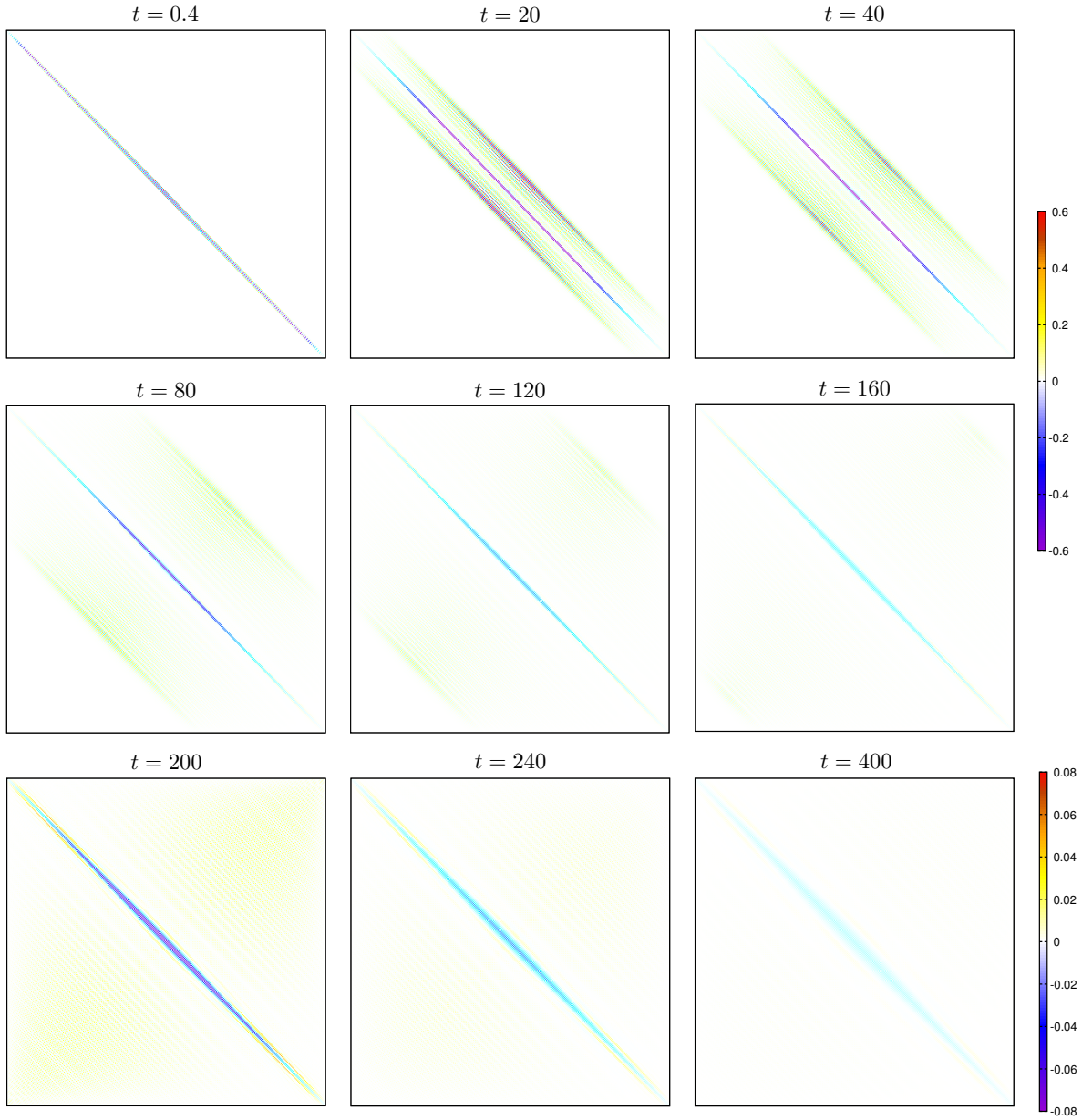

Figure 7.11: Temporal evolution of the real part of the entanglement Hamiltonian matrix (7.4.6) of an interval with $\ell = 400$ in the infinite chain of free fermions after the global quench (see Sec .7.4).

detailed analysis of this asymptotic regime is performed in Sec .7.4.4). We also checked numerically that the imaginary part of T vanishes for $t \to 0$, as expected. In the complex matrix T the odd diagonals are real, while the even diagonals are purely imaginary, like in the correlation matrix (7.4.3).

As time evolves, the amplitude of the elements of T decreases; indeed, in Fig. 7.11 and Fig. 7.12 a zoom is needed for large values of t in order to appreciate the fact that T is non vanishing. It is straightforward to observe that at the beginning the main contribution is localised on the diagonals close to the main one and that, during the temporal evolution, also the diagonals corresponding to longer range interactions become more important.

In Fig. 7.13 we show the temporal evolution of the first four diagonals in the entanglement

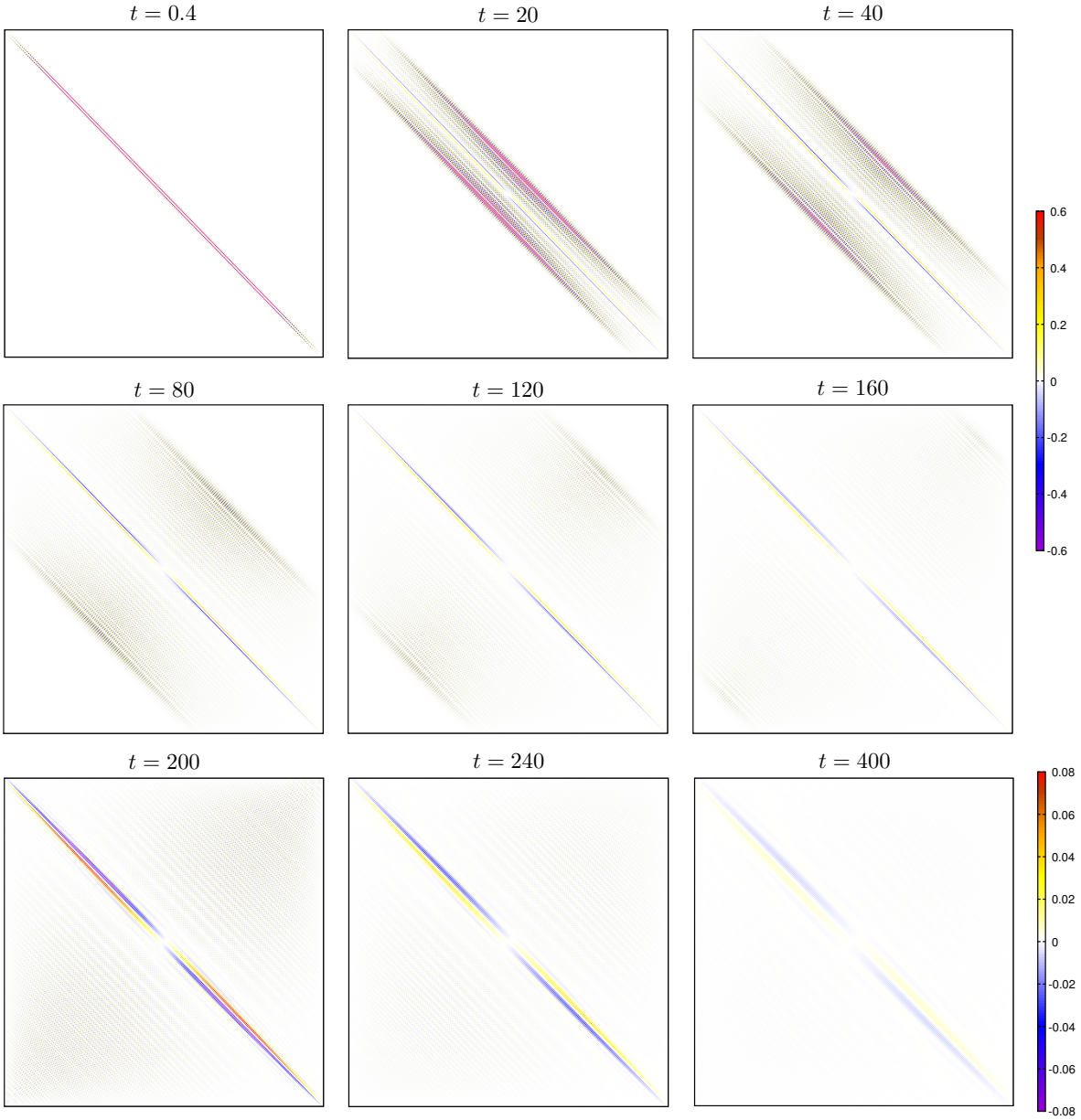

Figure 7.12: Temporal evolution of the imaginary part of the entanglement Hamiltonian matrix (7.4.6) of an interval with $\ell = 400$ in the infinite chain of free fermions after the global quench (see Sec .7.4).

Hamiltonian matrix. Notice that $T_{i,i+1}$ is always positive, while in the other panels also negative values occur. We find it worth remarking that all the curves displayed in this figure vanish at the endpoints of the interval.

In Fig. 7.11 and Fig. 7.12 it is straightforward to observe that the diagonals providing a long range interaction become more relevant as time evolves by forming a band around the main diagonal whose width $2d_0$ increases with time. A similar feature has been highlighted for the global quench in the harmonic chain discussed in Sec .7.3.1. This observation naturally leads to consider the antidiagonals in $\mathrm{Re}(T)$ and $\mathrm{Im}(T)$, that are shown in Fig. 7.14 and Fig. 7.15, making evident the occurrence of a band and the increasing of its width during the temporal evolution. The width

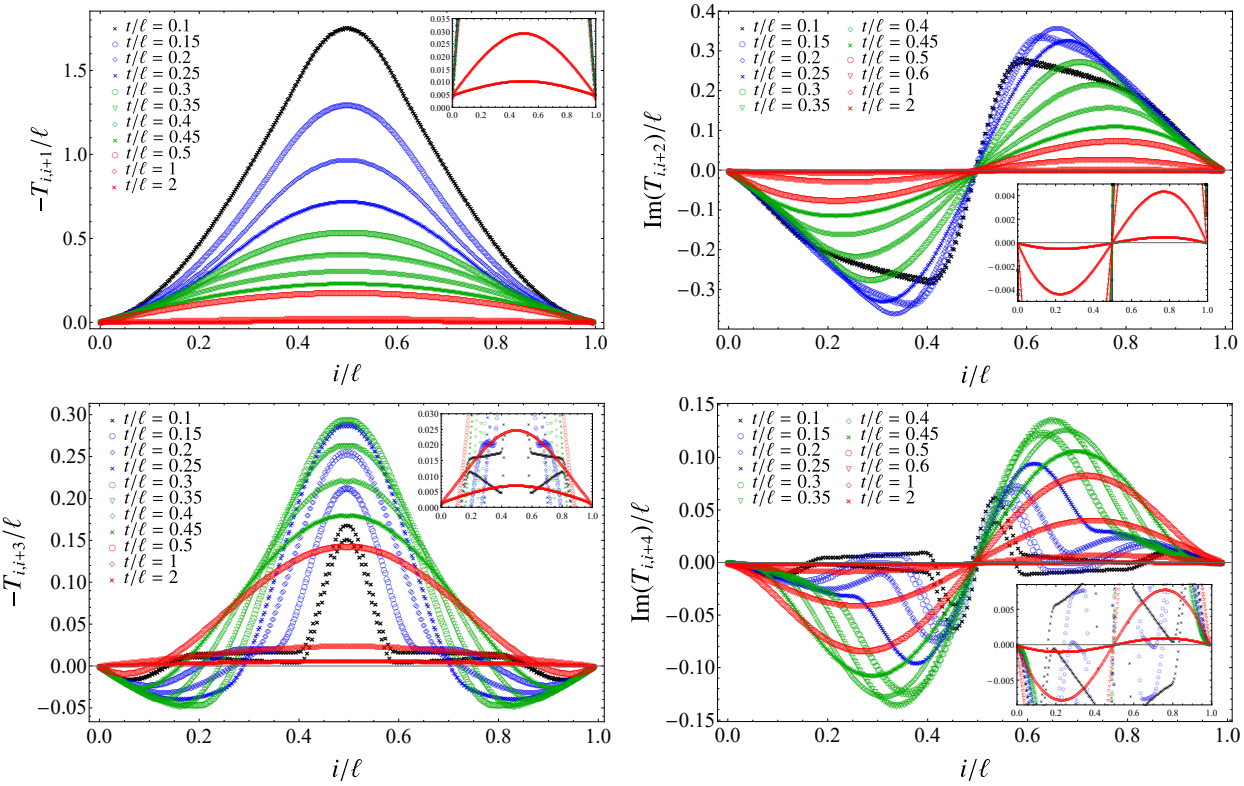

Figure 7.13: Chain of free fermions: Temporal evolution of the p-th diagonal with $1 \leqslant p \leqslant 4$ of the entanglement Hamiltonian matrix (7.4.6) of an interval with $\ell = 400$ after the global quench. The insets zoom in on small values, in order to show the curves for large times.

$2d_0$ of this band can be defined by taking the distance between the two minima for $\mathrm{Re}(T)$ and the distance between the minimum and the maximum for $\mathrm{Im}(T)$. In the bottom panels of Fig. 7.16 we show that $d_0(t)$ defined in this way increases linearly with velocity equal to one as time evolves.

7.4.2 Entanglement spectrum

Also for this global quench we find it worth considering the temporal evolution of some quantities related to the entanglement spectrum. In the top left panel of Fig. 7.17, the eigenvalues $\eta_k = \log(1/\zeta_k - 1)$ of the hermitian matrix T obtained from the eigenvalues ζ_k of the reduced correlation matrix $C_A(t)$ are shown for different values of time. The solid black curve corresponds to the asymptotic curve for $t \to \infty$ obtained in [85]. Since $\eta_k = -\eta_{\ell-k+1}$ and only even values of ℓ are considered, we find it convenient to label these eigenvalues as η_k with $k = \pm\frac{1}{2}, \pm\frac{3}{2}, \cdots \pm\frac{\ell-1}{2}$. This gives $\eta_k = -\eta_{-k}$.

The eigenvalues η_k, also called single particle entanglement energies, provide the entanglement spectrum. Indeed, we can associate a value $n_k = \{0, 1\}$, with $k = \pm\frac{1}{2}, \pm\frac{3}{2}, \cdots \pm\frac{\ell-1}{2}$, to each eigenvalue η_k in such a way that the elements $\lambda_{\boldsymbol{n}}$ of the entanglement spectrum are determined by the all the possible vectors $\boldsymbol{n}$ with entries given by n_k as

$$\lambda_{\boldsymbol{n}} = \frac{e^{-\sum_{k=-(\ell-1)/2}^{(\ell-1)/2} \eta_k \, n_k}}{\prod_{k=-(\ell-1)/2}^{(\ell-1)/2} (1 + e^{-\eta_k})} \,. \tag{7.4.7}$$

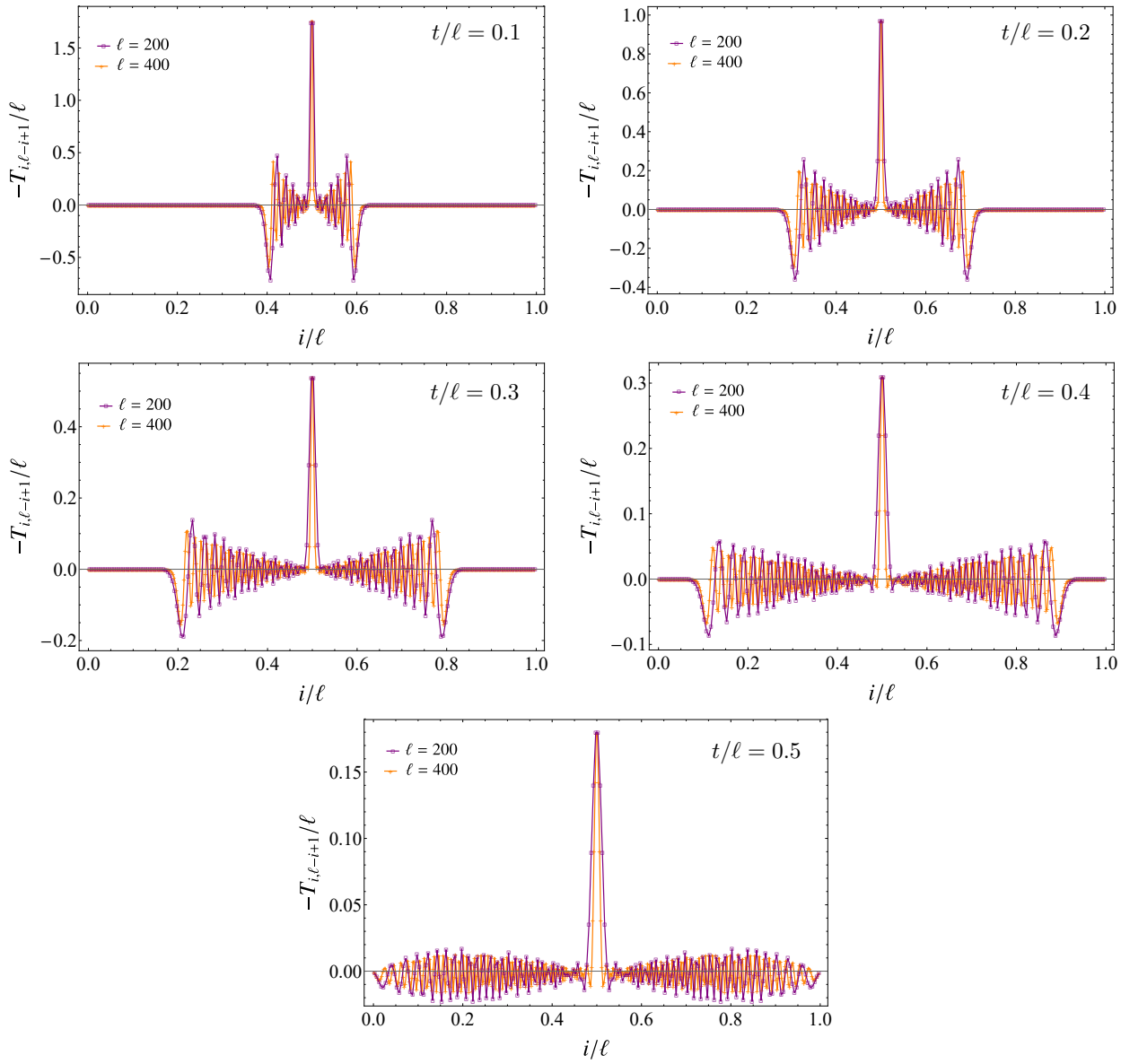

Figure 7.14: Chain of free fermions: Antidiagonal of the real part of the entanglement Hamiltonian matrix (7.4.6) (see also Fig. 7.11) for various times and two different lengths. The points corresponding to the two minima travel in opposite directions from the center of the interval towards the endpoints with velocity equal to one (see also the bottom panels in Fig. 7.16, where $2d_0$ denotes the distance between these two minima).

The largest eigenvalue is given by the configuration where all the modes with negative η_k are occupied and therefore can be written as $\lambda_{\max} = \big[\prod_k (1+e^{-\eta_k})\big]^{-1} \prod_{k<0} e^{-\eta_k}$, whose temporal evolution for $\ell = 200$ and $\ell = 400$ is shown in the top right panel of Fig. 7.17.

The gaps in the entanglement spectrum can be computed from the single particle entanglement energies η_k by considering the particle-hole excitations with respect to the Fermi level. For the first gaps $0 < g_1 < g_2 < \dots$, this analysis gives $g_1 = 2\eta_{\frac{1}{2}}$, $g_2 = \eta_{\frac{1}{2}} + \eta_{\frac{3}{2}}$ and $g_3 = \min\big\{\eta_{\frac{1}{2}} + \eta_{\frac{5}{2}}\,, 2\eta_{\frac{3}{2}}\big\}$. The expressions for the higher gaps become difficult to write as r increases, but this can be done

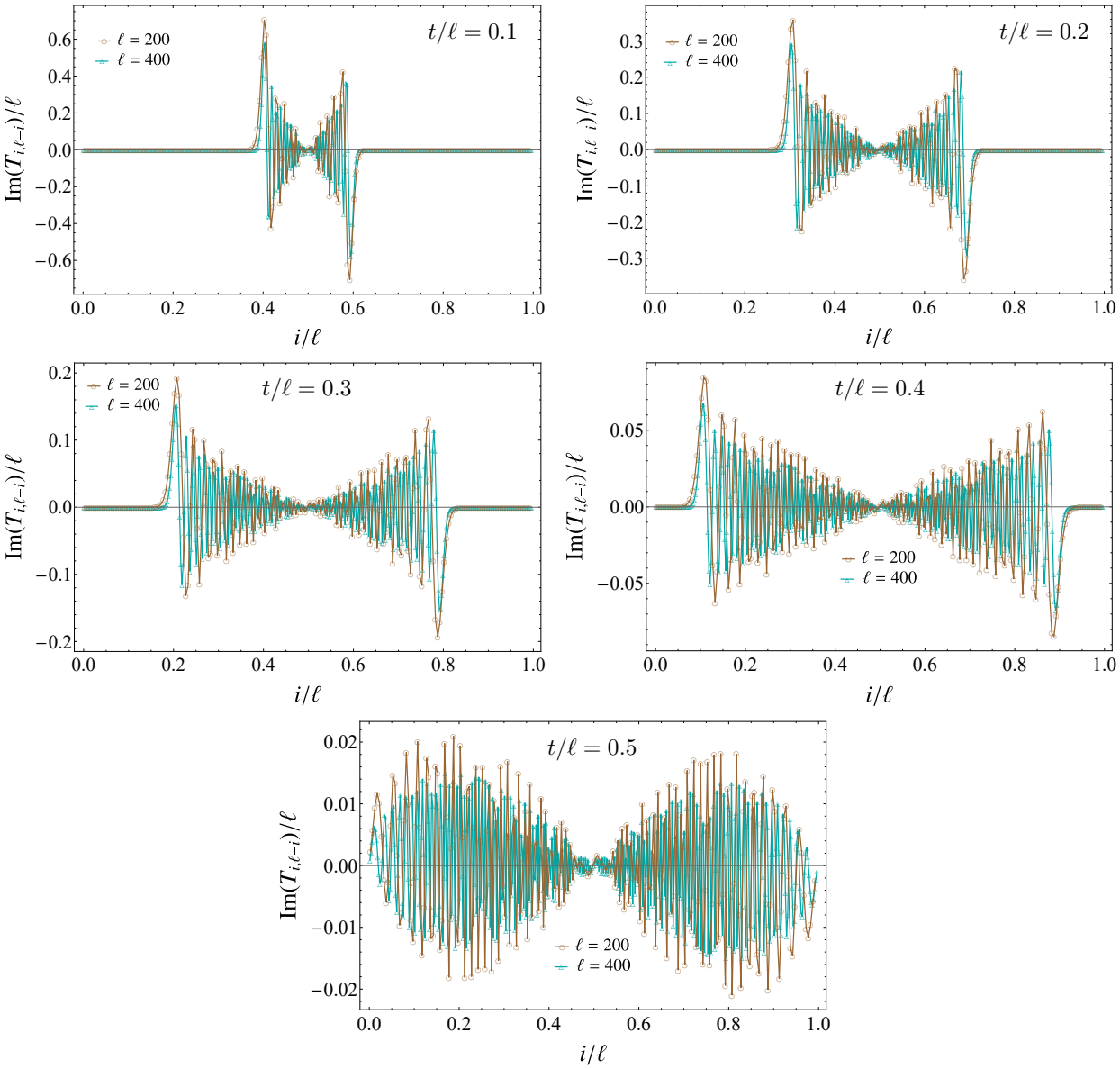

Figure 7.15: Chain of free fermions: Antidiagonal of the imaginary part of the entanglement Hamiltonian matrix (7.4.6) (see also Fig. 7.12) for various times and two different lengths. The points corresponding to the maximum and to the minimum travel in opposite directions from the center of the interval towards the endpoints with velocity equal to one (see also the bottom panels in Fig. 7.16, where $2d_0$ denotes the distance between the two extrema).

numerically in a systematic way. For these entanglement gaps we carry out an analysis similar to the one performed for the corresponding quantities in the harmonic chain (see Fig. 7.6), whose results are collected in the middle and bottom panels of Fig. 7.17. Also for this global quench the data about the temporal evolution of the entanglement gaps display two distinct regimes separated by $t/\ell \simeq 1/2$. In the middle left panel of Fig. 7.17 we show the temporal evolution of the inverse of the entanglement gaps, in order to highlight the linear growths predicted by the CFT formula (7.2.2) before $t/\ell \simeq 1/2$. The numerical value for τ_0 is obtained by fitting the linear growth of

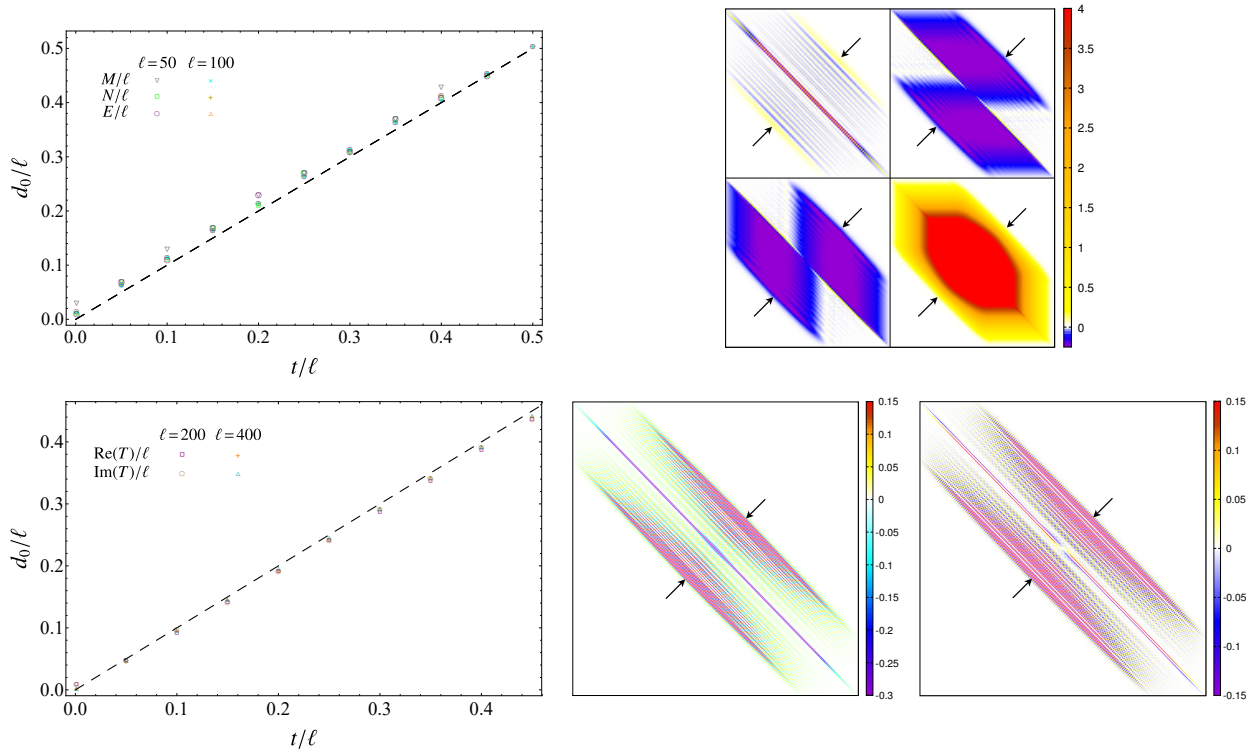

Figure 7.16: Linear growth of the width of the bands occurring in the blocks of the entanglement Hamiltonian matrices after the global quench. The width $2d_0$ of the various bands is highlighted by the black arrows in the panels on the right, where the entanglement Hamiltonian matrices are shown at a typical value t such that $t/\ell \in (0, 1/2)$ (see Fig. 7.2, Fig. 7.11 and Fig. 7.12). In the left panels the slope of the dashed lines is one. Top: Harmonic chain (see also Fig. 7.5). Bottom: Chain of free fermions (see also Fig. 7.14 and Fig. 7.15).

the entanglement entropy through the CFT formula $S_A \simeq 2\pi c\, t/(3\tau_0)$ of [81,82] (see Sec .7.2) with $c = 1$ for the free massless Dirac fermion, finding $\tau_0 \simeq 3.26$. This allows to fit the slope of the linear growths in the middle left panel of Fig. 7.17 through (7.2.2), finding $\Delta_1 = 1.224$, $\Delta_2 = 2.448$ and $\Delta_3 = 3.662$. We find it curious that the linear growths in the middle left panels of Fig. 7.6 and Fig. 7.17 basically coincide, despite the diversity of the underlying models (notice that the values of τ_0 are different in the two quenches).

As done for the harmonic chain, in order to reduce the influence of the parameter τ_0, we consider the temporal evolutions of $g_r S_A$ and of the ratios g_r/g_1. As for $g_r S_A$ (middle right panel of Fig. 7.17), the curves corresponding to different values of ℓ collapse much better than the ones obtained for the quench in the harmonic chain (middle right panel of Fig. 7.6) because the values of ℓ considered for this fermionic chain are large enough. Nonetheless, the zooms in the insets show that these curves are distinguishable.

Also for this quench the temporal evolutions of the ratios g_r/g_1 in the entanglement spectrum (bottom panel of Fig. 7.17) display the most interesting features. When $t/\ell < 1/2$, curves having different ℓ's nicely collapse identifying neatly plateaux that correspond to strictly positive integers. The same positive integers are obtained also in the asymptotic regime of long time and large ℓ. We checked numerically this result by plugging into the code employed to study g_r/g_1 the asymptotic values for η_k found in [85], that will be reported later in Sec .7.4.4 (see (7.4.12)). The

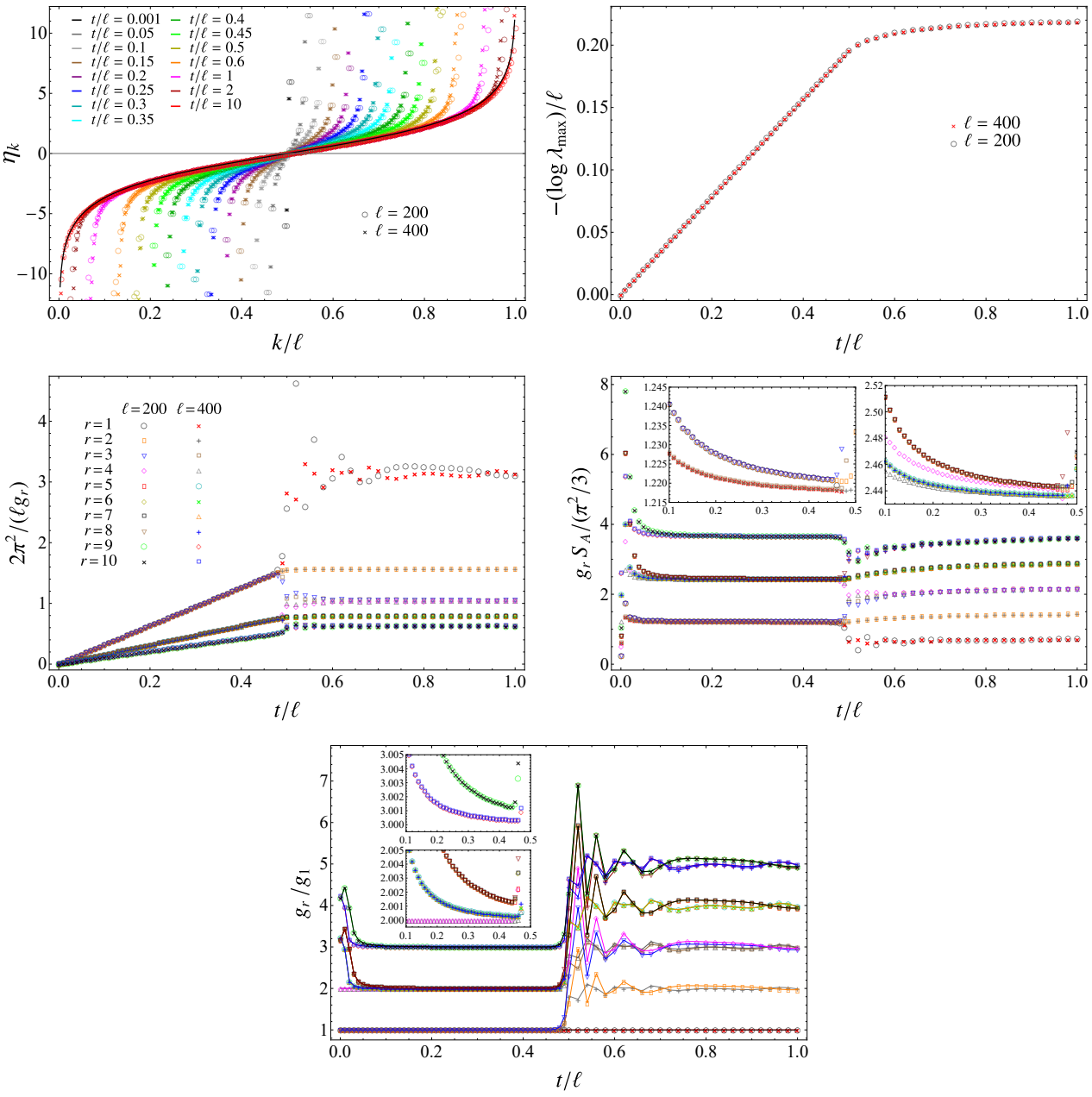

Figure 7.17: Chain of free fermions: Entanglement spectrum for an interval of length ℓ after the quench discussed in Sec .7.4. Top left: Single particle entanglement spectrum for different values of t (see also Fig. B.1 in [85]). Top right: Temporal evolution of the largest eigenvalue of the entanglement spectrum. Middle left: Temporal evolution of the first gaps in the entanglement spectrum. The legenda of this panel holds also in the remaining ones. Middle right: Temporal evolution of $g_r S_A$ (the insets zoom in on the two lower plateaux, showing that at a smaller scale the data having $\ell = 200$ and $\ell = 400$ do not overlap). Bottom: Temporal evolution of the ratios g_r/g_1 between the gaps in the entanglement spectrum (the insets zoom in on higher plateaux). The limits of the curves for $t \to \infty$ and large values of ℓ are the strictly positive integers.

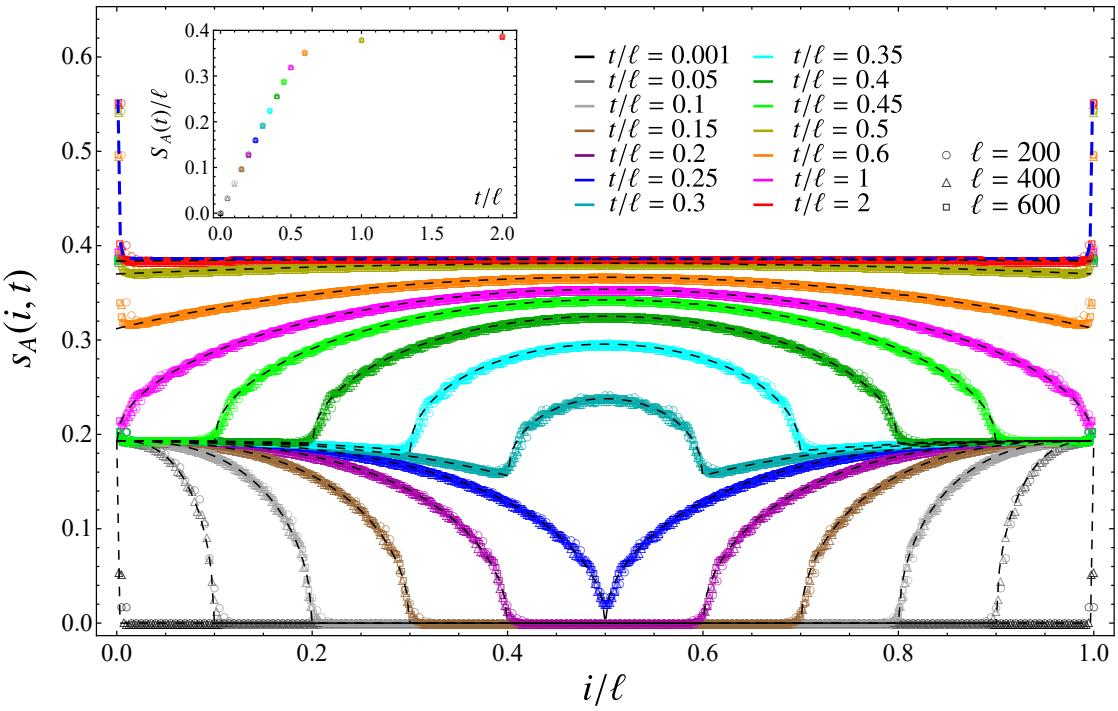

Figure 7.18: Chain of free fermions: Temporal evolution after the global quench of the contour for the entanglement entropy of an interval made by ℓ sites, evaluated from (A.1.8), (A.2.3) and (A.2.4). The inset shows the entanglement entropy for certain values of t, according to the same colour code of the main plot. The black dashed lines are obtained from the quasi-particle picture, by using (7.3.13) with $f_0(x) = 0$ and other expressions discussed in Sec .7.4.3. The blue dashed curve is obtained from (7.4.14) and it does not change significantly for the values of ℓ corresponding to these data.

plateaux before $t/\ell \simeq 1/2$ and for long time should correspond to the ratios between the conformal dimensions in the spectrum of the underlying CFT, and the data agree with the expected results for a massless Dirac fermion with free boundary conditions. We remark that in our analysis we considered only the particle-hole excitations. It would be interesting to improve this numerical analysis by including higher gaps or by considering other configurations.

In the Ising model, the entanglement spectrum after a global quench has been considered in [393] and also in this model the gaps close as time evolves when the evolution is determined by a critical Hamiltonian.

7.4.3 A contour function from the quasi-particle picture

In order to construct a contour function for the entanglement entropy by employing the quasi-particle picture, we need to know the dispersion relation of the model after the quench and the entropy density in momentum space of the quasi-particles (see Sec .7.3.3), which are quantities corresponding to the entire system. The dispersion relation of the Hamiltonian (7.4.2), which determines the evolution of the system after the quench, is given by $\omega(\theta) = \cos\theta$, where $-\pi \leqslant \theta \leqslant \pi$ [399]. In order to compute the entropy density, let us consider the asymptotic state of the system after the quench. For $t \to \infty$, the correlators are given by (7.4.4) with i and j labelling two generic sites of the infinite chain. Considering a periodic chain made by an even number

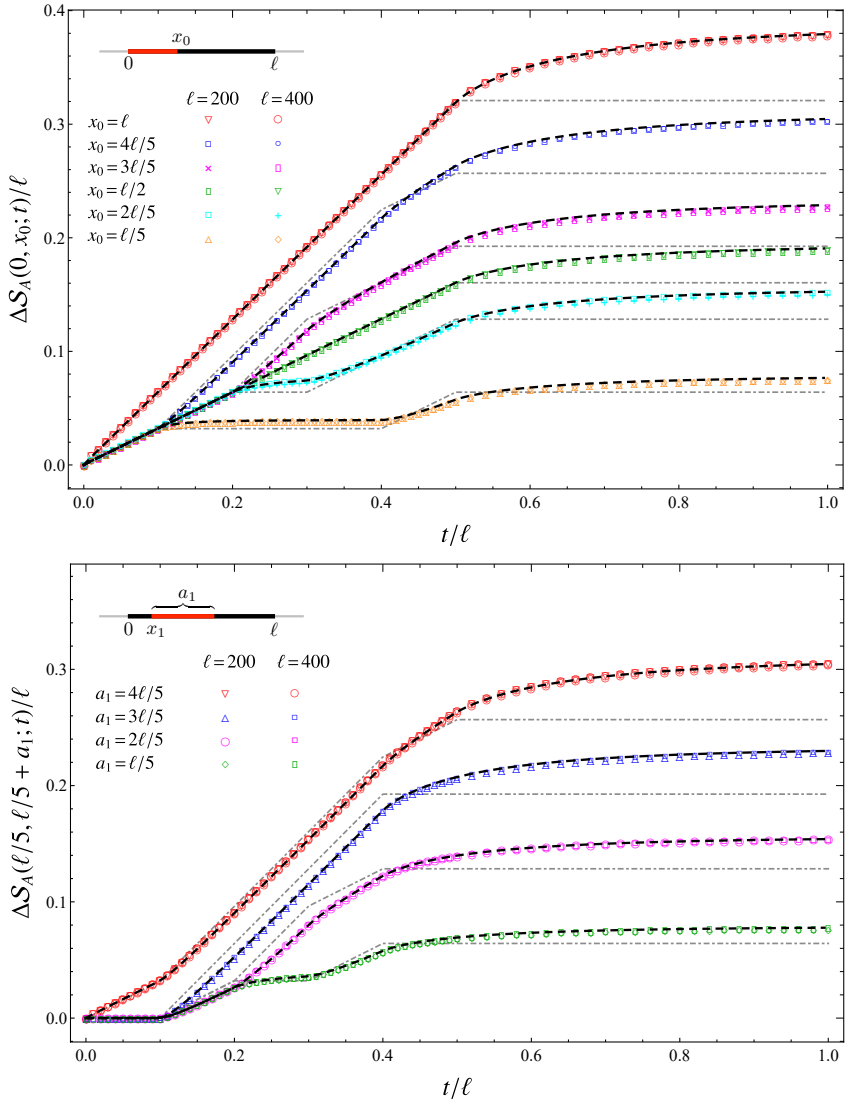

Figure 7.19: Chain of free fermions: Temporal evolution of (7.3.7) for $n=1$.

L of sites, a circulant matrix $\widetilde{C}^{(\infty)}_{i,j}$ with $i,j \in [-L/2, L/2]$ is obtained, whose eigenvalues are $\zeta_k = [1+\cos(2\pi k/L)]/2$, with $k \in [-L/2, L/2]$. From these eigenvalues, one finds the asymptotic entropy

$$S^{(\infty)} = -2\sum_{k=-L/2}^{L/2} \left\{ \cos^2\left(\frac{\pi k}{L}\right) \log\left[\cos\left(\frac{\pi k}{L}\right)\right] + \sin^2\left(\frac{\pi k}{L}\right) \log\left[\sin\left(\frac{\pi k}{L}\right)\right] \right\}. \qquad (7.4.8)$$

After introducing $\theta = 2\pi k/L$, we take the limit $L\to\infty$ of $S^{(\infty)}/L$ with $S^{(\infty)}$ given by (7.4.8), and the result provides the entropy density $s^{(\infty)}(\theta)$ as follows

$$-\frac{1}{\pi}\int_{-\pi}^{\pi} \Big[\big(\cos(\theta/2)\big)^2 \log[\cos(\theta/2)] + \big(\sin(\theta/2)\big)^2 \log[\sin(\theta/2)] \Big] d\theta \equiv \int_{-\pi}^{\pi} s^{(\infty)}(\theta)\, d\theta \qquad (7.4.9)$$

These observations lead to construct a contour function from the quasi-particle picture by employing $s^{(\infty)}(\theta)$ and $v(\theta) \equiv \omega'(\theta) = \sin\theta$ into (7.3.13), being $\theta \in [-\pi, \pi]$.

In Fig. 7.18 we show the temporal evolution of the contour for the entanglement entropy evaluated through the prescription of [28] discussed in Appendix A.2, namely by employing (7.3.5), (A.1.7), (A.2.2) and (A.2.4). Notice that the data corresponding to different values of ℓ collapse on the same curves. The black dashed curves are obtained from (7.3.13) with $f_0(x) = 0$ and (7.4.9) as explained above: they display perfect agreement with the data, except in the neighbourhoods of the endpoints. Similarly to the case of the harmonic chain described in Sec .7.3.3, the divergencies of the contour function close to the endpoints can be reproduced by choosing a suitable expression for $f_0(x)$ (e.g. (7.2.9) with $n = 1$ and the proper τ_0, as done for the harmonic chain in the right panel of Fig. 7.9). The qualitative behaviour of the curves in Fig. 7.18 is the same observed in [28] for a different global quench and it is roughly reproduced also by the naive CFT formula (7.2.8) discussed in Sec .7.2 (see the right panel in Fig. 7.1). The blue dashed line in Fig. 7.18 corresponds to the asymptotic regime $t \to \infty$ discussed below in Sec .7.4.4. Also for this global quench the numerical data display linear divergencies close to the endpoints of the interval that are independent of time.

In Fig. 7.19 we show the temporal evolution of (7.3.7) with $n = 1$ for the same choices of (i_1, i_2) considered in Fig. 7.10. The qualitative behaviour of the curves is similar to the corresponding curves obtained for the global quench in the harmonic chain, hence the qualitative arguments reported Sec .7.3.3 about the changes of the slopes holds also in this case. On the other hand, for $t/\ell > 1/2$ the asymptotic values for long times are different from the ones observed in the harmonic chain, as expected from the fact that the asymptotic value of the entanglement entropy depends both on the model and on the initial state. We find worth remarking that for the chain of free fermions we have access to larger values of ℓ with respect to the harmonic chain, hence the curves corresponding to different values of ℓ display a better collapse than the ones shown in Fig. 7.10 for the harmonic chain, capturing the asymptotic curves for $\ell \to \infty$. The black dashed lines, obtained from the quasi-particle picture analysis by using (7.3.6), (7.3.7) and (7.3.13), display a very good agreement with the numerical data. The data are also compared against the corresponding naive CFT expression (7.2.12) (grey dotted-dashed curves), where $\tau_0 = 3.26$ has been used.

7.4.4 Long time regime

In the asymptotic regime $t \to \infty$, the imaginary part of the correlation matrix (7.4.3) vanishes, as already remarked above. In particular, $C_{i,j}(t) \to C^{(\infty)}_{i,j}$ being $C^{(\infty)}_{i,j}$ the real symmetric and tridiagonal matrix defined in (7.4.4), which has the same value along a given diagonal. Because of the simple structure of $C^{(\infty)}_{i,j}$, analytic expressions for its eigenvalues and for the corresponding eigenvectors can be written. The eigenvalues of $C^{(\infty)}$ read [85]

$$\zeta_k = \frac{1 + \cos\theta_k}{2} \qquad\qquad \theta_k \equiv \frac{\pi\, k}{\ell + 1}\,. \tag{7.4.10}$$

In order to study the matrix occurring in the entanglement Hamiltonian, we also need the eigenvectors corresponding to the eigenvalues (7.4.10), that are given by

$$u_k(r) = \frac{\sin(r\,\theta_k)}{\sqrt{(\ell+1)/2}} \qquad\qquad 1 \leqslant r \leqslant \ell \tag{7.4.11}$$

where the normalisation condition $\sum_r u_k(r)^2 = 1$ has been imposed. Then, the generic element of the $\ell \times \ell$ entanglement Hamiltonian matrix (7.4.6) reads

$$T_{i,j} = \frac{2}{\ell+1} \sum_{k=1}^{\ell} \eta_k \, \sin(i\theta_k)\, \sin(j\theta_k) \qquad\qquad \eta_k = 2\log\big[\tan(\theta_k/2)\big] \tag{7.4.12}$$

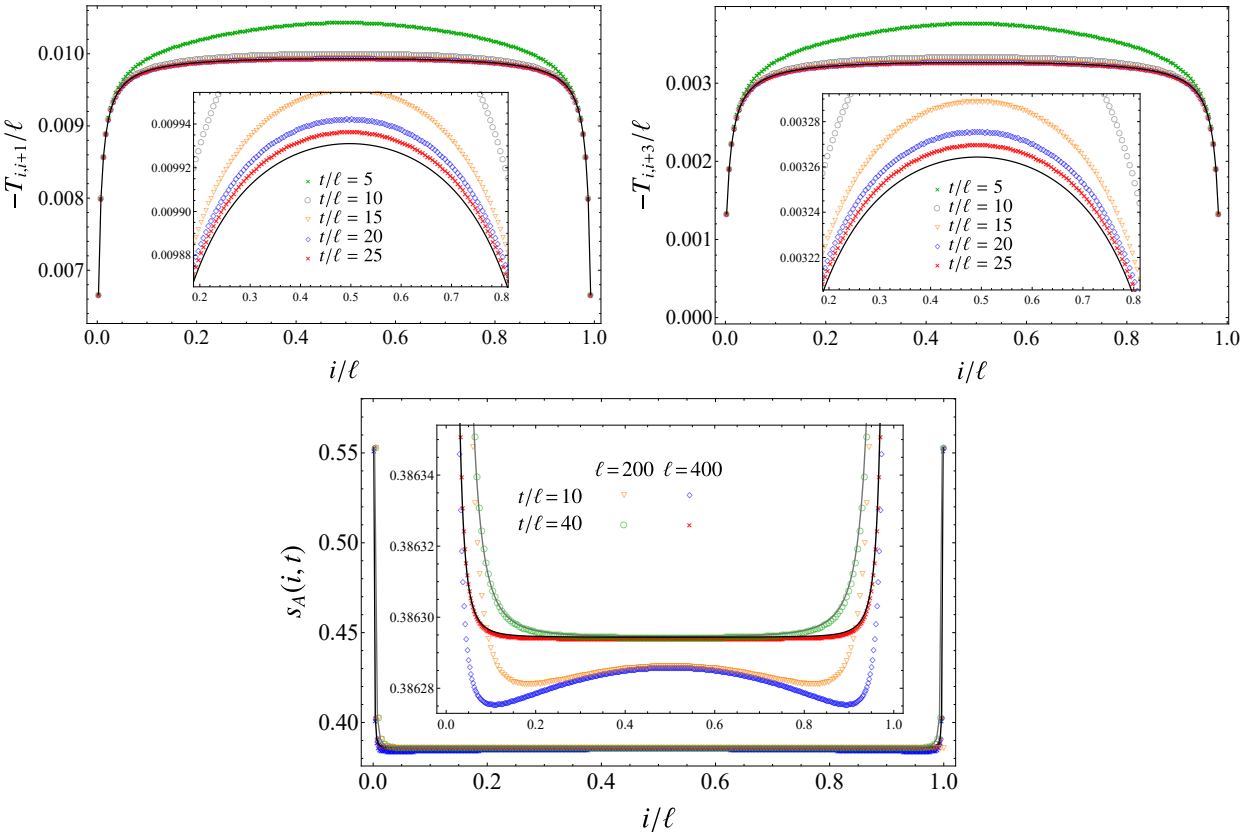

Figure 7.20: Chain of free fermions: Long time regime after the global quench (see Sec .7.4.4). Top: First diagonal (left) and third diagonal (right) of the entanglement Hamiltonian matrix of an interval with $\ell = 200$. The data points have been found by using (7.4.6), while the solid black curves correspond to (7.4.13) with $p = 1$ (left) and $p = 3$ (right). Bottom: Contour for the entanglement entropy for two values of ℓ and two (large) values of t for each length. The data points, obtained from (A.1.8), (A.2.3) and (A.2.4), agree with the solid lines found from (7.4.14) with $n = 1$.

where $1 \leqslant i, j \leqslant \ell$ and the single particle entanglement energies have been obtained from (7.4.6) and (7.4.10). Notice that $\sin(r\theta_k) = 0$ when $r = 0$ or $r = L + 1$. The matrix T in (7.4.12) is symmetric, as expected; hence we can focus on its p-th diagonal with $0 \leqslant p \leqslant \ell - 1$, whose generic element is

$$T_{i,i+p} = \frac{1}{\ell+1} \sum_{k=1}^{\ell} \eta_k \Big(\cos(p\,\theta_k) \big[1 - \cos(2i\theta_k)\big] + \sin(p\,\theta_k)\, \sin(2i\theta_k) \Big) \qquad 1 \leqslant i \leqslant \ell - p\,. \quad (7.4.13)$$

Notice that $\theta_{\ell-k+1} = \pi - \theta_k$, and this implies $\eta_{\ell-k+1} = -\eta_k$, as expected from the discussion in Sec. 7.4.2. Moreover, one can show that $T_{i,i+2p} = 0$ for non negative integers p, and that the p-th diagonal is symmetric with respect to its middle point, namely $T_{\ell-i-p+1,\ell-i+1} = T_{i,i+p}$.

In the top panels of Fig. 7.20, the expression (7.4.13) has been checked against numerical data corresponding to large values of t for $p = 1$ (left) and $p = 3$ (right). The agreement is satisfactory, but the insets show that larger values of t should be taken in order to improve it.

The asymptotic expressions (7.4.10) and (7.4.11) provide also the contour for the entanglement

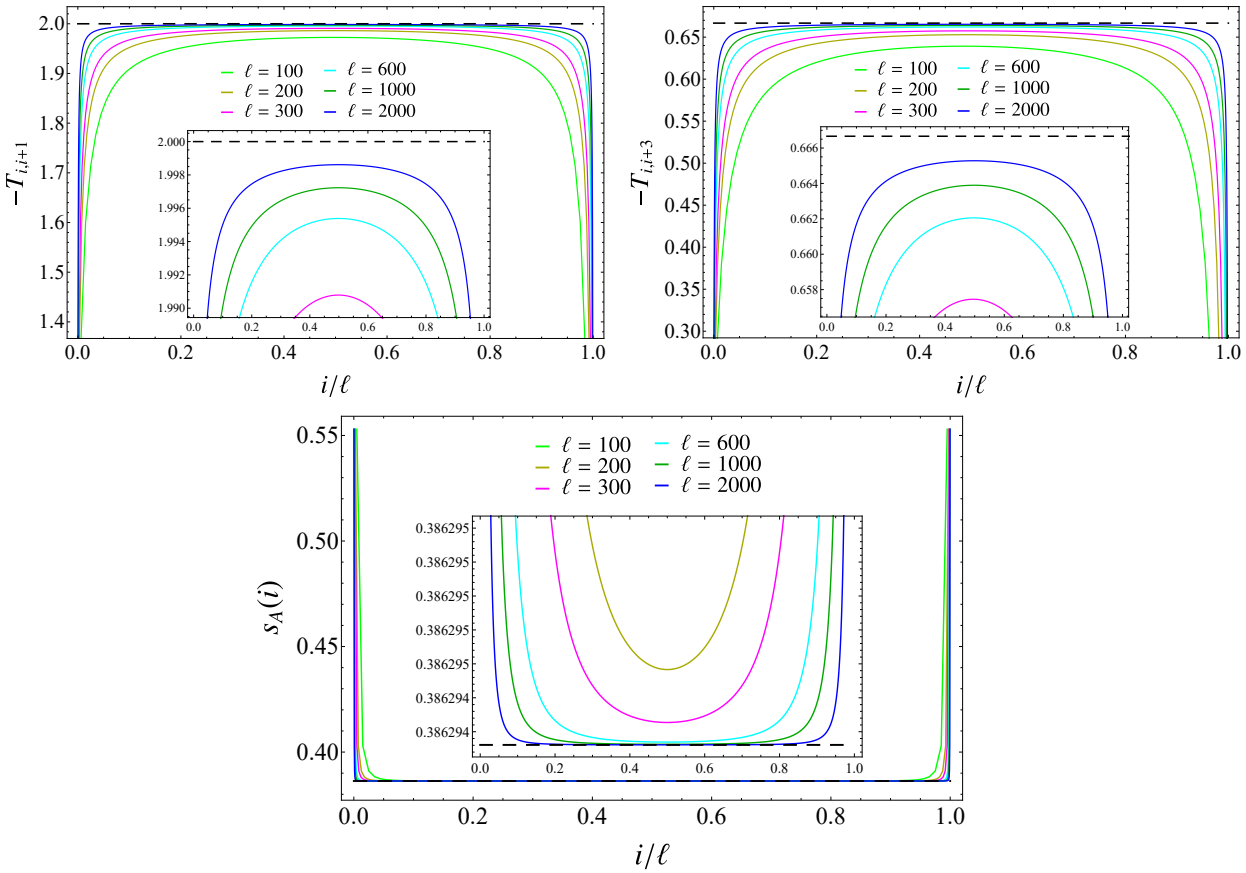

Figure 7.21: Chain of free fermions: $\ell \to \infty$ in the long time regime after the global quench (see Sec .7.4.4). Top: First diagonal (left) and third diagonal (right) of the entanglement Hamiltonian matrix for increasing values of ℓ. The solid curves are obtained from (7.4.13) and the dashed lines correspond to (7.4.15). Bottom: Contour for the entanglement entropy. The solid lines are obtained from (7.4.14) with $n = 1$, while the horizontal dashed line corresponds to (7.4.16).

entropies. It reads, using (A.1.8) and (A.2.4),

$$s_A^{(n)}(i) = \sum_{k=1}^{\ell} s_n(\zeta_k)\, u_k(i)^2 = \frac{2}{\ell+1} \sum_{k=1}^{\ell} s_n(\zeta_k) \left[\sin(i\theta_k)\right]^2 \tag{7.4.14}$$

where $s_n(\zeta_k)$ is obtained by evaluating (A.2.2) or (A.2.3) for the ζ_k's given in (7.4.10). The expression (7.4.14) corresponds to the black dashed curve in Fig. 7.18 and to the solid lines in the bottom panel of Fig. 7.20. Agreement is observed with the data points obtained for large values of time.

It is useful to consider the limit $\ell \to \infty$ of the above expressions holding in the asymptotic regime of long time. As the entanglement Hamiltonian matrix element (7.4.13), by neglecting the highly oscillating terms coming from $\cos(2i\theta_k)$ and $\sin(2i\theta_k)$, for i far enough from 1 and $\ell - p$, one finds (see also section 7.1 of [4])

$$-T_{i,i+p} \;\longrightarrow\; -\frac{1}{\pi}\int_0^{\pi} \eta(\theta)\, \cos(p\,\theta)\, d\theta \;=\; \begin{cases} 0 & \text{even } p \\ 2/p & \text{odd } p \end{cases} \tag{7.4.15}$$

where $\eta(\theta) \equiv 2\log[\tan(\theta/2)]$ (see (7.4.12)).

The limit (7.4.15) is checked in the top panels of Fig. 7.21 for $p = 1$ (left) and $p = 3$ (right).

As for the entanglement entropy, from (A.2.3) and the eigenvalues in (7.4.10), one obtains

$$\frac{S_A}{\ell} \longrightarrow \frac{1}{\pi}\int_0^\pi s(\theta)\, d\theta = -1 + \log 4 \simeq 0.386 \qquad \ell \to \infty \tag{7.4.16}$$

that is the flat value reached for $t \to \infty$ both in the inset and in the main plot of Fig. 7.18. Also the horizontal dashed line in the bottom panel of Fig. 7.21 corresponds to (7.4.16). The consistency of this result can be checked by employing (7.4.14), that for $\ell \to \infty$ gives

$$-\frac{2}{\pi}\int_0^\pi \Big[\big(\cos(\theta/2)\big)^2 \log[\cos(\theta/2)] + \big(\sin(\theta/2)\big)^2 \log[\sin(\theta/2)]\Big] d\theta = -1 + \log 4 \tag{7.4.17}$$

where we used that $1/2$ is the mean value constant coming from $[\sin(i\theta_k)]^2$. For the Rényi entropies, from (A.2.2) one finds

$$\frac{S_A^{(n)}}{\ell} \longrightarrow \frac{1}{(1-n)\pi}\int_0^\pi \log\Big[\big(\cos(\theta/2)\big)^{2n} + \big(\sin(\theta/2)\big)^{2n}\Big]\, d\theta \tag{7.4.18}$$

that can be evaluated for explicit values of n, finding e.g. $\log(24 - 16\sqrt{2})$ for $n = 2$ and $\log(4/3)$ for $n = 3$.

7.5 Discussion

We studied the temporal evolution of the entanglement Hamiltonian of an interval after a global quantum quench in two simple free lattice models: the harmonic chain and a chain of free fermions. In the harmonic chain (in the thermodynamic limit) we considered a quench of the frequency parameter such that the evolution Hamiltonian is massless. In the chain of free fermions at half filling, we explored the global quench introduced in [85], where the initial state is the ground state of a dimerised chain and the evolution Hamiltonian is determined by the homogenous hopping Hamiltonian. In these free models, the time dependent entanglement Hamiltonian is a quadratic operator; hence it is fully determined by a matrix that can be written explicitly as a function of the matrix whose elements are the two point correlators [10, 191, 194–196, 284]. The entanglement Hamiltonian matrix can be decomposed in terms of a diagonal matrix containing the single particle entanglement spectrum and another matrix that is symplectic for the harmonic chain or orthogonal for the chain of free fermions. The single particle entanglement spectrum and the matrix occurring in this decomposition can be employed to construct also a contour for the entanglement entropies [28, 29], that encodes information about the spatial structure of the bipartite entanglement. In this chapter we studied also the temporal evolution of the single particle entanglement spectrum and of the contour for the entanglement entropies after a global quench both in the harmonic chain and in the chain of free fermions.

During the temporal evolution, the entanglement Hamiltonian matrix is not block diagonal in the harmonic chain and it is complex in the chain of free fermions. Bands of diagonals around the main diagonal in the $\ell \times \ell$ blocks composing the entanglement Hamiltonian matrix in the harmonic chain and in the $\ell \times \ell$ real and imaginary parts of the entanglement Hamiltonian matrix in the chain of free fermions can be identified whose width grows linearly with velocity equal to one.

The analytic results obtained in CFT for the entanglement Hamiltonian of a semi-infinite line [147] have been exploited to write expressions for the finite interval in the continuum limit that reproduce qualitatively the behaviour of the numerical data of some quantities in some regimes.

In particular, the linear growth of the gaps in the entanglement spectrum before $t/\ell \simeq 1/2$ and the qualitative temporal evolution of the contour for the entanglement entropy have been obtained. In our numerical analysis we have also observed that the temporal evolution of the ratios of the gaps in the entanglement spectrum can be employed to read the ratios in the conformal spectrum of the underlying CFT when the evolution Hamiltonian is critical. This observation holds both for $t/\ell < 1/2$ (as predicted in [147]) and in the asymptotic regime of long time. Furthermore, it seems true also for different initial states. It would be interesting to further explore this idea by considering global quenches governed by different critical Hamiltonians.

The quasi-particle picture of [82] has been employed to obtain semi-empirical analytic expressions of the contour for the entanglement entropy, finding reasonable agreements with the numerical data, in particular for the chain of free fermions, where larger subsystems have been studied. For the harmonic chain, the formula for the contour is valid also for the global quenches where the mass in the evolution Hamiltonian is non vanishing; hence it would be interesting to test it also for these protocols. For the global quench in the chain of free fermions, the entanglement Hamiltonian matrix and the contour for the entanglement entropy have been studied in the asymptotic regime of $t \to \infty$.

The analysis of entanglement Hamiltonians and the contours for the entanglement entropies can be extended in many interesting directions. Other kinds of global quenches can be considered or also quenches of different nature, like the local quenches [86]. An interesting development is studying the temporal evolution of these quantities for more complicated bipartitions, like the one where A is made by disjoint intervals [147, 180–182] whose entanglement entropies have been studied in CFT, lattice models [233–237, 299, 364–367] and holography [300–303, 400–403].

It is worth studying the temporal evolutions of the entanglement Hamiltonians and of the contours for the entanglement entropies after global and local quenches also in interacting models and in higher dimensions. Indeed, in this chapter we have highlighted the role of the entanglement gaps to obtain the conformal dimensions of the underlying CFT when the evolution Hamiltonian is critical; hence it would be interesting to test this idea also in interacting models. In the context of the gauge/gravity correspondence, the bit threads approach to the holographic entanglement entropy [404] suggests a possible gravitational dual of the contour for the entanglement entropy [405].

Part III

Symmetry resolved entanglement

Chapter 8

Symmetry resolved entanglement entropies in quantum field theories

8.1 Introduction

As explained in Sec. 1.2.3, a recent line of research is devoted to understand the interplay between entanglement and symmetries in many-body quantum systems and quantum field theories through the study of the *symmetry resolved entanglement entropies* defined in (1.2.26) and (1.2.27). The direct computation of these quantities from their definitions require the analytic knowledge of the symmetry resolution of the entanglement spectrum, which is possible to achieve in a limited number of cases. To overcome this issue, a very useful approach has been developed in [96] and it consists in defining the charged moments of the reduced density matrix $\hat{\rho}_A$ as

$$Z_n(\alpha) \equiv \mathrm{Tr}\hat{\rho}_A^n e^{\mathrm{i}\widehat{Q}_A\alpha}, \tag{8.1.1}$$

with $Z_1(\alpha=0)=1$, being $\mathrm{Tr}\hat{\rho}_A=1$. The setup we consider here is the one of Sec. 1.2.3 with $\widehat{Q}_A$ providing the $U(1)$ conserved charge restricted to the subsystem A. Charged moments similar to (8.1.1) have been already considered in the context of free field theories [406, 407], in holographic settings [408, 409], as well as in the study of entanglement in mixed states [410, 411]. In this specific case, the charged moments are not the main goal of our computation, but they represent a fundamental tool, because their Fourier transforms are the moments of the reduced density matrix restricted to the sector of fixed charge $q \in \mathbb{Z}$ [96], i.e.

$$\mathcal{Z}_n(q) \equiv \mathrm{Tr}(\Pi_q\,\hat{\rho}_A^n) = \int_{-\pi}^{\pi} \frac{d\alpha}{2\pi} e^{-\mathrm{i}q\alpha} Z_n(\alpha). \tag{8.1.2}$$

Let us stress that the probability $p(q)$ of finding q in a measurement of $\widehat{Q}_A$ in the reduced density matrix $\hat{\rho}_A$ is simply related to the moments $\mathcal{Z}_n$ as

$$p(q) = \mathcal{Z}_1(q)\,. \tag{8.1.3}$$

Finally the symmetry resolved entropies (1.2.26) and (1.2.27) are obtained as

$$S_n(q) = \frac{1}{1-n}\ln\left[\frac{\mathcal{Z}_n(q)}{\mathcal{Z}_1^n(q)}\right], \qquad S_1(q) = \lim_{n\to 1} S_n(q). \tag{8.1.4}$$

Let us stress, as specified later in this section, that the notation in (8.1.4) for the symmetry resolved entanglement entropies, adopted in this chapter and in chapter 9, is different from the one introduced in (1.2.26) and (1.2.27).

This theoretical framework and the possibility of measuring in an experiment the internal symmetry structure of the entanglement [25] paved the way to study different symmetry-resolved contributions in various theoretical contexts such as Conformal Field Theories (CFTs) [96, 97, 254, 412–416], free [104, 417] and interacting integrable quantum field theories [418, 419], holographic settings [420], spin chains [95, 105, 106, 246–248, 251, 255–257, 421–429], disordered systems [249, 250, 430, 431] and for non-trivial topological phases [252, 258, 432]

The main goal of this chapter is to investigate the field theoretical techniques for the computation of the charged moments in relativistic free two-dimensional quantum field theories (QFTs). In the following sections we will mainly deal with a free fermionic field theory and with a complex scalar one, whose Euclidean actions are given, respectively, by

$$\begin{aligned} S_D =& \frac{1}{4\pi}\int dz d\bar{z}\,(\psi_R^*\partial_z\psi_R + \psi_L^*\partial_{\bar{z}}\psi_L + m(\psi_L^*\psi_R + \psi_R^*\psi_L)\,, \\ S_S =& \frac{1}{4\pi}\int dz d\bar{z}\,\left(\partial_z\varphi^*\partial_{\bar{z}}\varphi + \partial_{\bar{z}}\varphi^*\partial_z\varphi + m^2\varphi^*\varphi\right), \end{aligned} \tag{8.1.5}$$

where we employ complex coordinates $(z, \bar{z})$ for the 2D spacetime. In S_D the fields $\psi_{R/L}$ are the chiral (right-moving R) and anti-chiral (left-moving L) components of the Dirac fermion. In S_S the field φ is a complex scalar. The actions in (8.1.5) exhibit a $U(1)$ symmetry, i.e. a symmetry under phase transformations of the fields given, respectively, by

$$\psi_{R/L} \to e^{\mathrm{i}\alpha}\psi_{R/L}, \quad \psi^*_{R/L} \to e^{-\mathrm{i}\alpha}\psi^*_{R/L}, \qquad \varphi \to e^{\mathrm{i}\alpha}\varphi, \quad \varphi^* \to e^{-\mathrm{i}\alpha}\varphi^*. \tag{8.1.6}$$

By Noether's theorem, this continuous symmetry transformation leads to a conserved quantity.

The chapter is organised as follows. In Sec. 8.2 we briefly recall two tools for the computation of the entanglement in QFT, i.e. the twist fields [11, 216, 224] and the Green's function technique in the replica space [10, 217, 218]. Our main findings, obtained when A is a single interval of length ℓ, are reported in sections 8.3, 8.4 and 8.5: in the first we employ the twist fields to compute the charged moments both in the massless and in the massive context (in the limit $m\ell \gg 1$). These results are extended in sections 8.4 and 8.5, where we write down the explicit form of the charged moments for arbitrary $m\ell$ and provide analytic asymptotic expansions valid for large and small $m\ell$. These outcomes are the starting point for the computation of the symmetry resolved entanglement entropies. Numerical checks for free fermions and bosons on the lattice are also provided as a benchmark of the analytical results. We draw our conclusions in Section 8.6.

Notations: in this chapter and in chapter 9, following [104, 105], we denote by $S_1(q)$ and $S_n(q)$ the symmetry resolved entanglement entropies (see (8.1.4)) and, consistently, by S_1 and S_n the total entanglement entropies. In this notation the dependence of the entropies on the subsystem A is implicit, while in the one adopted in Sec. 1.2 it was explicitly reported.

8.2 Replica method and quantum field theory

In this section, we recall two powerful methods used to compute the entanglement entropy in relativistic free QFT.

Starting from the replica trick described in Sec. 1.2.3, the first approach is based on a particular type of twist fields in quantum field theory that are related to branch points in the Riemann surface $\mathcal{R}_n$. We denote them by $\mathcal{T}_n$ and $\tilde{\mathcal{T}}_n$. Their action, in operator formalism, is defined by [11, 216, 224, 433, 434]

$$\begin{aligned} \mathcal{T}_n(z_1)\ \phi_i(z') &= \phi_{i+1}(z')\mathcal{T}_n(z_1), \\ \tilde{\mathcal{T}}_n(z_2)\phi_i(z') &= \phi_{i-1}(z')\tilde{\mathcal{T}}_n(z_2), \end{aligned} \tag{8.2.1}$$

where z_1 and z_2 are the endpoints of A, $z' \in A$ and $i = 1, \dots, n$ with $n+1 \equiv 1$. The two-point function of the twist fields directly gives [11]

$$\mathrm{Tr}\hat{\rho}_A^n \propto \langle \mathcal{T}_n(z_1)\tilde{\mathcal{T}}_n(z_2)\rangle \,. \tag{8.2.2}$$

In conformal invariant theories (e.g. when the mass terms in the actions (8.1.5) vanish) the two-point function of twist fields is fixed by their scaling dimension, leading to Eq. (1.2.23). In the case of free theories, a simplification arises by the diagonalisation in the replica space: the n-sheeted problem can be mapped to an equivalent one in which one deals with n decoupled and multivalued free fields, generically referred as $\tilde{\phi}_k$. Thus, also the twist fields can be written as products of fields acting only on $\tilde{\phi}_k$, denoted as $\mathcal{T}_{n,k}$ and $\tilde{\mathcal{T}}_{n,k}$. The total partition function is a product of n partition functions, ζ_k, each one given by (up to unimportant multiplicative constant)

$$\zeta_k \propto \langle \mathcal{T}_{n,k}(z_1)\tilde{\mathcal{T}}_{n,k}(z_2)\rangle \,. \tag{8.2.3}$$

The second approach is the one used in [217, 218] for a fermionic and a complex scalar theory, respectively: it also relies on mapping the problem from the determination of the partition function on $\mathcal{R}_n$, to the computation of n partition functions of a free field on a cut plane. However, the difference with respect to the previous approach is that each ζ_k is not computed as a two point-function of twist fields, but using the relation between the free energy and the Green's function of each sector k. Denoting by G_D the Green's function for the Dirac field and by G_S the one for the scalar (in each sector k of the n copies), they are related to the corresponding partition function ζ_k by, respectively,

$$\partial_m \ln \zeta_k = \mathrm{tr}\, G_D, \qquad \partial_{m^2} \ln \zeta_k = -\int dr^2\, G_S(\mathbf{r}, \mathbf{r}'). \tag{8.2.4}$$

The strategy of Refs. [217, 218] was to exploit the rotational and translational symmetry of the Helmholtz equations satisfied by G_D and G_S and analyse their behaviour at the singular endpoints of the cut A so to determine the right hand sides of the above equations. The final expressions for ζ_k can be expressed in terms of the solution of second order non linear differential equations of the Painlevé V type. Here we only report the final results for the Rényi entropies of free fields in the limit $m\ell \to 0$ [217, 218]

$$\begin{aligned} S_n^D =& \frac{n+1}{6n}\left(\ln\frac{\ell}{\epsilon} - \frac{(m\ell)^2}{2}\ln^2 m\ell\right) + O((m\ell)^2 \ln m\ell), \\ S_n^S =& \frac{n+1}{3n}\ln\frac{\ell}{\epsilon} + \ln\frac{\ln m\ell}{\ln m\epsilon} + O(m\ell). \end{aligned} \tag{8.2.5}$$

These formulas have been obtained in the scaling regime with $t = m\ell$ fixed, in the conformal limit $m\ell \to 0$ and after taking the limit of large ℓ. Eq. (8.2.5) shows the leading mass corrections to Eq. (1.2.23) for the theories in Eq. (8.1.5) strongly depend on the statistics of the particles. The leading mass correction vanishes for a Dirac field, while it is singular (like $\ln(-\ln(m))$) for a Klein-Gordon field (both real and complex). In the literature, this infrared divergence is ascribed to the zero mode of the massless scalar theory [226, 435].

8.3 Twist Field Approach

In this section we consider 1D critical and close to critical systems. We obtain a general exact result for the conformal invariant charged moments by exploiting the properties of some local operators known as modified or fluxed twist fields [406–408]. This result includes and generalises the ones in Ref. [96]. The same approach also provides the leading asymptotic behaviour of the charged moments for (free) massive field theories.

8.3.1 Modified Twist Fields

In a generic QFT, the replica trick for computing $Z_n(\alpha)$ defined in (8.1.1) can be implemented by inserting an Aharonov-Bohm flux through a multi-sheeted Riemann surface $\mathcal{R}_n$, such that the total phase accumulated by the field upon going through the entire surface is α [96]. The result is that $Z_n(\alpha)$ is the partition function on such modified surface, that, following Ref. [96], we dub $\mathcal{R}_{n,\alpha}$. In QFT language, the insertion of the flux corresponds to a twisted boundary condition. This boundary condition fuses with the twist fields at the endpoints of the subsystem A resulting into two local operators $\mathcal{T}_{n,\alpha}$ and $\tilde{\mathcal{T}}_{n,\alpha}$. These are modified versions of the standard twist fields $\mathcal{T}_n$ and $\tilde{\mathcal{T}}_n$ which take into account not only the internal permutational symmetry among the replicas but also the presence of the flux. Thus, the partition function on $\mathcal{R}_{n,\alpha}$ is determined by their two-point correlation function, that is the main object of interest in this section.

Rather than dealing with fields defined on a non trivial manifold $\mathcal{R}_{n,\alpha}$, it is more convenient to work on a single plane with a n-component field

$$\Phi = \begin{pmatrix} \phi_1 \\ \phi_2 \\ \vdots \\ \phi_n \end{pmatrix}, \tag{8.3.1}$$

where ϕ_j is the field on the j-th copy (here the field ϕ_j generically refers to either a scalar field φ_j or a chiral Dirac one ψ_j; the same applies to $\tilde{\phi}_k$ that we are going to introduce soon). Upon crossing the cut A, the vector field Φ transforms according to the transformation matrix T_α

$$T_\alpha = \begin{pmatrix} 0 & e^{i\alpha/n} & & \\ & 0 & e^{i\alpha/n} & \\ & & \ddots & \ddots \\ (-1)^{(n+1)f} e^{i\alpha/n} & & & 0 \end{pmatrix}, \tag{8.3.2}$$

where $f = 1$ for free Dirac fermions and $f = 0$ for free complex scalars. When $\alpha = 0$ we recover the usual transformations for the fields across the different replicas [10]. The matrix T_α has eigenvalues

$$\begin{aligned} f = 0: &\qquad \lambda_k = e^{\mathrm{i}\frac{\alpha}{n}} e^{2\pi \mathrm{i}\frac{k}{n}}, \quad k = 0, \dots, n-1, \\ f = 1: &\qquad \lambda_k = e^{\mathrm{i}\frac{\alpha}{n}} e^{2\pi \mathrm{i}\frac{k}{n}}, \quad k = -\frac{n-1}{2}, \dots, \frac{n-1}{2}. \end{aligned} \tag{8.3.3}$$

By diagonalising T_α with a unitary transformation, the problem is reduced to n decoupled fields $\tilde{\phi}_k$ in a two dimensional spacetime. Thus, since we are dealing with free theories, the total partition function is a product of the partition functions for each k and the twist fields can be written as products of fields each acting on a different $\tilde{\phi}_k$, i.e.

$$\begin{aligned} f = 0: &\qquad \mathcal{T}_{n,\alpha} = \prod_{k=0}^{n-1} \mathcal{T}_{n,k,\alpha}, \qquad \tilde{\mathcal{T}}_{n,\alpha} = \prod_{k=0}^{n-1} \tilde{\mathcal{T}}_{n,k,\alpha}, \\ f = 1: &\qquad \mathcal{T}_{n,\alpha} = \prod_{k=-\frac{n-1}{2}}^{\frac{n-1}{2}} \mathcal{T}_{n,k,\alpha}, \qquad \tilde{\mathcal{T}}_{n,\alpha} = \prod_{k=-\frac{n-1}{2}}^{\frac{n-1}{2}} \tilde{\mathcal{T}}_{n,k,\alpha}, \end{aligned} \tag{8.3.4}$$

with $\mathcal{T}_{n,k,\alpha}\tilde{\phi}_{k'} = \delta_{k,k'} e^{\mathrm{i}\alpha/n} e^{2\pi \mathrm{i}k/n} \tilde{\phi}_k$ and $\tilde{\mathcal{T}}_{n,k,\alpha}\tilde{\phi}_{k'} = \delta_{k,k'} e^{-\mathrm{i}\alpha/n} e^{-2\pi \mathrm{i}k/n} \tilde{\phi}_k$. Since the partition function on $\mathcal{R}_{n,\alpha}$ can be written as the two-point function of the modified twist fields, from (8.3.4)

we have

$$\begin{aligned} f=0: &\qquad \ln Z_n(\alpha)=\sum_{k=0}^{n-1}\ln\langle \mathcal{T}_{n,k,\alpha}\tilde{\mathcal{T}}_{n,k,\alpha}\rangle\,,\\ f=1: &\qquad \ln Z_n(\alpha)=\sum_{k=-(n-1)/2}^{(n-1)/2}\ln\langle \mathcal{T}_{n,k,\alpha}\tilde{\mathcal{T}}_{n,k,\alpha}\rangle\,. \end{aligned} \tag{8.3.5}$$

When dealing with a CFT (e.g. when $m=0$ in (8.1.5)) $\mathcal{T}_{n,k,\alpha}$ and $\tilde{\mathcal{T}}_{n,k,\alpha}$ are primary operators and their two-point function is fixed by conformal invariance to be

$$\langle \mathcal{T}_{n,k,\alpha}\tilde{\mathcal{T}}_{n,k,\alpha}\rangle \propto \frac{1}{|u-v|^{4\Delta_k(\alpha)}}, \tag{8.3.6}$$

where

$$\begin{aligned} f=0: &\qquad \Delta_k(\alpha)=\frac{1}{2}\left(\frac{k}{n}+\frac{|\alpha|}{2\pi n}\right)\left(1-\frac{k}{n}-\frac{|\alpha|}{2\pi n}\right),\\ f=1: &\qquad \Delta_k(\alpha)=\frac{1}{2}\left(\frac{k}{n}+\frac{\alpha}{2\pi n}\right)^2. \end{aligned} \tag{8.3.7}$$

Let us stress that, in order to have operators with positive conformal dimension, the phase that bosons pick up going around one of the entangling points must be $0<\frac{k}{n}+\frac{\alpha}{2\pi n}<1$. This can be achieved, since $\alpha\in[-\pi,\pi]$, by trading α with $|\alpha|$ when we deal with scalar field theories.

Finally, the logarithm of the partition function on $\mathcal{R}_{n,\alpha}$ given by (8.3.5) reads

$$\begin{aligned} f=0: &\quad \ln Z_n(\alpha)=-4\ln\ell\sum_{k=0}^{n-1}\Delta_k(\alpha)=-\left[\frac{1}{3}\left(n-\frac{1}{n}\right)-\frac{\alpha^2}{2\pi^2 n}+\frac{|\alpha|}{\pi n}\right]\ln\ell,\\ f=1: &\quad \ln Z_n(\alpha)=-4\ln\ell\sum_{k=-\frac{n-1}{2}}^{\frac{n-1}{2}}\Delta_k(\alpha)=-\left[\frac{1}{6}\left(n-\frac{1}{n}\right)+\frac{2}{n}\left(\frac{\alpha}{2\pi}\right)^2\right]\ln\ell. \end{aligned} \tag{8.3.8}$$

The charged moments for the free massless Dirac field theory ($f=1$) have been already worked out in the literature with different techniques [96,97,406–408]. Instead, the charged moments for a free massless complex scalar field ($f=0$) represent a new result (actually in Appendix A of [408] a result consistent with (8.3.8) has been obtained using the heat kernel techniques).

Let us stress that the presence of a flux in the Riemann surface changes some features of the twist fields in CFT: they remain primary operators, but they do depend on the theory and are not anymore identified only by the central charge (see also [96]).

8.3.2 Massive field theory and flux insertion

In this section we compute the charged moments $Z_n(\alpha)$ of a massive relativistic 2D QFT on the infinite line for a bipartition in two semi-infinite lines. Thus, we follow the same logic as in [9] (i.e. the continuum version of Baxter corner transfer matrix approach [259] for the reduced density matrix [9, 262, 436, 437]), which in turn parallels the proof of the c-theorem by Zamolodchikov [157]. The results of this section are not limited to free theories but hold for *generic massive relativistic* QFT. Exploiting the rotational invariance about the origin of the Riemann surface $\mathcal{R}_{n,\alpha}$,

the expectation values of the stress tensor of a massive euclidean QFT in complex coordinates, $T \equiv T_{zz}, \bar{T} \equiv T^*_{\bar{z}\bar{z}}$, and the trace, $\Theta \equiv 4T_{z\bar{z}}$, have the form

$$\begin{aligned} \langle T(z,\bar{z})\rangle &= F_{n,\alpha}(z\bar{z})/z^2, \\ \langle \Theta(z,\bar{z})\rangle - \langle\Theta\rangle_{1,\alpha=0} &= G_{n,\alpha}(z\bar{z})/z\bar{z}, \\ \langle \bar{T}(z,\bar{z})\rangle &= F_{n.\alpha}(z\bar{z})/\bar{z}^2, \end{aligned} \tag{8.3.9}$$

where $\langle\Theta\rangle_{1,\alpha=0}$ is a non-vanishing constant measuring the explicit breaking of scale invariance in the non-critical system, while $\langle T\rangle_{1,\alpha=0}$ and $\langle\bar{T}\rangle_{1,\alpha=0}$ both vanish. These quantities are related by the conservation equations of the stress-energy tensor ($4\partial_{\bar{z}}T + \partial_z\Theta = 0$) as

$$(z\bar{z})\left(F'_{n,\alpha} + \frac{1}{4}G'_{n,\alpha}\right) = \frac{1}{4}G_{n,\alpha}. \tag{8.3.10}$$

The conservation equations as well as the rotational invariance are preserved in the presence of the flux α because the Riemann surface $\mathcal{R}_{n,\alpha}$ can be thought simply as a complex plane with the insertion of two modified twist fields, as discussed in the previous subsection. Both $F_{n,\alpha}$ and $G_{n,\alpha}$ approach zero for $|z| \gg \xi$, while when $|z| \ll \xi$, they approach the CFT values given by the conformal dimension of the modified twist field, $\Delta_n(\alpha)$ [96]. Hence we have

$$\begin{aligned} F^{CFT}_{n,\alpha} &\to \frac{c}{24}\left(1 - \frac{1}{n^2}\right) + \frac{\Delta_n(\alpha)}{n}, \\ G_{n,\alpha} &\to 0, \end{aligned} \tag{8.3.11}$$

and in particular for a massive Dirac field theory ($f = 1$) and for a complex massive scalar theory ($f = 0$), using the conformal weights (8.3.7), we have

$$\begin{aligned} F^{f=1}_{n,\alpha} &\to \frac{1}{24}\left(1 - \frac{1}{n^2}\right) + \frac{1}{2n^2}\left(\frac{\alpha}{2\pi}\right)^2, \\ F^{f=0}_{n,\alpha} &\to \frac{1}{12}\left(1 - \frac{1}{n^2}\right) + \frac{1}{2n^2}\left[\left(\frac{\alpha}{2\pi}\right)^2 - \frac{|\alpha|}{2\pi}\right]. \end{aligned} \tag{8.3.12}$$

At this point we have all the ingredients for generalising the computation of [9] to the case of our interest. The final result reads

$$\ln Z_n(\alpha) = \left[\frac{c}{12}\left(n - \frac{1}{n}\right) + 2\Delta_n(\alpha)\right]\ln(m\epsilon_{n,\alpha}), \tag{8.3.13}$$

or specialising to free Dirac ($f = 1$) or complex Klein-Gordon ($f = 0$) fields

$$f = 1: \qquad \ln Z_n(\alpha) = \left[\frac{1}{12}\left(n - \frac{1}{n}\right) + \frac{1}{n}\left(\frac{\alpha}{2\pi}\right)^2\right]\ln(m\epsilon_{n,\alpha}), \tag{8.3.14}$$

$$f = 0: \qquad \ln Z_n(\alpha) = \left[\frac{1}{6}\left(n - \frac{1}{n}\right) - \frac{1}{n}\left(\frac{\alpha}{2\pi}\right)^2 + \frac{|\alpha|}{2\pi n}\right]\ln(m\epsilon_{n,\alpha}). \tag{8.3.15}$$

where the UV cutoff $\epsilon_{n,\alpha}$ depends both on the Rényi index n and the parameter α (consistently with the lattice results in Ref. [251] and in chapter 9 for massless theories).

We can specialise (8.3.13) to a Luttinger liquid with parameter K, whose underlying field theory is a $c = 1$ CFT equivalent to a massless compact boson. In this case, one can use the results found in [96] for the conformal dimension of the modified twist field, obtaining

$$\ln Z_n(\alpha) = \left[\frac{1}{12}\left(n - \frac{1}{n}\right) + \frac{K}{n}\left(\frac{\alpha}{2\pi}\right)^2\right]\ln(m\epsilon_{n,\alpha}), \tag{8.3.16}$$

which for $K = 1$ gives the result found for fermions in (8.3.14), as it should.

8.3.3 From charged moments to symmetry resolved entropies

Performing the Fourier transforms of the charged moments above, one obtains symmetry resolved moments and entropies. For the Luttinger liquid, which includes Dirac Fermions at $K = 1$, the α dependence of the leading term is the same as in the massless cases [96,251]. The charged moments (ignoring for the time being the dependence on n and α of $\epsilon_{n,\alpha}$ in (8.3.16)), are

$$\mathcal{Z}_n(q) \simeq (m\epsilon)^{\frac{1}{12}\left(n-\frac{1}{n}\right)} \sqrt{\frac{n\pi}{K|\ln m\epsilon|}}\, e^{-\frac{n\pi^2 q^2}{K|\ln m\epsilon|}}, \tag{8.3.17}$$

and hence symmetry resolved entropies

$$S_n(q) = S_n - \frac{1}{2}\ln\left(\frac{K}{\pi}|\ln m\epsilon|\right) + O(1), \tag{8.3.18}$$

with S_n the total entropy. Exploiting the knowledge of $\mathcal{Z}_1(q)$ in (8.3.17) we also easily get the number or fluctuation entropy

$$S_{\rm num} = -\int_{-\infty}^{\infty} \mathcal{Z}_1(q)\ln\mathcal{Z}_1(q) = \frac{1}{2}\ln\left(\frac{K}{\pi}|\ln m\epsilon|\right) + O(1)\,, \tag{8.3.19}$$

that in the sum for the total entropy cancels exactly the double logarithmic term in (8.3.18).

As for the massive complex boson, we are interested in the Fourier transform of (8.3.15). In the saddle point approximation, we can neglect the term $\propto \alpha^2$ in (8.3.15) and the Fourier transform is

$$\mathcal{Z}_n(q) \simeq Z_n(0)\frac{2n|\ln(m\epsilon)|}{4n^2\pi^2q^2 + \ln^2(m\epsilon)} \simeq Z_n(0)\frac{2n}{|\ln(m\epsilon)|}\left(1 - \frac{4n^2\pi^2q^2}{\ln^2(m\epsilon)} + \dots\right), \tag{8.3.20}$$

and hence

$$S_n(q) = S_n - \ln|\ln m\epsilon| + O(1)\,, \tag{8.3.21}$$

with S_n the total entropy. Also in this case, one easily derives the number entropy from $\mathcal{Z}_1(q)$ obtaining again, at the leading order, the double logarithmic term in $S_n(q)$ in (8.3.21), i.e. $S_{\rm num} = \ln(|\ln m\epsilon|) + O(1)$.

8.4 The Green's function approach: The Dirac field

In this section we derive the charged moments for a massive Dirac field for arbitrary mass and then consider the limits of small and large mass. In Sec. 8.3.1 we showed that $Z_n(\alpha)$ can be written as product of partition functions ζ_a on the plane with proper boundary conditions along the cut A, explicitly given by

$$\tilde{\psi}_k(e^{2\pi \mathrm{i}}z, e^{-2\pi\mathrm{i}}\bar{z}) = e^{2\pi\mathrm{i}a}\tilde{\psi}_k(z,\bar{z}), \qquad a = \frac{k}{n} + \frac{\alpha}{2\pi n}, \qquad k = -\frac{n-1}{2}, \cdots, \frac{n-1}{2}. \tag{8.4.1}$$

Hence we have

$$\ln Z_n(\alpha) = \sum_{k=-\frac{n-1}{2}}^{\frac{n-1}{2}} \ln\zeta_{\frac{k}{n}+\frac{\alpha}{2\pi n}}. \tag{8.4.2}$$

Let us introduce the auxiliary *universal* quantities

$$w_a \equiv \ell\partial_\ell \ln\zeta_a, \qquad c_n(\alpha) \equiv \sum_k w_{\frac{k}{n}+\frac{\alpha}{2\pi n}}, \tag{8.4.3}$$

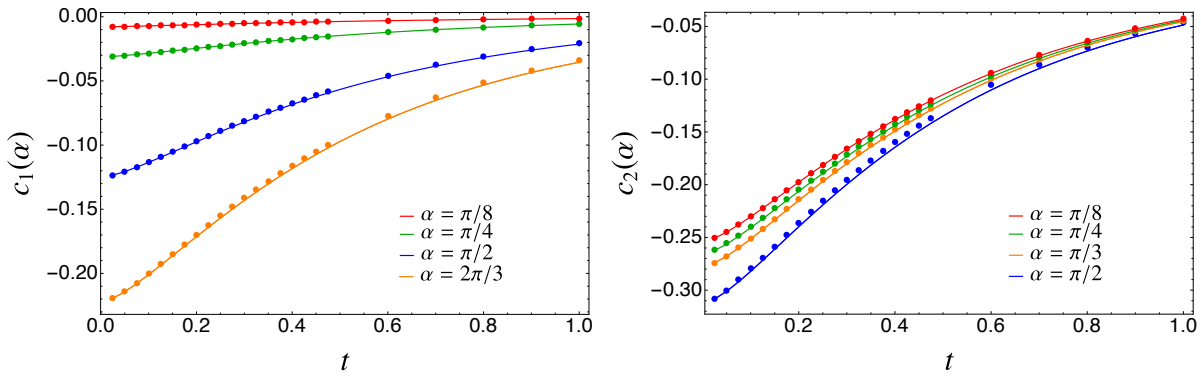

Figure 8.1: The universal constant $c_n(\alpha)$ extracted from the numerical solution of the Painlevé equation (8.4.7) for different values of α and n as a function of $t = m\ell$ (full lines). The numerical data are obtained varying ℓ between 200 and 400 lattice points and properly choosing m in such a way $t = m\ell \in (0, 1)$. For larger α and n, we need larger subsystem size to have a good match between field theory and lattice calculation because lattice corrections become stronger.

that, using (8.4.2), allow us to write the logarithmic derivative of the partition function in $\mathcal{R}_{n,\alpha}$ as

$$c_n(\alpha) = \ell \frac{\partial \ln Z_n(\alpha)}{\partial \ell} \qquad \Rightarrow \qquad \ln Z_n(\alpha) = \int_\epsilon^\ell \frac{c_n(\alpha)}{\ell'} d\ell'. \tag{8.4.4}$$

For $n = 1$, the function $c_n(\alpha)$ is the analogue of Zamolodchikov's c-function [157] in the presence of the flux α. The cutoff ϵ, in analogy to what discussed in Sec. 8.3.2 depends on both α and n, although we almost always omit such a dependence for conciseness.

The key observation of this approach relies on the following identity between the partition function ζ_a and the Green's function G_D in the same geometry

$$\partial_m \ln \zeta_a = \operatorname{tr} G_D \,. \tag{8.4.5}$$

Through this relation, the function w_a has been already obtained for generic values of a for the massive Dirac fermion [10, 217].

The method that we just reviewed provides exact results for the charged moments of a free Dirac field. Indeed, in Ref. [217] it has been shown that the function w_a defined in (8.4.3) can be written as

$$w_a(t) = -\int_t^\infty y v_a^2(y) dy, \tag{8.4.6}$$

where $t = m\ell$ and v_a is the solution of the Painlevé V equation

$$v_a'' + \frac{v_a'}{t} = -\frac{v_a}{1 - v_a^2}(v_a')^2 + v_a(1 - v_a^2) + 4\frac{\left(a - \frac{1}{2}\right)^2}{t^2(1 - v_a^2)} v_a. \tag{8.4.7}$$

This equation can be straightforwardly solved numerically with any standard algorithm for ordinary differential equations, once we impose the boundary condition as $t \to 0$ [217]

$$v_a(t) = -2a(\ln t + \kappa_D(a)) + O(t^2), \tag{8.4.8}$$

where

$$\kappa_D(a) = -\ln 2 + 2\gamma_E + \frac{1}{2}(\psi(a) + \psi(-a)), \tag{8.4.9}$$

with $\psi(z) \equiv \Gamma'(z)/\Gamma(z)$ the digamma function and γ_E the Euler-Mascheroni constant. Plugging the numerical solution of the differential equation (8.4.7) into (8.4.3), we obtain the universal constant $c_n(\alpha)$. Then, with the further integration (8.4.4), the desired $\ln Z_n(\alpha)$ is found to the price of introducing the non-universal cutoff ϵ. As examples we report in Fig. 8.1 the plots of the resulting $c_n(\alpha)$ for few values of α and n as functions of $t = m\ell$. In the figure we also compare our exact solution with the numerical results obtained from a lattice discretisation of the free Dirac theory (see Sec. 8.4.4 for details). The agreement is excellent. We stress that in Fig. 8.1 there is no free parameter in matching analytical and numerical data for $c_n(\alpha)$ (as a difference compared to $Z_n(\alpha)$).

The method we just outlined provides exact results for the desired charged moments and, by Fourier transform, the symmetry resolved entropies. However, the procedure is completely numerical and we would appreciate an analytic handle on the subject. While in general this is not feasible, the limits of small and large t are analytically treatable, as we are going to show.

8.4.1 The expansion close to the conformal point $m\ell = 0$

Here we use the methods just introduced to derive an asymptotic expansion of the charged moments close to the conformal point, i.e. for $t = m\ell \to 0$. In this limit, the expansion of the function $w_a(t)$ has been worked out in Ref. [217], obtaining

$$w_a = -2a^2 + a^2(1 - 2\kappa_D + 2\kappa_D^2 + (4\kappa_D - 2)\ln t + 2\ln^2 t)t^2 - 2a^4 t^4 \ln^4 t + O(t^4 \ln^3 t), \quad (8.4.10)$$

where we omitted the dependence on a of κ_D. In order to compute $c_n(\alpha)$ through (8.4.3), we again set $a = \frac{k}{n} + \frac{\alpha}{2\pi n}$ and we define the following functions

$$\Omega_n(\alpha) \equiv \sum_k a^2(\psi(a) + \psi(-a)) \equiv \Omega_n(0) + \frac{\alpha^2}{2\pi^2 n}\omega_n + \rho_n^{\omega}(\alpha), \quad (8.4.11a)$$

$$\Lambda_n(\alpha) \equiv \sum_k a^2(\psi(a) + \psi(-a))^2 \equiv \Lambda_n(0) + \frac{\alpha^2}{2\pi^2 n}\lambda_n + \rho_n^{\lambda}(\alpha), \quad (8.4.11b)$$

where $\omega_n = \pi^2 n \Omega_n''(\alpha)$ and $\lambda_n = \pi^2 n \Lambda_n''(\alpha)$ so that the remainder functions $\rho_n^{\omega/\lambda}(\alpha)$ are $O(\alpha^4)$. All the sums over k run from $-\frac{n-1}{2}$ to $\frac{n-1}{2}$. The quantities $\Omega(n,\alpha)$ and $\Lambda(n,\alpha)$ (and their derivatives) can be rewritten using the integral representation $\psi(x) = -\gamma_E + \int_0^1 dy \frac{1-y^{x-1}}{1-y}$ for the digamma function $\psi(x)$, allowing for an analytic continuation in n (the technical details of this procedure can be found in [104]).

From Eqs. (8.4.10)-(8.4.11) we obtain up to $O(t^2)$

$$\begin{aligned} c_n(\alpha) =& \frac{\partial \ln Z_n(\alpha)}{\partial \ln \ell} = \sum_{k=-(n-1)/2}^{(n-1)/2} w_{\frac{k}{n}+\frac{\alpha}{2\pi n}} = \left(\frac{1-n^2}{6n} - \frac{\alpha^2}{2\pi^2 n}\right)(1 - t^2 \ln^2 t) + \\ &+ \left[\left(\frac{1-n^2}{6n} - \frac{\alpha^2}{2\pi^2 n}\right)(1 + 2\ln 2 - 4\gamma_E) + 2\Omega_n(\alpha)\right] t^2 \ln t + \\ &- \Big[\left(\frac{1-n^2}{12n} - \frac{\alpha^2}{4\pi^2 n}\right)(1 + 2\ln 2 - 4\gamma_E + 2(\ln 2 - 2\gamma_E)^2) + \\ &+ (1 - 4\gamma_E + 2\ln 2)\Omega_n(\alpha) - \frac{\Lambda_n(\alpha)}{2}\Big] t^2 + O(t^4 \ln^3 t). \end{aligned} \quad (8.4.12)$$

The expression (8.4.12) can be now integrated analytically, getting

$$\ln Z_n(\alpha) = -\left(\frac{1}{6}\left(n - \frac{1}{n}\right) + \frac{\alpha^2}{2\pi^2 n}\right)\ln\frac{\ell}{\epsilon} + y_n(t) - \frac{\alpha^2}{2\pi^2 n} z_n(t) + \rho_n^z(\alpha, t) + o(t^3), \quad (8.4.13)$$

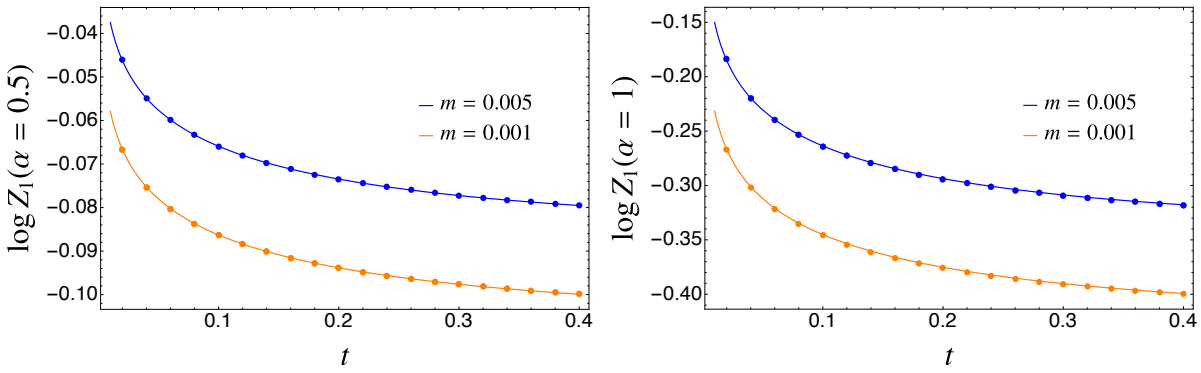

Figure 8.2: Leading scaling behaviour of the charged Rényi entropies with the insertion of a flux α. The numerical results (symbols) for two different values of α and masses m are reported as functions of $t = m\ell$ when $n = 1$. The data match well the prediction in (8.4.13) (solid lines) which includes lattice corrections as explained in the text.

where we defined

$$y_n(t) = \frac{t^2}{6}\left(n-\frac{1}{n}\right)\left(\frac{1}{2}\ln t^2 - \ln t(1-2\gamma_E+\ln 2)+\frac{3}{4}+2\gamma_E^2+\frac{\ln^2 2}{2}\right. \tag{8.4.14}$$
$$\left.-2\gamma_E(1+\ln 2)+\ln 2\right)+(\ln t-(\ln 2+1-2\gamma_E))t^2\Omega_n(0)+\frac{t^2}{4}\Lambda_n(0),$$

$$z_n(t) = t^2\Big[-\frac{\ln t^2}{2}+\ln t(1-2\gamma_E+\ln 2-\omega_n)+ \tag{8.4.15}$$
$$-\frac{3}{4}-2\gamma_E^2-\frac{\ln^2 2}{2}+2\gamma_E(1+\ln 2)-\ln 2+(\ln 2+1-2\gamma_E)\omega_n-\frac{\lambda_n}{4}\Big],$$

$$\rho_n^z(\alpha,t) = t^2[(\ln t-(\ln 2+1-2\gamma_E))\rho_n^\omega(\alpha)+\rho_n^\lambda(\alpha)], \tag{8.4.16}$$

and $\rho_n^z(\alpha)$ is defined so that $\rho_n^z(\alpha) = O(\alpha^4)$. Notice, as we already stressed a few times, that in (8.4.13) the cutoff ϵ comes as an additive constant of integration and it generically depends on both n and α.

The expression (8.4.13) represents our final field theoretical result for the charged entropies. We wish to test this prediction against exact lattice computations obtained with the methods reported in Sec. 8.4.4. However, in order to perform a direct comparison with lattice data, we have to take into account the additional non-universal contribution coming from the discretisation of the spatial coordinate, i.e. the explicit expression for the cutoff ϵ in (8.4.13) that, as already mentioned, does depend on α and cannot be simply read off from the result at $\alpha = 0$. We assume here (as (8.4.13) suggests at leading order) that the cutoff does not depend on the mass; consequently we can use the exact value for $m = 0$ [251] obtained with the use of Fisher-Hartwig techniques. The final result of Ref. [251] may be written as

$$\left(\frac{1}{6}\left(n-\frac{1}{n}\right)+\frac{\alpha^2}{2\pi^2 n}\right)\ln(2\epsilon) =$$
$$\Upsilon_n(\alpha) = n\mathrm{i}\int_{-\infty}^{\infty} dw[\tanh(\pi w)-\tanh(\pi n w+\mathrm{i}\alpha/2)]\ln\frac{\Gamma(\frac{1}{2}+\mathrm{i}w)}{\Gamma(\frac{1}{2}-\mathrm{i}w)}, \tag{8.4.17}$$

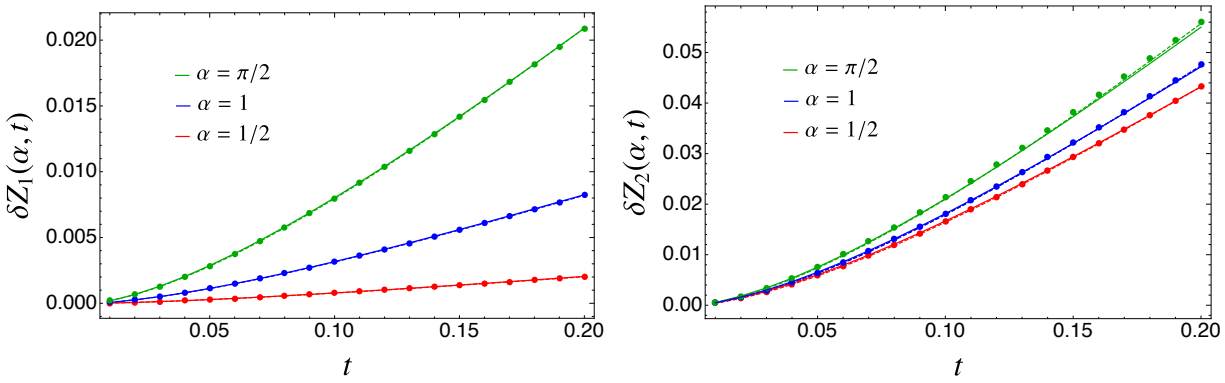

Figure 8.3: Subtracted universal charged entropy $\delta Z(\alpha, t)$ in (8.4.19). Left (right) panel is for $n = 1$ ($n = 2$). The dashed lines are the small t expansion in (8.4.13) for $n = 1$ while the solid lines are the Painlevé exact solution. The tiny discrepancies observed in some cases are finite ℓ corrections.

and in particular we will use

$$\gamma(n) \equiv \frac{1}{2}\frac{\partial^2 \Upsilon_n(\alpha)}{\partial \alpha^2}\Big|_{\alpha=0} = \frac{n\mathrm{i}}{4}\int_{-\infty}^{\infty} dw[\tanh^3(\pi n w) - \tanh(\pi n w)] \ln \frac{\Gamma(\frac{1}{2} + \mathrm{i}w)}{\Gamma(\frac{1}{2} - \mathrm{i}w)}. \tag{8.4.18}$$

In Ref. [251] it has been shown that the cutoff in (8.4.17) is very well described by the quadratic expansion in α and higher corrections $O(\alpha^4)$ are negligible for most practical purposes.

In Fig. 8.2 we report the numerical data for the charged moments with the insertion of a flux α for two values of α and m with $n = 1$. The data are well described by the theoretical prediction (8.4.13) with the cutoff (8.4.17). Finally, in order to have a test of the prediction (8.4.13) that does not rely on an independent lattice calculation we can consider the difference between the charged entropy at finite t (i.e. finite mass) and the massless one. Specifically we consider

$$\delta Z(\alpha, t) = \ln Z_n(\alpha, m) - \ln Z_n(\alpha, m = 0), \tag{8.4.19}$$

in which both the cutoff and ℓ dependences cancel and it becomes a *universal* function solely of t (closely related to $c_n(\alpha)$). The results for $\delta Z(\alpha, t)$ are reported in Fig. 8.3. The agreement of the numerics with the prediction (8.4.13) is perfect for small t. Furthermore, the differences emerging for larger t are correctly captured by the numerical exact solution of the Painlevé equation (8.4.7). The small discrepancies visible in the figure are just finite size effects that are stronger for larger values of n and α.

8.4.2 From the charged moments to symmetry resolution

We are now ready to study the true symmetry resolution by performing the Fourier transform of $Z_n(\alpha)$. In this Fourier transform we ultimately use a saddle-point approximation in which $Z_n(\alpha)$ is Gaussian and hence we truncate hereafter (8.4.13) at quadratic order in α. Consequently, the charged partition function can be well approximated as

$$Z_n(\alpha) = Z_n(0) e^{-b_n \alpha^2/2}, \tag{8.4.20}$$

where

$$b_n(\ell, t) = \frac{1}{\pi^2 n}(\ln \ell + z_n(t)) - 2\gamma(n) + \frac{\ln 2}{\pi^2 n} \equiv \frac{1}{\pi^2 n} \ln \ell - h_n, \tag{8.4.21}$$

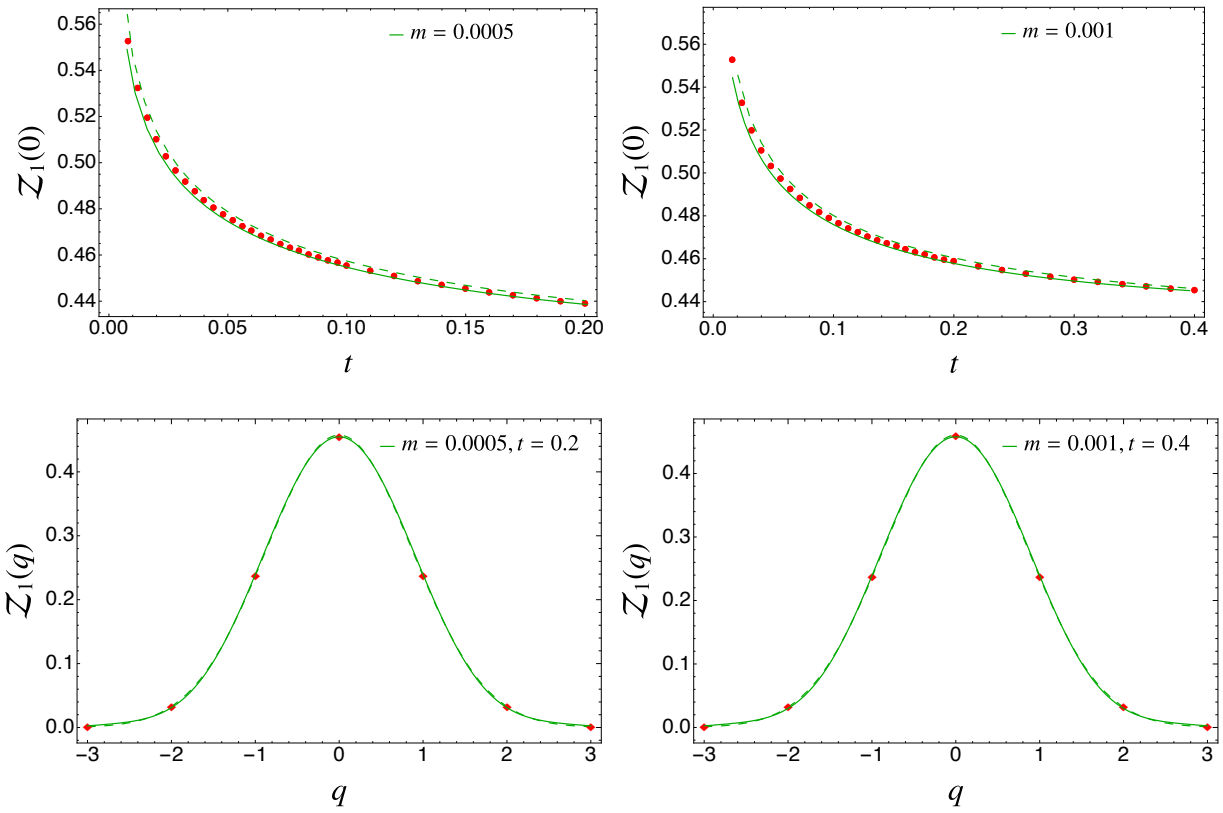

Figure 8.4: The probability $\mathcal{Z}_1(q)$. Top: As a function of $t = m\ell$ at fixed $q = 0$ for mass $m = 0.0005$ (left) and $m = 0.001$ (right). The dashed green line is $\mathcal{Z}_1(q)$ obtained by the saddle point approximation, i.e. (8.4.23). The solid green line is the exact Fourier transform without taking the quadratic approximation. For large ℓ (and t as a consequence) the saddle-point approximation converges to the exact value, as expected. Bottom: The same at fixed t as function of q.

where we consistently approximated the cutoff at quadratic level and used the lattice cutoff with $\gamma(n)$ given in (8.4.18). A different cutoff just leads to a different additive constant in b_n (i.e., a different definition of h_n), but we will use its precise form only for the comparison with numerics and so all the following formulas are completely general.

Now we can compute the Fourier transform (8.1.2) that reads

$$\mathcal{Z}_n(q) = Z_n(0) \int_{-\pi}^{\pi} \frac{d\alpha}{2\pi} e^{-iq\alpha} e^{-\alpha^2 b_n(\ell,t)/2}. \tag{8.4.22}$$

When $\ell \to \infty$, we can perform the integral by saddle point approximation and the integration domain can be extended to the whole real line. We end up in a simple Gaussian integral, obtaining

$$\mathcal{Z}_n(q) = \frac{Z_n(0)}{\sqrt{2\pi b_n(\ell,t)}} e^{-\frac{q^2}{2b_n(\ell,t)}}. \tag{8.4.23}$$

We check (8.4.23) against numerical computations in Figure 8.4 focusing on $n = 1$ and the agreement is perfect. We test both the scaling with $t = m\ell$ for fixed q and at fixed t as a function of q.

Now we are ready to compute the symmetry resolved Rényi entropies. From the definition

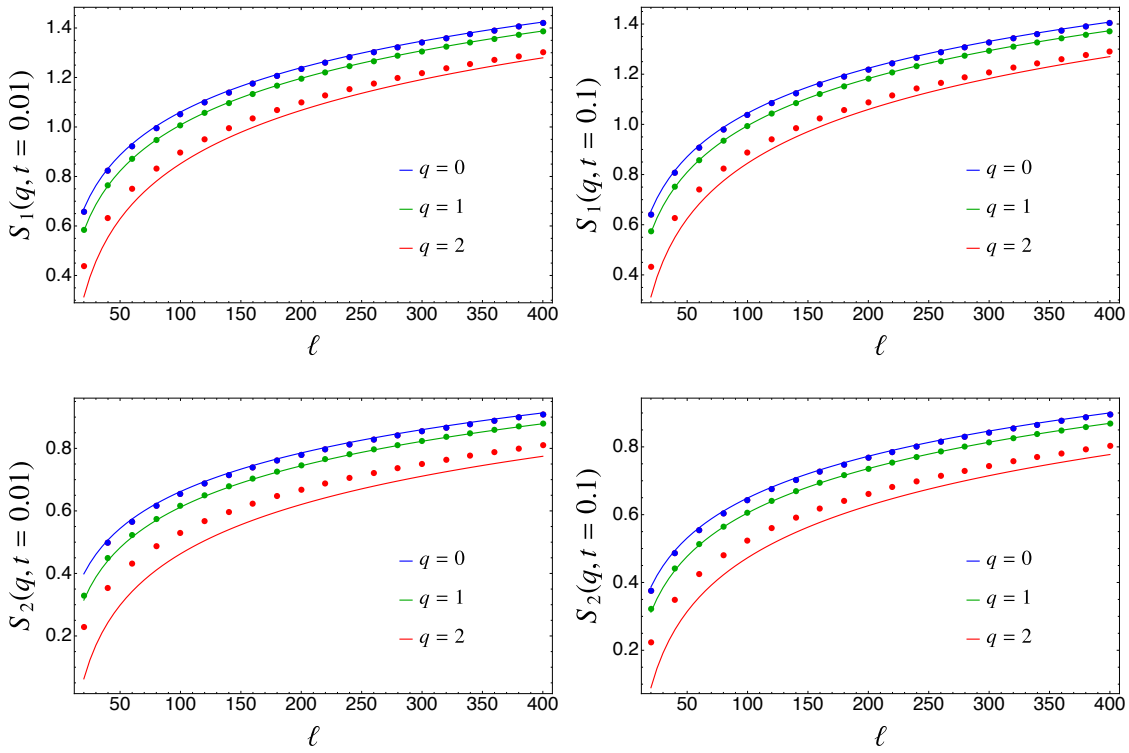

Figure 8.5: Symmetry resolved entanglement entropies for a few different values of q and n as functions of ℓ. The field theory prediction is tested against exact lattice computations. The agreement with (8.4.26), that includes lattice effects, is remarkable. For large $|q|$, the approximation at the order q^2 is no longer sufficient and neglected corrections to the scaling become important, as well known for the massless case [251].

(8.1.4) we have

$$S_n(q) = S_n^D - \frac{1}{2}\ln(2\pi) + \frac{1}{1-n}\ln\frac{b_1(\ell,t)^{n/2}}{b_n(\ell,t)^{1/2}} - \frac{q^2}{2(1-n)}\left(\frac{1}{b_n(\ell,t)} - \frac{n}{b_1(\ell,t)}\right), \tag{8.4.24}$$

where S_n^D is the total n-th Rényi entropy for the Dirac fields, which reads [217]

$$S_n^D = \frac{n+1}{6n}\left(\ln\frac{\ell}{\epsilon} - \frac{t^2}{2}\ln^2 t\right) + O(t^2 \ln t)\,. \tag{8.4.25}$$

We can further expand the above equation for $\ell \to \infty$ since $b_n(\ell, t)$ diverges logarithmically, obtaining

$$S_n(q) = S_n^D - \frac{1}{2}\ln\left(\frac{2}{\pi}\ln\delta_n\ell\right) + \frac{\ln n}{2(1-n)} - \frac{\pi^4 n(h_1 - nh_n)^2}{4(1-n)^2(\ln\ell)^2} + \\ + q^2 n\pi^4 \frac{h_1 - nh_n}{2(1-n)(\ln\ell\kappa_n)^2} + o(\ln\ell^{-2}), \tag{8.4.26}$$

where

$$\ln\delta_n = -\frac{\pi^2 n(h_n - h_1)}{1-n}, \tag{8.4.27}$$

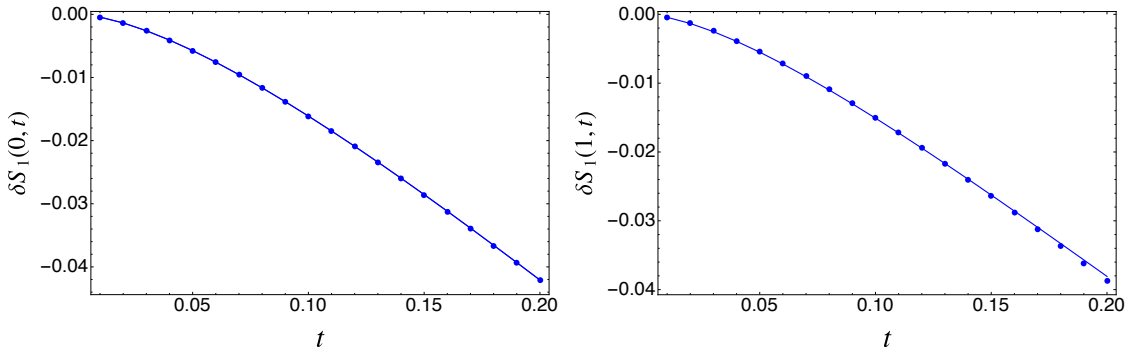

Figure 8.6: Subtracted symmetry resolved von Neumann entropy $\delta S_1(q,t) \equiv S_1(q,t) - S_1(q,t=0)$ for $q = 0$ (left) and $q = 1$ (right) as a function of t (fixing $\ell = 600$ and varying m). This subtracted quantity highlights the mass dependence of symmetry resolved entropies. The continuous lines are just the difference of the same subtracted entropies as obtained from the field theory expansion (8.4.26).

and

$$\ln \kappa_n = -\pi^2 \frac{(h_1 + n h_n)}{2}. \tag{8.4.28}$$

The above formula is valid also for the symmetry resolved Von Neumann entropy taking properly the limits of the various pieces as $n \to 1$.

Let us critically discuss the result in (8.4.26). The leading terms for large ℓ (up to $O((\ln \ell)^{-2})$) do not depend on q and they are given by the total entropies S_n^D in (8.4.25). We then conclude that at this order, the presence of the mass does not break entanglement equipartition found in conformal field theory [97]. The first term breaking equipartition is at order $O((\ln \ell)^{-2})$ and its amplitude is governed by the constant h_n defined in (8.4.21). This constant gets contributions both from the non-universal cutoff and from the mass; the two contributions have the same analytic features. In Fig. 8.5 we test the accuracy of our total prediction against exact lattice numerical calculations. The agreement is remarkable for small values of $|q|$, but it worsens already at $q = 2$; this does not come as a surprise since the same trend was already observed in the massless case [251]. Such discrepancies are entirely due to corrections of order $o(q^2)$ and are expected to reduce as ℓ gets larger. The drawback of the data reported in Fig. 8.5 is that universal field theory mass contributions and the lattice non-universal terms are mixed up and the latter are, by far, the largest one. It is then very difficult to observe the dependence on the mass in these plots. An effective and easy way to highlight the role of the mass is to subtract from the symmetry resolved entropies their value for the massless case, i.e. considering the numerical evaluation of the $\delta S_n(q,t) \equiv S_n(q,t) - S_n(q,0)$. Such subtracted entropies for $n = 1$ and $q = 0, 1$ are reported in Fig. 8.6, showing that the entropy is a monotonous decreasing function of t (and hence of m at fixed ℓ).

8.4.3 The long distance expansion

In this subsection we move to the analysis of the charged and symmetry resolved entropies in the limit of large t. The most effective way to proceed is, following Ref. [217], to employ in (8.4.7) a boundary condition for $t \to \infty$, that takes the form [217]

$$v_a(t) \sim \frac{2}{\pi} \sin(\pi a) K_{2a}(t), \tag{8.4.29}$$

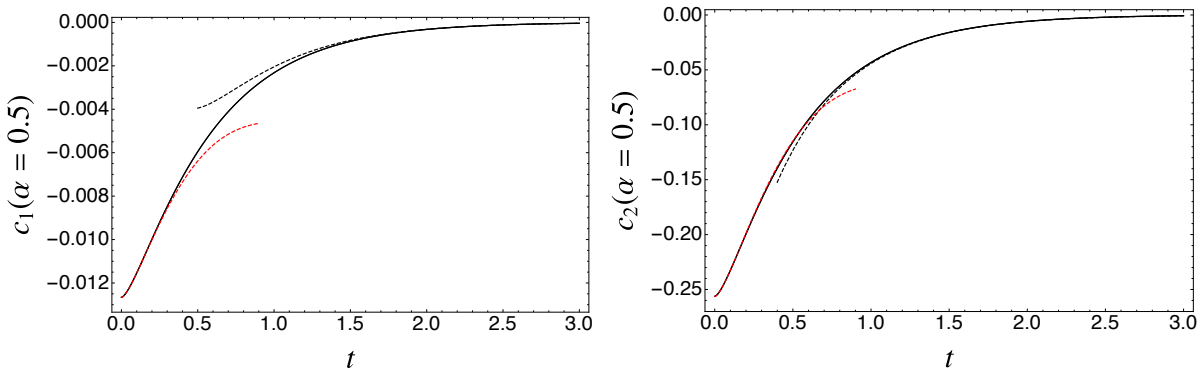

Figure 8.7: The solid lines are the functions $c_n(\alpha)$ obtained as exact numerical solutions of the differential equation (8.4.7). The dashed lines are the leading terms in the expansions for short (red) and long (black) distances, i.e. Eqs. (8.4.12) and (8.4.31), respectively.

where $K_{2a}(t)$ is the modified Bessel function of the second kind. This is the starting point for a systematic expansion for large t of the solution $v_a(t)$ of the differential equation (8.4.7). Plugging the resulting expansion into the integral (8.4.6) for $w_a(t)$, we get

$$w_a(t) = -e^{-2t}\frac{\sin^2(a\pi)}{\pi}\left(1 + \frac{-1+16a^2}{4t} + O(t^{-2})\right). \tag{8.4.30}$$

Summing over $a = \frac{k}{n} + \frac{\alpha}{2\pi n}$, we obtain the long distance asymptotic expansion for the universal factor $c_n(\alpha)$

$$c_n(\alpha) = \frac{e^{-2t}}{2\pi}\left(-n + \frac{(4-n^2)\pi^2 - 12\alpha^2}{12nt\pi^2} - \frac{2\csc\frac{\pi}{n}(\pi\cot\frac{\pi}{n}\cos\frac{\alpha}{n} + \alpha\sin\frac{\alpha}{n})}{\pi nt} + O(t^{-2})\right), \tag{8.4.31}$$

and for $n = 1$

$$c_1(\alpha) = -\frac{e^{-2t}}{\pi}\sin^2\frac{\alpha}{2}\left(1 + \frac{\frac{4\alpha^2}{\pi^2} - 1}{4t} + O(t^{-2})\right). \tag{8.4.32}$$

This is consistent with the exact result $c_1(0) = 0$ coming from the normalisation of the reduced density matrix. For $\alpha = 0$, (8.4.31) reproduces the known results [217].

In Fig. 8.7 we report the numerical exact solution of the Painlevé equation (8.4.7) for $c_n(\alpha)$; we focus on $n = 1, 2$ and plot $c_n(\alpha)$ as a function of t. For large t, the solutions perfectly match the asymptotic expansions (8.4.31) and (8.4.32) (for completeness we also show the small t expansion in (8.4.12)). Let us emphasise the presence of a discontinuity in $c_n(\alpha)$ for $n \to 1$ as a function of n: it is due to the non-commutativity of the limits $n \to 1$ and $t \to \infty$, as well known and discussed at length in the literature for $\alpha = 0$ [217, 224]. We show here that the presence of α does not cancel such a discontinuity, although for $\alpha \neq 0$ the leading term is of the same order e^{-2t}.

The charged entropy is simply given by the integral

$$\ln Z_n(\alpha) = \int_{m\epsilon}^{m\ell}\frac{c_n(\alpha)}{t}dt. \tag{8.4.33}$$

At large t, the function $c_n(\alpha)$ goes to zero exponentially in t for any n; hence the charged entropies approach asymptotically a finite value for large ℓ. This saturation value is determined entirely by the infrared physics, i.e. by the value of $c_n(\alpha)$ at small t, indeed

$$\ln Z_n(\alpha) \simeq \ln Z_n^{(0)}(\alpha) \equiv \int_{m\epsilon}^{\infty}\frac{c_n(\alpha)}{t}dt \simeq \left(\frac{1}{6}\left(n - \frac{1}{n}\right) + \frac{\alpha^2}{2\pi^2 n}\right)\ln m\epsilon. \tag{8.4.34}$$

This dependence on $\ln(m\epsilon)$ coincides with the result in Sec. 8.3.2 (following the analysis of the properties of the energy momentum tensor on $\mathcal{R}_{n,\alpha}$), up to a factor 2 due to the number of the endpoints (cf. (8.3.14)).

The corrections in $m\ell$ to the ℓ-independent result (8.4.34) are obtained expanding the integral (8.4.33) in the ultraviolet. Keeping for conciseness only the leading order in t of Eqs. (8.4.31) and (8.4.32) and performing the integration, we get

$$\ln Z_n(\alpha) = \ln Z_n^{(0)}(\alpha) + \frac{ne^{-2t}}{4\pi t}, \qquad \ln Z_1(\alpha) = \ln Z_1^{(0)}(\alpha) + \frac{e^{-2t}}{2\pi t}\sin^2\frac{\alpha}{2}. \tag{8.4.35}$$

Once again, $Z_n(\alpha)$ are not continuous functions of n close to $n = 1$ (as it was already known for $\alpha = 0$, see [217]) and, above all, the correction of $\ln Z_n(\alpha)$ does not depend on α for $n \neq 1$ at this order. Subleading corrections to (8.4.35) can be straightforwardly and systematically worked out, but they are not illuminating, although they do depend on α also for $n \neq 1$.

For $n \neq 1$, since the leading correction does not depend on α, the Fourier transform is not affected and the symmetry resolved moments with $n \neq 1$ just get a multiplicative correction to $\mathcal{Z}_n(q)$ in (8.3.17) (so additive for the logarithm), given by

$$\delta \ln \mathcal{Z}_n(q) = \frac{ne^{-2t}}{4\pi t}\,. \tag{8.4.36}$$

For $n = 1$ the net effect of the $\sin^2(\alpha/2)$ term in (8.4.35) is to renormalise the variance with an exponential additive correction, i.e. the desired probability is

$$\mathcal{Z}_1(q) = e^{-\frac{2q^2\pi^2}{4|\ln(m\epsilon)| - \pi e^{-2t}/t}} \sqrt{\frac{2\pi}{4|\ln(m\epsilon)| - \pi e^{-2t}/t}} \tag{8.4.37}$$

The symmetry resolved Rényi entropies with $n \neq 1$ are straightforwardly obtained from (8.1.4). Indeed, plugging Eqs. (8.4.36) and (8.4.37) in (8.1.4), we get

$$S_n(q) = -\frac{n+1}{6n}\ln(m\epsilon) + \frac{ne^{-2m\ell}}{4\pi m\ell(1-n)} + \frac{\ln n}{2(1-n)} - \frac{1}{2}\ln\left(\frac{2}{\pi}|\ln m\epsilon| + \frac{ne^{-2m\ell}}{(1-n)2m\ell}\right) + \\ + O((\ln m\epsilon)^{-1}, e^{-3m\ell}). \tag{8.4.38}$$

Such a result shows exact equipartition (at this order) which is a clear consequence of the simple form of (8.4.36). This is reminiscent of the exact results for integrable models studied in chapter 9.

The limit $n \to 1$ for the von Neumann entropy should be handled with care. We start rewriting (8.1.4) as

$$S_1(q) = \ln \mathcal{Z}_1(q) - \frac{1}{\mathcal{Z}_1(q)}\int_{-\pi}^{\pi}\frac{d\alpha}{2\pi}e^{-\mathrm{i}q\alpha}Z_1(\alpha)\partial_n \ln Z_n(\alpha)|_{n=1}. \tag{8.4.39}$$

We use this equation to obtain the entire correction in t due to the Bessel function and not only the leading exponential term (as done in (8.4.35)). The crucial computation is

$$\begin{aligned}\partial_n c_n(\alpha)|_{n=1} &= -\partial_n \int_t^\infty dy\, y \sum_{k=-(n-1)/2}^{(n-1)/2} v_a^2(y)\Big|_{n=1} = \\ &= -\left(\frac{2}{\pi}\right)^2 \partial_n \int_t^\infty dy\, y \sum_{k=-(n-1)/2}^{(n-1)/2} \sin^2(\pi a) K_{2a}^2(y)\Big|_{n=1},\end{aligned} \tag{8.4.40}$$

where $a = \frac{k}{n} + \frac{\alpha}{2\pi n}$. We can use the integral representation for the Bessel function

$$K_a(y) = \int_1^\infty du\, e^{-yu} \frac{(u+\sqrt{u^2-1})^a + (u+\sqrt{u^2-1})^{-a}}{2\sqrt{u^2-1}}, \tag{8.4.41}$$

to perform the sum over k in Eq. (8.4.40). Once we plug Eq. (8.4.41) into Eq. (8.4.40) , we get

$$\begin{aligned} c_n(\alpha) = &- \frac{2}{\pi^2} \int_t^\infty dy\, y \int_1^\infty du \int_1^\infty dv \frac{e^{-y(u+v)}}{\sqrt{u^2-1}\sqrt{v^2-1}} \times \\ &\times \left(F_{n,\alpha}((u+\sqrt{u^2-1})(v+\sqrt{v^2-1})) + F_{n,\alpha}\left(\frac{(u+\sqrt{u^2-1})}{(v+\sqrt{v^2-1})}\right)\right), \end{aligned} \tag{8.4.42}$$

where

$$F_{n,\alpha}(z) = \frac{z^{\frac{\pi-\alpha}{n\pi}}}{4}\left(z-\frac{1}{z}\right)\left(\frac{1+z^{\frac{2\alpha}{n\pi}}}{z^{\frac{2}{n}}-1} + \frac{(z^{\frac{2(\pi+\alpha)}{n\pi}}-1)\cos\frac{\pi-\alpha}{n} + (z^{\frac{2}{n}} - z^{\frac{2\alpha}{n\pi}})\cos\frac{\pi+\alpha}{n}}{1+z^{\frac{4}{n}} - 2z^{\frac{2}{n}}\cos(\frac{2\pi}{n})}\right). \tag{8.4.43}$$

We now study the behaviour of $F_{n,\alpha}(z)$ when $n \to 1$. For $z = 1$, the limit $n \to 1$ is singular. We can isolate this singularity using the polar variables $(n-1, z-1) \to (\rho\cos\theta, \rho\sin\theta)$ and expanding in the radial coordinate ρ. The result of this procedure is

$$F_{n,\alpha}(z) = \frac{1}{2} - \frac{1}{2}\frac{(z-1)^2\cos\alpha}{\pi^2(n-1)^2 + (z-1)^2} + O(n-1, z-1), \tag{8.4.44}$$

whose derivative with respect to n is

$$\partial_n F_{n,\alpha}(z)\Big|_{n\to1} = \lim_{n\to1}\frac{F_{n,\alpha}(z) - F_{1,\alpha}(z)}{n-1} = \pi^2\left(\frac{1}{2} - \sin^2\frac{\alpha}{2}\right)\delta(z-1). \tag{8.4.45}$$

Plugging this result in Eq. (8.4.42) and taking the derivative wrt n, we get

$$\partial_n c_n(\alpha)\big|_{n\to1} = -\left(1 - 2\sin^2\frac{\alpha}{2}\right)\int_t^\infty dy y K_0(2y) = -\left(\frac{1}{2} - \sin^2\frac{\alpha}{2}\right) tK_1(2t), \tag{8.4.46}$$

which, once integrated in t according to Eq. (8.4.33), gives the full ultraviolet behaviour of $\partial_n \ln Z_n(\alpha)\big|_{n\to1}$, i.e.

$$\partial_n \ln Z_n(\alpha)\big|_{n\to1} = \left(\frac{1}{3} - \frac{\alpha^2}{2\pi^2}\right)\ln(m\epsilon) + \left(\frac{1}{4} - \frac{1}{2}\sin^2\frac{\alpha}{2}\right)K_0(2t). \tag{8.4.47}$$

Plugging the above derivative into (8.4.39) finally yields

$$S_1(q) = -\frac{1}{3}\ln(m\epsilon) - \frac{1}{4}K_0(2m\ell) - \frac{1}{2}\ln\left(\frac{2|\ln(m\epsilon)|}{\pi}\right) - \frac{1}{2} + O((\ln m\epsilon)^{-1}). \tag{8.4.48}$$

The first two terms in (8.4.48) are respectively the leading and the subleading terms in the total entanglement entropy of a massive Dirac field, in agreement with the known results in Refs. [216, 217, 224]. The double logarithmic term appears only in the symmetry resolved result and, as already discussed in (8.3.18), it is related to the number entropy. The above derivation clearly highlight this correspondence. As for the Rényi entropy, at this order in $\ln m\epsilon$, there is perfect entanglement equipartition that will be broken by higher order terms.

8.4.4 Lattice discretisation of the massive Dirac fermion

For the numerical test of our field theory results we consider the following lattice discretisation of the Dirac fermion [217]

$$\widehat{H} = -\frac{\mathrm{i}}{2}\sum_{j=0}^{L-1}(\hat{c}_{j+1}^\dagger \hat{c}_j - \hat{c}_j^\dagger \hat{c}_{j+1}) + m\sum_{j=0}^{L-1}(-1)^j \hat{c}_j^\dagger \hat{c}_j, \tag{8.4.49}$$

where $\hat{c}_j$ satisfy the anti-commutation relations $\{\hat{c}_j, \hat{c}_k^\dagger\} = \delta_{jk}$ and L denotes the number of sites of the chain. The correlators in the thermodynamic limit, *i.e.* for $L \to \infty$, are

$$\begin{aligned}
\langle \hat{c}_j^\dagger \hat{c}_k \rangle &= \frac{1}{2}\delta_{(j-k),0} + (-1)^j \int_0^{\frac{1}{2}} dx \frac{m\cos(2\pi x(j-k))}{\sqrt{m^2+\sin(2\pi x)^2}} \qquad \text{for} \qquad |j-k| \quad \text{even}, \\
\langle \hat{c}_j^\dagger \hat{c}_k \rangle &= \mathrm{i}\int_0^{\frac{1}{2}} dx \frac{\sin(2\pi x)}{\sqrt{m^2+\sin(2\pi x)^2}} \sin(2\pi x(j-k)) \qquad \text{for} \qquad |j-k| \quad \text{odd}.
\end{aligned} \tag{8.4.50}$$

Denoting by ν_j the eigenvalues of the correlation matrix restricted to the subsystem A made by ℓ sites (with $j \in [1,\ell]$), simple algebra leads to the moments $\mathrm{Tr}\hat{\rho}_A^n$ and to the Rényi entropies [4,191]. The α-dependent moments $Z_n(\alpha)$ can be also easily written in terms of the eigenvalues of the correlation matrix $C_{jk} = \langle \hat{c}_j^\dagger \hat{c}_k \rangle$. For this purpose, it is necessary to write down the charge operator $\widehat{Q}_A$ in terms of $\hat{c}_j$ and $\hat{c}_j^\dagger$ operators in (8.4.49), i.e. [438]

$$\widehat{Q}_A = \sum_{j=0}^{\ell-1}\left(\hat{c}_j^\dagger \hat{c}_j - \frac{1}{2}\right) = \sum_{j=0}^{\ell-1}\hat{c}_j^\dagger \hat{c}_j - \frac{\ell}{2}. \tag{8.4.51}$$

Therefore, the charged moments read [96]

$$Z_n(\alpha) = \prod_{j=1}^{\ell}[(\nu_j)^n e^{\mathrm{i}\alpha/2} + (1-\nu_j)^n e^{-\mathrm{i}\alpha/2}], \tag{8.4.52}$$

which provides a very simple formula for its numerical computation. The Fourier transform of $Z_n(\alpha)$ gives the symmetry resolved moments and entropies.

8.5 The Green's function approach: The complex scalar field

In this section we present a derivation of the charged moments for a complex massive scalar by generalising to $\alpha \neq 0$ the results obtained in [10,218]. In Sec. 8.3.1 we showed that $Z_n(\alpha)$ can be written as product of partition functions on the plane with boundary conditions along the cut A

$$\tilde{\varphi}_k(e^{2\pi\mathrm{i}}z, e^{-2\pi\mathrm{i}}\bar{z}) = e^{2\pi\mathrm{i}a}\tilde{\varphi}_k(z,\bar{z}), \qquad a = \frac{k}{n} + \frac{\alpha}{2\pi n}, \qquad k = 0, \cdots n-1. \tag{8.5.1}$$

Denoting by ζ_a these partition functions we have

$$\ln Z_n(\alpha) = \sum_{k=0}^{n-1} \ln \zeta_{\frac{k}{n}+\frac{\alpha}{2\pi n}}. \tag{8.5.2}$$

As for the analogous case of fermions, cf. Eq. (8.4.3), we define the auxiliary quantities

$$w_a \equiv \ell\partial_\ell \ln \zeta_a, \qquad c_n(\alpha) \equiv \sum_{k=0}^{n-1} w_{\frac{k}{n}+\frac{\alpha}{2\pi n}}, \tag{8.5.3}$$

that, using (8.5.2), allow us to write the logarithmic derivative of the partition function in $\mathcal{R}_{n,\alpha}$ as

$$c_n(\alpha) = \ell \frac{\partial \ln Z_n(\alpha)}{\partial \ell} \qquad \Rightarrow \qquad \ln Z_n(\alpha) = \int_\epsilon^\ell \frac{c_n(\alpha)}{\ell'} d\ell'. \tag{8.5.4}$$

Even here, for $n = 1$, the function $c_n(\alpha)$ is the analogue of Zamolodchikov's c-function [157] in the presence of the flux α.

The key observation of this approach relies on the identity between the partition function ζ_a and the Green's function G_S, which reads

$$\partial_{m^2} \ln \zeta_k = -\int dr^2\, G_S(\mathbf{r}, \mathbf{r}')\,. \tag{8.5.5}$$

Through this relation, the function w_a has been obtained for generic values of a also for bosonic free massive field theories [10]. As already found in Sec. 8.3.1 using twist fields, also this approach requires that $0 < a < 1$ for the scalar theory (see [218] for details). Thus, in order to compute $Z_n(\alpha)$, we will use the results in [10] setting $a = \frac{k}{n} + \frac{|\alpha|}{2\pi n}$ for the complex Klein Gordon theory.

Here we consider the complex massive non-compact bosonic field theory with action given by (8.1.5) and mass m. The function w_a with $0 < a < 1$ defined in (8.5.3) can be written as [218]

$$w_a = -\int_t^\infty y u_a^2(y) dy, \tag{8.5.6}$$

where $t = m\ell$ and u_a is the solution of the Painlevé V equation

$$u_a'' + \frac{u_a'}{t} = \frac{u_a}{1+u_a^2}(u_a')^2 + u_a(1+u_a^2) + 4\frac{\left(a-\frac{1}{2}\right)^2}{t^2(1+u_a^2)} u_a. \tag{8.5.7}$$

The solution of (8.5.7) is showed in Fig. 8.8: the function w_a for a generic value of t can be obtained solving numerically (8.5.7) with the initial condition for $t \to 0$

$$u_a(t) = \frac{-1}{t\,(\ln t + \kappa_S(a))} - a(a-1)t(\ln t + \kappa_S(a)) + O(t), \tag{8.5.8}$$

where [10]

$$\kappa_S(a) = 2\gamma_E + \frac{\psi(1-a) + \psi(a)}{2} - \ln 2. \tag{8.5.9}$$

In the figure we compare the exact result from field theory with numerical data for a chain of complex oscillators, obtained exploiting the techniques reviewed in Sec. 8.5.3. We have a fairly good agreement between lattice and field theory, although for small values of α the agreement gets worse and one needs a larger and larger subsystem length ℓ on the lattice to match the continuum limit. In the following we will further discuss this issue in the limits when we have an analytic handle on the problem.

8.5.1 The expansion close to the conformal point

In the conformal limit $t \to 0$ we have that the solution of the Painlevé equation admits the expansion [218]

$$w_a = -2a(1-a) - \frac{1}{\ln(t) + \kappa_S(a)} + O(t). \tag{8.5.10}$$

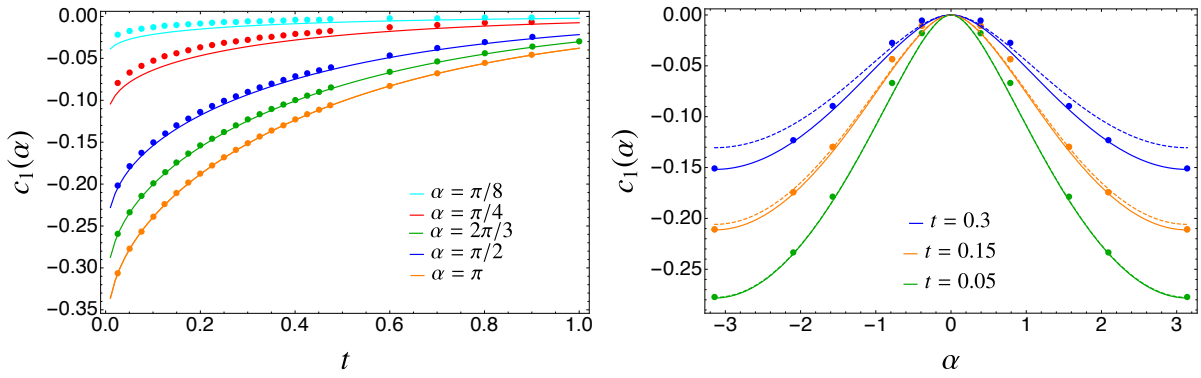

Figure 8.8: Left panel: Logarithmic derivative of the charged moments, $c_1(\alpha)$, as a function of $t = m\ell$ obtained by solving numerically the Painléve equation (8.5.7) (solid lines). The data (symbols) are obtained fixing (from top to bottom) $\ell = 720, 620, 420, 420, 320$ and varying properly m in such a way that $m\ell \in (0, 1)$. As discussed in the main text, the agreement with the numerical data worsens as α decreases. Right panel: the same quantity is plotted as a function of α from the numerical solution of the Painlevé equation (solid lines), showing also in this case that the agreement as $\alpha \to 0$ is not excellent. The dashed lines represent the small t expansion in (8.5.11): the smaller is t, the better the approximation works.

Using (8.5.3) we get

$$c_n(\alpha) = \sum_{k=0}^{n-1} w_{\frac{k}{n}+\frac{|\alpha|}{2\pi n}} = \frac{1-n^2}{3n} + \frac{\alpha^2}{2\pi^2 n} - \frac{|\alpha|}{\pi n} - \sum_{k=0}^{n-1} \frac{1}{\ln t + \kappa_S(a(k))} + \dots . \tag{8.5.11}$$

Let us discuss first at the level of the universal function $c_n(\alpha)$ the origin of the non uniform behaviour in α. Eq. (8.5.11) is an exact asymptotic expansion valid for any $\alpha \neq 0$. For $\alpha \to 0$, there is a clear problem with the constant $\kappa_S(a(0))$ (i.e. of the mode with $k = 0$) which diverges as $\pi/|\alpha|$. Hence, since $\ln t$ grows very slowly with t, the true asymptotic behaviour is attained only for $t \gtrsim e^{\pi/|\alpha|}$. For smaller values of t, the mode $k = 0$ looks almost constant ($\sim |\alpha|/\pi$) and similar to the leading term. Exactly for $\alpha = 0$, the mode $k = 0$ diverges, so its inverse is just zero and it does not affect the calculation. It is then clear that the approach to the asymptotic behaviour cannot be uniform in α, as already observed numerically in Fig. 8.8.

After having discussed this caveat with the small α behaviour, we are ready to integrate (8.5.11) to get the charged moments, according to (8.5.4), obtaining

$$\ln Z_n(\alpha) = \left(\frac{1-n^2}{3n} + \frac{\alpha^2}{2\pi^2 n} - \frac{|\alpha|}{\pi n} \right) \ln\left(\frac{\ell}{\epsilon}\right) + \sum_{k=0}^{n-1} \ln \left| \frac{\ln(m\epsilon) + \kappa_S(a(k))}{\ln(m\ell) + \kappa_S(a(k))} \right| . \tag{8.5.12}$$

Let us remark that when $n = 1$, the last sum reduces to the term with $k = 0$. We recall that the cutoff ϵ depends both on n and α making the analysis even more troubling.

Even though we are in the conformal limit in which $m\ell \ll 1$, the additional constant $\kappa_S(a(0))$ cannot be neglected because of its divergent behaviour when $k = 0$ and $\alpha = 0$. The terms with $k > 0$ do not present any problem and $\kappa_S(a(k))$ can be safely neglected. The mode with $k = 0$ instead has three different regimes, depending on the value of $\kappa_S(k = 0)$ which is governed by α as follows:

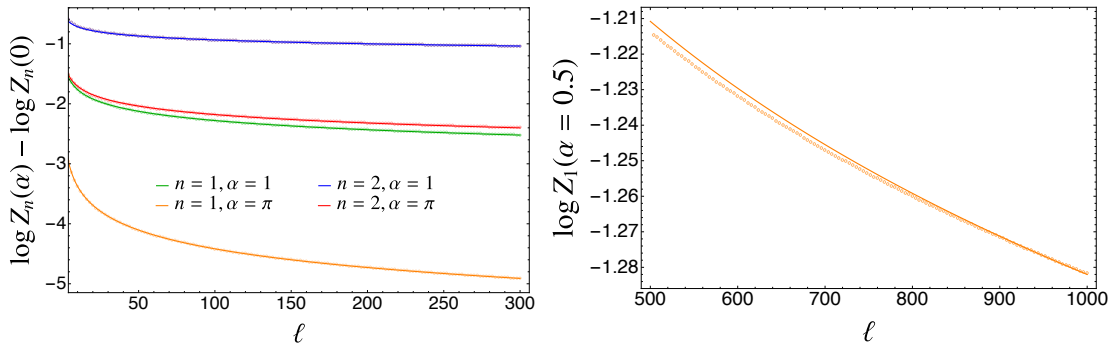

Figure 8.9: Charged moments for the free massive boson close to the critical regime. We benchmark the analytical prediction (8.5.12) (solid lines) with the numerical data (symbols) for different values of n and α at fixed $m = 10^{-10}$: the analytical formula matches well the data for large values of α (left), but for smaller α (right) much larger values of ℓ are necessary to observe a fair match, as explained in the text.

- for very small α, i.e. such that $\alpha \lesssim n\pi/|\ln(m\epsilon/2)+\gamma_E|$, $\kappa_S(k=0)$ diverges faster than both $\ln m\ell$ and $\ln m\epsilon$. Hence, expanding the ratio in (8.5.12), this subleading term becomes of the same order of the leading one, i.e.

$$\ln\left|\frac{\ln(m\epsilon)+\kappa_S(a(0))}{\ln(m\ell)+\kappa_S(a(0))}\right| \xrightarrow{\alpha\to 0} \frac{|\alpha|}{\pi n}\ln\frac{\ell}{\epsilon}+\ldots, \tag{8.5.13}$$

- for intermediate values of α, i.e. when $n\pi/|\ln(m\epsilon/2)+\gamma_E| \lesssim \alpha \lesssim n\pi/|\ln(m\ell/2)+\gamma_E|$, we have

$$\ln\left|\frac{\ln(m\epsilon)+\kappa_S(a(0))}{\ln(m\ell)+\kappa_S(a(0))}\right| \sim \ln\left|\frac{\ln(m\epsilon)}{\kappa_S(a(0))}\right|+\ldots, \tag{8.5.14}$$

  and hence this produces just an additive correction in ℓ, but depending on $m\epsilon$;

- for larger α, i.e. for $\alpha \gtrsim n\pi/|\ln(m\ell/2)+\gamma_E|$, the term κ_S is a correction both for numerator and denominator and so

$$\ln\left|\frac{\ln(m\epsilon)+\kappa_S(a(0))}{\ln(m\ell)+\kappa_S(a(0))}\right| \simeq \ln\left|\frac{\ln(m\epsilon)}{\ln(m\ell)}\right|+\ldots, \tag{8.5.15}$$

  as for the terms with $k \neq 0$. We stress that this third regime is the true asymptotic one for large ℓ at fixed α.

This competition among the three terms makes difficult the analytical treatment of the last sum in (8.5.12), and, at the same time, the non trivial dependence on the cutoff ϵ (that we recall also depends on α and n) complicates the comparison with the numerics. For this reason, we consider only the leading term in (8.5.12), which, strictly speaking, is valid in the massless case and in the third regime above. Such a leading term is the same provided as in the twist field approach (cf. Eq. (8.3.8)) and coincides with some equivalent ones in literature [408]. The main advantage of (8.5.12) is that it clearly shows what are the problems one faces when considering only the leading term. The comparisons with the numerics are shown in Figure 8.9: we report the numerical data for different values of n and α; as expected from our previous discussion, the agreement with the predictions is very good for large α, but it worsens as α gets smaller and n gets larger. Smaller is α, larger is the value of ℓ on the lattice necessary to observe the true asymptotic behaviour.

Symmetry resolution

The symmetry resolved moments of the reduced density matrix can be computed through the Fourier transform of the leading term of the charged moments in (8.5.12)

$$\mathcal{Z}_n(q) = \tag{8.5.16}$$
$$= Z_n(0)\left(\frac{\ell}{\epsilon}\right)^{-\frac{1}{2n}}\sqrt{\frac{n\pi}{8\ln(\ell/\epsilon)}}(-1)^q e^{\frac{n\pi^2q^2}{2\ln(\ell/\epsilon)}}\left[\mathrm{Erfi}\left(\frac{\ln(\ell/\epsilon)-n\pi\mathrm{i}q}{\sqrt{2n\ln(\ell/\epsilon)}}\right)+\mathrm{Erfi}\left(\frac{\ln(\ell/\epsilon)+n\pi\mathrm{i}q}{\sqrt{2n\ln(\ell/\epsilon)}}\right)\right],$$

where $\mathrm{Erfi}(x)$ is the imaginary error function (the overall result is real and positive for $q\in\mathbb{Z}$)

$$\mathrm{Erfi}(x)=\frac{-2\mathrm{i}}{\sqrt{\pi}}\int_0^{\mathrm{i}x}dt\,e^{-t^2}\xrightarrow{x\to\infty}\frac{e^{x^2}}{\sqrt{\pi}x}. \tag{8.5.17}$$

In the large ℓ limit, using the expansion in (8.5.17), the charged moments in (8.5.16) can be can be approximated as

$$\mathcal{Z}_n(q)=Z_n(0)\frac{n\ln\ell/\epsilon}{n^2\pi^2q^2+\ln^2\ell/\epsilon}, \tag{8.5.18}$$

and hence the symmetry resolved entropies are given by

$$S_n(q)=\frac{1}{1-n}\ln\frac{\mathcal{Z}_n(q)}{\mathcal{Z}_1(q)^n}\simeq S_n-\ln\ln\frac{\ell}{\epsilon}+\frac{\ln n}{1-n},\quad S_1(q)\simeq S_1-\ln\ln\frac{\ell}{\epsilon}-1. \tag{8.5.19}$$

The leading behaviour is described by the total Rényi entropies, with the usual correction $\ln\ln\ell$ that is independent on q, confirming the equipartition of the entanglement entropy for a complex massive scalar field theory. Let us mention that a further expansion of (8.5.16) leads to subleading corrections behaving as $q^2/(\ln\ell)^2$ which explicitly depend on q, breaking the equipartition of the entanglement.

Let us now discuss the effect of the term that we disregarded in (8.5.12), namely the sum over k. The mode with $k\neq 0$ would provide double logarithimic corrections encountered also in other contexts, like non unitary CFTs [230, 439]. These in principle are calculable and partially under control. We mention that such terms have a non-trivial dependence on n in $\mathcal{Z}_n(q)$ and hence they are responsible of a further breaking of equipartition. Unfortunately, the determination of this correction is not easy because it is influenced by the precise dependence on α and n of the non-universal cutoff ϵ (as it should be clear from (8.5.12)). Finally, as discussed for the charged moments, the effect of the mode $k=0$ is even more dramatic and too difficult to keep under control.

8.5.2 The long distance expansion

The boundary condition for (8.5.7) in the limit in which $t\to\infty$ is [218]

$$u_a(t)\sim\frac{2}{\pi}\sin(\pi a)K_{1-2a}(t). \tag{8.5.20}$$

The solution of (8.5.7) in the long distance regime together with (8.5.6) gives

$$w_a(t)=-e^{-2t}\frac{\sin^2(a\pi)}{\pi}\left(1+\frac{3-16a+16a^2}{4t}\right). \tag{8.5.21}$$

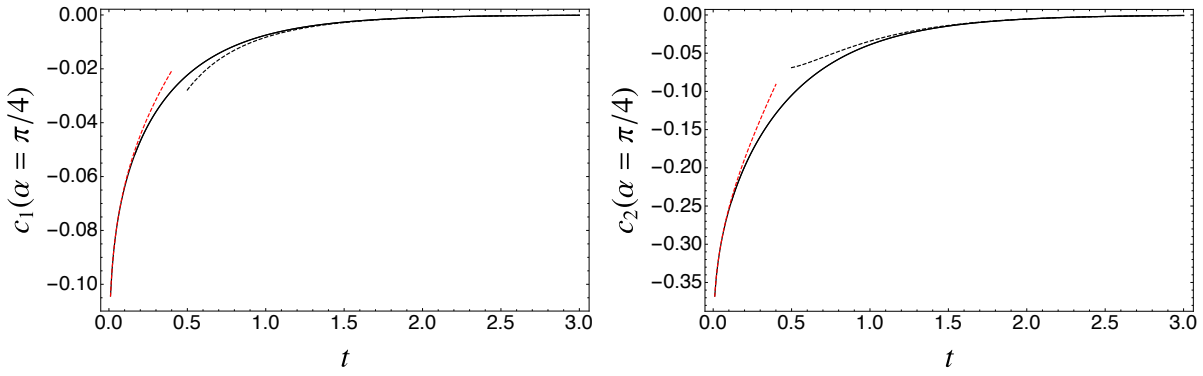

Figure 8.10: The solid lines are the functions $c_n(\alpha)$ as solutions of (8.5.7). The dashed lines are the short (red) and long (black) distance leading terms we evaluated analytically in (8.5.11) and (8.5.22), respectively.

Summing over $a = \frac{k}{n} + \frac{|\alpha|}{2\pi n}$, we get

$$\begin{aligned} c_n(\alpha) &= \frac{e^{-2t}}{2\pi n t}\left(-n^2 t - \frac{8+n^2}{12} + \frac{2|\alpha|}{\pi} - \frac{\alpha^2}{\pi^2} + 2\Big(\csc^2\frac{\pi}{n} - \frac{|\alpha|}{\pi}\Big)\cos\frac{\alpha}{n} + \frac{2\alpha}{\pi}\cot\frac{\pi}{n}\sin\frac{\alpha}{n}\right), \\ c_1(\alpha) &= -\frac{e^{-2t}}{\pi}\sin^2\frac{\alpha}{2}\left(1 + \frac{3 + \frac{4\alpha^2}{\pi^2} - \frac{8|\alpha|}{\pi}}{4t}\right). \end{aligned} \tag{8.5.22}$$

The long distance leading term in (8.5.22) is showed in Fig. 8.10 for two different values of n: it approximates well the solution of the Painlevé equation (8.5.7) in the regime $t \gg 1$. The same feature was observed in Sec. 8.4.3 for the corresponding equations in fermionic systems as also the discontinuity for $n \to 1$, which can be ascribed to the non-commutativity of the limits $n \to 1$ and $t \to \infty$. Also for a complex scalar field, Eqs. (8.5.22) show that the functions $c_n(\alpha)$ vanish for large t and the charged moments stop growing. Hence,

$$\ln Z_n(\alpha) \simeq \ln Z_n^{(0)}(\alpha) \equiv \int_{m\epsilon}^{\infty} \frac{c_n(\alpha)}{t} dt \simeq -\Big(\frac{1-n^2}{3n} + \frac{\alpha^2}{2\pi^2 n} - \frac{|\alpha|}{\pi n}\Big)\ln m\epsilon. \tag{8.5.23}$$

As expected, the dependence on $\ln(m)$ coincides with the one reported in (8.3.15), up to a factor 2 due to the number of endpoints.

Integrating $c_n(\alpha)$, we obtain up to order $O(e^{-2t}/t)$

$$\ln Z_n(\alpha) = \ln Z_n^{(0)}(\alpha) + \frac{n e^{-2t}}{4\pi t}, \qquad \ln Z_1(\alpha) = \ln Z_1^{(0)}(\alpha) + \frac{e^{-2t}}{2\pi t}\sin^2\frac{\alpha}{2}, \tag{8.5.24}$$

which are the same expressions found for fermions in Sec. 8.4.3. The expression for $\delta\mathcal{Z}_n(q)$ is the same as in (8.4.36) for fermions, while $\mathcal{Z}_1(q)$ is given by

$$\mathcal{Z}_1(q) = \frac{|\ln m\epsilon|}{\pi^2 q^2 + \ln^2 m\epsilon} + O(1/(\ln^2 m\epsilon)), \tag{8.5.25}$$

so that all contributions coming from the long-distance behaviour are negligible at order $O(1/(\ln m\epsilon))$. The resolved entropies are the ones given in (8.3.21), where S_n also takes into account the term $\frac{n e^{-2t}}{4\pi t}$. The limit $n \to 1$ can be solved through a technique similar to the one used in Sec. 8.4.3.

8.5.3 The complex harmonic chain

For the discretisation of the scalar field theory, we consider a harmonic chain made up of L sites described by the Hamiltonian (the mass of the oscillators and the spring constant have been set to one)

$$\widehat{H} = \frac{1}{2}\sum_{i=0}^{L-1} \hat{p}_i^2 + \omega_0^2 \hat{q}_i^2 + (\hat{q}_{i+1} - \hat{q}_i)^2 \tag{8.5.26}$$

where the $\hat{p}_i$ and $\hat{q}_i$ satisfy the canonical commutation relations $[\hat{q}_i, \hat{q}_j] = [\hat{p}_i, \hat{p}_j] = 0$ and $[\hat{q}_i, \hat{p}_j] = \mathrm{i}\delta_{ij}$. To have a continuous symmetry, we consider a complex bosonic theory which on the lattice is a chain of complex oscillators. It is the sum of two real harmonic chains in the variables $(\hat{q}^{(1)}, \hat{p}^{(1)})$ and $(\hat{q}^{(2)}, \hat{p}^{(2)})$, i.e.

$$\widehat{H}_{\mathbb{C}}(\hat{q}^{(1)} + \mathrm{i}\hat{q}^{(2)}, \hat{p}^{(1)} + \mathrm{i}\hat{p}^{(2)}) = \widehat{H}(\hat{q}^{(1)}, \hat{p}^{(1)}) + \widehat{H}(\hat{q}^{(2)}, \hat{p}^{(2)}). \tag{8.5.27}$$

The Hamiltonian (8.5.27) can be also written in terms of particles and antiparticles mode operators, $\hat{a}_k$ and $\hat{b}_k$, satisfying $[\hat{a}_k, \hat{a}_j^\dagger] = \delta_{j,k}$, $[\hat{b}_k, \hat{b}_j^\dagger] = \delta_{j,k}$. In terms of these operators, the Hamiltonian (8.5.27) is

$$\widehat{H}_{\mathbb{C}} = \sum_{k=0}^{L-1} \Omega_k (\hat{a}_k^\dagger \hat{a}_k + \hat{b}_k^\dagger \hat{b}_k) \tag{8.5.28}$$

where, assuming that periodic boundary conditions are imposed, $\Omega_k = \sqrt{\omega_0^2 + 4\big[\sin\big(\pi k/L\big)\big]^2}$. The conserved charge operator reads

$$\widehat{Q} = \sum_{k=0}^{L-1} (\hat{a}_k^\dagger \hat{a}_k - \hat{b}_k^\dagger \hat{b}_k), \tag{8.5.29}$$

i.e. the total number of particles *minus* the number of antiparticles. The operator $\widehat{Q}$ can be as well written in real space and its value in a given subsystem A is the same sum restricted to A, i.e.

$$\widehat{Q}_A = \sum_{j\in A} \hat{a}_j^\dagger \hat{a}_j - \hat{b}_j^\dagger \hat{b}_j. \tag{8.5.30}$$

For the charged moments (8.1.1), we need to compute $\mathrm{Tr}(\hat{\rho}_A^n e^{\mathrm{i}\widehat{Q}_A\alpha})$, but, using the form in (8.5.30) for $\widehat{Q}_A$, the trace factorises as

$$Z_n(\alpha) = \mathrm{Tr}\hat{\rho}_A^n e^{\mathrm{i}\widehat{Q}_A\alpha} = \mathrm{Tr}[(\hat{\rho}_A^a)^n e^{\mathrm{i}\widehat{N}_A^a\alpha}] \times [\mathrm{Tr}(\hat{\rho}_A^b)^n e^{-\mathrm{i}\widehat{N}_A^b\alpha}], \tag{8.5.31}$$

where $\widehat{N}_A^a = \sum_{j\in A} \hat{a}_j^\dagger \hat{a}_j$ and $\widehat{N}_A^b = \sum_{j\in A} \hat{b}_j^\dagger \hat{b}_j$. The two factors in (8.5.31) are equal, except for the sign of α. If we introduce

$$e^{F_n(\alpha)} \equiv \mathrm{Tr}[\hat{\rho}_A^n e^{\mathrm{i}\widehat{N}_A\alpha}] \qquad \Rightarrow \qquad Z_n(\alpha) = \big|e^{F_n(\alpha)}\big|^2. \tag{8.5.32}$$

We stress that $e^{F_n(\alpha)}$ is not a charged moment because in the single harmonic chain there is no $U(1)$ symmetry. Moreover, (8.5.32) ensures that the charged moments $Z_n(\alpha)$ are real quantities.

From the definition (8.5.32), we observe that $e^{F_n(\alpha)}$ can be computed focusing on a single harmonic chain. Let us consider Q_A and P_A obtained by restricting to the subsystem A the indices of $Q_{i,j} = \langle \hat{q}_i \hat{q}_j \rangle$ and $P_{i,j} = \langle \hat{p}_i \hat{p}_j \rangle$ respectively. The expressions of these two-point correlators are reported in Appendix C.1.1 (in particular, the ones for an infinite harmonic chain in its ground state are given by (C.1.5) and (C.1.6)). If the subsystem A is made by ℓ sites, the elements σ_k,

with $k = 1, \dots, \ell$, of the symplectic spectrum of $\gamma_A = Q_A \oplus P_A$ are provided by the eigenvalues of $\sqrt{Q_A P_A}$ [191].

If we introduce the vectors $|\boldsymbol{n}\rangle \equiv \bigotimes_{k=1}^{\ell} |n_k\rangle$, products of Fock states of the number operator in the subsystem A, namely $\widehat{N}_A$, the reduced density matrix of A can be written as [266, 278]

$$\hat{\rho}_A = \sum_{\boldsymbol{n}} \prod_{k=1}^{\ell} \frac{1}{\sigma_k + 1/2} \left(\frac{\sigma_k - 1/2}{\sigma_k + 1/2} \right)^{n_k} |\boldsymbol{n}\rangle\langle\boldsymbol{n}|, \tag{8.5.33}$$

where the non-negative integer n_k is the k-th element of the ℓ-dimensional vector $\boldsymbol{n}$. Since $\widehat{N}_A$ appearing in the definition (8.5.32) of $F_n(\alpha)$ is the number operator in the orthonormal basis made of the states $|\boldsymbol{n}\rangle$, we can write

$$e^{F_n(\alpha)} = \sum_{\boldsymbol{n}} \prod_{k=1}^{\ell} \left[\frac{1}{\sigma_k + 1/2} \left(\frac{\sigma_k - 1/2}{\sigma_k + 1/2} \right)^{n_k} \right]^n e^{i n_k \alpha} = \prod_{k=1}^{\ell} \frac{1}{\left(\sigma_k + \frac{1}{2}\right)^n - e^{\mathrm{i}\alpha} \left(\sigma_k - \frac{1}{2}\right)^n} \,. \tag{8.5.34}$$

This relation holds also in higher dimensions and for a generic shape of the subsystem A provided that ℓ is the number of sites in A. In the Sec. 8.5.1 we have exploited (8.5.32) and (8.5.34) to compare our field theoretical predictions for the charged moments with the numerical data.

The computation of $Z_n(\alpha)$ through (8.5.32) and (8.5.34) is the starting point for the computation of the symmetry resolved moments and entropies by a Fourier transform.

8.6 Discussion

In this chapter we characterised the symmetry resolved entanglement for free massive fields in two dimensions, presenting the results for a Dirac field and a complex scalar theory. We showed that two well known techniques in the framework of the replica trick can be adapted –by modifying the n-sheeted Riemann surface and the corresponding partition function– to the calculation of charged moments. Both computations (via modified twist fields and the Green's function approach of Ref. [10]) mainly rely on the boundary conditions of the fields at the endpoints of the entangling region. From the Fourier transform of these charged moments, we extract the symmetry resolved Rényi entropies, stressing the relevant universal aspects. At leading order, even in the massive case, the symmetry resolved entropies for both theories satisfy equipartition of entanglement [95, 97]. We also show that the entanglement equipartition is broken by the mass at order $(\ln \ell)^{-2}$, which is the same one found in other circumstances [105, 251, 412, 423].

There are two main aspects that our analysis leaves open for further study. The first one concerns the calculation of charged and symmetry resolved entropies in free scalars and fermions in arbitrary dimension. To this aim, we expect that some of the existing techniques in the literature, as e.g. in Refs. [22, 153, 175, 219, 221–223, 440–443], should be readily adapted to our problem. Furthermore, as discussed in [420], important insights could also come from the holographic correspondence for the entanglement entropy [49, 244, 444]. The other point is whether interacting QFTs can be handled in two dimensions, e.g. exploiting integrability techniques as those of Refs. [216, 224, 226, 227, 445]. This program, which has been initiated in [418, 419], deserves further investigations.

Chapter 9

Symmetry resolved entanglement entropies in gapped systems

9.1 Introduction

The universal logarithmic behaviour of the entanglement entropies given by (1.2.23) is not strictly a prerogative of the gapless models, but it also occurs for gapped models in the vicinity of a quantum phase transition in the regime in which the correlation length ξ is large but finite [9]. Indeed, using ideas from the famous proof of the c-theorem by Zamolodchikov [157], it has been shown that for a bipartition of an infinite system into two semi-infinite halves, the leading behaviour of entanglement entropies is generically [9]

$$S_n \simeq \frac{c}{12}\left(1+\frac{1}{n}\right)\log\xi. \tag{9.1.1}$$

This result can be elegantly recovered for integrable lattice models through the Baxter corner transfer matrix (CTM) [259], as reported (and generalised) in many references [9, 388, 436, 437, 446–453]. We will discuss explicitly this technique in the following sections. The CTM approach provided exact results not only close to the critical point, but gave generalisations also to the regime in which the correlation length is small. When the subsystem A is a finite interval of length ℓ, as long as $\ell \gg \xi$, the Rényi entropies are just twice the value in (9.1.1) as a consequence of cluster decomposition in the ground-state of these theories. However, as ℓ becomes of the order of ξ, a complicated crossover takes place that is not captured by CTM and requires more complicated techniques, see e.g. Refs. [216, 224, 227, 454].

The goal of this chapter is to study how the total entanglement splits into the contributions coming from disjoint symmetry sectors in gapped integrable models, using CTM techniques. We carry out this analysis for two non-critical quantum lattice models with a $U(1)$ symmetry, namely the double or complex harmonic chain (which is a free model) and the XXZ chain (which is genuinely interacting). To this aim, we first calculate the charged moments of the reduced density matrix (RDM) (8.1.1), and then obtain the contributions of the sectors by Fourier transform.

The chapter is organised as follows. In Sec. 8.2 we briefly give an overview of how the RDM of an off-critical quantum chain is related to Baxter's CTM. For integrable models whose weights satisfy a Yang-Baxter relation, the eigenvalues of the RDM can be determined exactly. In sections 9.3 and 9.4 we exploit these exact results for the computation of the symmetry resolved entanglement entropies, for the complex harmonic chain and XXZ spin-chain respectively. We also benchmark the analytic results in Sec. 9.3 against exact numerical computations. In Sec. 9.5 we find analytic

results for the full counting statistics in gapped XXZ chains, highlighting its relation with the symmetry resolved entanglement. We conclude in Sec. 9.6 with some remarks and discussions.

9.2 The corner transfer matrix and the entanglement entropy

In dealing with the geometric bipartition considered in this chapter (i.e. two semi-infinite half lines) the corner transfer matrix provides an exact form for the reduced density matrix [262] and hence it is a formidable tool for the derivation of the charged moments and symmetry resolved entropies. In order to understand how the CTM works, we give a brief review of the construction of the RDM.

Generally, a direct computation of the density matrix of a system is tough. A trick to address this problem is to use the fact that the density matrix of the quantum chain is the partition function of a two-dimensional classical system on a strip [260, 455, 456]. The latter can be solved by means of the transfer matrix T and we can identify the eigenstate $|\Psi\rangle$ of T corresponding to its maximal eigenvalue. Given the Hamiltonian of the quantum chain $\widehat{H}$ and its lattice spacing a, the transfer matrix is $T = e^{-a\widehat{H}}$ up to a prefactor; hence $|\Psi\rangle$ is the ground state of $\widehat{H}$. One then obtains the reduced density matrix of a subsystem A of the chain by tracing over all the coordinates belonging to the complement of A. Therefore $\hat{\rho}_A$ is the partition function of two half-infinite strips, one extending from $-\infty$ to 0 and the other from 0 to $+\infty$.

The CTM plays a crucial role: it connects a horizontal row to a vertical one. Choosing the lattice in a clever way [259], when the model is isotropic, the four possible corner transfer matrices [259] are all equivalent and the partition function is just $\mathrm{Tr}\hat{A}^4$, with $\hat{A}$ the CTM. Going back to our quantum problem, the reduced density matrix is [262]

$$\hat{\rho}_A = \frac{\hat{A}^4}{\mathrm{Tr}\hat{A}^4}. \tag{9.2.1}$$

We will deal with integrable massive models satisfying the Yang-Baxter equations; in this case, it is possible to show that (9.2.1) has an exponential form given by [260, 262]

$$\hat{\rho}_A = \frac{e^{-\widehat{H}_{\mathrm{CTM}}}}{\mathrm{Tr}e^{-\widehat{H}_{\mathrm{CTM}}}}. \tag{9.2.2}$$

In the cases we are interested in the entanglement Hamiltonian $\widehat{H}_{\mathrm{CTM}}$ can be diagonalised as [262]

$$\widehat{H}_{\mathrm{CTM}} = \sum_{j=0}^{\infty} \epsilon_j \hat{n}_j, \tag{9.2.3}$$

where $\hat{n}_j$ are number operators and ϵ_j are the single-particle levels of the entanglement Hamiltonian. The result (9.2.3) provides exact eigenvalues and degeneracies of the RDM (i.e. the entanglement spectrum of the system [26, 370]), from which one calculates straightforwardly the entanglement entropies [9].

However, (9.2.3) contains no information about the distributions of the eigenvalues ϵ_j into the various symmetry sectors (indeed, it has exactly the same form for models with discrete and continuous symmetries). In order to use it to compute the symmetry resolved entropies in gapped integrable models, we should complement (9.2.3) with some other input providing the symmetry resolution, but this should be done on a case by case basis. The rest of the chapter is devoted exactly to solve this problem for two specific 1D integrable lattice models: the complex harmonic chain and the non-critical XXZ chain in which we will exploit the results of Refs. [194,383] and [263, 457] respectively.

9.3 The complex harmonic chain

In this section we use the CTM to derive the symmetry resolved entanglement entropies for a double or complex harmonic chain that is $U(1)$ symmetric and whose continuum limit is the non-compact massive *complex* boson discussed in chapter 8. We will find an analytic expression for the charged moments as functions of α and we will discuss its limit close to the conformal invariant critical point, when the correlation length ξ is finite but large. Then we will use this result to compute the symmetry resolved entropies. All the analytical results will be compared against exact numerical computations based on correlation matrix techniques discussed in Sec. 8.5.3. (see also [4, 191, 458] and Appendix A.1).

9.3.1 Reduced density matrix of the half complex harmonic chain

The Hamiltonian describing an infinite complex harmonic chain is provided by (8.5.27), where the two real Hamiltonians in the right hand side are given by (5.2.1). Let us call $\omega_0 = 1 - \kappa$ the frequency parameter of the two real harmonic chains that, in the continuum limit, provides the mass of the complex scalar field. Furthermore, we set $m = 1$ in the two real chains. The conserved charge restricted to the subsystem A, which in our case is half of the chain, is given by (8.5.30).

The reduced density matrix, $\hat{\rho}_A^{(\mathrm{r})}$, for half of the real harmonic chain made by L sites was explicitly constructed by Peschel and Chung in [194] in the large L limit. The trick is to relate $\hat{\rho}_A^{(\mathrm{r})}$ to the partition function of a two-dimensional massive Gaussian model in the geometry of an infinite strip of width L with a cut perpendicular to it [383]. Due to the integrability of the Gaussian model, in the case where L is much larger than the correlation length, the $\widehat{H}_{\mathrm{CTM}}$ for the harmonic chain may be written in a diagonal form as in (9.2.3), where now we explicitly have

$$\widehat{H}_{\mathrm{CTM}} = \sum_{j=0}^{\infty} (2j+1)\epsilon\, \hat{\beta}_j^\dagger \hat{\beta}_j, \qquad \epsilon = \frac{\pi I(\sqrt{1-\kappa^2})}{I(\kappa)}. \tag{9.3.1}$$

Here $I(\kappa)$ is the complete elliptic integral of the first kind, i.e.

$$I(\kappa) = \int_0^{\pi/2} \frac{d\theta}{\sqrt{1-\kappa^2 \sin^2\theta}}, \tag{9.3.2}$$

and $\hat{\beta}_j, \hat{\beta}_j^\dagger$ are bosonic annihilation and creation operators (satisfying $[\hat{\beta}_i, \hat{\beta}_j^\dagger] = \delta_{i,j}$).

One can find, consistently with the discussion in Sec. 8.5.3, that if A is half of the complex harmonic chain, the charged moments defined in (8.1.1) factorises as follows

$$Z_n(\alpha) = \mathrm{Tr}\hat{\rho}_A^n e^{\mathrm{i}\widehat{Q}_A\alpha} = \mathrm{Tr}[(\hat{\rho}_A^\alpha)^n e^{\mathrm{i}\widehat{N}_A^\alpha \alpha}] \times [\mathrm{Tr}(\hat{\rho}_A^\gamma)^n e^{-\mathrm{i}\widehat{N}_A^\gamma \alpha}]. \tag{9.3.3}$$

where $\widehat{N}_A^\alpha = \sum_{j\in A} \hat{\alpha}_j^\dagger \hat{\alpha}_j$ and $\widehat{N}_A^\gamma = \sum_{j\in A} \hat{\gamma}_j^\dagger \hat{\gamma}_j$ and $\hat{\rho}_A^\alpha$ and $\hat{\rho}_A^\gamma$ can be written in terms of the entanglement Hamiltonian (9.3.1) with $\hat{\beta}_j$ replaced by $\hat{\alpha}_j$ and $\hat{\gamma}_j$ respectively. Let us stress that $\hat{\alpha}_j, \hat{\alpha}_j^\dagger$ and $\hat{\gamma}_j, \hat{\gamma}_j^\dagger$ are two pairs of bosonic annihilation and creation operators

Thus, the strategy is to compute $F_n(\alpha) = \mathrm{Tr}[\hat{\rho}_A^n e^{\mathrm{i}\widehat{N}_A\alpha}]$ exploiting (9.3.1) and then obtain $Z_n(\alpha)$ from (8.5.32).

9.3.2 Charged moments from CTM

In the above subsection, $\widehat{N}_A$ and $\hat{\rho}_A$ for the single chain have been already written in the same basis and the derivation of $F_n(\alpha)$ amounts to compute the trace

$$e^{F_n(\alpha)} = \frac{\mathrm{Tr} e^{-\sum_{j=0}^{\infty}(\epsilon_j n - \mathrm{i}\alpha)\hat{n}_j}}{\left(\mathrm{Tr} e^{-\sum_{j=0}^{\infty}\epsilon_j \hat{n}_j}\right)^n} = \frac{\prod_{j=0}^{\infty}\sum_{k=0}^{\infty} e^{-((2j+1)\epsilon n - \mathrm{i}\alpha)k}}{\left(\prod_{j=0}^{\infty}\sum_{k=0}^{\infty} e^{-(2j+1)\epsilon\, k}\right)^n} = \frac{\prod_{j=0}^{\infty}(1-e^{-(2j+1)\,\epsilon})^n}{\prod_{j=0}^{\infty}(1-e^{-(2j+1)\,\epsilon n + \mathrm{i}\alpha})}, \tag{9.3.4}$$

whose logarithm is given by

$$F_n(\alpha) = \sum_{j=0}^{\infty} n \log[1-e^{-(2j+1)\epsilon}] - \sum_{j=0}^{\infty}\log[1-e^{-(2j+1)\epsilon n + \mathrm{i}\alpha}]. \tag{9.3.5}$$

This formula is exact and can be easily computed numerically, since it converges very quickly. It is plotted in Figure 9.1 as a function of α for various values of ω_0 and n, but we will discuss its properties later.

Using (8.5.32), the charged moments for the complex harmonic chain are

$$Z_n(\alpha) = \frac{\prod_{j=0}^{\infty}(1-e^{-(2j+1)\epsilon})^{2n}}{\prod_{j=0}^{\infty}(1-e^{-(2j+1)\epsilon n + \mathrm{i}\alpha})\prod_{j=0}^{\infty}(1-e^{-(2j+1)\epsilon n - \mathrm{i}\alpha})} = Z_n \frac{\theta_4(0|e^{-\epsilon n})}{\theta_4(\frac{\alpha}{2}|e^{-\epsilon n})}, \tag{9.3.6}$$

where in the last equality we use that

$$Z_n \equiv Z_n(\alpha=0) = \prod_{j=0}^{\infty}\frac{(1-e^{-(2j+1)\epsilon})^{2n}}{(1-e^{-(2j+1)\epsilon n})^2}, \qquad \theta_4(z|u) = \sum_{k=-\infty}^{\infty}(-1)^k\, u^{k^2}\, e^{2\mathrm{i}kz}\,. \tag{9.3.7}$$

Notice that the entire α dependence is encoded in the denominator of (9.3.6) and that $Z_1 = 1$, but $Z_1(\alpha) \neq 1$. Also the total Rényi entropies of the complex harmonic chains are

$$S_n = \frac{1}{1-n}\log Z_n = \frac{2}{1-n}\sum_{j=0}^{\infty}[n\log(1-e^{-(2j+1)\epsilon}) - \log(1-e^{-(2j+1)\epsilon n})], \tag{9.3.8}$$

i.e. the double of a real harmonic chain.

Poisson resummation and critical regime

A drawback of the form (9.3.5) is that it does not directly allow a direct expansion in the critical regime, i. e. for small ϵ. Moreover, we cannot perform an Euler Mac-Laurin summation (as for $\alpha = 0$, see [9]) since the function $f(x) = \log(1-e^{-2x})$ diverges for $x \to 0$. However, following Ref. [436], we can obtain the asymptotic expansion for small ϵ by using the (generalised) Poisson resummation formula:

$$\sum_{j=-\infty}^{\infty} f(|\epsilon(bj+a)|) = \frac{2}{\epsilon b}\sum_{k=-\infty}^{\infty}\hat{f}\left(\frac{2\pi k}{\epsilon b}\right)e^{2\pi\mathrm{i}ka/b}, \tag{9.3.9}$$

where

$$\hat{f}(y) = \int_0^\infty f(x)\cos(yx)dx. \tag{9.3.10}$$

In order to use this resummation formula for (9.3.5), we must choose $a = 1/2$, $b = 1$ and

$$f_{n,\alpha}(x) = -\log(1 - e^{-2nx+\mathrm{i}\alpha})\,. \tag{9.3.11}$$

The final result reads

$$\begin{aligned} F_n(\alpha) =& \frac{\mathrm{Li}_2(e^{\mathrm{i}\alpha})}{2\epsilon n} - \frac{n\pi^2}{12\epsilon} + \sum_{k=1}^{\infty}\left[(-1)^k\frac{n\epsilon}{2\pi^2k^2} + (-1)^{k+1}\frac{n}{2k}\coth\frac{\pi^2 k}{\epsilon}\right] + \\ & \frac{\mathrm{i}e^{\mathrm{i}\alpha}}{2\pi}\sum_{k=1}^{\infty}\frac{(-1)^k}{k}\left[\Phi(e^{\mathrm{i}\alpha},1,1-\frac{\mathrm{i}\pi k}{\epsilon n}) - \Phi(e^{\mathrm{i}\alpha},1,1+\frac{\mathrm{i}\pi k}{\epsilon n})\right]. \end{aligned} \tag{9.3.12}$$

where we have isolated the contribution from the term $k = 0$ of the sum in (9.3.9) which gives the leading divergence in the limit $\epsilon \to 0$. Here we have introduced the polylogarithm of order two Li_2 and the Lerch transcendent function Φ

$$\mathrm{Li}_2(z) = \sum_{m=1}^{\infty}\frac{z^m}{m^2}, \qquad \Phi(z,s,a) = \sum_{j=0}^{\infty}\frac{z^j}{(j+a)^s}\,. \tag{9.3.13}$$

We are now interested in the critical region of the parameter space in which the correlation length ξ (inverse gap) is large but finite. In the critical regime $\xi \gg 1$ (or equivalently $\epsilon \ll 1$), the correlation length of the model behaves like

$$\log\xi \simeq \frac{\pi^2}{\epsilon} + \mathcal{O}(\epsilon^0). \tag{9.3.14}$$

Using the results of Ref. [459] for computing the limit $\epsilon \to 0$ of the last sum over k in (9.3.12) we find that the only non-vanishing terms in the asymptotic expansion close to $\epsilon = 0$ are

$$F_n(\alpha) = \frac{\mathrm{Li}_2(e^{\mathrm{i}\alpha})}{2\epsilon n} - \frac{n\pi^2}{12\epsilon} + \frac{n}{2}\log 2 + \mathcal{O}(\epsilon), \tag{9.3.15}$$

whose real part is

$$\mathrm{Re}[F_n(\alpha)] = \left[\frac{1}{2n}\left(\frac{\alpha}{2\pi}\right)^2 - \frac{|\alpha|}{4\pi n} + \frac{1}{12n} - \frac{n}{12}\right]\log\xi + \frac{n}{2}\log 2 + \mathcal{O}(\epsilon), \tag{9.3.16}$$

because

$$\frac{\mathrm{Re}[\mathrm{Li}_2(e^{\mathrm{i}\alpha})]}{n} = \frac{1}{n}\left(\frac{\alpha}{2}\right)^2 - \frac{\pi|\alpha|}{2n} + \frac{\pi^2}{6n}. \tag{9.3.17}$$

The charged moments for the complex harmonic chain are now given by (8.5.32), i.e. $\log Z_n(\alpha) = F_n(\alpha) + F_n(-\alpha)$ and, in the limit $\epsilon \to 0$,

$$\log Z_n(\alpha) = \left[\frac{1}{n}\left(\frac{\alpha}{2\pi}\right)^2 - \frac{|\alpha|}{2\pi n} + \frac{1}{6n} - \frac{n}{6}\right]\log\xi + n\log 2 + \mathcal{O}(\epsilon). \tag{9.3.18}$$

Notice that while $F_n(\alpha)$ is generically complex, $\log Z_n(\alpha)$ for the complex chain is real and even in α.

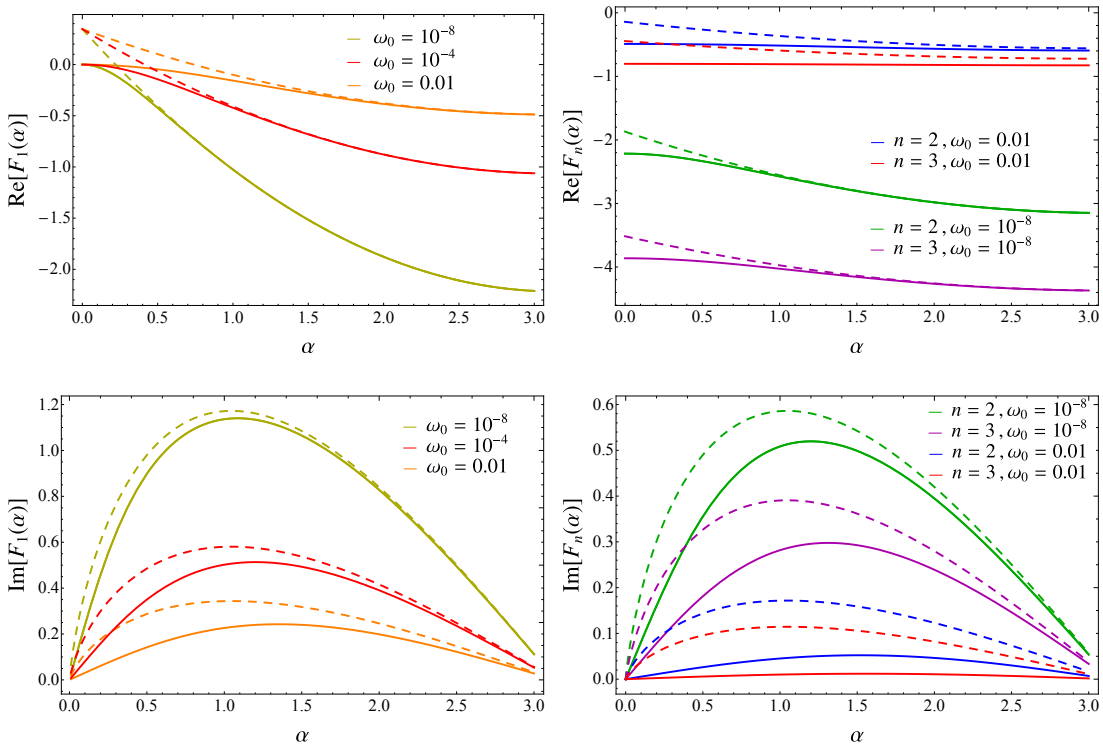

Figure 9.1: Charged moments for the harmonic chain: we report the real (top) and the imaginary (bottom) part of $F_n(\alpha)$, Eq. (9.3.5), as function of α for different values of ω_0. Everywhere, the dashed lines are the asymptotic expansions for $\epsilon \to 0$ and $\alpha \neq 0$ up to $\mathcal{O}(\epsilon)$, cf. Eq. (9.3.15). As discussed in the text, the convergence to the critical result is not uniform and it is slower for smaller $\alpha \neq 0$. The function $\log Z_n(\alpha)$ for the complex chain is twice the real part of $F_n(\alpha)$.

Discussions

We concluded our exact computation of the charged moments and we are now ready to critically discuss our findings. The expression (9.3.18) tells us that the leading term in the "charged entropies" diverges logarithmically with ξ and matches the result found in (8.3.15) replacing ξ with the inverse of the mass of the continuum theory.

Another interesting fact is that the limit $\alpha \to 0$ and the expansion for ϵ around 0 do not commute, as a difference with other known cases (we believe that the origin of the non-commutativity is the non compact nature of the continuum limit). Indeed, if we consider first the limit $\alpha \to 0$ in (9.3.12), the last sum gives

$$\sum_{k=1}^{\infty} (-1)^k \left[-\frac{\epsilon n}{2k^2\pi^2} + \frac{1}{2k} \coth\left(\frac{k\pi^2}{\epsilon n}\right) \right], \tag{9.3.19}$$

leading to the known formula of the Rényi entropies of a real harmonic chain, that in the critical regime $\epsilon \to 0$ is [9, 436] (see (9.3.8))

$$S_n = \frac{\pi^2}{12\epsilon} \frac{1+n}{n} - \frac{\log 2}{2} + \mathcal{O}(\epsilon). \tag{9.3.20}$$

On the other hand, if we invert the order of these two operations, we obtain the divergent term

$$\frac{\mathrm{i}e^{\mathrm{i}\alpha}}{2\pi}\sum_{k=1}^{\infty}\frac{(-1)^k}{k}\left[\Phi(e^{\mathrm{i}\alpha},1,1-\frac{\mathrm{i}\pi k}{\epsilon n})-\Phi(e^{\mathrm{i}\alpha},1,1+\frac{\mathrm{i}\pi k}{\epsilon n})\right]\to\frac{n\epsilon}{12}\frac{e^{\mathrm{i}\alpha}}{1-e^{\mathrm{i}\alpha}}. \tag{9.3.21}$$

Considering now the charged moments of the complex chain, $\ln Z_n(\alpha)=2\mathrm{Re}F_n(\alpha)$, the divergent term (9.3.21) cancels, but the finite part is not the total moment $\ln Z_n$ in (9.3.7). This fact implies that the approach of $\ln Z_n(\alpha)$ to the critical limit $\epsilon\to 0$ is non-uniform in α: exactly at $\alpha=0$ the charged entropy approaches (9.3.8), but for any non-zero α the limit is (9.3.15) that as a consequence is reached for smaller and smaller ϵ (i.e. ω_0) as α gets closer to 0. This feature was already observed in Sec. 8.5, where it was shown that the lattice results approach the field theoretical ones in a non uniform way in α.

All these aspects are evident in Figure 9.1 where we show (for $\alpha\geq 0$ since $F_n(-\alpha)=F_n^*(\alpha)$) the exact result (9.3.12) (or equivalently (9.3.5)) together with its critical limit (9.3.15). As we discussed above, the former converges to the latter as ω_0, therefore ϵ, decreases, but in a non-uniform way. Indeed, while for large α (i.e. close to π) the two curves are very close also when ω_0 is not so small, for smaller and non-zero values of α, we need much smaller ω_0 to approach the critical limit. For $\alpha=0$ the limit is different. It is also clear that for higher values of n, the convergence is slower and starts at smaller values of ω_0. The last observation is a well known fact for $\alpha=0$, cf. Ref. [436], and it is not surprising that the effect is amplified in the presence of a flux.

9.3.3 Symmetry resolved moments and entropies via Fourier trasform

The symmetry resolved moments $\mathcal{Z}_n(q)$ are obtained as Fourier transform of $Z_n(\alpha)$ in (9.3.6), i.e.

$$\mathcal{Z}_n(q)=\int_{-\pi}^{\pi}\frac{d\alpha}{2\pi}e^{-\mathrm{i}q\alpha}Z_n(\alpha)=Z_n\theta_4(0|e^{-\epsilon n})\int_{-\pi}^{\pi}\frac{d\alpha}{2\pi}e^{-\mathrm{i}q\alpha}\frac{1}{\theta_4(\frac{\alpha}{2}|e^{-\epsilon n})}. \tag{9.3.22}$$

The integral in the right hand side of the above equation can be found in Ref. [460] (exercise 14 at page 489), obtaining

$$\frac{\mathcal{Z}_n(q)}{Z_n}=\prod_{k=1}^{\infty}\left(\frac{1-e^{-n\epsilon(2k-1)}}{1-e^{-2n\epsilon k}}\right)^2 e^{-n\epsilon|q|}\sum_{k=0}^{\infty}(-1)^k e^{-n\epsilon k^2}e^{-n\epsilon(2|q|+1)k}\,, \tag{9.3.23}$$

which is our final result for the symmetry resolved moments. It is likely that the sum in (9.3.23) can be rewritten in terms of some special functions, but we did not find any particularly useful expression. We define the sum as

$$\Phi_q(u)=u^{|q|}\sum_{k=0}^{\infty}(-1)^k u^{k^2}u^{(2|q|+1)k}. \tag{9.3.24}$$

and in terms of this function we have

$$\mathcal{Z}_n(q)=\prod_{k=1}^{\infty}\left(\frac{(1-e^{-\epsilon(2k-1)})^n}{1-e^{-2n\epsilon k}}\right)^2\Phi_q(e^{-n\epsilon}), \tag{9.3.25}$$

where we used the explicit form of Z_n in (9.3.7).

The symmetry resolved Rényi entropies are now easily deduced from (8.1.4), obtaining

$$S_n(q) = \frac{2}{1-n}\sum_{k=1}^{\infty}\Big[n\log(1-e^{-2\epsilon k}) - \log(1-e^{-2n\epsilon k})\Big] + \frac{1}{1-n}\log\frac{\Phi_q(e^{-n\epsilon})}{(\Phi_q(e^{-\epsilon}))^n}. \tag{9.3.26}$$

Taking the limit $n \to 1$, we get the von Neumann entropy

$$S_1(q) = -2\sum_{j=1}^{\infty}\left[\log(1-e^{-2\epsilon j}) - \frac{2\epsilon j e^{-2\epsilon j}}{1-e^{-2\epsilon j}}\right] + \log\Phi_q(e^{-n\epsilon}) + \epsilon e^{-\epsilon}\frac{\Phi_q'(e^{-n\epsilon})}{\Phi_q(e^{-n\epsilon})}. \tag{9.3.27}$$

As a non-trivial consistency check of our results, we have computed the total von Neumann entanglement entropy starting from the symmetry resolved ones in (9.3.27) and using (1.2.28) and we have recovered the limit $n \to 1$ of (9.3.8).

The critical limit $\epsilon \to 0$ is easily understood if one focuses on the variation in q of moments and entropies, rather than on their absolute values. Indeed from (9.3.25), it is easy to see that

$$\frac{\mathcal{Z}_n(q)}{\mathcal{Z}_n(q=0)} = \frac{\Phi_q(e^{-n\epsilon})}{\Phi_0(e^{-n\epsilon})} \xrightarrow{\epsilon\to 0} e^{-n^2q^2\epsilon^2/2}\,, \tag{9.3.28}$$

where the last limit is performed by expanding to the second order in ϵ each term in the sum (9.3.24), making carefully the sum in terms of ζ functions, and finally re-exponentiating the result. We stress that this critical limit is *not* the Fourier transform of the critical limit for $Z_n(\alpha)$ in (9.3.18) because the two limiting procedures do not commute. This explains why the expression (9.3.28) is different from (8.5.18) obtained directly in a field theoretical setup. The critical behaviour of the resolved entropies is then easily worked out as

$$S_n(q) = \frac{1}{1-n}\log\frac{\mathcal{Z}_n(q)}{\mathcal{Z}_1^n(q)} = S_n(q=0) + \frac{n\epsilon^2q^2}{2} + O(\epsilon^3), \tag{9.3.29}$$

which is valid also for $n = 1$ without any particular limit. Also in the critical limit, it is worth to mention the behaviour

$$S_n(q=0) = S_n - \log\frac{8\pi}{\epsilon} + \frac{\log n}{1-n} + o(1)\,, \tag{9.3.30}$$

which signals the presence of a subleading term proportional to $\log\epsilon \sim \log(\log\xi)$. Such a term has not a unique interpretation and origin for the (complex) harmonic chain. Indeed, we know that the total entropy of a massive free non-compact boson has such subleading terms in $\log(\log\xi)$ [218] in the small mass limit, but even that double logarithmic terms appear generically in the symmetry resolution (see (8.5.19) for the massive complex scalar field theory and [96, 251] for the critical compact boson).

Let us now critically discuss our results. First of all, there is a very important difference compared to the conformal gapless case [96], i.e. the absence of equipartition of entanglement [97]: the Rényi entropies (9.3.26) depend explicitly on q. This dependence is explicitly reported in Figure 9.2 (a) where, in order to show its variation, we plot it as a continuous function of q, although only integer values are physical. The lack of exact equipartition is not surprising; also in critical models the leading terms for large ℓ show equipartition [97], while some subleading terms depend explicitly on q [96, 251]. In panel (b) of Figure 9.2 we focus on the critical limit of Rényi entropies (9.3.29) plotting $S_n(q) - S_n(q=0)$. As $\epsilon \to 0$, the result approaches the critical form (9.3.29), but clearly the convergence is not uniform: it is faster for smaller q and n. Indeed, since this dependence is all encoded in the function $\Phi_q(e^{-n\epsilon})$, the parameter that must be small is not ϵ, but $n\epsilon$. On the other hand, the higher order terms in ϵ, that have been neglected in (9.3.29), become important for large q.

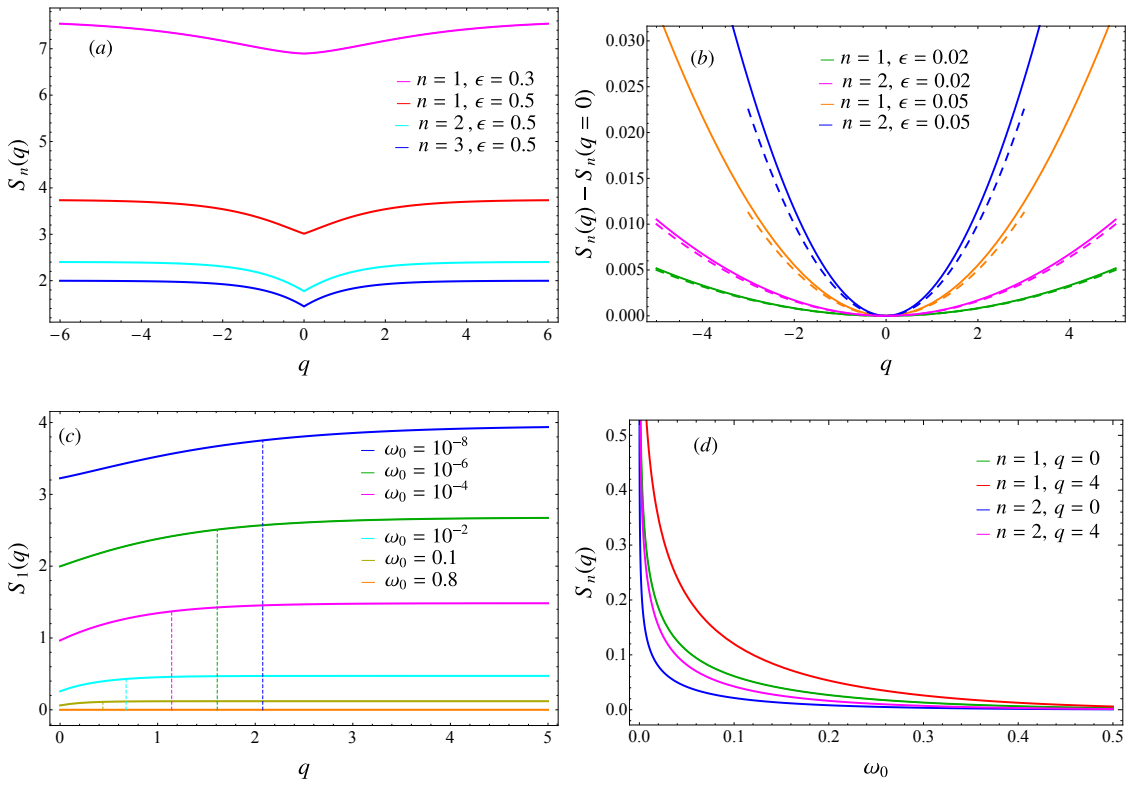

Figure 9.2: Symmetry resolved entanglement entropies for the complex harmonic chain. Panel (a) shows $S_n(q)$ as functions of q for different values of ϵ and n. Panel (b) reports $S_n(q) - S_n(q = 0)$ for small values of ϵ, showing the validity of the expansion in the critical regime (9.3.29). The critical limits in (9.3.29) are also reported as dashed lines showing its accuracy for small $n\epsilon$. The panel (c) shows the effective equipartition of entanglement for $q \gtrsim 1/\epsilon$ (these crossover values are reported as dashed vertical lines). The panel (d) shows $S_n(q)$ as function of ω_0 for different values of q and n.

Another interesting feature of the symmetry resolved entropies for this complex harmonic chain is an *effective equipartition* in two limits. The first one is the limit of large q. Indeed, in (9.3.26) the entire q-dependence is encoded in the function $\Phi_q(e^{-n\epsilon})$. Looking at (9.3.24), it should be clear that all the terms with $qn\epsilon \gg 1$ are exponentially suppressed. Practically, the total sum is more or less the same for all q such that $n\epsilon q \gtrsim 1$ (from (9.3.14) this is equivalent to $nq\pi^2 \gtrsim \log \xi$ in the critical region). Hence, there is an *effective equipartition* among all $q \gtrsim 1/(n\epsilon)$. Actually, since the only physical values of q are the integers, this fact implies that there is an almost exact equipartition (with the exception of $S_n(0)$) of the entropy if $n\epsilon \gtrsim 1$, which corresponds to $\omega_0 \gtrsim 10^{-4}$ (for $n = 1$). In panel (c) we report the von Neumann entropies $S_1(q)$ for several values of ω_0, showing that, as q becomes large enough, the entropies $S_n(q)$ do not depend on q anymore. We also explicitly report the (approximate) crossover values for $q \sim 1/\epsilon$ (as function of ω_0 is given by (9.3.1)), showing that it correctly captures the change of behaviour. Finally, we have effective equipartition also in the critical regime, but in this case also for small q. In fact, (9.3.29) shows that the q-dependent term is proportional to ϵ^2, while the leading term of $S_n(q)$ (say for $q = 0$) diverges as ϵ^{-1}. Thus the q-dependence is suppressed as ϵ^3 and there is an effective equipartition. Even if for large q, the expansion (9.3.29) breaks down, we do not expect that $S_n(q) - S_n(0)$ becomes of the order $S_n(0)$ and so there is an effective equipartition for all q: the numerical analysis of (9.3.26) seems to

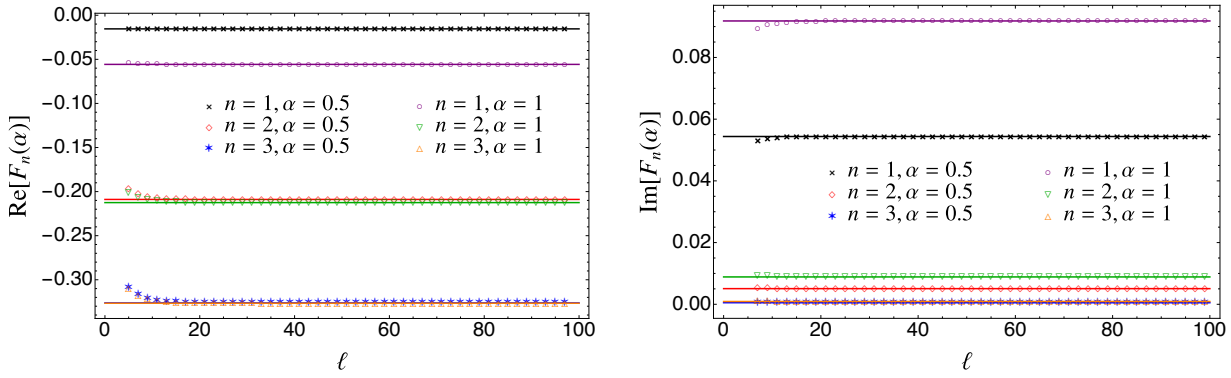

Figure 9.3: Numerical results for the charged moments for an interval of length ℓ embedded in the infinite harmonic chain. We report the real (left) and the imaginary (right) parts of $F_n(\alpha)$ as a function of the subsystem length ℓ, for different values of $n = 1, 2, 3$ and fixed $\omega_0 = 0.1$. The numerical data for an interval of length ℓ (divided by 2) are compared to the analytic CTM prediction (9.3.5): as ℓ is moderately large, the agreement is perfect. The charged moments are just $\log Z_n(\alpha) = 2\mathrm{Re}[F_n(\alpha)]$.

confirm this expectation. The effective equipartition in the critical limit is in agreement with the results for the massive complex scalar field theory in Sec. 8.5.1 (although, as discussed just below (9.3.28), the critical limit considered there is different from the one here). The functional form of the leading q-dependent term in (9.3.29) is reminiscent of the one found for free fermions [251].

9.3.4 Numerical checks

In this subsection we test the validity of the results in the previous ones against exact numerical computations.

The numerical data for $F_n(\alpha)$, obtained from (8.5.34) for an interval of length ℓ, should converge to the double (because of the two end-points) of the CTM prediction for the semi-infinite line (with one-endpoint) as soon as ℓ becomes larger than the correlation length ξ. In Figure 9.3 we report the numerical data for (half of) the real and the imaginary parts of $F_n(\alpha)$ for different values of n and α. We have set $\omega_0 = 0.1$, so that after a short crossover in ℓ, the data saturate. The CTM prediction (9.3.5) is also reported for comparison, showing that the analytical result perfectly describes the saturation values. The charged moments for the complex harmonic chain are just $\log Z_n(\alpha) = 2\mathrm{Re}[F_n(\alpha)]$ both for numerics and analytics and so Figure 9.3 is a direct test also for them.

We now take the Fourier transform of the numerical data for $Z_n(\alpha)$ to test the validity and the accuracy of the CTM predictions for the symmetry resolved moments and entropies. In Figure 9.4 we report the (square roots of the) numerically calculated symmetry resolved partition sums $\mathcal{Z}_n(q)$. We compare the data for $n = 1, 2, 3$ with the CTM prediction (9.3.23). The latter perfectly captures the q-dependence, as shown in the panel (a), and gives the value at which the data saturate when studied as functions of ℓ, panel (b). Finally, in Figure 9.5 we report the symmetry resolved entropies for several values of q, n, ω_0. For large ℓ, the numerical data converge to (twice) the CTM predictions in Eqs. (9.3.26) and (9.3.27). Notice that for the larger values of ω_0 the saturation values do not depend on q because of the effective equipartition, but for smaller ω_0 they clearly do. As ω_0 becomes much smaller (such that $\epsilon \sim 0.1$), we expect again effective equipartition, although we do not report such data here because they require very large ℓ.

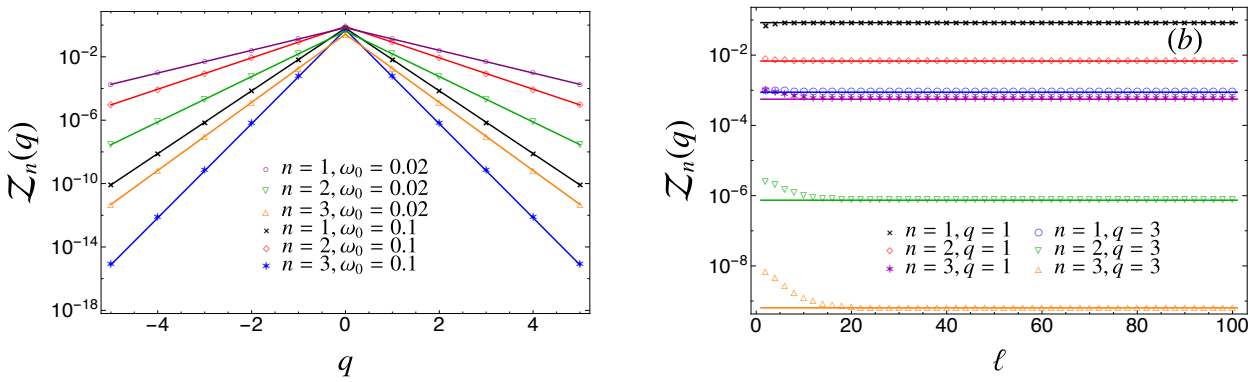

Figure 9.4: Numerical results for the symmetry resolved moments for the complex harmonic chain. (a): (Square root of the) symmetry resolved partition sums $\mathcal{Z}_n(q)$ as function of q. The numerical data for $n = 1, 2, 3$ are compared with the CTM prediction (9.3.23) for two values of ω_0. (b): The same quantity is plotted against the subsystem size ℓ for different values of $q = 20, 40$ and fixed $\omega_0 = 0.1$, showing the convergence towards the CTM prediction (9.3.23) for $n = 1, 2, 3$.

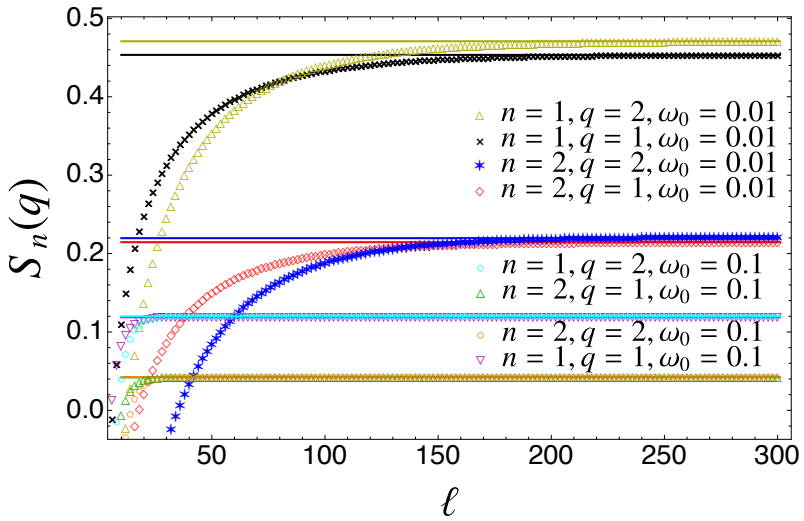

Figure 9.5: Numerical results for the symmetry resolved entropies for the complex harmonic chain. The numerical data for $q = 1, 2$, $n = 1, 2$ and $\omega_0 = 0.1$ and 0.01 are compared with the CTM predictions (9.3.26) and (9.3.27), to which they clearly approach. Notice that the convergence is slower for smaller ω_0. For $\omega_0 = 0.1$ we have an approximate equipartition, but this is not the case for $\omega_0 = 0.01$.

9.4 Gapped XXZ spin-chain

In this section we study the symmetry resolved entanglement in the anisotropic Heisenberg model in the gapped antiferromagnetic regime using the CTM approach. The resolved moments are computed starting from the explicit expressions for the eigenvalues of the RDM and their degeneracies. Then the symmetry resolved entropies are deduced and their critical regime is investigated. The discrete Fourier transform of the resolved moments allows to compute the charged moments and to discuss their behaviour in the critical regime.

9.4.1 Symmetry resolved moments and entropies

The Hamiltonian of the anisotropic Heisenberg model (also known as XXZ chain) is

$$\widehat{H}_{\rm XXZ} = \sum_j \left[\hat{\sigma}^x_j \hat{\sigma}^x_{j+1} + \hat{\sigma}^y_j \hat{\sigma}^y_{j+1} + \Delta \hat{\sigma}^z_j \hat{\sigma}^z_{j+1}\right], \tag{9.4.1}$$

where $\hat{\sigma}^i$, $i = x, y, z$ are the Pauli matrices. The model has a conformal quantum critical point for $\Delta = 1$, it is gapless when $|\Delta| \leq 1$ and gapped when $|\Delta| > 1$. We consider this model in the antiferromagnetic gapped regime with $\Delta > 1$.

The XXZ chain is solvable by Bethe Ansatz techniques; unfortunately this framework is not very effective to study the entanglement properties both in the coordinate [231] and in the algebraic [202, 461–468] approach. On the other hand, the CTM solution for the XXZ chain is a powerful tool to compute the entanglement entropies; in this approach, the reduced density matrix is related to the partition function of the six-vertex model on a strip with a cut. In Ref. [262] $\widehat{H}_{\rm CTM}$ has been found to be of the form (9.2.3) with

$$\epsilon_j = 2\epsilon j, \qquad \epsilon = {\rm arccosh}\Delta, \tag{9.4.2}$$

and n_j being some fermionic number operators. Since in the thermodynamic limit, the ground-state of the gapped XXZ spin-chain is doubly degenerate we should clarify which state we are going to deal with in this section. The entanglement Hamiltonian (9.2.3) together with (9.4.2) selects by construction the ground state that does not break the inversion symmetry, i.e. the one that in the limit of large Δ is $(|N_1\rangle + |N_2\rangle)/\sqrt{2}$ where $|N_i\rangle$ are the two possible Néel states. However, we prefer to work with the more physical symmetry breaking state $|N_i\rangle$. In CTM approach this can be constructed with an entanglement Hamiltonian of the form (9.2.3) where the sum over j starts from 1 rather than 0, i.e.

$$\widehat{H}_{\rm CTM} = \sum_{j=1}^{\infty} \epsilon_j \hat{n}_j, \qquad \epsilon_j = 2\epsilon j, \qquad \epsilon = {\rm arccosh}\Delta. \tag{9.4.3}$$

In the remaining part of this section we always focus on the symmetry breaking ground state with the above $\widehat{H}_{\rm CTM}$. If one is interested into the other state, analogous results may easily be derived.

The entanglement spectrum is obtained by filling in all the possible ways the single particle levels in (9.4.3) (i.e. setting all n_j equal either to 0 or 1). The resulting levels are equally spaced with spacing 2ϵ and highly degenerate. The degeneracy of the level $2\epsilon s$, with $s = \sum_j j$ (see (9.4.2)) is $D_{\rm h}(s)$, the number of partitions of s into smaller non-repeated integers (including zero) [1].

We want to characterise how the entanglement of the semi-infinite line A with respect to its complement splits into the different sectors with fixed magnetisation $\hat{S}_z \equiv \sum_j \hat{\sigma}^z_j/2$. We indicate with q the possible values, in the subsystem A, of the *difference* of the magnetisation with respect to the antiferromagnetic Néel state chosen as a reference configuration. Such variable q is quantised in terms of integer numbers (each spin flip leads to a change of magnetisation of ± 1), i.e. $q \in \mathbb{Z}$. With a slight abuse of language, we will refer to q as the magnetisation, although it is a magnetisation difference. To derive the symmetry resolved entanglement, we first write $\mathcal{Z}_n(q)$, defined in (8.1.2), as

$$\mathcal{Z}_n(q) = \sum_{s \in \mathcal{S}_q} \lambda_s^n, \tag{9.4.4}$$

[1] We use the subscript "h" for the degeneracy and for some of the quantities we are going to introduce in order to stress that we are considering half of the infinite chain as subsystem. This notation will be particularly useful in the next section.

where λ_s are the eigenvalues of the RDM and the sum is restricted to the levels with fixed value of q. Using (9.2.2) and the explicit expression of the entanglement spectrum from (9.4.3), we can write

$$\mathcal{Z}_n(q) = \frac{\sum_s \mathcal{F}_{\rm h}(q,s) e^{-2n\epsilon s}}{\Big(\sum_s D_{\rm h}(s) e^{-2\epsilon s}\Big)^n}\,, \tag{9.4.5}$$

where $\mathcal{F}_{\rm h}(q,s)$ is the number of eigenvalues at level s with magnetisation q. The degeneracies $\mathcal{F}_{\rm h}(q,s)$ have been studied in Ref. [263] with a combination of perturbation theory and integrability arguments. The final result for the bipartition of our interest is $\mathcal{F}_{\rm h}(q,s) = \mathcal{P}_{\rm h}(\frac{s-m_{\rm h}(q)}{2})$ [263], with $\mathcal{P}_{\rm h}(n)$ the number of integer partitions of n and $m_{\rm h}(q) = q(2q-1)$. Using this result and changing variable in the sum of the numerator in (9.4.5) as $(s - m_{\rm h}(q))/2 \to s$, we obtain

$$\mathcal{Z}_n(q) = e^{-2n\epsilon q(2q-1)} \frac{\sum_s \mathcal{P}_{\rm h}(s) e^{-4n\epsilon s}}{\Big(\sum_s D_{\rm h}(s) e^{-2\epsilon s}\Big)^n}, \tag{9.4.6}$$

where we have also exploited that $\mathcal{P}_{\rm h}(n)$ is non vanishing only if n is a positive integer.

Setting $x = e^{-4n\epsilon}$ and $y = e^{-2\epsilon}$, the two sums in (9.4.6) can be conveniently rewritten in terms of generating functions

$$\sum_{s=0} \mathcal{P}_{\rm h}(s) x^s = \prod_{k=1}^{\infty} \frac{1}{1-x^k}, \qquad \sum_{s=0} D_{\rm h}(s) y^s = \prod_{k=1}^{\infty} (1+y^k). \tag{9.4.7}$$

and $\mathcal{Z}_n(q)$ can be expressed in terms of elliptic theta functions as

$$\mathcal{Z}_n(q) = \frac{2^{\frac{1+n}{3}} \left[\kappa(e^{-\epsilon})\right]^{\frac{n}{12}} e^{-4n\epsilon(q-\frac{1}{4})^2}}{\left[\kappa(e^{-2\epsilon n})\kappa'(e^{-2\epsilon n})\right]^{\frac{1}{6}} \left\{\left[\kappa'(e^{-\epsilon})\right]^{-\frac{2}{3}} - \left[\kappa'(e^{-\epsilon})\right]^{\frac{4}{3}}\right\}^{\frac{n}{8}} \theta_3\left(0|e^{-2\epsilon n}\right)}, \tag{9.4.8}$$

where

$$\theta_3(z|u) = \sum_{k=-\infty}^{\infty} u^{k^2} e^{2ikz}\,, \qquad \kappa'(u) = \frac{\theta_4^2(0|u)}{\theta_3^2(0|u)}\,, \qquad \kappa'(u) = \sqrt{1-\kappa'(u)^2} \tag{9.4.9}$$

and $\theta_4(z|u)$ is defined in (9.3.7). We remark that $\mathcal{Z}_1(q)$ is normalised to one, i.e. $\sum_{q\in\mathbb{Z}} \mathcal{Z}_1(q) = 1$, as it should be from the definition (9.4.4). This is consistent with the interpretation of $\mathcal{Z}_1(q)$ as a probability, see Section 8.2. Notice that $q = 1/4$ is exactly the mean magnetisation of the subsystem in the critical limit $\epsilon \to 0$, as we can check by computing $\bar{q} = \int dq q \mathcal{Z}_1(q)$, since we are dealing with the symmetry breaking ground state. Notice that the dependence on q in (9.4.8) is entirely encoded in the Gaussian factor and it is symmetric for $q \to 1/2 - q$. Moreover, exploiting the asymptotic behaviours of the elliptic functions (9.4.1) [469], we have that in the critical regime $\mathcal{Z}_n(q)$ becomes

$$\mathcal{Z}_n(q) \simeq \sqrt{\frac{2^{1+n}\epsilon n}{\pi}} e^{-\frac{\pi^2}{24\epsilon}\left(n-\frac{1}{n}\right)} e^{-4n\epsilon(q-\frac{1}{4})^2}, \tag{9.4.10}$$

where we keep the Gaussian factor in order to have a meaningful result. Once the resolved moments $\mathcal{Z}_n(q)$ have been worked out, the symmetry resolved entropies follow straightforwardly

$$S_n(q) = \frac{1}{1-n} \sum_{k=1}^{\infty} \left[n \log\left(1 - e^{-4\epsilon k}\right) - \log\left(1 - e^{-4n\epsilon k}\right)\right], \tag{9.4.11}$$

and, taking the limit $n \to 1$,

$$S_1(q) = \sum_{k=1}^{\infty} \left[\frac{4\epsilon k}{e^{4\epsilon k} - 1} - \log\left(1 - e^{-4\epsilon k}\right) \right]. \tag{9.4.12}$$

Notice that as $\Delta \gg 1$, $S_n(q) \to 0$ (see also Figure 9.6), since in this limit the selected antiferromagnetic ground state is a product state. If we would have considered the non-symmetry breaking ground state $(|N_1\rangle + |N_2\rangle)/\sqrt{2}$, $\Delta \gg 1$ we would have found $S_n(q) \to \log 2$, as for the total entropy [9, 436, 453]. We stress that although there is entanglement equipartition, the functions $S_n(q)$ are not equal to the total entropies S_n because there is a non-vanishing fluctuation term like in (1.2.28) for $n = 1$.

Remarkably, the expressions (9.4.11) and (9.4.12) for the symmetry resolved Rényi and von Neumann entanglement entropies do not depend on q for any value of n, i.e. they *exactly satisfy the equipartition of entanglement* for any value of Δ. In the critical case, only the leading terms satisfy such equipartition [97, 251].

The relation between the correlation length of the model and ϵ, in the critical regime $\xi \gg 1$, is [259]

$$\log \xi \simeq \frac{\pi^2}{2\epsilon} + O(\epsilon^0), \tag{9.4.13}$$

which combined with Eqs. (9.4.10) provides the expansions of the symmetry resolved entropies in the critical regime

$$\begin{aligned} S_n(q) &= \frac{1}{12}\left(1 + \frac{1}{n}\right)\log \xi - \frac{1}{2}\log\left(\frac{\log \xi}{\pi}\right) + \frac{1}{2}\log 2 + \frac{\log n}{2(1-n)}, \\ S_1(q) &= \frac{1}{6}\log \xi - \frac{1}{2}\log\left(\frac{\log \xi}{\pi}\right) + \frac{\log 2 - 1}{2}. \end{aligned} \tag{9.4.14}$$

We notice that the term $-\frac{1}{2} - \frac{1}{2}\log(\log \xi/\pi)$ appearing in $S_1(q)$ in (9.4.14) is canceled exactly by the fluctuation entanglement entropy once we consider the total von Neumann entanglement entropy. Indeed, using that the probability is $p(q) = \mathcal{Z}_1(q)$, we write the fluctuation entropy as $-\int dq \mathcal{Z}_1(q) \log \mathcal{Z}_1(q)$. Using (9.4.8), computing the gaussian integral in q and then taking the critical limit, we find

$$-\int_{-\infty}^{\infty} dq \mathcal{Z}_1(q) \log \mathcal{Z}_1(q) = \frac{1}{2} + \frac{1}{2}\log(\log \xi/\pi), \tag{9.4.15}$$

which exactly cancels the contribution from the configurational entropy. This is in complete analogy with what has been found for critical systems for the $\log \log \ell$ term [251].

As stressed in Sec. 9.3.3 for the harmonic chain, one can check that known total entanglement entropy found in [9, 453] for the symmetry breaking ground state can be recovered from (1.2.28) using the total von Neumann entanglement entropy from $S_1(q)$ in (9.4.12) and $\mathcal{Z}_1(q) = p(q)$ in (9.4.8).

In Figure 9.6 we report symmetry resolved moments and entropies. The possible values of q are just integers, but since $\mathcal{Z}_n(q)$ becomes quickly small as q increases, we consider arbitrary real values. As anticipated, $\mathcal{Z}_n(q)$ has a peak at $q = 1/4$ and shows a clear Gaussian shape for all Δ. The exact result (9.4.8) is well approximated by its critical limit (9.4.10) for Δ close to 1, but the approach is not uniform and it is worse for larger q (as well as larger n). Clearly, the maximum of $\mathcal{Z}_n(q)$ is a decreasing function of n. In the last panel of Figure 9.6, we report the symmetry resolved entropies as functions of Δ (as we stressed because of equipartition, they do not depend on q). Notice that the window of Δ for which the critical limit of $S_n(q)$ in (9.4.14) is a good approximation of the exact expression (9.4.11) is wider for smaller values of q.

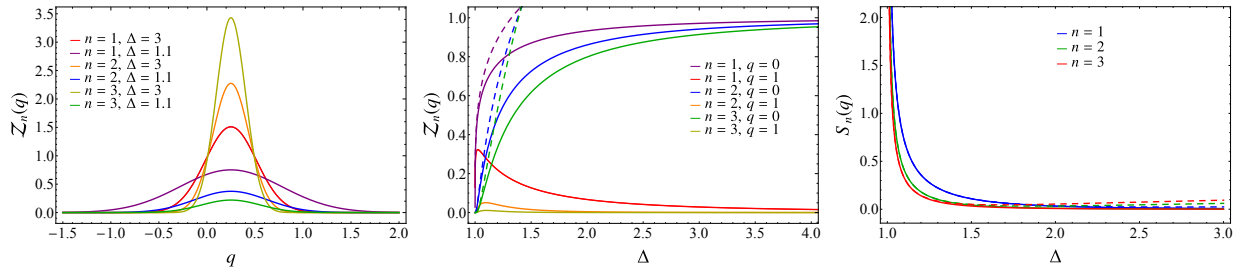

Figure 9.6: Magnetisation resolved moments and entropies for the XXZ spin-chain. The left panel shows the results for $\mathcal{Z}_n(q)$, Eq. (9.4.8), against q for different values of $n = 1, 2, 3$ and $\Delta = 1.1, 3$. In the middle panel, we report again $\mathcal{Z}_n(q)$ at fixed q and as function of Δ (full lines). As a comparison, we also report the asymptotic expansion (9.4.10) for Δ close to 1 (dashed lines). In the right panel, we report $S_n(q)$ and its critical limit, respectively Eq. (9.4.11) and Eq. (9.4.14), as function of Δ for $n = 1, 2, 3$. We recall that $S_n(q)$ does not depend on q because of entanglement equipartition.

9.4.2 Charged moments via Fourier series

The charged moments are obtained from the resolved ones $\mathcal{Z}_n(q)$ by inverting the formula (8.1.2), i.e.

$$Z_n(\alpha) = \sum_{q=-\infty}^{\infty} \mathcal{Z}_n(q) e^{\mathrm{i}q\alpha}. \tag{9.4.16}$$

Plugging in the above equation the result for $\mathcal{Z}_n(q)$ in (9.4.8) and using the definitions in (9.4.1), we obtain

$$Z_n(\alpha) = \frac{2^{\frac{1+n}{3}} e^{-\frac{n}{4}\epsilon} \left[\kappa(e^{-\epsilon})\right]^{\frac{n}{12}}}{\left[\kappa(e^{-2\epsilon n})\kappa'(e^{-2\epsilon n})\right]^{\frac{1}{6}} \left\{\left[\kappa'(e^{-\epsilon})\right]^{-\frac{2}{3}} - \left[\kappa'(e^{-\epsilon})\right]^{\frac{4}{3}}\right\}^{\frac{n}{8}}} \frac{\theta_3(\frac{\alpha}{2} - \mathrm{i}n\epsilon \,|\, e^{-4\epsilon n})}{\theta_3\left(e^{-2\epsilon n}\right)}. \tag{9.4.17}$$

Setting $\alpha = 0$ and exploiting the infinite product representations of the elliptic theta function [460], we get

$$Z_n(0) = \frac{\prod_{k=1}^{\infty} \left(1 + e^{-2\epsilon n k}\right)}{\prod_{k=1}^{\infty} \left(1 + e^{-2\epsilon k}\right)^n}, \tag{9.4.18}$$

as found in [9]. The charged moment $Z_n(\alpha)$ in the critical regime is obtained using the asymptotic expansions of the elliptic functions [469], finding

$$Z_n(\alpha) \simeq 2^{-\frac{1-n}{2}} e^{-\frac{\pi^2}{24\epsilon}\left(n - \frac{1}{n}\right)} e^{-\frac{\alpha^2}{16n\epsilon} + \mathrm{i}\frac{\alpha}{4}}. \tag{9.4.19}$$

Taking the logarithm of $Z_n(\alpha)$ and using (9.4.13) we have

$$\log Z_n(\alpha) \simeq \left[\frac{1}{12}\left(\frac{1}{n} - n\right) - \frac{\alpha^2}{8\pi^2 n}\right] \log \xi + \mathrm{i}\frac{\alpha}{4} - (1-n)\frac{\log 2}{2}. \tag{9.4.20}$$

Here, the linear term in α is just the mean magnetisation in A, $\bar{q} = 1/4$.

We find it worth comparing this finding with the results obtained in a field theoretical setting in Sec. 8.3.2. The continuum limit of the XXZ chain in the gapless phase is described by the

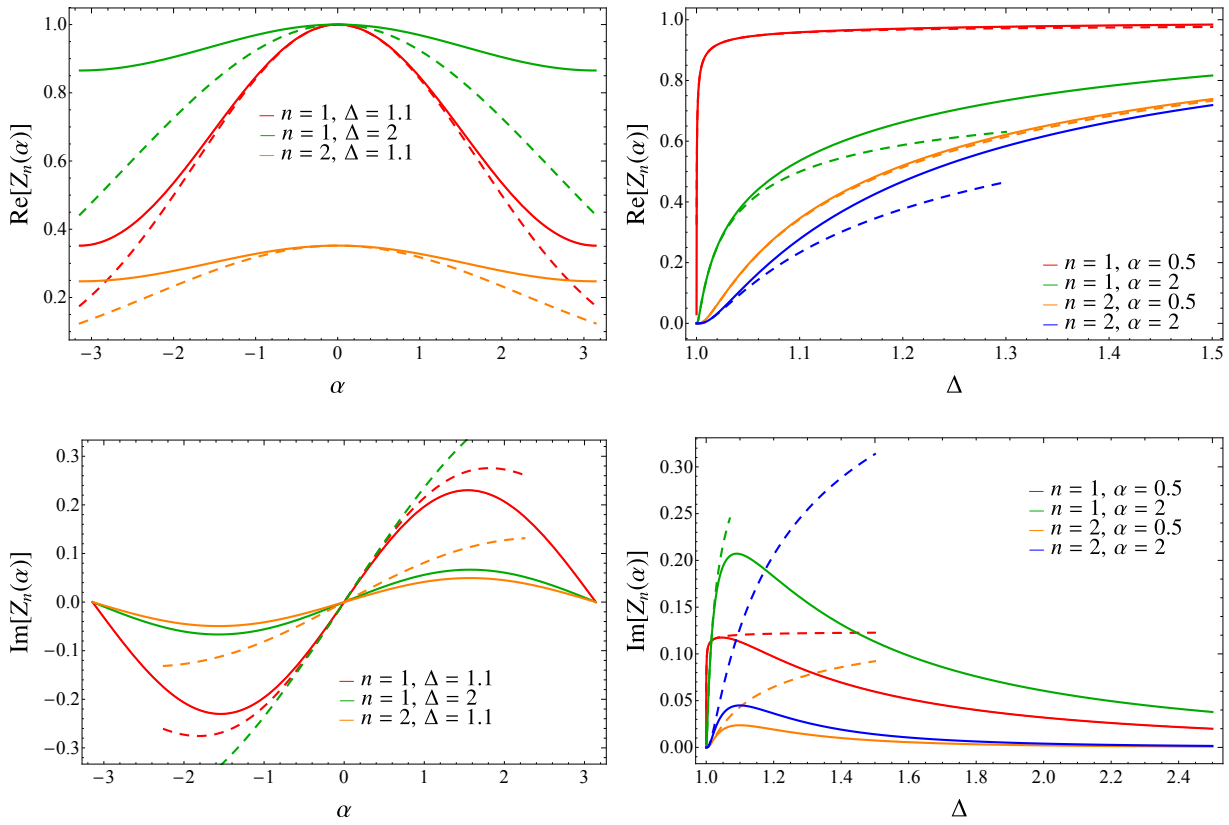

Figure 9.7: Charged moments for the XXZ spin chain. Top and Bottom plots correspond to real and imaginary parts respectively. In the left panels, the plots are against α for different values of Δ, while in the right panels are against Δ at fixed α. The dashed lines are the expansions close to the critical points (Eq. (9.4.19)) that are approached only for Δ very close to 1.

critical compact boson (aka, Luttinger liquid), where the parameter Δ is related to the Luttinger parameter K. Consistently, we find that the leading term in (9.4.20) is equal to the one in (8.3.16) for $K = \frac{1}{2}$, which is the Luttinger parameter at $\Delta = 1$, and $\xi \to 1/(m\epsilon_{n,\alpha})$.

Moreover, for the symmetry resolved entropies, the CFT result for the compact boson is $S_n(q) - S_n = -\frac{1}{2}\log((2K/\pi)\log\ell) + O(\ell^0)$ [96, 97], which is the same as in (9.4.14) with the replacement $\ell \to \xi$ and with $K = 1/2$.

In Figure 9.7 we report the plots of the charged moments as functions of α and Δ. Also in this case, the approach to the critical regime is not uniform and it is faster for α closer to 0 (and n close to 1). This is very different compared to what we have seen in the previous section for the harmonic chain for which the limit $\alpha \to 0$ is singular. This is a further confirmation that the anomalous behaviour of the harmonic chain is due to its non-compact nature of the continuum limit.

9.5 Full counting statistics in the gapped XXZ spin chain

The process of measurement in quantum mechanics is intrinsically probabilistic: the measure of a given observable generically provides different outcomes in identically prepared systems. Hence, the probability distribution (PDF) of an observable is a natural quantity to consider in any quan-

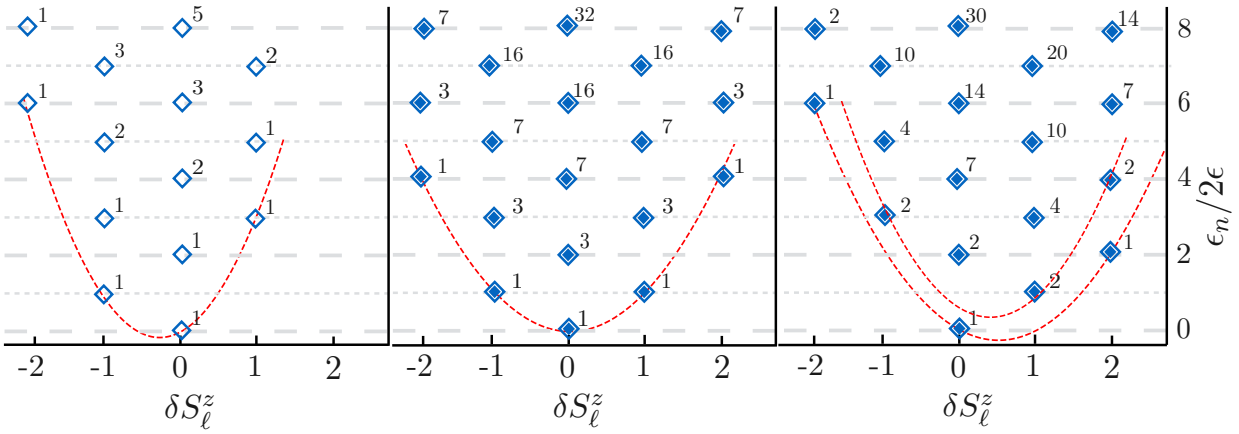

Figure 9.8: Entanglement spectra of the gapped XXZ spin chain in the three configurations we consider here. Left: Semi-infinite line. Center: A block of ℓ contiguous spins with ℓ even. Right: A block with ℓ odd. We report the logarithm of the eigenvalues of the reduced density matrix ϵ in units of 2ϵ, with $\epsilon = \text{arccosh}\Delta$, as function of δS^z_ℓ (see (9.5.1)). Each tilted square signals the presence of an eigenvalue with degeneracy given by the nearby number. The dashed-red parabolas are envelopes of the location of the largest eigenvalue of the RDM at fixed δS^z_ℓ. Notice that in the left and in the center, the towers of degeneracies are independent of δS^z_ℓ. Conversely, on the right, i.e. for odd blocks, there are two towers depending on the parity of δS^z_ℓ.

tum mechanical system and provides much more information than the average value of the same observable. In many-body systems, these PDFs, or equivalently their full counting statistics (FCS), have been the subject of intensive investigations since many years with a focus mainly on local observables (i.e. defined in a given point or lattice site) or global ones (i.e. extensive quantities involving the entire system). Only in recent time, the attention shifted to observables with support on a finite, but large, subsystem embedded in a thermodynamic one, partially motivated by cold atomic experiments [470–475] and by the connection with the entanglement entropy of the same subsystem [476–485]. In spite of a large recent literature on the subject [486–511], results based on integrability for one-dimensional exactly solvable *interacting* models are still scarse (see [499,500]).

The full counting statistics (FCS) of a conserved charge within an extended subsystem is strictly related to the charged moments introduced in (8.1.1) in order to study the symmetry resolved entanglement entropies. Thus, it is natural to adapt the techinques developed in the previous sections of this chapter to the computation of the FCS. In this section, we provide an explicit exact calculation for the PDF and for the FCS of the total transverse magnetisation within an extended subsystem in an infinite XXZ spin chain. As a byproduct, we also derive some results for the symmetry resolved entanglement of blocks made by a finite number of spins.

9.5.1 Full counting statistics

We consider the ground state of the XXZ spin chain defined by the Hamiltonian (9.4.1) and we focus on the antiferromagnetic gapped regime with $\Delta > 1$. As discussed in Sec. 9.4.1, the total transverse magnetisation ($\sum_j \hat\sigma^z_j/2$) is conserved and therefore the reduced density matrix $\hat\rho_\ell$ of the subsystem made by ℓ contiguous spins can be organised in blocks of fixed magnetisation (quantised in terms of integers or half-integers up to $\ell/2$ depending on the parity of ℓ). This property allows to compute the FCS directly from the entanglement spectrum, as explained in the

following subsections.

As already done in Sec. 9.4, in order to work with an observable with integer eigenvalues for any ℓ, it is convenient to focus on the difference of the block magnetisation with respect to the Néel state, denoted here by

$$\delta\hat{S}^z_\ell \equiv \sum_{j=1}^{\ell} \Big(\frac{\hat{\sigma}^z_j}{2} - \frac{(-1)^j}{2} \Big) \,. \tag{9.5.1}$$

The probability of a measurement of the subsystem magnetisation with outcome $\delta S^z_\ell = q$ is just the trace of the block of ρ_ℓ in the sector with $\delta S^z = q$, i.e.

$$p(q) = \mathrm{Tr}\hat{\rho}_\ell \Pi_q = \sum_{s \,\in\, \mathcal{S}_q} \lambda_s \,, \tag{9.5.2}$$

where Π_q is the projector on the sector of magnetisation $\delta\hat{S}^z = q$, λ_s are the eigenvalues of ρ_ℓ, and $\mathcal{S}_q$ stands for all the eigenvalues in that magnetisation sector (notice that $\sum_q p(q) = \mathrm{Tr}\rho_\ell = 1$ by construction). Let us remark that the probability in (9.5.2) is the same quantity introduced in (8.1.3). The FCS generating function is defined as

$$G(\lambda) \equiv \mathrm{Tr}\hat{\rho}_\ell e^{\mathrm{i}\lambda\delta\hat{S}^z_\ell} = \sum_q p(q) e^{\mathrm{i}q\lambda}; \tag{9.5.3}$$

its derivatives in $\lambda = 0$ provide the moments of the observables δS^z_ℓ. Hence the exact knowledge of the entanglement spectrum also provides the FCS of the total transverse magnetisation (in general it provides the FCS of any conserved charge). As discussed in Sec. 9.4, for the ground state of the XXZ spin chain in the gapped regime, the entanglement spectrum has been obtained in Ref. [263]. We exploit its knowledge here to reconstruct the PDF and the FCS of the subsystem magnetisation also when the block ℓ is made by a finite number of sites.

Let us stress that the FCS in (9.5.3) coincides with the charged moment in (9.4.16) evaluated for $n = 1$ after the renaming of the variable $\alpha \to \lambda$. This makes evident the connection between the FCS and the symmetry resolved entanglement.

9.5.2 Entanglement spectrum of blocks with odd and even number of sites

As done in Sec. 9.4.1, in the following we consider an infinite XXZ chain in the symmetry broken ground state, i.e. the one that for large Δ converges to the Néel state. This state is doubly degenerate, so there are two equivalent states which are mapped into each other by the translation of one site. As already discussed in Sec. 9.4.1, when the subsystem is half of the chain, the result for the degeneracy of the eigenvalues of $\hat{\rho}_\ell$ with $\delta S^z_\ell = q$ at level s is given by $\mathcal{F}_{\mathrm{h}}(q,s) = \mathcal{P}_{\mathrm{h}}(\frac{s - m_{\mathrm{h}}(q)}{2})$ [263], with $\mathcal{P}_{\mathrm{h}}(n)$ the number of integer partitions [2] of n and $m_{\mathrm{h}}(q) = q(2q+1)$ (the other degenerate state –sometimes called Antineel for $\Delta \to \infty$– is obtained by sending $q \to -q$ with the net effect of having $m_{\mathrm{h}}(q) = q(2q-1)$). The first panel of Fig. 9.8 reports the structure of the entanglement spectrum of a semi-infinite subsystem based on this result. Exploting (9.4.8) with $n = 1$ and (8.1.3), we obtain $p(q)$ defined in (9.5.2) when the subsystem is half of the inifinite chain. It reads

$$p_{\mathrm{h}}(q) = \frac{e^{-2\epsilon q(2q+1)}}{\theta_3\left(i\epsilon | e^{-4\epsilon}\right)} \tag{9.5.4}$$

where ϵ is given by (9.4.2) and θ_3 is defined in (9.4.1). The subscript h has been introduced just to stress that the result (9.5.4) holds for the case of semi-infinite subsystem, in contrast with the results reported in the following subsections for finite blocks.

[2] We use the convention that $\mathcal{P}_{\mathrm{h}}(x) = 0$ for negative integers and half-integers.

Now, still following the approach of Ref. [263], we explain how to use these results to obtain the entanglement spectrum of a finite large interval. As long as ℓ is larger than the correlation length, the reduced density matrix ρ_ℓ of a single interval with two boundaries factorises into $\rho_L \otimes \rho_R$, where $\rho_{L/R}$ are the reduced density matrices for the semi-infinite lines having the left/right end-point of the interval. The combination of these two spectra into a single one is graphically reported in Fig. 9.8. We show both cases for even and odd subsystems (center and right respectively).

For an even subsystem we should combine two different spectra $m_L(x) = x(2x+1)$ and $m_R(x) = x(2x-1)$ from left and right. Conversely, for odd blocks, the left and the right spectra to combine are equal, e.g. $m_L(x) = m_R(x) = x(2x+1)$. The final results for the degeneracies are reported in the figure. In the even case, we have that the degeneracy at fixed q at level s can be written as $\mathcal{F}_{\rm e}(q,s) = \mathcal{P}_{\rm e}(\frac{s-m_{\rm e}(q)}{2})$ with $m_{\rm e}(q) = q^2$ and $\mathcal{P}_{\rm e}$ generated by

$$\sum_{s=0} \mathcal{P}_{\rm e}(s) x^s = \prod_{k\geq 1} \frac{(1+x^k)^2}{1-x^k}\,, \tag{9.5.5}$$

leading to the generating function for the total degeneracy $D_{\rm e}(s)$ of level s

$$\sum_{s=0} D_{\rm e}(s) x^s = \prod_{k\geq 1} (1+x^k)^2. \tag{9.5.6}$$

Notice that, while the generating function for $D_{\rm e}(s)$ is the square of the one for $D_{\rm h}(s)$ reported in (9.4.7), the same is not true for $\mathcal{P}_{\rm e}$ and $\mathcal{P}_{\rm h}$ [3].

For odd blocks, it is more complicated to combine the two spectra for even and odd q. The degeneracies of both sectors have the generating function

$$\sum_{s=0} \mathcal{P}^{\rm b}_{\rm o}(s) x^s = \prod_{k\geq 1} \frac{(1-x^{2k})^3}{(1-x^k)^2(1-x^{4k})^2}, \tag{9.5.7}$$

where even (odd) powers of x correspond to even (odd) values of q. However, a single generating function for different q is not a too useful tool to write symmetry resolved quantities. Exploiting some identities of elliptic theta functions $\theta_{2,3}$, we can extract the even and the odd part of (9.5.7) we are interested in. After some algebra we get (for $x > 0$)

$$\sum_{s=0} \mathcal{P}_{\rm o}(s,q) x^s = \frac{(\theta_2(0|x^4))^{\frac{1-(-1)^q}{2}} (\theta_3(0|x^4))^{\frac{1+(-1)^q}{2}}}{\prod_{k\geq 1}(1+x^{2k})(1-(-x)^k)(1-x^k)}, \tag{9.5.8}$$

which does depend on the parity of q. For the sake of completeness, let us remind the definition of the elliptic function θ_2 given by

$$\theta_2(z|u) = \sum_{k=-\infty}^{\infty} u^{\left(k+\frac{1}{2}\right)^2} e^{i(2k+1)z}\,. \tag{9.5.9}$$

Hence, from (9.5.8), the degeneracy of the level s with fixed q is

$$\mathcal{F}_{\rm o}(q,s) = \mathcal{P}_{\rm o}(s - m_{\rm o}(q), q), \tag{9.5.10}$$

with $m_{\rm o}(q) = q^2 - q$. Indeed $m_{\rm o}(q)$ and $m_{\rm o}(q)+1$ are the two parabolas in Fig. 9.8, envelopes of the largest eigenvalues of the RDM for even and odd q respectively. The generating function for the total degeneracy $D_{\rm o}(s)$ of level s is the same as $D_{\rm e}(s)$ in (9.5.6).

[3] Again we employ the convention $\mathcal{P}_{\rm e}(x) = 0$ for negative numbers and for half-integers.

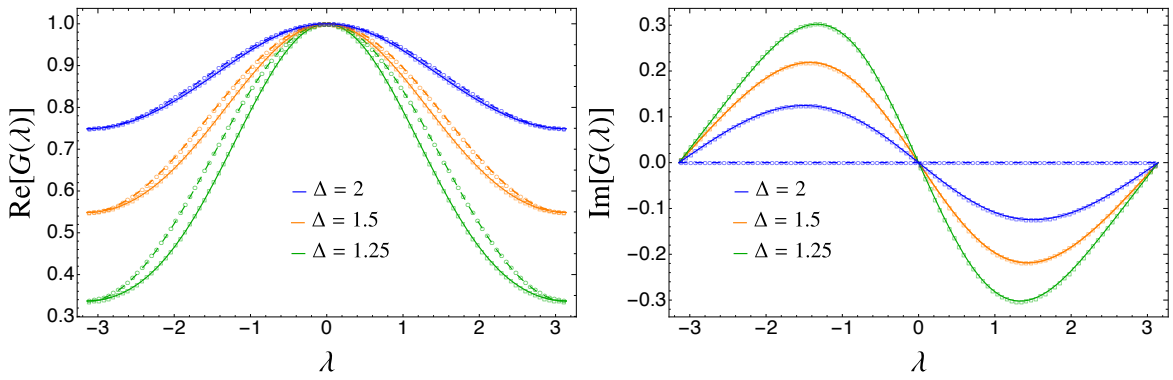

Figure 9.9: Full counting statistics generating functions $G(\lambda)$ for the gapped XXZ spin chain for three values of Δ. The left (right) panel is the real (imaginary) part of $G(\lambda)$. The symbols are the iTEBD data that perfectly match the superimposed analytic predictions (full lines for odd ℓ and dashed for even ℓ). The data are for infinite chains and subsystems equal to $\ell = 200$ (circles) or 201 (squares). Notice that the real parts for even and odd q are qualitatively similar, but quantitatively different.

9.5.3 Full counting statistics: even number of sites

The easiest way to get the PDF $p_{\rm e}(q)$ for the interval is to combine the PDFs at the right and left boundary as

$$p_{\rm e}(q) = \sum_{q_1=-\infty}^{\infty} p_L(q_1) p_R(q-q_1) = \sum_{q_1=-\infty}^{\infty} p_{\rm h}(q_1) p_{\rm h}(q_1-q), \tag{9.5.11}$$

where we used that the PDF at the two boundaries are $p_L(q) = p_{\rm h}(q_1)$ and $p_R(q) = p_{\rm h}(-q)$ with $p_{\rm h}$ given by (9.5.4). The sum is easily rewritten as

$$p_{\rm e}(q) = \frac{e^{-2\epsilon(q^2-1/4)}}{\left[\theta_3\left(i\epsilon|e^{-4\epsilon}\right)\right]^2} \sum_{q_1=-\infty}^{\infty} e^{-2\epsilon(2q_1+q+1/2)^2}\,. \tag{9.5.12}$$

The remaining sum over q_1 does not depend on q, for integer q. Hence the PDF is Gaussian

$$p_{\rm e}(q) = \frac{e^{-2q^2\epsilon}}{\theta_3(0|e^{-2\epsilon})}, \tag{9.5.13}$$

where θ_3 is defined in (9.4.1). The FCS is the Fourier series (9.4.16) which immediately leads to

$$G_{\rm e}(\lambda) = \frac{\theta_3\left(\frac{\lambda}{2}|e^{-2\epsilon}\right)}{\theta_3(0|e^{-2\epsilon})}. \tag{9.5.14}$$

Notice that this is real and even in λ. As a cross check, the same result is re-obtained by directly summing over the eigenvalues of the RDM with the degeneracies reported in Fig. 9.8 (to perform the sum, one exploits (9.5.5) the product representation of the θ_3 function).

The FCS generating function is directly measured in iTEBD simulations [512], as explained in details, e.g., in Refs. [496, 508]. The results in the thermodynamic limit for three values of $\Delta > 1$ and for $\ell = 200$ are shown in Figure 9.9. The agreement is always excellent (data and predictions are superimposed) for all considered values of Δ. We mention that as Δ gets close to 1, one should consider much larger values of ℓ to reach such good agreement due to the diverging correlation length at the isotropic point.

9.5.4 Full counting statistics: odd number of sites

Also for this case, the PDF can be obtained combining two single-boundary ones as

$$p_{\rm o}(q) = \sum_{q_1=-\infty}^{\infty} p_L(q_1)p_R(q-q_1) = \sum_{q_1=-\infty}^{\infty} p_{\rm h}(q_1)p_{\rm h}(q-q_1), \tag{9.5.15}$$

where we used that the PDF at the two boundaries are the same and given by (9.5.4). Again, the sum is easily rewritten as

$$p_{\rm o}(q) = \frac{e^{-2\epsilon(q^2-q)}\sum_{q_1=-\infty}^{\infty} e^{-2\epsilon(2q_1-q)^2}}{\left[\theta_3\left(\mathrm{i}\epsilon|e^{-4\epsilon}\right)\right]^2}\,. \tag{9.5.16}$$

However, this time the remaining sum *does* depend on the parity of q. Performing this sum, the PDF is

$$p_{\rm o}(q) = \mathcal{N}_{\rm o} e^{-2\epsilon(q^2-q)} \times \begin{cases} \theta_3(0|e^{-8\epsilon})\,, & q \text{ even}, \\ \theta_2(0|e^{-8\epsilon})\,, & q \text{ odd}, \end{cases} \tag{9.5.17}$$

with $\mathcal{N}_{\rm o}$ easily obtained from the normalisation and θ_3 and θ_2 given by (9.4.1) and (9.5.9) respectively.

The FCS is the Fourier series (9.4.16) which, after some manipulations using the properties of elliptic functions, leads to

$$G_{\rm o}(\lambda) = \left(\frac{\theta_3\left(\mathrm{i}\epsilon - \frac{\lambda}{2}|e^{-4\epsilon}\right)}{\theta_3(\mathrm{i}\epsilon|e^{-4\epsilon})}\right)^2. \tag{9.5.18}$$

Notice that this FCS has a non-vanishing and non-trivial imaginary part, but satisfy $G_{\rm o}(\lambda)^* = G_{\rm o}(-\lambda)$. Again, as a cross check, this result is re-obtained by directly summing over the eigenvalues of the RDM with the degeneracies reported in Fig. 9.8.

Also for odd ℓ, the analytical prediction (9.5.18) is tested against iTEBD simulations in Figure 9.9. In these simulations, we measure the FCS of the operator S^z_ℓ and not δS^z_ℓ; hence the numerical data have been divided by $e^{\mathrm{i}\lambda/2}$. After this normalisation, the agreement between data and prediction is extremely good in all considered cases.

9.5.5 Byproduct: symmetry resolved entropies

In order to further highlight the relation between the FCS and the symmetry resolved entanglement, in this subsection we compute the symmetry resolved entanglement entropies for subsystems made by a finite number of sites. The symmetry resolution of the entanglement spectrum reported in Figure 9.8 allows us to access the symmetry resolved moments (8.1.2) as

$$\mathcal{Z}_n(q) \equiv \sum_{s\in\mathcal{S}_q} \lambda_s^n = \frac{\sum_j \mathcal{F}_\alpha(q,s)e^{-2n\epsilon s}}{\left(\sum_j D_\alpha(s)e^{-2\epsilon s}\right)^n}\,, \tag{9.5.19}$$

where $\alpha \in \{\mathrm{h},\mathrm{e},\mathrm{o}\}$ and $\mathcal{F}_\alpha(q,s)$ and $D_\alpha(s)$ are respectively the degeneracies of the s-th eigenvalue for fixed q and total for the three cases of interest (whose generating functions have been reported in Sec. 9.5.2). In the definition of symmetry resolved entropies given by (8.1.4) only the ratio $\mathcal{Z}_n(q)/\mathcal{Z}_1^n(q)$ matters and therefore the dependence on $D_\alpha(s)$ cancels leading to

$$\frac{\mathcal{Z}_n(q)}{\mathcal{Z}_1^n(q)} = \frac{\sum_s \mathcal{F}_\alpha(q,s)e^{-2n\epsilon s}}{\left(\sum_s \mathcal{F}_\alpha(q,s)e^{-2\epsilon s}\right)^n} = \frac{\sum_s \mathcal{P}_\alpha(s)e^{-2an\epsilon s}}{\left(\sum_s \mathcal{P}_\alpha(s)e^{-2a\epsilon s}\right)^n}, \tag{9.5.20}$$

where $\alpha \in \{\mathrm{h}, \mathrm{e}, \mathrm{o}\}$ and in the last equality we used $\mathcal{F}_\alpha(q,s) = \mathcal{P}_\alpha(\frac{s-m_\alpha(q)}{a})$ (with $a=2$ for semi-infinite and even ℓ, while $a=1$ for odd ℓ) and shifted the sum as $(s-m_\alpha(q))/a \to s$ (notice that the actual value of $m_\alpha(q)$ is unessential).

Combining (9.5.20) with $\alpha = \mathrm{h}$ and (9.4.7), we recover the symmetry resolved entropies for the semi-infinite line given by (9.4.11).

Now we derive the entropies for a finite interval of both even and odd length. For even ℓ, the two sums in (9.5.20) with $\alpha = \mathrm{e}$ can be rewritten in terms of generating functions (9.5.5) (with $x = e^{-4n\epsilon}$), obtaining

$$S_n^{\mathrm{e}}(q) = \frac{\displaystyle\sum_{k=1}^{\infty} \Big[\ln \frac{(1+e^{-4n\epsilon k})^2}{1-e^{-4n\epsilon k}} - n \ln \frac{(1+e^{-4\epsilon k})^2}{1-e^{-4\epsilon k}} \Big]}{1-n}. \tag{9.5.21}$$

Very importantly, the symmetry resolved entropies are *not the double* of the single resolved entropies (9.4.11) for the half line as it is the case for the total one (mathematically this is a consequence of the relation between the generating function for $D_{\mathrm{e}}(s)$ and $D_{\mathrm{h}}(s)$, but not for $\mathcal{P}_{\mathrm{e}}$ and $\mathcal{P}_{\mathrm{h}}$). Also, these symmetry resolved entanglement entropies are independent of q and hence satisfy the equipartition of entanglement [97] exactly.

In the very same fashion, we can repeat the calculation for odd ℓ, setting $\alpha = \mathrm{o}$ in (9.5.20) and obtaining the more cumbersome expression

$$\begin{aligned} S_n^{\mathrm{o}}(q) = \frac{1}{1-n} \Bigg[\sum_{k=1}^{\infty} \Bigg(& n \ln(1+e^{-4\epsilon k})(1-e^{-2\epsilon k})(1-(-)^k e^{-2\epsilon k}) \\ & - \ln(1+e^{-4\epsilon nk})(1-e^{-2\epsilon nk})(1-(-)^k e^{-2\epsilon nk}) \Bigg) \\ & + \frac{1+(-)^q}{2} (\ln \theta_3(e^{-8\epsilon n}) - n \ln \theta_3(e^{-8\epsilon}) + \frac{1-(-)^q}{2} (\ln \theta_2(e^{-8\epsilon n}) - n \ln \theta_2(e^{-8\epsilon}) \Bigg], \end{aligned} \tag{9.5.22}$$

with θ_3 and θ_2 given by (9.4.1) and (9.5.9) respectively. Hence, for odd ℓ, the symmetry resolved entropies do depend on the parity of q and the equipartition of entanglement is explicitly broken.

We finally mention, as a highly non-trivial crosscheck, that it is possible, but cumbersome, to sum over the various sectors q in order to recover the total entanglement through (1.2.28), both for even and odd ℓ.

9.6 Discussion

In this chapter we found exact results for the symmetry resolved entanglement entropies of half line in infinite integrable systems in the gapped regime. We considered two models for which the RDM (and therefore the entanglement spectrum) of the subsystem can be obtained through the Baxter CTM. We also discuss the relation between the symmetry resolved entanglement entropies and the full counting statistics obtaining, for the latter, exact results.

In Section 9.3 we considered the massive regime of the complex harmonic chain that has a $U(1)$ symmetry corresponding to the conservation of the electric charge. In order to obtain the symmetry resolved entanglement entropies, we first computed the charged moments of the RDM in Eqs. (9.3.3), (9.3.5), and (9.3.12). Then we computed the Fourier transform of the charged moments and the symmetry resolved entanglement entropies (see Eqs. (9.3.26) and (9.3.27)). Interestingly we found that there is no entanglement equipartition, i.e. the symmetry resolved entropies $S_n(q)$

explicitly depend on q. However, entanglement equipartition is effectively recovered in two limits: i) for large q, i.e. as soon as q becomes larger than the logarithm of the correlation length and ii) in the critical region for $n\epsilon \ll 1$. All our analytical results have been checked numerically using (8.5.32) and (8.5.34).

In Section 9.4 the symmetry resolved entanglement entropies have been computed for the XXZ chain in the antiferromagnetic gapped regime (Eqs. (9.4.11) and (9.4.12)). Here, the conserved $U(1)$ symmetry corresponds to the rotations in the plane perpendicular to the anisotropy. Somehow surprisingly, for this model, the symmetry resolved entropies *exactly satisfy the equipartition of entanglement* for any anisotropy $\Delta \geq 1$. We found this result very remarkable, although its physical origin is not clear: it would be very interesting to establish a priori which properties guarantee an exact equipartition of entanglement and how they are related to integrability. The computation has been performed exploiting the explicit expressions of the elements of the entanglement spectrum and the degeneracies of each level in a given magnetisation sector [263]. These results allow also to find exact expressions for the FCS of the magnetisation within finite blocks of ℓ contiguous spins. This is discussed in Sec. 9.5 and our main findings are reported in (9.5.14) and (9.5.18) for even and odd values of ℓ respectively.

Let us conclude this chapter with some possible directions for future investigations motivated by the results we have found. A first question to ask is what happens when integrability is absent: while a general treatment seems impossible, the results for the entanglement spectrum in Refs. [263, 264] suggests that in some non-trivial regimes general results may be derived. Another natural extension is to study symmetry resolved entanglement in higher dimension for which there are only few works for free fermions [256, 257, 423]. The equations (8.5.32) and (8.5.34) pave the way for general numerical studies in arbitrary dimension for bosonic systems as well, also in the presence of a spherical constraint [513]. In some cases, also analytical results can be explicitly worked out [423]. Finally, one expects that the symmetry resolved entanglement should help in reconstructing the entanglement Hamiltonian, but it is still unclear how.

Conclusions

The goal of this thesis is to study the quantum circuit complexity of mixed states and some aspects of entanglement in many-body quantum systems. The intertwinement between these two topics can be explained as follows. Many entanglement quantifiers are defined for a certain spatial bipartition $A \cup B$ and can be computed from the reduced density matrix of the subsystem A, which characterises a mixed state. Thus, in order to determine the complexity between reduced density matrices associated to the same subsystem (subsystem complexity $\mathcal{C}_A$), it is necessary to provide a prescription for computing the complexity of mixed states. This is the content of the Part I of this thesis, where we employ the Fisher information geometry [91–93, 125] of the covariance matrices for providing the optimal circuit connecting two bosonic Gaussian mixed states with vanishing first moments and its length, that we identify with the complexity of the circuit. These two results are given in (2.2.20) and (2.2.24) respectively, providing an extension of the findings obtained for pure states in [35,40]. Some applications are then discussed in the context of harmonic lattices (or their one dimensional version given by the harmonic chain); among these, it is worth mentioning the complexity between thermal states reported in (2.2.54), the subsystem complexity (2.7.40), a precise prescription for computing spectrum and basis complexity explained in Sec. 2.3 and the temporal evolution of the subsystem complexity after a global and a local quantum quench analysed in Secs. 3.4 and 3.5 and Sec. 4.4 respectively.

Throughout this part, in some interesting cases, we have compared the entanglement entropy S_A defined in (1.2.3) with the subsystem complexity $\mathcal{C}_A$ in (2.7.40) obtained for the same subsystem. At equilibrium, the major distinction between these two quantities occurs in the leading divergence: while for S_A it is determined by the volume of the boundary of A (this law is violated in a two-dimensional conformal field theory in its ground state, e.g. when A is an interval and therefore the boundary of A is made by two points [6, 8, 9]), for $\mathcal{C}_A$ it grows like the volume of A, with a power that depends on the choice of the cost function [79, 98]. This is shown, for instance, in (2.7.41) when A is a block of consecutive sites in an infinite harmonic chain in its ground state (see also Fig. 2.7).

A comparison between $\mathcal{C}_A$ and S_A, when A is a single block in harmonic chains out of equilibrium, has been made in chapters 3 and 4. In particular, these quantities have been considered after a global quench in Secs. 3.4 and 3.5 and after a local quench in Sec. 4.4, finding that, in most cases we have analysed, there are remarkable qualitative differences between the subsystem complexity and the entropy. The only case when we have observed a strikingly similar qualitative behaviour is provided by the local quench considered in chapter 4 when the joining point of the two harmonic chains lies outside the subsystem. This can be observed, for instance, in (4.4.2) and (4.4.3) for S_A and $\mathcal{C}_A$ respectively and, correspondingly, in the left panels of Figs. 4.5 and 4.6. The comparison between entanglement entropy and subsystem complexity has been discussed also in various gravitational backgrounds within the holographic correspondence [46, 55, 59, 143–145, 297, 298, 316, 514]. It is important to further study $\mathcal{C}_A$ and S_A (or other entanglement measures computed for the same spatial subsystem) in parallel in order to gain a deeper understanding of differences and

similarities of these two quantities.

We find it worth remarking that intriguing qualitative similarities are observed between the temporal evolution of the subsystem complexity of a block of consecutive sites in an infinite harmonic chain after a global quench (see the black data points in the top panel of Fig. 3.14 and in Fig. 3.16) and the holographic results obtained for the corresponding gravitational background in [145, 316] (see also Fig. 1.5). Despite the results obtained for lattice models can be compared only qualitatively with the holographic findings, it would be interesting to extend this analysis to more complicated bipartitions and to other critical systems.

In Part II we focus on entanglement Hamiltonians and entanglement spectra in free lattice models. In chapter 5 we have studied the continuum limit of the entanglement Hamiltonian of an interval in massless harmonic chains in their ground states showing that, in order to recover the result (1.2.13) from conformal field theory (CFT), also the long range couplings of the matrices M and N in the lattice expression (1.2.17) have to be taken into account (see Fig. 5.5 and Fig. 5.11). On the other hand, considering a harmonic chain far away from criticality as done in chapter 6, the on-site and nearest-neighbour terms of M and N are found to be more and more dominant as the mass increases, exhibiting triangular profiles that can be understood from the analytical results for a half-infinite interval (see Fig. 6.3). Unfortunately, we are not able to obtain a well-defined continuum limit of the entanglement Hamiltonian in the massive case exploiting the procedure introduced in chapter 5. We argue this is due to the non-negligible contributions from the antidiagonals of M and N showed in Fig. 6.10. As for the gaps in the entanglement spectrum (1.2.18), from a numerical analysis of free critical lattice models at equilibrium (Secs. 5.3.2 and 5.4.2) and out of equilibrium (Secs. 7.3.2 and 7.4.2), the expected results (1.2.19) for the underlying BCFTs have been recovered. Moreover, exploiting the quasi-particle picture [82], the formula (7.3.13) for the temporal evolution of the contour for the entanglement entropies after a global quench has been obtained and it has been checked against numerical computations on a free fermionic chain (see Fig. 7.18).

Our analysis not only provides new insights about the entanglement properties of free models, but also leads to a better understanding of the structure of the reduced density matrices, which might turn out to be useful in the study of the quantum circuits connecting these particular mixed states. An explicit example of interplay and cross-fertilisation between entanglement and complexity is the following. As just remarked above, the subsystem complexity is obtained by connecting two reduced density matrices through a quantum circuit. The entanglement Hamiltonians provide an alternative way to characterise the reduced density matrices. Thus, it is natural to ask whether we can consider quantum circuits that allow to construct a target entanglement Hamiltonian from a reference one and compute their complexity. This idea has been implemented in Sec. 2.4 for the entanglement Hamiltonians in harmonic lattices, where the optimal circuit and the corresponding complexity have been found to be (2.4.4) and (2.4.5) respectively. Through this approach one can hopefully exploit the results discussed in Sec. 1.2.2 and in the chapters 5, 6 and 7 to get more insights about the subsystem complexity. On the other hand, the geometric approaches developed for studying the quantum circuits can surely shed new light on the structure of the set of entanglement Hamiltonians, which, as stressed often in the previous sections, are objects typically very hard to study. This is just an example of how the physics of the entanglement can improve the understanding of the circuit complexity in many-body systems and viceversa. We hope in the future to find further cases of this cross-fertilisation.

Finally, in Part III we have collected the results about the symmetry resolved entanglement, focussing in particular on gapped systems. In chapter 8 we have considered the free massive Dirac and complex scalar field theories and we have shown that, despite the presence of the mass, at leading order both theories satisfy the equipartition of entanglement [97]. In chapter 9, exploiting

CTM techniques [259, 262, 383], interesting exact results have been obtained for the symmetry resolved entanglement entropies of half infinite subsystems in the complex harmonic chain (see (9.3.26) and (9.3.27)) and in the XXZ spin chain (see (9.4.11) and (9.4.12)). Remarkably, while for the spin chain we have found exact equipartition of entanglement, this is not the case for the harmonic system where equipartition is effectively recovered only in some limits.

To the best of our knowledge, a proposal for the symmetry resolved complexity has not been formulated yet. It would be very interesting to investigate this aspect in order to see if the interplay between complexity and symmetries leads to features already observed for the entanglement, as for instance some form of equipartition.

The study of the circuit complexity and the entanglement in many-body quantum systems leaves open various interesting directions of research concerning relevant aspects and problems of condensed matter theory and high energy physics.

As discussed in Sec. 1.2.3, the replica trick for the entanglement entropy provides a powerful computational approach in quantum field theories that has been generalised to compute various entanglement measures in several different systems. It would be very useful to have a counterpart for the circuit complexity, but, currently, such a method is not available. Thus, it is of crucial importance to pursue this line of research, developing new possible approaches or exploiting the existing ones [60–76]. A similar technology in the context of CFTs would allow to understand in a more systematic way whether the complexity is, as the entanglement is known to be, a good diagnostic tool for detecting criticality in quantum systems. Furthermore, it would provide results capable for a quantitative comparison with the holographic findings obtained through the proposals (1.1.18) and (1.1.21).

A pivotal role in the study of the emergence of universal properties from lattice systems is played by exactly solvable models, which, allowing for analytical solutions, are interesting "theoretical laboratories" for testing various physical aspects ranging from critical behaviours to out of equilibrium dynamics. Well-known examples are the integrable systems which show a rich and fascinating mathematical structure. The Bethe Ansatz techniques [515, 516], successfully applied for the computations of various observables in integrable models, have been also employed to study the entanglement properties [202, 231, 461–468]. It would be intriguing to apply this formalism in constructing quantum circuits connecting states of integrable systems and in evaluating their complexity. It might be that the profound mathematical structure due to the integrability can provide remarkable insights about the geometry of these quantum states.

Entanglement has found considerable applications in the context of tensor networks [517–519]. Indeed, the efficiency of numerical algorithms based on these techniques can be quantified by the entanglement [520]. The Multi-scale Entanglement Renormalisation Ansatz is an example of tensor network which is known to approximate accurately a CFT ground state [521, 522]. These networks are defined on a discretised version of hyperbolic spaces and therefore have been used to realise various statements from holography [523, 524]. In [51] it has been observed that the CV proposal (1.1.18) for the holographic complexity has a simple realisation through tensor networks and this has led to further applications, as for instance the definition in this context of the holographic subsystem complexity [64]. The approaches for the complexity based on tensor networks deserves further studies. Indeed, these systems realise one of the most natural definition of complexity in many-body systems and can be used to obtain insights about this quantity in continuum theories [525, 526]. Moreover, this would allow to keep on investigating the relation between entanglement and subsystem complexity.

The capacity of entanglement of a given bipartition is the quantum information theoretic counterpart of heat capacity and it is intimately related to the corresponding entanglement Hamiltonian, since it is defined as the variance of this operator. It would be interesting to study this

quantity in various settings in order to understand whether it can detect physical features that the entanglement entropy is not able to see [527–530].

Complexity and entanglement have been intensively studied also in the context of AdS/CFT correspondence. The Ryu-Takayanagi formula (1.2.24) for the entanglement entropy is considered one of the most important insights connecting quantum information theory and quantum gravity and has inspired many subsequent results in holography, as for instance the proposals (1.1.18) and (1.1.21) for the holographic complexity. Entanglement has been found to be an extraordinary tool for studying some aspect of black holes. Among these, it is worth mentioning the relation between black holes and quantum chaos [53,531,532], in turn connected with the chaotic dynamics of the strongly coupled dual CFTs. Moreover, in this context, intriguing paradoxes have been formulated [533, 534] and their discussion has led to deep insights for black hole physics, as for instance the ER=EPR principle [535, 536] and the notion of firewall [537, 538]. One of the most celebrated paradoxes is the information paradox, raised by Hawking in [539]. According to this, if a pure state of matter collapses to form a black hole which evaporates through Hawking radiation, the final quantum state appears to be mixed, breaking the unitarity of quantum gravity. To recover the unitary evolution, Page proposed a mechanism which predicts that, after an initial growth, the radiation entropy decreases to zero as the black hole evaporates [540]. Reproducing the Page curve for a model of a black hole with radiation is a challenging task that has produced remarkable efforts (see the reviews [541,542]). In the last years, many progresses in this direction have been obtained exploiting a generalisation of the Ryu-Takayanagi formula, which includes quantum corrections, that leads to the so-called *island rule* [543–549].

A further aspect of the AdS/CFT correspondence where entanglement has led to considerable contributions is the emergence of spacetime [550]. The so-called bulk reconstruction program aims to discover CFT operators representing bulk fields at all the points [551, 552]. Recently, in this framework, a technique has been developed for constructing local bulk fields starting from the knowledge of the entanglement Hamiltonian in the CFT at the boundary of the AdS space [553]. Possible new results might be obtained by applying in this framework the progresses concerning the entanglement Hamiltonians in the context of many-body systems and, in particular, of CFT.

There is still a lot to understand about the interplay between quantum information theory and gauge/gravity dualities. This topic deserves further investigations and important insights can be achieved exploiting the great efforts done in literature on the application of quantum information techniques to many-body quantum systems. Also other branches of information theory, rooted in a more mathematical framework, can be helpful for this purpose. It is the case of the information geometry [93,121], which has been recently applied in the study of the circuit complexity [98] and of the AdS/CFT correspondence [554].

Acknowledgments

The last four years spent in Trieste have been extremely significant for my growth both from a professional and a human point of view. In addition to the experiences and skills acquired, I will carry inside myself many people without whom my path would have been much more complicated. For this reason, I cannot help but thank them all.

First of all, I would like to express gratitude to my supervisor Erik. I thank him not only for teaching me most I know about the profession of research, but also (and above all) for his help, his constant presence and his incessant encouragement.

During these years I have had the honour and the privilege of collaborating with excellent and brilliant physicists, each of whom taught me a lot. I want to thank them all for that. Lots of thanks, far beyond the scientific aspects, go to Pasquale for his help and his precious advice in complicated moments.

Huge thanks go to the whole group of Statistical Physics: first of all to the faculties, for giving me the opportunity to live this experience, and then to fellow students and postdocs I have had the luck to interact with, for having made the work environment full of motivations and moments of human and professional growth.

The entire SISSA community, from students to professors, from the technical and administrative staff to bar and canteen workers, has demonstrated to be a real family capable of giving me moments of joy, fun, discussion and thinking. Special thanks are for those with whom I have shared most of the time in SISSA (and not only). Saman, Jackie, Mattia, Piero, Paolo and all the others: thank you for all the moments of leisure and the experiences lived together. Thanks to Pierpaolo for the fantastic year as a flatmate and the beautiful friendship which was born later and to Gianluca for the mutual support during the first year and for teaching me to go beyond appearances.

C'è poi la parte della mia vita precedente alla SISSA, che continuerà ad essere per me un punto di riferimento fondamentale. Grazie a Gigi e Lore (gli altri due del *tridente*) per aver mantenuto la promessa di sopravvivere al dottorato; sono sicuro che prima o poi arriverà anche il nostro articolo a sei mani. Grazie a tutti gli amici di Prato che, ad ogni mio ritorno, fanno sembrare che il tempo si sia fermato a quattro anni fa, prima della mia partenza. Un ringraziamento speciale a Pucci, Stefano, Paia e Mirco (*que' ragazzi*, insomma) per tutti i viaggi folli a Trieste e a Mogliano, per i meeting di allineamento durante il lockdown e soprattutto per esserci sempre nei momenti più duri.

Sono profondamente grato a Giuliana e Rocco, la mia famiglia, per tutto ciò che hanno fatto per me. Dopo aver trascorso tanto tempo lontano da casa mi accorgo ancora di più dell'importanza dei loro insegnamenti e dei loro consigli. Li ringrazio per il loro amore incondizionato e per aver dolcemente atteso per tutti i mesi di lockdown passati senza poterci abbracciare.

Mille e più pagine di ringraziamenti non basterebbero a contenere tutto quello che vorrei dire a Sara ed esprimere in poche righe cosa sia stata per me in questi anni è un'impresa impossibile. Più di ogni altra cosa, però, la voglio ringraziare per avermi sopportato e supportato ogni giorno, ogni ora e ogni istante, per avermi insegnato, forse un po' inconsapevolmente, il significato della parola *determinazione*, per aver coltivato pazientemente il nostro rapporto e per averlo reso un faro anche e soprattutto nei momenti più difficili.

Appendix A

Entanglement entropies and contour functions in free systems on a lattice

In this appendix we report the main formulas which allow to compute the entanglement entropies and the contour functions for the entanglement entropies in free lattice models.

If we consider a subsystem A made by L sites of a given lattice, the contour function for the entanglement entropies $s_A^{(n)} : A \to \mathbb{R}$ has to satisfy the following properties

$$S_A^{(n)} = \sum_{i=1}^{L} s_A^{(n)}(i) \qquad\qquad s_A^{(n)}(i) \geqslant 0\,. \tag{A.0.1}$$

In Appendix A.1 we consider harmonic lattices, while in in Appendix A.2 we focus on free fermionic lattices.

A.1 Harmonic lattices

The harmonic lattice made by N sites with nearest neighbour spring-like interaction is described by the hamiltonian (2.2.1). If the whole lattice is in a Gaussian state (see Sec. 2.2.1) the key object for computing the entanglement entropies is the $2L \times 2L$ reduced covariance matrix γ_A defined as

$$\gamma_A = \begin{pmatrix} Q_A & M_A \\ M_A^{\mathrm{t}} & P_A \end{pmatrix}. \tag{A.1.1}$$

in terms of the correlators $(Q_A)_{i,j} = \langle \hat{q}_i \hat{q}_j \rangle$, $(P_A)_{i,j} = \langle \hat{p}_i \hat{p}_j \rangle$ and $(M_A)_{i,j} = \mathrm{Re}\big[\langle \hat{q}_i \hat{p}_j \rangle\big]$, with $i, j \in A$ (see Appendix C for a review of the correlators of harmonic chains in some relevant Gaussian states).

A very important tool employed to quantify the bipartite entanglement in harmonic lattices is the Williamson's theorem (see Sec. 2.2.3), which leads, for the reduced covariance matrix γ_A, to

$$\gamma_A = W^{\mathrm{t}}\, \mathcal{D}\, W \tag{A.1.2}$$

where $\mathcal{D} \equiv \mathrm{diag}(\sigma_1, \dots, \sigma_L) \oplus \mathrm{diag}(\sigma_1, \dots, \sigma_L)$ and the diagonal matrix $\mathrm{diag}(\sigma_1, \dots, \sigma_L)$ collects the symplectic eigenvalues $\sigma_k > 0$ of γ_A.

The symplectic spectrum of γ_A provides the entanglement entropy S_A and the Rényi entropies $S_A^{(n)}$ as follows [4, 5, 27, 77, 191, 275–277, 555]

$$S_A = \sum_{k=1}^{L} s(\sigma_k) \qquad S_A^{(n)} = \sum_{k=1}^{L} s_n(\sigma_k) \tag{A.1.3}$$

where $s(y)$ and $s_n(y)$ are the analytic functions given by

$$s(y) \equiv (y+1/2)\log(y+1/2) - (y-1/2)\log(y-1/2) \tag{A.1.4}$$

and

$$s_n(y) \equiv \frac{1}{n-1}\,\log\left[(y+1/2)^n - (y-1/2)^n\right]. \tag{A.1.5}$$

The parameter n is an integer $n \geqslant 2$. Performing an analytic continuation of this integer parameter, the entanglement entropy S_A can be obtained as $S_A^{(1)} \equiv \lim_{n\to 1} S_A^{(n)}$, that is the replica limit for the entanglement entropy (see Sec. 1.2.1). The expressions (A.1.3) with (A.1.4) and (A.1.5) have been employed to compute numerically the entanglement entropies in chapters 3 and 4 (in order to compare S_A with the corresponding subsystem complexity) and in chapters 6 and 7.

The symplectic spectrum of γ_A is obtained by diagonalising $(\mathrm{i}J\gamma_A)^2$. Indeed, by employing that W is symplectic and that $J^{\mathrm{t}}\mathcal{D}^r J = \mathcal{D}^r$ (J is the standard symplectic matrix (2.2.2)) for any non negative integer r, it is not difficult to realise that

$$(\mathrm{i}J\gamma_A)^2 = W^{-1}\,\mathcal{D}^2\,W\,. \tag{A.1.6}$$

The contour for the entanglement entropies in harmonic lattices has been studied in [27,29,103] (see also [28, 177, 556] for analyses of this quantity in other lattice models). The prescription we have employed in this thesis has been proposed in [29] and it satisfies the two conditions in (A.0.1) and a weakened version of other three conditions proposed in [28]. Another expression fulfilling (A.0.1) has been suggested in [29], but the remaining three properties have not been proved for this proposal. A third contour function has been considered in [27, 556]: it satisfies the first condition in (A.0.1) but numerical violations of the positivity condition $s_A^{(n)}(i) \geqslant 0$ have been observed for some configurations [29].

A contour function $s_A^{(n)}(i)$ can be constructed by associating L real numbers $p_k(i)$ to every symplectic eigenvalue σ_k, where $1 \leqslant i, k \leqslant L$. The function $p_k(i)$ is often called mode participation function [27] and it fulfils the following conditions

$$\sum_{i=1}^{L} p_k(i) = 1 \qquad\qquad p_k(i) \geqslant 0\,. \tag{A.1.7}$$

A mode participation function $p_k(i)$ allows to write the entanglement entropies (A.1.3) as in (A.0.1) with

$$s_A^{(n)}(i) = \sum_{k=1}^{L} p_k(i)\; s_n(\sigma_k) \tag{A.1.8}$$

being $s_n(y)$ the functions defined in (A.1.4) and (A.1.5) for $n \geqslant 1$. The contour function (A.1.8) is not unique because any mode participation function fulfilling (A.1.7) provides a contour function (A.1.8) that satisfies (A.0.1). Furthermore, any $2L \times 2L$ orthogonal matrix O can be employed to construct a mode participation function $p_k(i)$. In order to make contact with the reduced covariance matrix γ_A, in [29] the Euler decomposition (see (2.2.16)) of the symplectic matrix W in (A.1.2) has been employed to construct an orthogonal matrix K leading to a reasonable candidate for the contour function $s_A^{(n)}(i)$. This orthogonal matrix can be written in terms of W as follows

$$K \equiv (WW^{\mathrm{t}})^{-1/2}\,W = W(W^{\mathrm{t}}W)^{-1/2}. \tag{A.1.9}$$

Partitioning this $2L \times 2L$ orthogonal matrix into $L \times L$ blocks

$$K = \begin{pmatrix} U_K & Y_K \\ Z_K & V_K \end{pmatrix} \tag{A.1.10}$$

the contour function for the entanglement entropies in harmonic lattices proposed in [29] is (A.1.8) with the mode participation function given by

$$p_k(i) = \frac{1}{2}\Big([(U_K)_{k,i}]^2 + [(Y_K)_{k,i}]^2 + [(Z_K)_{k,i}]^2 + [(V_K)_{k,i}]^2 \Big) . \tag{A.1.11}$$

The prescription (A.1.8) with mode partecipation function given by (A.1.11) has been employed in Sec. 7.3.3 for computing the temporal evolution the contour for the entanglement entropies in a harmonic chain after a global quench of the fequency parameter.

A.2 Free fermionic lattices

In this appendix we consider a system of free fermions hopping between lattice sites described by the following Hamiltonian

$$\hat{H} = \sum_{i,j} t_{i,j}\, \hat{c}_i^\dagger\, \hat{c}_j \tag{A.2.1}$$

where for the operators $\hat{c}_i$ and $\hat{c}_i^\dagger$ the canonical anticommutation relations $\{\hat{c}_i, \hat{c}_j^\dagger\} = \delta_{i,j}$ and $\{\hat{c}_i, \hat{c}_j\} = \{\hat{c}_i^\dagger, \hat{c}_j^\dagger\} = 0$ hold. Given a subsystem A made by L sites, let us define the correlation matrix C_A whose generic element is $(C_A)_{i,j} = \langle \hat{c}_i^\dagger\, \hat{c}_j \rangle$, with $i, j \in A$. The matrix C_A is hermitian and therefore it is diagonalised by a unitary matrix that we call $\widetilde{U}$. If we call ζ_k, with $k = 1, \dots, L$, the real eigenvalues of C_A, the Rényi entropies can be written as [3–5, 10, 77, 191]

$$S_A^{(n)} = \sum_{k=1}^{\ell} s_n(\zeta_k) \qquad s_n(y) \equiv \frac{1}{1-n}\, \log\big[y^n + (1-y)^n \big] . \tag{A.2.2}$$

The limit $n \to 1$ of these expressions provides the entanglement entropy as

$$S_A = \sum_{k=1}^{\ell} s(\zeta_k) \qquad s(y) \equiv -\, y \log(y) - (1-y) \log(1-y) . \tag{A.2.3}$$

These relations have been used to compute numerically the entanglment entropies for free fermionic chains both in static cases (chapter 6) and in out-of-equilibrium settings (chapter 7).

An exhaustive analysis of a contour function for the entanglement entropy in chains of free fermions has been carried out in [28]. We employ this prescription in our analysis and refer the reader interested in further details to this reference. In [28] a natural contour for the entanglement entropies is obtained as explained in Appendix A.1 (see (A.1.8)) with a mode partecipation function obtained through the unitary matrix $\widetilde{U}$ as

$$p_k(i) = \big| \widetilde{U}_{k,i} \big|^2 . \tag{A.2.4}$$

As consistency check, let us observe that the i-th element of the diagonal of the matrix relation $\widetilde{U}^\dagger \widetilde{U} = \mathbf{1}$ gives the condition $\sum_{k=1}^{L} p_k(i) = 1$ for $1 \leqslant i \leqslant L$.

The proposal (A.1.8) with mode partecipation function given by (A.2.4) has been used in Sec. 7.4.3 to determine numerically the temporal evolution of the contour for the entanglement entropies in a free fermionic chain after a global quench

Appendix B

Complexity of thermofield double states

In this appendix we consider the thermofield double states (TFD's) for the harmonic lattices [557], whose circuit complexity has been explored in various studies over the last few years [40, 42, 43].

In Appendix B.1 we define the thermofield double states and we compute their covariance matrices. In Appendix B.2 the circuit complexity for these states is discussed, while in Appendix B.3 we study the mutual complexity for the TFD's.

B.1 The thermofield double state

The TFD's are pure states constructed by entangling two equal copies of the harmonic lattice in such a way that a thermal state of the original system is obtained by tracing out one of the two copies.

Consider two harmonic lattices (that will be denoted as "left" and "right" in the following) made by the same number N of sites. These two systems can be combined creating a system made by $2N$ sites (denoted as "doubled" system) whose hamiltonian reads

$$\widehat{H}_{\rm d} \equiv \frac{1}{2}\, \hat{\boldsymbol{r}}_{\rm d}^{\rm t}\, H_{\rm d}^{\rm phys}\, \hat{\boldsymbol{r}}_{\rm d} = \frac{1}{2}\, \hat{\boldsymbol{r}}_{\rm d}^{\rm t} \Big(Q_{\rm d}^{\rm phys} \oplus \frac{1}{m}\, \mathbf{1} \Big)\, \hat{\boldsymbol{r}}_{\rm d} \qquad Q_{\rm d}^{\rm phys} = Q^{\rm phys} \oplus Q^{\rm phys} \tag{B.1.1}$$

where $\hat{\boldsymbol{r}}_{\rm d}^{\rm t} \equiv (\hat{\boldsymbol{q}}_{\rm l}^{\rm t}, \hat{\boldsymbol{q}}_{\rm r}^{\rm t}, \hat{\boldsymbol{p}}_{\rm l}^{\rm t}, \hat{\boldsymbol{p}}_{\rm r}^{\rm t})$, where the subindices refer to the left and right part of the doubled system, and $Q^{\rm phys}$ has been introduced in (2.2.41). For the periodic chain the matrix $Q^{\rm phys}$ has been written explicitly in (2.7.3).

It is not difficult to adapt the diagonalisation procedure described in Sec. 2.2.6 to (B.1.1). This leads to construct the $4N \times 4N$ matrix $H_{\rm d}^{\rm phys}$ defined in (B.1.1) as follows (see (2.2.43))

$$H_{\rm d}^{\rm phys} = V_{\rm d}\, \mathcal{X}_{\rm d}\, \mathcal{D}_{\rm d}\, \mathcal{X}_{\rm d}\, V_{\rm d}^{\rm t} \tag{B.1.2}$$

where we have introduced the diagonal matrix $\mathcal{D}_{\rm d} \equiv \mathcal{D}_{\rm phys} \oplus \mathcal{D}_{\rm phys}$, the symplectic and orthogonal matrix $V_{\rm d} \equiv V \oplus V$ and the symplectic diagonal matrix

$$\mathcal{X}_{\rm d} = S \oplus S^{-1} \qquad S \equiv \mathcal{S} \oplus \mathcal{S} \tag{B.1.3}$$

where

$$\mathcal{S} \equiv \sqrt{m}\, {\rm diag}\Big(\sqrt{\Omega_1}, \dots, \sqrt{\Omega_N} \Big) \tag{B.1.4}$$

with Ω_k dispersion relation introduced through (2.2.42). These matrices are defined in terms of the $2N \times 2N$ matrices V and $\mathcal{D}_{\text{phys}}$ in (2.2.42) and (2.2.45) respectively.

Since V_{d} and $\mathcal{X}_{\text{d}}$ are symplectic matrices, the expression (B.1.2) leads us to write the Williamson's decomposition of $H_{\text{d}}^{\text{phys}}$ as follows

$$H_{\text{d}}^{\text{phys}} = W_{\text{d}}^{\text{t}}\, \mathcal{D}_{\text{d}}\, W_{\text{d}} \qquad W_{\text{d}} = \mathcal{X}_{\text{d}}\, V_{\text{d}}^{\text{t}}\,. \tag{B.1.5}$$

This decomposition suggests to introduce the following set of canonical conjugated variables (see Sec. 2.2.6)

$$\hat{\boldsymbol{s}}_{\text{d}} \equiv W_{\text{d}}\, \hat{\boldsymbol{r}}_{\text{d}} \qquad \hat{\boldsymbol{s}}_{\text{d}}^{\text{t}} \equiv (\hat{\mathfrak{q}}_{\text{l},1}, \dots, \hat{\mathfrak{q}}_{\text{l},N}, \hat{\mathfrak{q}}_{\text{r},1}, \dots, \hat{\mathfrak{q}}_{\text{r},N}, \hat{\mathfrak{p}}_{\text{l},1}, \dots, \hat{\mathfrak{p}}_{\text{l},N}, \hat{\mathfrak{p}}_{\text{r},1}, \dots, \hat{\mathfrak{p}}_{\text{r},N})\,. \tag{B.1.6}$$

Defining the annihilation operators and the creation operators for the two parts of the system as in (2.2.48), one obtains a vector $\hat{\boldsymbol{b}}_{\text{d}}^{\text{t}} \equiv \big(\hat{\boldsymbol{b}}_{\text{l}}^{\text{t}}, \hat{\boldsymbol{b}}_{\text{r}}^{\text{t}}, (\hat{\boldsymbol{b}}_{\text{l}}^{\dagger})^{\text{t}}, (\hat{\boldsymbol{b}}_{\text{r}}^{\dagger})^{\text{t}}\big)$, where $\hat{\mathfrak{b}}_{l,k}$ and $\hat{\mathfrak{b}}_{r,k}$ are the k-th element of $\hat{\boldsymbol{b}}_{\text{l}}$ and $\hat{\boldsymbol{b}}_{\text{r}}$ respectively. In terms of the components of $\hat{\boldsymbol{b}}_{\text{d}}$, the hamiltonian (B.1.1) becomes

$$\widehat{H}_{\text{d}} = \sum_{k=1}^{N} \Omega_k \Big(\hat{\mathfrak{b}}_{l,k}^{\dagger}\, \hat{\mathfrak{b}}_{l,k} + \hat{\mathfrak{b}}_{r,k}^{\dagger}\, \hat{\mathfrak{b}}_{r,k} + 1 \Big)\,. \tag{B.1.7}$$

The standard quantisation procedure leads to introduce the eigenstates $|\boldsymbol{n}_{\text{r}}, \boldsymbol{n}_{\text{l}}\rangle \equiv |\boldsymbol{n}_{\text{l}}\rangle_{\text{l}}\, |\boldsymbol{n}_{\text{r}}\rangle_{\text{r}}$ of the number operator, that can be factorised through the eigenstates $|\boldsymbol{n}_{\text{l}}\rangle_{\text{l}}$ and $|\boldsymbol{n}_{\text{r}}\rangle_{\text{r}}$ of the number operators corresponding to the two parts. The eigenstates with $\boldsymbol{n}_{\text{r}} = \boldsymbol{n}_{\text{l}} \equiv \boldsymbol{n}$ allow to define the thermofield double state (TFD) as follows [557]

$$|\text{TFD}\rangle = \prod_{k=1}^{N} \sqrt{1 - e^{-\beta\Omega_k}} \sum_{\boldsymbol{n}} e^{-\frac{\beta}{2}\sum_{k=1}^{N} \Omega_k n_k} |\boldsymbol{n}\rangle_{\text{l}}\, |\boldsymbol{n}\rangle_{\text{r}}\,. \tag{B.1.8}$$

When $\beta \to \infty$, the TFD becomes the product state of the two ground states $|\boldsymbol{0}\rangle_{\text{l}}\, |\boldsymbol{0}\rangle_{\text{r}}$.

Tracing out the degrees of freedom corresponding to one of the two parts, e.g. the right part, in (B.1.8) one obtains

$$\text{Tr}_{\mathcal{H}_{\text{r}}}\big(|\text{TFD}\rangle\langle\text{TFD}|\big) = \prod_{k=1}^{N} \big(1 - e^{-\beta\Omega_k}\big) \sum_{\boldsymbol{n}} e^{-\beta\sum_{k=1}^{N} \Omega_k n_k}\, |\boldsymbol{n}\rangle_{\text{l}}\, {}_{\text{l}}\langle\boldsymbol{n}| \tag{B.1.9}$$

which is the thermal density matrix for the left half system at temperature $1/\beta$.

The covariance matrix of the TFD can be found through a slight generalisation of the procedure described in Sec. 2.2.6 for the thermal states. From (2.2.9) and (B.1.6), the covariance matrix of this pure state can be written as

$$\gamma_{\text{TFD}} = \text{Re}\langle\text{TFD}|\, \hat{\boldsymbol{r}}_{\text{d}}\, \hat{\boldsymbol{r}}_{\text{d}}^{\text{t}}\, |\text{TFD}\rangle = W_{\text{d}}^{-1}\, \text{Re}\big[\langle\text{TFD}|\, \hat{\boldsymbol{s}}_{\text{d}} \hat{\boldsymbol{s}}_{\text{d}}^{\text{t}}\, |\text{TFD}\rangle\big]\, W_{\text{d}}^{-\text{t}}\,. \tag{B.1.10}$$

In order to compute the matrix $\text{Re}\langle\text{TFD}|\hat{\boldsymbol{s}}_{\text{d}} \hat{\boldsymbol{s}}_{\text{d}}^{\text{t}}|\text{TFD}\rangle$, one first expresses the operators in $\hat{\boldsymbol{s}}_{\text{d}}$ in terms of the creation and annihilation operators in $\hat{\boldsymbol{b}}_{\text{d}}$ and then exploits their action on (B.1.8). The non vanishing elements of $\text{Re}\langle\text{TFD}|\hat{\boldsymbol{s}}_{\text{d}} \hat{\boldsymbol{s}}_{\text{d}}^{\text{t}}|\text{TFD}\rangle$, are

$$\begin{aligned}
&\text{Re}\langle\hat{\mathfrak{q}}_{l,k}\hat{\mathfrak{q}}_{l,k}\rangle = \text{Re}\langle\hat{\mathfrak{q}}_{r,k}\hat{\mathfrak{q}}_{r,k}\rangle = \text{Re}\langle\hat{\mathfrak{p}}_{l,k}\hat{\mathfrak{p}}_{l,k}\rangle = \text{Re}\langle\hat{\mathfrak{p}}_{r,k}\hat{\mathfrak{p}}_{r,k}\rangle = \frac{1}{2}\coth(\beta\Omega_k/2) \\
&\text{Re}\langle\hat{\mathfrak{q}}_{r,k}\hat{\mathfrak{q}}_{l,k}\rangle = \text{Re}\langle\hat{\mathfrak{q}}_{l,k}\hat{\mathfrak{q}}_{r,k}\rangle = -\text{Re}\langle\hat{\mathfrak{p}}_{r,k}\hat{\mathfrak{p}}_{l,k}\rangle = -\text{Re}\langle\hat{\mathfrak{p}}_{l,k}\hat{\mathfrak{p}}_{r,k}\rangle = \frac{1}{2}\,\frac{1}{\sinh(\beta\Omega_k/2)}
\end{aligned} \tag{B.1.11}$$

where the notation $\langle \widehat{O} \rangle \equiv \langle \mathrm{TFD}| \, \widehat{O} \, |\mathrm{TFD}\rangle$ has been adopted. By using (B.1.11), the covariance matrix $\mathrm{Re}\langle \mathrm{TFD}|\hat{\boldsymbol{s}}_{\mathrm{d}}\hat{\boldsymbol{s}}_{\mathrm{d}}^{\mathrm{t}}|\mathrm{TFD}\rangle$ in (B.1.10) can be written as

$$\mathrm{Re}\langle \hat{\boldsymbol{s}}_{\mathrm{d}} \, \hat{\boldsymbol{s}}_{\mathrm{d}}^{\mathrm{t}} \rangle = \Upsilon_{\mathrm{TFD}}^{(+)} \oplus \Upsilon_{\mathrm{TFD}}^{(-)} \qquad \Upsilon_{\mathrm{TFD}}^{(\pm)} \equiv \begin{pmatrix} \Lambda_{\mathrm{TFD}} & \pm\tilde{\Lambda}_{\mathrm{TFD}} \\ \pm\tilde{\Lambda}_{\mathrm{TFD}} & \Lambda_{\mathrm{TFD}} \end{pmatrix} \tag{B.1.12}$$

where we have introduced the following $N \times N$ diagonal matrices

$$\begin{aligned} \Lambda_{\mathrm{TFD}} &\equiv \frac{1}{2}\,\mathrm{diag}\Big(\coth(\beta\Omega_1/2), \dots, \coth(\beta\Omega_N/2) \Big) \\ \tilde{\Lambda}_{\mathrm{TFD}} &\equiv \frac{1}{2}\,\mathrm{diag}\Big(\frac{1}{\sinh(\beta\Omega_1/2)}, \dots, \frac{1}{\sinh(\beta\Omega_N/2)} \Big) \end{aligned} \tag{B.1.13}$$

which satisfy

$$\Lambda_{\mathrm{TFD}}^2 - \tilde{\Lambda}_{\mathrm{TFD}}^2 = \frac{1}{4}\,\mathbf{1} \tag{B.1.14}$$

and

$$\big(\Lambda_{\mathrm{TFD}} + \tilde{\Lambda}_{\mathrm{TFD}}\big)\big(\Lambda_{\mathrm{TFD}} - \tilde{\Lambda}_{\mathrm{TFD}}\big)^{-1} = \mathrm{diag}\big(\coth^2\big(\beta\Omega_1/4\big), \dots, \coth^2\big(\beta\Omega_N/4\big) \big) \, . \tag{B.1.15}$$

Plugging (B.1.12) into (B.1.10) and employing the definition of W_{d} in (B.1.5), for the covariance matrix of the TFD we find

$$\gamma_{\mathrm{TFD}} = V_{\mathrm{d}}\, \mathcal{X}_{\mathrm{d}}^{-1} \Big(\Upsilon_{\mathrm{TFD}}^{(+)} \oplus \Upsilon_{\mathrm{TFD}}^{(-)} \Big) \mathcal{X}_{\mathrm{d}}^{-1}\, V_{\mathrm{d}}^{\mathrm{t}} = Q_{\mathrm{TFD}} \oplus P_{\mathrm{TFD}} \tag{B.1.16}$$

where (B.1.3) and $V_{\mathrm{d}} \equiv V \oplus V$ have been employed to write the last expression, which is given in terms of the following $2N \times 2N$ symmetric matrices

$$Q_{\mathrm{TFD}} = V S^{-1}\, \Upsilon_{\mathrm{TFD}}^{(+)}\, S^{-1}\, V^{\mathrm{t}} \qquad P_{\mathrm{TFD}} = V S\, \Upsilon_{\mathrm{TFD}}^{(-)}\, S\, V^{\mathrm{t}} \, . \tag{B.1.17}$$

By using that V is an orthogonal matrix and that

$$\Upsilon_{\mathrm{TFD}}^{(+)}\, \Upsilon_{\mathrm{TFD}}^{(-)} = \frac{1}{4}\,\mathbf{1} \tag{B.1.18}$$

which can be obtained from (B.1.12) and (B.1.14), one finds

$$Q_{\mathrm{TFD}}\, P_{\mathrm{TFD}} = \frac{1}{4}\,\mathbf{1} \tag{B.1.19}$$

as expected, since the TFD is a pure state whose covariance matrix has non vanishing blocks only along the diagonal.

In order to write the Williamson's decompositions of γ_{TFD}, let us observe that the matrices $\Upsilon_{\mathrm{TFD}}^{(\pm)}$ can be diagonalised by the $2N \times 2N$ symplectic and orthogonal matrix O as follows

$$\Upsilon_{\mathrm{TFD}}^{(\pm)} = O^{\mathrm{t}} \Big(\big(\Lambda_{\mathrm{TFD}} \pm \tilde{\Lambda}_{\mathrm{TFD}}\big) \oplus \big(\Lambda_{\mathrm{TFD}} \mp \tilde{\Lambda}_{\mathrm{TFD}}\big) \Big) O \qquad O = \frac{1}{\sqrt{2}} \begin{pmatrix} \mathbf{1} & \mathbf{1} \\ -\mathbf{1} & \mathbf{1} \end{pmatrix} . \tag{B.1.20}$$

By using (B.1.14) and (B.1.15), these matrices can be written as

$$\Upsilon_{\mathrm{TFD}}^{(\pm)} = \frac{1}{2}\, O^{\mathrm{t}} \mathcal{X}_{\mathrm{TFD}}^{\pm 2}\, O \tag{B.1.21}$$

where

$$\mathcal{X}_{\text{TFD}} = \text{diag}\Big(\sqrt{\coth\left(\beta\Omega_1/4\right)}\,,\ldots,\sqrt{\coth\left(\beta\Omega_N/4\right)}\,,\sqrt{\tanh\left(\beta\Omega_1/4\right)}\,,\ldots,\sqrt{\tanh\left(\beta\Omega_N/4\right)}\Big). \tag{B.1.22}$$

Plugging (B.1.3) and (B.1.21) into (B.1.16), one gets the Williamson's decompositions of γ_{TFD} as

$$\gamma_{\text{TFD}} = \frac{1}{2}\, W_{\text{TFD}}^{\text{t}}\, W_{\text{TFD}} \tag{B.1.23}$$

where the $4N \times 4N$ symplectic matrix W_{TFD} is

$$W_{\text{TFD}} = \left(\mathcal{X}_{\text{TFD}}\, O\, S^{-1} V^{\text{t}}\right) \oplus \left(\mathcal{X}_{\text{TFD}}^{-1}\, O\, S\, V^{\text{t}}\right). \tag{B.1.24}$$

It is instructive to express the fact that the TFD is a particular purification of a thermal state (see (B.1.9)) by identifying it within the analysis reported in Sec. 2.6. This can be done by setting $N_{\text{anc}} = N$ and by rewriting the covariance matrix of the TFD in terms of the matrices occurring in (2.6.8).

Comparing (B.1.16) with (2.6.3), we easily conclude that in this case Q_{TFD} and P_{TFD} correspond to Q_{ext} and P_{ext} respectively, while $M_{\text{ext}} = \mathbf{0}$. Then, by employing the block diagonal matrices (B.1.3), (B.1.12) and $V = \widetilde{V} \oplus \widetilde{V}$, where $\widetilde{V}$ is the $N \times N$ orthogonal matrix (see (2.2.42) and (2.7.5)-(2.7.6) for the periodic harmonic chain), we can write Q_{TFD} and P_{TFD} as the partitioned matrices in (2.6.8) with

$$Q = Q_{\text{anc}} = \widetilde{V}\, \mathcal{S}^{-1} \Lambda_{\text{TFD}}\, \mathcal{S}^{-1}\, \widetilde{V}^{\text{t}} \qquad P = P_{\text{anc}} = \widetilde{V}\, \mathcal{S}\, \Lambda_{\text{TFD}}\, \mathcal{S}\, \widetilde{V}^{\text{t}} \tag{B.1.25}$$

and

$$\Gamma_Q \,=\, \widetilde{V}\, \mathcal{S}^{-1} \tilde{\Lambda}_{\text{TFD}}\, \mathcal{S}^{-1}\, \widetilde{V}^{\text{t}} \qquad \Gamma_P \,=\, -\,\widetilde{V}\, \mathcal{S}\, \tilde{\Lambda}_{\text{TFD}}\, \mathcal{S}\, \widetilde{V}^{\text{t}}\,. \tag{B.1.26}$$

We remark that (B.1.25) and (B.1.26) satisfy the conditions in (2.6.18). Furthermore, $Q \oplus P = Q_{\text{anc}} \oplus P_{\text{anc}}$ constructed from (B.1.25) provides the covariance matrix of a thermal state given in (2.2.50), as expected. Thus, the TFD is a purification of the thermal state and its covariance matrix satisfies (2.6.17).

B.2 Complexity of TFD's

The TFD are pure states; hence the complexity of a target TFD with respect to a reference TFD can be computed by employing (2.2.36). In the most general case where the target TFD and the reference TFD originate from different hamiltonians, complicated expressions occur because W_{TFD} depends on the physical hamiltonian through S and V in a non trivial way.

For the sake of simplicity, let us focus on the special case where the same hamiltonian underlies both the target TFD and the reference TFD, which are only distinguished by their inverse temperatures β_{R} and β_{T}. In this case both the reference state and the target state have the same S and V. Moreover, since (B.1.20) tells us that O does not contain parameters, the reference and target states that we are considering can be distinguished only through their matrices $\mathcal{X}_{\text{TFD,R}}$ and $\mathcal{X}_{\text{TFD,T}}$. In this case, by employing (B.1.24) we find that the matrix defined in (2.2.31) crucially simplifies to the following diagonal matrix

$$W_{\text{TFD,TR}} = \left(\mathcal{X}_{\text{TFD,T}}\, \mathcal{X}_{\text{TFD,R}}^{-1}\right) \oplus \left(\mathcal{X}_{\text{TFD,T}}^{-1}\, \mathcal{X}_{\text{TFD,R}}\right). \tag{B.2.1}$$

The circuit complexity corresponding to this choice of TFD's can be obtained by plugging (B.2.1) into (2.2.36). The result reads

$$\mathcal{C}_{\text{TFD}} = \frac{1}{2\sqrt{2}} \sqrt{\text{Tr}\left\{ \left[\log\!\big(\mathcal{X}^2_{\text{TFD,T}} \mathcal{X}^{-2}_{\text{TFD,R}}\big) \right]^2 \oplus \left[\log\!\big(\mathcal{X}^{-2}_{\text{TFD,T}} \mathcal{X}^{2}_{\text{TFD,R}}\big) \right]^2 \right\}} \tag{B.2.2}$$

which can be written more explicitly by employing (B.1.22) for these TFD's, finding

$$\mathcal{C}_{\text{TFD}} = \frac{1}{\sqrt{2}} \sqrt{\sum_{k=1}^{N} \left[\log\!\left(\frac{\coth\left(\beta_{\text{T}}\Omega_k/4\right)}{\coth\left(\beta_{\text{R}}\Omega_k/4\right)} \right) \right]^2} \,. \tag{B.2.3}$$

An interesting regime to consider corresponds to $\beta_{\text{R}}\Omega_k \gg 1$. In this limit the reference state is the product of the ground states of the two parts because only $\boldsymbol{n} = \boldsymbol{0}$ contributes in (B.1.8). In this regime the complexity (B.2.3) simplifies to

$$\mathcal{C}_{\text{TFD}} = \frac{1}{\sqrt{2}} \sqrt{\sum_{k=1}^{N} \left[\log\!\big(\coth\left(\beta_{\text{T}}\Omega_k/4\right)\big) \right]^2} \tag{B.2.4}$$

which is consistent with the results reported in [40].

We find it worth generalising (B.2.3) by considering a circuit where the reference state and the target state correspond to different hamiltonians (with $m_{\text{R}} = m_{\text{T}} \equiv m$) that have the same matrix V_{d} in their decompositions (B.1.2). This is the case e.g. for the periodic harmonic chain explored in Sec. 2.7.1, where $\widetilde{V}$ defined in (2.7.5) and (2.7.6) depends only on the number of sites of the chain, hence it is independent of the parameters occurring in the hamiltonian of the chain. From (B.1.16) and (B.1.19), we have that $\gamma_{\text{TFD}} = Q_{\text{TFD}} \oplus 4Q^{-1}_{\text{TFD}}$, which implies

$$\gamma_{\text{TFD,T}}\, \gamma^{-1}_{\text{TFD,R}} = Q_{\text{TFD,T}}\, Q^{-1}_{\text{TFD,R}} \oplus Q^{-1}_{\text{TFD,T}}\, Q_{\text{TFD,R}} \,. \tag{B.2.5}$$

This allows to write the complexity (2.2.24) as follows

$$\mathcal{C}_{\text{TFD}} = \frac{1}{2\sqrt{2}} \sqrt{\text{Tr}\Big\{ \left[\log(Q_{\text{TFD,T}}\, Q^{-1}_{\text{TFD,R}} \oplus Q^{-1}_{\text{TFD,T}}\, Q_{\text{TFD,R}}) \right]^2 \Big\}} = \frac{1}{2} \sqrt{\text{Tr}\Big\{ \left[\log(Q_{\text{TFD,T}}\, Q^{-1}_{\text{TFD,R}}) \right]^2 \Big\}} \,. \tag{B.2.6}$$

By applying (B.1.17) to this case, where the reference and target states have the same matrix V, the argument of the logarithm in (B.2.6) becomes

$$Q_{\text{TFD,T}}\, Q^{-1}_{\text{TFD,R}} \;=\; V\, S_{\text{T}}^{-1}\, \Upsilon^{(+)}_{\text{TFD,T}}\, S_{\text{T}}^{-1}\, S_{\text{R}}\, \big(4\Upsilon^{(-)}_{\text{TFD,R}}\big)\, S_{\text{R}} V^{\text{t}} \tag{B.2.7}$$

where we have used that $\big(\Upsilon^{(+)}_{\text{TFD,R}}\big)^{-1} = 4\Upsilon^{(-)}_{\text{TFD,R}}$ (see (B.1.18)). The relations in (B.1.3), (B.1.4), (B.1.12) and (B.1.13) lead to write (B.2.7) as follows

$$Q_{\text{TFD,T}}\, Q^{-1}_{\text{TFD,R}} = V \begin{pmatrix} \Lambda_{\text{TR}} & \tilde{\Lambda}_{\text{TR}} \\ \tilde{\Lambda}_{\text{TR}} & \Lambda_{\text{TR}} \end{pmatrix} V^{\text{t}} \tag{B.2.8}$$

where Λ_{TR} and $\tilde{\Lambda}_{\text{TR}}$ are $N \times N$ diagonal matrices whose entries read

$$\begin{aligned} \big(\Lambda_{\text{TR}}\big)_{k,k} &= \frac{\Omega_{\text{R},k}}{\Omega_{\text{T},k}} \left[\coth\left(\beta_{\text{R}}\Omega_{\text{R},k}/2\right) \coth\left(\beta_{\text{T}}\Omega_{\text{T},k}/2\right) - \frac{1}{\sinh\left(\beta_{\text{R}}\Omega_{\text{R},k}/2\right) \sinh\left(\beta_{\text{T}}\Omega_{\text{T},k}/2\right)} \right] \\ \big(\tilde{\Lambda}_{\text{TR}}\big)_{k,k} &= \frac{\Omega_{\text{R},k}}{\Omega_{\text{T},k}} \left[\frac{\coth\left(\beta_{\text{R}}\Omega_{\text{R},k}/2\right)}{\sinh\left(\beta_{\text{T}}\Omega_{\text{T},k}/2\right)} - \frac{\coth\left(\beta_{\text{T}}\Omega_{\text{T},k}/2\right)}{\sinh\left(\beta_{\text{R}}\Omega_{\text{R},k}/2\right)} \right] \qquad 1 \leqslant k \leqslant N \,. \end{aligned} \tag{B.2.9}$$

By adapting the result given in (B.1.20) for $\Upsilon^{(+)}_{\text{TFD}}$, we can diagonalise the matrix containing Λ_{TR} and $\tilde{\Lambda}_{\text{TR}}$ in the r.h.s. of (B.2.8) through the orthogonal matrix O. This leads to write (B.2.8) as follows

$$Q_{\text{TFD,T}}Q^{-1}_{\text{TFD,R}} = VO^{\text{t}}\Big[\big(\Lambda_{\text{TR}}+\tilde{\Lambda}_{\text{TR}}\big)\oplus\big(\Lambda_{\text{TR}}-\tilde{\Lambda}_{\text{TR}}\big)\Big]OV^{\text{t}} \tag{B.2.10}$$

where the entries of the diagonal matrices within the square brackets are given by

$$\big(\Lambda_{\text{TR}}+\tilde{\Lambda}_{\text{TR}}\big)_{k,k} = \frac{\Omega_{\text{R},k}\coth\big(\beta_{\text{T}}\Omega_{\text{T},k}/4\big)}{\Omega_{\text{T},k}\coth\big(\beta_{\text{R}}\Omega_{\text{R},k}/4\big)} \qquad \big(\Lambda_{\text{TR}}-\tilde{\Lambda}_{\text{TR}}\big)_{k,k} = \frac{\Omega_{\text{R},k}\coth\big(\beta_{\text{R}}\Omega_{\text{R},k}/4\big)}{\Omega_{\text{T},k}\coth\big(\beta_{\text{T}}\Omega_{\text{T},k}/4\big)}\,. \tag{B.2.11}$$

Plugging (B.2.10) into (B.2.6), we find that the orthogonal matrices V and O do not contribute to the complexity. By employing also (B.2.11), one obtains

$$\mathcal{C}_{\text{TFD}} = \frac{1}{2}\sqrt{\sum_{k=1}^{N}\left\{\left[\log\left(\frac{\Omega_{\text{R},k}\coth\big(\beta_{\text{R}}\Omega_{\text{R},k}/4\big)}{\Omega_{\text{T},k}\coth\big(\beta_{\text{T}}\Omega_{\text{T},k}/4\big)}\right)\right]^2+\left[\log\left(\frac{\Omega_{\text{R},k}\coth\big(\beta_{\text{T}}\Omega_{\text{T},k}/4\big)}{\Omega_{\text{T},k}\coth\big(\beta_{\text{R}}\Omega_{\text{R},k}/4\big)}\right)\right]^2\right\}}\,. \tag{B.2.12}$$

In the regime $\beta_{\text{R}}\Omega_{\text{R},k}\gg 1$ this expression simplifies to

$$\mathcal{C}_{\text{TFD}} = \frac{1}{2}\sqrt{\sum_{k=1}^{N}\left\{\left[\log\left(\frac{\Omega_{\text{T},k}\coth\big(\beta_{\text{T}}\Omega_{\text{T},k}/4\big)}{\Omega_{\text{R},k}}\right)\right]^2+\left[\log\left(\frac{\Omega_{\text{R},k}\coth\big(\beta_{\text{T}}\Omega_{\text{T},k}/4\big)}{\Omega_{\text{T},k}}\right)\right]^2\right\}} \tag{B.2.13}$$

which is consistent with the results reported in [40][1].

B.3 Mutual complexity of TFD's

It is worth comparing the circuit complexity of two thermal states with the one obtained from the corresponding TFD's. In this subsection we focus on one-dimensional TFD states constructed from two entangled harmonic chains with N sites each, but this analysis can be straightforwardly adapted to higher dimensional lattices. In particular, we consider the one-dimensional version of the Hamiltonian (B.1.1) and then we perform the canonical transformation discussed above (2.7.2). Thus, the parameters determining both the reference and the target states are the dimensionless frequency $\tilde{\omega}$ defined in (2.7.4) and the inverse of the dimensionless temperature $\tilde{\beta}=1/\widetilde{T}$, with $\widetilde{T}$ given by (2.7.26).

Following [79], we introduce the mutual complexity for the TFD's as

$$\mathcal{M}_{\text{TFD}}\big(\tilde{\omega}_{\text{R}},\tilde{\omega}_{\text{T}},\tilde{\beta}_{\text{R}},\tilde{\beta}_{\text{T}}\big) = 2\,\mathcal{C}^2_{\text{th}}\big(\tilde{\omega}_{\text{R}},\tilde{\omega}_{\text{T}},\tilde{\beta}_{\text{R}},\tilde{\beta}_{\text{T}}\big)-\mathcal{C}^2_{\text{TFD}}\big(\tilde{\omega}_{\text{R}},\tilde{\omega}_{\text{T}},\tilde{\beta}_{\text{R}},\tilde{\beta}_{\text{T}}\big) \tag{B.3.1}$$

where $\mathcal{C}_{\text{th}}$ and $\mathcal{C}_{\text{TFD}}$ are given by (2.7.30) and (B.2.12) respectively and, for the sake of clarity, we have specified all the parameters on which these quantities depend. More explicitly, (B.3.1) reads

$$\begin{aligned}\mathcal{M}_{\text{TFD}}\big(\tilde{\omega}_{\text{R}},\tilde{\omega}_{\text{T}},\tilde{\beta}_{\text{R}},\tilde{\beta}_{\text{T}}\big) &= \\ &= \frac{1}{4}\sum_{k=1}^{N}\left\{\left[\log\left(\frac{\Omega_{\text{R},k}\coth\big(\tilde{\beta}_{\text{R}}\Omega_{\text{R},k}/2\big)}{\Omega_{\text{T},k}\coth\big(\tilde{\beta}_{\text{T}}\Omega_{\text{T},k}/2\big)}\right)\right]^2-\left[\log\left(\frac{\Omega_{\text{R},k}\coth\big(\tilde{\beta}_{\text{R}}\Omega_{\text{R},k}/4\big)}{\Omega_{\text{T},k}\coth\big(\tilde{\beta}_{\text{T}}\Omega_{\text{T},k}/4\big)}\right)\right]^2\right. \\ &\qquad\left.+\left[\log\left(\frac{\Omega_{\text{R},k}\coth\big(\tilde{\beta}_{\text{T}}\Omega_{\text{T},k}/2\big)}{\Omega_{\text{T},k}\coth\big(\tilde{\beta}_{\text{R}}\Omega_{\text{R},k}/2\big)}\right)\right]^2-\left[\log\left(\frac{\Omega_{\text{R},k}\coth\big(\tilde{\beta}_{\text{T}}\Omega_{\text{T},k}/4\big)}{\Omega_{\text{T},k}\coth\big(\tilde{\beta}_{\text{R}}\Omega_{\text{R},k}/4\big)}\right)\right]^2\right\}\end{aligned} \tag{B.3.2}$$

[1] See Eq. (192) of [40] at $t=0$.

where the dispersion relations $\Omega_{\mathrm{S},k}$ are given by (2.7.19). The mutual complexity in (B.3.2) can be written also in terms of $\Omega_{\mathrm{M,N},k}$ defined in (2.7.31) as follows

$$\begin{aligned}\mathcal{M}_{\mathrm{TFD}}\big(\tilde{\omega}_{\mathrm{R}},\tilde{\omega}_{\mathrm{T}},\tilde{\beta}_{\mathrm{R}},\tilde{\beta}_{\mathrm{T}}\big) \;=\; & \frac{1}{4}\sum_{k=1}^{N}\Bigg\{\left[\log\left(\frac{\Omega_{\mathrm{R,R},k}}{\Omega_{\mathrm{T,T},k}}\right)\right]^2+\left[\log\left(\frac{\Omega_{\mathrm{R,T},k}}{\Omega_{\mathrm{T,R},k}}\right)\right]^2 \\ & -\left[\log\left(\frac{\Omega_{\mathrm{R,R},k}}{\Omega_{\mathrm{T,T},k}}\right)+\log\left(\frac{\cosh\left(\tilde{\beta}_{\mathrm{T}}\Omega_{\mathrm{T},k}/2\right)\left(\cosh\left(\tilde{\beta}_{\mathrm{R}}\Omega_{\mathrm{R},k}/2\right)-1\right)}{\cosh\left(\tilde{\beta}_{\mathrm{R}}\Omega_{\mathrm{R},k}/2\right)\left(\cosh\left(\tilde{\beta}_{\mathrm{T}}\Omega_{\mathrm{T},k}/2\right)-1\right)}\right)\right]^2 \\ & -\left[\log\left(\frac{\Omega_{\mathrm{R,T},k}}{\Omega_{\mathrm{T,R},k}}\right)+\log\left(\frac{\cosh\left(\tilde{\beta}_{\mathrm{R}}\Omega_{\mathrm{R},k}/2\right)\left(\cosh\left(\tilde{\beta}_{\mathrm{T}}\Omega_{\mathrm{T},k}/2\right)-1\right)}{\cosh\left(\tilde{\beta}_{\mathrm{T}}\Omega_{\mathrm{T},k}/2\right)\left(\cosh\left(\tilde{\beta}_{\mathrm{R}}\Omega_{\mathrm{R},k}/2\right)-1\right)}\right)\right]^2\Bigg\}.\end{aligned} \tag{B.3.3}$$

After expanding the squares and a bit of manipulation, one obtains

$$\begin{aligned}\mathcal{M}_{\mathrm{TFD}}\big(\tilde{\omega}_{\mathrm{R}},\tilde{\omega}_{\mathrm{T}},\tilde{\beta}_{\mathrm{R}},\tilde{\beta}_{\mathrm{T}}\big) \;&=\; \frac{1}{2}\sum_{k=1}^{N}F_{\mathrm{TR},k}\left\{2\log\left[\frac{\coth\left(\tilde{\beta}_{\mathrm{T}}\Omega_{\mathrm{T},k}/2\right)}{\coth\left(\tilde{\beta}_{\mathrm{R}}\Omega_{\mathrm{R},k}/2\right)}\right]-F_{\mathrm{TR},k}\right\} \\ &=\; \frac{1}{2}\sum_{k=1}^{L}F_{\mathrm{TR},k}\left\{\log\left[\frac{\coth^2\left(\tilde{\beta}_{\mathrm{T}}\Omega_{\mathrm{T},k}/2\right)\cosh\left(\tilde{\beta}_{\mathrm{R}}\Omega_{\mathrm{R},k}/2\right)\left(\cosh\left(\tilde{\beta}_{\mathrm{T}}\Omega_{\mathrm{T},k}/2\right)-1\right)}{\coth^2\left(\tilde{\beta}_{\mathrm{R}}\Omega_{\mathrm{R},k}/2\right)\cosh\left(\tilde{\beta}_{\mathrm{T}}\Omega_{\mathrm{T},k}/2\right)\left(\cosh\left(\tilde{\beta}_{\mathrm{R}}\Omega_{\mathrm{R},k}/2\right)-1\right)}\right]\right\}\end{aligned} \tag{B.3.4}$$

where

$$F_{\mathrm{TR},k}=\log\left(\frac{\cosh\left(\tilde{\beta}_{\mathrm{T}}\Omega_{\mathrm{T},k}/2\right)\left(\cosh\left(\tilde{\beta}_{\mathrm{R}}\Omega_{\mathrm{R},k}/2\right)-1\right)}{\cosh\left(\tilde{\beta}_{\mathrm{R}}\Omega_{\mathrm{R},k}/2\right)\left(\cosh\left(\tilde{\beta}_{\mathrm{T}}\Omega_{\mathrm{T},k}/2\right)-1\right)}\right). \tag{B.3.5}$$

For fixed k, the argument of the sum in (B.3.4) only depends on $\tilde{\beta}_{\mathrm{T}}\Omega_{\mathrm{T},k}$ and $\tilde{\beta}_{\mathrm{R}}\Omega_{\mathrm{R},k}$ and it is symmetric under the exchange of T and R; hence we can fix $\tilde{\beta}_{\mathrm{T}}\Omega_{\mathrm{T},k}>\tilde{\beta}_{\mathrm{R}}\Omega_{\mathrm{R},k}$ for every k without loss of generality. This allows to show that every term of the sum (B.3.4) is negative[2] and therefore $\mathcal{M}_{\mathrm{TFD}}\big(\tilde{\omega}_{\mathrm{R}},\tilde{\omega}_{\mathrm{T}},\tilde{\beta}_{\mathrm{R}},\tilde{\beta}_{\mathrm{T}}\big)$ is always negative.

The thermodynamic limit $N\to\infty$ of (B.3.2) gives

$$\mathcal{M}_{\mathrm{TFD}}\big(\tilde{\omega}_{\mathrm{R}},\tilde{\omega}_{\mathrm{T}},\tilde{\beta}_{\mathrm{R}},\tilde{\beta}_{\mathrm{T}}\big)\;=\;a_{\mathrm{TFD}}\big(\tilde{\omega}_{\mathrm{R}},\tilde{\omega}_{\mathrm{T}},\tilde{\beta}_{\mathrm{R}},\tilde{\beta}_{\mathrm{T}}\big)\,N+\dots \tag{B.3.6}$$

where the coefficient of the linear divergence can be written in terms $\Omega_{\mathrm{S},\theta}$ in (2.7.22) as

$$\begin{aligned}a_{\mathrm{TFD}}\big(\tilde{\omega}_{\mathrm{R}},\tilde{\omega}_{\mathrm{T}},\tilde{\beta}_{\mathrm{R}},\tilde{\beta}_{\mathrm{T}}\big) \;&= \\ &=\;\frac{1}{4\pi}\int_0^{\pi}\Bigg\{\left[\log\left(\frac{\Omega_{\mathrm{R},\theta}\coth\left(\tilde{\beta}_{\mathrm{R}}\Omega_{\mathrm{R},\theta}/2\right)}{\Omega_{\mathrm{T},\theta}\coth\left(\tilde{\beta}_{\mathrm{T}}\Omega_{\mathrm{T},\theta}/2\right)}\right)\right]^2-\left[\log\left(\frac{\Omega_{\mathrm{R},\theta}\coth\left(\tilde{\beta}_{\mathrm{R}}\Omega_{\mathrm{R},\theta}/4\right)}{\Omega_{\mathrm{T},\theta}\coth\left(\tilde{\beta}_{\mathrm{T}}\Omega_{\mathrm{T},\theta}/4\right)}\right)\right]^2 \\ &\qquad+\left[\log\left(\frac{\Omega_{\mathrm{R},\theta}\coth\left(\tilde{\beta}_{\mathrm{T}}\Omega_{\mathrm{T},\theta}/2\right)}{\Omega_{\mathrm{T},\theta}\coth\left(\tilde{\beta}_{\mathrm{R}}\Omega_{\mathrm{R},\theta}/2\right)}\right)\right]^2-\left[\log\left(\frac{\Omega_{\mathrm{R},\theta}\coth\left(\tilde{\beta}_{\mathrm{T}}\Omega_{\mathrm{T},\theta}/4\right)}{\Omega_{\mathrm{T},\theta}\coth\left(\tilde{\beta}_{\mathrm{R}}\Omega_{\mathrm{R},\theta}/4\right)}\right)\right]^2\Bigg\}\,d\theta\,.\end{aligned} \tag{B.3.7}$$

We remark that the massless limit of $\mathcal{M}_{\mathrm{TFD}}/N$ diverges when $N<\infty$, while it is finite once $N\to\infty$ is considered. Indeed, by setting $\tilde{\omega}_{\mathrm{R}}=\tilde{\omega}_{\mathrm{T}}=0$ in (B.3.7) we find

$$\begin{aligned}a_{\mathrm{TFD}}\big(\tilde{\omega}_{\mathrm{R}}=0,\tilde{\omega}_{\mathrm{T}}=0,\tilde{\beta}_{\mathrm{R}},\tilde{\beta}_{\mathrm{T}}\big) \;&= \\ &=\int_0^{\pi}\left\{\left[\log\left(\frac{\coth\left(\tilde{\beta}_{\mathrm{R}}\sin\theta\right)}{\coth\left(\tilde{\beta}_{\mathrm{T}}\sin\theta\right)}\right)\right]^2-\left[\log\left(\frac{\coth\left(\tilde{\beta}_{\mathrm{R}}\sin\theta/2\right)}{\coth\left(\tilde{\beta}_{\mathrm{T}}\sin\theta/2\right)}\right)\right]^2\right\}\frac{d\theta}{2\pi}\,.\end{aligned} \tag{B.3.8}$$

[2] We use that $\frac{\cosh(x/2)}{\cosh(x/2)-1}$ is a monotonically decreasing function and that $\frac{\coth^2(x/2)(\cosh(x/2)-1)}{\cosh(x/2)}$ is a monotonically increasing function when $x>0$. This implies that $F_{\mathrm{TR},k}<0$, while the function within the curly brackets in the last sum of (B.3.4) is positive for any value of k.

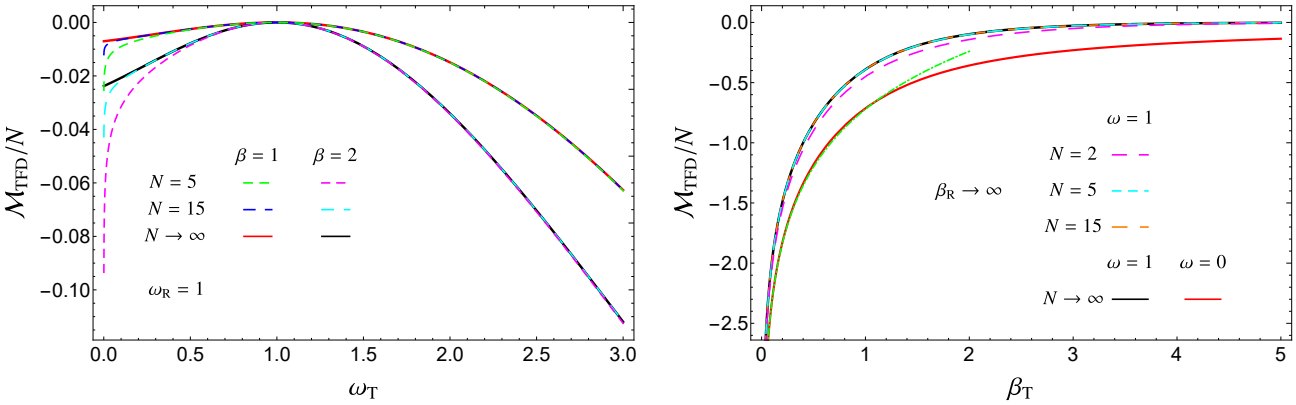

Figure B.1: Comparison between the mutual complexity for the TFD state (B.3.2) and its thermodynamic limit in the periodic harmonic chain (here $m = 1$ and $\kappa_{\rm R} = \kappa_{\rm T} = 1$). In the left panel we show $\mathcal{M}_{\rm TFD}/N$ as function of $\omega_{\rm T}$ setting $\omega_{\rm R} = 1$ and considering two values of $\beta_{\rm R} = \beta_{\rm T} \equiv \beta$ and two values of N (dashed curves). We also report $a_{\rm TFD}$ in (B.3.7) for the same values of the parameters (solid curves). In the right panel the dependence on $\beta_{\rm T}$ is investigated by plotting (B.3.2) for three different values of N (dashed curves) and (B.3.7) (black solid curve) both for $\beta_{\rm R} \to \infty$ and $\omega_{\rm R} = \omega_{\rm T} \equiv \omega = 1$. The massless limit in (B.3.9) is also reported (red solid curve) and its small $\beta_{\rm T}$ behaviour in (B.3.10) is checked (green dot-dashed curve).

This feature has been observed also for the complexity of pure states (Sec. 2.7.2) and for the complexity of thermal states (Sec. 2.7.3).

In the limit $\tilde{\beta}_{\rm R} \to \infty$ both the TFD in (B.1.8) and the thermal reference state become the product of two ground states. In this regime, (B.3.8) slightly simplifies to

$$a_{\rm TFD}\big(\tilde{\omega}_{\rm R} = 0, \tilde{\omega}_{\rm T} = 0, \tilde{\beta}_{\rm R} \to \infty, \tilde{\beta}_{\rm T}\big) \;\; = \;\; = \int_0^\pi \left\{ \left[\log\left(\coth\left(\tilde{\beta}_{\rm T} \sin\theta \right) \right) \right]^2 - \left[\log\left(\coth\left(\tilde{\beta}_{\rm T} \sin\theta/2 \right) \right) \right]^2 \right\} \frac{d\theta}{2\pi} \tag{B.3.9}$$

which depends only on $\tilde{\beta}_{\rm T}$ and can be easily studied. This function is negative for every value of $\tilde{\beta}_{\rm T}$ and it vanishes when $\tilde{\beta}_{\rm T} \to \infty$, as expected. When $\tilde{\beta}_{\rm T} \to 0$ in (B.3.9), we find the following logarithmic divergence

$$a_{\rm TFD}\big(\tilde{\omega}_{\rm R} = 0, \tilde{\omega}_{\rm T} = 0, \tilde{\beta}_{\rm R} \to \infty, \tilde{\beta}_{\rm T}\big) \;=\; \log 2 \left(\log \tilde{\beta}_{\rm T} - \frac{3}{2} \log 2 \right) + \dots \; . \tag{B.3.10}$$

In Fig. B.1 we compare the mutual complexity for the TFD in (B.3.2) with its thermodynamic limit in (B.3.6) for various values of the parameters. In the left panel we show $\mathcal{M}_{\rm TFD}/N$ (dashed lines) as function of $\omega_{\rm T}$ for fixed $\omega_{\rm R} = 1$ and for two values of $\beta_{\rm R} = \beta_{\rm T} \equiv \beta$. As N increases, the dashed curves approach the solid curves representing $a_{\rm TFD}$ given in (B.3.7). When $\omega_{\rm T} \to 0$, $\mathcal{M}_{\rm TFD}/N$ evalueted for finite N diverges, while its thermodynamic limit is finite, as observed above. In the right panel we show $\mathcal{M}_{\rm TFD}/N$ as function of $\beta_{\rm T}$ when $\beta_{\rm R} \to \infty$ and $\omega_{\rm R} = \omega_{\rm T} \equiv \omega = 1$. Remarkably, the curves obtained for finite number of sites coincide with their thermodynamic limit already for $N = 5$. In the same panel we plot $a_{\rm TFD}\big(\omega_{\rm R} = 0, \omega_{\rm T} = 0, \beta_{\rm R} \to \infty, \beta_{\rm T}\big)$ in (B.3.9) (red solid curve), checking also that its behaviour for $\beta_{\rm T} \ll 1$ is well reproduced by (B.3.10) (green dot-dashed curve).

Let us conclude this appendix by mentioning that a holographic proposal for the mutual complexity of the TFD states have been investigated in [79]. When the gravitational background is

the eternal black hole, which is the gravitational dual of the TFD state [139], and the subregions L and R are constant time-slices of the two disconnected boundaries where the two copies of the same CFT are defined, the definition of the holographic mutual complexity (2.7.48) becomes [79]

$$\mathcal{M}_{\rm AdS}({\rm TFD}) = \mathcal{C}_{\rm AdS}({\rm L}) + \mathcal{C}_{\rm AdS}({\rm R}) - \mathcal{C}_{\rm AdS}({\rm TFD}) \tag{B.3.11}$$

It has been shown that the mutual complexity (B.3.11) is negative in any number of spacetime dimensions for all the three proposals for the holographic complexity mentioned in Sec. 2.7.7 [46,79]. This qualitatively agrees with the results that we have obtained in this appendix for the mutual complexity given in (B.3.1) and (B.3.2).

Appendix C

Correlators in harmonic chains

In this appendix we report the two-point correlation functions of the harmonic chains employed throughout the thesis. In Appendix C.1 we consider harmonic chains at equilibrium either in their ground state or in a thermal state, while in Appendix C.2 we focus on harmonic chains driven out of equilibrium by a global quantum quench of the frequency parameter.

C.1 Harmonic chains at equilibrium

In this appendix we report the correlators of harmonic chains at equilibrium. We consider finite chains either with periodic boundary conditions (Appendix C.1.1) or with Dirichlet boundary conditions imposed at their endpoints (Appendix C.1.2). In both the cases we also take the thermodynamic limit which leads to harmonic chains respectively on the infinite line and on the semi-infinite line with Dirichlet boundary conditions imposed at its origin.

C.1.1 Harmonic chains with periodic boundary conditions

The periodic harmonic chain made by N sites is defined by the Hamiltonian (2.7.1) with boundary conditions given by $\hat{q}_{N+1} = \hat{q}_1$ and $\hat{p}_{N+1} = \hat{p}_1$. By introducing the creation and annihilation operators in the standard way, for the ground state one finds the following two-point correlators

$$\langle \hat{q}_i \hat{q}_j \rangle = \frac{1}{2N} \sum_{k=1}^{N} \frac{1}{m\Omega_k} \cos[2\pi k\,(i-j)/N] \qquad \langle \hat{p}_i \hat{p}_j \rangle = \frac{1}{2N} \sum_{k=1}^{N} \Omega_k \cos[2\pi k\,(i-j)/N] \tag{C.1.1}$$

where the dispersion relation is given by

$$\Omega_k = \sqrt{\omega^2 + \frac{4\kappa}{m} \big[\sin\big(\pi k/N\big)\big]^2} \qquad 1 \leqslant k \leqslant N\,. \tag{C.1.2}$$

The translation invariance induces the occurrence of the zero mode, that corresponds to $k = N$. Since $\Omega_N = \omega$, it is straightforward to observe that $\langle \hat{q}_i \hat{q}_j \rangle$ diverges as $\omega \to 0$; hence the mass cannot be set to zero in the numerical analysis of this system.

We also consider the periodic harmonic chain in the thermal state with temperature T. For this state the correlators read

$$\langle \hat{q}_i \hat{q}_j \rangle_T = \frac{1}{2N} \sum_{k=1}^{N} \frac{\coth[\Omega_k/(2T)]}{m\Omega_k} \cos[2\pi k\,(i-j)/N] \tag{C.1.3}$$

$$\langle \hat{p}_i \hat{p}_j \rangle_T = \frac{1}{2N} \sum_{k=1}^{N} m\Omega_k \coth[\Omega_k/(2T)] \cos[2\pi k\,(i-j)/N] \tag{C.1.4}$$

where Ω_k is given by (C.1.2). Also in this case the correlator in (C.1.3) diverges as $\omega \to 0$ because of the occurrence of the zero mode at $k = N$. Let us stress that when $T \to 0$ the correlators (C.1.1) are retrieved from (C.1.3) and (C.1.4).

In the thermodynamic limit $N \to \infty$ the correlators (C.1.1) for the ground state become [27]

$$\langle \hat{q}_i \hat{q}_j \rangle \;=\; \frac{\zeta^{i-j+1/2}}{2\sqrt{\kappa m}} \binom{i-j-1/2}{i-j} {}_2F_1\big(1/2\,, i-j+1/2\,, i-j+1\,, \zeta^2\big) \tag{C.1.5}$$

$$\langle \hat{p}_i \hat{p}_j \rangle \;=\; \frac{\sqrt{\kappa m}\;\zeta^{i-j-1/2}}{2} \binom{i-j-3/2}{i-j} {}_2F_1\big(-1/2\,, i-j-1/2\,, i-j+1\,, \zeta^2\big) \tag{C.1.6}$$

where $\zeta \equiv \big(\omega - \sqrt{\omega^2 + 4\kappa/m}\,\big)^2 (4\kappa/m)$. As for the correlators (C.1.3) and (C.1.4) at finite temperature, in the thermodynamic limit they become

$$\langle \hat{q}_i \hat{q}_j \rangle_T \;=\; \frac{1}{2\pi} \int_0^\pi \frac{\coth[\Omega_\theta/(2T)]}{m\Omega_\theta} \cos[2\theta\,(i-j)]\, d\theta \tag{C.1.7}$$

$$\langle \hat{p}_i \hat{p}_j \rangle_T \;=\; \frac{1}{2\pi} \int_0^\pi m\Omega_\theta \coth[\Omega_\theta/(2T)] \cos[2\theta\,(i-j)]\, d\theta\,. \tag{C.1.8}$$

where $\Omega_\theta \equiv \sqrt{\omega^2 + (4\kappa/m)\,(\sin\theta)^2}$.

These two-point functions have been exploited in chapter 2 and in the numerical analyses reported in chapters 5, 6, 8 and 9.

C.1.2 Harmonic chains with Dirichlet boundary conditions

The harmonic chain made by N sites on a segment with Dirichlet boundary conditions is defined by the Hamiltonian (2.7.1) with $\hat{q}_0 = \hat{q}_N = \hat{q}_{N+1} = 0$ and $\hat{p}_0 = \hat{p}_N = 0$ imposed at its endpoints.

The two-point correlators $\langle \hat{q}_i \hat{q}_j \rangle$ and $\langle \hat{p}_i \hat{p}_j \rangle$ in the ground state read respectively [558]

$$\langle \hat{q}_i \hat{q}_j \rangle = \frac{1}{N} \sum_{k=1}^{N-1} \frac{1}{m\Omega_k} \sin(\pi k\, i/N) \sin(\pi k\, j/N) \tag{C.1.9}$$

$$\langle \hat{p}_i \hat{p}_j \rangle = \frac{1}{N} \sum_{k=1}^{N-1} m\Omega_k \sin(\pi k\, i/N) \sin(\pi k\, j/N) \tag{C.1.10}$$

where the dispersion relation is

$$\Omega_k \equiv \sqrt{\omega^2 + \frac{4\kappa}{m} \big[\sin(\pi k/(2N))\big]^2} \qquad 1 \leqslant k \leqslant N-1\,. \tag{C.1.11}$$

In contrast with the harmonic chain in the infinite line (see Appendix C.1.1), this harmonic chain is not translation invariant; hence the zero mode does not occur and the massless limit $\omega \to 0$ is well defined because the correlators (C.1.9) and (C.1.10) are finite.

In the thermodynamic limit, the correlators (C.1.9) and (C.1.10) can be written respectively as follows

$$\langle \hat{q}_i \hat{q}_j \rangle \;=\; \frac{1}{m\omega\sqrt{1+\kappa_\omega}} \Big\{ F_+(|i-j|) - F_+(i+j) \Big\} \tag{C.1.12}$$

$$\langle \hat{p}_i \hat{p}_j \rangle \;=\; m\omega\sqrt{1+\kappa_\omega} \Big\{ F_-(|i-j|) - F_-(i+j) \Big\} \tag{C.1.13}$$

where the functions $F_{\pm}(n)$ are defined as follows

$$F_{\pm}(n) \equiv \left(\frac{2(1+\kappa_\omega)}{\kappa_\omega}\right)^{\pm 1/2} \frac{\Gamma(n \pm 1/2)\,\zeta^{n\pm 1/2}}{n!\,2\,\Gamma(\pm 1/2)}\; {}_2F_1\big(\pm 1/2\,, n \pm 1/2\,, n+1\,, \zeta^2\big) \tag{C.1.14}$$

with $\kappa_\omega \equiv 2\kappa/(m\omega^2)$ and ζ given below (C.1.6).

In the massless regime, which corresponds to $\omega = 0$, the expressions (C.1.12) and (C.1.13) significantly simplify and become the correlators found in [211], which are written in terms of the digamma function $\psi(z)$ respectively as

$$\langle \hat{q}_i \hat{q}_j \rangle = \frac{1}{2\pi\sqrt{\kappa m}} \Big(\psi(1/2+i+j) - \psi(1/2+i-j) \Big) \tag{C.1.15}$$

$$\langle \hat{p}_i \hat{p}_j \rangle = \frac{2\sqrt{\kappa m}}{\pi} \left(\frac{1}{4(i+j)^2-1} - \frac{1}{4(i-j)^2-1} \right). \tag{C.1.16}$$

These two-point functions have been exploited for obtaining some of the numerical results reported in chapter 5 (see Sec. 5.4).

C.2 Harmonic chains after a global quantum quench

In this appendix we discuss the temporal evolution of the correlators of harmonic chains after a global quantum quench of the frequency parameter. In Appendix C.2.1 we report the explicit expressions of the two-point functions both for finite and infinite chains, while in Appendix C.2.2 we discuss their large time limit which can also be obtained through the Generalised Gibbs Ensamble.

C.2.1 Temporal evolution of the correlators

In this appendix we report the correlators of the harmonic chain made by N sites defined by the Hamiltonian (2.7.1) after the global quench $\omega_0 \to \omega$ of the frequency parameter.

When PBC are imposed, the two-point correlators read

$$\begin{aligned}
\langle \psi_0 |\, \hat{q}_i(t)\, \hat{q}_j(t)\, | \psi_0 \rangle &= \frac{1}{N} \sum_{k=1}^{N} Q_k(t)\, \cos\big[(i-j)\, 2\pi k/N\big] \\
\langle \psi_0 |\, \hat{p}_i(t)\, \hat{p}_j(t)\, | \psi_0 \rangle &= \frac{1}{N} \sum_{k=1}^{N} P_k(t)\, \cos\big[(i-j)\, 2\pi k/N\big] \\
\mathrm{Re}\big[\langle \psi_0 |\, \hat{q}_i(t)\, \hat{p}_j(t)\, | \psi_0 \rangle\big] &= \frac{1}{N} \sum_{k=1}^{N} M_k(t)\, \cos\big[(i-j)\, 2\pi k/N\big]
\end{aligned} \tag{C.2.1}$$

where $1 \leqslant i, j \leqslant N$; while for DBC one has the following correlators

$$\begin{aligned}
\langle \psi_0 |\, \hat{q}_i(t)\, \hat{q}_j(t)\, | \psi_0 \rangle &= \frac{2}{N} \sum_{k=1}^{N} Q_k(t)\, \sin\big(i\,\pi k/N\big)\, \sin\big(j\,\pi k/N\big) \\
\langle \psi_0 |\, \hat{p}_i(t)\, \hat{p}_j(t)\, | \psi_0 \rangle &= \frac{2}{N} \sum_{k=1}^{N} P_k(t)\, \sin\big(i\,\pi k/N\big)\, \sin\big(j\,\pi k/N\big) \\
\mathrm{Re}\big[\langle \psi_0 |\, \hat{q}_i(t)\, \hat{p}_j(t)\, | \psi_0 \rangle\big] &= \frac{2}{N} \sum_{k=1}^{N} M_k(t)\, \sin\big(i\,\pi k/N\big)\, \sin\big(j\,\pi k/N\big)
\end{aligned} \tag{C.2.2}$$

where $1 \leqslant i, j \leqslant N-1$. In these correlators, the functions $Q_k(t)$, $P_k(t)$ and $M_k(t)$ are given by (3.2.5), with either (3.3.1) for PBC or (3.3.3) for DBC.

For the infinite harmonic chain on the line, we take $N \to \infty$ of (C.2.1), finding

$$\begin{aligned}
\langle\psi_0|\,\hat{q}_i(t)\,\hat{q}_j(t)\,|\psi_0\rangle &= \frac{1}{\pi}\int_0^\pi Q_\theta(t)\cos\big[2\theta\,(i-j)\,\big]\,d\theta \\
\langle\psi_0|\,\hat{p}_i(t)\,\hat{p}_j(t)\,|\psi_0\rangle &= \frac{1}{\pi}\int_0^\pi P_\theta(t)\cos\big[2\theta\,(i-j)\,\big]\,d\theta \\
\mathrm{Re}\big[\langle\psi_0|\,\hat{q}_i(t)\,\hat{p}_j(t)\,|\psi_0\rangle\big] &= \frac{1}{\pi}\int_0^\pi M_\theta(t)\cos\big[2\theta\,(i-j)\,\big]\,d\theta
\end{aligned} \tag{C.2.3}$$

where $i, j \in \mathbb{Z}$; while, for the harmonic chain on the semi-infinite line with DBC, the limit $N \to \infty$ of (C.2.2) leads to

$$\begin{aligned}
\langle\psi_0|\,\hat{q}_i(t)\,\hat{q}_j(t)\,|\psi_0\rangle &= \frac{2}{\pi}\int_0^\pi Q_\theta(t)\sin(i\theta)\sin(j\theta)\,d\theta \\
\langle\psi_0|\,\hat{p}_i(t)\,\hat{p}_j(t)\,|\psi_0\rangle &= \frac{2}{\pi}\int_0^\pi P_\theta(t)\sin(i\theta)\sin(j\theta)\,d\theta \\
\mathrm{Re}\big[\langle\psi_0|\,\hat{q}_i(t)\,\hat{p}_j(t)\,|\psi_0\rangle\big] &= \frac{2}{\pi}\int_0^\pi M_\theta(t)\sin(i\theta)\sin(j\theta)\,d\theta
\end{aligned} \tag{C.2.4}$$

where $i, j > 0$. The functions $Q_\theta(t)$, $P_\theta(t)$ and $M_\theta(t)$ in these integrands are given by (3.2.5) where $\Omega_{0,k}$ and Ω_k are replaced respectively by $\Omega_{0,\theta}$ and Ω_θ, which are (3.3.20) for the infinite line and

$$\Omega_{0,\theta} = \sqrt{\omega_0^2 + \frac{4\kappa}{m}\,[\sin(\theta/2)]^2} \qquad \Omega_\theta = \sqrt{\omega^2 + \frac{4\kappa}{m}\,[\sin(\theta/2)]^2}\,. \tag{C.2.5}$$

for the semi-infinite line.

These correlators have been exploited in chapter 3 and in the numerical analyses reported in chapters 3 and 7.

C.2.2 GGE correlators

In the following we report the explicit expressions of the correlators for the harmonic chains in the GGE state which have been employed to construct the reduced covariance matrix $\gamma_{\mathrm{GGE},A}$ from the covariance matrix γ_{GGE} defined in (3.5.4). The matrix $\gamma_{\mathrm{GGE},A}$ occurs in the expression (3.5.24) for the complexity $\mathcal{C}_{\mathrm{GGE},A}$.

For PBC, we obtain

$$\mathrm{Tr}\big(\hat{q}_i\,\hat{q}_j\,\hat{\rho}_{\mathrm{GGE}}\big) = \frac{1}{N}\sum_{k=1}^{N}\frac{\Omega_{0,k}^2+\Omega_k^2}{4\,\Omega_k^2\,\Omega_{0,k}}\,\cos\big[(i-j)\,2\pi k/N\,\big] \tag{C.2.6}$$

$$\mathrm{Tr}\big(\hat{p}_i\,\hat{p}_j\,\hat{\rho}_{\mathrm{GGE}}\big) = \frac{1}{N}\sum_{k=1}^{N}\frac{\Omega_{0,k}^2+\Omega_k^2}{4\,\Omega_{0,k}}\,\cos\big[(i-j)\,2\pi k/N\,\big] \tag{C.2.7}$$

in terms of the dispersion relations (3.3.1). Notice that the correlators (C.2.6) diverge when $\omega = 0$; hence for PBC the massless limit must be studied by taking ω very small, but non vanishing. In the thermodynamic limit $N \to \infty$, these correlators become respectively

$$\int_0^\pi \frac{\Omega_{0,\theta}^2+\Omega_\theta^2}{\Omega_\theta^2\,\Omega_{0,\theta}}\,\cos\big[2\theta\,(i-j)\,\big]\,\frac{d\theta}{4\pi} \qquad \int_0^\pi \frac{\Omega_{0,\theta}^2+\Omega_\theta^2}{\Omega_{0,\theta}}\,\cos\big[2\theta\,(i-j)\,\big]\,\frac{d\theta}{4\pi} \tag{C.2.8}$$

where the dispersion relations are given in (3.3.20).

When DBC are imposed, we obtain

$$\mathrm{Tr}\big(\hat{q}_i\,\hat{q}_j\,\hat{\rho}_{\rm GGE}\big) \;=\; \frac{2}{N}\sum_{k=1}^{N-1}\frac{\Omega_{0,k}^2+\Omega_k^2}{4\,\Omega_k^2\,\Omega_{0,k}}\,\sin\big(\pi ki/N\big)\,\sin\big(\pi kj/N\big) \tag{C.2.9}$$

$$\mathrm{Tr}\big(\hat{p}_i\,\hat{p}_j\,\hat{\rho}_{\rm GGE}\big) \;=\; \frac{2}{N}\sum_{k=1}^{N-1}\frac{\Omega_{0,k}^2+\Omega_k^2}{4\,\Omega_{0,k}}\,\sin\big(\pi ki/N\big)\,\sin\big(\pi kj/N\big) \tag{C.2.10}$$

in terms of the dispersion relations (3.3.3). Notice that, in this case, all these correlators are finite when $\omega = 0$. The thermodynamic limit $N \to \infty$ of these correlators gives respectively

$$\int_0^\pi \frac{\Omega_{0,\theta}^2+\Omega_\theta^2}{\Omega_\theta^2\,\Omega_{0,\theta}}\sin(i\theta)\sin(j\theta)\,\frac{d\theta}{2\pi} \qquad\qquad \int_0^\pi \frac{\Omega_{0,\theta}^2+\Omega_\theta^2}{\Omega_{0,\theta}}\sin(i\theta)\sin(j\theta)\,\frac{d\theta}{2\pi} \tag{C.2.11}$$

where (C.2.5) must be employed.

These correlators have been used in chapter 3 (see Sec. 3.5) for studying the asymptotic values of the subsystem complexity after a global quench.

As consistency check of the fact that the GGE describes the limit $t \to \infty$ after the global quench, one observes that the correlators in (C.2.8) and (C.2.11) are recovered by taking (C.2.3) and (C.2.4) respectively and replacing all the oscillatory functions with their averages (i.e. $[\sin(\Omega_\theta t)]^2$ and $[\cos(\Omega_\theta t)]^2$ by $1/2$ and $\sin(\Omega_\theta t)$ by 0).

Bibliography

[1] E. Schrödinger, *"Probability relations between separated systems"*, Math. Proc. Camb. Philos. Soc. 32, 446–4520 (1936).

[2] A. Einstein, B. Podolsky and N. Rosen, *"Can Quantum-Mechanical Description of Physical Reality Be Considered Complete?"*, Phys. Rev. 47, 777 (1935).

[3] L. Amico, R. Fazio, A. Osterloh and V. Vedral, *"Entanglement in many-body systems"*, Rev. Mod. Phys. 80, 517 (2008), quant-ph/0703044.

[4] I. Peschel and V. Eisler, *"Reduced density matrices and entanglement entropy in free lattice models"*, J. Phys. A 42, 504003 (2009), arxiv:0906.1663.

[5] J. Eisert, M. Cramer and M. Plenio, *"Area laws for the entanglement entropy - a review"*, Rev. Mod. Phys. 82, 277 (2010), arxiv:0808.3773.

[6] C. Holzhey, F. Larsen and F. Wilczek, *"Geometric and renormalized entropy in conformal field theory"*, Nucl. Phys. B 424, 443 (1994), hep-th/9403108.

[7] G. Vidal, J. Latorre, E. Rico and A. Kitaev, *"Entanglement in quantum critical phenomena"*, Phys. Rev. Lett. 90, 227902 (2003), quant-ph/0211074.

[8] C. G. Callan and F. Wilczek, *"On geometric entropy"*, Phys. Lett. B 333, 55 (1994), hep-th/9401072.

[9] P. Calabrese and J. L. Cardy, *"Entanglement entropy and quantum field theory"*, J. Stat. Mech. 0406, P06002 (2004), hep-th/0405152.

[10] H. Casini and M. Huerta, *"Entanglement entropy in free quantum field theory"*, J. Phys. A 42, 504007 (2009), arxiv:0905.2562.

[11] P. Calabrese and J. Cardy, *"Entanglement entropy and conformal field theory"*, J. Phys. A 42, 504005 (2009), arxiv:0905.4013.

[12] J. H. Bardarson, F. Pollmann and J. E. Moore, *"Unbounded Growth of Entanglement in Models of Many-Body Localization"*, Phys. Rev. Lett. 109, 017202 (2012), arxiv:1202.5532.

[13] M. Serbyn, Z. Papic and D. A. Abanin, *"Universal Slow Growth of Entanglement in Interacting Strongly Disordered Systems"*, Phys. Rev. Lett. 110, 260601 (2013), arxiv:1304.4605.

[14] M. Levin and X.-G. Wen, *"Detecting Topological Order in a Ground State Wave Function"*, Phys. Rev. Lett. 96, 110405 (2006), cond-mat/0510613.

[15] A. Kitaev and J. Preskill, *"Topological entanglement entropy"*, Phys. Rev. Lett. 96, 110404 (2006), hep-th/0510092.

[16] J. D. Bekenstein, *"Black holes and the second law"*, Lett. Nuovo Cim. 4, 737 (1972).

[17] J. D. Bekenstein, *"Black holes and entropy"*, Phys. Rev. D 7, 2333 (1973).

[18] J. D. Bekenstein, *"Generalized second law of thermodynamics in black hole physics"*, Phys. Rev. D 9, 3292 (1974).

[19] S. W. Hawking, *"Particle Creation by Black Holes"*, Commun. Math. Phys. 43, 199 (1975), [Erratum: Commun.Math.Phys. 46, 206 (1976)].

[20] L. Bombelli, R. K. Koul, J. Lee and R. D. Sorkin, *"A Quantum Source of Entropy for Black Holes"*, Phys. Rev. D 34, 373 (1986).

[21] M. Srednicki, *"Entropy and area"*, Phys. Rev. Lett. 71, 666 (1993), hep-th/9303048.

[22] S. N. Solodukhin, *"Entanglement entropy of black holes"*, Living Rev. Rel. 14, 8 (2011), arxiv:1104.3712.

[23] R. Islam, R. Ma, P. M. Preiss, M. Eric Tai, A. Lukin, M. Rispoli and M. Greiner, *"Measuring entanglement entropy in a quantum many-body system"*, Nature 528, 77 (2015).

[24] A. M. Kaufman, M. E. Tai, A. Lukin, M. Rispoli, R. Schittko, P. M. Preiss and M. Greiner, *"Quantum thermalization through entanglement in an isolated many-body system"*, Science 353, 794 (2016), arxiv:1603.04409.

[25] A. Lukin, M. Rispoli, R. Schittko, M. E. Tai, A. M. Kaufman, S. Choi, V. Khemani, J. Leonard and M. Greiner, *"Probing entanglement in a many-body localized system"*, Science 364, 256 (2019), arxiv:1805.09819.

[26] H. Li and F. Haldane, *"Entanglement Spectrum as a Generalization of Entanglement Entropy: Identification of Topological Order in Non-Abelian Fractional Quantum Hall Effect States"*, Phys. Rev. Lett. 101, 010504 (2008), arxiv:0805.0332.

[27] A. Botero and B. Reznik, *"Spatial structures and localization of vacuum entanglement in the linear harmonic chain"*, Phys. Rev. A 70, 052329 (2004), quant-ph/0403233.

[28] Y. Chen and G. Vidal, *"Entanglement contour"*, J. Stat. Mech. 2014, P10011 (2014), arxiv:1406.1471.

[29] A. Coser, C. De Nobili and E. Tonni, *"A contour for the entanglement entropies in harmonic lattices"*, J. Phys. A 50, 314001 (2017), arxiv:1701.08427.

[30] J. Watrous, *"Quantum Computational Complexity"*, Encyclopedia of Complexity and Systems Science , 7174 (2009), arxiv:0804.3401.

[31] S. Aaronson, *"The Complexity of Quantum States and Transformations: From Quantum Money to Black Holes"*, arxiv:1607.05256.

[32] M. A. Nielsen, *"A Geometric Approach to Quantum Circuit Lower Bounds"*, Quantum Info. Comput. 6, 213–262 (2006), quant-ph/0502070.

[33] M. A. Nielsen, M. R. Dowling, M. Gu and A. Doherty, *"Quantum computation as geometry"*, Science 311, 1133–1135 (2006), quant-ph/0603161.

[34] M. R. Dowling and M. A. Nielsen, *"The Geometry of Quantum Computation"*, Quantum Info. Comput. 8, 861–899 (2008), quant-ph/0701004.

[35] R. Jefferson and R. C. Myers, *"Circuit complexity in quantum field theory"*, JHEP 1710, 107 (2017), arxiv:1707.08570.

[36] M. Guo, J. Hernandez, R. C. Myers and S.-M. Ruan, *"Circuit Complexity for Coherent States"*, JHEP 1810, 011 (2018), arxiv:1807.07677.

[37] R. Khan, C. Krishnan and S. Sharma, *"Circuit Complexity in Fermionic Field Theory"*, Phys. Rev. D 98, 126001 (2018), arxiv:1801.07620.

[38] L. Hackl and R. C. Myers, *"Circuit complexity for free fermions"*, JHEP 1807, 139 (2018), arxiv:1803.10638.

[39] A. Bhattacharyya, A. Shekar and A. Sinha, *"Circuit complexity in interacting QFTs and RG flows"*, JHEP 1810, 140 (2018), arxiv:1808.03105.

[40] S. Chapman, J. Eisert, L. Hackl, M. P. Heller, R. Jefferson, H. Marrochio and R. C. Myers, *"Complexity and entanglement for thermofield double states"*, SciPost Phys. 6, 034 (2019), arxiv:1810.05151.

[41] P. Braccia, A. L. Cotrone and E. Tonni, *"Complexity in the presence of a boundary"*, JHEP 2002, 051 (2020), arxiv:1910.03489.

[42] S. Chapman and H. Z. Chen, *"Charged Complexity and the Thermofield Double State"*, JHEP 2102, 187 (2021), arxiv:1910.07508.

[43] M. Doroudiani, A. Naseh and R. Pirmoradian, *"Complexity for Charged Thermofield Double States"*, JHEP 2001, 120 (2020), arxiv:1910.08806.

[44] M. Guo, Z.-Y. Fan, J. Jiang, X. Liu and B. Chen, *"Circuit complexity for generalized coherent states in thermal field dynamics"*, Phys. Rev. D 101, 126007 (2020), arxiv:2004.00344.

[45] N. Jaiswal, M. Gautam and T. Sarkar, *"Complexity and information geometry in spin chains"*, arxiv:2005.03532.

[46] C. A. Agón, M. Headrick and B. Swingle, *"Subsystem Complexity and Holography"*, JHEP 1902, 145 (2019), arxiv:1804.01561.

[47] J. M. Maldacena, *"The Large N limit of superconformal field theories and supergravity"*, Int. J. Theor. Phys. 38, 1113 (1999), hep-th/9711200.

[48] S. Ryu and T. Takayanagi, *"Holographic derivation of entanglement entropy from AdS/CFT"*, Phys. Rev. Lett. 96, 181602 (2006), hep-th/0603001.

[49] S. Ryu and T. Takayanagi, *"Aspects of Holographic Entanglement Entropy"*, JHEP 0608, 045 (2006), hep-th/0605073.

[50] L. Susskind, *"Computational Complexity and Black Hole Horizons"*, Fortsch. Phys. 64, 24 (2016), arxiv:1403.5695.

[51] D. Stanford and L. Susskind, *"Complexity and Shock Wave Geometries"*, Phys. Rev. D 90, 126007 (2014), arxiv:1406.2678.

[52] L. Susskind and Y. Zhao, *"Switchbacks and the Bridge to Nowhere"*, arxiv:1408.2823.

[53] D. A. Roberts, D. Stanford and L. Susskind, *"Localized shocks"*, JHEP 1503, 051 (2015), arxiv:1409.8180.

[54] L. Susskind, *"Entanglement is not enough"*, Fortsch. Phys. 64, 49 (2016), arxiv:1411.0690.

[55] M. Alishahiha, *"Holographic Complexity"*, Phys. Rev. D 92, 126009 (2015), arxiv:1509.06614.

[56] A. R. Brown, D. A. Roberts, L. Susskind, B. Swingle and Y. Zhao, *"Holographic Complexity Equals Bulk Action?"*, Phys. Rev. Lett. 116, 191301 (2016), arxiv:1509.07876.

[57] A. R. Brown, D. A. Roberts, L. Susskind, B. Swingle and Y. Zhao, *"Complexity, action, and black holes"*, Phys. Rev. D 93, 086006 (2016), arxiv:1512.04993.

[58] J. L. Barbon and E. Rabinovici, *"Holographic complexity and spacetime singularities"*, JHEP 1601, 084 (2016), arxiv:1509.09291.

[59] D. Carmi, R. C. Myers and P. Rath, *"Comments on Holographic Complexity"*, JHEP 1703, 118 (2017), arxiv:1612.00433.

[60] P. Caputa, N. Kundu, M. Miyaji, T. Takayanagi and K. Watanabe, *"Anti-de Sitter Space from Optimization of Path Integrals in Conformal Field Theories"*, Phys. Rev. Lett. 119, 071602 (2017), arxiv:1703.00456.

[61] B. Czech, *"Einstein Equations from Varying Complexity"*, Phys. Rev. Lett. 120, 031601 (2018), arxiv:1706.00965.

[62] P. Caputa, N. Kundu, M. Miyaji, T. Takayanagi and K. Watanabe, *"Liouville Action as Path-Integral Complexity: From Continuous Tensor Networks to AdS/CFT"*, JHEP 1711, 097 (2017), arxiv:1706.07056.

[63] S. Chapman, M. P. Heller, H. Marrochio and F. Pastawski, *"Toward a Definition of Complexity for Quantum Field Theory States"*, Phys. Rev. Lett. 120, 121602 (2018), arxiv:1707.08582.

[64] R. Abt, J. Erdmenger, H. Hinrichsen, C. M. Melby-Thompson, R. Meyer, C. Northe and I. A. Reyes, *"Topological Complexity in AdS_3/CFT_2"*, Fortsch. Phys. 66, 1800034 (2018), arxiv:1710.01327.

[65] A. Bhattacharyya, P. Caputa, S. R. Das, N. Kundu, M. Miyaji and T. Takayanagi, *"Path-Integral Complexity for Perturbed CFTs"*, JHEP 1807, 086 (2018), arxiv:1804.01999.

[66] P. Caputa and J. M. Magan, *"Quantum Computation as Gravity"*, Phys. Rev. Lett. 122, 231302 (2019), arxiv:1807.04422.

[67] H. A. Camargo, P. Caputa, D. Das, M. P. Heller and R. Jefferson, *"Complexity as a novel probe of quantum quenches: universal scalings and purifications"*, Phys. Rev. Lett. 122, 081601 (2019), arxiv:1807.07075.

[68] S. Chapman, D. Ge and G. Policastro, *"Holographic Complexity for Defects Distinguishes Action from Volume"*, JHEP 1905, 049 (2019), arxiv:1811.12549.

[69] H. A. Camargo, M. P. Heller, R. Jefferson and J. Knaute, *"Path integral optimization as circuit complexity"*, Phys. Rev. Lett. 123, 011601 (2019), arxiv:1904.02713.

[70] D. Ge and G. Policastro, *"Circuit Complexity and 2D Bosonisation"*, JHEP 1910, 276 (2019), arxiv:1904.03003.

[71] P. Bueno, J. M. Magan and C. Shahbazi, *"Complexity measures in QFT and constrained geometric actions"*, arxiv:1908.03577.

[72] Y. Sato and K. Watanabe, *"Does Boundary Distinguish Complexities?"*, JHEP 1911, 132 (2019), arxiv:1908.11094.

[73] J. Erdmenger, M. Gerbershagen and A.-L. Weigel, *"Complexity measures from geometric actions on Virasoro and Kac-Moody orbits"*, JHEP 2011, 003 (2020), arxiv:2004.03619.

[74] M. Flory and M. P. Heller, *"Geometry of Complexity in Conformal Field Theory"*, Phys. Rev. Res. 2, 043438 (2020), arxiv:2005.02415.

[75] M. Flory and M. P. Heller, *"Conformal field theory complexity from Euler-Arnold equations"*, JHEP 2012, 091 (2020), arxiv:2007.11555.

[76] N. Chagnet, S. Chapman, J. de Boer and C. Zukowski, *"Complexity for Conformal Field Theories in General Dimensions"*, arxiv:2103.06920.

[77] C. Weedbrook, S. Pirandola, R. García-Patrón, N. J. Cerf, T. C. Ralph, J. H. Shapiro and S. Lloyd, *"Gaussian quantum information"*, Rev. Mod. Phys. 84, 621 (2012), arxiv:1110.3234.

[78] A. Serafini, *"Quantum Continuous Variables: A Primer of Theoretical Methods"*, CRC Press (2017).

[79] E. Caceres, S. Chapman, J. D. Couch, J. P. Hernandez, R. C. Myers and S.-M. Ruan, *"Complexity of Mixed States in QFT and Holography"*, JHEP 2003, 012 (2020), arxiv:1909.10557.

[80] F. H. L. Essler and M. Fagotti, *"Quench dynamics and relaxation in isolated integrable quantum spin chains"*, J. Stat. Mech. 1606, 064002 (2016), arxiv:1603.06452.

[81] P. Calabrese and J. Cardy, *"Quantum quenches in 1 + 1 dimensional conformal field theories"*, J. Stat. Mech. 1606, 064003 (2016), arxiv:1603.02889.

[82] P. Calabrese and J. L. Cardy, *"Evolution of entanglement entropy in one-dimensional systems"*, J. Stat. Mech. 2005, P04010 (2005), cond-mat/0503393.

[83] P. Calabrese and J. L. Cardy, *"Time-dependence of correlation functions following a quantum quench"*, Phys. Rev. Lett. 96, 136801 (2006), cond-mat/0601225.

[84] P. Calabrese and J. Cardy, *"Quantum Quenches in Extended Systems"*, J. Stat. Mech. 0706, P06008 (2007), arxiv:0704.1880.

[85] V. Eisler and I. Peschel, *"Evolution of entanglement after a local quench"*, J. Stat. Mech. 2007, P06005 (2007), cond-mat/0703379.

[86] P. Calabrese and J. Cardy, *"Entanglement and correlation functions following a local quench: a conformal field theory approach"*, J. Stat. Mech. 0710, P10004 (2007), arxiv:0708.3750.

[87] M. Nozaki, T. Numasawa and T. Takayanagi, *"Quantum Entanglement of Local Operators in Conformal Field Theories"*, Phys. Rev. Lett. 112, 111602 (2014), arxiv:1401.0539.

[88] M. Nozaki, *"Notes on Quantum Entanglement of Local Operators"*, JHEP 1410, 147 (2014), arxiv:1405.5875.

[89] M. Rigol, V. Dunjko, V. Yurovsky and M. Olshanii, *"Relaxation in a Completely Integrable Many-Body Quantum System: An Ab Initio Study of the Dynamics of the Highly Excited States of 1D Lattice Hard-Core Bosons"*, Phys. Rev. Lett. 98, 050405 (2007), cond-mat/0604476.

[90] L. Vidmar and M. Rigol, *"Generalized Gibbs ensemble in integrable lattice models"*, J. Stat. Mech. 1606, 064007 (2016), arxiv:1604.03990.

[91] C. Rao, *"Information and the accuracy attainable in the estimation of statistical parameters"*, Bull. Calcutta Math. Soc. 37, 81 (1945).

[92] C. Atkinson and A. Mitchell, *"Rao's Distance Measure"*, Sankhyā: The Indian Journal of Statistics 43, 345 (1981).

[93] S. Amari, *"Information Geometry and Its Applications"*, Springer (2016).

[94] J. Williamson, *"On the Algebraic Problem Concerning the Normal Forms of Linear Dynamical Systems"*, American Journal of Mathematics 58, 141 (1936).

[95] N. Laflorencie and S. Rachel, *"Spin-resolved entanglement spectroscopy of critical spin chains and Luttinger liquids"*, J. Stat. Mech. 2014, P11013 (2014), arxiv:1407.3779.

[96] M. Goldstein and E. Sela, *"Symmetry-resolved entanglement in many-body systems"*, Phys. Rev. Lett. 120, 200602 (2018), arxiv:1711.09418.

[97] J. C. Xavier, F. C. Alcaraz and G. Sierra, *"Equipartition of the entanglement entropy"*, Phys. Rev. B 98, 041106 (2018), arxiv:1804.06357.

[98] G. Di Giulio and E. Tonni, *"Complexity of mixed Gaussian states from Fisher information geometry"*, JHEP 2012, 101 (2020), arxiv:2006.00921.

[99] G. Di Giulio and E. Tonni, *"Subsystem complexity after a global quantum quench"*, JHEP 2105, 022 (2021), arxiv:2102.02764.

[100] G. Di Giulio and E. Tonni, *"Subsystem complexity after a local quantum quench"*, arxiv:2106.08282, accepted by JHEP.

[101] G. Di Giulio and E. Tonni, *"On entanglement hamiltonians of an interval in massless harmonic chains"*, J. Stat. Mech. 2003, 033102 (2020), arxiv:1911.07188.

[102] V. Eisler, G. Di Giulio, E. Tonni and I. Peschel, *"Entanglement Hamiltonians for non-critical quantum chains"*, J. Stat. Mech. 2010, 103102 (2020), arxiv:2007.01804.

[103] G. Di Giulio, R. Arias and E. Tonni, *"Entanglement hamiltonians in 1D free lattice models after a global quantum quench"*, J. Stat. Mech. 1912, 123103 (2019), arxiv:1905.01144.

[104] S. Murciano, G. Di Giulio and P. Calabrese, *"Entanglement and symmetry resolution in two dimensional free quantum field theories"*, JHEP 2008, 073 (2020), arxiv:2006.09069.

[105] S. Murciano, G. Di Giulio and P. Calabrese, *"Symmetry resolved entanglement in gapped integrable systems: a corner transfer matrix approach"*, SciPost Phys. 8, 046 (2020), arxiv:1911.09588.

[106] P. Calabrese, M. Collura, G. Di Giulio and S. Murciano, *"Full counting statistics in the gapped XXZ spin chain"*, EPL 129, 60007 (2020), arxiv:2002.04367.

[107] S. Wiesner, *"Conjugate Coding"*, SIGACT News 15, 78–88 (1983).

[108] S. Aaronson, *"Quantum Copy-Protection and Quantum Money"*, 24th Annual IEEE Conference on Computational Complexity 15, 229–242 (2009), arxiv:1110.5353.

[109] S. Aaronson and P. Christiano, *"Quantum Money from Hidden Subspaces"*, Proceedings of the Forty-Fourth Annual ACM Symposium on Theory of Computing 15, 41–60 (2012), arxiv:1203.4740.

[110] S. Aaronson, J. Liu, Q. Liu, M. Zhandry and R. Zhang, *"New Approaches for Quantum Copy-Protection"*, arxiv:2004.09674.

[111] P. Ananth and R. L. La Placa, *"Secure Software Leasing"*, Advances in Cryptology – EUROCRYPT 2021 15, 501 (2021), arxiv:2005.05289.

[112] L. Susskind, *"Butterflies on the Stretched Horizon"*, arxiv:1311.7379.

[113] L. Susskind, *"Three Lectures on Complexity and Black Holes"*, Springer (2018).

[114] A. R. Brown, L. Susskind and Y. Zhao, *"Quantum Complexity and Negative Curvature"*, Phys. Rev. D 95, 045010 (2017), arxiv:1608.02612.

[115] H. W. Lin, *"Cayley graphs and complexity geometry"*, JHEP 1902, 063 (2019), arxiv:1808.06620.

[116] L. J. Boya, E. Sudarshan and T. Tilma, *"Volumes of compact manifolds"*, Rep. Math. Phys. 52, 401 (2003), math-ph/0210033.

[117] A. R. Brown and L. Susskind, *"Second law of quantum complexity"*, Phys. Rev. D 97, 086015 (2018), arxiv:1701.01107.

[118] E. Knill, *"Approximation by quantum circuits"*, quant-ph/9508006.

[119] P. Bocchieri and A. Loinger, *"Quantum Recurrence Theorem"*, Phys. Rev. 107, 337 (1957).

[120] D. Aharonov, A. Kitaev and N. Nisan, *"Quantum Circuits with Mixed States"*, quant-ph/9806029.

[121] N. Chentsov, *"Statistical Decision Rules and Optimal Inference"*, Translations of Mathematical Monographs vol. 53, American Mathematical Society (1982).

[122] F. Nielsen, *"An elementary introduction to information geometry"*, arxiv:1808.08271.

[123] D. Felice, M. H. Quang and S. Mancini, *"The volume of Gaussian states by information geometry"*, J. Math. Phys. 58, 012201 (2017), arxiv:1509.01049.

[124] W. Förstner and B. Moonen, *"A Metric for Covariance Matrices"*, in: *"Geodesy-The Challenge of the 3rd Millennium"*, Springer Berlin Heidelberg (2003), 299–309p.

[125] R. Bhatia, *"Positive Definite Matrices"*, Princeton University Press (2007).

[126] R. Bhatia and T. Jain, *"On symplectic eigenvalues of positive definite matrices"*, J. Math. Phys. 56, 112201 (2015), arxiv:1803.04647.

[127] J. Lawson and Y. Lim, *"The Geometric Mean, Matrices, Metrics, and More"*, The American Mathematical Monthly 108, 797 (2001).

[128] J. Pinele, S. I. R. Costa and J. E. Strapasson, *"On the Fisher-Rao Information Metric in the Space of Normal Distributions"*, Geometric Science of Information , 676 (2019).

[129] S.-M. Ruan, *"Purification Complexity without Purifications"*, JHEP 2101, 092 (2021), arxiv:2006.01088.

[130] H. A. Camargo, L. Hackl, M. P. Heller, A. Jahn, T. Takayanagi and B. Windt, *"Entanglement and complexity of purification in (1+1)-dimensional free conformal field theories"*, Phys. Rev. Res. 3, 013248 (2021), arxiv:2009.11881.

[131] I. Bengtsson and K. Życzkowski, *"Geometry of quantum states: an introduction to quantum entanglement"*, Cambridge University Press (2017).

[132] M. Nielsen and I. Chuang, *"Quantum Computation and Quantum Information"*, Cambridge University Press (2000).

[133] D. Spehner, F. Illuminati, M. Orszag and W. Roga, *"Geometric measures of quantum correlations with Bures and Hellinger distances"*, arxiv:1611.03449.

[134] D. Petz, *"Monotone metrics on matrix spaces"*, Linear Algebra and its Applications 244, 81 (1996).

[135] E. Witten, *"Anti-de Sitter space and holography"*, Adv. Theor. Math. Phys. 2, 253 (1998), hep-th/9802150.

[136] S. Gubser, I. R. Klebanov and A. M. Polyakov, *"Gauge theory correlators from noncritical string theory"*, Phys. Lett. B 428, 105 (1998), hep-th/9802109.

[137] O. Aharony, S. S. Gubser, J. M. Maldacena, H. Ooguri and Y. Oz, *"Large N field theories, string theory and gravity"*, Phys. Rept. 323, 183 (2000), hep-th/9905111.

[138] P. Hayden and J. Preskill, *"Black holes as mirrors: Quantum information in random subsystems"*, JHEP 0709, 120 (2007), arxiv:0708.4025.

[139] J. M. Maldacena, *"Eternal black holes in anti-de Sitter"*, JHEP 0304, 021 (2003), hep-th/0106112.

[140] M. Moosa, *"Evolution of Complexity Following a Global Quench"*, JHEP 1803, 031 (2018), arxiv:1711.02668.

[141] S. Chapman, H. Marrochio and R. C. Myers, *"Holographic complexity in Vaidya spacetimes. Part I"*, JHEP 1806, 046 (2018), arxiv:1804.07410.

[142] S. Chapman, H. Marrochio and R. C. Myers, *"Holographic complexity in Vaidya spacetimes. Part II"*, JHEP 1806, 114 (2018), arxiv:1805.07262.

[143] D. S. Ageev, I. Y. Aref'eva, A. A. Bagrov and M. I. Katsnelson, *"Holographic local quench and effective complexity"*, JHEP 1808, 071 (2018), arxiv:1803.11162.

[144] D. Ageev, *"Holographic complexity of local quench at finite temperature"*, Phys. Rev. D 100, 126005 (2019), arxiv:1902.03632.

[145] B. Chen, W.-M. Li, R.-Q. Yang, C.-Y. Zhang and S.-J. Zhang, *"Holographic subregion complexity under a thermal quench"*, JHEP 1807, 034 (2018), arxiv:1803.06680.

[146] K. Ohmori and Y. Tachikawa, *"Physics at the entangling surface"*, J. Stat. Mech. 1504, P04010 (2015), arxiv:1406.4167.

[147] J. Cardy and E. Tonni, *"Entanglement hamiltonians in two-dimensional conformal field theory"*, J. Stat. Mech. 1612, 123103 (2016), arxiv:1608.01283.

[148] A. Hamma, R. Ionicioiu and P. Zanardi, *"Bipartite entanglement and entropic boundary law in lattice spin systems"*, Phys. Rev. A 71, 022315 (2005), quant-ph/0409073.

[149] P. V. Buividovich and M. I. Polikarpov, *"Entanglement entropy in lattice gauge theories"*, PoS CONFINEMENT8, 039 (2008), arxiv:0811.3824.

[150] P. V. Buividovich and M. I. Polikarpov, *"Entanglement entropy in gauge theories and the holographic principle for electric strings"*, Phys. Lett. B 670, 141 (2008), arxiv:0806.3376.

[151] W. Donnelly, *"Decomposition of entanglement entropy in lattice gauge theory"*, Phys. Rev. D 85, 085004 (2012), arxiv:1109.0036.

[152] C. A. Agon, M. Headrick, D. L. Jafferis and S. Kasko, *"Disk entanglement entropy for a Maxwell field"*, Phys. Rev. D 89, 025018 (2014), arxiv:1310.4886.

[153] H. Casini, M. Huerta and J. A. Rosabal, *"Remarks on entanglement entropy for gauge fields"*, Phys. Rev. D 89, 085012 (2014), arxiv:1312.1183.

[154] H. Casini, M. Huerta, J. M. Magan and D. Pontello, *"Logarithmic coefficient of the entanglement entropy of a Maxwell field"*, Phys. Rev. D 101, 065020 (2020), arxiv:1911.00529.

[155] R. Haag, *"Local quantum physics: Fields, particles, algebras"*, Springer (1992).

[156] G. Vidal, *"Entanglement monotones"*, J. Mod. Opt. 47, 355 (2000), quant-ph/9807077.

[157] A. B. Zamolodchikov, *"Irreversibility of the Flux of the Renormalization Group in a 2D Field Theory"*, JETP Lett. 43, 730 (1986).

[158] H. Casini, *"Geometric entropy, area, and strong subadditivity"*, Class. Quant. Grav. 21, 2351 (2004), hep-th/0312238.

[159] H. Casini and M. Huerta, *"A Finite entanglement entropy and the c-theorem"*, Phys. Lett. B 600, 142 (2004), hep-th/0405111.

[160] H. Casini and M. Huerta, *"A c-theorem for the entanglement entropy"*, J. Phys. A 40, 7031 (2007), cond-mat/0610375.

[161] H. Casini, I. Salazar Landea and G. Torroba, *"The g-theorem and quantum information theory"*, JHEP 1610, 140 (2016), arxiv:1607.00390.

[162] H. Casini, M. Huerta, R. C. Myers and A. Yale, *"Mutual information and the F-theorem"*, JHEP 1510, 003 (2015), arxiv:1506.06195.

[163] H. Casini, E. Testé and G. Torroba, *"Markov Property of the Conformal Field Theory Vacuum and the a Theorem"*, Phys. Rev. Lett. 118, 261602 (2017), arxiv:1704.01870.

[164] E. H. Lieb and M. B. Ruskai, *"A Fundamental Property of Quantum-Mechanical Entropy"*, Phys. Rev. Lett. 30, 434 (1973).

[165] E. H. Lieb and M. B. Ruskai, *"Proof of the strong subadditivity of quantum-mechanical entropy"*, J. Math. Phys. 14, 1938 (1973).

[166] G. Vidal and R. F. Werner, *"Computable measure of entanglement"*, Phys. Rev. A 65, 032314 (2002), quant-ph/0102117.

[167] M. B. Plenio, *"Logarithmic Negativity: A Full Entanglement Monotone That is not Convex"*, Phys. Rev. Lett. 95, 090503 (2005), quant-ph/0505071.

[168] C. H. Bennett, D. P. DiVincenzo, J. A. Smolin and W. K. Wootters, *"Mixed state entanglement and quantum error correction"*, Phys. Rev. A 54, 3824 (1996), quant-ph/9604024.

[169] E. Schmidt, *"Zur Theorie der linearen und nichtlinearen Integralgleichungen"*, Math. Ann. 81, 433–476 (1907).

[170] M. Nielsen and I. Chuang, *"Quantum Computation and Quantum Information"*, Cambridge University Press (2010).

[171] J. Bisognano and E. Wichmann, *"On the Duality Condition for a Hermitian Scalar Field"*, J. Math. Phys. 16, 985 (1975).

[172] J. Bisognano and E. Wichmann, *"On the Duality Condition for Quantum Fields"*, J. Math. Phys. 17, 303 (1976).

[173] W. G. Unruh, *"Notes on black hole evaporation"*, Phys. Rev. D 14, 870 (1976).

[174] P. D. Hislop and R. Longo, *"Modular Structure of the Local Algebras Associated With the Free Massless Scalar Field Theory"*, Commun. Math. Phys. 84, 71 (1982).

[175] H. Casini, M. Huerta and R. C. Myers, *"Towards a derivation of holographic entanglement entropy"*, JHEP 1105, 036 (2011), arxiv:1102.0440.

[176] G. Wong, I. Klich, L. A. Pando Zayas and D. Vaman, *"Entanglement Temperature and Entanglement Entropy of Excited States"*, JHEP 1312, 020 (2013), arxiv:1305.3291.

[177] E. Tonni, J. Rodríguez-Laguna and G. Sierra, *"Entanglement hamiltonian and entanglement contour in inhomogeneous 1D critical systems"*, J. Stat. Mech. 1804, 043105 (2018), arxiv:1712.03557.

[178] V. Eisler and I. Peschel, *"Properties of the entanglement Hamiltonian for finite free-fermion chains"*, J. Stat. Mech. 1810, 104001 (2018), arxiv:1805.00078.

[179] V. Eisler, E. Tonni and I. Peschel, *"On the continuum limit of the entanglement Hamiltonian"*, J. Stat. Mech. 1907, 073101 (2019), arxiv:1902.04474.

[180] H. Casini and M. Huerta, *"Reduced density matrix and internal dynamics for multicomponent regions"*, Class. Quant. Grav. 26, 185005 (2009), arxiv:0903.5284.

[181] R. Longo, P. Martinetti and K.-H. Rehren, *"Geometric modular action for disjoint intervals and boundary conformal field theory"*, Rev. Math. Phys. 22, 331 (2010), arxiv:0912.1106.

[182] R. E. Arias, H. Casini, M. Huerta and D. Pontello, *"Entropy and modular Hamiltonian for a free chiral scalar in two intervals"*, Phys. Rev. D 98, 125008 (2018), arxiv:1809.00026.

[183] M. Mintchev and E. Tonni, *"Modular Hamiltonians for the massless Dirac field in the presence of a boundary"*, JHEP 2103, 204 (2021), arxiv:2012.00703.

[184] M. Mintchev and E. Tonni, *"Modular Hamiltonians for the massless Dirac field in the presence of a defect"*, JHEP 2103, 205 (2021), arxiv:2012.01366.

[185] I. Klich, D. Vaman and G. Wong, *"Entanglement Hamiltonians for chiral fermions with zero modes"*, Phys. Rev. Lett. 119, 120401 (2017), arxiv:1501.00482.

[186] I. Klich, D. Vaman and G. Wong, *"Entanglement Hamiltonians and entropy in 1+1D chiral fermion systems"*, Phys. Rev. B 98, 035134 (2018), arxiv:1704.01536.

[187] G. Wong, *"Gluing together Modular flows with free fermions"*, JHEP 1904, 045 (2019), arxiv:1805.10651.

[188] D. Blanco, A. Garbarz and G. Pérez-Nadal, *"Entanglement of a chiral fermion on the torus"*, JHEP 1909, 076 (2019), arxiv:1906.07057.

[189] D. Blanco and G. Pérez-Nadal, *"Modular Hamiltonian of a chiral fermion on the torus"*, Phys. Rev. D 100, 025003 (2019), arxiv:1905.05210.

[190] P. Fries and I. A. Reyes, *"Entanglement Spectrum of Chiral Fermions on the Torus"*, Phys. Rev. Lett. 123, 211603 (2019), arxiv:1905.05768.

[191] I. Peschel, *"Calculation of reduced density matrices from correlation functions"*, J. Phys. A 36, L205 (2003), cond-mat/0212631.

[192] V. Eisler and I. Peschel, *"Analytical results for the entanglement Hamiltonian of a free-fermion chain"*, J. Phys. A 50, 284003 (2017), arxiv:1703.08126.

[193] R. Arias, D. Blanco, H. Casini and M. Huerta, *"Local temperatures and local terms in modular Hamiltonians"*, Phys. Rev. D 95, 065005 (2017), arxiv:1611.08517.

[194] I. Peschel and M.-C. Chung, *"Density matrices for a chain of oscillators"*, J. Phys. A 32, 8419 (1999), cond-mat/9906224.

[195] M.-C. Chung and I. Peschel, *"Density-matrix spectra for two-dimensional quantum systems"*, Phys. Rev. B 62, 4191 (2000), cond-mat/0004222.

[196] M.-C. Chung and I. Peschel, *"Density-matrix spectra of solvable fermionic systems"*, Phys. Rev. B 64, 064412 (2001), cond-mat/0103301.

[197] S.-A. Cheong and C. L. Henley, *"Operator-based truncation scheme based on the many-body fermion density matrix"*, Phys. Rev. B 69, 075112 (2004), cond-mat/0307172.

[198] V. Eisler, D. Karevski, T. Platini and I. Peschel, *"Entanglement evolution after connecting finite to infinite quantum chains"*, J. Stat. Mech. 2008, P01023 (2008), arxiv:0711.0289.

[199] V. Eisler and I. Peschel, *"Free-fermion entanglement and spheroidal functions"*, J. Stat. Mech. 2013, P04028 (2013), arxiv:1302.2239.

[200] R. Arias, H. Casini, M. Huerta and D. Pontello, *"Anisotropic Unruh temperatures"*, Phys. Rev. D 96, 105019 (2017), arxiv:1707.05375.

[201] I. Peschel, *"On the reduced density matrix for a chain of free electrons"*, J. Stat. Mech. 0406, P06004 (2004), cond-mat/0403048.

[202] B. Nienhuis, M. Campostrini and P. Calabrese, *"Entanglement, combinatorics and finite-size effects in spin chains"*, J. Stat. Mech. 2009, P02063 (2009), arxiv:0808.2741.

[203] F. Parisen Toldin and F. F. Assaad, *"Entanglement Hamiltonian of Interacting Fermionic Models"*, Phys. Rev. Lett. 121, 200602 (2018), arxiv:1804.03163.

[204] J. L. Cardy, *"Effect of Boundary Conditions on the Operator Content of Two-Dimensional Conformally Invariant Theories"*, Nucl. Phys. B 275, 200 (1986).

[205] J. L. Cardy, *"Boundary Conditions, Fusion Rules and the Verlinde Formula"*, Nucl. Phys. B 324, 581 (1989).

[206] H. Saleur and M. Bauer, *"On Some Relations Between Local Height Probabilities and Conformal Invariance"*, Nucl. Phys. B 320, 591 (1989).

[207] A. M. Läuchli, *"Operator content of real-space entanglement spectra at conformal critical points"*, arxiv:1303.0741.

[208] A. Roy, F. Pollmann and H. Saleur, *"Entanglement Hamiltonian of the 1+1-dimensional free, compactified boson conformal field theory"*, J. Stat. Mech. 2008, 083104 (2020), arxiv:2004.14370.

[209] J. Surace, L. Tagliacozzo and E. Tonni, *"Operator content of entanglement spectra in the transverse field Ising chain after global quenches"*, Phys. Rev. B 101, 241107(R) (2020), arxiv:1909.07381.

[210] P. Calabrese, J. Cardy and E. Tonni, *"Entanglement negativity in quantum field theory"*, Phys. Rev. Lett. 109, 130502 (2012), arxiv:1206.3092.

[211] P. Calabrese, J. Cardy and E. Tonni, *"Entanglement negativity in extended systems: A field theoretical approach"*, J. Stat. Mech. 1302, P02008 (2013), arxiv:1210.5359.

[212] N. Lashkari, *"Relative Entropies in Conformal Field Theory"*, Phys. Rev. Lett. 113, 051602 (2014), arxiv:1404.3216.

[213] N. Lashkari, *"Modular Hamiltonian for Excited States in Conformal Field Theory"*, Phys. Rev. Lett. 117, 041601 (2016), arxiv:1508.03506.

[214] J. Zhang, P. Ruggiero and P. Calabrese, *"Subsystem Trace Distance in Quantum Field Theory"*, Phys. Rev. Lett. 122, 141602 (2019), arxiv:1901.10993.

[215] J. Zhang, P. Ruggiero and P. Calabrese, *"Subsystem trace distance in low-lying states of $(1+1)$-dimensional conformal field theories"*, JHEP 1910, 181 (2019), arxiv:1907.04332.

[216] J. L. Cardy, O. A. Castro-Alvaredo and B. Doyon, *"Form factors of branch-point twist fields in quantum integrable models and entanglement entropy"*, J. Statist. Phys. 130, 129 (2008), arxiv:0706.3384.

[217] H. Casini, C. Fosco and M. Huerta, *"Entanglement and alpha entropies for a massive Dirac field in two dimensions"*, J. Stat. Mech. 0507, P07007 (2005), cond-mat/0505563.

[218] H. Casini and M. Huerta, *"Entanglement and alpha entropies for a massive scalar field in two dimensions"*, J. Stat. Mech. 0512, P12012 (2005), cond-mat/0511014.

[219] H. Casini and M. Huerta, *"Universal terms for the entanglement entropy in 2+1 dimensions"*, Nucl. Phys. B 764, 183 (2007), hep-th/0606256.

[220] H. Casini and M. Huerta, *"Analytic results on the geometric entropy for free fields"*, J. Stat. Mech. 0801, P01012 (2008), arxiv:0707.1300.

[221] H. Casini, M. Huerta and L. Leitao, *"Entanglement entropy for a Dirac fermion in three dimensions: Vertex contribution"*, Nucl. Phys. B 814, 594 (2009), arxiv:0811.1968.

[222] S. N. Solodukhin, *"Entanglement entropy, conformal invariance and extrinsic geometry"*, Phys. Lett. B 665, 305 (2008), arxiv:0802.3117.

[223] S. N. Solodukhin, *"Entanglement Entropy in Non-Relativistic Field Theories"*, JHEP 1004, 101 (2010), arxiv:0909.0277.

[224] O. A. Castro-Alvaredo and B. Doyon, *"Bi-partite entanglement entropy in massive 1+1-dimensional quantum field theories"*, J. Phys. A 42, 504006 (2009), arxiv:0906.2946.

[225] O. Blondeau-Fournier, O. A. Castro-Alvaredo and B. Doyon, *"Universal scaling of the logarithmic negativity in massive quantum field theory"*, J. Phys. A 49, 125401 (2016), arxiv:1508.04026.

[226] D. Bianchini and O. A. Castro-Alvaredo, *"Branch Point Twist Field Correlators in the Massive Free Boson Theory"*, Nucl. Phys. B 913, 879 (2016), arxiv:1607.05656.

[227] O. A. Castro-Alvaredo, *"Massive Corrections to Entanglement in Minimal E8 Toda Field Theory"*, SciPost Phys. 2, 008 (2017), arxiv:1610.07040.

[228] O. A. Castro-Alvaredo and B. Doyon, *"Bi-partite entanglement entropy in integrable models with backscattering"*, J. Phys. A 41, 275203 (2008), arxiv:0802.4231.

[229] O. A. Castro-Alvaredo and E. Levi, *"Higher particle form factors of branch point twist fields in integrable quantum field theories"*, J. Phys. A 44, 255401 (2011), arxiv:1103.2069.

[230] D. Bianchini, O. A. Castro-Alvaredo, B. Doyon, E. Levi and F. Ravanini, *"Entanglement Entropy of Non Unitary Conformal Field Theory"*, J. Phys. A 48, 04FT01 (2015), arxiv:1405.2804.

[231] J. Latorre, E. Rico and G. Vidal, *"Ground state entanglement in quantum spin chains"*, Quant. Inf. Comput. 4, 48 (2004), quant-ph/0304098.

[232] J. I. Latorre and A. Riera, *"A short review on entanglement in quantum spin systems"*, J. Phys. A 42, 504002 (2009), arxiv:0906.1499.

[233] P. Calabrese, J. Cardy and E. Tonni, *"Entanglement entropy of two disjoint intervals in conformal field theory"*, J. Stat. Mech. 0911, P11001 (2009), arxiv:0905.2069.

[234] P. Calabrese, J. Cardy and E. Tonni, *"Entanglement entropy of two disjoint intervals in conformal field theory II"*, J. Stat. Mech. 1101, P01021 (2011), arxiv:1011.5482.

[235] J. Cardy, *"Some results on the mutual information of disjoint regions in higher dimensions"*, J. Phys. A 46, 285402 (2013), arxiv:1304.7985.

[236] A. Coser, L. Tagliacozzo and E. Tonni, *"On Rényi entropies of disjoint intervals in conformal field theory"*, J. Stat. Mech. 1401, P01008 (2014), arxiv:1309.2189.

[237] A. Coser, E. Tonni and P. Calabrese, *"Spin structures and entanglement of two disjoint intervals in conformal field theories"*, J. Stat. Mech. 1605, 053109 (2016), arxiv:1511.08328.

[238] F. C. Alcaraz, M. I. Berganza and G. Sierra, *"Entanglement of low-energy excitations in Conformal Field Theory"*, Phys. Rev. Lett. 106, 201601 (2011), arxiv:1101.2881.

[239] M. I. Berganza, F. C. Alcaraz and G. Sierra, *"Entanglement of excited states in critical spin chians"*, J. Stat. Mech. 1201, P01016 (2012), arxiv:1109.5673.

[240] J. Dubail, J.-M. Stephan, J. Viti and P. Calabrese, *"Conformal Field Theory for Inhomogeneous One-dimensional Quantum Systems: the Example of Non-Interacting Fermi Gases"*, SciPost Phys. 2, 002 (2017), arxiv:1606.04401.

[241] J. Rodríguez-Laguna, J. Dubail, G. Ramírez, P. Calabrese and G. Sierra, *"More on the rainbow chain: entanglement, space-time geometry and thermal states"*, J. Phys. A 50, 164001 (2017), arxiv:1611.08559.

[242] S. Murciano, P. Ruggiero and P. Calabrese, *"Entanglement and relative entropies for low-lying excited states in inhomogeneous one-dimensional quantum systems"*, J. Stat. Mech. 2019, pages =, P. Calabrese (2018), arxiv:1810.02287.

[243] V. E. Hubeny, M. Rangamani and T. Takayanagi, *"A Covariant holographic entanglement entropy proposal"*, JHEP 0707, 062 (2007), arxiv:0705.0016.

[244] T. Nishioka, S. Ryu and T. Takayanagi, *"Holographic Entanglement Entropy: An Overview"*, J. Phys. A 42, 504008 (2009), arxiv:0905.0932.

[245] M. Rangamani and T. Takayanagi, *"Holographic Entanglement Entropy"*, Springer (2017).

[246] H. M. Wiseman and J. A. Vaccaro, *"Entanglement of Indistinguishable Particles Shared between Two Parties"*, Phys. Rev. Lett. 91, 097902 (2003), quant-ph/0210002.

[247] H. Barghathi, C. M. Herdman and A. Del Maestro, *"Renyi Generalization of the Accessible Entanglement Entropy"*, Phys. Rev. Lett. 121, 150501 (2018), arxiv:1804.01114.

[248] H. Barghathi, E. Casiano-Diaz and A. Del Maestro, *"Operationally accessible entanglement of one-dimensional spinless fermions"*, Phys. Rev. A 100, 022324 (2019), arxiv:1905.03312.

[249] M. Kiefer-Emmanouilidis, R. Unanyan, J. Sirker and M. Fleischhauer, *"Bounds on the entanglement entropy by the number entropy in non-interacting fermionic systems"*, SciPost Phys. 8, 83 (2020), arxiv:2003.03112.

[250] M. Kiefer-Emmanouilidis, R. Unanyan, M. Fleischhauer and J. Sirker, *"Evidence for Unbounded Growth of the Number Entropy in Many-Body Localized Phases"*, Phys. Rev. Lett. 124, 243601 (2020), arxiv:2003.04849.

[251] R. Bonsignori, P. Ruggiero and P. Calabrese, *"Symmetry resolved entanglement in free fermionic systems"*, J. Phys. A 52, 475302 (2019), arxiv:1907.02084.

[252] K. Monkman and J. Sirker, *"Operational entanglement of symmetry-protected topological edge states"*, Phys. Rev. Res. 2, 043191 (2020), arxiv:2005.13026.

[253] R. Vosk and E. Altman, *"Dynamical Quantum Phase Transitions in Random Spin Chains"*, Phys. Rev. Lett. 112, 217204 (2014), arxiv:1307.3256.

[254] E. Cornfeld, M. Goldstein and E. Sela, *"Imbalance entanglement: Symmetry decomposition of negativity"*, Phys. Rev. A 98, 032302 (2018), arxiv:1804.00632.

[255] N. Feldman and M. Goldstein, *"Dynamics of Charge-Resolved Entanglement after a Local Quench"*, Phys. Rev. B 100, 235146 (2019), arxiv:1905.10749.

[256] M. T. Tan and S. Ryu, *"Particle number fluctuations, Rényi entropy, and symmetry-resolved entanglement entropy in a two-dimensional Fermi gas from multidimensional bosonization"*, Phys. Rev. B 101, 235169 (2020), arxiv:1911.01451.

[257] S. Fraenkel and M. Goldstein, *"Symmetry resolved entanglement: Exact results in 1D and beyond"*, J. Stat. Mech. 2003, 033106 (2020), arxiv:1910.08459.

[258] E. Cornfeld, L. A. Landau, K. Shtengel and E. Sela, *"Entanglement spectroscopy of non-Abelian anyons: Reading off quantum dimensions of individual anyons"*, Phys. Rev. B 99, 115429 (2019), arxiv:1810.01853.

[259] R. Baxter, *"Exactly Solved Models in Statistical Mechanics"*, Academic Press (1982).

[260] H. Itoyama and H. Thacker, *"Lattice Virasoro Algebra and Corner Transfer Matrices in the Baxter Eight Vertex Model"*, Phys. Rev. Lett. 58, 1395 (1987).

[261] I. Peschel and T. T. Truong, *"Corner transfer matrices and conformal invariance"*, Z. Phys. B 69, 385 (1987).

[262] I. Peschel, M. Kaulke and O. Legeza, *"Density-matrix spectra for integrable models"*, Annalen der Physik 8, 153 (1999).

[263] V. Alba, M. Haque and A. M. Läuchli, *"Boundary-Locality and Perturbative Structure of Entanglement Spectra in Gapped Systems"*, Phys. Rev. Lett. 108, 227201 (2012), arxiv:1107.1726.

[264] V. Alba, M. Haque and A. M. Läuchli, *"Entanglement Spectrum of the Two-Dimensional Bose-Hubbard Model"*, Phys. Rev. Lett. 110, 260403 (2013), arxiv:1212.5634.

[265] A. Ferraro, S. Olivares and M. G. A. Paris, *"Gaussian states in continuous variable quantum information"*, quant-ph/0503237.

[266] A. Holevo, *"Probabilistic and Statistical Aspects of Quantum Theory"*, Edizioni della Normale (2011).

[267] G. Adesso, S. Ragy and A. R. Lee, *"Continuous Variable Quantum Information: Gaussian States and Beyond"*, Open Systems and Information Dynamics 21, 1440001 (2014), arxiv:1401.4679.

[268] A. Bernamonti, F. Galli, J. Hernandez, R. C. Myers, S.-M. Ruan and J. Simón, *"First Law of Holographic Complexity"*, Phys. Rev. Lett. 123, 081601 (2019), arxiv:1903.04511.

[269] A. Bernamonti, F. Galli, J. Hernandez, R. C. Myers, S.-M. Ruan and J. Simón, *"Aspects of The First Law of Complexity"*, J. Phys. A 53, 294002 (2020), arxiv:2002.05779.

[270] R. Simon, E. Sudarshan and N. Mukunda, *"Gaussian-Wigner distributions in quantum mechanics and optics"*, Phys. Rev. A 36, 3868 (1987).

[271] R. Simon, N. Mukunda and B. Dutta, *"Quantum-noise matrix for multimode systems: U(n) invariance, squeezing, and normal forms"*, Phys. Rev. A 49, 1567 (1994).

[272] Arvind, B. Dutta, N. Mukunda and R. Simon, *"The Real symplectic groups in quantum mechanics and optics"*, Pramana 45, 471 (1995), quant-ph/9509002.

[273] R. Simon, S. Chaturvedi and V. Srinivasan, *"Congruences and canonical forms for a positive matrix: Application to the Schweinler–Wigner extremum principle"*, J. Math. Phys. 40, 3632 (1999), math-ph/9811003.

[274] M. de Gosson, *"Symplectic Geometry and Quantum Mechanics"*, Birkhäuser Verlag (2006).

[275] K. Audenaert, J. Eisert, M. Plenio and R. Werner, *"Entanglement Properties of the Harmonic Chain"*, Phys. Rev. A 66, 042327 (2002), quant-ph/0205025.

[276] M. Plenio, J. Eisert, J. Dreissig and M. Cramer, *"Entropy, entanglement, and area: analytical results for harmonic lattice systems"*, Phys. Rev. Lett. 94, 060503 (2005), quant-ph/0405142.

[277] M. Cramer, J. Eisert, M. Plenio and J. Dreissig, *"An Entanglement-area law for general bosonic harmonic lattice systems"*, Phys. Rev. A 73, 012309 (2006), quant-ph/0505092.

[278] A. Holevo, *"Some statistical problems for quantum Gaussian states"*, IEEE Transactions on Information Theory 21, 533 (1975).

[279] R. Fisher, *"On the mathematical foundations of theoretical statistics"*, Philos. Trans. R. Soc. Lond. 222, 309–368 (1921).

[280] J. Pinele, J. E. Strapasson and S. I. R. Costa, *"The Fisher-Rao Distance between Multivariate Normal Distributions: Special Cases, Boundsand Applications"*, Entropy 22, 404 (2020).

[281] S. I. Costa, S. A. Santos and J. E. Strapasson, *"Fisher information distance: A geometrical reading"*, Discrete Applied Mathematics 197, 59 (2015), arxiv:1210.2354.

[282] J. Strapasson, J. Pinele and S. Costa, *"A totally geodesic submanifold of the multivariate normal distributions and bounds for the Fisher-Rao distance"*, 2016 IEEE Information Theory Workshop (ITW) , 61 (2016).

[283] A. Holevo and R. F. Werner, *"Evaluating capacities of Bosonic Gaussian channels"*, Phys. Rev. A 63, 032312 (2001), quant-ph/9912067.

[284] L. Banchi, S. L. Braunstein and S. Pirandola, *"Quantum Fidelity for Arbitrary Gaussian States"*, Phys. Rev. Lett. 115, 260501 (2015), arxiv:1507.01941.

[285] F. Benatti and R. Floreanini, *"Open quantum dynamics: complete positivity and entanglement"*, Int. J. Mod. Phys. B 19, 3063 (2005), quant-ph/0507271.

[286] G. Giedke and I. J. Cirac, *"Characterization of Gaussian operations and distillation of Gaussian states"*, Phys. Rev. A 66, 042327 (2002), quant-ph/0204085.

[287] F. W. Stinespring, *"Positive Functions on C*-Algebras"*, Proceedings of the American Mathematical Society 6, 211 (1955).

[288] F. Caruso, J. Eisert, V. Giovannetti and A. Holevo, *"Multi-mode bosonic Gaussian channels"*, New J. Phys. 10, 083030 (2008), arxiv:0804.0511.

[289] B. M. Terhal, M. Horodecki, D. W. Leung and D. P. DiVincenzo, *"The entanglement of purification"*, J. Math. Phys. 43, 4286–4298 (2002), quant-ph/0202044.

[290] T. Takayanagi and K. Umemoto, *"Entanglement of purification through holographic duality"*, Nature Phys. 14, 573 (2018), arxiv:1708.09393.

[291] P. Nguyen, T. Devakul, M. G. Halbasch, M. P. Zaletel and B. Swingle, *"Entanglement of purification: from spin chains to holography"*, JHEP 1801, 098 (2018), arxiv:1709.07424.

[292] A. Bhattacharyya, T. Takayanagi and K. Umemoto, *"Entanglement of Purification in Free Scalar Field Theories"*, JHEP 1804, 132 (2018), arxiv:1802.09545.

[293] V. Eisler and Z. Zimborás, *"Entanglement negativity in the harmonic chain out of equilibrium"*, New J. Phys. 16, 123020 (2014), arxiv:1406.5474.

[294] A. Coser, E. Tonni and P. Calabrese, *"Entanglement negativity after a global quantum quench"*, J. Stat. Mech. 1412, P12017 (2014), arxiv:1410.0900.

[295] J. S. Cotler, M. P. Hertzberg, M. Mezei and M. T. Mueller, *"Entanglement Growth after a Global Quench in Free Scalar Field Theory"*, JHEP 1611, 166 (2016), arxiv:1609.00872.

[296] A. Altland and B. Simons, *"Condensed Matter Field Theory"*, Cambridge University Press (2010).

[297] M. Alishahiha, K. Babaei Velni and M. R. Mohammadi Mozaffar, *"Black hole subregion action and complexity"*, Phys. Rev. D 99, 126016 (2019), arxiv:1809.06031.

[298] R. Auzzi, S. Baiguera, A. Legramandi, G. Nardelli, P. Roy and N. Zenoni, *"On subregion action complexity in AdS_3 and in the BTZ black hole"*, JHEP 2001, 066 (2020), arxiv:1910.00526.

[299] C. De Nobili, A. Coser and E. Tonni, *"Entanglement entropy and negativity of disjoint intervals in CFT: Some numerical extrapolations"*, J. Stat. Mech. 1506, P06021 (2015), arxiv:1501.04311.

[300] V. E. Hubeny and M. Rangamani, *"Holographic entanglement entropy for disconnected regions"*, JHEP 0803, 006 (2008), arxiv:0711.4118.

[301] M. Headrick, *"Entanglement Renyi entropies in holographic theories"*, Phys. Rev. D 82, 126010 (2010), arxiv:1006.0047.

[302] E. Tonni, *"Holographic entanglement entropy: near horizon geometry and disconnected regions"*, JHEP 1105, 004 (2011), arxiv:1011.0166.

[303] P. Fonda, L. Giomi, A. Salvio and E. Tonni, *"On shape dependence of holographic mutual information in AdS_4"*, JHEP 1502, 005 (2015), arxiv:1411.3608.

[304] P. Calabrese, L. Tagliacozzo and E. Tonni, *"Entanglement negativity in the critical Ising chain"*, J. Stat. Mech. 1305, P05002 (2013), arxiv:1302.1113.

[305] V. Eisler and Z. Zimborás, *"On the partial transpose of fermionic Gaussian states"*, New J. Phys. 17, 053048 (2015), arxiv:1502.01369.

[306] A. Coser, E. Tonni and P. Calabrese, *"Partial transpose of two disjoint blocks in XY spin chains"*, J. Stat. Mech. 1508, P08005 (2015), arxiv:1503.09114.

[307] V. Eisler and Z. Zimborás, *"Entanglement negativity in two-dimensional free lattice models"*, Phys. Rev. B 93, 115148 (2016), arxiv:1511.08819.

[308] C. De Nobili, A. Coser and E. Tonni, *"Entanglement negativity in a two dimensional harmonic lattice: Area law and corner contributions"*, J. Stat. Mech. 1608, 083102 (2016), arxiv:1604.02609.

[309] J. Couch, W. Fischler and P. H. Nguyen, *"Noether charge, black hole volume, and complexity"*, JHEP 1703, 119 (2017), arxiv:1610.02038.

[310] E. Ilievski, J. De Nardis, B. Wouters, J.-S. Caux, F. H. L. Essler and T. Prosen, *"Complete Generalized Gibbs Ensembles in an Interacting Theory"*, Phys. Rev. Lett. 115, 157201 (2015), arxiv:1507.02993.

[311] D. W. Alves and G. Camilo, *"Evolution of complexity following a quantum quench in free field theory"*, JHEP 1806, 029 (2018), arxiv:1804.00107.

[312] T. Ali, A. Bhattacharyya, S. Shajidul Haque, E. H. Kim and N. Moynihan, *"Time Evolution of Complexity: A Critique of Three Methods"*, JHEP 1904, 087 (2019), arxiv:1810.02734.

[313] J. Jiang, J. Shan and J. Yang, *"Circuit complexity for free Fermion with a mass quench"*, Nucl. Phys. B 954, 114988 (2020), arxiv:1810.00537.

[314] T. Ali, A. Bhattacharyya, S. Shajidul Haque, E. H. Kim and N. Moynihan, *"Post-Quench Evolution of Complexity and Entanglement in a Topological System"*, Phys. Lett. B 811, 135919 (2020), arxiv:1811.05985.

[315] A. Bhattacharyya, S. S. Haque and E. H. Kim, *"Complexity from the Reduced Density Matrix: a new Diagnostic for Chaos"*, arxiv:2011.04705.

[316] R. Auzzi, G. Nardelli, F. I. Schaposnik Massolo, G. Tallarita and N. Zenoni, *"On volume subregion complexity in Vaidya spacetime"*, JHEP 1911, 098 (2019), arxiv:1908.10832.

[317] Y. Ling, Y. Liu, C. Niu, Y. Xiao and C.-Y. Zhang, *"Holographic Subregion Complexity in General Vaidya Geometry"*, JHEP 1911, 039 (2019), arxiv:1908.06432.

[318] Y.-T. Zhou, X.-M. Kuang, Y.-Z. Li and J.-P. Wu, *"Holographic subregion complexity under a thermal quench in an Einstein-Maxwell-axion theory with momentum relaxation"*, Phys. Rev. D 101, 106024 (2020), arxiv:1912.03479.

[319] S. Sotiriadis and J. Cardy, *"Quantum quench in interacting field theory: A Self-consistent approximation"*, Phys. Rev. B 81, 134305 (2010), arxiv:1002.0167.

[320] V. Alba and P. Calabrese, *"Entanglement dynamics after quantum quenches in generic integrable systems"*, SciPost Physics 4, 17 (2018), arxiv:1712.07529.

[321] J. Abajo-Arrastia, J. Aparicio and E. Lopez, *"Holographic Evolution of Entanglement Entropy"*, JHEP 1011, 149 (2010), arxiv:1006.4090.

[322] X. Wen, S. Ryu and A. W. W. Ludwig, *"Entanglement hamiltonian evolution during thermalization in conformal field theory"*, J. Stat. Mech. 1811, 113103 (2018), arxiv:1807.04440.

[323] J. Cardy, *"Thermalization and Revivals after a Quantum Quench in Conformal Field Theory"*, Phys. Rev. Lett. 112, 220401 (2014), arxiv:1403.3040.

[324] V. Kac and P. Cheung, *"Quantum Calculus"*, Springer (2002).

[325] V. Balasubramanian, A. Bernamonti, J. de Boer, N. Copland, B. Craps, E. Keski-Vakkuri, B. Muller, A. Schafer, M. Shigemori and W. Staessens, *"Holographic Thermalization"*, Phys. Rev. D 84, 026010 (2011), arxiv:1103.2683.

[326] V. Balasubramanian, A. Bernamonti, N. Copland, B. Craps and F. Galli, *"Thermalization of mutual and tripartite information in strongly coupled two dimensional conformal field theories"*, Phys. Rev. D 84, 105017 (2011), arxiv:1110.0488.

[327] A. Allais and E. Tonni, *"Holographic evolution of the mutual information"*, JHEP 1201, 102 (2012), arxiv:1110.1607.

[328] R. Callan, J.-Y. He and M. Headrick, *"Strong subadditivity and the covariant holographic entanglement entropy formula"*, JHEP 1206, 081 (2012), arxiv:1204.2309.

[329] V. E. Hubeny, M. Rangamani and E. Tonni, *"Thermalization of Causal Holographic Information"*, JHEP 1305, 136 (2013), arxiv:1302.0853.

[330] V. E. Hubeny and H. Maxfield, *"Holographic probes of collapsing black holes"*, JHEP 1403, 097 (2014), arxiv:1312.6887.

[331] Z.-Y. Fan and M. Guo, *"Holographic complexity under a global quantum quench"*, Nucl. Phys. B 950, 114818 (2020), arxiv:1811.01473.

[332] H. Liu and S. J. Suh, *"Entanglement growth during thermalization in holographic systems"*, Phys. Rev. D 89, 066012 (2014), arxiv:1311.1200.

[333] M. G. Nezhadhaghighi and M. A. Rajabpour, *"Entanglement dynamics in short- and long-range harmonic oscillators"*, Phys. Rev. B 90, 205438 (2014), arxiv:1408.3744.

[334] R. G. Unanyan and M. Fleischhauer, *"Entanglement dynamics in harmonic-oscillator chains"*, Phys. Rev. A 89, 062330 (2014), arxiv:1011.4838.

[335] T. Barthel and U. Schollwock, *"Dephasing and the Steady State in Quantum Many-Particle Systems"*, Phys. Rev. Lett. 100, 100601 (2008), arxiv:0711.4896.

[336] M. Cramer, C. Dawson, J. Eisert and T. Osborne, *"Exact Relaxation in a Class of Nonequilibrium Quantum Lattice Systems"*, Phys. Rev. Lett. 100, 030602 (2008), cond-mat/0703314.

[337] M. Cramer and J. Eisert, *"A quantum central limit theorem for non-equilibrium systems: exact local relaxation of correlated states"*, New J. Phys. 12, 055020 (2010), arxiv:0911.2475.

[338] S. Sotiriadis and P. Calabrese, *"Validity of the GGE for quantum quenches from interacting to noninteracting models"*, J. Stat. Mech. 1407, P07024 (2014), arxiv:1403.7431.

[339] E. Ilievski, M. Medenjak, T. Prosen and L. Zadnik, *"Quasilocal charges in integrable lattice systems"*, J. Stat. Mech. 1606, 064008 (2016), arxiv:1603.00440.

[340] P. Calabrese, *"Entanglement spreading in non-equilibrium integrable systems"*, arxiv:2008.11080, in: *"Les Houches Summer School: Integrability in Atomic and Condensed Matter Physics"*.

[341] M. Fagotti and F. H. L. Essler, *"Reduced density matrix after a quantum quench"*, Physical Review B 87, 245107 (2013), arxiv:1302.6944.

[342] J.-M. Stéphan and J. Dubail, *"Local quantum quenches in critical one-dimensional systems: entanglement, the Loschmidt echo, and light-cone effects"*, J. Stat. Mech. 2011, P08019 (2011), arxiv:1105.4846.

[343] C. T. Asplund and A. Bernamonti, *"Mutual information after a local quench in conformal field theory"*, Phys. Rev. D 89, 066015 (2014), arxiv:1311.4173.

[344] M. Nozaki, T. Numasawa and T. Takayanagi, *"Holographic Local Quenches and Entanglement Density"*, JHEP 1305, 080 (2013), arxiv:1302.5703.

[345] T. Ugajin, *"Two dimensional quantum quenches and holography"*, arxiv:1311.2562.

[346] A. F. Astaneh and A. E. Mosaffa, *"Quantum Local Quench, AdS/BCFT and Yo-Yo String"*, JHEP 1505, 107 (2015), arxiv:1405.5469.

[347] C. T. Asplund, A. Bernamonti, F. Galli and T. Hartman, *"Holographic Entanglement Entropy from 2d CFT: Heavy States and Local Quenches"*, JHEP 1502, 171 (2015), arxiv:1410.1392.

[348] A. Jahn and T. Takayanagi, *"Holographic entanglement entropy of local quenches in AdS4/CFT3: a finite-element approach"*, J. Phys. A 51, 015401 (2018), arxiv:1705.04705.

[349] T. Shimaji, T. Takayanagi and Z. Wei, *"Holographic Quantum Circuits from Splitting/Joining Local Quenches"*, JHEP 1903, 165 (2019), arxiv:1812.01176.

[350] P. Caputa, T. Numasawa, T. Shimaji, T. Takayanagi and Z. Wei, *"Double Local Quenches in 2D CFTs and Gravitational Force"*, JHEP 1909, 018 (2019), arxiv:1905.08265.

[351] T. Takayanagi, *"Holographic Dual of BCFT"*, Phys. Rev. Lett. 107, 101602 (2011), arxiv:1105.5165.

[352] M. Fujita, T. Takayanagi and E. Tonni, *"Aspects of AdS/BCFT"*, JHEP 1111, 043 (2011), arxiv:1108.5152.

[353] J. Cardy, *"Measuring Entanglement Using Quantum Quenches"*, Phys. Rev. Lett. 106, 150404 (2011), arxiv:1012.5116.

[354] P. Calabrese, J. Cardy and E. Tonni, *"Finite temperature entanglement negativity in conformal field theory"*, J. Phys. A 48, 015006 (2015), arxiv:1408.3043.

[355] V. Eisler and Z. Zimborás, *"Entanglement negativity in two-dimensional free lattice models"*, Phys. Rev. B 93, 115148 (2016), arxiv:1511.08819.

[356] D. D. Blanco, H. Casini, L.-Y. Hung and R. C. Myers, *"Relative Entropy and Holography"*, JHEP 1308, 060 (2013), arxiv:1305.3182.

[357] A. Liguori and M. Mintchev, *"Quantum field theory, bosonization and duality on the half line"*, Nucl. Phys. B 522, 345 (1998), hep-th/9710092.

[358] C. G. Callan, Jr. and I. R. Klebanov, *"Exact $C = 1$ boundary conformal field theories"*, Phys. Rev. Lett. 72, 1968 (1994), hep-th/9311092.

[359] C. G. Callan, I. R. Klebanov, A. W. W. Ludwig and J. M. Maldacena, *"Exact solution of a boundary conformal field theory"*, Nucl. Phys. B 422, 417 (1994), hep-th/9402113.

[360] R. Blumenhagen and E. Plauschinn, *"Introduction to Conformal Field Theory"*, Springer (2009).

[361] B. Herwerth, G. Sierra, J. I. Cirac and A. E. B. Nielsen, *"Bosonic Gaussian states from conformal field theory"*, Phys. Rev. B 98, 115156 (2018), arxiv:1807.01943.

[362] G. Mussardo, *"Statistical Field Theory: An Introduction to Exactly Solved Models in Statistical Physics"*, Oxford University Press (2010).

[363] L. Taddia, J. C. Xavier, F. C. Alcaraz and G. Sierra, *"Entanglement entropies in conformal systems with boundaries"*, Phys. Rev. B 88, 075112 (2013), arxiv:1302.6222.

[364] S. Furukawa, V. Pasquier and J. Shiraishi, *"Mutual Information and Compactification Radius in a c=1 Critical Phase in One Dimension"*, Phys. Rev. Lett. 102, 170602 (2009), arxiv:0809.5113.

[365] M. Caraglio and F. Gliozzi, *"Entanglement Entropy and Twist Fields"*, JHEP 0811, 076 (2008), arxiv:0808.4094.

[366] M. Fagotti and P. Calabrese, *"Entanglement entropy of two disjoint blocks in XY chains"*, J. Stat. Mech. 1004, P04016 (2010), arxiv:1003.1110.

[367] V. Alba, L. Tagliacozzo and P. Calabrese, *"Entanglement entropy of two disjoint intervals in c=1 theories"*, J. Stat. Mech. 1106, P06012 (2011), arxiv:1103.3166.

[368] N. Allegra, J. Dubail, J.-M. Stephan and J. Viti, *"Inhomogeneous field theory inside the arctic circle"*, J. Stat. Mech. 1605, 053108 (2016), arxiv:1512.02872.

[369] G. Y. Cho, A. W. W. Ludwig and S. Ryu, *"Universal entanglement spectra of gapped one-dimensional field theories"*, Phys. Rev. B 95, 115122 (2017), arxiv:1603.04016.

[370] P. Calabrese and A. Lefevre, *"Entanglement spectrum in one-dimensional systems"*, Phys. Rev. A 78, 032329 (2008), arxiv:0806.3059.

[371] V. Alba, P. Calabrese and E. Tonni, *"Entanglement spectrum degeneracy and the Cardy formula in 1+1 dimensional conformal field theories"*, J. Phys. A 51, 024001 (2018), arxiv:1707.07532.

[372] F. F. Assaad, T. C. Lang and F. Parisen Toldin, *"Entanglement spectra of interacting fermions in quantum Monte Carlo simulations"*, Phys. Rev. B 89, 125121 (2014), arxiv:1311.5851.

[373] F. F. Assaad, *"Stable quantum Monte Carlo simulations for entanglement spectra of interacting fermions"*, Phys. Rev. B 91, 125146 (2015), arxiv:1501.01418.

[374] M. Dalmonte, B. Vermersch and P. Zoller, *"Quantum Simulation and Spectroscopy of Entanglement Hamiltonians"*, Nature Phys. 14, 827 (2018), arxiv:1707.04455.

[375] G. Giudici, T. Mendes-Santos, P. Calabrese and M. Dalmonte, *"Entanglement Hamiltonians of lattice models via the Bisognano-Wichmann theorem"*, Phys. Rev. B 98, 134403 (2018), arxiv:1807.01322.

[376] W. P. Su, J. R. Schrieffer and A. J. Heeger, *"Solitons in polyacetylene"*, Phys. Rev. Lett. 42, 1698 (1979).

[377] A. J. Heeger, S. Kivelson, J. R. Schrieffer and W. P. Su, *"Solitons in conducting polymers"*, Rev. Mod. Phys. 60, 781 (1988).

[378] T. Nishino and K. Okunishi, *"Corner Transfer Matrix Algorithm for Classical Renormalization Group"*, J. Phys. Soc. Jpn. 66, 3040 (1997), cond-mat/9705072.

[379] T. Mendes-Santos, G. Giudici, M. Dalmonte and M. A. Rajabpour, *"Entanglement Hamiltonian of quantum critical chains and conformal field theories"*, Phys. Rev. B 100, 155122 (2019), arxiv:1906.00471.

[380] J. Zhang, P. Calabrese, M. Dalmonte and M. A. Rajabpour, *"Lattice Bisognano-Wichmann modular Hamiltonian in critical quantum spin chains"*, SciPost Phys. Core 2, 007 (2020), arxiv:2003.00315.

[381] V. Eisler, M.-C. Chung and I. Peschel, *"Entanglement in composite free-fermion systems"*, J. Stat. Mech. 2015, P07011 (2015), arxiv:1503.09116.

[382] K. Okamoto, *"Longitudinal Spin Correlation in Spin-1/2 Dimerized XY Chain"*, J. Phys. Soc. Japan 57, 2947 (1988).

[383] I. Peschel and T. T. Truong, *"Corner Transfer Matrices for the Gaussian Model"*, Annalen der Physik 503, 185 (1991).

[384] F. Iglòi and R. Juhàsz, *"Exact relationship between the entanglement entropies of XY and quantum Ising chains"*, EPL 81, 57003 (2008), arxiv:0709.3927.

[385] B. Davies, *"Corner transfer matrices for the Ising model"*, Physica A 154, 1 (1988).

[386] T. T. Truong and I. Peschel, *"Diagonalisation of finite-size corner transfer matrices and related spin chains"*, Z. Phys. B 75, 119–125 (1989).

[387] J. Sirker, M. Maiti, N. P. Konstantinidis and N. Sedlmayr, *"Boundary fidelity and entanglement in the symmetry protected topological phase of the SSH model"*, J. Stat. Mech. 1410, P10032 (2014), arxiv:1406.7832.

[388] I. Peschel, *"On the entanglement entropy for an XY spin chain"*, J. Stat. Mech. 0412, P12005 (2004), cond-mat/0410416.

[389] P. Kim, H. Katsura, N. Trivedi and J. H. Han, *"Entanglement and corner Hamiltonian spectra of integrable open spin chains"*, Phys. Rev. B 94, 195110 (2016), arxiv:1512.08597.

[390] J. Cardy, *"Quantum quenches to a critical point in one dimension: some further results"*, J. Stat. Mech. 2016, 023103 (2016), arxiv:1507.07266.

[391] S. Sotiriadis, P. Calabrese and J. Cardy, *"Quantum quench from a thermal initial state"*, EPL 87, 20002 (2009), arxiv:1002.0167.

[392] J.-S. Caux and F. H. L. Essler, *"Time evolution of local observables after quenching to an integrable model"*, Phys. Rev. Lett. 110, 257203 (2013), arxiv:1301.3806.

[393] G. Torlai, L. Tagliacozzo and G. D. Chiara, *"Dynamics of the entanglement spectrum in spin chains"*, J. Stat. Mech. 2014, P06001 (2014), arxiv:1311.5509.

[394] S. R. Das, D. A. Galante and R. C. Myers, *"Universal scaling in fast quantum quenches in conformal field theories"*, Phys. Rev. Lett. 112, 171601 (2014), arxiv:1401.0560.

[395] H. Casini, H. Liu and M. Mezei, *"Spread of entanglement and causality"*, JHEP 1607, 077 (2016), arxiv:1509.05044.

[396] J. Surace, M. Piani and L. Tagliacozzo, *"Simulating the out-of-equilibrium dynamics of local observables by trading entanglement for mixture"*, Phys. Rev. B 99, 235115 (2019), arxiv:1810.01231.

[397] I. Affleck and A. W. W. Ludwig, *"Universal noninteger 'ground state degeneracy' in critical quantum systems"*, Phys. Rev. Lett. 67, 161 (1991).

[398] J. L. Cardy, *"Boundary conformal field theory"*, hep-th/0411189.

[399] E. Lieb, T. Schultz and D. Mattis, *"Two soluble models of an antiferromagnetic chain"*, Annals of Physics 16, 407 (1961).

[400] P. Hayden, M. Headrick and A. Maloney, *"Holographic Mutual Information is Monogamous"*, Phys. Rev. D 87, 046003 (2013), arxiv:1107.2940.

[401] T. Faulkner, *"The Entanglement Renyi Entropies of Disjoint Intervals in AdS/CFT"*, arxiv:1303.7221.

[402] T. Hartman, *"Entanglement Entropy at Large Central Charge"*, arxiv:1303.6955.

[403] P. Fonda, D. Seminara and E. Tonni, *"On shape dependence of holographic entanglement entropy in AdS_4/CFT_3"*, JHEP 1512, 037 (2015), arxiv:1510.03664.

[404] M. Freedman and M. Headrick, *"Bit threads and holographic entanglement"*, Commun. Math. Phys. 352, 407 (2017), arxiv:1604.00354.

[405] J. Kudler-Flam, I. MacCormack and S. Ryu, *"Holographic entanglement contour, bit threads, and the entanglement tsunami"*, J. Phys. A 52, 325401 (2019), arxiv:1902.04654.

[406] J. S. Dowker, *"Conformal weights of charged Rényi entropy twist operators for free scalar fields in arbitrary dimensions"*, J. Phys. A 49, 145401 (2016).

[407] J. S. Dowker, *"Charged Renyi entropies for free scalar fields"*, J. Phys. A 50, 165401 (2017), arxiv:1512.01135.

[408] A. Belin, L.-Y. Hung, A. Maloney, S. Matsuura, R. C. Myers and T. Sierens, *"Holographic Charged Renyi Entropies"*, JHEP 1312, 059 (2013), arxiv:1310.4180.

[409] P. Caputa, M. Nozaki and T. Numasawa, *"Charged Entanglement Entropy of Local Operators"*, Phys. Rev. D 93, 105032 (2016), arxiv:1512.08132.

[410] H. Shapourian, K. Shiozaki and S. Ryu, *"Partial time-reversal transformation and entanglement negativity in fermionic systems"*, Phys. Rev. B 95, 165101 (2017), arxiv:1611.07536.

[411] H. Shapourian, P. Ruggiero, S. Ryu and P. Calabrese, *"Twisted and untwisted negativity spectrum of free fermions"*, SciPost Phys. 7, 037 (2019), arxiv:1906.04211.

[412] L. Capizzi, P. Ruggiero and P. Calabrese, *"Symmetry resolved entanglement entropy of excited states in a CFT"*, J. Stat. Mech. 2007, 073101 (2020), arxiv:2003.04670.

[413] S. Murciano, R. Bonsignori and P. Calabrese, *"Symmetry decomposition of negativity of massless free fermions"*, SciPost Phys. 10, 111 (2021), arxiv:2102.10054.

[414] H.-H. Chen, *"Symmetry decomposition of relative entropies in conformal field theory"*, JHEP 2107, 084 (2021), arxiv:2104.03102.

[415] L. Capizzi and P. Calabrese, *"Symmetry resolved relative entropies and distances in conformal field theory"*, arxiv:2105.08596.

[416] P. Calabrese, J. Dubail and S. Murciano, *"Symmetry-resolved entanglement entropy in Wess-Zumino-Witten models"*, arxiv:2106.15946.

[417] D. X. Horvath, L. Capizzi and P. Calabrese, *"U(1) symmetry resolved entanglement in free 1+1 dimensional field theories via form factor bootstrap"*, JHEP 2105, 197 (2021), arxiv:2103.03197.

[418] D. X. Horváth and P. Calabrese, *"Symmetry resolved entanglement in integrable field theories via form factor bootstrap"*, JHEP 2011, 131 (2020), arxiv:2008.08553.

[419] D. X. Horvath, P. Calabrese and O. A. Castro-Alvaredo, *"Branch Point Twist Field Form Factors in the sine-Gordon Model II: Composite Twist Fields and Symmetry Resolved Entanglement"*, arxiv:2105.13982.

[420] S. Zhao, C. Northe and R. Meyer, *"Symmetry-resolved entanglement in AdS_3/CFT_2 coupled to U(1) Chern-Simons theory"*, JHEP 2107, 030 (2021), arxiv:2012.11274.

[421] S. Fraenkel and M. Goldstein, *"Entanglement Measures in a Nonequilibrium Steady State: Exact Results in One Dimension"*, arxiv:2105.00740.

[422] R. Bonsignori and P. Calabrese, *"Boundary effects on symmetry resolved entanglement"*, J. Phys. A 54, 015005 (2021), arxiv:2009.08508.

[423] S. Murciano, P. Ruggiero and P. Calabrese, *"Symmetry resolved entanglement in two-dimensional systems via dimensional reduction"*, J. Stat. Mech. 2008, 083102 (2020), arxiv:2003.11453.

[424] H. Barghathi, J. Yu and A. Del Maestro, *"Theory of noninteracting fermions and bosons in the canonical ensemble"*, Phys. Rev. Res. 2, 043206 (2020), arxiv:2007.15661.

[425] B. Estienne, Y. Ikhlef and A. Morin-Duchesne, *"Finite-size corrections in critical symmetry-resolved entanglement"*, SciPost Phys. 10, 054 (2021), arxiv:2010.10515.

[426] A. Elben et al., *"Mixed-state entanglement from local randomized measurements"*, Phys. Rev. Lett. 125, 200501 (2020), arxiv:2007.06305.

[427] V. Vitale, A. Elben, R. Kueng, A. Neven, J. Carrasco, B. Kraus, P. Zoller, P. Calabrese, B. Vermersch and M. Dalmonte, *"Symmetry-resolved dynamical purification in synthetic quantum matter"*, arxiv:2101.07814.

[428] G. Parez, R. Bonsignori and P. Calabrese, *"Quasiparticle dynamics of symmetry resolved entanglement after a quench: the examples of conformal field theories and free fermions"*, Phys. Rev. B 103, L041104 (2021), arxiv:2010.09794.

[429] G. Parez, R. Bonsignori and P. Calabrese, *"Exact quench dynamics of symmetry resolved entanglement in a free fermion chain"*, arxiv:2106.13115.

[430] X. Turkeshi, P. Ruggiero, V. Alba and P. Calabrese, *"Entanglement equipartition in critical random spin chains"*, Phys. Rev. B 102, 014455 (2020), arxiv:2005.03331.

[431] M. Kiefer-Emmanouilidis, R. Unanyan, M. Fleischhauer and J. Sirker, *"Slow delocalization of particles in many-body localized phases"*, Phys. Rev. B 103, 024203 (2021).

[432] D. Azses and E. Sela, *"Symmetry-resolved entanglement in symmetry-protected topological phases"*, Phys. Rev. B 102, 235157 (2020), arxiv:2008.09332.

[433] L. J. Dixon, D. Friedan, E. J. Martinec and S. H. Shenker, *"The Conformal Field Theory of Orbifolds"*, Nucl. Phys. B 282, 13 (1987).

[434] V. G. Knizhnik, *"Analytic Fields on Riemann Surfaces. 2"*, Commun. Math. Phys. 112, 567 (1987).

[435] W. G. Unruh, *"Comment on 'Proof of the quantum bound on specific entropy for free fields'"*, Phys. Rev. D 42, 3596 (1990).

[436] P. Calabrese, J. Cardy and I. Peschel, *"Corrections to scaling for block entanglement in massive spin chains"*, Journal of Statistical Mechanics: Theory and Experiment 2010, P09003 (2010), http://dx.doi.org/10.1088/1742-5468/2010/09/P09003.

[437] E. Ercolessi, S. Evangelisti and F. Ravanini, *"Exact entanglement entropy of the XYZ model and its sine-Gordon limit"*, Phys. Lett. A 374, 2101 (2010), arxiv:0905.4000.

[438] F. Berruto, G. Grignani, G. W. Semenoff and P. Sodano, *"Chiral symmetry breaking on the lattice: A Study of the strongly coupled lattice Schwinger model"*, Phys. Rev. D 57, 5070 (1998), hep-lat/9710066.

[439] R. Couvreur, J. L. Jacobsen and H. Saleur, *"Entanglement in nonunitary quantum critical spin chains"*, Phys. Rev. Lett. 119, 040601 (2017), arxiv:1611.08506.

[440] S. N. Solodukhin, *"Entanglement entropy of round spheres"*, Phys. Lett. B 693, 605 (2010), arxiv:1008.4314.

[441] C. P. Herzog, *"Universal Thermal Corrections to Entanglement Entropy for Conformal Field Theories on Spheres"*, JHEP 1410, 028 (2014), arxiv:1407.1358.

[442] C. P. Herzog and T. Nishioka, *"Entanglement Entropy of a Massive Fermion on a Torus"*, JHEP 1303, 077 (2013), arxiv:1301.0336.

[443] L.-Y. Hung, R. C. Myers and M. Smolkin, *"Twist operators in higher dimensions"*, JHEP 1410, 178 (2014), arxiv:1407.6429.

[444] T. Nishioka, *"Entanglement entropy: holography and renormalization group"*, Rev. Mod. Phys. 90, 035007 (2018), arxiv:1801.10352.

[445] O. A. Castro-Alvaredo, M. Lencsés, I. M. Szécsényi and J. Viti, *"Entanglement Dynamics after a Quench in Ising Field Theory: A Branch Point Twist Field Approach"*, JHEP 1912, 079 (2019), arxiv:1907.11735.

[446] R. Weston, *"The Entanglement entropy of solvable lattice models"*, J. Stat. Mech. 0603, L03002 (2006), math-ph/0601038.

[447] E. Ercolessi, S. Evangelisti, F. Franchini and F. Ravanini, *"Essential singularity in the Renyi entanglement entropy of the one-dimensional XYZ spin-1/2 chain"*, Phys. Rev. B 83, 012402 (2011), arxiv:1008.3892.

[448] E. Ercolessi, S. Evangelisti, F. Franchini and F. Ravanini, *"Correlation Length and Unusual Corrections to the Entanglement Entropy"*, Phys. Rev. B 85, 115428 (2012), arxiv:1201.6367.

[449] E. Ercolessi, S. Evangelisti, F. Franchini and F. Ravanini, *"Modular invariance in the gapped XYZ spin-$\frac{1}{2}$ chain"*, Phys. Rev. B 88, 104418 (2013), arxiv:1301.6758.

[450] G. B. Mbeng, V. Alba and P. Calabrese, *"Negativity spectrum in 1D gapped phases of matter"*, J. Phys. A 50, 194001 (2017), arxiv:1612.05172.

[451] A. De Luca and F. Franchini, *"Approaching the restricted solid-on-solid critical points through entanglement: One model for many universalities"*, Phys. Rev. B 87, 045118 (2013), arxiv:1205.6426.

[452] D. Bianchini and F. Ravanini, *"Entanglement Entropy from Corner Transfer Matrix in Forrester Baxter non-unitary RSOS models"*, arxiv:1509.04601.

[453] V. Alba, P. Calabrese and E. Tonni, *"Entanglement spectrum degeneracy and the Cardy formula in 1+1 dimensional conformal field theories"*, Journal of Physics A: Mathematical and Theoretical 51, 024001 (2017), http://dx.doi.org/10.1088/1751-8121/aa9365.

[454] E. Levi, O. A. Castro-Alvaredo and B. Doyon, *"Universal corrections to the entanglement entropy in gapped quantum spin chains: a numerical study"*, Phys. Rev. B 88, 094439 (2013), arxiv:1304.6874.

[455] T. Nishino, *"Density Matrix Renormalization Group Method for 2D Classical Models"*, J. Phys. Soc. Jpn. 64, 3598 (1995), cond-mat/9508111.

[456] T. Nishino and K. Okunishi, *"Density matrix and renormalization for classical lattice models"*, Lecture Notes in Physics 478, 167 (1996), cond-mat/9610107.

[457] V. Alba, M. Haque and A. M. Läuchli, *"Entanglement spectrum of the Heisenberg XXZ chain near the ferromagnetic point"*, J. Stat. Mech. 2012, P08011 (2012), arxiv:1206.0131.

[458] I. Peschel, *"Special Review: Entanglement in Solvable Many-Particle Models"*, Braz. J. Phys 42, 267–291 (2012), arxiv:1109.0159.

[459] C. Ferreira and J. L. López, *"Asymptotic expansions of the Hurwitz–Lerch zeta function"*, J. Math. Anal. Appl 298, 210 (2004).

[460] E. Whittaker and G. Watson, *"A course of modern analysis"*, Cambridge University Press (1996).

[461] H. Boos, M. Jimbo, T. Miwa, F. Smirnov and Y. Takeyama, *"Density matrix of a finite sub-chain of the Heisenberg anti-ferromagnet"*, Lett. Math. Phys. 75, 201 (2006), hep-th/0506171.

[462] J. Sato, M. Shiroishi and M. Takahashi, *"Exact evaluation of density matrix elements for the Heisenberg chain"*, J. Stat. Mech. 0612, P12017 (2006), hep-th/0611057.

[463] J. Sato and M. Shiroishi, *"Density matrix elements and entanglement entropy for the spin-1/2 XXZ chain at $\Delta = 1/2$"*, J. Phys. A 40, 8739 (2007), arxiv:0704.0850.

[464] V. Alba, M. Fagotti and P. Calabrese, *"Entanglement entropy of excited states"*, J. Stat. Mech. 0910, P10020 (2009), arxiv:0909.1999.

[465] H. Katsura and I. Maruyama, *"Derivation of Matrix Product Ansatz for the Heisenberg Chain from Algebraic Bethe Ansatz"*, J. Phys. A 43, 175003 (2010), arxiv:0911.4215.

[466] T. Miwa and F. Smirnov, *"New exact results on density matrix for XXX spin chain"*, Lett. Math. Phys. 109, 675 (2019), arxiv:1802.08491.

[467] F. Smirnov, *"Exact density matrix for quantum group invariant sector of XXZ model"*, arxiv:1804.08974.

[468] F. Göhmann, *"Statistical mechanics of integrable quantum spin systems"*, SciPost Phys. Lect. Notes 16, F. Göhmann (2020), arxiv:1909.09967.

[469] S. Banerjee and B. Wilkerson, International Journal of Number Theory 16, 2097.

[470] S. Hofferberth, I. Lesanovsky, T. Schumm, A. Imambekov, V. Gritsev, E. Demler and J. Schmiedmayer, *"Probing quantum and thermal noise in an interacting many-body system"*, Nature Physics 4, 489–495 (2008), arxiv:0710.1575.

[471] T. Kitagawa, S. Pielawa, A. Imambekov and J. Schmiedmayer.

[472] T. Kitagawa, A. Imambekov, J. Schmiedmayer and E. Demler, *"The dynamics and prethermalization of one-dimensional quantum systems probed through the full distributions of quantum noise"*, New J. Phys. 13, 073018 (2011), arxiv:1104.5631.

[473] M. Gring, M. Kuhnert, T. Langen, T. Kitagawa, B. Rauer, M. Schreitl, I. Mazets, D. A. Smith, E. Demler and J. Schmiedmayer, *"Relaxation and Prethermalization in an Isolated Quantum System"*, Science 337, 1318 (2012), arxiv:1112.0013.

[474] J. Armijo, T. Jacqmin, K. V. Kheruntsyan and I. Bouchoule, *"Probing Three-Body Correlations in a Quantum Gas Using the Measurement of the Third Moment of Density Fluctuations"*, Phys. Rev. Lett. 105, 230402 (2010), arxiv:1007.3713.

[475] T. Jacqmin, J. Armijo, T. Berrada, K. V. Kheruntsyan and I. Bouchoule, *"Sub-Poissonian Fluctuations in a 1D Bose Gas: From the Quantum Quasicondensate to the Strongly Interacting Regime"*, Phys. Rev. Lett. 106, 230405 (2011), arxiv:1103.3028.

[476] I. Klich and L. Levitov, *"Quantum Noise as an Entanglement Meter"*, Phys. Rev. Lett. 102, 100502 (2009), arxiv:0804.1377.

[477] I. Klich and L. Levitov, *"Many-Body Entanglement: a New Application of the Full Counting Statistics"*, Adv. Theor. Phys. 1134, 36 (2009), arxiv:0901.3391.

[478] B. Hsu, E. Grosfeld and E. Fradkin, *"Quantum noise and entanglement generated by a local quantum quench"*, Phys. Rev. B 80, 235412 (2009), arxiv:0908.2622.

[479] H. F. Song, C. Flindt, S. Rachel, I. Klich and K. Le Hur, *"Entanglement entropy from charge statistics: Exact relations for noninteracting many-body systems"*, Phys. Rev. B 83, 161408 (2011), arxiv:1008.5191.

[480] H. F. Song, S. Rachel, C. Flindt, I. Klich, N. Laflorencie and K. Le Hur, *"Bipartite Fluctuations as a Probe of Many-Body Entanglement"*, Phys. Rev. B 85, 035409 (2012), arxiv:1109.1001.

[481] P. Calabrese, M. Mintchev and E. Vicari, *"Exact relations between particle fluctuations and entanglement in Fermi gases"*, EPL 98, 20003 (2012), arxiv:1111.4836.

[482] G. C. Levine, M. J. Bantegui and J. A. Burg, *"Full counting statistics in a disordered free fermion system"*, Phys. Rev. B 86, 174202 (2012), arxiv:1201.3933.

[483] R. Susstrunk and D. A. Ivanov, *"Free fermions on a line: Asymptotics of the entanglement entropy and entanglement spectrum from full counting statistics"*, EPL 100, 60009 (2012), arxiv:1208.5845.

[484] P. Calabrese, P. Le Doussal and S. N. Majumdar, *"Random matrices and entanglement entropy of trapped Fermi gases"*, Phys. Rev. A 91, 012303 (2015), arxiv:1411.4421.

[485] Y. Utsumi, *"Full counting statistics of information content"*, Eur. Phys. J. Spec. Top. 227, 1911–1928 (2019), arxiv:1807.04338.

[486] R. W. Cherng and E. Demler, *"Quantum noise analysis of spin systems realized with cold atoms"*, New J. Phys. 9, 7 (2007), cond-mat/0609748.

[487] M. Bortz, J. Sato and M. Shiroishi, *"String correlation functions of the spin-1/2 Heisenberg XXZ chain"*, J. Phys. A 40, 4253 (2007), cond-mat/0612348.

[488] D. B. Abraham, F. H. L. Essler and A. Maciolek, *"Effective Forces Induced by a Fluctuating Interface: Exact Results"*, Phys. Rev. Lett. 98, 170602 (2007), cond-mat/0703815.

[489] A. Lamacraft and P. Fendley, *"Order parameter statistics in the critical quantum Ising chain"*, Phys. Rev. Lett. 100, 165706 (2008), arxiv:0802.1246.

[490] D. A. Ivanov and A. G. Abanov, *"Characterizing correlations with full counting statistics: Classical Ising and quantum XY spin chains"*, Phys. Rev. E 87, 022114 (2013), arxiv:1203.6325.

[491] Y. Shi and I. Klich, *"Full counting statistics and the Edgeworth series for matrix product states"*, J. Stat. Mech. 2013, P05001 (2013), arxiv:1212.6965.

[492] V. Eisler, *"Universality in the Full Counting Statistics of Trapped Fermions"*, Phys. Rev. Lett. 111, 080402 (2013), arxiv:1304.1413.

[493] I. Klich, *"A note on the full counting statistics of paired fermions"*, J. Stat. Mech. 2014, P11006 (2014), arxiv:1403.7824.

[494] M. Moreno-Cardoner, J. F. Sherson and G. D. Chiara, *"Non-Gaussian distribution of collective operators in quantum spin chains"*, New J. Phys. 18, 103015 (2016), arxiv:1510.05959.

[495] J.-M. Stéphan and F. Pollmann, *"Full counting statistics in the Haldane-Shastry chain"*, Phys. Rev. B 95, 035119 (2017), arxiv:1608.06856.

[496] M. Collura, F. H. L. Essler and S. Groha, *"Full counting statistics in the spin-1/2 Heisenberg XXZ chain"*, J. Phys. A 50, 414002 (2017), arxiv:1706.07939.

[497] K. Najafi and M. A. Rajabpour, *"Full counting statistics of the subsystem energy for free fermions and quantum spin chains"*, Phys. Rev. B 96, 235109 (2017), arxiv:1710.08814.

[498] S. Humeniuk and H. P. Buchler, *"Full Counting Statistics for Interacting Fermions with Determinantal Quantum Monte Carlo Simulations"*, Phys. Rev. Lett. 119, 236401 (2017), arxiv:1706.08951.

[499] A. Bastianello, L. Piroli and P. Calabrese, *"Exact Local Correlations and Full Counting Statistics for Arbitrary States of the One-Dimensional Interacting Bose Gas"*, Phys. Rev. Lett. 120, 190601 (2018), arxiv:1802.02115.

[500] A. Bastianello and L. Piroli, *"From the sinh-Gordon field theory to the one-dimensional Bose gas: exact local correlations and full counting statistics"*, J. Stat. Mech. 1811, 113104 (2018), arxiv:1807.06869.

[501] G. Perfetto, L. Piroli and A. Gambassi, *"Quench action and large deviations: Work statistics in the one-dimensional Bose gas"*, Phys. Rev. E 100, 032114 (2019), arxiv:1904.06259.

[502] G. D. V. Del Vecchio, A. Bastianello, A. De Luca and G. Mussardo, *"Exact out-of-equilibrium steady states in the semiclassical limit of the interacting Bose gas"*, SciPost Phys. 9, 002 (2020), arxiv:2002.01423.

[503] V. Gritsev, E. Altman, E. Demler and A. Polkovnikov, *"Full quantum distribution of contrast in interference experiments between interacting one-dimensional Bose liquids"*, Nature Phys. 2, 705–709 (2006), cond-mat/0602475.

[504] V. Eisler and Z. Ràcz, *"Full Counting Statistics in a Propagating Quantum Front and Random Matrix Spectra"*, Phys. Rev. Lett. 110, 060602 (2013), arxiv:1211.2321.

[505] I. Lovas, B. Dòra, E. Demler and G. ZaràND, *"Full counting statistics of time-of-flight images"*, Phys. Rev. A 95, 053621 (2017), arxiv:1612.02837.

[506] S. Groha, F. H. L. Essler and P. Calabrese, *"Full counting statistics in the transverse field Ising chain"*, SciPost Phys. 4, 43 (2018), arxiv:1803.09755.

[507] M. Collura, A. De Luca, P. Calabrese and J. Dubail, *"Domain wall melting in the spin-$\frac{1}{2}$ XXZ spin chain: Emergent Luttinger liquid with a fractal quasiparticle charge"*, Phys. Rev. B 102, 180409 (2020), arxiv:2001.04948.

[508] M. Collura and F. H. L. Essler, *"How order melts after quantum quenches"*, Phys. Rev. B 101, 041110 (2020), arxiv:1901.04402.

[509] M. Collura, *"Relaxation of the order-parameter statistics in the Ising quantum chain"*, SciPost Phys. 7, 72 (2019), arxiv:1906.00948.

[510] M. Arzamasovs and D. M. Gangardt, *"Full Counting Statistics and Large Deviations in a Thermal 1D Bose Gas"*, Phys. Rev. Lett. 122, 120401 (2019), arxiv:1807.09381.

[511] M. N. Najafi and M. A. Rajabpour, *"Formation probabilities and statistics of observables as defect problems in free fermions and quantum spin chains"*, Phys. Rev. B 101, 165415 (2020), arxiv:1911.04595.

[512] G. Vidal, *"Efficient Simulation of One-Dimensional Quantum Many-Body Systems"*, Phys. Rev. Lett. 93, 040502 (2004), quant-ph/0310089.

[513] S. Wald, R. Arias and V. Alba, *"Entanglement and classical fluctuations at finite-temperature critical points"*, J. Stat. Mech. 2003, 033105 (2020), arxiv:1911.02575.

[514] R. Abt, J. Erdmenger, M. Gerbershagen, C. M. Melby-Thompson and C. Northe, *"Holographic Subregion Complexity from Kinematic Space"*, JHEP 1901, 012 (2019), arxiv:1805.10298.

[515] H. Bethe, *"Zur Theorie der Metalle. I. Eigenwerte und Eigenfunktionen der linearen Atomkette"*, Zeitschrift für Physik 71, 205 (1931).

[516] V. E. Korepin, N. Bogoliubov and A. Izergin, *"Quantum Inverse Scattering Method and Correlation Functions"*, Cambridge University Press (1993).

[517] S. Ostlund and S. Rommer, *"Thermodynamic Limit of Density Matrix Renormalization for the spin-1 heisenberg chain"*, Phys. Rev. Lett. 75, 3537 (1995), cond-mat/9503107.

[518] S. Rommer and S. Ostlund, *"Class of ansatz wave functions for one-dimensional spin systems and their relation to the density matrix renormalization group"*, Phys. Rev. B 55, 2164 (1997), cond-mat/9606213.

[519] J. I. Cirac and F. Verstraete, *"Renormalization and tensor product states in spin chains and lattices"*, J. Phys. A 42, 504004 (2009), arxiv:0910.1130.

[520] L. Tagliacozzo, T. R. de Oliveira, S. Iblisdir and J. I. Latorre, *"Scaling of entanglement support for Matrix Product States"*, Phys. Rev. B 78, 024410 (2008), arxiv:0712.1976.

[521] G. Vidal, *"Class of Quantum Many-Body States That Can Be Efficiently Simulated"*, Phys. Rev. Lett. 101, 110501 (2008), quant-ph/0610099.

[522] G. Evenbly and G. Vidal, *"Tensor Network States and Geometry"*, J. Stat. Phys. 145, 891–918 (2011), arxiv:1106.1082.

[523] B. Swingle, *"Entanglement Renormalization and Holography"*, Phys. Rev. D 86, 065007 (2012), arxiv:0905.1317.

[524] F. Pastawski, B. Yoshida, D. Harlow and J. Preskill, *"Holographic quantum error-correcting codes: Toy models for the bulk/boundary correspondence"*, JHEP 1506, 149 (2015), arxiv:1503.06237.

[525] F. Verstraete and J. I. Cirac, *"Continuous Matrix Product States for Quantum Fields"*, Phys. Rev. Lett. 104, 190405 (2010), arxiv:1002.1824.

[526] J. Haegeman, T. J. Osborne, H. Verschelde and F. Verstraete, *"Entanglement Renormalization for Quantum Fields in Real Space"*, Phys. Rev. Lett. 110, 100402 (2013), arxiv:1102.5524.

[527] H. Yao and X.-L. Qi, *"Entanglement entropy and entanglement spectrum of the Kitaev model"*, Phys. Rev. Lett. 105, 080501 (2010), arxiv:1001.1165.

[528] Y. O. Nakagawa and S. Furukawa, *"Capacity of entanglement and the distribution of density matrix eigenvalues in gapless systems"*, Phys. Rev. B 96, 205108 (2017), arxiv:1708.08924.

[529] J. De Boer, J. Jarvela and E. Keski-Vakkuri, *"Aspects of capacity of entanglement"*, Phys. Rev. D 99, 066012 (2019), arxiv:1807.07357.

[530] K. Kawabata, T. Nishioka, Y. Okuyama and K. Watanabe, *"Probing Hawking radiation through capacity of entanglement"*, JHEP 2105, 062 (2021), arxiv:2102.02425.

[531] S. H. Shenker and D. Stanford, *"Black holes and the butterfly effect"*, JHEP 1403, 067 (2014), arxiv:1306.0622.

[532] S. H. Shenker and D. Stanford, *"Multiple Shocks"*, JHEP 1412, 046 (2014), arxiv:1312.3296.

[533] A. Almheiri, D. Marolf, J. Polchinski and J. Sully, *"Black Holes: Complementarity or Firewalls?"*, JHEP 1302, 062 (2013), arxiv:1207.3123.

[534] D. Marolf and J. Polchinski, *"Gauge/Gravity Duality and the Black Hole Interior"*, Phys. Rev. Lett. 111, 171301 (2013), arxiv:1307.4706.

[535] J. Maldacena and L. Susskind, *"Cool horizons for entangled black holes"*, Fortsch. Phys. 61, 781 (2013), arxiv:1306.0533.

[536] L. Susskind, *"ER=EPR, GHZ, and the consistency of quantum measurements"*, Fortsch. Phys. 64, 72 (2016), arxiv:1412.8483.

[537] K. Papadodimas and S. Raju, *"An Infalling Observer in AdS/CFT"*, JHEP 1310, 212 (2013), arxiv:1211.6767.

[538] A. Almheiri, D. Marolf, J. Polchinski, D. Stanford and J. Sully, *"An Apologia for Firewalls"*, JHEP 1309, 018 (2013), arxiv:1304.6483.

[539] S. W. Hawking, *"Breakdown of Predictability in Gravitational Collapse"*, Phys. Rev. D 14, 2460 (1976).

[540] D. N. Page, *"Information in black hole radiation"*, Phys. Rev. Lett. 71, 3743 (1993), hep-th/9306083.

[541] A. Almheiri, T. Hartman, J. Maldacena, E. Shaghoulian and A. Tajdini, *"The entropy of Hawking radiation"*, Rev. Mod. Phys. 93, 035002 (2021), arxiv:2006.06872.

[542] S. Raju, *"Lessons from the Information Paradox"*, arxiv:2012.05770.

[543] G. Penington, *"Entanglement Wedge Reconstruction and the Information Paradox"*, JHEP 2009, 002 (2020), arxiv:1905.08255.

[544] G. Penington, S. H. Shenker, D. Stanford and Z. Yang, *"Replica wormholes and the black hole interior"*, arxiv:1911.11977.

[545] A. Almheiri, R. Mahajan and J. Maldacena, *"Islands outside the horizon"*, arxiv:1910.11077.

[546] A. Almheiri, T. Hartman, J. Maldacena, E. Shaghoulian and A. Tajdini, *"Replica Wormholes and the Entropy of Hawking Radiation"*, JHEP 2005, 013 (2020), arxiv:1911.12333.

[547] A. Almheiri, R. Mahajan, J. Maldacena and Y. Zhao, *"The Page curve of Hawking radiation from semiclassical geometry"*, JHEP 2003, 149 (2020), arxiv:1908.10996.

[548] A. Almheiri, R. Mahajan and J. E. Santos, *"Entanglement islands in higher dimensions"*, SciPost Phys. 9, 001 (2020), arxiv:1911.09666.

[549] A. Almheiri, N. Engelhardt, D. Marolf and H. Maxfield, *"The entropy of bulk quantum fields and the entanglement wedge of an evaporating black hole"*, JHEP 1912, 063 (2019), arxiv:1905.08762.

[550] M. Van Raamsdonk, *"Building up spacetime with quantum entanglement"*, Gen. Rel. Grav. 42, 2323 (2010), arxiv:1005.3035.

[551] A. Hamilton, D. N. Kabat, G. Lifschytz and D. A. Lowe, *"Local bulk operators in AdS/CFT: A Boundary view of horizons and locality"*, Phys. Rev. D 73, 086003 (2006), hep-th/0506118.

[552] A. Hamilton, D. N. Kabat, G. Lifschytz and D. A. Lowe, *"Holographic representation of local bulk operators"*, Phys. Rev. D 74, 066009 (2006), hep-th/0606141.

[553] D. Kabat and G. Lifschytz, *"Emergence of spacetime from the algebra of total modular Hamiltonians"*, JHEP 1905, 017 (2019), arxiv:1812.02915.

[554] J. Erdmenger, K. T. Grosvenor and R. Jefferson, *"Information geometry in quantum field theory: lessons from simple examples"*, SciPost Phys. 8, 073 (2020), arxiv:2001.02683.

[555] N. Schuch, J. I. Cirac and M. M. Wolf, *"Quantum States on Harmonic Lattices"*, Communications in Mathematical Physics 267, 65–92 (2006).

[556] I. Frérot and T. Roscilde, *"Area law and its violation: A microscopic inspection into the structure of entanglement and fluctuations"*, Phys. Rev. B 92, 115129 (2015), arxiv:1506.00545.

[557] F. Khanna, A. Malbouisson, J. Malbouisson and A. Santana, *"Thermal quantum field theory - Algebraic aspects and applications"*, World Scientific (2009).

[558] S. Lievens, N. I. Stoilova and J. Van der Jeugt, *"Harmonic oscillator chains as Wigner Quantum Systems: Periodic and fixed wall boundary conditions in gl(1—n) solutions"*, J. Math. Phys. 49, 073502 (2008), arxiv:0709.0180.